

SCHOLARLY PUBLICATIONS

*A CURRENT AWARENESS BULLETIN
OF RESEARCH OUTPUT*

@DTU

(61st Edition)

JANUARY, 2018

BY: CENTRAL LIBRARY

DELHI TECHNOLOGICAL UNIVERSITY

(FORMERLY *DELHI COLLEGE OF ENGINEERING*)

GOVT. OF N.C.T. OF DELHI

SHAHBAD DAULATPUR, MAIN BAWANA ROAD

DELHI 110042

PREFACE

This is the **Sixty One** Issue of Current Awareness Bulletin started by Delhi Technological University, Central Library. The aim of the bulletin is to compile, preserve and disseminate information published by the faculty, students and alumni for mutual benefits. The bulletin also aims to propagate the intellectual contribution of Delhi Technological University (DTU) as a whole to the academia.

The bulletin contains information resources available in the internet in the form of articles, reports, presentations published in international journals, websites, etc. by the faculty and students of DTU. The publications of faculty and student which are not covered in this bulletin may be because of the reason that the full text either was not accessible or could not be searched by the search engine used by the library for this purpose.

The learned faculty and students are requested to provide their uncovered publications to the library either through email or in CD, etc. to make the bulletin more comprehensive.

This issue contains the information published during **January, 2018**. The arrangement of the contents is alphabetical. The full text of the article which is either subscribed by the university or available in the web is provided in this bulletin.

Central Library

CONTENTS

1. A Review on Medicinal Plants against Cancer, **6.Arпита Roy**, **7.Shruti Ahuja** and **3.Navneeta Bharadvaja**, Biotechnology, DTU
2. A review on pharmaceutically important medical plant: Plumbago zeylanica, **6.Arпита Roy** and **3.Navneeta Bharadvaja**, Biotechnology, DTU
3. An intelligent, adaptive, performance-sensitive, and virtual reality-based gaming platform for the upper limb, **7.1.Ashish Dhiman**, Dhaval Solanki, Ashu Bhasin, Abhijit Das and Uttama Lahiri, Electronics, DTU
4. Critical Review of Fabrication & Characterisation of Metal Matrix Composites, **6.Ankit Tyagi** and **6.Yashwant koli**, Mechanical, DTU
5. Development of Hybrid Model with Feasibility Analysis for UN-electrified Households in Developing Countries, Priyanka Anand, Sarbjeet Kaur Bath and **3.Mohammad Rizwan**, Electrical, DTU
6. E-Catalyst Learning System, **8.1.Rajiv Roy**, Computer, DTU
7. EFFECT OF BOAT TAIL PROFILE ON DRAG COEFFICIENT OF A SEDAN USING CFD, **6.Salman Javed**, **6.Farhan Javed** and **3.Samsher**, Mechanical, DTU
8. ELECTRONICALLY TUNABLE LC HIGH PASS LADDER FILTER USING OTRA, **3.Neeta Pandey**, **6.Venkatesh Kumar**, **6.Aayush Goel** and **6.Ankit Gupta**, ECE, DTU
9. Establishment of the Shoot and Callus Culture of an Important Medicinal Plant Plumbago zeylanica, **6.Arпита Roy** and **3.Navneeta Bharadvaja**, Biotechnology, DTU
10. Experimental Investigation of Influence of SiO₂ Nanoparticles on the Tribological and Rheological properties of SAE 40 Lubricating Oil, **i**, **3.Ramesh Chandra Singh** and **3.Rajiv Chaudhary**, Mechanical, DTU

11. Fabrication of Sensitive Bioelectrode Based on Atomically Thin CVD Grown Graphene for Cancer Biomarker Detection, Vijay K. Singh, **3.Saurabh Kumar**, Sumit Kumar Pandey, **6.Saurabh Srivastava**, Monu Mishra, Govind Gupta, **3.B.D. Malhotra**, R.S. Tiwari and Anchal Srivastava, Biotechnology, DTU
12. Identification of LTI Autonomous All Pole System Using Eigenvector Algorithm, **3.Sudipta Majumdar**, Electronics and Communication, DTU
13. Implementation of Extended Kalman Filter on Stochastic Model of LPF, **6.Rahul Bansal** and **3.Sudipta Majumdar**, ECE, DTU
14. Influence of Interface Trap Charge Density on Reliability Issues of Transparent Gate Recessed Channel (TGRC) MOSFET, **6.Ajay Kumar**¹, **3.M.M. Tripathi**¹ and **3.Rishu Chaujar**², ¹Electrical and ²Physics, DTU
15. Influence of various Carbon and Nitrogen sources on Lipid productivity of *Chlorella minutissima* and *Scenedesmus* sp. and their FAME analysis, **6.Tushita Attre**, **6.Arpita Roy** and **3.Navneeta Bharadvaja**, Biotechnology, DTU
16. Micro-Diversity Analysis of Error Probability and Channel Capacity over Hoyt-Gamma Fading, **6.Sandeep KUMAR**, Sanjay Kumar SONI and **3.Priyanka JAIN**, Electronics and Communication, DTU
17. Movie recommender system with metaheuristic artificial bee, **3.Rahul Katarya**, IT, DTU
18. New Configuration for OFCC-Based CM SIMO Filter and its Application as Shadow Filter, **3.Deva Nand** and **3.Neeta Pandey**, Electronics and Communications, DTU
19. Optimal automatic generation control of two-area power systems with energy storage units under deregulated environment, **6.Yogendra Arya**, **3.Narendra Kumar** and S. K. Gupta, Electrical, DTU
20. PID Based Impedance Control Scheme for Flexible Single Arm Underwater Robot Manipulator, Sunil Kumar, **3.Vikas Rastogi** and Pardeep Gupta, Mechanical, DTU

21. Realization of Current Mode Universal Filter and a Dual-Mode Single Resistance Controlled Quadrature Oscillator Employing VDCC and Only Grounded Passive Elements, **7.1.Manish GUPTA** and Tajinder Singh ARORA, Electronics and Communication, DTU
22. Significant enhancement in structural, dielectric, piezoelectric and ferromagnetic properties of Ba_{0.9}Sr_{0.1}Zr_{0.1}Ti_{0.9}O₃-CoFe₂O₄ multiferroic composites, **6.Aditya Jain**, **3.Amrish K. Panwar** and A.K. Jha, Physics, DTU
23. Source Material Assessment of Heterojunction DG-TFET for Improved Analog Performance, **6.Jaya Madan**, **6.Skanda Shekhar** and **3.Rishu Chaujar**, Physics, DTU
24. Stability Analysis of Job Shop Problem, **3.Nilam Rathi**, Applied Mathematics, DTU

1. *Chancellor*

2. *Pro Vice Chancellor*

3. *Faculty*

4. *Teaching-cum-Research Fellow*

5. *Alumni*

6. *Research Scholar*

7. *PG Scholar*

8. *Undergraduate Student*

2.1. *Ex Pro Vice Chancellor*

3.1. *Ex Faculty*

4.1. *Asst. Librarian*

6.1. *Ex Research Scholar*

7.1. *Ex PG Scholar*

8.1. *Ex Undergraduate Student*

A Review on Medicinal Plants against Cancer

Arpita Roy*, Shruti Ahuja and Navneeta Bharadvaja

Department of Biotechnology, Delhi Technological University, New Delhi, India

*Corresponding Author: Arpita Roy, Department of Biotechnology, Delhi Technological University, New Delhi, India, E-mail: arbt2014@gmail.com

Received date: September 29, 2017; Accepted date: November 01, 2017; Published date: November 10, 2017

Copyright: © 2017 Arpita Roy, et al. This is an open-access article distributed under the terms of the Creative Commons Attribution License, which permits unrestricted use, distribution, and reproduction in any medium, provided the original author and source are credited.

Citation: Arpita Roy, Shruti Ahuja, Navneeta Bharadvaja (2017) A Review on Medicinal Plants against Cancer. J Plant Sci Agric Res. Vol. 1 No. 2:008.

Abstract

Cancer is one of the life-threatening diseases which creates major problem in both the developing and developed countries. Demand for new methods to prevent this disease is growing increasingly. Plants have always been a basis for the traditional medicine systems and they have provided continuous remedies to the mankind for thousands of years. Medicinal plants are considered as a repository of various bioactive compounds and used for long time due to its therapeutic properties. Plant derived product has benefits over synthetic medicine which increased the utilization of medicinal plants in the healthcare sector as several plants' derived compounds show potential role against cancer treatment. Plant based anticancer agents includes vincristine, taxol, vinblastin, stigmasterol, camptothecin, resveratrol, etc., are in clinical use all over the world. In the present review, an effort has been made to provide the information about the role of various medicinal plants against cancer.

Keywords: Cancer; Anticancer agent; Medicinal plants; Bioactive compounds; Cytotoxicity

naturally occurring compounds known to possess cytotoxicity effects, as they display potential to destroy cancer cells. Due to these advantages of medicinal plants they are in high demand and several species of medicinal plants have been investigated and selected for the preparation of cancer medicines. Recently, there has been an increased scientific interest in the study of materials from plant source as an anticancer compound. Several studies have found the role of medicinal plants in prevention and treatment of cancer [2]. National Cancer Institute has approximately screened 35,000 plant species for their potential anticancer activities and they have found that among them about 3,000 plant species have shown reproducible anticancer activity [3]. Emergence of important anti-cancer agents from natural source requires more research in order to develop more drugs to treat this disease. Medicinal plants contain wide ranges of secondary metabolites which include flavonoids, flavones, anthocyanins, lignans, coumarins, isocatechins and catechins [4]. These bioactive compounds are mainly responsible for the antioxidant prosperity of medicinal plants. The increasing side effects and expensive medication has tilted the focus of researches on herbal medicines. Therefore in this review an effort has been made to provide information about the medicinal plants that possesses anticancer activity.

Introduction

Cancer is one of the deadly diseases which are characterized by the irregular cell proliferation. The most common reason behind the cancer is lifestyle changes and therefore an urgent need to find a better treatment for the disease is required. According to World Health Organization [1], more than 14 million people diagnosed with cancer and 8 million died in 2012 (www.who.int). High mortality and incidence make it an important public health and economic issue which requires an effective prevention. Medicinal plants have various advantages over chemical products, because plant derived compounds are more tolerant and non-toxic to the normal human cells. Already available conventional therapies for the treatment of cancer are radiotherapy and chemotherapy which have various side effects like neurological, cardiac, renal and pulmonary toxicity, seriously affecting the health of the person. Therefore, an alternative method is required to develop that include less toxic and more potent anticancer drug as compare to the drugs available in the market. Several studies [2] have been made on

Anticancer Activity of Medicinal Plants

Actaea racemosa

Belonging to the family Ranunculaceae is commonly known as black cohosh and black snakeroot. It contains cycloartenol type triterpenoids, cinnamic acid derivatives and cimicifugoside. This plant is also well known for its role in amenorrhea and ovaritis [5]. The main compound of this plant is actein and it shows inhibition of human HepG2 liver cancer cells growth by reducing the cholesterol and free fatty acid levels in liver [6].

Ardisia crenata

It belongs to the Myrsinaceae family and commonly known as coral bush, spice berry, red berries and coralberry. It is commonly found in warm climate of tropical and sub-tropical regions. It contains cyclic depsopeptide, triterpenoid saponins and alkenylphenol [7]. Anticancer activity of this plant is due to the presence of ardisiacrispin, which is a mixture of two triterpenoid saponins i.e. ardisiacrispin A and B. One study

showed that the ardisiacrispin inhibits proliferation of uncontrolled liver cancer cell line (Bel-7402) by microtubule disruption and induction of proapoptotic activities [8].

Bacopa Monnieri

It belongs to the Scrophulariaceae family and found throughout the plains in India. It is reported to contain tetracyclic triterpenoid saponins, bacosides A and B, herpestine, brahmine, flavonoids, stigmasterol [9]. Stigmasterol is known to possess anticancer activity by inducing apoptosis mediated by the activation of protein phosphatase 2A by ceramide. Study conducted by Ghosh [10] evaluated the antitumor activity of stigmasterol isolated from *Bacopa Monnieri* on Ehrlich Ascites Carcinoma in swiss albino mice and found that stigmasterol enhanced the life span of tumor bearing mice by decreasing the tumor volume and viable cell count.

Bidens Pilosa

It belongs to the Asteraceae family and native to the America. It contains polyacetylenes, flavonoids, phenylpropanoids terpenoids, and others compounds. Phenyl-1, 3, 5-heptatriyn possesses toxicity profile on normal blood cells in erythrocyte osmotic fragility experiments along with other extracts [11]. Hexane, methanol and chloroform extracts of *Bidens pilosa* and their fractions were tested on various cancer cell lines. Results showed the antitumor activity of extracts among which hexane extract showed maximum activity [12].

Catharanthus roseus

It belongs to the Apocynaceae family and commonly known as rosyperiwinkle or Madagascar periwinkle. Its main compound is alkaloids, and used for the circulatory diseases treatment and provide relief to the normal cerebral blood flow obstruction. Vinblastin and vincristine are the two well-known compounds which significantly effects against the human neoplasm. Vincristin sulfate arrest mitosis and utilized for the treatment of acute leukemia in children and vinblastin sulfate is utilized for the treatment of choriocarcinoma, lymphosarcoma, neuroblastoma and carcinoma of lung, breast and other organs [13].

Centella asiatica

It belongs to the Apiaceae family and commonly known as brahmamanduki in Hindi, mandukaparni in Sanskrit and pennywort in English. It is commonly found in India, Australia, Pacific Islands, New Guinea, Iran and Malaysia. It contains numerous compounds such as asiaticoside, pectic acid, hydrocotyline, sterol, flavonoid, vallerine, ascorbic acid and thankunosides [14]. Partially purified fraction of *Centella asiatica* suppressed mouse lung fibroblast cell proliferation and oral administration slowed the solid development and ascites tumours [15]. Pre-treatment with this plant increase the survival time of irradiated animals and show protection against radiation induces damage in liver [16]. This plant shows inhibition in lipid peroxidation in various organs like lungs, liver, heart, brain,

spleen and kidney and shows potential towards the cancer inhibition [3].

Cedrus deodara

It is belongs to the Pinaceae family and found in the Western Himalaya, northern Pakistan, north central India, eastern Afghanistan, western Nepal and south-western Tibet. It is known as deodar in Hindi and devdar in Sanskrit. It contains taxifolin, cedrin, cedreoside, cedrin, cedreoside and deodarin. Stem wood extract of *C. deodara* which contains lignin composition exhibits cytotoxicity to the human cancer cell lines [17] and also induce tumor regression in murine models [18]. Bark of this plant shows potential in the rheumatoid arthritis inflammation, fever, cancer, dysentery, diarrhea and ulcer [3].

Citrus

Citrus fruits belong to the family, Rutaceae found all over the world and top the world fruit market. There are four important species in citrus fruit with a wide variety of hybrid species as well. Several reports show citrus as a potent anti-tumor agent. Citrus peels are a rich source of phytochemicals such as phenols, limonoids, flavonoids and polysaccharides. Zhao et al. [19] extracted and purified an acidic polysaccharide from the peels of *Citrus aurantifolia*. The main components of the acidic polysaccharides (CA) are rhamnose (Rha), arabinose (Ara), galactose (Gal), glucose (Glu), mannose (Man) and galacturonic acid (GalA). The antitumor activity of CAs was evaluated in mice transplanted H22 hepatoma cells. CA restricted the tumor cell cycle in S phase and stimulated the expression of proapoptotic factor caspase 3. CA enhances immune response against cancer cells by increasing the levels of tumor infiltrating CD8+ T lymphocytes. It inhibits the expression of anti-apoptotic protein BclxL and Mcl-1. The results conclude that acidic polysaccharides from citrus peels could be used as an adjuvant in treating hepatocellular carcinoma [19]. Park et al. [20] characterized a pectic polysaccharide, rhamnogalacturonan II (CPE-II) from peels of *Citrus unshiu*. Citrus peels are an abundant source of polyhydroxyl flavonoids (PHFs) such as hesperidin, neohesperidin and naringin; and polymethoxyflavones (PMFs), most of these components act as potent antitumor compounds. PMFs are reported to significantly inhibit metastasis by restricting cell adhesion and its invasion [20]. It enhances cytotoxicity by increasing the expression of NK cells. Cell cycle is arrested in G1 phase by inhibiting cyclin-dependent kinases (Cdk) and enhancing Cdk inhibitor proteins. The efficacy of citrus peels against skin cancer has been studied in a two stage skin carcinogenesis model [20].

Cynodon dactylon

It belongs to the Poaceae family and possesses several medicinal activities which include anti-helminthic, anti-diuretic, hepatoprotective, anti-inflammatory activity, prostatitis, dysentery, etc. The nontoxic dose of the petroleum ether of *Cynodon dactylon* on normal vero cell line showed the cell viability of 97% at a concentration of 0.007 mg/ml which decreased with increase in concentration. Extract showed a potential cytotoxic activity against Hep-2 laryngeal cancer cell

line. Cyclophosphamide served as pcontrol and 96.2% cancer inhibition was observed. The concentration of petroleum ether extract of *Cynodon dactylon* at 10 mg/ml showed inhibition percent with regard to cytotoxicity of 93.5% that was comparable to the positive control [21].

Languas galangal

It belongs to the Zingiberaceae family and commonly known as the blue ginger or Thai ginger is a common culinary herb used in Thai cuisines. 1'-Acetoxychavicol acetate (ACA) extract from *Languas galanga* and *Alpinia galangal* is a potent anti-tumor agent. It has been documented to suppress chemical and virus induced tumor initiation and proliferation. A study reported that ACA mediated its antitumor activity by modulating the activity of transcription factor, NF-kappa B which regulates metastasis and cellular proliferation [22].

Piper longum

It belongs to the Peparaceae family and used as a spice. It contains longumine and used for the treatment of cough, chronic bronchitis, and cough. *Piper longum* extract showed inhibitory effects on the growth of Human lung cancer (HCC-827 cell line) and recorded in term of viable cell count decrease as compared to the control value and inhibition is dose dependent [23]. It is also used as an antidote in scorpion sting and snake biting [24].

Picrorhiza kurroa

It belongs to the Plantaginaceae and found in the Himalayan region and Nepal. It contains a bitter glycoside which is known as kutkin. It is used for the treatment of digestive problems, liver damage, asthma, vitiligo and wound healing (Kumar and Ramesh, 2014). Rhizome extract of *Picrorhiza kurroa* is rich in caffeic esters, apiocynin and *cucurbitacines aglycone* compounds and they possess cytotoxic effects on mammalian cell lines [25].

Plumbago zeylanica

It belongs to the Plumbaginaceae family and commonly known as white leadwort, chitrak and Ceylon leadwort. It is found in the warmer part of India and Sri Lanka. Several studies reveal the presence of various phytochemicals in this plant which includes plumbagin, plumbagin acid, coumarins, saponaretin, isoaffinetin, isoorientin, steroids, glucosides and psoralen. This plant shows therapeutic activity against skin diseases, rheumatic pain, wounds and scabies [26]. Plumbagin is a naphthoquinone which is isolated from the roots of this plant and it possess anti-tumor activity by controlling the hormone refractory invasive prostate cancer. Inhibitory effect of plumbagin against various molecular targets (STAT-3, AKT and PI-3K) results in the growth inhibition and invasion of prostate cancer. Plumbagin shows apoptosis induction in cancer cells and also inhibits growth of these cells [27,28].

Punica granatum

It belongs to the Lythraceae family and commonly known as Pomegranate. Pomegranate is a rich source of phenolic compounds, Ellagitannins (ETs) and ellagic acid (EA) that metabolically convert to urolithins by the gut microbiota. Urolithins are found in high concentrations in colorectal cancer (CRC) patients. This has diverted researches towards the anticancer activity of pomegranate. Urolithins inhibit proliferation of cancer cells and interfere with cell cycle and induce apoptosis. In a randomized clinical trial by Syed et al. [29] colorectal cancer patients were orally administered ellagitannin-containing pomegranate extract.

Tinospora cordifolia

It belongs to Menispermaceae family and commonly found in Sri Lanka, India, Myanmar and China. Stem and roots contain important alkaloids. It is known as 'giloya' in Hindi, 'guduchi' in Sanskrit and heartleaf moonseed plant in English. Root of this plant contains various alkaloids which includes tinosporin, choline, isocolumbin, columbin, tetrahydroplamatin, magnoflorimine and palmatin [30,21]. *Tinospora cordifolia* stem is generally used for the treatment of fever, dyspepsia, jaundice, skin and urinary disease [31]. *In vitro* study shows *Tinospora cordifolia* able to kill HeLa cells; this shows the potential of this plant as an anticancer agent. *Tinospora cordifolia* extract shows dose dependent cell death as compared to the controls [32]. Dichloromethane extract of *T. cordifolia* showed anticancer activity in mice transplanted with Ehrlich ascites carcinoma [33].

Thymus vulgaris

It belongs to the Lamiaceae family and commonly known as the German thyme or Garden thyme. Sertel et al. (2011) studied the cytotoxic activity of thyme against head and neck squamous cell carcinoma. The essential oils in Thyme induced cancer cell death by regulating interferon signaling, N-glycan biosynthesis and extracellular signal-regulated kinase 5 (ERK5) signaling [34].

Zanthoxylum nitidum

It belongs to the Rutaceae family and found in the Australia and Southeast Asian countries. It contains flavonoids, alkaloids, carbohydrates and amino acids [35]. It root contains nitidine chloride, dihydronitidines, oxinitidine, skimmianine, α -allocryptopine and 6-methoxy-5,6-dihydrochelerythrine. It is used for the treatment of stomachache, toothache, rheumatism, cough, vomiting, cholera and diarrhea. Nitidine possesses the anti-cancer activity and shows cytotoxic activity against the LLC (DNA intercalator which is generally classified as topoisomerases I and II inhibitor) and which leads to the cancer cells apoptosis [36,37].

Conclusions

Cancer is one of major problem in both developing and developed countries. Chemotherapy and radiation therapy causes various side effects therefore there is requirement of an alternative medicine to treat cancer. Medicinal plant contains

various secondary metabolites which show their potential activity against various diseases. Anti-cancer agents derived from the plant source have largely contributed to the development of new drugs. This review provides the information about medicinal plants with their secondary metabolites that show anti-cancer activity. So it can be concluded that herbal medicinal plants and its derivatives are active against different type of cancers. Herbal drug treatment may be recommended to the rural and poor people to treat effectively the cancers as it is cheaper. Screening of medicinal plants for anticancer activity provides a huge space for development of strong anticancer agents.

References

- WHO (2017) fact sheet. World Health Organisation committee 186.
- Greenwell M, Rahman PKSM (2015) Medicinal Plants: Their Use in Anticancer Treatment. International journal of pharmaceutical sciences and research 6: 4103-4112.
- Desai AG, Qazi GN, Ganju RK, El-Tamer M, Singh J, et al. (2008) Medicinal Plants and Cancer Chemoprevention. Curr Drug Metab 9: 581-591.
- Sumner J (2000) The Natural History of Medicinal Plants. Timber Press 17. ISBN 0-88192-483-0
- Mahady GB, Fabricant D, Chadwick LR, Dietz B (2002) Black cohosh: an alternative therapy for menopause. Nutr Clin Care 5: 283-289.
- Einbond LS, Soffritti M, Esposti DD, Park T, Cruz E, et al. (2009) Actein activates stressand statin-associated responses and is bioavailable in Sprague-Dawley rats. Fund Clin Pharmacol 23: 311-321.
- Horgen FD, Guinaudeau H, Pezzuto JM, Soejarto DD, Farnsworth NR et al. (1997) Isolation and structure elucidation of ardisenone a new, cytotoxic alkenylphenol from *Ardisia iwahigensis*. J Nat Prod 60: 533-535.
- Li M, Wei SY, Xu B, Guo W, Liu DL, et al. (2008) Proapoptotic and microtubule-disassembly effects of ardisiacrispin (A+B), triterpenoid saponins from *Ardisia crenata* on human hepatoma Bel-7402 cells. J Asian Nat Prod Res 10: 729-736.
- Das M, Shrestha B, Datta S, Das S, Deb J (2010) Phyto-pharmacological review of *Bacopa monnieri* Linn. Natural Product anIndian Journal 6: 1-4.
- Ghosh T, Maity TK, Singh J (2011) Evaluation of antitumor activity of stigmaterol, a constituent isolated from *Bacopa monnieri* Linn aerial parts against Ehrlich Ascites Carcinoma in mice. Orient Pharm Exp Med 11: 41-49.
- Kumari P, Misra K, Sisodia BS, Faridi U, Srivastava S, et al. (2009) A promising anticancer and antimalarial component from the leaves of *Bidens pilosa*. Planta Medica 5: 59.
- Sundararajan P, Dey A, Smith A, Doss AG, Rajappan M (2006) Studies of anticancer and antipyretic activity of *Bidens pilosa* whole plant. Africa Health Sciences 6: 27.
- Noble RL (1990) The discovery of the vinca alkaloids--chemotherapeutic agents against cancer. Biochem Cell Biol 68: 1344-1351.
- Roy A, Kundu K, Saxena G, Kumar L, Bharadvaja N (2016) Effect of different media and growth hormones on shoot multiplication of in-vitro grown *Centella asiatica* accessions. Adv Tech Biol Med 4: 12.
- Babu TD, Kuttan G, Padikkala J (1995) Cytotoxic and anti-tumour properties of certain taxa of Umbelliferae with special reference to *Centella asiatica* (L.) Urban. J Ethnopharmacol 48: 53-57.
- Sharma J, Sharma R (2002) Radioprotection of Swiss albino mouse by *Centella asiatica* extract. Phytother Res 16: 785-786.
- Shashi B, Jaswant S, Madhusudana RJ, Kumar SA, Nabi QG (2006) A novel lignan composition from *Cedrus deodara* induces apoptosis and early nitric oxide generation in human leukemia Molt-4 and HL-60 cells. Nitric Oxide 14: 72-88.
- Singh SK, Shanmugavel M, Kampasi H, Singh R, Mondhe DM, et al. (2007) Qazi GN Chemically standardized isolates from *Cedrus deodara* stem wood having anticancer activity. Planta Med 73: 519-526.
- Zhao Y, Sun H, Ma L, Liu A (2017) Polysaccharides from the peels of *Citrus aurantifolia* induce apoptosis in transplanted H22 cells in mice. Int. J. Biol. Macromolec 29: 680-689
- Park HR, Park SB, Hong HD, Suh HJ, Shin KS (2017) Structural elucidation of anti-metastatic rhamnogalacturonan II from the pectinase digest of citrus peels (*Citrus unshiu*). Int J Biol Macromol 94: 161-169.
- Sultana N, Lee NH (2007) Antielastase and free radical scavenging activities of compounds from the stems of *Cornus kousa*. Phytother Res 21: 1171-1176.
- Ichikawa H, Takada Y, Murakami Aggarwal BB (2005) Identification of a novel blocker of I κ B α kinase that enhances cellular apoptosis and inhibits cellular invasion through suppression of NF- κ B regulated gene products. J Immunol 174: 7383-7392.
- Sawhney SS, Painuli RM, Singh D (2011) Antioxidant and antimicrobial activity of *phyllanthus emblica* for its application in treatment of ophthalmic disorders. Int J Pharm Pharm Sci 4: 129-132.
- Kayande N, Patel R (2016) Review on: Indian Medicinal plants having anticancer property. Pharma Tutor 4: 25-28.
- Kumar MH, Ramesh C (2014) Antimutagenic Activity of Root Extract of *Picrorhiza kurroa* Using Ames test in Both Dose Dependant Cytotoxic Assay and Mutagenicity Study. J Pharmacogn Phytochem 2: 48-52.
- Gupta MM, Verma RK, Uniyal GC, Jain SP (1993) Determination of plumbagin by normal-phase high-performance liquid chromatography. J Chromatogr A 637: 209-212.
- Roy A, Bharadvaja N (2017) Effect of different culture medias on shoot multiplication and stigmaterol content in accessions of *Centella asiatica*. International Journal of Ayurvedic and Herbal Medicine 7: 2643-2650.
- Roy A, Attre T, Bharadvaja N (2017) Anticancer agent from medicinal plants: A Review. New aspects in medicinal plants and pharmacognosy. JB Books Publisher, Poland 154.
- Syed DN, Chamcheu JC, Adhami VM, Mukhtar H (2013) Pomegranate Extracts and Cancer Prevention: Molecular and Cellular Activities. Anti-cancer agents in medicinal chemistry 13: 1149-1161.
- Pahadiya S, Sharma J (2003) Alteration of lethal effects of gamma rays in Swiss albino mice by *Tinospora cordifolia*. Phytother Res 17: 552-554.

31. Singh SS, Srivastava S, Gupta VS, Patro B, Ghosh AC (2003) Chemistry and medicinal properties of *Tinospora cordifolia* (guduchi). *Ind J Pharmacol* 35: 83-91.
32. Jagetia GC, Nayak V, Vidyasagar MS (1998) Evaluation of the antineoplastic activity of guduchi (*Tinospora cordifolia*) in cultured HeLa cells. *Cancer Lett* 127: 71-82.
33. Jagetia GC, Rao SK (2006) Evaluation of the antineoplastic activity of guduchi (*Tinospora cordifolia*) in Ehrlich ascites carcinoma bearing mice. *Biol Pharm Bull* 29: 460-466.
34. Sertel S, Eichhorn T, Plinkert PK, Efferth T (2011) Cytotoxicity of *Thymus vulgaris* essential oil towards human oral cavity squamous cell carcinoma. *Anticancer Res* 31: 81-87.
35. Bhattacharya S, Zaman MK (2009) Pharmacognostical evaluation of *Zanthoxylum nitidum* bark. *Int J PharmTech Res* 1: 292-298.
36. Fang SD, Wang LK, Hecht SM (1993) Inhibitors of DNA topoisomerase I isolated from the roots of *Zanthoxylum nitidum*. *J Org Chem* 58: 5025-5027.
37. Venkateswaralu G, Swarupa Rani T, Vani M, Vineela PAJ (2015) In-Vitro anticancer activity of petroleum ether extracts of *Cynodon dactylon*. *Journal of pharmacognosy and Phytochemistry* 4: 164-168.



Review Article

ISSN: 2454-5023

J. Ayu. Herb. Med.

2017; 3(4): 225-228

© 2017, All rights reserved

www.ayurvedjournal.com

Received: 02-09-2017

Accepted: 02-11-2017

A review on pharmaceutically important medical plant: *Plumbago zeylanica*

Arpita Roy¹, Navneeta Bharadva¹

¹ Plant Biotechnology Laboratory, Department of Biotechnology, Delhi Technological University, New Delhi-110042, India

ABSTRACT

Medicinal plants have been used as a source of medicine and they are in great demand worldwide. They have been used for many years to treat health disorders and prevent diseases. *Plumbago zeylanica* is one of the medicinal plants which are widely used for its therapeutic value. It contains several bioactive compounds like naphthoquinones, flavonoids, alkaloids, glycosides, steroids, tri-terpenoids, tannins, fixed oils, fats, proteins, etc among all plumbagin is most important bioactive compounds. It possesses wide range of pharmaceutical activities such as anti-cancer, anti-diabetic, anti-malarial, anti-microbial, etc. Several studies have been done in evaluation of its pharmaceutical activities. The aim of the present review is to provide a comprising knowledge related to the chemical composition and pharmaceutical activity of *P. zeylanica*.

Keywords: *Plumbago zeylanica*, chemical composition, plumbagin, pharmaceutical activity.

INTRODUCTION

Plants are the important source of various useful materials and provide food, shelter, medicine etc. Detailed descriptions of plant and plant's products about 700 herbs used for medicinal purposes to cure various ailments have been mentioned in various literatures like *Ayurveda*, *Charak samhita* and *Susrut Samhita*. *P. zeylanica* is a medicinal plant which commonly known as "White leadwort" or "Chitrak". It belongs to the *Plumbaginaceae* family and a perennial herb which is found in Uttar Pradesh, West Bengal, Maharashtra and also to some parts of South India [1]. It is one of the oldest herbs which are reported to be used in Ayurveda for several disorders over thousands of years. It contains various bioactive compounds like alkaloids, flavonoids, naphthoquinones, glycoside, saponins, steroids, tri-terpenoids, coumarins, phenolic compounds, tannins, carbohydrate, fixed oils, fats and proteins [2, 3]. This plant have been reported to show anti-bacterial, anti-plasmodial, anti-tumour, hepatoprotective, central nervous system stimulatory activity, anti-fungal, anti-inflammatory, anti-hyperglycemic, anti-cancer, anti-atherosclerotic activity etc [4].

Leaves of *P. zeylanica* are dark green in colour and are simple, elliptical with hairy margins along with alternate placement on the stem with the distance of up to 3 inches and thickness of 1.5 inches. Petioles are thin and with an approximate length of 0.5 mm and native stipules are present [5]. Plants breed flower white in colour with diameter of 1/2 to 3/4 inch having the stalk measuring 4 to 12 inches along with a terminal raceme-type of inflorescence. Roots of *P. zeylanica* are long and slightly branched with very less secondary roots, having a smooth and unbroken texture, colour of the roots is light yellow when the plant is freshly plucked out of the ground and changes to reddish brown in colour when it is dried which often initiates in the form of hard pieces. These roots are usually very strong having a bitter taste and a distinct odour with acrid [4].

Chemical composition

P. zeylanica contains variety of secondary metabolites like flavonoids, alkaloids, glycosides, saponins, steroids, tannins, tri-terpenoids, coumarins, carbohydrates, phenolic compounds, fixed oils, fats, proteins and naphthoquinones [6]. Naphthoquinones present in the plant are plumbagin, chitrone, 3-biplumbagin, chloroplumbagin, elliptone. Coumarins are seselin, 5-methoxy seselin, xanthyletin, suberosin. Other compounds present in the plant are Plumbagin acid, β sitosterol, 2, 2-dimethyl-5-hydroxy-6-acetylchromene, saponaretin, isoaffinetin, etc. Among all these Plumbagin, is the most important bioactive compounds present in *P. zeylanica*.

*Corresponding author:

Arpita Roy

Plant Biotechnology Laboratory,
Department of Biotechnology,
Delhi Technological University,
New Delhi-110042, India

Email: arbt2014[at]gmail.com

Plumbagin

Plumbagin (5-hydroxy-2-methyl-1, 4- naphthoquinones- $C_{11}H_8O_3$) (Figure 1) is a naphthoquinones which is mostly present in roots of this plant [7]. It is a stirring yellow pigment that patently appears in the *Plumbaginaceae* family. Plumbagin is soluble in organic solvents like acetone, chloroform, alcohol, benzene and acetic acid [8].

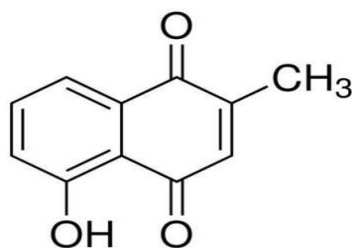


Figure 1: Structure of Plumbagin

Pharmaceutical activity of *Plumbago zeylanica*

P. zeylanica has been reported to possess wide range of pharmacological activities like anti-inflammatory, anti-diabetic, memory inducing, lipid metabolism, anti-malarial, allergic and modulatory, anti-fertility, anti-bacterial, anti-viral, anti-cancer, anti-oxidant, larvicidal. Roots are used as a traditional medicine in various regions like in Ethiopia the root, bark or leaf powder is used for treatment of syphilis, tuberculosis and gonorrhoea and in Zambia the root and leaf is used as a remedy for inflammation of mouth, chest and throat by boiling the plant part in milk and consuming it.

Anti-microbial activity

Crude alcoholic extract of *P. zeylanica* showed anti-bacterial property against the growth of multi-resistant strains of *E. coli* and *Shigella*. MIC value of 0.64-10.24mg/ml obtained when compared with other plant extract [9]. A study reported that methanolic extract of *P. zeylanica* root showed the anti-bacterial effect against *Bacillus subtilis* cultures [10]. Ethanolic extract of *P. zeylanica* showed anti-microbial activity against *Salmonella typhi*, *Pseudomonas aeruginosa*, *Bacillus subtilis* and *Staphylococcus aureus* where as acetone and chloroform showed moderate activity [11]. Effect of crude extract of *P. zeylanica* leaves against *E.coli*, *Bacillus cereus*, *Staphylococcus aureus*, and *Candida* was observed and it was found that they exhibits inhibition zones which indicates the potential anti- microbial activity of *P. zeylanica* [12].

Anti-diabetic activity

A study investigated that 500mg of *Plumbago zeylanica* and 1gm of haridra powder in form of capsules given 4 times for 45 days with restricted diet schedule of low calorie diet to the obese patient [13]. Results showed that *P. zeylanica* is highly significant in the weight loss of the patient as compared to the haridra. Another studied reported the effect of *Plumbago zeylanica* extract on diabetic rats. Extract reported to decrease the activity of glucose-6-phosphate and meanwhile increasing the activity of hexokinase when the ethanolic extract at a concentration of 100mg. 200mg/kg along with tolbutamide was administered orally to the streptozotocin treated diabetic rats [14]. Plumbagin isolated from the *P. zeylanica* enhance the protein and GLUT4 mRNA expression in diabetic rats and thus indicates the enhanced GLUT4 translocation and contribution to the glucose homeostasis [15].

Anti- inflammatory activity

A study reported that hydro-alcoholic extract of *P. zeylanica* leaf showed anti-inflammatory activity [16]. A study showed that *P. zeylanica* reduces the oedema thus comforting the body part, it is also investigated to suppress the NF-kappa B activation in the tumour cells

and also prevention of graft versus host disease [17, 18, 19]. A study revealed the anti-inflammatory effect of *P. zeylanica* in carrageenin induced raw paw oedema in rats. In the investigation four groups were taken where two groups were treated with 300mg/kg and 500mg/kg which confirm the 31.03 and 60.30% acute inflammation inhibition [7]. A clinical study conducted on 30 patients who were taken from the OPD and IPD of National Institute of Ayurveda, Jaipur by Napalchyal *et al.*, where 4mgs of chitraka churna was given to 15 patients for twice a day with lukewarm water for 15 days. And they found a significant improvement in the pain, swelling, tenderness and dizziness cause due to inflammation of the body parts [20].

Anti-Cancer Activity

Various reports state that the plant *P. zeylanica* consists of bioactive compound which possess anti-cancer activity against various cancer cell lines. A study also reveals that Plumbagin can inhibit cell proliferation, block cell cycle and induce apoptosis of APL cell line NB4 cells [21]. Ethanolic extract of *P. zeylanica* possess significant anti-cancer activity against Ehrlich Ascites Carcinoma in animal model, and also it reduces elevated level of lipid per-oxidation having presence of higher terpenoids and flavonoids [22]. A report showed that methanolic extract of *P. zeylanica* were used against MCF-7 and HT-29 and it results in moderate anti-cancer activity and the inhibitory property compared with the standard tamoxifen for MCF-7 and 5-fluoro Uracil for HT-29. 50.23% of MCF-7 cell death and 25.17% of HT-29 cell inhibition were observed [23]. A study reported that plumbagin suppressed the BAX, BCL-2, pro-caspase-3 expression and cleaved caspase-3 in gastric cancer cells. Plumbagin inhibits the apoptosis in human gastric cancer cells that may be due to its ability to suppress the STAT3 and Akt phosphorylation [24].

Larvicidal activity

Maniafu *et al.*, reported the larvicidal activity of three *Plumbago* spp. Hexane and chloroform crude extracts of *P. zeylanica* showed highest larvicidal activity against *A. gambiae* i.e. LC50 6.4 and 6.7 μ g/ml respectively [25]. A reported show that *P. zeylanica* extract possesses larvicidal activity against second, third, and fourth instar larvae of *Aedes aegypti*. LC (50) values of all the extracts in different solvents of *P. zeylanica* were less than 50 ppm against all tested larval instars [26].

Central nervous system activity

A study reported that hydro-alcoholic leaf extract of *P. zeylanica* were evaluated for its CNS activity and it was found that the extract showed significant CNS depressant activity with the muscle relaxant properties [27]. Vishnukanta *et al.*, also investigated the anti-convulsant activity of hydro-alcoholic leaf extract of *P. zeylanica* and results showed that it did not possess the anti-convulsant activity [28].

Hypo-cholesterolemic activity

A clinical study carried by Sharma *et al.*, which utilized the root extract of *P.zeylanica* containing Plumbagin, when administered to the hyper-lipidemic rabbits reduced the serum cholesterol and LDL by a 53% to 86% and 61% to 91% respectively. The compound Plumbagin restricts the cholesterol and triglyceride accumulation in the liver and aorta [29]. A study also reveals a significant decrease in the serum cholesterol, LDL, cholesterol and triglyceride when 500mg/kg ethanolic extract of *P. zeylanica* was administered to hyper-lipidemic rabbits [30].

Wound healing activity

Wound healing activity of methanolic extract of *P. zeylanica* root reported in wistar albino rats [31]. A study investigated the wound healing activity of ethanolic root extract of *P. zeylanica* in wistar rats and found that the activity is due to the presence of phytochemicals such as terpenoids, alkaloids, flavonoids, saponins etc. and these

compounds are responsible for the wound healing activity of the plant [32]. Another study reported the evidence of oxidative stress in pathogenesis of non-healing ulcers. As the wound healing mainly depends on low level of oxidant so the antioxidant nature of the plant extract obtained from *P. zeylanica* helps in controlling the wound oxidative stress thus accelerating wound healing [33].

In-vitro studies in *Plumbago zeylanica*

P. zeylanica is grown and propagated mostly by seed cultivation, semi-ripe cuttings which are preserved with growth regulators. Due to the long time sprouting of seed in 21-30 days and the deterioration in germination rate by extended storage, traditional approaches for proliferation are problematic and less efficient, also the secondary metabolite content is very low. Hence, to minimize the growth time as well as to enhance the biomass and biochemical content of the plant, *in-vitro* cultivation of this plant is an efficient tool. A study reported the maximum shooting in MS media supplemented with 27.2 µM Adenine Sulphate + 2.46 µM IBA and rooting in MS media supplemented with 4.92 µM IBA [34]. Dohare *et al.*, observed maximum number of shoots in MS media supplemented with 1mg/l BA+ 1mg/l NAA and maximum number of roots in half strength MS media supplemented with 1mg/l IAA [35]. A report shows the maximum number of roots in MS media containing 0.1 mg/l NAA+ 1.5 mg/l Kinetin from nodal explants [36]. Similarly, another study reported that MS media containing 2mg/l BAP+ 0.2mg/l NAA showed the maximum number of shoots from nodal explants where as MS media containing 1mg/l IBA showed the maximum number of roots [37].

CONCLUSION

Medicinal plants are the prime source of effective conventional drugs for the treatment of different diseases. Herbal medicines have been used for the past decade due to their several pharmacological activities. They have provided opportunities to the researchers for future research and development in this field. *Plumbago zeylanica* is one of the important medicinal plants which have several pharmacological properties such as anticancer activity, antimicrobial activity, antioxidant activity, etc. Due to the medicinal importance of this plant, pharmaceutical industries do random sampling from the natural environment and there is a decrease in the population of *P. zeylanica* which make it an over-exploited plant. So there is a need of an alternative process for mass propagation of this plant. This review suggests that *P. zeylanica* shows various pharmacological actives against several diseases. It is an effective bioactive compound and has a great potential to be integrated into conventional medical practices for the treatment of various diseases. *P. zeylanica* is an important plant in herbal manufacturing but still there is a requirement of strong determination to fine an alternative process for mass proliferation of this plant. Using *in-vitro* methods at huge scale for development and successive ground plantations should be immeasurably valuable for the growing demands of *P. zeylanica*. Aim of this review is to bring attention towards importance of *Plumbago zeylanica* and its potential pharmaceutical activity for the development of new herbal formulations.

Source of Support: Nil.

Conflict of Interest: None Declared.

REFERENCES

- Mandavkar YD, Jalalpure SS. A comprehensive review on *Plumbago zeylanica* Linn. African journal of Pharmacy and Pharmacology African Journal of Pharmacy and Pharmacology. 2011; 5(25):2738-2747.
- Roy A, Bharadvaja N. Silver nanoparticles synthesis from pharmaceutically important medicinal plant *Plumbago zeylanica*. MOJ Bioequivalence and Bioavailability. 2017; 3(5):00046.

- Roy A, Attre T, Bharadvaja N. Anticancer agent from medicinal plants: A Review. New aspects in medicinal plants and pharmacognosy. JB Books Publisher, Poland, 2017.
- Kumar R, Kumar S, Patra A, Jayalakshmi S. Hepatoprotective activity of aerial parts of *Plumbago zeylanica* linn against carbon tetrachloride-induced hepatotoxicity in rats. International Journal of Pharmacy and Pharmaceutical Sciences. 2009; 1:171-175.
- Kapoor LD. Handbook of Ayurvedic Medicinal plants. CRC Press, London, 1990.
- Ming Y, Wang J, Yang J, Liu W. Chemical constituents of *Plumbago zeylanica*. Advanced Materials Research, 2011; 308-310:1662-1664.
- Arunachalam KD, Velmurugan P, Raja RB. Anti-inflammatory and cytotoxic effects of extract from *Plumbago zeylanica*. African Journal of Microbiology Research. 2010; 4(12):1239-1245.
- Budavari S, O'Neal M, Smith A, Heckelman P, Kinneary J. The Merck index: an encyclopedia of chemicals, drugs, and biologicals, 12th edn, Whitehouse Station, NJ: Merck & Co. Inc., 1996.
- Ahmad I, Aquil F. *In vitro* efficacy of bioactive extracts of 15 medicinal plants against ESBL-producing multidrug-resistant enteric bacteria. Microbiological Research, 2007; 162(3):264-275.
- Devi CK, Krishna DG. Pharmacognostic, phytochemical and biological study of *Plumbago zeylanica*. International Journal of Natural Products Research. 2012; 1(2):21-23.
- Banik B, Sarkar P, Sultana F, Saikia M, Dey A. *In-vitro* antimicrobial screening with phytochemical study of *Plumbago zeylanica* L. collected from two regions of Eastern Himalayas- A comparative study. International Journal of Phytopharmacy. 2014; 4(5):120-123.
- Shweta S, Dubey S. Antimicrobial Activity of Leaves Extract of *Plumbago zeylanica* Plant against Known Drugs. International Journal of Research Studies in Biosciences. 2015; 3(6):1-6.
- Kotecha M, Rao KS. Clinical evaluation of haridra & chitrak in the management of medoroga (obesity). Journal of Ayurveda. 2007; 1:226-28.
- Zarmouh MM, Subramaniam K, Viswanathan S, Kumar PG. Cause and effect of *Plumbago zeylanica* root extract on blood glucose and hepatic enzymes in experimental diabetic rats. African Journal of Microbiology Research. 2010; 4(24):2674-2677.
- Sunil C, Duraipandiyar V, Agastian P, Ignacimuthu S. Antidiabetic effect of plumbagin isolated from *Plumbago zeylanica* L. root and its effect on GLUT4 translocation in streptozotocin-induced diabetic rats. Food and Chemical Toxicology, 2012; 50(12):4356-63.
- Vishnukanta, Rana AC. Analgesic and anti-inflammatory activity of hydroalcoholic extract of *Plumbago zeylanica* leaf extract. Pharmacognosy Magazine, 2008; 15: S133-136.
- Sheeja E, Joshi SB, Jain DC. Bioassay guided isolation of anti-inflammatory & anti compound from *Plumbago zeylanica* leaf. *Pharmaceutical Biology*, 2010; 48:381-7.
- Dang GK, Parekar RR, Kamal SK, Scindia AM, Rege NN. Anti-inflammatory activity of phyllanthus emblica, *Plumbago zeylanica* & cyperus rotundus in acute models of inflammation. *Phytotherapy Research*, 2011; 25:904-8.
- Checker R, Sharma D, Sandur SK, Khanam S, Poduval TB. Anti-inflammatory effects of plumbagin are mediated by inhibition of NF- κ B activation in lymphocytes. *International Immunopharmacology*, 2009; 9:949-58.
- Napalchyal KS, Shinde S, Singh JP, Mishra DS. Clinical evaluation of Chitrakadi Churnav combined with the Kshar Vasti in the management of Amavata (Rheumatoid Arthritis). Journal of Ayurveda. 2013; 7(3):73-80.
- Zhao YL, Lu DP. Effects of plumbagin on the human acute promyelocytic leukaemia cells in vitro. Recent Activity Export, 2006; 14(2):208-211.
- Hiradeve S, Danao K, Kharabe V, Mendhe B. Evaluation of anticancer activity of *Plumbago zeylanica* Linn leaf extract. International Journal of Biomedical Research. 2010; 1(2):01-09.
- Sankara Aditya J VSPK, Naresh KL, Animisha M. *In-vitro* anti-cancer activities of few plant extracts against MCF-7 and HT-29 cell lines. International Journal of Pharma Sciences. 2013; 3(2):185-188.
- Li J, Li J, Cai G, Shen L, Lu F. Proapoptotic and Growth-inhibitory Effects of Plumbagin on Human Gastric Cancer Cells Via Suppression of Signal Transducer and Activator of Transcription 3 and Protein Kinase B. *Alternative Therapies, Health and Medicine*, 2017; 5382.
- Maniafu BM, Wilber L, Ndiege IO, Wanjala CC, Akenga TA. Larvicidal activity of extracts from three *Plumbago* spp against *A. gambiae*. Mem Inst Oswaldo Cruz, 2009; 104(6):813-817.
- Patil CD, Patil SV, Salunke BK, Salunkhe RB. Bioefficacy of *Plumbago zeylanica* (Plumbaginaceae) and *Cestrum nocturnum* (Solanaceae) plant Extracts against *Aedes aegypti* (Diptera: Culicidae) and- *Poecili areticulata*. Parasitol. Res., 2011; 108(5):1253-1263.

27. Vishnukanta, Rana AC. Evaluation of central nervous system activities of *Plumbago zeylanica* l. leaf extract. Pharmacologyonline, 2009; 2:575-585.
28. Vishnukanta, Rana AC. Evaluation of anticonvulsant activity of *Plumbago zeylanica* Linn leaf extract. Asian Journal of Pharmaceutical and Clinical Research. 2010; 3(1):76-78.
29. Sharma I, Gusain D, Dixit VP. Hypolipidaemic and atherosclerotic effects of plumbagin in rabbits. Indian Journal of Physiology and Pharmacology. 1991; 35:10-4.
30. Ram A. Effect of *Plumbago zeylanica* in hyperlipidaemic rabbits and its modification by vitamin E. Indian Journal of Pharmacology. 1996; 28:161-166.
31. Kodati DR, Shashidher B, Kumar GP. Evaluation of wound healing activity of methanolic root extract of *Plumbago zeylanica* L. in wistar albino rats. Asian Journal of Plant Science and Research. 2011; 1(2):26-34.
32. Jyothi VA, Fathima. Phytochemical evaluation & pharmaceutical screening of wound healing & antioxidant activity of *Plumbago zeylanica*. International Journal of Pharmacy & Technology. 2013; 5:5879-5891.
33. Kumar P, Udupa EGP, Sharan A, Singh R, Prasad Hk, Rao P. Effects of Limited Access Dressing In Chronic Wounds: A Biochemical and Histological Study. Indian Journal of Plastic Surgery. 2015; 22-28.
34. Selvakumar V, Anbudurai PR, Balakumar T. *In-vitro* propagation of the medicinal plant *Plumbago zeylanica* L through nodal explants. *In Vitro Cellular & Developmental Biology - Plant*, 2001; 37(2):280-284.
35. Dohare B, Jain K, Jain B, Khare S. Efficient micropropagation protocol for a valued endangered medicinal plant-chitrak (*Plumbago zeylanica* Linn.). International Journal of Current Research and Review. 2012; 4:21.
36. Dasgupta S, Reddy MN. Rapid direct root induction of *Plumbago zeylanica* Linn. European Journal of Experimental Biology. 2013; 3(5):447-451.
37. Chatterjee T, Ghosh B. Simple Protocol for Micropropagation and *in-vitro* conservation of *Plumbago zeylanica* L: An Important Indigenous Medicinal Plant. International Journal of Bio-resource and Stress Management. 2015; 6(1):068-075.

HOW TO CITE THIS ARTICLE

Roy A, Bharadvaja N. A review on pharmaceutically important medical plant: *Plumbago zeylanica*. Journal of Ayurvedic and Herbal Medicine 2017; 3(4):225-228.

An intelligent, adaptive, performance-sensitive, and virtual reality-based gaming platform for the upper limb

Ashish Dhiman¹  | Dhaval Solanki¹ | Ashu Bhasin² | Abhijit Das³ | Uttama Lahiri¹

¹Department of Electrical Engineering,
Indian Institute of Technology
Gandhinagar, Gandhinagar, Gujarat
382355, India

²Department of Neurology, All India
Institute of Medical Sciences, New Delhi
110029, India

³Department of Neurorehabilitation,
AMRI Institute of Neurosciences, Kolkata
700099, India

Correspondence

Ashish Dhiman, Department of Electrical
Engineering, Indian Institute of
Technology Gandhinagar, Gandhinagar,
Gujarat 382355, India.
Email: ashish.dhiman1@gmail.com

Funding information

Department of Science and Technology,
Ministry of Science and Technology,
Grant/Award Number:
RES/DST-SEED/EE/UL/201314-049

Abstract

Stroke is a leading cause of adult disability, characterized by a spectrum of muscle weakness and movement abnormalities related to the upper limb. About 80% of individuals who had a stroke suffer from upper limb dysfunction. Conventional rehabilitation aims to improve one's ability to use paralyzed limbs through repetitive exercise under one-on-one supervision by physiotherapists. This poses difficulty given the limited availability of healthcare resources and the high cost of availing specialized services at healthcare centers, particularly in developing countries like India. Thus, the design of cost-effective, home-based, and technology-assisted individualized rehabilitation platform that can deliver real-time feedback on one's skill progress is critical. This paper describes the design of a novel, multimodal, virtual reality (VR)-based, and performance-sensitive exercise platform that can intelligently adapt its task presentation to one's performance. Here, we aim to address unilateral shoulder abduction and adduction that are essential for the performance of daily living activities. We designed an experimental study in which six individuals who had chronic stroke (post-stroke period: >6 months) participated. While they interacted with our VR-based tasks, we recorded their physiological signals in a synchronized manner. Preliminary results indicate the potential of our VR-based, adaptive individualized system in the performance of individuals who had a stroke suffering from upper limb movement disorders.

KEYWORDS

physiology, stroke, upper limb, virtual reality

1 | INTRODUCTION

Global Burden of Disease estimates that nearly 15 million people suffer from stroke every year with a prediction that 80% of stroke events will occur in low-to-middle income countries such as India by 2050,^{1,2} making the incidence of stroke a public health issue. Stroke causes several disabilities such as loss of control on the contralesional side and loss of limb coordination and dexterity of hands. Research studies depict that 80% of stroke patients suffer from upper limb movement disorder, with only 20% achieving some functional recovery during the first 6 months of post-stroke.^{3–6} Movement disorder in the upper limb often adversely affects an individual's ability to independently perform activities of daily living, for example, self-feeding, dressing, bathing, and brushing the teeth, thereby making the affected individual dependent on caregivers with subsequently reduced community life. Often, execution of these tasks needs one's shoulder abduction

and adduction capability. With stroke, the abnormal joint torque often gets manifested as an inadequate shoulder abduction and adduction capability,⁷ which makes it difficult for them to carry out reaching tasks required in activities of daily living. Conventional rehabilitation aims to address such disorders through physical therapy,^{8,9} which has been promising for such patients for recuperating limb function. However, this needs one-on-one sitting with skilled clinicians and physiotherapists who can decide the right dosage of rehabilitation and timely access to specialized health care centers offering such services. For middle-income countries like India, limited availability of specialized healthcare resources, the high cost of availing specialized and private-owned services, and limited access to health care centers in rural areas are some of the main deterrents. Even when patients do receive rehabilitation, the upper limb receives scant attention, with a recent systematic review reporting that the average time spent on upper limb activities during a session is 0.9–7.9 min.¹⁰ Also, a perception of treatment regimen as rigid and immutable often leads to exhausting patients' capabilities and motivation.¹¹

Faced with these challenges, researchers have been investigating the use of technology-assisted platforms to deliver rehabilitation services that are intensive, quantitative, individualized, and cost effective. For example, investigators have used robot-assisted,^{12–15} computer-based,^{16–18} and wearable, sensor-based platforms¹⁹ to address rehabilitation needs for individuals with upper limb movement disorder. However, the robot-assisted and wearable, sensor-based platforms such as CyberGrasp, although powerful, are often costly and, in some cases, might pose safety issues for the patient. Thus, computer-based platforms using virtual reality (VR) have been studied for their potential use in rehabilitation. This is because VR offers several advantages, for example, proponents highlighted the capability of VR systems to contribute to repetitive task practice with variations that are often motivating, real-time feedback, safety, controllability, etc.^{9,20} Also, VR provides the flexibility to manipulate the rehabilitation paradigm, along with qualitative and quantitative feedback to the therapist and to the patient.²¹ This flexibility in designing a suitable rehabilitation paradigm is important for individualized rehabilitation that is critical, given the spectrum nature of the disorder. Thus, in our present research, we have designed a VR-based exercise platform targeting an individual's upper limb movement.

In the recent years, the use of VR in stroke rehabilitation has increased, for example, Broeren et al.²² developed VR-based 3D games to promote motor skills and pattern of arm movements of patients suffering from left arm paresis; Holden,²³ Saposnik et al.,²⁴ and Adams et al.²⁵ showed the importance of designing skill-specific meaningful activities in the VR environment for rehabilitation; Sucar et al.¹⁹ presented VR-based Gesture Therapy platform for upper limb rehabilitation; and Ballester et al.²⁶ showed the efficacy of the VR-based intervention in enhancing motor skills of the paretic limb in hemiparetic stroke patients. Also, researchers have used VR in conjunction with external peripherals, for example, Wii (Nintendo),²⁷ Kinect Sensor (Microsoft),²⁸ and haptic devices,²⁹ which add to delivering a feeling of immersion in the task environment, thereby making the task motivating.

The currently existing VR-based systems offer exercises that can monitor one's performance in a task. However, tasks are not designed to offer different levels of challenge within the VR environment to the users. Given the spectrum nature of the disorder with varying residual motor abilities in post-stroke, it is critical to individualize the exercise platform such that the task is effective in spite of the individual variability evident in patients with different stroke severities.^{30–32} One of the ways can be to design applications that are adaptive to individual capabilities by offering tasks of varying challenges based on individualized performance, similar to that practiced by expert clinicians. The estimation of patient's health condition while performing rehabilitation exercise is done by the clinician's expert eyes that are often subjective in nature and not quantitative. Literature studies indicate that various physiological signals showing cardiovascular, electrodermal activity, etc., are often considered as valuable health indicators to the physiotherapist.^{33–35} Further, it has also been shown that monitoring physiological indices including heart rate³⁶ and galvanic skin response³⁷ is crucial during exercise, which is always helpful for clinicians to understand the patient's physiological profile and their exercise stress level.³⁸ However, none of the currently existing VR-based systems have investigated the implications of such technology-assisted exercise on one's health as can be evident through the monitoring of physiological indices during exercise. Thus, given the criticality of monitoring the health status or the physiological profile of patient, particularly during rehabilitation exercise sessions, it would be beneficial to make the rehabilitation platform with physiology. With this rationale, in our proof-of-concept study, we have considered physiology as an offline analysis with our performance in a self-adaptive system.

1.1 | Contribution and objectives

The **main contribution** of our present work is the development of VR-based adaptive task platform coupled with a peripheral device such as haptic device. Our VR-based, haptic-enabled task platform can (a) offer tasks of varying challenges based on individualized performance and (b) provide an avenue to monitor one's health status through real-time

measure of physiological indices. The current paper focuses on three research objectives: (a) to develop a VR-based stroke rehabilitation platform equipped with force feedback facility, (b) to make the interactive system intelligent such that it can adapt to one's task performance ability by offering tasks of varying difficulty in a controlled manner, and (c) to understand the implications of such a system on an individual's task performance, namely, task progression, task completion time, performance errors, and performance score (PF) while doing a VR-based task. Additionally, we acquired their heart rate and galvanic skin response in a time-synchronized manner for subsequent offline analysis.

This paper is organized as follows. Section 2 describes the system design. Section 3 presents the experimental setup and the methodology used. Section 4 presents the results obtained in our experimental study. Finally, Section 5 summarizes the research findings, limitations of the current study, and the direction of our future research.

2 | SYSTEM DESIGN

Our system is composed of four modules: (1) VR-based task module, (2) physical interface module, (3) task switching rationale, and (4) physiological data acquisition module (Figure 1).

2.1 | VR-based task module

We designed the VR-based tasks using the Vizard software (marketed by Worldviz Llc.) and Google sketch-up (3D modeling program provided by Google). The VR-based tasks were of two different types, namely, (i) *Reaching* and (ii) *Coordination* tasks to trigger abduction and adduction movement of the shoulder joint. In order to facilitate repetitive practice as practiced by physiotherapists and mentioned in physiotherapy guidelines,^{30–32} we designed a repository of 48 templates of VR-based tasks (24 each for *Reaching* and *Coordination* tasks) distributed over 3 difficulty levels (DL1–DL3) to avoid monotony of practice. Also, severity of the stroke is one of the important factors that influences the needs and preferences of the individuals who had a stroke.³⁹ Hence, three difficulty levels were designed while performing the reaching and coordination movements as an initial approximation to make the task effective in spite of the individual variability. However, based on the rehabilitation paradigm, more difficulty levels can be designed.

2.1.1 | Design of VR-based reaching task

For the *Reaching* task, we designed park environments composed of static and dynamic obstacles (e.g., crates and birds, respectively) and target objects (e.g., balloons of different sizes, shapes, and colors) as shown in Figure 2(a). The balloons were located randomly throughout the park with variations in the surrounding environment. The task was to reach out with the help of tabletop-mounted haptic stylus (stylus tip shown as an arrow in Figure 2(a)) and puncture the balloons by avoiding both the static and dynamic obstacles within a specified duration. “Crate”-shaped static obstacles were placed in front of the balloons to increase the difficulty in reaching out the balloons. Any collision of the haptic stylus with an obstacle was counted as an error. The number of balloons (3, 6, and 9) to be punctured within a specified duration decided the task difficulty level (DL1, DL2, and DL3, respectively).

2.1.2 | Design of VR-based coordination task

A car navigation task was designed as the VR-based *Coordination* task. A navigation environment consisted of a car, a track, and dynamic obstacles in the form of pedestrians crossing the track and static obstacles as tree pots at the edge of

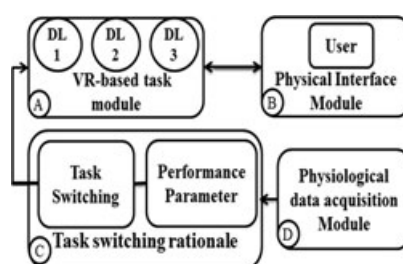


FIGURE 1 System design block diagram. VR = virtual reality, DL = Difficulty Level

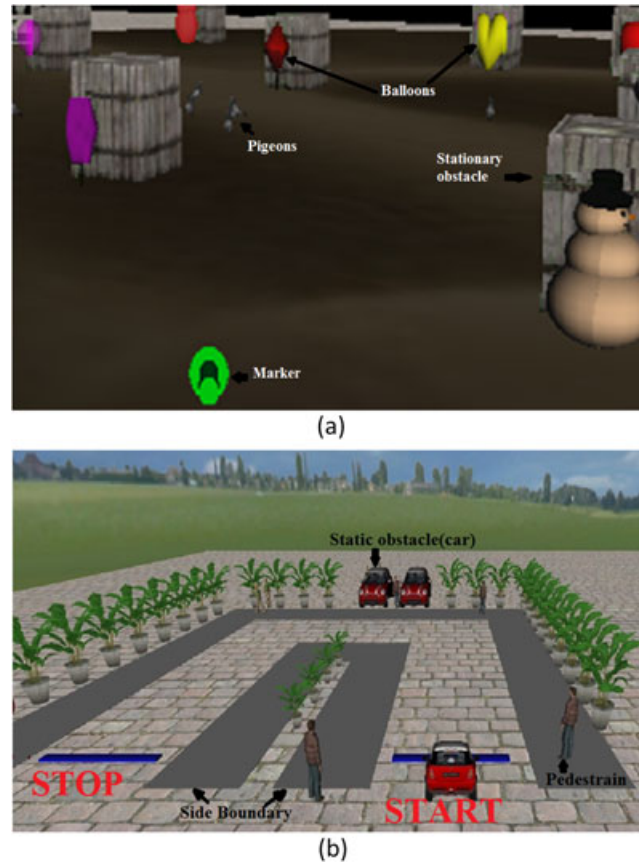


FIGURE 2 Screenshot of VR-based tasks in (a) reaching task and (b) coordination task [Colour figure can be viewed at wileyonlinelibrary.com]

the track (Figure 2(b)). A participant was asked to navigate the virtual car from a start line to stop line drawn on each track within a specified duration with the help of the haptic stylus while avoiding collision with the obstacles. The tracks were of different shapes to challenge the coordination skills of the participants. For example, DL1 task was kept fairly easy with a straight track. Tracks were curved to challenge the coordination skills for increased difficulty. The DL2 task has a semicircular track where the participant would need to continuously change the shoulder movements in order to follow the track and avoid collision with the pillars at the edge of the track. The DL3 has a semisquare track where the participant has to start from the start line, move through a straight track, change hand orientation, follow a straight track, change hand orientation, and finally follow a straight track to reach the end line of the track (Figure 2(b)).

2.2 | Physical interface module

Our participants interacted with the VR-based platform with the help of haptic device (“Phantom Omni” from Geomagic) as shown in Figure 3(a). The haptic device (integrated to the VR-based objects by dynamic linked library) provided tactile feedback to the participants during the interaction. We considered the haptic stylus movement along the x and y directions that maneuvered objects right/left and forward/backward, respectively, in the VR environment. This stylus movement corresponded to the patient's horizontal shoulder adduction/abduction.

In the *Reaching tasks*, one had to translate the haptic stylus on a physical workspace (x, y) of 30 mm × 70 mm for DL1, 60 mm × 70 mm for DL2, 90 mm × 70 mm for DL3 that accounted for an angular displacement range ($x(\min, \max), y(\min, \max)$) of 0° – 20° , 0° – 52° for DL1, $\{0^\circ$ – $55^\circ, 0^\circ$ – $52^\circ\}$ for DL2, and $\{0^\circ$ – $90^\circ, 0^\circ$ – $52^\circ\}$ for DL3 for completing each task (i.e., punching of all the balloons: 3 for DL1, 6 for DL2, and 9 for DL3). Thus, with the increase in difficulty level, the horizontal displacement (along x) varied from 30 mm to 90 mm, and angular displacement range extends from 0° (DL1) to 90° (DL3). Similarly, in the *Coordination tasks*, physical workspace (x, y) varies from (0 mm × 70 mm) for DL1, (60 mm × 70 mm) for DL2, (120 mm × 70 mm) for DL3, which accounted for an angular displacement range ($x(\min, \max), y(\min, \max)$) of $\{(0^\circ$ – $20^\circ), (0^\circ$ – $52^\circ)\}$ for DL1, $\{(0^\circ$ – $55^\circ), (0^\circ$ – $52^\circ)\}$ for DL2, and $\{(0^\circ$ – $120^\circ), (0^\circ$ – $52^\circ)\}$ for DL3

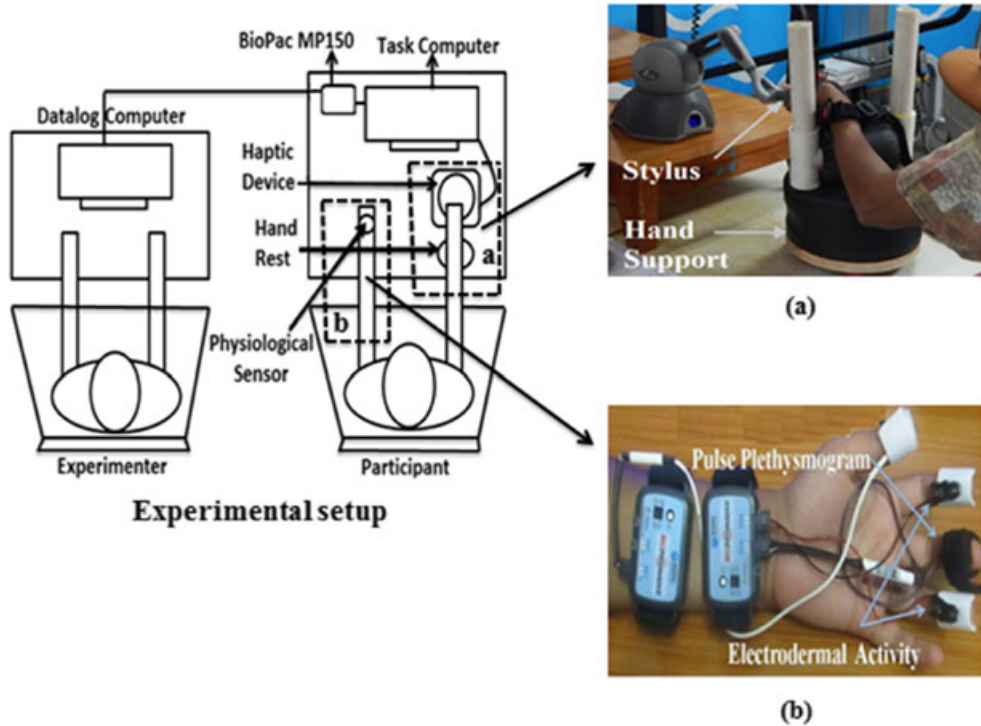


FIGURE 3 Block diagram of physical interface module. PPG = pulse plethysmogram; EDA = electrodermal activity. (a) A participant holding the stylus of the haptic device (b) Setup for sensors PPG and EDA [Colour figure can be viewed at wileyonlinelibrary.com]

for completing each task (i.e., traversing the VR track from the Start Line to the Stop Line). Thus, the horizontal displacement range extends from 0 mm to 120 mm with angular displacement from 0° to 120° , keeping the displacement along the z direction at 70 mm and 52° for all the cases. The idea of variability in range/angular movements was to encourage the participants to make shoulder movements while doing the tasks. Please note that our system was programmed to make one's shoulder movement on a restricted workspace based on the limited movement capability of our post-stroke participants. Although the participants came with some residual shoulder abduction and adduction capability, they faced difficulty in making large displacement of their hand through shoulder abduction/adduction. The patient's affected hand was tied to the haptic stylus with a Velcro belt to prevent it from falling, and his hand was provided with a hand support (Figure 3(a)). We hope that with the knowledge of performance and repeated exposure, this haptic device can be replaced with one that allows increased movement. Additionally, the haptic device was programmed to provide tactile feedback (approximately 1.6 N) to the user upon colliding with an obstacle (static or dynamic) in the VR environment. For our experimental study, we used Equations (1) and (2) and did not use the turret-like movement of the haptic stylus because we did not focus on the roll capability of one's wrist joint, as follows:

$$\Delta Z_{\text{DIST}} = W_Z^* (z + z_{\text{OFFSET}}) \quad (1)$$

$$\Delta X_{\text{DIST}} = W_X^* (x + x_{\text{OFFSET}}), \quad (2)$$

where ΔZ_{DIST} and ΔX_{DIST} represent the distance of the virtual car (for *Coordination task*) or haptic pointer (for *Reaching task*) traversed in the VR environment corresponding to the stylus displacement along z and x directions, respectively. W_Z and W_X are the weight factors used to render a smoother and controlled maneuver of the virtual car/haptic pointer along the track/park environment. The z_{OFFSET} and x_{OFFSET} are the offsets used for getting the coordinates of the virtual car/haptic pointer on a 0–1 scale. These weight factors and offset values were chosen as an initial approximation for our experimental study, and these can be changed in future. For the *Reaching task*, the weight factors and offset values were $W_Z (=0.2)$, $W_X (=10)$, and $z_{\text{OFFSET}} (=0)$, $x_{\text{OFFSET}} (=0)$, respectively. For *Coordination task*, the weight factors and offset values were $W_Z (=0.5)$, $W_X (=4.5)$, and $z_{\text{OFFSET}} (=0.5)$, $x_{\text{OFFSET}} (=0)$, respectively.

2.3 | Task switching rationale

Our VR-based system was adaptive to the participant's PF while the participant interacted with the VR-based tasks. Here, a cutoff score of 70% was used in tasks across different difficulty levels, similar to that used for robot-assisted rehabilitation

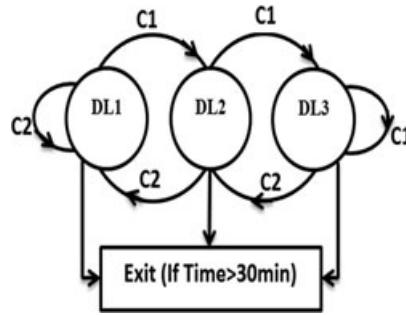


FIGURE 4 State machine representation

tasks, for outpatient clinics, and technology-assisted skill learning.^{40–42} The task switching module offered tasks (chosen randomly) of varying challenges (difficulty level) based on one's PF using a state machine representation (Figure 4).⁴³

If a participant's performance in a task belonging to a particular difficulty level was "Adequate" ($\geq 70\%$; condition C1), say DL1, then our task switching module offered tasks of higher difficulty (DL2), except for DL3, because DL3 was the highest difficulty level. If one's performance was "Inadequate" (condition C2), then the module switched to a task of lower difficulty level (except for DL1). Care was taken that different task templates were offered to the participants in order to avoid the feeling of monotony that the participant might experience while performing tasks. While offering tasks of varying difficulty levels, our algorithm also took care on the presentation of *Reaching (R)* and *Coordination (C)* tasks such that an *R* task of lower difficulty level was presented before an *R* task of higher difficulty level. Likewise was the case for *C* tasks. For example, if $1_R, 2_R, 3_R, 1_C, 2_C, 3_C$ represent *R* tasks and *C* tasks in DL1, DL2, and DL3, respectively, then, if the first task was 1_C ; this could be followed by 1_R for "Inadequate" performance or by 2_C (but not 2_R) for "Adequate" performance. This was because the first game offered was 1_C and not 1_R . The task repository was sufficient to offer tasks that ended on completion of 30 min of task performance, similar to that reported in literature.⁴⁴

2.3.1 | Computation of PF

PF was evaluated based on the time (T) taken by a participant to complete a given task and the number of collision errors (E) made by the participant while performing the task. Our algorithm calculated time fraction (TF) and error fraction (EF) from T and E . From our previous pilot study with age-matched healthy participants ($n = 6$; mean (sd) = 48 (18.23) years), we decided the threshold values of T and E as $T_{TH} = 50$ (DL1), 80 (DL2), 110 (DL3), respectively, for *Coordination*; $T_{TH} = 225$ (DL1), 525 (DL2), 825 (DL3) for *Reaching*; and $E_{TH} = 5$ for DL1–DL3 for both the tasks.

The TF is defined by Equations (3)–(5) as follows:

$$\text{If } T \leq T_{TH}, \text{ then } TF = 1 \quad (3)$$

$$\text{If } T_{TH} < T \leq 2 * T_{TH}, \text{ then } TF = \frac{2 * T_{TH} - T}{T_{TH}} \quad (4)$$

$$\text{If } T > 2 * T_{TH}, \text{ then } TF = 0 \quad (5)$$

Likewise was the case for EF .

Speed–accuracy trade-off is critical while taking an errorless (or reduced error) approach, particularly seen in exercises related to upper limb rehabilitation.⁴⁵ Keeping this trade-off in mind, as a first approximation, we have considered a weight distribution of 60% for EF and 40% for TF (Equation 6). Although both the speed and accuracy of task execution are important, we allotted more weightage to accuracy than the time taken, because performing a task accurately with less number of errors was considered as more important from the standpoint of rehabilitation. For example, if a individual who had a stroke was asked to brush his teeth, then satisfactory ability to complete brushing is more important than completing brushing unsatisfactorily within a shorter duration.

$$PF = 100 * ((0.6 * EF) + (0.4 * TF)) \quad (6)$$

2.4 | Physiological data acquisition module

While our participants interacted with VR-based systems, physiological signals, namely, pulse plethysmogram and electrodermal activity, were acquired by Biopac MP150 (from Biopac Systems Inc.) operated in wireless mode with sampling

frequency of 1,000 Hz. The acquired signals were processed to extract two physiological indices, for example, mean pulse rate (PR_{MEAN}) and tonic mean ($Tonic_{\text{MEAN}}$) synchronized with VR-based task propagation.⁴⁶ We chose these signals, because literature indicates the importance of monitoring these signals as possible window to one's health condition during exercise. Specifically, pulse rate, an important indicator of one's physical fitness, is often used by clinicians in deciding the exercise intensity.³⁴ Also, tonic activity has been reported to be used as a metric of post-stroke functional recovery.³⁵ Even for VR-based exercises, investigators have used pulse rate and galvanic skin response to provide additional user state information to the clinician, thereby helping in making informed decisions on the pacing of the VR-based exercises.³³

3 | EXPERIMENTAL SETUP AND METHODOLOGY

3.1 | Participants

We included six individuals who had a stroke (mean (SD) = 50 (8.50) years) in the study. These patients were recruited through referral from a local civil hospital where they were undergoing therapy. Once their questions related to our system were answered, their consent for voluntary participation in the study was sought. The participants' characteristics are shown in Table 1. The study was approved by the Institutional Ethics Committee.

3.2 | Inclusion and exclusion criteria

Patients aged 18–75 years and having a post-stroke period of >3 months were included in the study. Individuals with a history of recent surgery (<3 months) and having a skeletal injury or pace maker were excluded. Patients were also screened by a physiotherapist through the range of motion of horizontal abduction and adduction measures of their shoulder joint on the first day (Fday) to see whether it was less than the corresponding values for healthy adults as reported in the literature.³³

3.3 | Experimental procedure

The experimental setup (Figure 3) was composed of (a) a chair placed in front of a task computer mounted on a table along with a haptic device, (b) a real-time data acquisition module connected to a data logger computer through an Ethernet port, and (c) a height-adjustable hand support. We invited participants for multiple exposures. However, based on the availability, most of the participants were given 3 exposures on 3 different days. Our study required an involvement of approximately 1 hr on the Fday including the patient's screening by the physiotherapist, signing of the consent forms, task demonstration by the experimenter, and interaction with VR-based tasks. Subsequent exposures lasted for approximately 30 min of the VR-based task. Also, the experimenter informed the participant that he was free to quit from the study at any point if he felt uncomfortable. Although we designed *Reaching* and *Coordination* tasks that were of two different task types, in our present experimental study, we offered both the task types to the participants in each session. The motivation was to expose each participant to a mix of *Reaching* and *Coordination* tasks on each day, similar to that required in real-life scenarios while executing daily living activities. However, care was taken to offer *Reaching/Coordination* tasks while keeping an eye on the fact that the participant was exposed to a task of lower difficulty level before being exposed

TABLE 1 Participant characteristics

Participants	Age (Years)	Affected hand	Post-stroke period (Years)	Days of exposure	Range of motion (in degrees) (Shoulder)
P1 (m)	52	Left	1	3	Ab:0–40°, Ad:0–40°
P2 (m)	48	Right	2	4	Ab: 0–80°, Ad: 0–70°
P3(m)	52	Right	8	3	Ab:0–90°, Ad:0–80°
P4 (f)	35	Left	0.58	3	Ab:0–75°, Ad: 0–60°
P5 (f)	61	Left	1	3	Ab: 0–60°, Ad:0–60°
P6 (f)	52	Left	2	2	Ab:0–75°, Ad:0–60°

Note. m = Male; f = female; Ab = abduction; Ad = adduction.

to a task of higher difficulty level. After completion of each task, our system delivered audiovisual feedback, for example, “Good job!” and PF points (0–100).

4 | RESULTS

Here, we present the findings of the experimental study carried out with our VR-based task platform that offered tasks of varying difficulty levels based on one's task performance. Specifically, we report our observations on one's task performance measured between the Fday and the Lday of interaction in terms of (a) task progression, (b) task execution time, and (c) accuracy while performing the tasks (i.e., reduced errors). Additionally, we present the implications of VR-based tasks on the participants' physiological indices such as PR_{MEAN} and $Tonic_{MEAN}$.

4.1 | Effect of our VR-based system on participants' task progression

Figure 5 shows the task progression pattern of all the participants for both Fday and Lday along with the distribution of *Reaching* and *Coordination* tasks of varying challenges.

It can be seen from Figure 5 that the pattern of task progression changed considerably on the Lday compared with that on the Fday of interaction for almost all the participants. On the Lday, all the participants were able to reach the highest difficulty level (DL3). Although P2 and P4–P6 also could reach DL3 on the Fday, there was an improvement in performance. For example, although P2, P4, and P5 interacted with the same number of trials on Fday and Lday, the

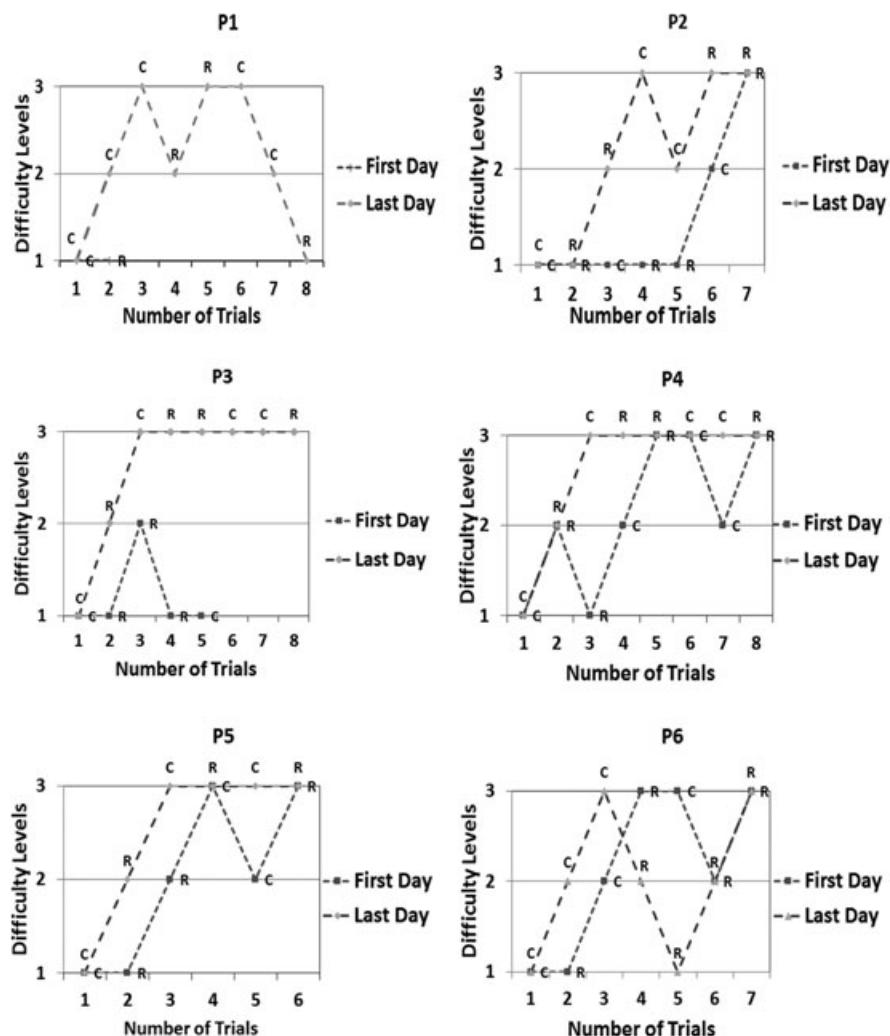


FIGURE 5 Comparative representation of task progression of P1–P6 between the first day and last day. R: Reaching; C: Coordination

number of trials in DL3 on Lday were more than that on Fday. However, for P6, although the number of trials in DL3 on Lday was less than that on Fday, there was a better controlled hand movement in terms of reduced collision error ($\Delta = 32\%$ for DL1, $\Delta = 44\%$ for DL2, $\Delta = 40\%$ for DL3) and improved performance in certain tasks of DL1 and DL2 ($\Delta = 57\%$ for *Coordination* task (DL1) and $\Delta = 14\%$ for *Reaching* task (DL2)).

4.2 | Effect of our VR-based system on participants' task execution time

Improvement in skill learning depends not only on one's capability of completing more task trials (as is evident from the task progression) but also on the ability to achieve improved task execution speed, without compensating for the PF. From Figure 6, we find that on an average, the *Reaching* tasks took more time than the *Coordination* tasks, possibly due to the fact that the *Reaching* tasks required the participants to search the targets distributed throughout the VR environment. Again, for both the *Reaching* and *Coordination* tasks, there was reduction in Task Execution Time from the Fday to the Lday across different difficulty levels, although by varying amounts. The decrease in task execution time indicates increase in speed of execution, which can be considered as an improvement in performance, provided that it comes with decrease in collision errors.

4.3 | Effect of our VR-based system on participants' performance errors

For improvement in skill, one needs to be able to do a task not only with increased speed but also with improved accuracy, that is, fewer collision errors in our case. Thus, we compared the average number of errors performed by the participants while interacting with our VR-based tasks for each difficulty level between the Fday and Lday. From Figure 7, we observe that the group average errors reduced for both the *Reaching* and *Coordination* tasks from Fday to Lday across all the difficulty levels, except DL3 of *Coordination* tasks (for which the error counts were comparable). In fact, the number of collision errors reduced from Fday to Lday for all the participants, except P5 for DL3. A possible reason behind this can be that P5 was hurrying to complete the tasks on the Lday, making more collision errors, as reported by the experimenter.

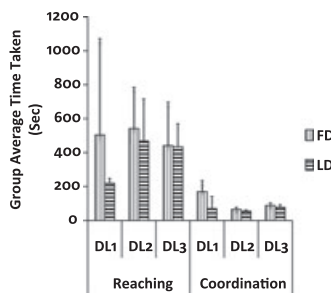


FIGURE 6 Group average interaction time of participants from (a) first day to (b) last day in reaching (R) and coordination (C) task with standard deviation bars. FD = First day, LD = Last day, DL = Difficulty Level

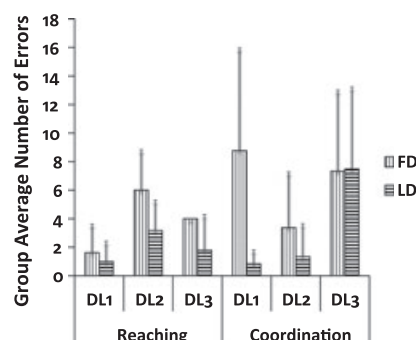


FIGURE 7 Group average number of errors of participants from (a) first day to (b) last day in reaching (R) and coordination (C) task with standard deviation bars. FD = First day, LD = Last day, DL = Difficulty Level

4.4 | Effect of our VR-based system on participants' PF

While our participants interacted with the VR-based tasks, our system computed their PF by using Equation (6). Figure 8 presents the group average PF (%) for both the *Reaching* and *Coordination* tasks on Fday and Lday across all the difficulty levels. There was an improvement in performance (%) from Fday to Lday for all the difficulty levels, except marginal change for DL3 trials of *Reaching* tasks and DL2 trials of *Coordination* tasks. A possible reason behind this can be that the participants took considerable time (that was comparable on Fday and Lday) to complete the DL3 trials of *Reaching* tasks and DL2 trials of *Coordination* tasks (Figure 6). Again, as far as the *Reaching* tasks were concerned, the group showed *Adequate* performance even on the Fday. However, that was not the case for the *Coordination* tasks (except DL2 tasks). A possible reason might be that the number of collision errors was more for the *Coordination* tasks on the Fday (except DL2 tasks) compared with the *Reaching* tasks (Figure 7). As reported by the experimenter, the participants were unable to make controlled maneuver of the VR cars with increased collisions with the walls at the side of the tracks on the Fday.

4.5 | Effect on PR_{MEAN}

Figure 9 shows the variation in the group PR_{MEAN} . On average, the PR_{MEAN} reduced on Lday than that on the Fday for both the *Reaching* and *Coordination* tasks and across all the difficulty levels, except *Reaching* tasks of DL1. This might infer that the participants were more comfortable while interacting with the *Reaching* and *Coordination* tasks on Lday than that on the Fday across the varying task difficulty levels. The increase in PR_{MEAN} on the Lday for the *Reaching* tasks, particularly for DL1, can be attributed to the fact that as the participants were excited to interact with our system (that most of the participants told the experimenter post our study) due to that they pressed themselves hard to perform well in the tasks, with the *Reaching* tasks requiring them to search the VR environment, accounting for maximum increase ($\% \Delta Performance_{Fday-to-Lday} = 37\%$ for DL1, 22% for DL2, -3% for DL3) in the % performance (Figure 8) for *Reaching* tasks.

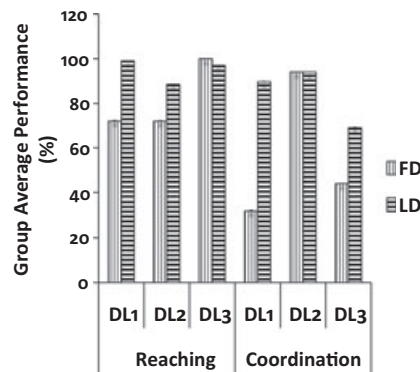


FIGURE 8 Group average performance score (%) of participants from first day to last day. Note that here, standard deviation is very less, therefore not visible. FD = First day, LD = Last day, DL = Difficulty Level

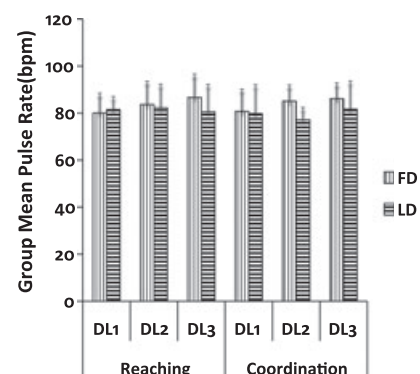


FIGURE 9 Group mean pulse rate of participants from (a) Fday to (b) Lday in reaching (R) and coordination (C) task with standard deviation bars. FD = First day, LD = Last day, DL = Difficulty Level

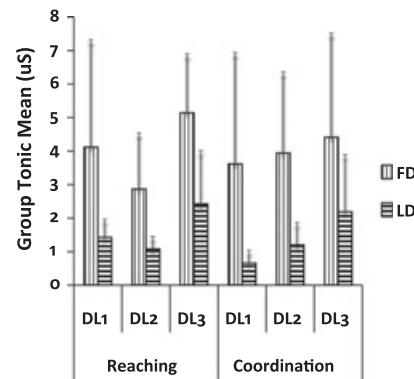


FIGURE 10 Group average tonic mean of participants from (a) first day to (b) last day in reaching (R) and coordination (C) task with standard deviation bars. FD = First day, LD = Last day, DL = Difficulty Level

4.6 | Effect on Tonic_{MEAN}

Similar to that for PR_{MEAN}, we find from Figure 10 that the participants' group Tonic_{MEAN} indicated that for both the *Reaching* and *Coordination* tasks across different difficulty levels, the participants were more comfortable on the Lday as compared to the Fday.

5 | DISCUSSION AND CONCLUSION

The results of our VR-based experimental study indicate that our system can have implications on one's task performance. Specifically, the preliminary results indicate that the performance improved in terms of task progression pattern, task completion time, performance errors, and PF while doing the VR-based tasks. Additionally, the results on the physiological indices, such as PR_{MEAN} and Tonic_{MEAN}, indicate that the participants' improvement in performance across tasks of varying difficulty from Fday to Lday was accompanied with themselves being more comfortable on the Lday as compared with the Fday. The decrease in pulse rate and tonic inhibition, which are valuable indicators of health condition during post-stroke recovery, indicates the potential of such a system to promote rehabilitation while contributing to improvement in health condition and physical fitness. However, in comparison with previous studies,³⁵ which speaks on tonic inhibition as an indicator of post-stroke functional recovery, similar trends (reduction in Tonic_{MEAN}) shown with our system indicate less stress level and further promote post-stroke recovery. Pioneering contributions^{13,17–26,32,47} used for stroke rehabilitation are powerful; often employ robots that are costly and heavy, posing financial and safety burdens on the patient; and, in some cases, have been reported to be limited in their ability to have a significant impact on one's daily living activities. Wearable sensors, such as CyberGrasp, used in stroke rehabilitation can provide force feedback to the user; besides being expensive, such wearable sensors often require uncomfortable mechanical plug for mounting on one's hand, making it inconvenient for use by patients. Additionally, these applications were not adaptive to offer tasks of varying challenges to the participants based on their individualized performance in a controlled manner and also do not provide individualized feedback on one's physiological profile, to the participants and also to the clinicians.

Our system is different compared with abovementioned pioneering studies, as users can repeatedly practice specific movements in a variety of environments in a controlled manner to achieve adequate performance; their physiological profile brings the added potential advantage to the physiotherapist, thereby providing a window into the quantitative estimates of one's health status. Passive device does not generate any power, is portable, cost effective, and suitable for home rehabilitation compared with clinical assistive devices having mechanical complexity. Our system also includes audiovisual feedback, as recent studies indicate that learning can be enhanced by visual and/or auditory cues.^{17,20}

Although the preliminary results are promising, our study had certain limitations. One of the limitations was a small sample size. However, the **main focus** of our paper was to design an individualized VR-based system that can offer *Reaching* and *Coordination* tasks (frequently used in daily living) to the participants as a technological platform rather than an intervention platform. In order to understand whether our system was operating as desired, we designed a preliminary experimental study with a small sample size and for a limited duration. However, in the future, for a full-fledged intervention study, we plan to carry out a longitudinal study with a larger number of participants. Another limitation of our study was the usage of the haptic device with a limited maneuvering capability. While considering the upper limb

movement capability of our participants, we used this haptic device with limited maneuverability. However, in the future, with longitudinal study, we plan to use haptic devices that have increased maneuverability.

With promising results of the present study, we hope that such a system can be used at least as a complementary tool in the hands of the therapists. Also, information on the real-time physiological measures of the patients during exercise can help the therapists to get an estimate of the physiological profile of the patients and accordingly decide the intervention paradigm. The low-cost portable exercise platform can reach households and thereby can be potent to bring in paradigm shift even in rural healthcare.

ACKNOWLEDGEMENTS

The authors are thankful to the Department of Science and Technology-Technology Interventions for Disabled and Elderly (DST-TIDE) program for partly supporting this research.

Conflict of Interest: The authors declare that they have no conflict of interest.

ORCID

Ashish Dhiman  <http://orcid.org/0000-0002-6168-7868>

REFERENCES

1. Feigin V. Stroke in developing countries: Can the epidemic be stopped and outcomes improved? *L Neurol*. 2007;6(2):94–97.
2. Turolla A, Dam M, Ventura L, et al. Virtual reality for the rehabilitation for the upper limb motor function after stroke: A prospective controlled trial. *J Neuroeng Rehabil*. 2013;10:85.
3. Langhorne P, Bernhardt J, Kwakkel G. Stroke rehabilitation. *Lancet*. 2011;377(9778):1693–1702. [https://doi.org/10.1016/s0140-6736\(11\)60325-5](https://doi.org/10.1016/s0140-6736(11)60325-5)
4. Ward NS. Stroke: mechanisms, stratification and implementation. *J Neurol Neurosurg Psychiatry*. 2013;84(3):237–8.
5. Pandian J, Sudhan P. Stroke epidemiology and stroke care services in India. *J Stroke*. 2013;15(3):128–134.
6. Santisteban L, Teremetz M, Blenton J-P, et al. Upper limb outcome measures used in stroke rehabilitation studies: A systematic literature review. *PLOS ONE*. 2016;11(50):e0154792. <https://doi.org/10.1371/journal.pone.0154792>
7. Ellis MD, Sukal-Moulton T, Dewald JPA. Progressive shoulder abduction loading is a crucial element of arm rehabilitation in chronic stroke. *Neurorehabil Neural Repair*. 2009;23(8):862–869.
8. Winstein CJ, Stein J, Arena R, et al. Guidelines for adult stroke rehabilitation and recovery. *Stroke*. 2016;47(6):e98–e169.
9. Levin MF. Emergence of virtual reality as a tool for upper limb rehabilitation: incorporation of motor control and motor learning principles. *Phys Ther*. 2015;95(3):415–425.
10. Kaur G, English C, Hillier S. How physically active are people with stroke in physiotherapy sessions aimed at improving motor function? A systematic review. *Stroke Res Treat*. 2012;(2012). Art. no. 820673.
11. Standen PJ, Threapleton K, Connell L, et al. Patients use of a home-based virtual reality system to provide rehabilitation of the upper limb following stroke. *Phys Ther*. 2015;95(3):350–359.
12. Zhang C., Li-Tsang CW, Au RK. Robotic approaches for the rehabilitation of upper limb recovery after stroke: a systematic review and meta-analysis. *Int J Rehabil Res*. 2016.
13. Squeri V, Masia L, Giannoni P, Sandini G, Morasso P. Wrist rehabilitation in chronic stroke patients by means of adaptive, progressive robot-aided therapy. *IEEE Trans Neural Syst Rehabil Eng*. 2014;22(2):312–325.
14. Zhang J, Cheah CC. Passivity and stability of human–robot interaction control for upper-limb rehabilitation robots. *IEEE Trans Robot*. 2015;31(2):233–245.
15. Maciejasz P, Eschweiler J, Hahn K, Troy A, Leonhardt S. A survey on robotic devices for upper limb rehabilitation. *J Neuroeng Rehabil*. 2014;11(3). <https://doi.org/10.1186/1743-0003-11-3>
16. Khor K, Chin P, Rahman H, et al. A novel haptic interface and control algorithm for robotics rehabilitation of stroke patients. Paper presented at: Haptics Symposium (HAPTICS), IEEE; 2014. p. 421–426.
17. da Silva Cameirão M, Bermúdez i Badia S, Duarte E, Verschure PF. Virtual reality based rehabilitation speeds up functional recovery of the upper extremities after stroke: a randomized controlled pilot study in the acute phase of stroke using the rehabilitation gaming system. *Restor Neurol Neurosci*. 2011;29(5):287–298.
18. Yeh S, Rizzo A, Zhu W et al. An integrated system: Virtual reality, haptics a technique (VHS) for post-stroke rehabilitation. Paper presented at: Proceedings of the ACM Symposium on Virtual Reality Software and Technology; 2005. p. 59–62.
19. Sucar L, Orihuela-Espina F, Velazquez R, et al. Gesture therapy: an upper limb virtual reality-based motor rehabilitation platform. *Trans Neural Syst Rehabil Eng*. 2014;22(3):634–643.
20. Soares AV, Woellner SS, Andrade CDS, et al. The use of virtual reality for upper limb rehabilitation of hemiparetic stroke patients. *Fisioter em Mov*. 2014;27(3):309–317.

21. Levin MF, Magdalon EC, Michaelsen SM, Quevedo AA. Quality of grasping and the role of haptics in a 3-D immersive virtual reality environment in individuals with stroke. *IEEE Trans Neural Syst Rehabil Eng*. 2015;23(6):1047–1055.
22. Broeren J, Georgsson M, Rydmark M, Sunnerhagen K. Virtual reality in stroke rehabilitation with the assistance of haptics and telemedicine. Paper presented at: 4th International Conference Disability, Virtual Reality and Associated Technologies; 2002; Hungary; p. 71–76.
23. Holden M. Virtual environments for motor rehabilitation: Review. *Cyberpsychol Behav*. 2005;8(3):187–211.
24. Saposnik G, Teasell R, Mamdani M, et al. Effectiveness of virtual reality using Wii gaming technology in stroke rehabilitation: A pilot randomized clinical trial and proof of principle. *Stroke*. 2010;41(7):1477–484.
25. Adams R, Lichter M, Krepkovich E, et al. Assessing upper extremity motor function in practice of virtual activities of daily living. *IEEE Trans Neural Syst Rehabil Eng*. 2015;23(2):287–96.
26. Ballester B, Nirme J, Duarte E, et al. The visual amplification of goal-oriented movements counteracts acquired non-use in hemiparetic stroke patients. *J Neuroeng Rehabil*. 2015;12(50). <https://doi.org/10.1186/s12984-015-0039-z>
27. Kumar D, Das A, Lahiri U, Dutta A. A human-machine-interface integrating low-cost sensors with a neuromuscular electrical stimulation system for post-stroke balance rehabilitation. *J Vis Exp*. 2016;12(110). <https://doi.org/10.3791/52394>
28. Kumar D, Aggarwal G, Sehgal R, Das A, Lahiri U, Dutta A. Engagement-sensitive interactive neuromuscular electrical therapy system for post-stroke balance rehabilitation—A concept study. Paper presented at: 2015 7th International IEEE/EMBS Conference on Neural Engineering (NER), IEEE; Montpellier, France. 2015.
29. Dhiman A, Solanki D, Bhasin A, et al. Design of adaptive haptic-enabled virtual reality based system for upper limb movement disorders: A usability study. Paper presented at: 6th IEEE International Conference on Biomedical Robotics and Biomechatronics (BioRob), IEEE; 2016; Singapore.
30. Luke LM, Allred RP, Jones TA. Unilateral ischemic sensorimotor cortical damage induces contralesional synaptogenesis and enhances skilled reaching with the ipsilateral forelimb in adult male rats. *Synapse*. 2004;54(4):187–99.
31. Löwquist E, Dreifaldt U. The design of a haptic exercise for post-stroke arm rehabilitation. Paper presented at: Proceedings of the 6th International Conference on Disability, Virtual Reality and Associated Technologies; 2006; Esbjerg, Denmark; p. 18–20.
32. Blennerhassett J, Dite W. Additional task-related practice improves mobility and upper limb function early after stroke: a randomised controlled trial. *Aust J Physiother*. 2004;50(4):219–224.
33. Rizzo A, Parsons TD, Lange B, et al. Virtual reality goes to war: A brief review of the future of military behavioral healthcare. *J Clin Psychol Med Settings*. 2011;18(2):176–187.
34. Warburton DE, Bredin SS, Horita LT, et al. The health benefits of interactive video game exercise. *Appl Physiol Nutr Metab*. 2007;32(4):655–663.
35. Clarkson AN, Huang BS, MacIsaac SE, Mody I, Carmichael ST. Reducing excessive GABA-mediated tonic inhibition promotes functional recovery after stroke. *Nature*. 2010;468(7321):305–309. <https://doi.org/10.1038/nature09511>
36. Jouven X, Empana J-P, Schwartz PJ, Desnos M, Courbon D. Heart-rate profile during exercise as a predictor of sudden death. *N Engl J Med*. 2005;352(19):1951–1958.
37. Cotter JD, Patterson MJ, Taylor NAS. The topography of eccrine sweating in humans during exercise. *Eur J Appl Physiol Occup Physiol*. 1995;71(6):549–554.
38. Thayer JF, et al. A meta-analysis of heart rate variability and neuroimaging studies: implications for heart rate variability as a marker of stress and health. *Neurosci Biobehav Rev*. 2012;36(2):747–756.
39. Ballester, BR, Badia SBI, Verschure PF. Including social interaction in stroke VR-based motor rehabilitation enhances performance: A pilot study. *PRESENCE: Teleoperators and Virtual Environments*. 2012;21(4):490–501.
40. Metzger J-C, Lambercy O, Califfi A, et al. Assessment-driven selection and adaptation of exercise difficulty in robot-assisted therapy: A pilot study with a hand rehabilitation robot. *J Neuro Engineering Rehabil*. 2014;11(154). <https://doi.org/10.1186/1743-0003-11-154>
41. Jack K, Mclean SM, Moffett JK, Gardiner E. Barriers to treatment adherence in physiotherapy outpatient clinics: A systematic review. *Man Ther*. 2010;15(3):220–228.
42. Young BM, Nigogosyan Z, Remsik A, et al. Changes in functional connectivity correlate with behavioral gains in stroke patients after therapy using a brain-computer interface device. *Front Neuroeng*. 2014;7(25). <https://doi.org/10.3389/fneng.2014.00025>
43. Booth T. Sequential machines and automata theory. Vol. 3. New York: Wiley; 1967.
44. Feys P, Coninx K, Kerkhofs L, et al. Robot-supported upper limb training in a virtual learning environment: a pilot randomized controlled trial in persons with MS. *J Neuroeng Rehabil*. 2015;12(60). <https://doi.org/10.1186/s12984-015-0043-3>
45. Krebs HI, Palazzolo JJ, Dipietro L, et al. Rehabilitation robotics: Performance-based progressive robot-assisted therapy. *Auton Robot*. 2003;15(1):7–20.
46. Kuriakose S, Lahiri U. Understanding the psycho-physiological implications of interaction with a virtual reality based system in adolescents with autism: A feasibility study. *IEEE Trans Neural Syst Rehabil Eng*. 2015;23(4):665–675.
47. Song Z, Guo S, Yazid M. Development of a potential system for upper limb rehabilitation training based on virtual reality. Paper presented at: 4th International Conference on Human System Interactions (HSI); 2011. p. 352–356.



Ashish Dhiman received the B.E. degree in Electronics and Communication Engineering from Panjab University, Chandigarh and completed Master's in Signal Processing & Digital Design from Delhi Technological University (Formerly Delhi College of Engineering) in 2011 and 2014, respectively. He worked as Junior Research Fellow in IIT Gandhinagar at Department of Electrical Engineering (Jan 2015- Jul, 16) and currently working as Software Algorithm developer in Continental Automotive Pvt. Ltd. at Bangalore. His research interest includes signal processing, image processing, pattern recognition, robotics and medical imaging.



Dhaval Solanki received M.Tech degree in Electrical Engineering from Indian Institute of Technology Gandhinagar, India. Currently, he is pursuing his Ph.D. degree in Electrical Engineering at Indian Institute of Technology Gandhinagar, India. His current research interests include signal processing, robotics, Virtual Reality for Stroke Rehabilitation and machine learning.



Ashu Bhasin received the Ph.D. degree in Neurology from All India Institute of Medical Sciences, New Delhi in 2011. Presently, she is working as Assistant Professor (DST-INSPIRE Faculty Fellow) in Department of Neurology, AIIMS, New Delhi, India. She is also honoured with Young Neurologist Scholarship from World Stroke Congress, awarded with Victor and Clara Young Scientist from World Stroke Congress and also awarded with Sewa Rattan Gold Medal from Global Economic Research Foundation in 2014.



Abhijit Das is a neurologist and received the DM Neurology degree from the SCTIMST, Trivandrum, India in 2009 & fellowship in Neurorehabilitation from Kessler Foundation/Rutgers University, USA in 2013. He is currently the Director of Neurorehabilitation at AMRI Institute of Neurosciences, Kolkata, India. His research area includes neurorehabilitation including virtual reality based motor/cognitive training, functional neuroimaging, non-invasive brain stimulation and eye tracking and physiology based brain-computer interfaces.



Uttama Lahiri received the Ph.D. degree from Vanderbilt University, Nashville, TN, USA, in 2011. Currently, she is an Associate Professor at the Indian Institute of Technology, Gandhinagar, India. Her research interests include Virtual Reality-based human-computer interaction, eye tracking and physiology based modeling techniques, human-robot interaction, adaptive intelligent techniques in cognitive research and robot-assisted surgical techniques.

How to cite this article: Dhiman A, Solanki D, Bhasin A, Das A, Lahiri U. An intelligent adaptive performance-sensitive virtual reality based gaming platform for upper limb. *Comput Anim Virtual Worlds*. 2018;e1800. <https://doi.org/10.1002/cav.1800>

Critical Review of Fabrication & Characterisation of Metal Matrix Composites

Ankit Tyagi*

Deptt. of Mechanical Engineering
Delhi Technological University
New Delhi, India

e-mail: tyagiankit10506@yahoo.com

Yashwant koli

Deptt. of Mechanical Engineering
Delhi Technological University
New Delhi, India

e-mail: yashwantkoli5@gmail.com

Abstract— Metal Matrix Composites (MMC) have been broadly considered as an alternative for the engineering materials due to their tremendous mechanical properties like high strength to weight ratio, wear resistance, high specific modulus, stiffness, damping capacity etc. Metal matrix composites specially aluminium based metal matrix composites (AMC) are getting popular day by day due to their diverse applications such as aerospace, aircrafts, automobile parts, electronic parts, turbine blades, golf clubs etc. Over the years, AMC have several operational, non-operational and functional uses in numerous engineering fields due to their better performance, environmental and economic benefits. AMC have been widely used in transportation industries because of less noise, lower fuel consumption and lower aerial emissions. It is now accepted that in order to empower the AMC substitution for engineering materials and to make it wide spread, there is a fascinating need to redesign the whole engineering system to reduce weight and volume.

Keywords - Composite; AMC; stir casting; fabrication.

I. INTRODUCTION

1.1 COMPOSITES

Composites comprise of reinforcement distributed in a continuous phase called matrix. The matrix develops its various characteristics from the geometry of constituents and the properties of interfaces between different constituents. Composite materials are typically characterized on the basis of the chemical and physical nature of matrix material and types of reinforcement. A composite is designed to show the characteristics of constituent materials.

Composite materials are getting popular due to their diverse applications and advantages over traditional engineering materials. Composites may have polymer matrix, ceramic matrix, metal matrix or carbon & graphite matrix and may have reinforcements in the form of particulates, whiskers, short fibers or long fibers. Hybrid composites consist of more than one reinforcing materials which helps attain desired properties. Composite materials have been widely used in aerospace, aircrafts, automobile parts, diesel piston, electronic parts, brake-shoes, turbine blades, golf clubs, armors of tanks, transportation industries etc.

1.2 PROPERTIES OF COMPOSITES

The properties of the composite materials depends predominantly on arrangement and type of reinforcements. Composites have many advantages over traditional engineering materials such as:

- Higher strength-to-density ratios
- Better fatigue resistance

- Higher strength
- Higher stiffness-to-density ratios
- Better wear resistance
- Better elevated temperature tolerance properties
- Lower creep rate
- Lower coefficients of thermal expansion

1.3 TYPES OF COMPOSITES BASED ON MATRIX MATERIAL

1.3.1 Polymer Matrix Composites (PMC)

Polymers can be ideally used as matrix materials as they possess good mechanical properties, can be processed easily and have light weight. High temperature synthetic materials are extensively used in aeronautical applications. Thermosets and thermoplastics are two different kinds of polymers used mainly. Polymeric materials have a tendency to degrade when they are exposed to elevated temperatures above 300°C. Hence Most of the PMC operate at temperatures below 300°C.

1.3.2 Ceramic Matrix Composites (CMC)

Ceramic matrix composites (CMC) have been established to overcome the drawbacks of monolithic ceramics such as intrinsic brittleness and lack of reliability of ceramics. CMC are used in place of heavy super alloys in order to reduce the weight of components. CMC have been widely used in gas turbines for power plants, fusion reactor first wall, heat shields for space vehicles, heat treatment furnaces, aircraft brakes etc.; but still they have limited application due to high cost, lack of suitable reinforcements lesser lifetime and difficulties in processing.

1.3.3 Carbon and Graphite matrix composites (CGMC)

Carbon and graphite have high temperature friendly materials with their rigidity and strength that are not affected by temperature ranges up to 2300°C. They can be fabricated through chemical vapor deposition of pyrolytic carbon.

1.3.4 Metal Matrix Composites (MMC)

MMC are made by scattering of reinforcing material into a metal matrix. Matrix is characteristically a lighter metal such as magnesium, titanium or aluminium which provide yielding support for the reinforcement. Cobalt and cobalt-nickel alloy matrices are generally used for high temperature applications. The reinforcing particles increase physical properties such as wear resistance, thermal conductivity, friction coefficient etc. of the matrix material. The reinforcing particles may have continuous or discontinuous phase in the metal matrix composites.

MMC possess diverse characteristics over conventional polymer matrix composites such as:

- MMC are resistant to fire
- They are resistant to radiation
- They are Damp proof
- They can function in wider range of temperatures
- They have better electrical and thermal conductivity

1.4 ALUMINIUM BASED METAL MATRIX COMPOSITES

Among MMC, aluminium matrix composites (AMC) are getting popular day by day and finding numerous applications. In AMC one of the constituent is aluminium based alloy known as matrix phase and other constituent is reinforcement, which is generally a ceramic such as SiC, Si₃N₄, TiC, BN, B₄C and Al₂O₃ are most commonly used. AMC properties can be tailored by varying the constituents and their volume fraction. Over the years, AMC have several operational, non-operational and functional applications in numerous engineering fields due to their better performance, environmental and economic benefits. AMC are being widely used in transportation industries because of less noise, lower fuel consumption and lower aerial emissions. With increasing environmental rules & regulations to enhancing fuel economy and efficiency, use of AMC in transport industries will be appropriate option in upcoming years. It is now accepted that in order to empower the AMC substitution for engineering materials and to make it wide spread, there is a fascinating need to redesign the whole engineering system to increase further weight and volume savings. AMC can be categorized into four types based on the type of reinforcement.

1.4.1 Particle reinforced Aluminium Matrix Composites (PAMC)

PAMC contain equiaxed ceramic reinforcements having aspect ratio less than 5. Ceramic reinforcements are usually oxides, borides or carbides (Al₂O₃, TiB₂ or SiC) and are present in metal matrix by volume fraction of less than 30%, when used for wear resistance and structural application. In general, PAMC can be fabricated either by solid state or liquid state fabricated processes. PAMC are least expensive when compared with CFAMC. Mechanical properties of PAMC are lower as compared to whisker/continuous fiber/ short fiber reinforced AMC but there properties are far superior to unreinforced aluminium alloys. They are isotropic in nature and can have many applications in forming operations such as rolling, extrusion and forging.

1.4.2 Short fiber and whisker reinforced Aluminium Matrix Composites (SFAMC)

SFAMC contain reinforcements having an aspect ratio greater than 5, but they are not continuous fiber. Most popular AMC is Short alumina fiber reinforced in aluminium matrix composites which is used in pistons. Short fiber reinforced composites are fabricated by using squeeze infiltration process, while Whisker reinforced composites are fabricated either by powder metallurgy (PM) process or by infiltration process. Mechanical properties of whisker reinforced composites are superior than short fiber reinforced composites. However; usage of whiskers as reinforcements in AMC is restricted due to their apparent health hazards. Short fiber reinforced AMC have characteristics of continuous fiber and particle reinforced AMC.

1.4.3 Continuous Fiber-reinforced Aluminium Matrix Composites (CFAMC)

CFAMC are continuous fibers of SiC, alumina or carbon with a diameter less than 20µm. AMC having fiber volume fraction of about 40% are fabricated by squeeze infiltration process. Recently CFAMC with 60 vol% alumina fiber (continuous fiber) reinforced composites with an ultimate tensile strength and elastic modulus of 1500 MPa and 240 GPa respectively have been fabricated by 3M corporation. These composites were fabricated by using pressure infiltration process.

1.4.4 Mono Filament reinforced Aluminium Matrix Composites (MFAMC)

Monofilaments are generally fabricated by chemical vapor deposition (CVD) of either Boron carbide or SiC into a core of Tungsten wire or of carbon fiber. Bending flexibility of monofilaments is less as compared to multi filaments. Diffusion bonding technique is often used to fabricate mono filament reinforced composites and is restricted to super plastic forming aluminium alloy matrices.

1.5 MANUFACTURING OF AMC

Fabrication techniques help in governing microstructure behavior, interfacial bond etc. in the composites Metal matrix composites specially aluminium based MMC can be fabricated by various techniques such as:

1.5.1 Solid State Processing

1.5.1.1 Powder Metallurgy (PM)

Mixing powder of ceramic whisker particle/short fiber in aluminium alloy is a valuable technique for the fabrication of AMC. Blending can be processed in dry or in liquid suspension. Blending generally have cold compaction followed by degassing and high temperature consolidation step such as extrusion. PM processed AMC, contain oxide constituent ranging from 0.05 to 0.5 depending on powder and processing conditions. These fine oxide particles have a tendency to act as a dispersion-strengthening agent and has strong influence predominantly during heat treatment on the matrix properties.

1.5.1.2 DIFFUSION BONDING PROCESS

Diffusion bonding technique is often used to fabricate mono filament reinforced composites. The technique is cumbersome and distribution of homogeneous fiber is difficult. The process is also not appropriated to fabricate complex shapes and components.

1.5.2 Liquid State Processing

1.5.2.1 STIR CASTING

In this process hard ceramic particles are fused into the molten aluminium melt and allowing the mixture to solidify. A good wettability is created between reinforcement and the molten aluminium alloy melt. Stir-casting technique is most simplest and economical fabrication process used for fabrication of AMC. The technique includes the addition of pre-heated reinforcing particles into the vortex of molten aluminium alloy created by the mechanical stirrer. After proper mixing of matrix and reinforcement, composite melt is casted into a suitable mould to get the desired shape of the AMC.

1.5.2.2 INFILTRATION PROCESS

Liquid aluminium alloy is intruded into the interstices of continuous fiber/whisker or short particle to fabricate AMC. Depending on the nature of reinforcement infiltration can be done with or without pressure application. AMC having volume fraction ranging from 10 to 70% of reinforcement can be fabricated using different infiltration techniques. In order to maintain its shape and integrity, it is necessary to use alumina and silica based mixtures as binder. During fabrication of

AMC by infiltration process may have porosity as casting defect in casted samples.

1.5.2.3 SPRAY DEPOSITION

Spray deposition process may have two different classes, depending on whether the droplet stream is fabricated from a molten bath or by continuous serving of cold metal into a region of rapid heat injection. The spray deposition has been extensively explored for the fabrication of AMC by injecting ceramic particle/short fiber/ whisker into the spray. There is inhomogeneous distribution of ceramic particles in fabricated AMC. The AMC produced by spray deposition process may possess porosity as casting defect in casted samples.

1.6 CHARACTERIZATION OF AMC

AMC are characterized in order to reveal microstructure, chemical composition etc. Distinct techniques may be used for observing microstructural constituents of fabricated metal matrix composites such as optical microscopy, Scanning electron microscopy (SEM), X-ray diffraction technique (XRD), Electron probe micro analyzer (EPMA), Energy dispersive X-ray spectroscopy (EDS), Energy dispersive analysis of X-ray (EDAX) etc.

1.6.1 Optical Microscopy

Optical microscopy technique is used to analyze the magnified image of microstructure of AMC. The optical microscopy is carried out using a metallurgical microscope. The microstructural specimens of AMC are prepared via standard polishing process and etching by a suitable etching agent. In this technique magnified images are detected and images are captured digitally.

1.6.2 Scanning Electron Microscopy–Energy Dispersive Analysis of X-Rays

SEM technique is used to generate variety of signal on the surface of fabricated composites. In this technique high resolution image of microstructure, chemical composition etc. is generated. EDAX technique is used for chemical characterization and elemental analysis of fabricated composites. This technique follows the fundamental principal that each element has a unique set of peaks on electromagnetic emission spectrum.

1.6.3 X-Ray Powder Diffraction Technique (XRD)

XRD technique is used for phase identification of crystalline material along with information about unit cell. This technique is used to detect constituent particles present in fabricated composites.

II. LITURATURE ANALYSIS

2.1 FABRICATION OF METAL MATRIX COMPOSITES

MMCs especially aluminium based MMCs have distinct techniques for fabrication of composites. Fabrication of MMCs is important in determining microstructure behavior, interfacial bond, defects such as misrun, porosity etc. in MMCs. Different fabrication techniques such as powder metallurgy, squeeze casting, diffusion bonding, spray & rheo casting, Stir casting etc. are used in fabrication of MMCs [21].

It is observed Al alloy reinforced with SiC using stir casting as fabrication process, porosity around SiC particles is observed [2, 3, 19] which can be reduce by preheated of mold [3]. It is researched Al alloy reinforced with groundnut shell ash & SiC using Stir casting, continuous phase of metal matrix along with dispersed reinforcement is observed [4]. It is investigated Mg MMCs reinforced with B₄C fabricated with powder metallurgy techniques using sintering cycle, clustering of B₄C particles in the MMCs is observed [6]

Al6082 reinforced with graphite [7], Al alloy reinforced with SiC [9], fabricated with stir casting techniques, clustering & non uniform distribution of reinforcement is observed [7, 9]. A356 reinforced with SiC, fabricated with Compo casting, porosity throughout the specimen is observed as a defect in MMCs [10]. Al alloy [A536, 6061] reinforced with SiC, fabricated with gravity casting, porosity & interdendritic micro shrinkage along with clustering of reinforcement is observed as defects in MMCs [12]. Al alloy reinforced with breadfruit seed hull ash fabricated with stir casting, density dislocation defect is observed in MMCs [13]. LM6 aluminium alloy reinforced with fly ash fabricated with stir–squeeze casting & gravity casting, no porosity & discontinuity is observed during stir–squeeze casting in metal matrix composites [16].

1) 2.2 STIR CASTING TECHNIQUE

Among distinct fabrication techniques stir casting is used for manufacturing MMCs because of its simplicity, low cost in fabrication and flexibility in production. In stir casting, reinforcing particles are mixed with molten metal matrix with the help of stirrer. After mixing molten metal matrix is pour into preheated mold. In order to fabricate MMCs distinct parameters are involved such as stirrer type, stirring time, pouring temperature, mold type, preheat of reinforcement, preheat of mold etc. Stirrer can be of stainless steel [10], coated with graphite [13] or BN coating [1], Mild steel [3, 9].

Stirring speed is important for enhancing wettability and controlling flow pattern of MMCs.

Stirring speed varying from 200-400 rpm [4, 7, 8, 10, 12, 15, 17], 500-800rpm [1, 2, 3, 9, 13, 16, 19, 20]. But optimum stirring speed ranging from 300-600rpm [24]. Stirring time helps in uniform distribution of reinforcement in MMCs along with proper bonding. Stirring time varying from 5 min. [4, 13, 16], 10 min. [2, 3, 5, 7, 9, 17, 19], 20 min [12, 15] etc. in order to maintain proper uniformity [24].

Reinforcement preheat temperature helps in enhancing wettability and removing moisture content from the reinforcement [1]. Preheat temperature of reinforcement varies from material to material used as reinforcement. Reinforcement such as fly ash 150-650°C [1, 16], SiC 800-1100°C [2, 3, 9, 10], Graphite 500°C [7] etc. have preheated temperature. Pouring temperature is used for determining grain orientation & structure of fabricated MMCs. Pouring temperature of distinct MMCs varies from 700-900°C. Mold governs the shape & size of fabricated MMCs. Mold may be permanent mold [5, 7, 12, 15], metallic mold [1, 2, 4, 8], Die mold [3, 16], sand mold [4, 9] with shape of cylindrical [2, 3, 5, 15], rectangular [1], circular [8], cast bar [12] etc. Preheat temperature of mold reduces porosity, misrun etc. in MMCs. Preheat temperature of mold varies 250°C [5, 7], 350°C [12, 15], 500°C [13] etc.

2) 2.3 CHARACTERIZATION OF FABRICATED METAL MATIX COMPOSITES

Fabricated metal matrix composites are characterized in order to reveal microstructure, chemical composition etc. of composites. Distinct techniques are used for observing microstructural constituents of fabricated metal matrix composites such as optical microscopy, Scanning electron microscopy (SEM), X-ray diffraction technique (XRD), Electron probe micro analyzer (EPMA), Energy dispersive X-ray spectroscopy (EDS), Energy dispersive analysis of X-ray (EDAX) etc.

It is observed from optical microscopy, SEM, EPMA, XRD techniques that fly ash particles reinforced with Al alloy shows shape of untreated fly ash particles are spherical with presence of Al, Si, O whereas treated fly ash particles have rod shaped with distinct aspect ratio, presence of Si, Al, O, C and conversion of SiO₂ into SiC is obtained in metal matrix composites [1]. It is investigated from optical micrograph that HE-30 Al alloy reinforced with SiC shows presence of porosity with uniform distribution of reinforcing particles is obtained in metal matrix composites [2]. It is researched from EDAX, EDX test sample that SiC reinforcement mixed with Al2024 shows chemical composition of fabricated metal matrix composites as shown in the table 2.3 [3].

Table 2.3 Chemical composition of 10 %wt. Al-SiC composites [3]

S.No	Element	Weight %
1	Caco3	24.19
2	SiO2	7.67
3	MgO	0.87
4	Al	64.79
5	Cu	2.47

It is investigated from SEM, EDS, XRD techniques that Mg MMCs reinforced with boron carbide (B_4C) shows uniform distribution of boron carbide (B_4C) with clustering particles, good interfacial bonding and presence of Al_2O_3 , MgO , MgB_2 in the composites samples [6]. It is observed from SEM, XRD, and test that Al6082 reinforced with graphite shows large impurities, non-uniform distribution and clustering of graphite particles at some places. The microstructures of MMCs shows inter-dendritic network of aluminium silicon eutectic. XRD results also reveal elements such as Al, C, Si peaks are present in fabricated MMCs [7]. It is investigated from metallurgical microscope that Al alloy reinforced with SiC shows at some location there are clustering of particles and without SiC particles inclusion when stirring process is not applied [9].

It is analyzed from optical microscopy that A356 alloy reinforced with SiC analysis perimeter (J. m), aspect ratio, sphericity, SiC area percentage and count. It also shows presence of porosity as isolated particles [10]. It is observed from optical microscopy that Al alloy reinforced with SiC shows plastic deformation is helpful in improving homogeneity of reinforcement [11]. It is investigated from Optical microscopy, SEM equipped with EDX & WDX that Al alloy (A536 & AA6061) reinforced with SiC shows presence of many phases such as primary, α -Al, SiC particles and eutectic structures. It is also observed that porosity & inter dendritic micro shrinkage are main defects in metal matrix composites [12].

It is analyzed from XRD, SEM/EDS, XRF (X-ray fluorescent) that Al-Si-Fe alloy reinforced with breadfruit seed hull ash particulates shows uniform distribution of reinforcement particles in Al alloy. XRF results shows chemical composition of breadfruit seed hull ash, while XRD shows count of various element present in the sample [13]. It is observed from optical microscopy and SEM that Al 6063, Al 6061 and Al 7072 matrix alloy reinforced with SiC shows non uniform distribution, clustering and agglomeration of SiC particles in metal matrix composites. There are many phases observed in microstructure such as Mg_2Si , Cu_2Si_6 , Al_5Mg_8 , Al_3Fe , Al_2Cu , and Al_3FeSi [14]. It is investigated from optical microscopy that Al6063 alloy reinforced with SiC shows uniform distribution of reinforcement and good homogeneous dispersion of SiC particles is observed in metal matrix composites [15]. It is analyzed from optical micrograph that LM6 Al alloy reinforced with fly ash shows uniform distribution, good retention of reinforcement, without any porosity, voids and discontinuities in MMCs. There are agglomeration of fly ash particles at some location in composites. It is also observed that there are good interfacial bonding between metal matrix and reinforcement particles in MMCs [16]. It is observed from metallurgical microscope that Al6061-SiC & Al7075- Al_2O_3 shows fairly uniform

distribution of reinforcement and homogeneity of fabricated composites [17].

It is investigated from metallographic examination that Al356 alloy reinforced with SiC shows non uniform distribution of reinforcement with agglomerations of particles at some location is observed. It is revealed that some particles have polygonal shape with sub angular edges and other have granular shape with aspect ratio of 1 [18]. It is observed from SEM that Al alloy reinforced with SiC shows porosity and clustering of reinforced particles is observed in metal matrix composites [19]. It is investigated from optical microscope & SEM that Al6061 alloy reinforced with SiC shows due to crack initiation and growth in composite matrix, there is fracture of coarse particles reinforced metal matrix composites [20].

III. CONCLUSION

It is observed & researched that powder metallurgy cause fracture damage to reinforcement & are expensive as reinforced particles required in this process is in powder form. Squeeze casting cause severe damage to reinforcement & moderate expensive with less or little porosity is observed in MMCs [23]. Stir casting cause less damage to reinforcement, flexible, economical and not restricted to shape & size, but porosity with non-uniform distribution of reinforcement is observed in MMCs [2, 3, 5, 9, 18, and 23]. Stir-Squeeze casting cause less or no damage to reinforcement and no or little porosity with uniform distribution of reinforcement in MMCs [16]. The main of this review paper is to establish an understanding of fabrication and characterization of MMCs.

REFERENCES

- [1] Ajit Kumar Senapati, R. I. Ganguly, R.R. Dash, P. C. Mishra and B. C. Routra, " production, characterization and analysis of mechanical properties of newly developed novel aluminium-silicon alloy based metal matrix composites", *Procedia Materials Science* 5 (2014) 472-481.
- [2] Pradyumna Phutane, Vijay Kumar S. Jatti, Ravi Sekhar and T. P. Singh, "Synthesis and characterization of SiC reinforced HE-30 Al alloy particulate MMCs", *International Journal of Engineering and Technology (IJET)* Vol. 5 No. 3 jun-jul 2013 ISSN: 0975-4024.
- [3] N. Subramani, M. Balamurugan and K. Vijayaraghavan, "Mechanical behavior of Al-SiC composites prepared by stir casting method", *International Journal of Innovation Research in Science, Engineering and Technology*, Vol. 3 Issue 3, March 2014.
- [4] Kenneth Kanayo Alanema, Michael Oluwatosin and Adebimpe A. Awe, "Microstructure, mechanical and fracture properties of groundnut shell ash and silicon carbide dispersion strengthened aluminium matrix composites", *Journal of King Saud University- Engineering Sciences* (2016).
- [5] Pardeep Sharma, Dinesh Khanduja and Satpal Sharma, "Parametric study of dry sliding wear of aluminium metal

- matrix composites by response surface methodology”, *Materials Today: Proceeding 2* (2015) 2687-2697.
- [6] L. F. Guleryuz, S. Ozan, D. Uzunsoy and R. Ipek, “An investigation of the microstructure and mechanical properties of B₄C reinforced PM magnesium matrix composites”, *Powder Metallurgy and Metal Ceramic*, Vol. 51, Nos. 7-8, November, 2012.
- [7] Pardeep Sharma, Satpal Sharma and Dinesh Khanduja, “A study on microstructure of aluminium matrix composites”, *Journal of Asian Ceramic Societies 3* (2015) 240-244.
- [8] Mohammed Imran, A.R. anwar Khan, Sadananda Megeri and Shoaib sadik, “Study of hardness and tensile strength of aluminium-7075 percentage varying reinforced with graphite and bagasse –ash composites”
- [9] Manoj Singla, D Deepak Dwivedi, Lakhvir Singh, Vikas Chawla, “Development of Aluminium Based Silicon Carbide Particulate Metal Matrix Composite”, *Journal of Minerals & Materials Characterization & Engineering*, Vol. 8, No.6, 2009, pp. 455-467.
- [10] S. Naher, D Brabazon and L Looney, “Development and Assessment of a New Quick Quench Stir Caster Design for the Production of Metal Matrix Composites”, *Journal of Material Processing Technology*, Vol. 166, 2004, pp. 430-439.
- [11] S. Das, R. Behera, A. Datta, G. Majumdar, B. Oraon, G. Sutradhar, “Experimental Investigation on the Effect of Reinforcement Particles on the Forgeability and the Mechanical Properties of Aluminum Metal Matrix Composites”, *Materials Sciences and Applications*, 2010, pp. 310-316.
- [12] W. Zhou, Z. M. Xu, “Casting of SiC Reinforced Metal Matrix Composites”, *Journal of Materials Processing Technology*, Vol. 63, 1997, pp. 358-363.
- [13] C. U. Atuanya, A. O. A. Ibhaddode, I. M. Dagwa, “Effects of breadfruit seed hull ash on the microstructures and properties of Al-Si-Fe alloy/breadfruit seed hull ash particulate composites”, *Results in Physics 2*, 2012, pp. 142–149.
- [14] A. Chennakesava Reddy and Essa Zitoun, “Matrix Al-alloys for Silicon Carbide Particle Reinforced Metal Matrix Composites”, *Indian Journal of Science and Technology*, Vol. 3, No. 12, 2010.
- [15] K. L. Meena, Dr. A. Manna, Dr. S. S. Banwait, Dr. Jaswanti, “An Analysis of Mechanical Properties of the Developed Al-SiC-MMC’s”, *American Journal of Mechanical Engineering*, 2013, Vol. 1, No. 1, pp. 14-19.
- [16] K. N. P. Prasad and M. Ramachandra, “ Effect of squeeze pressure on hardness and wear resistance of aluminium flyash composite manufactures by stir-squeeze casting”, *International Journal of Engineering Inventions*, e-ISSN:2278-7461, p-ISSN 2319-6491, Volume 3 Issue 4 (November 2013) PP: 01-08.
- [17] G. B. Veeresh Kumar, C. S. P. Rao, N. Selvaraj, M. S. Bhagyashekar, “ Studies on Al6061-SiC and Al7075 - Al₂O₃ Metal Matrix Composites”, *Journal of Minerals & Materials Characterization & Engineering*, Vol. 9, 2010, pp. 43-55.
- [18] Mohammad M. Ranjbaran, “Experimental Investigation of Fracture Toughness in Al 356- SiC Aluminium Matrix Composite” *American Journal of Scientific and Industrial Research*, 2010.
- [19] Hai Su, Jian Lu, Zheng Lu, Wenli Gao, Hui Zhang and Hongbo Liu, “Optimization of Stirring Parameters Through Numerical Simulation for the Preparation of Aluminum Matrix Composite by Stir Casting Process”, *Journal of Manufacturing Science and Engineering*. 132(6), 2010.
- [20] Lihe Qian, Toshiro Kobayashi, Hiroyuki Toda, Takashi Goda and Zhong-Guang Wang, “Fracture Toughness of a 6061 Al Matrix Composite Reinforced with Fine SiC Particles”, *Transactions*, Vol 43, No 11, 2002, pp. 2838 – 2842.
- [21] Sijo MT and KR Jayadevan, “Analysis of stir cast aluminium silicon carbide metal matrix composite: A comprehensive review”, *Procedia Technology 24* (2016) 379-385.
- [22] M. K. Surappa, “Aluminium Matrix Composites: Challenges and Opportunities”, *Sadhana Vol. 28, Parts 1 & 2*, February/April 2003, pp. 319–334.
- [23] Hashim, L Looney and M S J Hashmi, “Metal Matrix Composites: Production by the Stir Casting Method”, *Journal of Material Processing and Technology*, Vol. 92, 1999, pp. 1-7.
- [24] C. Saravanan, K. Subramanian, V. Ananda Krishnan and R. Sankara Narayanan, “Effect of particulate reinforced aluminium metal matrix composite- A review”, *Mechanics and Mechanical Engineering*, Vol. 19, No. 1 (2015) 23-30.

Development of Hybrid Model with Feasibility Analysis for Un-electrified Households in Developing Countries

Priyanka Anand¹, Sarbjeet Kaur Bath², Mohammad Rizwan³

¹Department of Electrical Engineering, I. K. Gujral Punjab Technical University, Kapurthala, India

²Department of Electrical Engineering, G. Z. S. Campus College of Engg & Tech, Bathinda, India

³Department of Electrical Engineering, Delhi Technological University, Delhi, India

¹anand_priyanka10@yahoo.co.in, ²sjkbath77@gmail.com, ³rizwan@dce.ac.in

Abstract: Rural electrification plays an essential role in socio - economic expansion of rural people and overall nation. However, there are many rural areas available in India which does not have access of electricity due to infeasibility of grid extension or limited availability. In addition, there are several rural households available in India which is not electrified till yet. Utilizing diesel generator (DG) in this situation is not a good alternative due to environmental impacts. In these circumstances, power generation through locally available renewable energy sources (RES) could be a viable solution due to cost-effectiveness, demand-supply gap, global warming & climate change, fossil fuel depletion etc. In the present investigation, feasibility analysis of hybrid power system utilizing locally available RES has been carried out for un-electrified rural households of Mewat district of Haryana state in India. Different possible configurations of off grid and grid connected mode has been developed and compared. It has been found that grid connected SPV/Wind/Biomass/Biogas hybrid system is most optimal solution in terms of net present cost (NPC) and cost of energy (COE).

Keywords: Solar photovoltaic, Biomass, Biogas, HOMER, Wind energy.

1. Introduction

Electrical energy plays a significant role in improving the socio-economic development of any nation. Further, in developing countries like India, a major portion of population is residing in rural areas. Presently, India has around 18452 villages and out of which 23% rural households are still un-electrified due to some technical and economical reasons [1]. In addition, the nation has an installed capacity of about 330 GW as on 30.06.2017 with a major share of approximately 70% from fossil fuels that leads towards greenhouse gas (GHG) emission, health issues etc. It has also been observed that only 18 % contribution from renewable energy sources (RES) that can be enhanced by harnessing more and more available RES [2]. In nutshell, power generation through locally available RES in these rural areas could be a viable solution due to several reasons such as non-feasibility of grid extension, environment friendly energy, improving health issues etc. Further, the power generation from RES is expected to increase drastically and is estimated to be around 175 GW by 2022 which would be a great achievement in Indian power sector [3]. Besides, Ministry of New and Renewable Energy (MNRE) provides several fiscal and non fiscal incentives like concessional custom duties, exemption of excise duties, subsidies, preferential tariff for purchase of renewable power, generation based incentives etc. [3].

However, RES like solar, wind energy are intermittent in nature, so combination of such sources called hybrid systems is recognized as a feasible solution to get economical, clean, green and reliable energy. The hybrid system may work in off grid and grid connected mode. Further, the performance of a hybrid system is highly dependent on the geographical locations; availability of RES; environmental conditions etc. Therefore, feasibility analysis at a particular site for the development of hybrid system is required to explore the cost, component size and overall economics. In this regards, several research has been carried out by several researchers by using several simulation tools and methods [4-24].

In light of the above discussion, the aim of the present work is to perform feasibility analysis of development hybrid power system for rural area of Haryana state in India has been carried out. This hybrid system will provide the reliable supply to un-electrified rural households. At first, the potential of different RES available at the study area has been estimated. Further, the total load demand of the selected site has been computed. Utilizing popular software, Hybrid Optimization Model for Electrical Renewable (HOMER), different feasible configurations in off grid and grid connected mode are compared and selected the most feasible in terms of techno-economic analysis.

2. Study area

Silkhoh is a village situated in Taoru block of the Mewat district of Haryana state in India. The longitude and latitude of the study area is 76.96° E and 28.15° N respectively [25]. According to census 2011, this village has a total population of 3467 alongwith 596 households. Based on the collected data, it has been found that the selected area has 398 un-electrified households [26]. Therefore, it is essential to design a power system in order to meet the energy needs of rural people.

3. Potential of different RES at selected site

In order to design a RES based hybrid system for a specific site, it is necessary to find out the potential of available RES and their capability to generate efficient and reliable power. Therefore, the potential of different RES viz. solar energy, wind energy, biomass and biogas has been calculated based on the site visits and collected data and is given in Table 1.

Table 1: RES Potential at Selected Site [27-30]

RES	Potential	Annual Energy Potential (kWh/year)
Solar energy (Daily solar radiation)	5.26 kWh/m ² /day	1919.9
Wind energy	Average annual wind Speed= 4.436 m/s Wind power density= 124W/m ²	1086.24
Biomass (Crop residue)	320 ton/year	290909
Biogas	170 m ³ /day	124100

From Table 2, it is observed that the selected site has huge potential of RES that can be utilized to fulfill the energy demand of rural people. Further, the power output of the solar photovoltaic (SPV) system ($P_{PV}(t)$) has been obtained using equation (1) as [24]:

$$P_{PV}(t) = R_{PV} \times DF \times \frac{Q_{PV}(t)}{Q_{PV,STC}} \quad (1)$$

Where, R_{PV} represents rated capacity of SPV array under standard test condition (STC); $Q_{PV}(t)$ is solar irradiance incident on SPV array in kW/m²; $Q_{PV,STC}$ depicts the solar radiation at STC (1 kW/m²). DF is derating factor of SPV array to consider reduced output under real world conditions like dust, shadow etc.

The power output of selected wind energy system at hour t can be calculated as per following equations [31]:

$$P_W(t) = \begin{cases} 0 & \text{when } V < V_{ci} \text{ and } V > V_{co} \\ x_1 V^2 + y_1 V + Z_1 & \text{when } V_{ci} \leq V < V_1 \\ x_2 V^2 + y_2 V + Z_2 & \text{when } V_1 \leq V < V_2 \\ x_3 V^2 + y_3 V + Z_3 & \text{when } V_2 \leq V < V_{co} \end{cases} \quad (2)$$

Where, V is wind speed in m/s; V_{ci} , and V_{co} is cut in and cut-out speed of wind turbine respectively. x , y , z represents coefficients of quadratic equation.

The power output obtained from biomass generator system ($P_M(t)$) has been computed using equation (3) as [24]:

$$P_M(t) = \frac{Q_{AM} \times CV_M \times \eta_M \times 1000}{365 \times 860 \times H_M} \quad (3)$$

Where, Q_{AM} represents yearly available amount of biomass (tons/yr), CV_M depicts biomass calorific value in kcal/kg, η_M is conversion efficiency and H_M represents operating hours per day of biomass generator system.

The output power ($P_G(t)$) of biogas generator system is computed as [32]

$$P_G(t) = \frac{Q_G \times F_G \times \eta_G}{860 \times H_G} \quad (4)$$

Where, Q_G is biogas availability per day (m^3/d), F_G is calorific value of biogas ($kcal/m^3$), η_G is overall conversion efficiency from biogas to electrical power production. H_G represents operating hours of biogas generator per day.

4. Assessment of Hourly Load Demand

The hourly load demand of the study area has been computed based on site visits, day to day use appliances by nearby villagers etc. The electrical appliances such as light emitting diode (LED), television (TV), fan, mobile charger, heater and water pump have been included while preparing the hourly load demand. Further, two seasons have been considered due to inclusion of temperature variation at study area in a year. The step time and day to day random variability of 5% each has been considered. The daily load profile of both the seasons has been depicted in Figure 1.

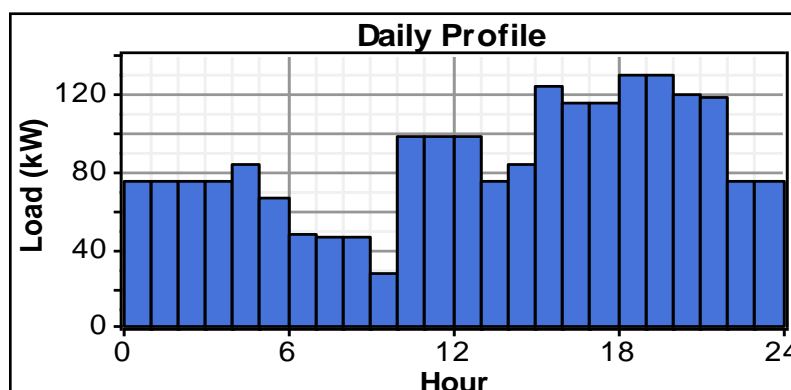


Figure 1(a). Daily load profile of study area during summer season

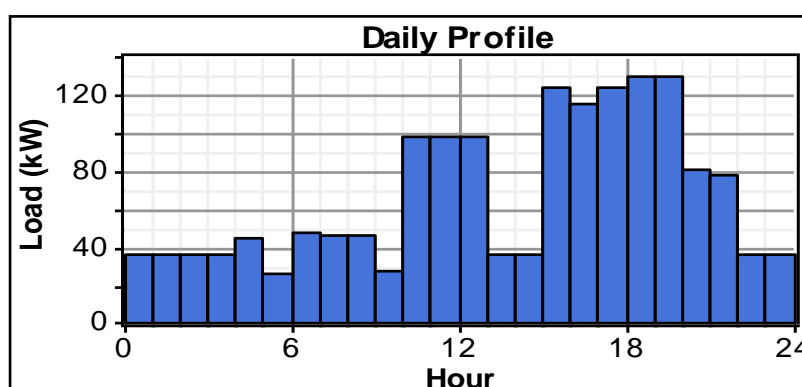


Figure 1(b). Daily load profile of study area during winter season

The daily energy requirement of the selected area during both the seasons is calculated as 2075 kWh/day and 1598 kWh/day respectively.

5. Methodology

Hybrid Optimization Model for Electrical Renewable (HOMER), well known software has been used for modeling of hybrid system. This software simulates several feasible configurations and ranked them on the basis of net present cost (NPC) [33]. In order to design and develop hybrid model in HOMER software, various technical and economical input database such as cost, size, lifetime etc. of system component are needed and is given in Table 2.

Table 2: Technical and Economical Input Database [16, 31]

Renewable energy technology	Capacity considered	Numbers considered	Capital cost	Replacement cost	O&M cost	Lifespan
SPV System	1kW	0- 100	\$ 1333/kW	\$1333 /kW	\$ 26/year	25 years
Wind turbine model (UE-33)	1kW	0-100	\$ 3500 /WT	\$ 3500 /WT	\$ 60/WT/year	25 years
Biomass gasifier system	1kW	0- 100	\$ 1033 /kW	\$ 750 /kW	\$ 0.01//kW/hour	15000 hours
Biogas generator system	1kW	23	\$ 660 /kW	\$ 450 /kW	\$ 0.01/kW/hour	20000 hours
Battery (VISION 6FM200D)	12V, 200 Ah	0-250	\$ 284 /kW	\$ 220/kW	\$6/battery/year	5 years/battery
Converter	1Kw	0-100	\$ 117 /kW	\$ 117 /kW	\$3/kW /year	10 years

6. Simulation Result and Discussion

Based on the locally available RES, the objective of the present work is to develop a hybrid model in order to fulfill the energy needs of the un-electrified rural households of the selected site. The hybrid model has been developed using HOMER software by providing technical and economical input database. At first, four feasible configurations in off grid mode have been considered and compared in terms of NPC and COE. Finally, best off grid configuration has been compared with grid connected and found most feasible. Further, the description of the four feasible off grid system is as follow:

- I. SPV/ Wind/Biomass/Biogas Generator with Battery
- II. Wind/Biomass/ Biogas Generator with Battery
- III. SPV/ Wind/Biomass Generator with Battery
- IV. SPV/ Biomass/Biogas Generator with Battery

6.1. Feasible off grid configurations

Four feasible off grid configurations are developed using HOMER software to meet out the hourly load demand of the selected site and their technical and economical results are presented in Table 3.

Table 3: Technical and Economical Results of Feasible Off Grid Configurations

Description	Parameter	SPV/ Wind/Biomass/ Biogas Generator with Battery	Wind/Biomass/ Biogas Generator with Battery	SPV/ Wind/Biomass Generator with Battery	SPV/ Biomass/ Biogas Generator with Battery
Technical parameters	SPV (kW)	35	-	15	130
	Wind turbine	231(70 nos.)	274 (83 nos.)	297 (90 nos.)	-
	Biomass generator	60	65	80	90
	Biogas generator	23	23	-	23
	Battery (nos.)	180	170	200	225
	Converter (kW)	60	50	60	100
Economical parameters	Total NPC (\$)	1005729	1005970	1173716	1339541
	Cost of energy (\$/kWh)	0.118	0.118	0.137	0.157

From Table 3, it is observed that the configuration SPV/Wind/Biomass/Biogas generator with Battery offer lowest NPC and COE of \$ 1005729 and \$ 0.118 respectively. The size of the configuration consists of 35 kW of SPV system, 231 kW of wind energy system, 65 kW biomass gasifier system, 23 kW of biogas generator and has 180 nos. of batteries along with 60 kW converter.

6.2. Comparison between grid connected and best off grid configuration

The best off-grid configuration has been compared with grid connected mode and it is observed that grid connected configuration has least NPC and COE of \$ 788780 and \$ 0.092 respectively. The system rating and economical parameters of grid connected configuration is given in Table 4.

Table 4: Results of Grid Connected Hybrid RES System

Configuration	SPV (kW)	UE-33 (kW)	Biomass generator (kW)	Biogas generator (kW)	Battery (no.)	Converter (kW)	Grid (kW)	NPC (\$)	COE (\$/kWh)
Grid connected SPV+ Wind +Biomass+ Biogas+Battery	40	271	60	23	140	50	5	788780	0.092

From Table 3 and Table 4, it is concluded that the grid connected SPV/Wind/Biomass/Biogas/Battery has been proposed for the selected site. The schematic diagram of proposed hybrid model is shown in Figure 2. Further, the cash flow summary in terms of NPC and monthly average energy generation of proposed configuration has been depicted in Figure 3 and Figure 4.

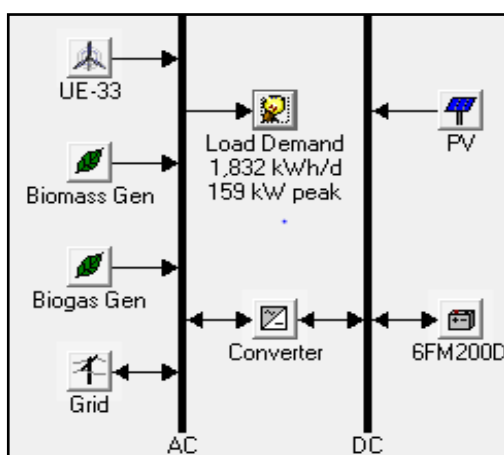


Figure 2: Schematic diagram of proposed hybrid model for selected site

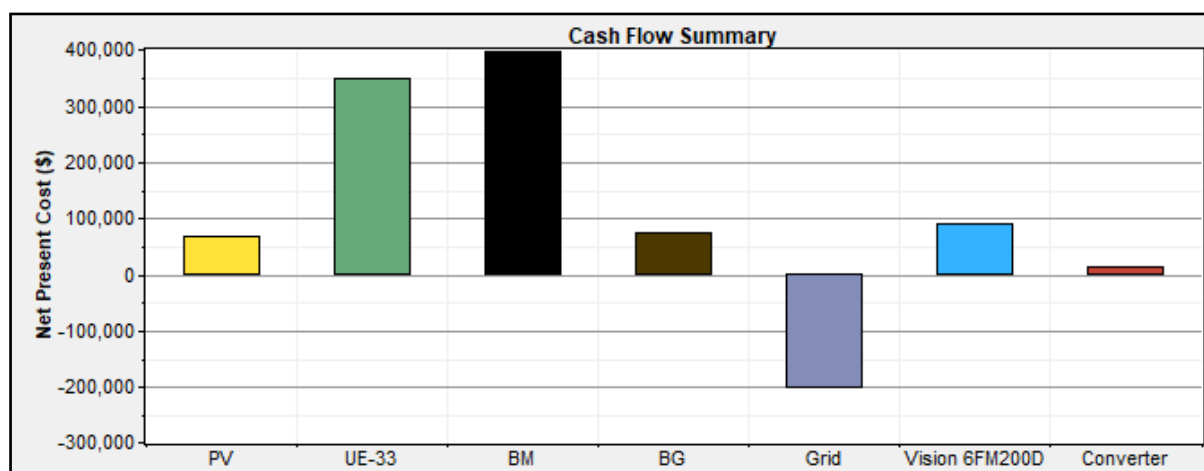


Figure 3: Cash flow summary in terms of NPC of proposed hybrid model

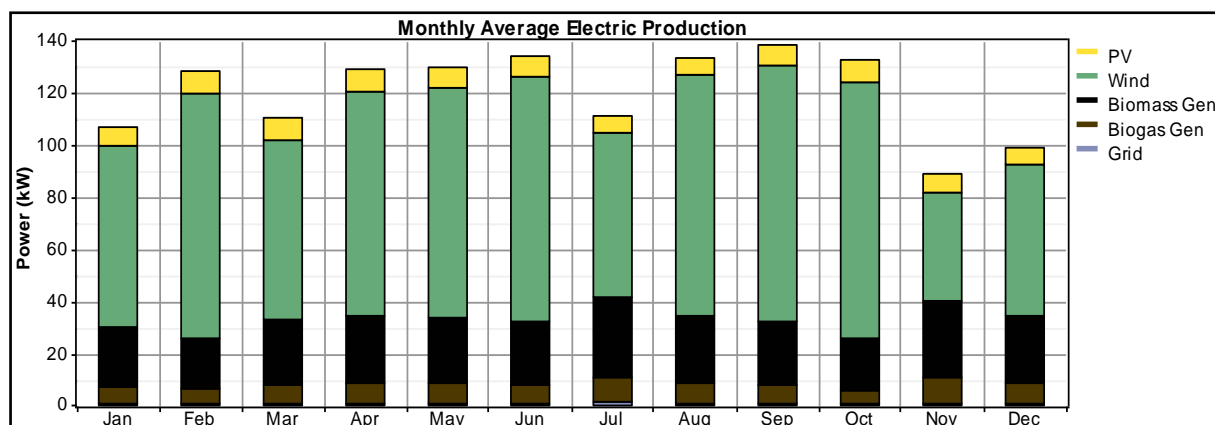


Figure 4: Monthly average energy generation of proposed grid connected hybrid model of study area

7. Conclusion

In the present work, RES based hybrid model has been developed for providing continuous supply to un-electrified rural households of Mewat district of Haryana state in India. Different possible configurations in off grid and grid connected mode has been considered and compared in terms of NPC and COE. The proposed grid connected hybrid model composed of 40 kW of SPV system, 271 kW (82 nos.) of wind energy system, 60 kW of biomass and 23 kW of biogas generator system alongwith 140 no. of batteries and 50 kW of converter. The proposed hybrid system would be very helpful in achieving the target of “Electricity to All” and rural electrification in India.

Acknowledgment

The corresponding author (Priyanka Anand) wishes to thank I. K. Gujral Punjab Technical University, Kapurthala (Punjab) for providing research facilities for pursuing research work.

References

- [1]. <http://garv.gov.in/garv2/dashboard#2>. Accessed 11 October 2017.
- [2]. Central Electricity Authority, Ministry of Power, Government of India, 2017: www.cea.nic.in
- [3]. www.mnre.gov.in.
- [4]. J. M. Khan, and T. M. Iqbal, “Pre-feasibility study of stand-alone hybrid energy systems for applications in Newfoundland”, *Renewable Energy*, vol. 30, pp. 835-854, 2005.
- [5]. S. Rehman, I. M. El-Amin, F. Ahmad, S. M. Shaahid, A. M. Al-Shehri, J. M. Bakhashwain, and A. Shash, “Feasibility study of hybrid retrofits to an isolated off-grid diesel power plant”, *Renewable and Sustainable Energy Reviews*, vol. 11, pp. 635-653, 2007.
- [6]. S. M. Shaahid, and M. A. Elhadidy, “Economic analysis of hybrid photovoltaic–diesel– battery power systems for residential loads in hot regions-A step to clean future”, *Renewable and Sustainable Energy Reviews*, vol. 12, pp. 488–503, 2008.
- [7]. G. Bekele, and B. Palm, “Feasibility study for a standalone solar–wind-based hybrid energy system for application in Ethiopia”, *Applied Energy*, vol. 87, pp. 487-495, 2010.
- [8]. A. B. Kanase-Patil, R. P. Saini, and M. P. Sharma, “ Sizing of integrated renewable energy system based on load profile and reliability index for the state of Uttarakhand in India”, *Renewable Energy*, vol. 36, pp. 2809-21, 2011.
- [9]. S. Kumaravel, and S. Ashok, “An optimal stand-alone biomass/solar-PV/pico-hydel hybrid energy system for remote rural area electrification of isolated village in western-ghats region of India”, *International Journal of Green Energy*, vol. 9, pp. 398-408, 2012.
- [10]. A. H. Al-Badi, and H. Bourdoucen, “Study and design of hybrid diesel–wind standalone system for remote area in Oman”, *International Journal of Sustainable Energy*, vol. 31, pp. 85-94, 2012.
- [11]. M. S. H. Lipu, M. S. Uddin, and M. A. R. Miah, “A feasibility study of solar-wind-diesel hybrid system in rural and remote areas of Bangladesh”, *International Journal of Renewable Energy Research*, vol. 3, pp. 892-900, 2013.
- [12]. M. Rizwan, R. Kumar, and D. Kumar, “Renewable energy based optimal hybrid system for distributed power generation”, *International Journal of Sustainable Development and Green Economics (IJSDEG)*, vol. 2, pp. 60-62, 2013.
- [13]. M. M. Rahman, M. M. Hasan, J. V. Paatero, and R. Lahdelma, “Hybrid application of biogas and solar resources to fulfill household energy needs: a potentially viable option in rural areas of developing countries”, *Renewable Energy*, vol. 68, pp. 35-45, 2014.

- [14].S. Bhardwaj, and S. K. Garg, "Rural electrification by effective mini hybrid PV solar, wind & biogas energy system for rural and remote areas of Uttar Pradesh", *International Journal of Computer Science and Electronics Engineering (IJCSEE)*, vol. 2, pp. 178-181, 2014.
- [15].S. Upadhyay, and M. P. Sharma, "Development of hybrid energy system with cycle charging strategy using particle swarm optimization for a remote area in India", *Renewable Energy*, vol. 77, pp. 586-598, 2015.
- [16].A. Chauhan, and R. P. Saini, "Techno-economic feasibility study on integrated renewable energy system for an isolated community of India", *Renewable and Sustainable Energy Reviews*, vol. 59, pp. 388-405, 2016.
- [17].P. Anand, S. K. Bath, and M. Rizwan, "Feasibility analysis of Solar-Biomass based standalone hybrid system for remote area", *American Journal of Electrical Power and Energy Systems*, vol.5, pp. 99-08, 2016.
- [18].P. Anand, S. K. Bath, and M. Rizwan, "Design and development of stand-alone renewable energy based hybrid power system for remote Base Transceiver Station", *International Journal of Computer applications*, vol. 169, pp. 34-41, 2017.
- [19].Priyanka, S. K. Bath, and M. Rizwan, "Design and Optimization of RES based Standalone Hybrid System for Remote Applications", *Proceeding of 8th IEEE conference on Innovative Smart Grid Technologies (ISGT 2017) sponsored by IEEE Power and Energy Society (PES), Washington DC, USA, April 23-26, 2017.*
- [20].M. J. Khan , A. K. Yadav, and L. Mathew, "Techno economic feasibility analysis of different combinations of PV-Wind- Diesel-Battery hybrid system for telecommunication applications in different cities of Punjab, India", *Renewable and Sustainable Energy Reviews*, vol. 76, pp. 577-607, 2017.
- [21].R. Rajbongshi, D. Borgohain, and S. Mahapatra, "Optimization of PV-biomass-diesel and grid base hybrid energy systems for rural electrification by using HOMER", *Energy*, vol. 126, pp. 461-474, 2017.
- [22].H. S. Das, C.W. Tan, A. H. M. Yatim , and K. Y. Lau , " Feasibility analysis of hybrid photovoltaic/battery/fuel cell energy system for an indigenous residence in East Malaysia", *Renewable and Sustainable Energy Reviews*, vol. 76, pp.1332-1347, 2017.
- [23].P. Anand, S.K. Bath, and M. Rizwan, "Design of Solar-Biomass-Biogas based hybrid system for Rural electrification with environmental benefits", *International Journal on Recent and Innovation Trends in Computing and Communication*, vol.5 (6), pp. 450 – 456, 2017.
- [24].P. Anand, S.K. Bath, and M. Rizwan, " Design and sizing of RES based hybrid system for rural applications of Haryana state in India", *International Journal of Electronics Engineering*, vol.9 (2), pp.79-85, 2017.
- [25].<http://mewat.gov.in/>. Accessed 04 October 2017.
- [26].<http://www.censusindia.gov.in/2011census/dchb/DCHB.html>.
- [27].NASA. Surface meteorology and solar energy: a renewable energy resource website. Available from: <https://eosweb.larc.nasa.gov/sse/>. Accessed 04 October 2017.
- [28].NIWE. National institute of wind energy. Ministry of New and Renewable Energy, Government of India; 2017. http://niwe.res.in/departments_wra_est.php. Accessed 04 October 2017.
- [29].Data collected, Agricultural department, Mewat district, Haryana state, India. Accessed 15 September 2017.
- [30].Data collected, Animal and Husbandary Department, Mewat district, Haryana state, India. Accessed 10 August 2017.
- [31].A. Chauhan, and R. P. Saini, "Size optimization and demand response of a stand-alone Integrated Renewable Energy System, *Energy*, vol. 124, pp. 59-73, 2017.
- [32].A. Chauhan, and R. P. Saini, "Techno-economic optimization based approach for energymangement of a stand-alone integrated renewable energy system for remote areas of India", *Energy*, vol. 94, pp. 138-56, 2016.
- [33].www.nrel.gov/homer.

E-Catalyst Learning System

by

Rajiv Roy

B.Eng., Delhi College of Engineering, Delhi University, 2010

A Project Submitted in Partial Fulfillment
of the Requirements for the Degree of
MASTER OF SCIENCE
in the Department of Computer Science

© Rajiv Roy, 2018

University of Victoria

All rights reserved. This project may not be reproduced in whole or in part, by photocopy
or other means, without the permission of the author.

Supervisory Committee

E-Catalyst Learning System

by

Rajiv Roy

B.Eng., Delhi College of Engineering, Delhi University, 2010

Supervisory Committee

Daniel M German, (Department of Computer Science)

Supervisor

Dr. Issa Traore, (Department of Electrical and Computer Engineering)

Co-Supervisor

Abstract

The e-catalyst Learning system is a user-friendly system, designed especially for the instructors to provide them an environment where they can teach and helps students to learn efficiently. The e-Catalyst learning system, built on top of the Salesforce platform, provides the foundation for the instructors, students, and institutions to connect to each other in new ways. In this learning system instructors can browse through their own courses, monitor the performance of the students, make direct call to the students through Skype, chat with the students, create tasks and events for the students, answers to the student's queries on the discussion board, check the schedule on calendar, add and delete courses, which are some of the features which available in e-Catalyst System. As the system is deployed in the cloud, it will be available online and accessible from anywhere in the world.

This system is developed in Canada, and it will be available as an open source system which will be later delivered over to a non-profit organization. This report gives the detailed overview of the e-Catalyst system. We will discuss the architecture of the system, model of the system, user interface overview, features of the system in detail, benefits and future work.

Table of Contents

Abstract	ii
Acknowledgements	v
1. Introduction	1
1.1 Problem Statement	2
1.2 e-Catalyst System Approaches and Characteristics	2
1.3 Benefits of e-Catalyst System	2
1.4 Report Outline	3
2. Cloud Computing Platform	4
3. E-Catalyst System Overview	5
4. System Modelling and Analysis	6
4.1 Design Analysis	6
4.2 Verification	7
<i>Figure 2 Verification of e-Catalyst system</i>	8
4.3 Entity–relationship model diagram	8
5. Implementation of E-catalyst system	10
5.1 Technologies and Tools	10
<i>Table 1 Technologies and Tools</i>	10
5.2 Framework	10
5.3 System architecture	11
5.4 Features of e-Catalyst System	11
<i>Figure 4 Home page</i>	12
<i>Figure 5 Instructor Personal Details Edit Mode</i>	12
<i>Figure 6 Calendar on Home Page</i>	13
<i>Figure 7 Calendar with Day View</i>	14
<i>Figure 8 Calendar with Week View</i>	14
<i>Figure 9 Calendar with Month View</i>	15
<i>Figure 10 Activities on Home Page</i>	15
<i>Figure 11 Assign Task</i>	16
<i>Figure 12 Assign Event</i>	17
<i>Figure 13 Students Enrolled</i>	17
<i>Figure 14 Skype Integration</i>	18
<i>Figure 15 Calling Student through Skype</i>	18
<i>Figure 16 Discussion Board</i>	19
<i>Figure 17 Survey posted on discussion board</i>	20
<i>Figure 18 Student Performance Dashboard</i>	21
<i>Figure 19 Course Inline Editing</i>	22
<i>Figure 20 Course Saved After Inline Editing</i>	22
<i>Figure 21 Add New Courses</i>	23

<i>Figure 22 New Course Saved</i>	23
<i>Figure 23 Delete Course</i>	24
<i>Figure 24 System throws Error Message when try to delete active course</i>	24
<i>Figure 25 Affiliated Institutions representation on google map</i>	25
6. E-Catalyst System Management	25
<i>Table 2 Detailed e-Catalyst System Management</i>	26
7. Conclusion and Future work	26
References	27

Acknowledgements

I would like to thank **Dr. Issa Traore** for his continuous support and mentoring throughout the project and my supervisor **Daniel M German** for his valuable feedback and suggestions.

Also, I would like to thank my friends and family who encouraged me during this project.

1. Introduction

Today's technology is changing and proliferating. With the growing of the internet and the World Wide Web, it becomes much easier to reach people around the world. Education is an essential part of human development; it gives us knowledge of the world around us, and the skills needed to succeed in the job market which has become so competitive. Standing out in the crowd is vital to be successful. Online education plays a significant role in the current market [1]. Nowadays education has become so expensive that people prefer to be more inclined to learn online compared to traditional methods like attending in-person universities or schools. Several institutions are now offering online education programmes [2]. Those institutions are competing for an increasingly sophisticated pool of students. To achieve success in the market, the online education platform should be reliable, trustworthy, efficient, and easy to use [3].

The objective of the project presented in this report is to develop a platform which attempts to address some of the aforementioned expectations. By keeping everything in mind we have built an e-learning platform called e-Catalyst system, which provides extensive functionalities for the instructors and students.

The e-catalyst system is an e-commerce software developed and deployed in the cloud where instructors and students from different universities collaborate with each other in an innovative way. It offers free online courses to the students wherein students can learn courses from renowned reputed instructors. e-Catalyst believes in collaborative work and sharing knowledge with each other, one of the ways to achieve this is Skype integration and a discussion board where students and instructors can share knowledge with each other. This system emphasizes user-friendliness. Instructors can log in, and view their teaching schedule on the calendar by day, weekly and monthly basis. Instructors can adjust their schedule and once the schedule changed a notification will be sent to the registered students. Instructors can add courses and change courses as per the course module. The instructor can view the number of students enrolled in each course and measure the performance of each student on the dashboard. They can assign tasks and events to a particular student or group of students as well. The instructor can call students directly using skype feature.

While the students and system managements modules are important functionalities of the system, this report will focus principally on the instructor module, and its related features.

1.1 Problem Statement

Education plays a meaningful role in the life and getting a good quality education nowadays has become hard because everything is expensive. There are many online education providers who offer online courses, but only a few providers are successful. Successful online education requires reliable, flexible and user-friendly learning system. The e-Catalyst system is easy to use and has out of the box functionalities. If the system is too complicated, hard to understand and to use then the instructor will lose interest, which could lead to the failure of the system. So, it is essential to make the learning system reliable, efficient and user friendly, by understanding and addressing the basic needs of the users. The e-catalyst system was developed by keeping all these things in mind.

1.2 e-Catalyst System Approaches and Characteristics

The design of e-Catalyst software architecture rely on two guiding principles as follows:

- 1) Instructor-led and facilitated learning: this method believes in collaborative work, where instructors can get connected directly to the learners and assist them directly if they need any help.
- 2) Self-paced learning: In self- paced Learning learners can learn from the course materials and the videos which are provided by the instructors. The materials are available all the time and accessible from anywhere.

1.3 Benefits of e-Catalyst System

Thee-Catalyst system provides several benefits including the following:

1. Commuting: the e-Catalyst system can be accessed from anywhere. Instructors don't need to commute, and this saves money and time.
2. Collaborative learning: the e-Catalyst system allows instructors to teach innovatively. The e-Catalyst system provides a common platform where instructors, students can share knowledge

and help each other. Chats, discussions forum, Skype are some of the standard features which are provided by the system.

3. Cost-effectiveness: As the e-Catalyst system is free, Instructors don't need to pay anything to use the system.

4. Student-Performance measurement: In e-Catalyst system instructors can measure the performance of each registered students into their courses. By monitoring performance, instructors can identify and help students who need more assistance and prepare unique materials for them.

5. Flexibility: As the system is in the cloud, the instructors can teach the students from anywhere at their convenience.

1.4 Report Outline

Section 2 describes the usage of cloud computing platform. The Salesforce force.com platform features which make it ideal for the -e-Catalyst system. Section 3 gives the overview of the e-catalyst system and defines all its features. In Section 4 we discuss the architecture of the e-Catalyst system, where we present design analysis using Tapaal, and Petri net formal model and check the system for deadlock and starvation. Verification of the system is performed to test whether the system is working as per the requirement or not. We have also provided the model diagram of the system to show the relationship between objects involved, it's attributes and how they are connected to each other. In section 5, we are discussing the implementation of the e-Catalyst system, by giving an outline of the technologies used, the architecture of the e-Catalyst system. Section 6 discusses the management of the e-Catalyst system, like the total cost involved, how much workforce will be needed to maintain the e-Catalyst system, how we are planning to continue the operation in future, maintenance cost, security, release, and storage information. Section 7 summarizes the outcome of the project, makes concluding remarks and discuss future work.

2. Cloud Computing Platform

The e-catalyst system is purely implemented on Salesforce Force.com cloud platform. Salesforce is a CRM (Customer Relationship Management) platform [6]. This cloud platform is available online and accessible from anywhere. As the system is deployed on the Cloud, end-users don't need to install anything on their system [10].

We have used Force.com platform for the following reasons:

- **Multitenant architecture:** Salesforce Force.com supports multitenant architecture [5], where all the users share the same infrastructure and follow the same version of Force.com platform. The multitenant architectures do the upgrades automatically for all the users, so no one has to worry about the version upgrade of the e-Catalyst system.
- **Cost Savings:** Force.com platform eliminates the capital expenses of buying hardware and software. We don't need to buy any software and install in the system; the platform itself is available online.
- **Security:** One of the primary concern nowadays is providing security to the system. Salesforce Force.com cloud platform provides security to all the applications which are built into their system. So, we don't have to worry about e-Catalyst system security as the Salesforce is taking care of them.
- **Flexibility:** Salesforce Force.com is an on-demand technology, so we can manage the bandwidth as per the usage of the system. If the number of users in the system is growing it is easy to scale up the cloud capacity as per the need for the system and it is also easy to scale down the cloud capacity anytime from anywhere. It makes the Force.com cloud system very user-friendly and business-centric platform.
- **Accessibility:** The cloud platform is a same single base platform where all the documents, files, and data are stored in one place in the cloud. Since everything is present in one place, all the data, documents and files are easily available and accessible.
- **Disaster Recovery:** Salesforce Force.com platform backs up all organization data. It helps from all kinds of an emergency scenario like natural disasters or human errors.

3. E-Catalyst System Overview

In the current market, there are many organizations which provide online education like Coursera, edX, etc [4]. e-Catalyst system provides out of the box functionalities especially for the instructors, which makes the system attractive. Online teaching is unique and different as compared to classroom instructing [2]. To make the system successful into the market, e-Catalyst provides the following features:

- **Manager timetable:** e-Catalyst offers an option to the instructors to manage their schedule, which shows when the instructors are available for teaching (i.e., number of days availability in a week, monthly, or daily basis). Once the schedule is fixed, a notification will be sent to the corresponding registered students.
- **Manage Courses:** Instructors can add new courses and can delete their existing courses as well provided the course is not ongoing. Any action in the course module by the instructor triggers a notification to the registered students.
- **Discussion Board:** Instructors can post questions or reply to the questions asked by the students on a discussion board. It makes the learners feel connected to each other.
- **Communication:** the e-Catalyst system provides different types of communication methods between the instructors and students.
 - **Chat:** Instructors can chat directly with the learners if they are online.
 - **Email:** Students can send email to the instructors where a case is generated inside the e-Catalyst system, and a notification sent to the instructor.
 - **Skype:** e-Catalyst provides an innovative feature in which instructors can call or video or chat directly to the students from within the e-Catalyst system.
 - **Discussion board:** Another way to communicate is the use of discussion board. The discussion board is used as a public forum, any questions asked will be visible to all users.
- **Inappropriate behavior:** If any learner misbehaves on the discussion board, instructors can send a private message to the learner as a reminder of him/her of the class policies.

- **Event/Task:** Instructors can create a task and assign work to the students; also, instructors can create events like for a meeting or exam schedules and send notifications to all the students.
- **Students Performance:** Instructors can view the performance of each registered students in their course on dashboards. It helps instructors to define the strategy like how to improve the performance of the students.
- **All affiliated institutions view:** Instructors can view all the affiliated institutions and can see all the details in a single place.

4. System Modelling and Analysis

In this section, we are performing the detailed analysis of the e-Catalyst system. In the system, there will be three actors, namely, instructors, students and Admin. Each actor will play a different type of roles in the system. In this report, we are focusing on instructor's modules.

4.1 Design Analysis

To implement the e-Catalyst system, first, we have designed the system and checked the system behavior whether the system is working without any deadlock and starvation or not. To do this, we have used Tapaal tool and Petri net mathematical [9] model (see Figure 1), and observed the whole system and checked how accurately the system would work in real time scenario.

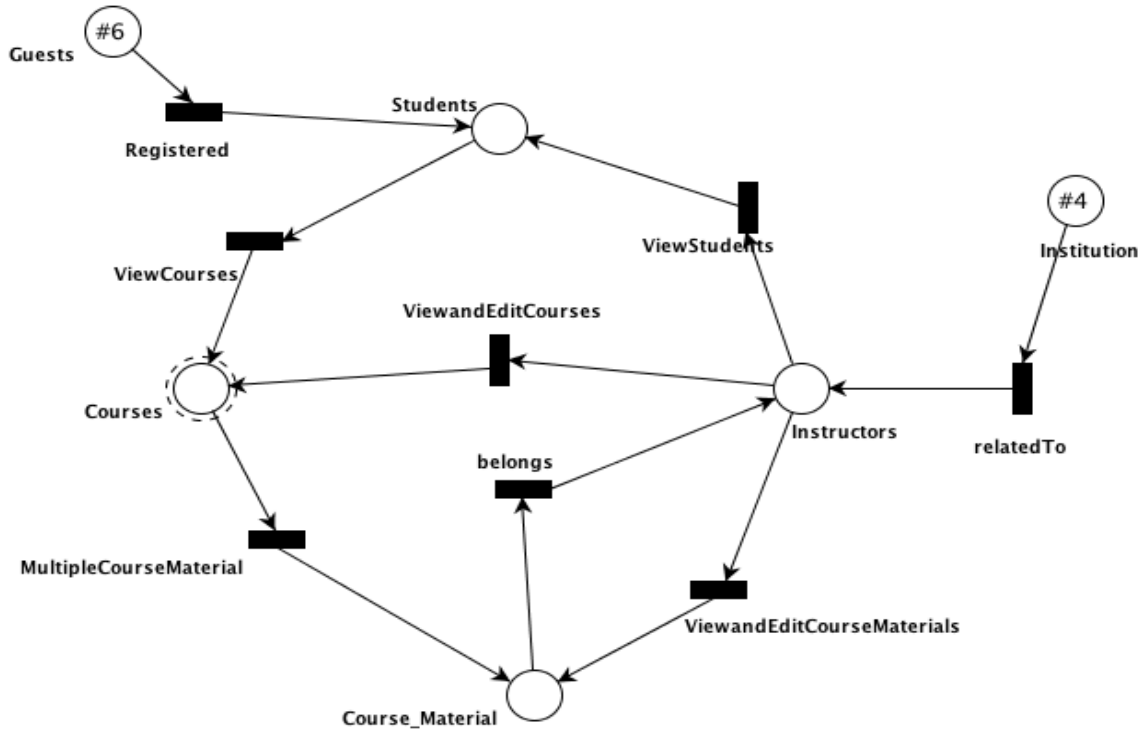


Figure 1 e-Catalyst System Design

As shown in Figure 1, Guest first registers to the e-Catalyst system, and after that, they become students to the system. Now Students can view all the courses and its respective course materials. Institution represents the university where instructors belong too. Instructors can see and make changes to the course materials. Instructors can also view the number of students present in the e-Catalyst system.

4.2 Verification

The e-catalyst system is verified by observing the simulation history results of the e-Catalyst Design depicted by Figure 2. Simulation history represents the outcomes of the e-Catalyst system, where the outcomes are validated with the real-time requirement and checked whether the system is behaving correctly or not and whether the system is working without deadlock or starvation or not.

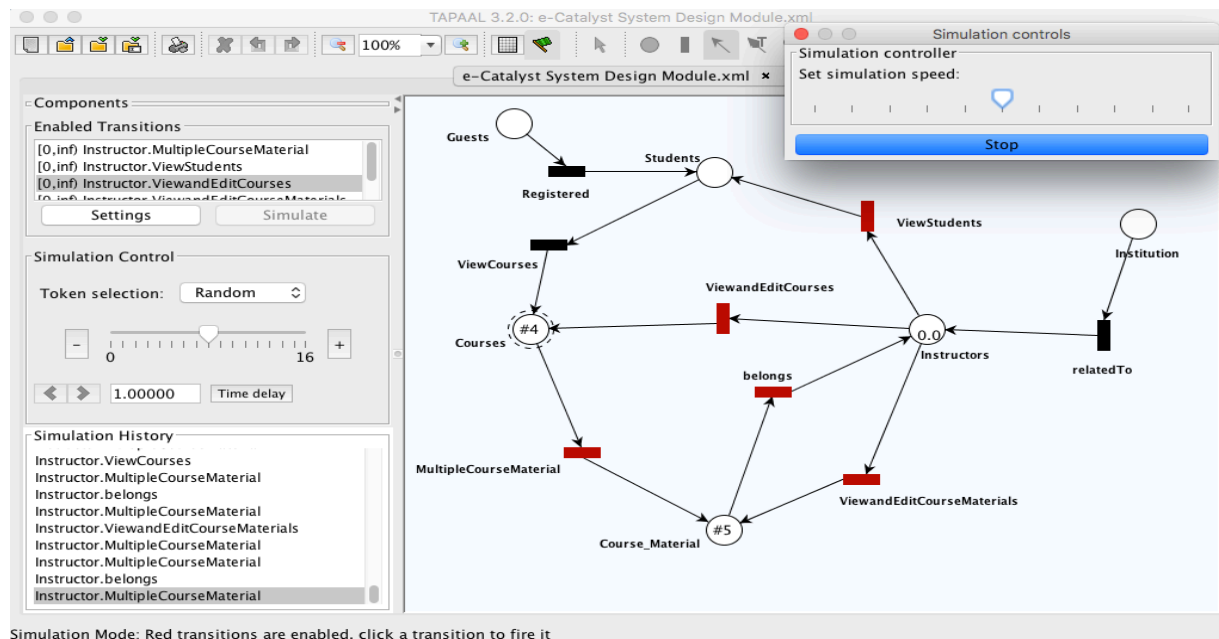


Figure 2 Verification of e-Catalyst system

4.3 Entity–relationship model diagram

An Entity relationship model diagram has been designed which indicates the relationship between each object of the e-Catalyst System as depicted in Figure 3. Each object performs some role which is associated with the functionality of an e-Catalyst system. The Entity-Relationship diagram represents the following:

- **Instructor Object:** Holds all the information of the instructors.
- **Course Object:** Hold information about the courses. One instructor can teach many courses.
- **User Object:** Holding information about the users.
- **Institution Object:** Holds information about institutions, which represents instructors from a different institution.
- **Course Material Object:** All course materials related to the courses are stored in this object, and the information about the users who have access to these course materials are also being stored.
- **InstructorsAndCourses Object:** Information about the instructors and courses they are teaching.

- The relationships between each object are represented by a color line which indicates the following:

-
- The diagram illustrates a database schema for a course management system. It features six main tables, each represented by a card with its fields and data types. Relationships are shown as lines connecting the tables.
- Course**: Fields include # of Students (Roll-Up Summary (COUNT Students)), Action (Checkbox), AttachmentId (Text(50)), CourseEndDate (Date), Course Id (Auto Number), Course Name (Text(80)), Created By (Lookup(User)), Description (Long Text Area(131072)), End Date (Date), End DateTime (Date/Time), End Date Time (Formula (Text)), End Time (Picklist), ExamDate (Date/Time), ExamDateChoice1 (Date/Time), ExamDateChoice2 (Date/Time), ExamDateChoice3 (Date/Time), ExamPage (Text(10)), Last Modified By (Lookup(User)), Level (Picklist), NumberOfDays (Formula (Number)), Owner (Lookup(User+1)), Start Date (Date), Start DateTime (Date/Time), Start Date Time (Formula (Text)), and Status (Picklist). A "Show More Fields" link is at the bottom.
 - Course Material**: Fields include AttachmentId (Text(255)), Course (Master-Detail(Course)), Course Material Name (Text(80)), Created By (Lookup(User)), Last Modified By (Lookup(User)), videoDuration (Text(100)), videoSeenTime (Text(100)), VideoTimeLeft (Text(100)), Week (Number(18, 0)), and weeklyStatus (Text(100)).
 - InstructorsAndCourses**: Fields include Course (Master-Detail(Course)), Courses Instructor Name (Auto Number), Created By (Lookup(User)), Email Instructor (Formula (Text)), Instructor (Master-Detail(Instructor)), and Last Modified By (Lookup(User)).
 - StudentsAndCourses**: Fields include Course (Master-Detail(Course)), Course Name & Completed Percenta (Formula (Text)), Created By (Lookup(User)), Last Modified By (Lookup(User)), Name (Auto Number), Percent (Formula (Number)), Percentage (Picklist), Status (Picklist), and Student (Master-Detail(Student)).
 - User**: Fields include About Me (Text Area(1000)), Active (Checkbox), Address (Address), Admin Info (Checkbox), Admin Info Emails (Text(8)), Alias (Text(8)), Allow Forecasting (Checkbox), Auth Token (Text(255)), Call Center (Lookup(Call Center)), Cell (Phone), Chatter Email Highlights Frequency (Picklist), Company Name (Text(80)), Contact (Lookup(Contact)), Data on Monthly Addition Limit (Number(9, 0)), Default Notification Frequency when (Picklist), Delegated Approver (Lookup(User+1)), Department (Text(80)), Division (Text(80)), Email (Email), Email Encoding (Picklist), Email Sender Address (Email), Email Sender Name (Text(80)), Email Signature (Text Area(1332)), Employee Number (Text(20)), and End of Day (Picklist). A "Show More Fields" link is at the bottom.
 - Institution**: Fields include AttachmentId (Text(50)), City (Text(255)), Country (Text(255)), Created By (Lookup(User)), Institution Name (Text(80)), Email (Email), Last Modified By (Lookup(User)), Location (Text Area(255)), Owner (Lookup(User+1)), Phone (Phone), State Province (Text(32)), Street (Text(255)), Website (Text(100)), and Zip Code (Text(32)).
- Relationships are indicated by lines connecting the tables. For example, 'Course' is linked to 'Course Material', 'InstructorsAndCourses', 'StudentsAndCourses', and 'User'. 'InstructorsAndCourses' is linked to 'User'. 'StudentsAndCourses' is linked to 'User'. 'User' is linked to 'Institution'.

9

5. Implementation of E-catalyst system

In this section, we present the implementation of e-Catalyst by discussing the technologies and tools involved and the implementation outcome.

5.1 Technologies and Tools

To design the e-Catalyst system efficiently, we used various technologies as described in table 1. First, we did design analysis and verification of the system and checked whether the system is working without deadlock or not. For that, we have used Tapaal Tool and Petri net mathematical model [9]. After completing the design and verification, we built the system on the Salesforce Force.com cloud platform. Cloud platform eliminated the installation of hardware and software in the system and helped us mainly focused on building the e-Catalyst system.

Technology	Description
Tapaal & Petri Net	Used to design the e-Catalyst system for verification and testing purposes.
Multitenant Architecture	All users are using the same platform where the resources are shared among the users by Salesforce.
Apex	A programming language which is used to perform business logic in the Salesforce Force.com Cloud platform.
Visualforce	A programming language which is used to design the user interface of the e-Catalyst system.
HTML, CSS, JavaScript, JQuery	Used primarily to enhance the user interface in the e-Catalyst system.

Table 1 Technologies and Tools

5.2 Framework

Salesforce Force.com cloud platform follows Model View Controller (MVC) Framework. This framework is the most popular design pattern in 3-tiered applications. MVC pattern contains three modules:

- **Model:** represent the data model of the system. The model includes all the objects which are provided by Salesforce. Controller access to this model to execute business logic in the system.
- **View:** representation of the schema and data. The view is used to show the data in a systematic way to the users. Any changes in the data model reflect in the view model [8].
- **Controller:** Represents the business logic of the system like what kind of functionalities need to be performed by the system. It is used to manipulate the data model of the system [7].

5.3 System architecture

e-Catalyst system deployment leverages the characteristics of the Salesforce multi-tenant architecture [5]. Salesforce follows multi-tenant architecture where all the users share the same infrastructure and the same version of the Force.com Platform. Multi-tenant architecture release upgrades automatically and concurrently for all the users. In this type of architecture, users don't have to worry about the operating system, virtualizations, server, storage and networking; everything is handled by Salesforce. This type of architecture enables lowering application cost, quick deployment, and greater flexibility and extensibility.

5.4 Features of e-Catalyst System


This section gives detailed overview of the features of the e-Catalyst system.

- **Home Page**

We have developed an interactive homepage where instructors can see their details (as shown in Figure 4).

Hello, Rajiv Roy

Edit Save



Instructor Name **Rajiv Roy**

Phone

Email rajivuvic@gmail.com

Institution

Choose File no file selected

Save

Edit Save

Calendar

1 7 31

All Activities

[Edit](#) | [Delete](#) | [Create New View](#)

[New Task](#)
[New Event](#)

A B C D E F G H I J K L M N O P Q R S T U V W X Y Z Other All

Action	Subject	Name	Related To	Due Date	Status	Priority	Assigned Alias	Last Modified Date...	Last Modified By ...
Edit Del	Call			10/23/2017	Not Started	Normal	RRoy	10/5/2017 2:29 PM	RRoy
Edit Del	Call				Not Started	Normal	RRoy	10/22/2017 1:47 AM	RRoy

Figure 4 Home page

The instructor is allowed to make changes (as shown in Figure 5) in their details by clicking on edit button. Once the new value is entered, instructors can save the new value by clicking Save button.

Edit Save

Instructor Name

Rajiv Roy

Phone

(887) 156-77870

Email

rajivuvic@gmail.com

Institution

Edit Save

Calendar

1 7 31

All Activities

[Edit](#) | [Delete](#) | [Create New View](#)

[New Task](#)
[New Event](#)

A B C D E F G H I J K L M N O P Q R S T U V W X Y Z Other All

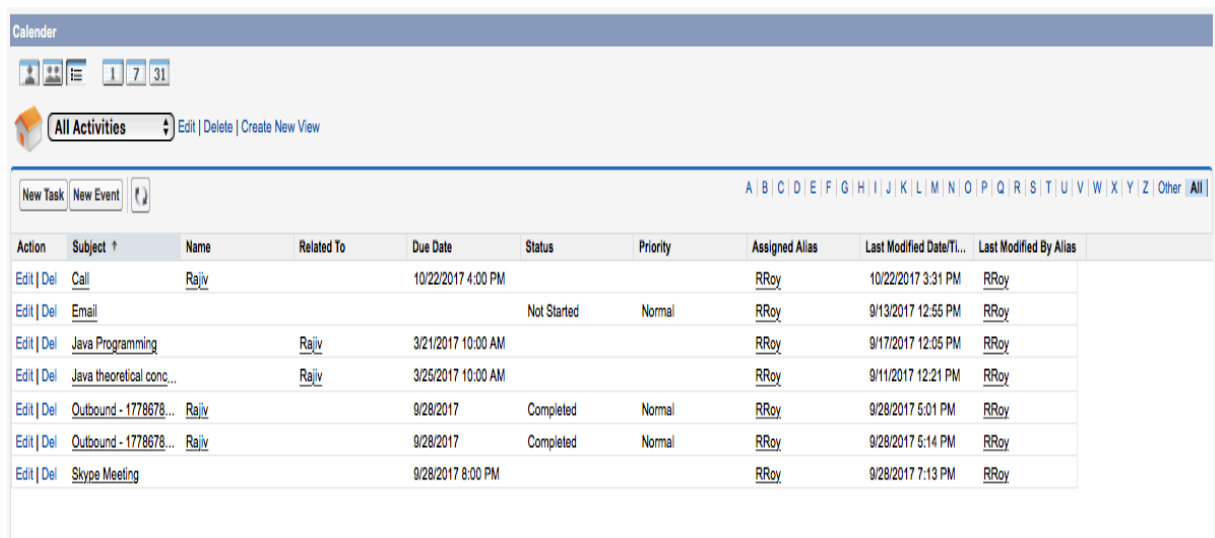
Action	Subject	Name	Related To	Due Date	Status	Priority	Assigned Alias	Last Modified Date/...	Last Modified By
Edit Del	Call	Rajiv		10/22/2017 4:00 PM			RRoy	10/22/2017 3:31 PM	RRoy
Edit Del	Email				Completed	Normal	RRoy	12/3/2017 2:12 AM	RRoy
Edit Del	Java Programming		Rajiv	12/5/2017 2:00 PM			RRoy	12/3/2017 2:11 AM	RRoy
Edit Del	Java theoretical con...		Rajiv	3/25/2017 10:00 AM			RRoy	9/11/2017 12:21 PM	RRoy
Edit Del	Outbound - 177867...	Rajiv		9/28/2017	Completed	Normal	RRoy	9/28/2017 5:01 PM	RRoy
Edit Del	Outbound - 177867...	Rajiv		9/28/2017	Completed	Normal	RRoy	9/28/2017 5:14 PM	RRoy
Edit Del	Skype Meeting			9/28/2017 8:00 PM			RRoy	9/28/2017 7:13 PM	RRoy

Figure 5 Instructor Personal Details Edit Mode

From the home page, Instructors can navigate to MyCourses, students enrolled, discussion board, student performance, and institution tabs. A calendar section is also visible on the home page as Shown in figure 5, wherein they can view their schedule by daily, weekly and on a monthly basis. Instructors can also view the tasks and events which are assigned to him/her and prioritize their work accordingly.

- **Calendar**

Instructors can view their schedule on a calendar from the home page itself. They can view the schedule on the calendar on daily, weekly, and monthly basis. As shown in the Figure 6, a tab named as “1”, “7” and “31” represents a day, week and month respectively. If the instructors click on one of the tabs then by mode of the selection a Calendar view will get opened.



The screenshot shows the 'Calendar' section of the e-Catalyst interface. At the top, there are icons for different views (1, 7, 31) and a dropdown menu set to 'All Activities'. Below this is a table with columns for Action, Subject, Name, Related To, Due Date, Status, Priority, Assigned Alias, Last Modified Date/Time, and Last Modified By Alias. The table contains several rows of tasks, including 'Call', 'Email', 'Java Programming', 'Java theoretical conc...', 'Outbound - 1778678...', and 'Skype Meeting'.

Action	Subject	Name	Related To	Due Date	Status	Priority	Assigned Alias	Last Modified Date/Time	Last Modified By Alias
Edit Del	Call	Rajiv		10/22/2017 4:00 PM			RRoy	10/22/2017 3:31 PM	RRoy
Edit Del	Email				Not Started	Normal	RRoy	9/13/2017 12:55 PM	RRoy
Edit Del	Java Programming	Rajiv		3/21/2017 10:00 AM			RRoy	9/17/2017 12:05 PM	RRoy
Edit Del	Java theoretical conc...	Rajiv		3/25/2017 10:00 AM			RRoy	9/11/2017 12:21 PM	RRoy
Edit Del	Outbound - 1778678...	Rajiv		9/28/2017	Completed	Normal	RRoy	9/28/2017 5:01 PM	RRoy
Edit Del	Outbound - 1778678...	Rajiv		9/28/2017	Completed	Normal	RRoy	9/28/2017 5:14 PM	RRoy
Edit Del	Skype Meeting			9/28/2017 8:00 PM			RRoy	9/28/2017 7:13 PM	RRoy

Figure 6 Calendar on Home Page

e-Catalyst provides **different types of Calendar view:**

1) When an Instructor clicks on tab 1 then a calendar with day view will get opened.

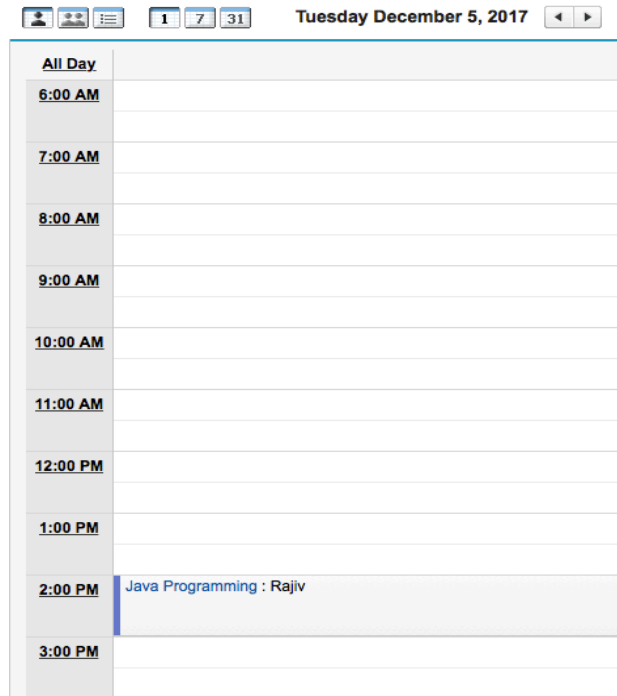


Figure 7 Calendar with Day View

The Figure 7 shows that the instructor is busy from 2 to 3 pm on Thursday.

2) When the Instructor clicks on tab 7 then a weekly view of the calendar will get opened.

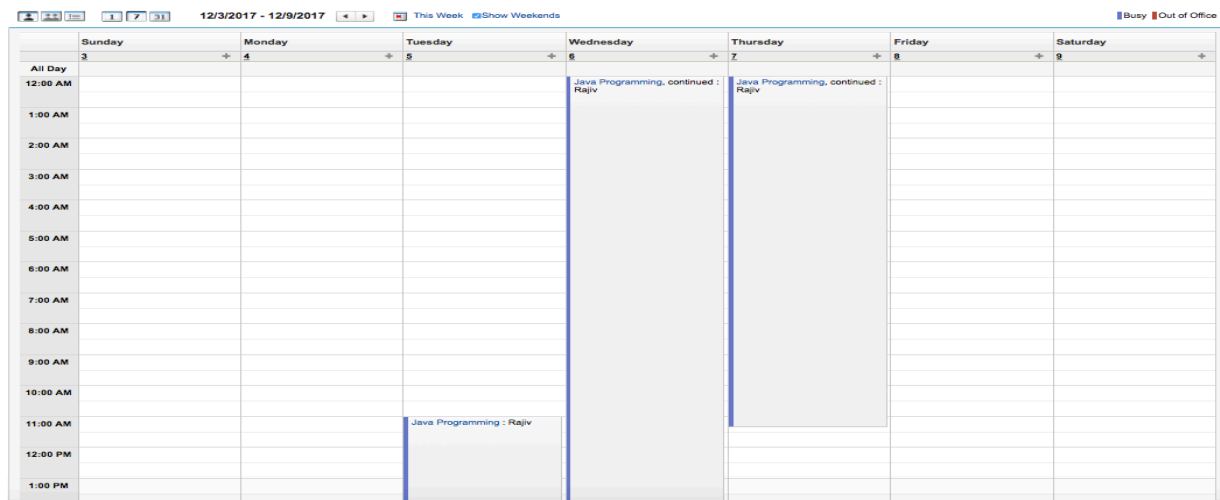


Figure 8 Calendar with Week View

By viewing Figure 8, we can see the instructor is busy on Tuesday, Wednesday, and Thursday and free on other days.

3) When the Instructor clicks on tab 31 then a monthly view will get opened. As you can see in Figure 9 the instructor is busy on Tuesday from 2:00 pm to 3:00 pm.

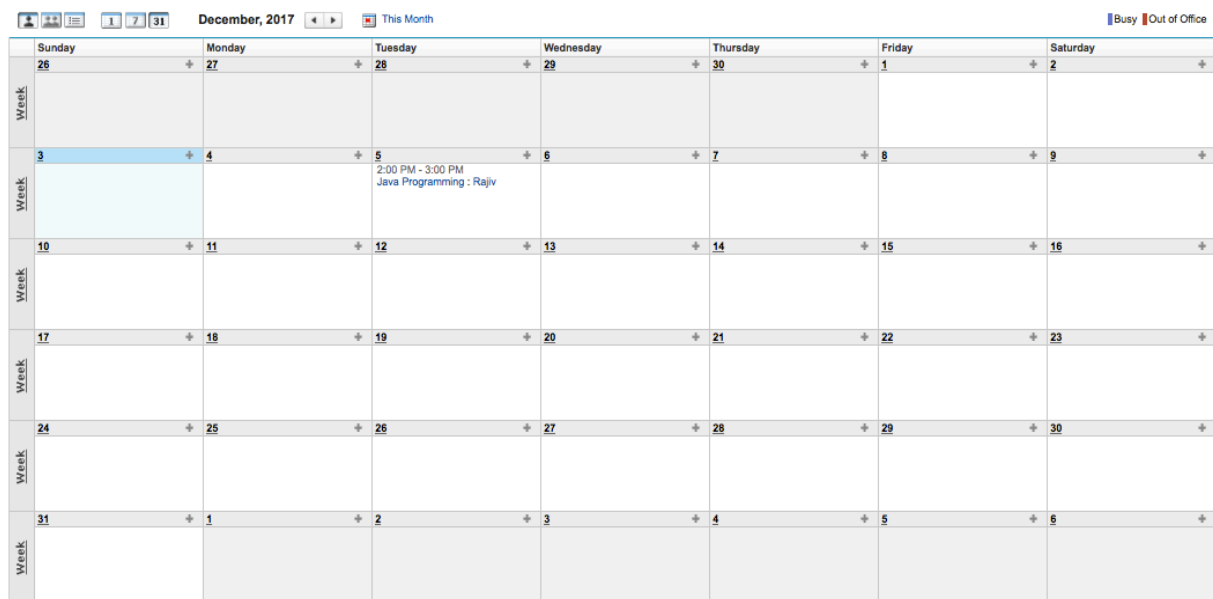


Figure 9 Calendar with Month View

Hence Calendar functionality helps the instructors to manage their schedule.

Activities are also visible on the home page. Instructors can assign a task and create events for the students. In Figure 10 we can see in e-Catalyst system on the home page there is a button called as New Task and New Event.

New Task New Event										A B C D E F G H I J K L M N O P Q R S T U V W X Y Z Other All									
Action	Subject	Name	Related To	Due Date	Status	Priority	Assigned Alias	Last Modified Date/Time	Last Modified By Alias										
Edit Del	Call	Rajiv		10/22/2017 4:00 PM			RRoy	10/22/2017 3:31 PM	RRoy										
Edit Del	Email				Completed	Normal	RRoy	12/3/2017 2:12 AM	RRoy										
Edit Del	Java Programming		Rajiv	12/5/2017 2:00 PM			RRoy	12/3/2017 2:11 AM	RRoy										
Edit Del	Java theoretical concepts		Rajiv	3/25/2017 10:00 AM			RRoy	9/11/2017 12:21 PM	RRoy										
Edit Del	Outbound - 17786783542	Rajiv		9/28/2017	Completed	Normal	RRoy	9/28/2017 5:01 PM	RRoy										
Edit Del	Outbound - 17786783542	Rajiv		9/28/2017	Completed	Normal	RRoy	9/28/2017 5:14 PM	RRoy										
Edit Del	Skype Meeting			9/28/2017 8:00 PM			RRoy	9/28/2017 7:13 PM	RRoy										

Figure 10 Activities on Home Page

- **Add Task**

Once we click on New Task button, an edit page gets opened as show in Figure 11, and then the instructor can assign a task to any registered student. Once the instructor clicks on save button, a task will be assigned to the assigned student.

Task Edit [Save] [Save & New Task] [Save & New Event] [Cancel]

Task Information ! = Required Information

Assigned To: User [v] Rajiv Roy [i]

Subject: [i]

Due Date: [12/3/2017]

Phone: []

Priority: Normal [v]

Status: Not Started [v]

Name: Contact [v] [i]

Related To: Opportunity [v] [i]

Email: []

Description Information

Comments: []

Recurrence

☐ Create Recurring Series of Tasks

Reminder

Reminder: ☒ 12/3/2017 8:00 AM [v]

Figure 11 Assign Task

- **Add Event**

Same with Event, once the instructor clicks on new event button as shown in Figure 12, an event page in edit mode gets opened where he/she can create an event and assign it to the student.

Calendar
New Event
Help for this Page

Event Edit
Save Save & New Task Save & New Event Cancel

Calendar Details
= Required Information

Assigned To User Rajiv Roy
Location
Subject
Start 12/3/2017 3:00 AM [2:25 AM]
Name Contact [Add to Invitees]
End 12/3/2017 4:00 AM [2:25 AM]
Phone
GoToMeeting Organiser
Email
GoToMeeting Status Scheduled
Related To Student

Description Information
Description

Notes
Notes

Recurrence

Figure 12 Assign Event

- Students Enrolled and Skype integration

Instructors can view the number of students enrolled in their courses, as shown in Figure 13. Wherein they can see all the essential information related to the students like student Name, Email, and Skype Id.

e-catalyst Learning
Logout

Home | My Courses | Student Enrolled | Discussion Board | Students Performance | Institutions

Hello, Rajiv Roy

Students Enrolled			
Students Name	Email	Skype ID	Skype
John	abc@gmail.com	abc@123	Chat Call Video Call
Robin		rizwana.rahman1	Chat Call Video Call

Figure 13 Students Enrolled

The instructor can interact directly with a student through skype either by chat, call or Video call. Suppose the instructor clicks on Call link, a message will be popped up as shown in Figure 14.

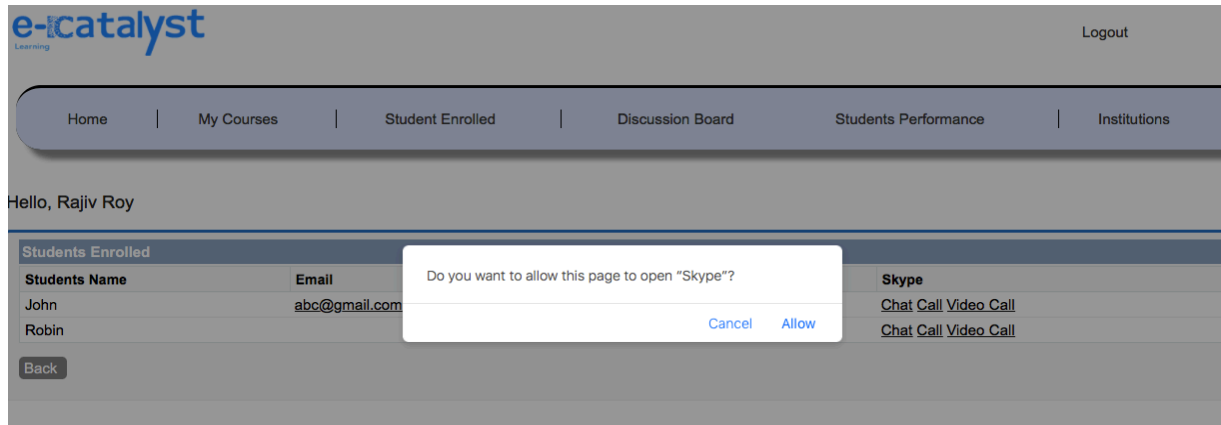


Figure 14 Skype Integration

Once the instructor presses “allows”, a skype panel will open automatically and start calling the student instantly as shown in Figure 15.

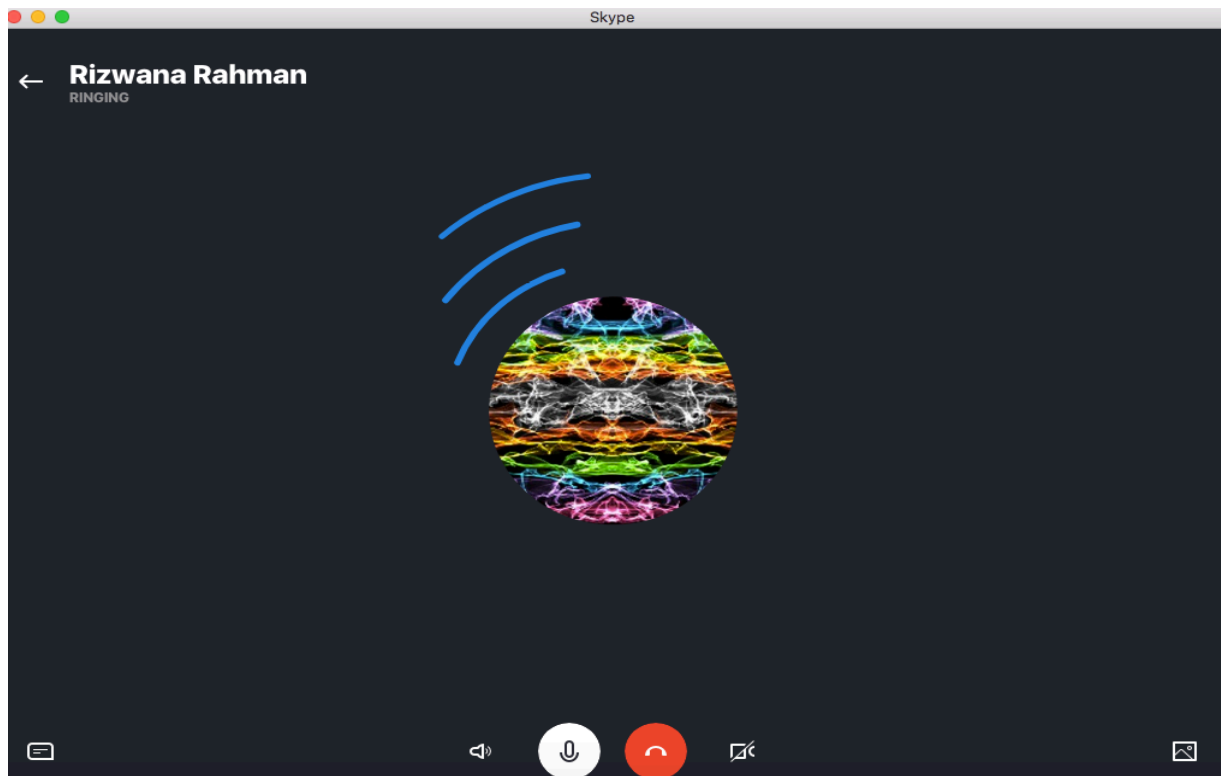


Figure 15 Calling Student through Skype

This functionality is specially built for the instructors and students so that they can interact directly with each other. This helps instructors to understand the student better, provide performance feedback to them and students can ask questions related to the course.

- **Discussion Board**

The design of e-Catalyst system stresses the importance of collaborative work. That is supported by the discussion board feature, depicted in Figure 16. Such feature is specially built for all the users present in an e-Catalyst system, and helps instructors and students to interact with each other and works together. This board is available openly in the confine of the course, where users can exchange information with each other. With the help of the discussion board, Instructors can make important announcements to the students or reply to the questions asked by the students. Important lectures notes, or videos can also be shared with the users.

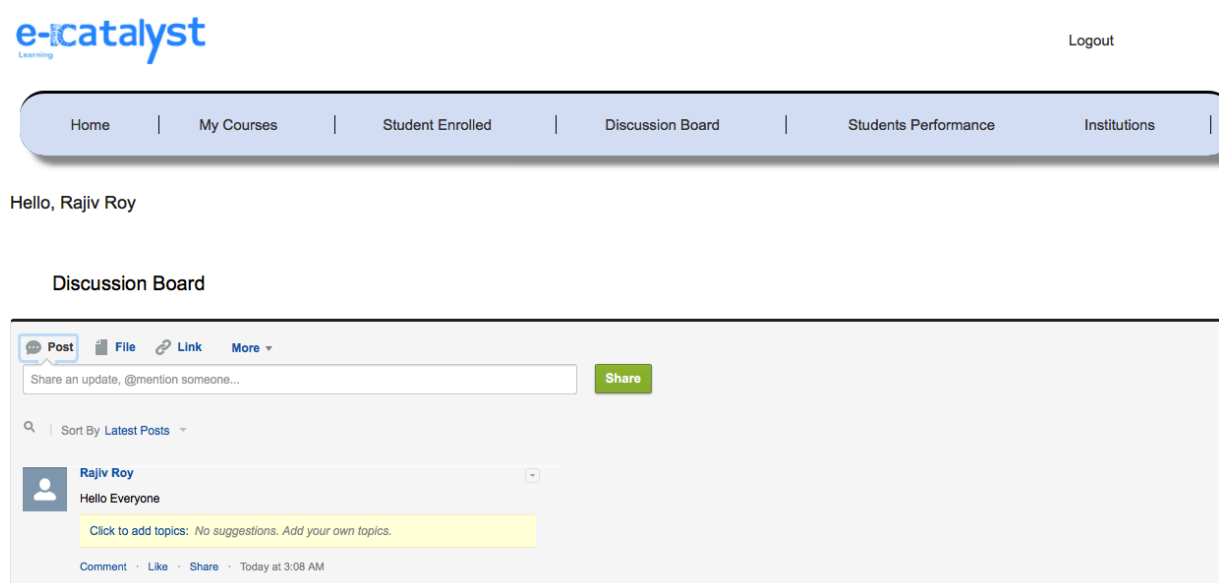


Figure 16 Discussion Board

- **Survey**

Instructors can create surveys and posts on the discussion board; students who are registered in their courses can fill the surveys. The feedback obtained from the students help instructors to improve the performance of their courses. For example, to improve the course content, instructors can create a survey and ask students questions and see the students' responses

received, as shown by Figure 17. On the basis of the responses, instructors can decide what next steps they should take to make the course better.

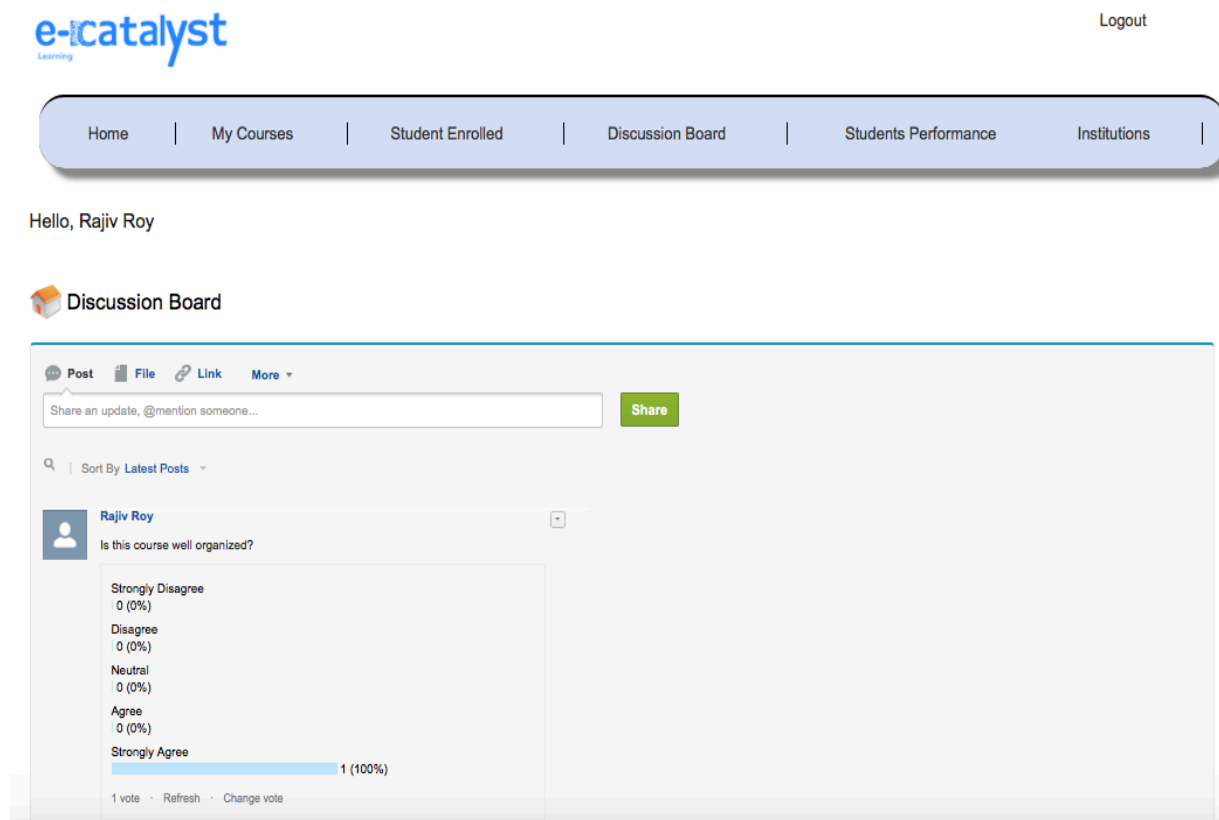


Figure 17 Survey posted on discussion board

- **Student Performance Dashboards**

e-Catalyst system design stresses the importance of interactive learning environment. So it is essential to know how much time students are spending on the e-Catalyst system and how active they are in studying the course material. To make better the learning environment and achieve successful learning outcome, instructors should know how well students are doing in their courses. That's why a Student performance dashboard, as shown in Figure 18, has been introduced. This helps the instructors to know how much students have progressed in the course material and shows students' progress and remaining percentage of coursework left to finish the course material. It helps the instructors to analyze each student progress and plan best practice strategies to assist students learning, define the timeline for next session, set the level of the course contents, and also determine the popularity of the course.

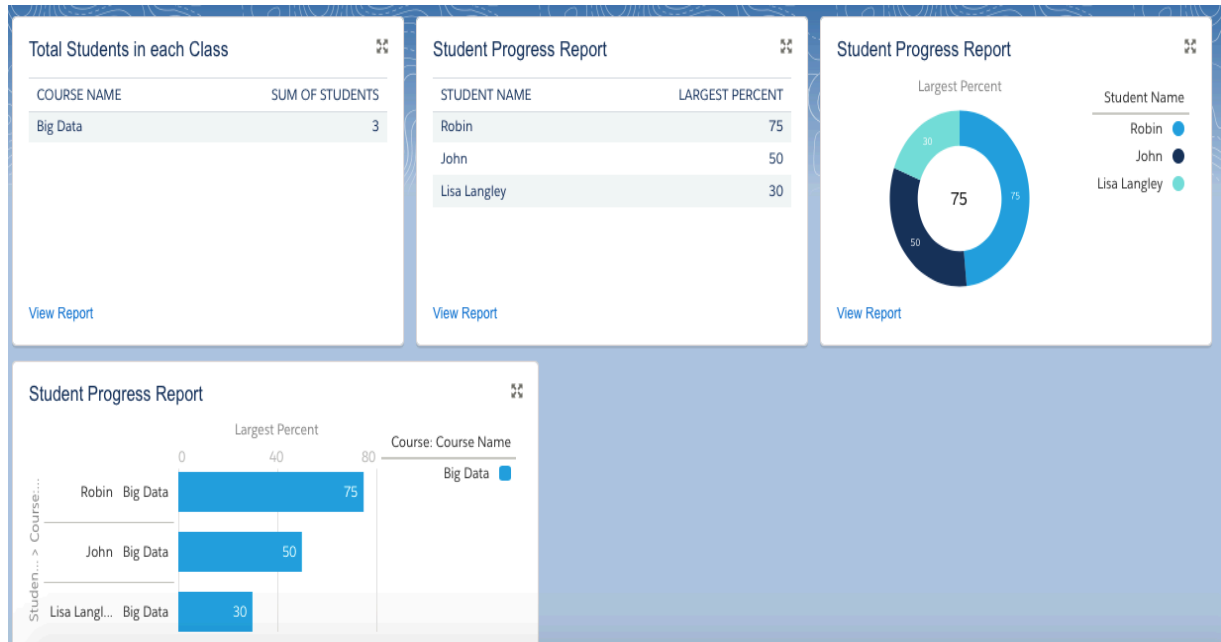


Figure 18 Student Performance Dashboard

Student performance dashboard figure encompasses the following features:

- 1) Total students registered in each course: E.g. in figure 18, In Big Data course, three students are registered.
- 2) Student progress table view: E.g. for the course Big data, percentage completed by each student, is showed in a tabular format.
- 3) Student progress chat view: E.g. Percentage completed by each student for the course big Data showed in a chat format.
- 4) Student Progress Bar chat view: E.g. Percentage completed by each student for the course big Data showed in Bar chat format.

- **Manage My Courses**

Inline editing

e-Catalyst allows Instructors to see all the courses they are teaching. All the necessary information like Course Name, Start Date, End Date, and course Description is visible to the instructor. If they would like to change any information about the course instructor, they just

need to double click on the field value. For instance, in Figure 19, if the instructor would like to change the start date of Big Data course, then he/she just need to double click on start date field, and the start date field will become editable; once it becomes editable, the instructor can enter a new value as shown in the Figure 19.

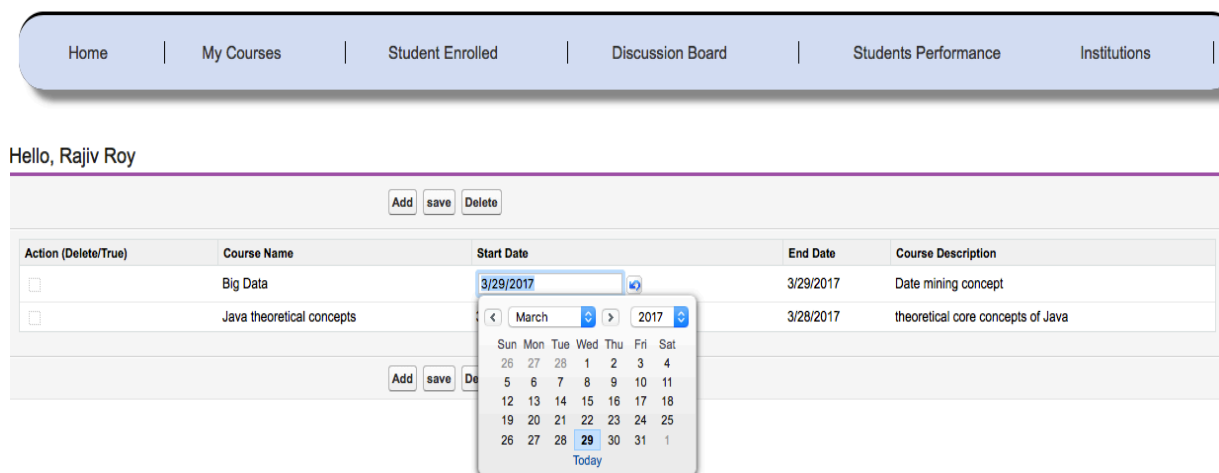


Figure 19 Course Inline Editing

Once the value is entered the instructor can click on Save button, and the record will be saved Figure 20.

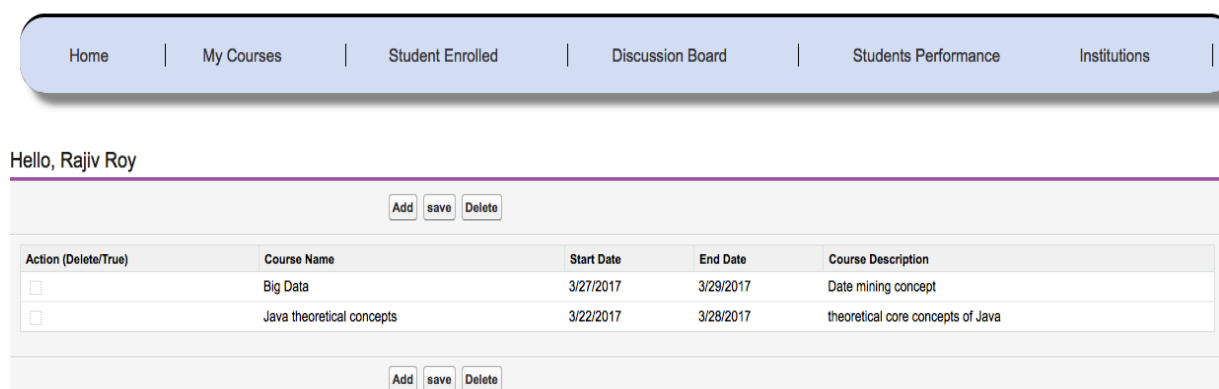


Figure 20 Course Saved After Inline Editing

e-Catalyst also provides the rights (i.e. privileges) to the instructors to manage their courses; they can either add or delete the courses.

Add Course

Instructors can add new courses by clicking on Add Button as shown in Figure 21. Once the button is clicked, a new page will get opened which allows instructors to enter all the required information related to the course.

Course Name	Start Date	End Date	Course Description
Data Structure	12/4/2017	12/19/2017	Linked list, Class, array etc

Figure 21 Add New Courses

Once the information is entered, the user can press the hit button, and the new course will be added to the database as shown in Figure 22.

Action (Delete/True)	Course Name	Start Date	End Date	Course Description
<input type="checkbox"/>	Big Data	11/28/2017	12/5/2017	Date mining concept
<input type="checkbox"/>	Java theoretical concepts	3/22/2017	3/28/2017	theoretical core concepts of Java
<input type="checkbox"/>	Data Structure	12/4/2017	12/19/2017	Linked list, Class, array etc

Figure 22 New Course Saved

Delete Course

To delete a particular course, the instructor needs to select the action corresponding to the course and then press the delete button as shown in Figure 23.

Home | My Courses | Student Enrolled | Discussion Board | Students Performance | Institutions |

Hello, Rajiv Roy

Add save Delete

Action (Delete/True)	Course Name	Start Date	End Date	Course Description
<input checked="" type="checkbox"/>	Big Data	11/28/2017	12/5/2017	Date mining concept
<input type="checkbox"/>	Java theoretical concepts	3/22/2017	3/28/2017	theoretical core concepts of Java

Add save Delete

Figure 23 Delete Course

Suppose if the instructor wants to delete Big Data course, in that case it will throw an error message, as shown in Figure 24. As this course is an active course, the system will not allow the instructor to delete this course. Only courses which are in planned phase and not started yet can be deleted.

Warning:
This course is already in progress. Sorry, this course is not allowed to delete.

Home | My Courses | Student Enrolled | Discussion Board | Students Performance | Institutions |

Hello, Rajiv Roy

Add save Delete

Action (Delete/True)	Course Name	Start Date	End Date	Course Description
<input type="checkbox"/>	Big Data	11/28/2017	12/5/2017	Date mining concept
<input type="checkbox"/>	Java theoretical concepts	3/22/2017	3/28/2017	theoretical core concepts of Java

Add save Delete

Figure 24 System throws Error Message when try to delete active course

- **Institutions Representation**

The e-catalyst system basic purpose is to provide students world-class instructors around the globe and help them to grow further in their career. Instructors are allowed to view all the details of the affiliated institutions on the Google map, as depicted by Figure 25. The instructors can use this information and connect directly to these institutions. The e-catalyst system not only brings students and instructors together, it also can be used to solve the big challenges facing today's generation in education by connecting the people around the globe.

Hello, Rajiv Roy

Affiliated Institutions

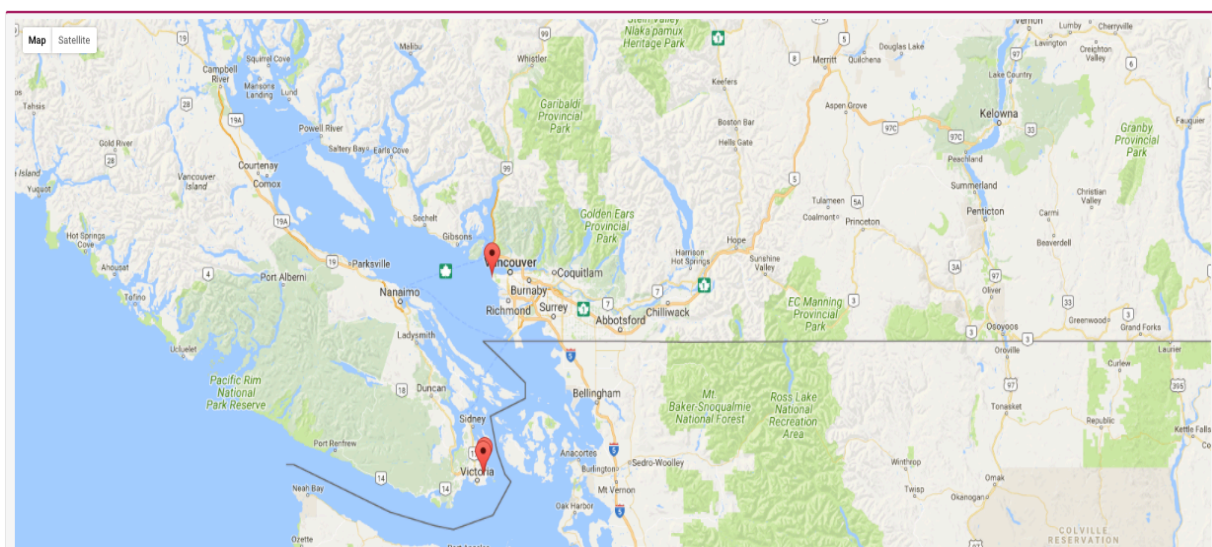


Figure 25 Affiliated Institutions representation on google map

6. E-Catalyst System Management

The e-Catalyst system provides out of the box functionalities to the instructors and students and to deliver positive outcome to the society, it is very important to maintain the system consistently. In order to achieve and maintain the system with all its functionalities, proper management of the system is needed. We have decided that the e-Catalyst system will be handed over to a non-profit educational organisation. The Non-profit organisation will not only maintain this system but also help students to learn from this system. Many instructors from reputed universities, software developer from big companies work for non-profit organisations without any pay for good cause. It will be easier for non-profit organisations to find good instructors and

software developers who are willing to teach and maintain the system pro bono or with limited fees. The detailed e-Catalyst system management and costs incurred are described in Table 2

Cost Items	e-Catalyst system
License Fee	No cost
Number of free License	100 beyond 100 each license will cost \$25
Source Code	Open, already developed
Development Team	Graduate students from Computer Science department at Uvic
Ownership	Handed over to non-Profit Organisation
Client support/maintenance services	Relies on developer forum, online documentation, development community
Support/maintenance cost	No Cost as maintained by the members of Non-Profit organisation
Verification of Product	Already done
Risk of product discontinuation	No
Ease of customization	Assured, performed by an engineer of non-profit organisation according to the specific needs
Security	Maintained by Salesforce
Version control	Automatically Update by Salesforce
Release process	Very easy
Storage	Initially free up to 1 GB More than 1 GB will cost per GB \$10

Table 2 Detailed e-Catalyst System Management

7. Conclusion and Future work

In this project, the “e-Catalyst Learning software system” is designed, verified, implemented and tested. The primary purpose of the system is to understand the basic needs of users who will use

the system and make the system more user-friendly. The system has introduced new functionalities which are easy to use and are beneficial for the instructors and students. Instructors can now schedule their calendar as per their convenience, can make Skype calls directly to the students, manage their courses, can check the student performance and give feedback to their students. Instructors can discuss topics and answers to the posts made by students on discussion board. Instructors can also see the institutions wherein they can contact the organizations and conduct seminars or group meetings with the instructors who work in those organizations to discuss the issues related to the education or to improve the performance of students. Thus, the features of the e-Catalyst system will not only help instructors to perform effectively their work but these will also make the system reliable, easy to use and user-friendly. There are still some features to be implemented in the future, including the following:

- Mobile application for e-Catalyst system
- Video Camera integration so that instructors can watch who is giving the exam
- Use of Artificial intelligence so that the instructors get best recommendations automatically like the performance of students, Other instructors interested areas, etc.

References

- [1] Bates, A.W. and Poole, G. (2003) Effective Teaching with Technology in Higher Education: Foundations for Success San Francisco: Jossey-Bass
- [2] Ragan, L.C. (1998). Good Teaching is Good Teaching: An Emerging Set of Guiding Principles and Practices for the Design and Development of Distance Education. DEOSNEWS (8), 12.
- [3] Bersin, Josh. (2002, March). Measuring E-Learning's Effectiveness: A Five-Step Program for Success. E-Learning.
- [4] eLearning Industry. Top eLearning statistics and facts.
<https://elearningindustry.com/elearning-statistics-and-facts-for-2015>

[5] Salesforce Developers. A Multitenant Architecture.

https://developer.salesforce.com/docs/atlas.en-us.fundamentals.meta/fundamentals/adg_intro_multitenant.htm

[6] Salesforce Developers. The technologies behind Force.com platform.

https://developer.salesforce.com/docs/atlas.en-us.fundamentals.meta/fundamentals/adg_intro_tech.htm

[7] Tutorials Point. Apex tutorial. <https://www.tutorialspoint.com/apex/>

[8] Tutorials Point. Salesforce Visualforce pages.

https://www.tutorialspoint.com/salesforce/salesforce_visualforce_pages.htm

[9] Cardoso, Janette; Camargo, Heloisa (1999). Fuzziness in Petri Nets and Tappal. Physica-Verlag. ISBN 3-7908-1158-0.

[10] Strowd, Harrison & Lewis, Grace. T-Check in System-of-Systems Technologies: Cloud Computing (CMU/SEI-2010-TN-009). Software Engineering Institute, Carnegie Mellon University, 2010. <http://www.sei.cmu.edu/library/abstracts/reports/10tn009.cfm>

ELECTRONICALLY TUNABLE LC HIGH PASS LADDER FILTER USING OTRA

Neeta Pandey, Venkatesh Kumar, Aayush Goel and Ankit Gupta

Department of Electronics and Communication Engineering, Delhi Technological University, India

Abstract

This paper presents Operational trans-resistance (OTRA) based electronically tunable high pass L-C based ladder filter. The proposed high pass filter is designed by following a systematic approach using leap frog simulation for ladder filters. The cut-off frequency of the proposed filter can be varied with the application of appropriate voltages to the gate of MOSFETs hence making the design electronically tunable. Therefore, it can be used for RF applications at 455kHz and 1MHz (intermediate frequencies for RF applications). Performance of the proposed circuit is verified through SPICE simulations employing a 0.5 μ m MOSIS AGILENT CMOS realization of OTRA.

Keywords:

OTRA, High Pass Filter, Tunable

1. INTRODUCTION

The conventional voltage mode circuits and filters realized using operational amplifiers suffer from limitations which include lower bandwidth for higher gains. On the contrary, current-mode circuits offer several advantages as compared to voltage mode circuits such as higher bandwidth, increased linearity and reduced power consumption [1]-[4]. Continuous Time (CT) filters find extensive applications in fields like communication, measurements, and instrumentation and offer simplicity, low power and no sampling noise as compared to the discrete time filters. High pass filters form a key component in R/F microwave wireless applications [5]. Hence design of a current mode high pass filter has been proposed in this paper.

The main approach for designing of filters involves the following steps: (a) choice of an appropriate order according to the required design specifications, (b) the derivation of the corresponding transfer function, (c) synthesis and implementation of the required circuit from the obtained transfer function [6]. The synthesis of CT filters generally follows the approach of doubly terminated lossless LC ladder realization [7]-[8]. The resulting filter is tolerant to component variations, and offers an improved dynamic range performance and enhanced accuracy of passband magnitude response. Inductors are bulky and their use in integrated circuits is costly [7]. We can overcome this non-feasibility of inductor realization in conventional LC ladder realization approach by using leap frog method, in which the relationship between various components is established through the signal flow graphs (SFG). Lossy and lossless active differentiators are then used to realize the obtained SFGs to implement the proposed design in this paper.

Literature survey of L-C ladder filters with different orders and approximation functions using leapfrog method [9]-[29] has been carried out. These configurations use variants of second generation current conveyors (CCII) namely dual/multiple output current controlled CCII (DOCCCII/ MOCCCII) [11]-[12],

multiple output CCII (MOCCCII) [10], differential voltage CC (DVCC) [14], differential voltage current controlled Current Feedback Operational amplifier (DVCCCFOA) [15] and differential voltage current controlled CCII (DVCCC), current feedback amplifier (CFA) [17], current feedback operational amplifier (CFOA) [16], current differencing buffer amplifier [18]-[20], current controlled current differencing buffer amplifier (CCCDDBA) [21], operational trans-conductance amplifier [24]-[26], current backward trans-conductance amplifier [27], current differencing trans-conductance amplifier (CDTA) [22]-[23], CMOS based differential integrators [9], CMOS based lossy and lossless integrators [28]-[29].

From the available pool of literature, it can be summarized that, Configurations [15], [16], [21], [24]-[26] and [9]-[14], [17]-[20], [22], [23], [27]-[29] provide voltage and current outputs respectively. There is no appropriate impedance level for the configurations [13]-[15], [17]-[20], [24]-[26]. Thus an additional active block may be required to access the output. There is a limited literature is available on structures providing voltage output [15]-[17], [21], [24]-[26]. Furthermore, these structures do not provide output at low impedance except for those presented in [16], [21].

Table.1. Full form of some acronyms

Acronym	Full form
OTRA	Operational Trans-Resistance Amplifier
SFG	Signal Flow Graphs
CCII	Second generation Current Conveyors
DVCC	Differential Voltage Current Conveyor
DVCCCFOA	Differential Voltage Current Controlled Current Feedback Operational Amplifier
DVCCC	Differential voltage current controlled CCII
CFA	Current Feedback Amplifier
CFOA	Current Feedback Operational Amplifier
CCCDDBA	Current Controlled Current Differencing Buffer Amplifier
CDTA	Current Differencing Trans-conductance Amplifier

OTRA is a current mode active device with voltage as the output. It does not have any limitations on the slew rate and gain bandwidth product [30]-[35]. The parasitic effects are negligible as the internal terminals are grounded. Therefore OTRA can be easily and appropriately utilized for the design of filter with voltage output based on LC ladder network with Leapfrog simulation method.

The paper presented has been divided into five sections as described: Section 2 highlights leapfrog based simulation of LC-

ladder, section 3 elaborates on the functioning of the proposed filter using OTRA block, section 4 describes the functioning of proposed filter considering non-idealities and section 5 presents simulation and results, which is finally followed by conclusion.

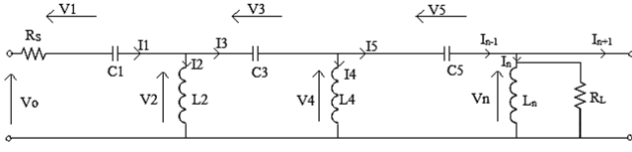


Fig.1. n^{th} order doubly terminated LC-Ladder

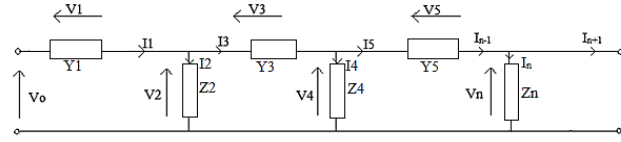


Fig.2. n^{th} order doubly terminated LC-Ladder with general immittances

2. LC HP LADDER FILTER USING LEAP FROG SIMULATION

This section illustrates and presents the realization of doubly terminated LC ladder with capacitors in series arm and inductors in the shunt arm to perform high pass operation. The currents and voltages in the shunt arm are given respectively as:

$$I_k = I_{k-1} - I_{k+1}, \text{ where } (k = 2, 4, 6, \dots, n-2) \quad (1)$$

and

$$V_k = V_{k-1} - V_{k+1}, \text{ where } (k = 1, 2, 3, \dots, n-1) \quad (2)$$

As the value of $I_n = 0$ and $I_n = I_{n-1}$

$$V_k = I_k sL_k \quad (3)$$

$$V_n = \frac{I_n}{\left[\frac{1}{sL_n} + G_L \right]} \text{ with } G_L = 1/R_L. \quad (4)$$

For the series arm, the currents are given as:

$$I_k = V_{k-1} - sC_{k+1}, \text{ where } (k = 4, 6, 8, \dots, n) \quad (5)$$

$$I_1 = \frac{V_n}{\left[\frac{1}{sL_1} + R_s \right]} \quad (6)$$

The elements in the series arms are rewritten as Admittances whereas those in the shunt arm as impedances. The Fig.2 shows modification over Fig.1.

The node voltages and the current in series arm are related as:

$$I_k = Y_k (V_{k-1} - V_{k+1}), \text{ where } (k = 1, 3, 5, \dots, n-1) \quad (7)$$

$$V_k = Z_k (I_{k-1} - I_{k+1}), \text{ where } (k = 2, 4, 6, \dots, n-2) \quad (8)$$

$$V_n = Z_n I_{n-1} \quad (9)$$

OTRA is used for the active realization of above equations. OTRA is a block which provides voltage output by processing input current difference. Therefore, the necessary changes for performing the voltage differencing operation are discussed in the following section.

3. PROPOSED CIRCUIT

The proposed sixth order high pass filter uses OTRA block which is in active building block. The first section briefly describes the properties and characteristics of OTRA block. The design of the proposed filter is described in the subsequent section.

3.1 OTRA

OTRA is an active three terminal device that consist of two input terminals and an output terminal as represented in Fig.3. It is a current mode device where the input terminals are virtually grounded leading to low input and output impedance. Thus, parasitic effects of OTRA can be neglected rendering it suitable for high frequency applications. The port relationship of OTRA is represented in Eq.(10).

$$\begin{bmatrix} V_p \\ V_n \\ V_o \end{bmatrix} = \begin{bmatrix} 0 & 0 & 0 \\ 0 & 0 & 0 \\ R_m & -R_m & 0 \end{bmatrix} \begin{bmatrix} I_p \\ I_n \\ I_o \end{bmatrix} \quad (10)$$

where, R_m represents the trans-resistance gain of OTRA, which approaches infinity for ideal operation. Due to the high value of R_m , the two input currents are of same value. Therefore, OTRA is used in negative feedback configuration for linear circuit applications.

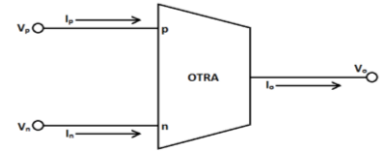


Fig.3. OTRA Circuit Symbol

3.2 OTRA BASED IMPLEMENTATION OF PROPOSED LC HIGH PASSED LADDER FILTER

Since OTRA provides current as output, for direct realization of Eq.(9) we multiply the equation by R_{sc} , the scaling resistance and Eq.(7) can be rewritten as:

$$R_{sc} I_k = R_{sc} Y_k (V_{k-1} - V_{k+1}), \text{ where } (k = 1, 3, 5, \dots, n-1) \quad (11)$$

$$V_{lk} = t_{Yk} [V_{k-1} - V_{k+1}], \text{ where } (k = 1, 3, 5, \dots, n-1) \quad (12)$$

where,

$$V_{lk} = R_{sc} I_k$$

$$Y_k = \frac{1}{\left[\frac{1}{sC_1} + R_s \right]},$$

$$Y_k = sC_k \text{ and } t_{Yk} = R_{sc} Y_k \quad (k = 1, 3, 5, \dots, n-1)$$

The node voltages in Eq.(8) and Eq.(9) are rewritten as Eq.(13), Eq.(14) and Eq.(15) with the help of Eq.(11) and Eq.(12).

$$V_k = \frac{Z_k}{R_{sc}} (R_{sc} I_{k-1} - R_{sc} I_{k+1}) \quad (k = 2, 4, 6, \dots, n-2) \quad (13)$$

$$V_k = t_{Zk} [V_{l(k-1)} - V_{l(k+1)}] \quad (k = 2, 4, 6, \dots, n-2) \quad (14)$$

$$V_n = t_{Zn} V_{l(n-1)} \quad (15)$$

where,

$$Z_k = sL_k,$$

$$Z_n = \frac{1}{\frac{1}{sL_n} + G_L}$$

and

$$t_{Zk} = Z_k/R_{SC}(k = 2,4,6,...,n-2)$$

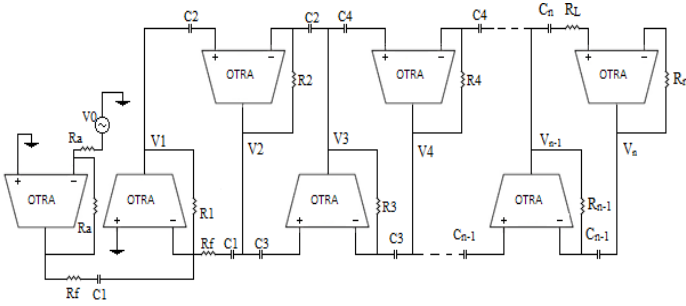


Fig.5. Proposed OTRA based n^{th} order doubly terminated HPF

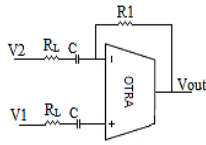


Fig.4. Non-Ideal Differentiator

OTRA block can be used to implement an ideal (lossless) and a non-ideal (lossy) differentiator. Using these two differentiators n^{th} order high pass filter has been proposed based on the leapfrog simulation.

The Eq.(11) to Eq.(15) are actively realized differencing lossy and lossless differentiators. A lossy differentiator as the first stage is followed by $(n-2)$ lossless differentiator stages. The n^{th} stage, i.e. the output stage is again a lossy differentiator.

The circuit for the non-ideal differentiator is represented in Fig.4. The output voltage in terms of V_1 and V_2 is given as:

$$V_{out} = R_1[V_1(sC + G_L) - V_2(sC + G_L)] \quad (16)$$

For the first stage the non-ideal circuit is designed using an inverter stage followed by a summer stage as shown in Fig.5.

3.3 ELECTRONIC TUNABILITY

More attention is being given to electronically tunable components as traditional electronic components may have deviations in fine-tuning the tolerances of the electronic components [36]. Electronic tunability enhances the controllability of a microcomputer or microcontroller [37]. A tunable high pass OTRA filter could be simulated by using NMOS instead of the feedback resistances so as to change the value of resistances w.r.t. the input voltages at the gate of NMOS and hence change the cut-off frequency of the proposed filter. The Fig.6 represents a single stage tunable lossy differentiator with the value of resistance given by Eq.(17).

$$R_i = \frac{1}{\mu_n C_{ox} \left(\frac{W}{L} \right) (V_{ai} - V_{bi})} \quad (17)$$

Thus, electronic tunability can be embedded by implementing resistors R_1 to R_n with the help of MOS based realization using method. This makes the design flexible and the filter can be fine-tuned in case there is any deviation from desired response. The modified Fig.7 shows tunable filter implementations where the gate voltages V_{ai} and V_{bi} realize the required resistors using MOS. ($i = 1,2,3,...,n$).

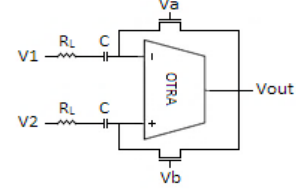


Fig.6. Single stage Tunable Differentiator

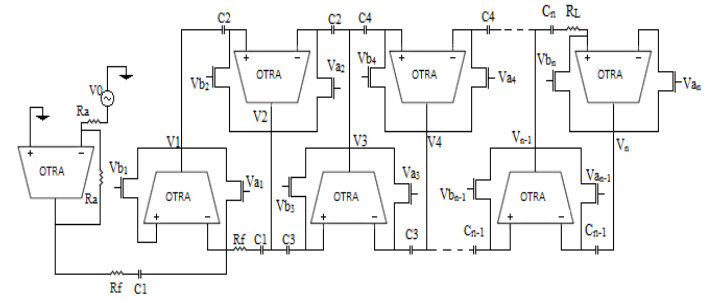


Fig.7. Electronically tunable Proposed OTRA based n^{th} order doubly terminated HPF

3.4 NON-IDEALITY ANALYSIS

The trans-resistance gain (g_m) of an ideal OTRA block is infinity causing the input currents to become equal. But in reality the gain is finite for small bandwidth and decreases further with increase in frequency. Therefore effects of this non-ideality should be included while deriving transfer functions.

The single pole model of the OTRA block will have trans-resistance gain of:

$$R_m(s) = R_0/(1 + (s/\omega_0)) \quad (18)$$

At high frequencies the Eq.(18) can be approximated to:

$$R_m(s) = 1/sC_p \quad (19)$$

where, the parasitic capacitance $C_p = 1/R_0\omega_0$, open loop DC trans-resistance gain is R_0 and trans-resistance cut-off frequency is ω_0 .

The transfer function of single stage differentiator is modified to

$$V_{out} = R_1 \{ V_1[s(C + C_p) + G_L] - V_2[s(C + C_p) + G_L] \} \quad (20)$$

4. SIMULATIONS AND RESULTS

The proposed high-pass filter is realised using lossy and lossless differentiator implementations of OTRA on the lines of a sixth-order Chebyshev filter with a 0.1dB ripple width in passband. The passive elements used in the prototype Chebyshev filter has normalized values of $C_1 = 0.8561$, $L_2 = 0.7122$, $C_3 = 0.4863$, $L_4 = 0.6592$, $C_5 = 0.5255$, $L_6 = 1.1604$ and $R_F = 0.7378$. For a cut-off frequency of 455kHz, $R_a = 1\text{k}\Omega$, $R_f = 0.599\text{k}\Omega$ and $C_a = C_b = C_c = C_d = C_e = C_f = 0.5\text{nF}$ the de-normalized values of

the feedback path resistors are $R_1 = 0.99\text{k}\Omega$, $R_2 = 0.299\text{k}\Omega$, $R_3 = 0.567\text{k}\Omega$, $R_4 = 0.277\text{k}\Omega$, $R_5 = 0.613\text{k}\Omega$, $R_6 = 0.487\text{k}\Omega$ and $R_L = 1.1\text{k}\Omega$.

Table.2. Aspect ratios of transistors in Fig.8

Transistor	$W(\mu\text{m})/L(\mu\text{m})$
$M_1 - M_3$	100/2.5
M_4	10/2.5
M_5, M_6	30/2.5
M_7	10/2.5
$M_8 - M_{11}$	50/2.5
M_{12}, M_{13}	100/2.5
M_{14}	50/2.5

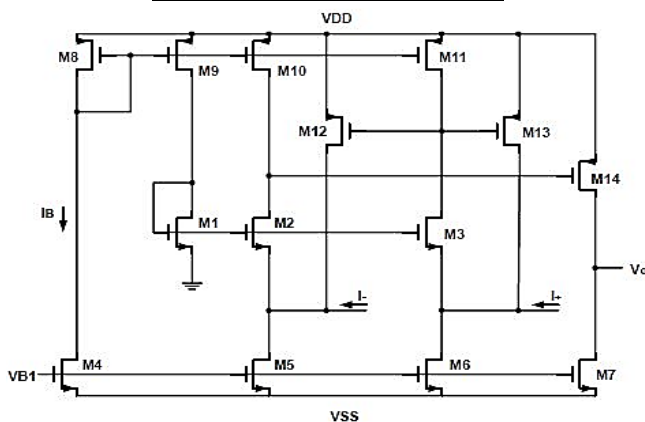


Fig.8. CMOS Implementation of OTRA [38]

The simulated frequency response of a high-pass LC-ladder filter is shown in Fig.9. Also the frequency response of OTRA based ladder filter in superimposed to know the deviations of the active realization. The simulated frequency response of a tunable OTRA based filter for cut-off frequencies of 455kHz and 1MHz are shown in Fig.10. Using Eq.(17) the aspect ratios (W/L) of the MOS transistors used to attain tunability are calculated as shown in Table.3. For achieving the cut-off frequency of 455kHz we have set the gate voltages of MOS resistors in feedback path to $V_{a_i} = 0.9\text{V}$ and $V_{b_i} = 1.2\text{V}$, while to achieve the cut-off frequency of 1MHz we have to set the gate voltages, V_{a_i} and V_{b_i} to 0.75V and 1.4V respectively ($i = 1, 2, 3, \dots, 6$).

Table.3. Aspect Ratios of Transistors in Fig.8

Transistor	$W(\mu\text{m})/L(\mu\text{m})$
$Ma_1 - Mb_1$	2.7/2.5
$Ma_2 - Mb_2$	4.33/5
$Ma_3 - Mb_3$	5/2.73
$Ma_4 - Mb_4$	4.75/5
$Ma_5 - Mb_5$	5/2.96
$Ma_6 - Mb_6$	2.68/5

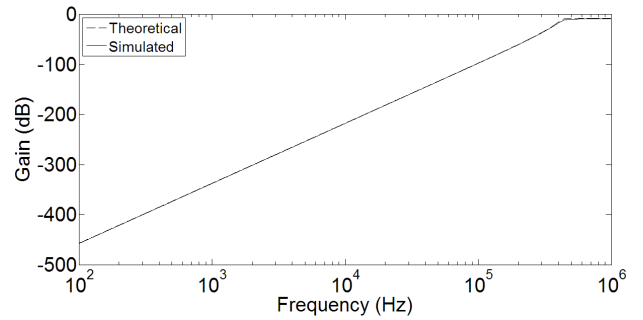


Fig.9. Simulated OTRA based vs Theoretical LC-ladder Filter Frequency Response

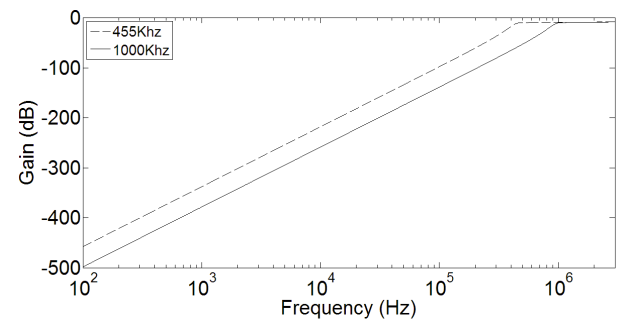


Fig.10. Simulated OTRA based Tunable Filter Frequency Response for 455kHz and 1MHz

5. CONCLUSION

OTRA based sixth order high-pass filter is presented and simulated in this paper. As compared to Current feedback operational amplifier (CFOA) based high pass ladder filter presented in [39], the proposed OTRA based sixth order high pass ladder filter is electronically tunable. The proposed topology also offers an advantage in terms of higher operating and cut-off frequencies as compared to existing high-pass ladder filter designs [39]. Simulation and results are presented for 455kHz and 1Mhz. Non-Ideality Analysis has been included along with electronic tunability specifications.

REFERENCES

- [1] H.P. Chen and P.L. Chu, "Versatile Universal Electronically Tunable Current-Mode Filter using CCII's", *IEICE Electronics Express*, Vol. 6, No. 2, pp. 122-128, 2009.
- [2] B. Wilson, "Recent Developments in Current Conveyor and Current-Mode Circuits", *IEE Proceedings-Circuits, Devices and Systems*, Vol. 137, No. 2, pp. 63-77, 1990.
- [3] G.W. Roberts and A.S. Sedra, "All Current-Mode Frequency Selective Circuits", *Electronics Letters*, Vol. 25, No. 12, pp. 759-761, 1989.
- [4] C.M. Chang, "Current Mode Allpass/Notch and Bandpass Filter using Single CCII", *Electronics Letters*, Vol. 27, No. 20, pp. 1812-1813, 1991.
- [5] Hui Chen, Di Jiang, Ke-Song Chen and Hong-Fei Zhao, "A Compact High-Pass Filter using Hybrid Microstrip/Nonuniform CPW with Dual-Mode Resonant Response", *International Journal of Antennas and Propagation*, Vol. 2016, pp. 1-7, 2016.

- [6] Suman Kumari, Stuti Gupta, Neeta Pandey, Rajeshwari Pandey and Rashika Anurag, "LC-Ladder Filter Systematic Implementation by OTRA", *International Journal Engineering Science and Technology*, Vol. 19, No. 4, pp. 1808-1814, 2016.
- [7] A. Thanachayanont and A. Payne, "CMOS Floating Active Inductor and its Application to Bandpass Filter and Oscillator Designs", *IEEE Proceedings-Circuits, Devices and Systems*, Vol. 147, No. 1, pp. 42-48, 2000.
- [8] R. Shumann and M.E. Van Valkenburg, "*Design of Analog Filters*", Oxford University Press, 2001.
- [9] S. Sa-Ad and D. Chaythong, "A High Frequency Current Mode Ladder Filter using Multiple Output Lossless Integrator", *Proceedings of International Symposium in Intelligent Signal Processing and Communication systems*, pp. 1-4, 2008.
- [10] J. Wu and E. El-Masry, "Current-Mode Ladder Filters using Multiple Output Current Conveyors", *IEEE Proceedings-Circuits, Devices and Systems*, Vol. 143, No. 4, pp. 218-222, 1996.
- [11] A. Jiraseree-Amornkunt, N. Fujii and W. Surakamponorn, "Realisation of Electronically Tunable Ladder Filters using Multi-Output Current Controlled Conveyors", *Proceedings of IEEE International Symposium on Circuits and Systems*, pp. 541-544, 2003.
- [12] A. Campeanu and J. Gal, "Systematic Implementation Method of LC-Ladder Filter by MO-CCCI Circuits", *Proceedings of 5th International Congress and Exhibition of Electrical and Electronic Engineering*, pp. 1-5, 2007.
- [13] X. Yanhui and H. Peng, "Realisation of Low Pass and Band-Pass Leapfrog Filters using OAs and CCCIs", *Proceedings of IEEE International Conference Management and Service Science*, pp. 1-4, 2009.
- [14] Y.H. Xi and X. Li, "Active Simulation of passive Leapfrog Ladder Filters Using DVCCs", *Proceedings of IEEE International Conference on Industrial Technology*, pp. 1-5, 2008.
- [15] C. Laoudias and C. Psychalinos, "Comparative Study of Resistor Less Filters using Differential Voltage Current Controlled Current Feedback Operational Amplifiers and Differential Voltage Current Controlled Current Conveyors", *International Scholarly Research Notices*, Vol. 2013, pp. 7-11, 2013.
- [16] P.K. Sinha, A. Saini, P. Kumar and S. Mishra, "CFOA based Low Pass and High Pass Ladder Filter-a New Configuration", *Circuits Systems*, Vol. 5, No. 12, pp. 293-300, 2014.
- [17] T.S. Rathore and U.P. Khot, "CFA-based Grounded-Capacitor Operational Simulation of Ladder Filters", *International Journal of Circuit Theory and Applications*, Vol. 36, No. 5-6, pp. 697-716, 2008.
- [18] W. Tangsrirat, N. Fujii and W. Surakamponorn, "Current-Mode Leapfrog Ladder Filters using CDBAs", *Proceedings of IEEE International Symposium on Circuits and Systems*, pp. 57-60, 2002.
- [19] W. Tangsrirat, W. Surakamponorn and N. Fujii, "Realization of Leapfrog Filters using Current Differential Buffered Amplifiers", *The Institute of Electronics, Information and Communication Engineers*, Vol. 86, No. 2, pp. 318-326, 2003.
- [20] W. Tangsrirat, K. Klahan, T. Dumawipata and W. Surakamponorn, "Low-Voltage NMOS-based Current Differencing Buffered Amplifier and its Application to Current-Mode Ladder Filter Design", *International Journal of Electronics*, Vol. 93, No. 11, pp. 777-791, 2006.
- [21] V. Ramola, S. Mishra, R.K. Singh and D.S. Chauhan, "CCCDDBA based Implementation of Voltage Mode Third Order Filter", *Proceedings of International Conference on Advances in Communication, Network, and Computing*, pp. 185-192, 2012.
- [22] A. Uygur and H. Kuntman, "Seventh-Order Elliptic Video Filter with 0.1 dB Pass Band Ripple Employing CMOS CDTAs", *AEU-International Journal of Electronics and Communications*, Vol. 61, No. 5, pp. 320-328, 2007.
- [23] J. Xu and C. Wang, "The Current Difference Transconductance Amplifier (CDTA)", Available at: <https://www.edn.com/design/analog/4405810/The-Current-Differencing-Transconductance-Amplifier-CDTA>.
- [24] Y. Sun, "Synthesis of leap-frog multiple-loop feedback OTA-C filters", *IEEE Transactions on Circuits and Systems II: Express Briefs*, Vol. 53, No. 9, pp. 961-965, 2006.
- [25] H.W. Su and Y. Sun, "A CMOS 100 MHz Continuous-Time Seventh Order 0.05 Equiripple Linear Phase Leapfrog Multiple Loop Feedback GM-C Filter", *Proceedings of IEEE International Symposium on Circuits and Systems*, pp. 17-20, 2002.
- [26] C. Feng, "The Design of OTA-C Filter based on the Prototype of Ladder LC-Filter", *Journal of Theoretical and Applied Information Technology*, Vol. 49, No. 1, pp. 144-148, 2013.
- [27] U.E. Ayten, M. Sagba and H. Sedef, "Current Mode Leap Frog Ladder Filters using a New Active Block", *AEU-International Journal of Electronics and Communications*, Vol. 64, No. 6, pp. 503-511, 2010.
- [28] P. Prommee and N. Wongprommoon, "Tunable CMOS-based Current Mode Fifth Order Ladder Low-Pass Filter", *Proceedings of 36th IEEE International Conference on Telecommunications and Signal Processing*, pp. 397-401, 2013.
- [29] T. Kunto, P. Prommee and M.T. Abuelmaatti, "Electronically Tunable Current-Mode High-Order Ladder Low-Pass Filters based on CMOS Technology", *Radioengineering*, Vol. 24, No. 4, pp. 974-987, 2015.
- [30] K.N. Salama and A.M. Soliman, "CMOS Operational Transresistance Amplifier for Analog Signal Processing", *Microelectronics Journal*, Vol. 30, No. 3, pp. 235-245, 1999.
- [31] R. Pandey, N. Pandey, M. Bothra and S.K. Paul, "Operational Transresistance Amplifier based Multiphase Sinusoidal Oscillator", *Journal of Electrical and Computer Engineering*, Vol. 2011, pp. 1-8, 2011.
- [32] C.L. Hou, H.C. Chien and Y.K. Lo, "Square Wave Generators Employing OTRAs", *IEEE Proceedings-Circuits, Devices and Systems*, Vol. 152, No. 6, pp. 718-722, 2005.
- [33] Y.K. Lo, H.C. Chien and H.G. Chiu, "Switch Controllable OTRA based Bistable Multivibrators", *IET Circuits, Devices and Systems*, Vol. 2, No. 4, pp. 373-382, 2008.
- [34] A. Gupta, R. Senani, D.R. Bhaskar and A.K. Singh, "OTRA-based Grounded-FDNR and Grounded-Inductance Simulators and their Applications", *Circuits, Systems, and Signal Processing*, Vol. 31, No. 2, pp. 489-499, 2012.

- [35] A. Gokcen, S. Kilinc and U. Cam, "Fully Integrated Universal Biquads using Operational Transresistance Amplifier with MOS-C Realisation", *Turkish Journal of Electrical Engineering and Computer Sciences*, Vol. 19, No. 3, pp. 363-372, 2011.
- [36] H.P. Chen, Y.S. Hwang and Y.T. Ku, "Voltage-Mode and Current-Mode Resistorless Third-Order Quadrature Oscillator", *Applied Sciences*, Vol. 7, No. 2, pp. 179-189, 2017.
- [37] Surasak Sangyaem, Surapong Siripongdee, Winai Jaikla and Fabian Khateb, "Five-Inputs Single-Output Voltage Mode Universal Filter with High Input and Low Output Impedance using VDDAs", *Optik-International Journal for Light and Electron Optics*, Vol. 128, pp. 14-25, 2017.
- [38] H. Mostafa and A.M Soliman, "A Modified CMOS Realization of the Operational Transresistance Amplifier (OTRA)", *Frequenz*, Vol. 60, No. 3-4, 2006.
- [39] P. Sinha, A. Saini, P. Kumar and S. Mishra, "CFOA based Low Pass and High Pass Ladder Filter-A New Configuration", *Circuits and Systems*, Vol. 5, No. 12, pp. 293-300, 2014.

Establishment of the Shoot and Callus Culture of an Important Medicinal Plant *Plumbago zeylanica*

Abstract

Plumbago zeylanica is an important medicinal plant which belongs to the Plumbaginaceae family. It possesses antibacterial, hepato protective, and central nervous system stimulatory activity, anti-fungal, anti-inflammatory, anti-hyperglycemic, anti-cancer and anti-atherosclerotic activity. The objective of this study was to assess the effect two cytokinins (BAP and Kinetin) on shoot growth and two auxin on callus induction (2, 4-D and NAA). Highest multiple shoots (4.33 ± 0.63) and length of shoot (5.01 ± 0.53) were induced from nodal explants on modified MS medium supplemented with the 1.0 mg/L 6-benzyladenine and 3%. Among the two auxin used for the investigation leaf explants showed highest callus induction in MS media supplement with 1.0 mg/L 2, 4-D.

Research Article

Volume 7 Issue 5 - 2017

Arpita Roy and Navneeta Bharadvaja*

Department of Biotechnology, Delhi Technological University, India

***Corresponding author:** Navneeta Bharadvaja, Plant Biotechnology Laboratory, Department of Biotechnology, Delhi Technological University, New Delhi-42, India, Email: navneetab@dtu.ac.in

Received: September 11, 2017 | **Published:** October 26, 2017

Introduction

Medicinal plants are one of the important sources of natural products, which include essential oils, fragrances, pigments, feedstock, and pharmaceuticals. They are of great interest to the researches in biotechnology field as most of the pharmaceutical industries depend on them Chand et al. [1]. *Plumbago zeylanica* is an important medicinal plant which belongs to the Plumbaginaceae family. It is commonly known as Chitrak and Lead word. The plants consists of various bioactive compounds like alkaloids, naphtha quinones, flavonoids, glycoside, steroids, Saponin, phenolic compounds, triterpenoids, coumarins, tannins, carbohydrate, fixed oils, fats, and proteins are present in different plant parts which has been reported to show antibacterial Uma Devi et al. [3], anti-plasmodial, hepato protective, central nervous system stimulatory activity, anti-fungal, anti-inflammatory, anti-hyperglycemic, anti-atherosclerotic activity Kumar et al. [3] anti-tumor, anti-cancer Roy et al. [4] etc. Propagation of this plant through seed is not reliable due to its poor germination under natural conditions. Pharmaceutical companies procured the plant material from wild and which leads to the depletion of this plant rapidly. This raises the concern about extinction of this. Due to the increasing need of this plant, an alternative technology to the conventional method in improvement of crop is to utilize the biotechnological approaches. *In-vitro* propagation is currently used to a large number of medicinally important plants for the multiplication and conservation. Earlier reports suggest that this plant can be multiplied by in-vitro propagation Rout, Wei & Sivanesan, et al. [5,6,7]. Looking at the importance of *Plumbago zeylanica*, in this study an effort has been done to investigate the role of different cytokinin and auxin elicitors on the growth of the plant. Different types of cytokinins and auxin provide shoot multiplication and callus induction. The present study describes the optimum condition for shoot multiplication and establishment of callus culture from nodal and leaf explants of *Plumbago zeylanica*.

Materials and Methods

Plant material

In-vitro grown *Plumbago zeylanica* accession number-524441 was collected from the National Bureau of Plant Genetic Resources (NBPGR). This accession was further maintained in MS (Murashige and Skoog medium) media containing 0.2 mg/l BAP in Plant Biotechnology Laboratory of Delhi Technological University.

Effect of different cytokinin concentration on shoot induction

Nodal explants were cultured in modified MS (NaNO₃ instead of NH₄NO₃) media containing BAP (benzyl amino purine) (1.0 mg/l, 1.5 mg/l and 2.0 mg/l) and Kinetin (1.0 mg/l, 1.5 mg/l and 2.0 mg/l) for shoot multiplication. pH of the medium was adjusted to 5.8 ± 0.2 by using 1N NaOH or 1N HCL before autoclaving at 121°C for 20 min. 0.8% (w/v) agar was used as a gelling agent. The culture was incubated at $25 \pm 2^\circ\text{C}$ with 16h/8h photoperiod. Visual observation was made weekly and data were recorded. After eight weeks shoot number and shoot length were recorded.

Effect of different auxin concentration on callus induction

For induction of callus, leaves from the in-vitro grown plant were excised (0.5 cm) and cultured on modified MS (NaNO₃ instead of NH₄NO₃) media supplemented with 2,4-D(2,4-dichlorophenoxyacetic acid) (1.0 mg/l), 2,4-D (1.0 mg/l) + BAP (0.5 mg/l), NAA (Naphthalene acetic acid) (1 mg/l) and NAA (1.0 mg/l) + BAP (0.5 mg/l).

Statistical analysis

Experiment was repeated thrice and each treatment had five replicates. The number of cultures per replicate varied for the experiments. Observations were recorded as the number of

shoots per explants and length of shoot per nodal explant. The data were analyzed using one-way analysis of variance (ANOVA) ($p < 0.05$).

Results and Discussion

Effect of different cytokinin concentration on shoot induction

In the present two different cytokinins were used i.e. BAP and Kinetin, BAP showed more effective proliferation of shoots than kinetin (Table 1), (Figure 1) express the effect of different concentration (1 mg/l, 1.5mg/l and 2mg/l) of cytokinins on the shoot number and shoot length. Proliferation of shoots was observed in all the culture media after two weeks of incubation. There was very less proliferation observed in MS media without any growth hormone. At high concentration of both the cytokinin, shoot proliferation rate declined. Highest shoot proliferation and length was achieved in the modified MS (NaNO_3 instead of NH_4NO_3) supplement with the 1.0 mg/l BAP. In the present study modified MS media was used for the first time to observe the effect on the growth of *P. zeylanica* and also the entire study was done on the *P. zeylanica* accession which was genetically identified and supplied by NBPGR.

Table 1: Effect of cytokinins on shoot multiplication.

Media	Number of Shoot	Length of Shoot
MS+1 mg/l BAP	4.33 ± 0.63	5.01 ± 0.53
MS+1.5mg/l BAP	2.6 ± 0.69	3.48 ± 0.44
MS+2mg/l BAP	1.8 ± 0.63	1.47 ± 0.43
MS+1 mg/l Kn	2.5 ± 0.53	2.62 ± 0.46
MS+1.5mg/l Kn	1.0 ± 0.48	1.08 ± 0.34
MS+2mg/l Kn	1.0 ± 0.42	0.74 ± 0.18

Sahoo [8] studied the role on BAP and Kinetin on shoot induction of *Plumbago zeylanica*, where BAP supplemented MS media produced more number of shoots that the kinetin supplemented MS media. Ceasar et al. [9] also reported similar kind of results in case of wild type *Plumbago zeylanica* plant. Gbadamosi & Egunyomi [10] reported the highest shoot multiplication in MS medium containing NAA (0.01 - 0.05 mg/l) and BAP (2.0 - 4.5 mg/l). Dohare et al. [11] reported highest shoot formation in the combination of 1mg/l BAP+ 1mg/l NAA and maximum length of shoot was recorded (5.38 ± 0.99 cm).

Effect of different auxin concentration on callus induction

Induction of callus was observed on the cut end of leaf explants after 2 weeks of incubation when modified MS (NaNO_3 instead of NH_4NO_3) supplemented with 1.0 mg/l 2, 4-D and 1.0 mg/l NAA. Whereas media supplemented with the 1.0 mg/l 2, 4-D+ 0.5 mg/l BAP and 1.0 mg/l NAA+ 0.5 mg/l BAP did not show any callus response. An media supplemented with IBA showed root induction. Highest amount of callus induction was obtained in modified MS (NaNO_3 instead of NH_4NO_3) supplemented with 1.0 mg/l 2, 4-D. Lubaina and Murugan (2012) reported that

maximum callus proliferation when MS media supplemented with 1 mg/l 2, 4-D along with 0.5 mg/l BA (Table 2), (Figure 2).

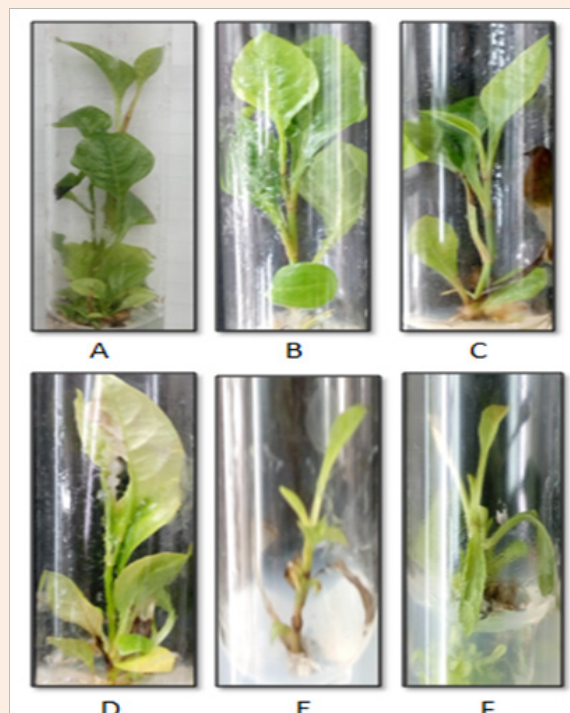


Figure 1: Effect of different cytokinin on shoot multiplication A) MS+1 mg/l BAP, B) MS+1.5mg/l BAP, C) MS+2mg/l BAP, D) MS+1 mg/l Kn, E) MS+1.5mg/l Kn, F) MS+2mg/l Kn.

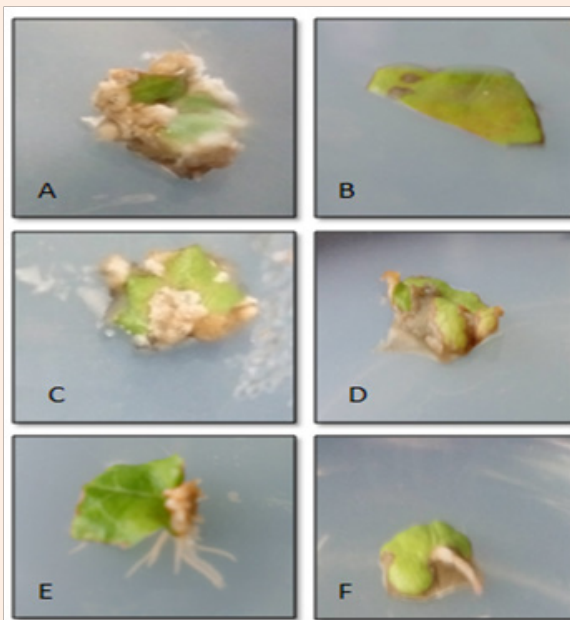


Figure 2: Effect of different auxins on callus induction A) MS+1 mg/l 2, 4-D, B) MS+ 1 mg/l 2, 4-D + 0.5mg/l BAP, C) MS+ 1mg/l NAA, D) MS+1mg/l NAA+ 0.5mg/l BAP, E) MS+1 mg/l IBA, F) MS+1mg/l IBA+ 0.5mg/l BAP.

Table 2: Effect of auxins on callus induction.

Media	Callus Induction
MS+1 mg/l 2, 4-D	+++
MS+ 1 mg/l 2, 4-D + 0.5mg/l BAP	-
MS+ 1mg/l NAA	++
MS+1mg/l NAA+ 0.5mg/l BAP	-
MS+1 mg/l IBA	Root induction
MS+1mg/l IBA+ 0.5mg/l BAP	Root induction

Conclusion

In this study, an attempt has been done to develop a method for the growth of *Plumbago zeylanica* by varying the cytokinin and auxin concentrations. Growth pattern was dependent on different growth hormones in both the shooting and rooting. 1.0 mg/l BAP results in the highest shoot multiplication. MS media supplemented with 1.0 mg/L 2, 4-D showed the faster callus induction rate. Mass propagation of this plant is feasible for field plantings to produce higher amount of roots which is the main source of plumbagin for the pharmaceutical industry. These *in-vitro* studies provide an efficient method for conservation and propagation this over exploited plant.

Acknowledgement

Our sincere thanks goes to Department of Biotechnology, Delhi Technological University for encouragement and providing necessary facilities during this investigation, Dr. Neelam Sharma, NBPGR, New Delhi for providing the plant materials.

Conflict of Interest

None.

References

1. Chand S, Sahrawat AK, Prakash D V S R (1997) *In vitro* culture of *Pimpinella anisum* L (anise) J. Plant Biochem Biotech 6(2): 91-95.

2. Uma Devi P, Soloman FE, Sharda AC (1999) Plumbagin, a plant naphthoquinone with radiomodifying properties. Pharmaceutical Biology 37(3): 231-236.
3. Kumar R, Kumar S, Patra A, Jayalakshmi S (2009) Hepatoprotective activity of aerial parts of *Plumbago zeylanica* linn against carbon tetrachloride-induced hepatotoxicity in rats. International Journal of Pharmacy and Pharmaceutical Sciences 1(Suppl 1): 171-175.
4. Roy A, Attre T, Bharadvaja N (2017) Anti cancer agent from medicinal plants: a review. New aspects in medicinal plants and pharmacognosy. (1st edn). JB Books, Poland.
5. Rout GR, Saxena C, Samantaray S, Das P (1999) Rapid plant regeneration from callus cultures of *Plumbago zeylanica*. Plant Cell, Tissue and Organ Culture 56(1): 47-51.
6. Wei X, Gou X, Yuan T, Russel SD (2006) A highly efficient *in vitro* plant regeneration system and Agrobacterium mediated transformation in *Plumbago zeylanica*. Plant Cell Rep 25(6): 513-521.
7. Sivanesan I (2007) Shoot regeneration and somaclonal variation from leaf callus cultures of *Plumbago zeylanica* Linn. Asian J Plant Sci 6: 83-86.
8. Sahoo S (1986) Micropropagation of *Plumbago zeylanica* Linn. J Herbs Spices Med Plants 5(4): 87-93.
9. Ceasar SA, Ayyanar M, Ignacimuthu S (2013) An Improved Micropropagation Protocol for *Plumbago zeylanica* L. An Important Medicinal Plant. Asian Journal of Biological Sciences, 6: 214-220.
10. Gbadamosi IT, Egunyomi A (2010) Micropropagation of *Plumbago zeylanica* L. (Plumbaginaceae) in Ibadan, Southwestern, Nigeria. Journal of Medicinal Plants Research 4(4): 293-297.
11. Dohare B, Jain K, Jain B, Khare S (2012) Rapid clonal propagation of an endangered medicinal plant *Plumbago zeylanica* Linn. International Journal of Pharmacy & Life Sciences 3(8): 1883- 1887.
12. Lubaina AS, Murugan K (2012) Effect of growth regulators in callus induction, plumbagin content and indirect organogenesis of *Plumbago zeylanica* International Journal of Pharmacy and Pharmaceutical Sciences 4(Suppl 1): 334-336.

Experimental Investigation of Influence of SiO₂ Nanoparticles on the Tribological and Rheological properties of SAE 40 Lubricating Oil

Sumit Chaudhary*¹, Ramesh Chandra Singh*², Rajiv Chaudhary*³

* Department of Mechanical Engineering, Delhi Technological University, Delhi, India

¹ mait.sumit@gmail.com

² rcsinghdelhi@gmail.com

³ rch_dce@rediffmail.com

Abstract: The SiO₂ nanoparticles have been used in the SAE 40 Lubricating oil upto 1% by weight considered as nano lubricant for testing of the rheological stability and tribological properties. The rheological properties of the nano lubricant were tested according to ASTM D 7552-09 for the various concentrations. The nano lubricant was found stable rheologically. The tribological analysis conducted on Pin on Disc test rig (ASTM G99) for fully flooded and starved conditions of lubrication. The nano lubricant showed the reduced coefficient of friction and negligible specific wear rate as compared to the plain SAE 40 lubricating oil. In the SEM images the thin layer of SiO₂ nanoparticles was observed on the surface of the pin. The SiO₂ nanoparticles present on the surface may enhance tribological properties of the material.

Keywords: Nanoparticles, Nano lubricant, Rheology, SEM, Tribology Coefficient of Friction, Specific Wear Rate.

1.0 INTRODUCTION

The recent study shows that almost 30-35% of the power produced by the internal combustion engine of the vehicle wasted in the form of tribological losses [1], [2]. These losses increase the fuel consumption in the engine [3], [4]. The burning of more fuel would raise the engine emission and harmful green house gasses [5], [6].

Various attempts have been made by the researches to overcome the tribological losses or to minimize the friction and wear between the mating surfaces by modifying the surfaces [7]–[10]. The lubricant plays a vital role for improving the tribological properties of the mating surface [11], [12]. Friction modifiers such as organomolybdenum compounds [13], [14], organic friction modifiers [15]–[17], used as lubricant additive has improved the tribological properties [18]. The friction modifiers are generally more effective in the boundary or mixed lubrication regime [18]. There is scope for improvement which the lubricant alone can't achieve. The lubricant enriched with nanoparticles may have the better tribological properties than the virgin lubricant or lubricant having other friction modifiers [19]–[22]. The nanoparticles as lubricant additive heals the cracks if the tribopairs hence improving the service life of the tribopairs [20].

SiO₂ nanoparticles had size 40-50 nm hardness 12 GPa [23], elastic modulus 150 GPa [24]. SiO₂ nanoparticle reduces the friction and wear at the mating surface by preventing the direct contact between the mating parts and enhance the rolling effect hence boost the tribological properties [25], [26].

2.0 EXPERIMENTAL SETUP

The experiment was performed on the Pin on Disc wear and friction test rig (ASTM G99). The mild steel disc diameter 165 mm and thickness 10 mm was casted. The disc was superfinished by surface grinding and lapping, the surface rms value roughness checked by the surface roughness tester in the circumferential direction at an angle of 30° radial outward directions around 2 µm.

The solid cylindrical pin of 10 mm diameter and length 32 mm made up of cast iron was casted. The face of the pin was made flat circular. The composition of the pin measured by spectroscopy came out to be C-3.51%, Cr-1.06%, Mn-0.56%, Si-2.97% Fe-91.9%. The length of the pin was kept such that the bending of pin would not occur.

The lubricant used at the interface of materials during experiment was 15W40 (SAE 40) which is the standard lubricant for the Diesel engine. The kinematic viscosity of the lubricant measured by (ASTMD-445) came out to be 98.922 mPa·s and the density measured by (ASTMD-4052) came out to be 871.82 kg/m³ at 40° C.

2.1 Test Rig: The pin on disc wear and friction testing test rig (ASTM G-99) as shown in Figure 1 was used for the tribotesting, the specification is given in table 1. The test rig is automatic computer controlled system having the speed range of 200 rpm to 2000 rpm. The counter disc was attached over a rotating plate with the help of bolts. The pin was kept in the plunger which is directly attached to the gravity assisted force. The force is transferred to the pin in vertically downward direction with the help of single lever mechanism with leverage 1:1.

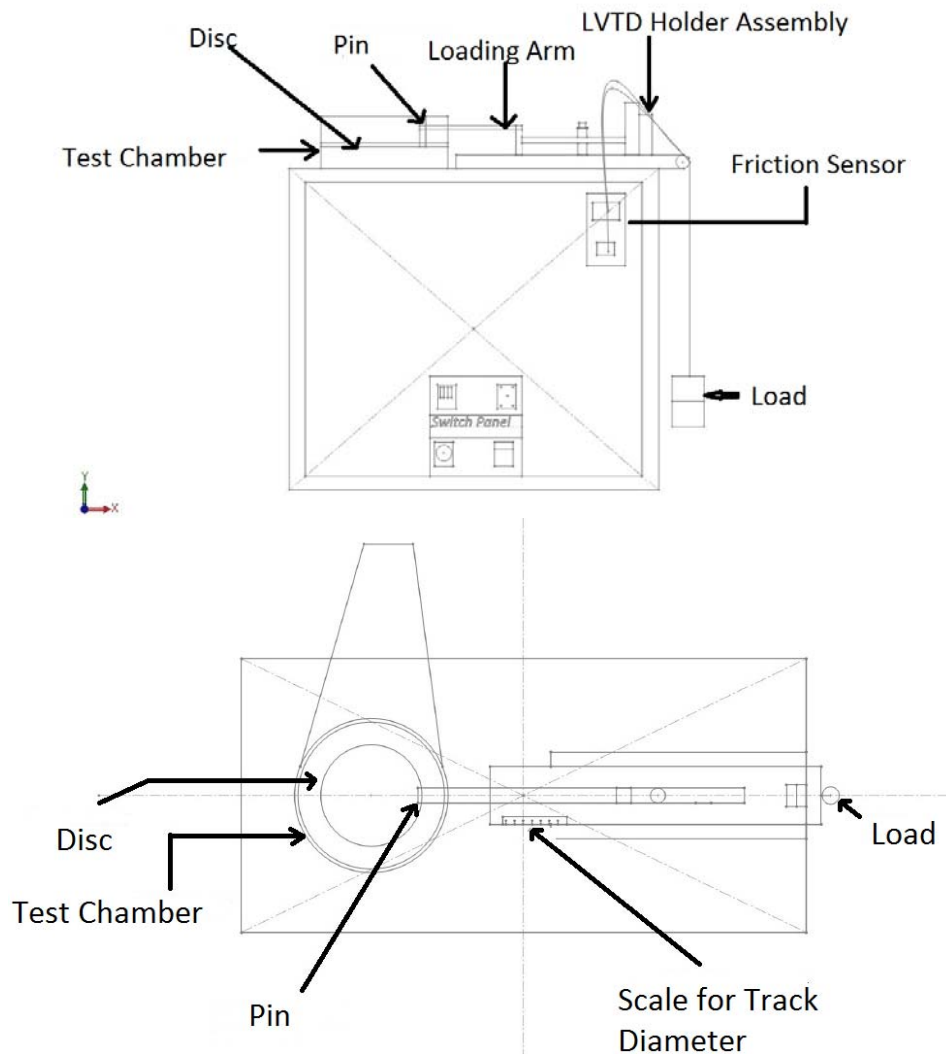


Figure 1: Pin on Disc Test Rig (a) Front View (b) Top View

Table 1: Specification of Pin on Disc Test Rig

S.No	Parameter	Unit	Minimum value	Maximum Value
1	Pin Diameter	mm	3	12
2	Track diameter	mm	0	165
3	Disk rotating speed	rpm	200	2000
4	Friction Force	N	0	200
5	Normal Force	N	1	200

2.2 Nano Lubricant: The nanoparticles of SiO₂ having the average particle size 50-60 nm were mixed in the lubricant SAE 40. The mixing of nanoparticles was done on weight ratio basis. The amount of nanoparticles to be mixed in the lubricant starts from 0.2% by weight upto 1% by weight in the successive increment of 0.2%. The nanofluid was not stable beyond 1% nanoparticles as the nanoparticles got sedimented.

2.3 Preparation of Nano Lubricant: The nano lubricant prepared by mixing the nanoparticles in the lubricant. The mixing carried out by continuous stirring by using the magnetic stirrer at 2000 rpm and 60⁰ C for

2 hours. The nanofluid was sonicated by ultrasonicator for 60 minutes. The nano lubricant was observed stable even after two months of preparation.

3.0 RESULT AND DISCUSSIONS

3.1 Rheological Analysis of Nano Lubricant: The Rheological study was carried as per (ASTM D 7552-09) at shear rate 20 s^{-1} , in the temperature range 0°C to 100°C .

There was no significant change in the Rheological properties of the nano lubricant as it compared to the standard lubricant (15W40). The nano lubricant was stable on the basis of rheology as the change in the viscosity with respect to amount of nanoparticles is less than 5%. The rheological investigation shows that as the amount of nanoparticles in the lubricant increased the viscosity of the lubricant decreased.

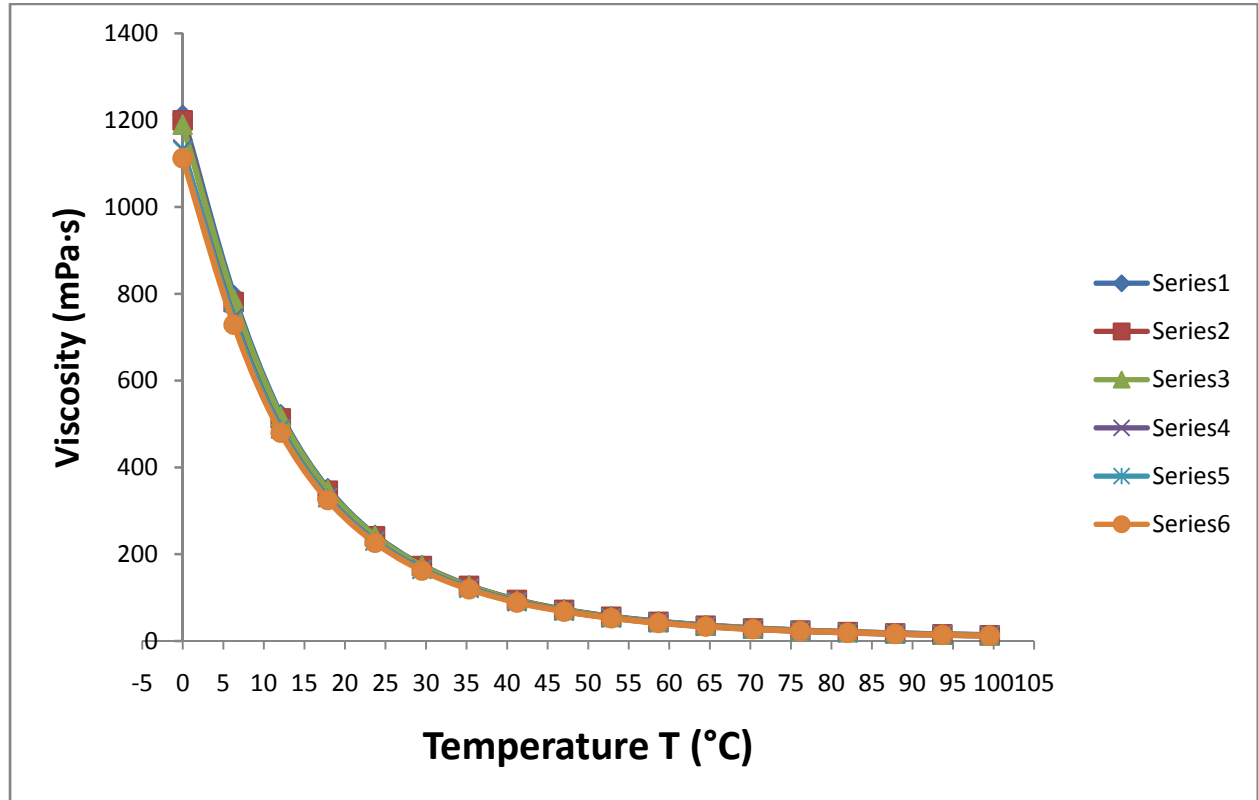


Figure 2: Rheological behavior of Lubricant

Relation between temperature and viscosity:

$$y = -8E-07T^5 + 0.000T^4 - 0.034T^3 + 2.215T^2 - 73.84T + 1110.$$

Where y: viscosity in $\text{mPa}\cdot\text{s}$

T: Temperature ($^\circ\text{C}$)

3.2 Tribological Study: The experiment was conducted at a load of 40 N with variable sliding speed, the sliding speed 3.663m/s, 5.2631m/s 7.3260 m/s, 10.4712 m/s, 13.6054m/s ranging from low speed range to medium and the high speed range. The atmospheric temperature at the time of testing was 28°C . The experiment was carried in fully flooded as well as starved lubrication condition.

In the tribological study coefficient of friction was derived from the friction force given by the software by dividing it with the applied load.

The specific wear rate was derived from the wear by the following relations:

$$S_w = \frac{V_w}{P \times D}$$

Where, S_w = specific wear rate, $\text{mm}^3 / \text{N}\cdot\text{m}$

V_w = Volume of wear loss, in mm^3

P = Applied load in Newton, N

D = Sliding Distance in meters, m

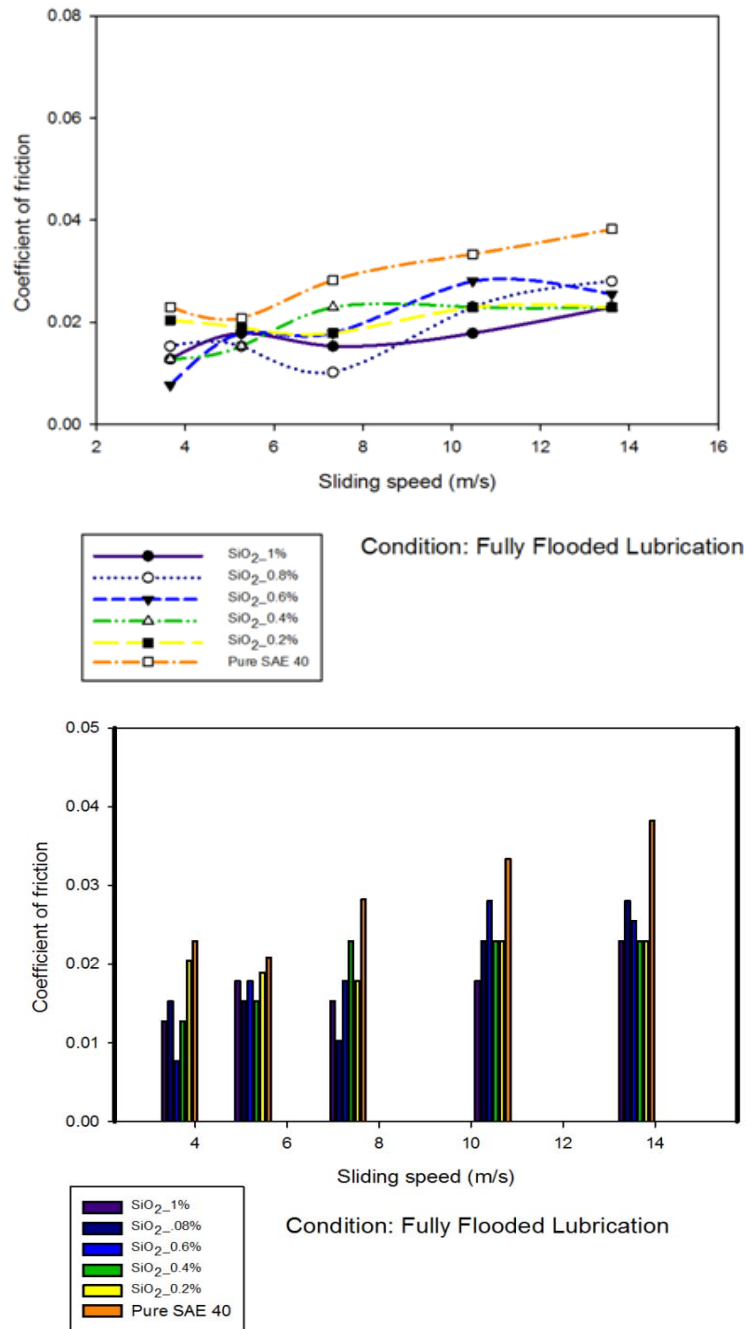


Figure 3: Variation of coefficient of friction with sliding speed for various compositions of Nanofluid in fully flooded Lubrication.

3.2.1 Study of Coefficient of friction for fully flooded condition: Figure 3 shows the variation of coefficient of friction with respect to speed at a constant load of 40 N for the different compositions of nanoparticles in the lubricant starting from 1%, 0.8%, 0.6%, 0.4%, 0.2% and Pure SAE 40 for fully flooded lubrication. The coefficient of friction in the low speed range is having higher values due to the boundary lubrication then the values of coefficient of friction decreases due to the hydrodynamic lubrication and in the high speed region the coefficient of friction again increases. The bar chart shows the comparison of coefficient of friction and the sliding speed in with composition of nanoparticles starting from the 1%, 0.8%, 0.6%, 0.4%, 0.2% and pure lubricant without nanoparticles. The coefficient of friction decreases as we increase the composition of nanoparticles due to the rolling action provided by the nanoparticles upto 0.6% and as we increase the composition of nanoparticles from 0.6% to 0.8% and then 1% the coefficient of friction again increased.

3.2.2 Study of Coefficient of friction for Starved condition: Figure 4 shows the variation of coefficient of friction with respect to speed at a constant load of 40 N for the different compositions of nanoparticles in the lubricant starting from 1%, 0.8%, 0.6%, 0.4%, 0.2% and Pure SAE 40 for starved lubrication. The coefficient of

friction in the low speed range is having higher values due to the higher shear force or contact of asperities then the values of coefficient of friction decreases due to the lesser time of contact between the contact surfaces. The bar chart shows the comparison of coefficient of friction and the sliding speed in with composition of nanoparticles starting from the 1%, 0.8%, 0.6%, 0.4%, 0.2% and pure lubricant without nanoparticles. The coefficient of friction decreases as we increase the composition of nanoparticles due to the rolling action provided by the nanoparticles upto 0.6% and as we increase the composition of nanoparticles from 0.6% to 0.8% and then 1% the coefficient of friction again increased.

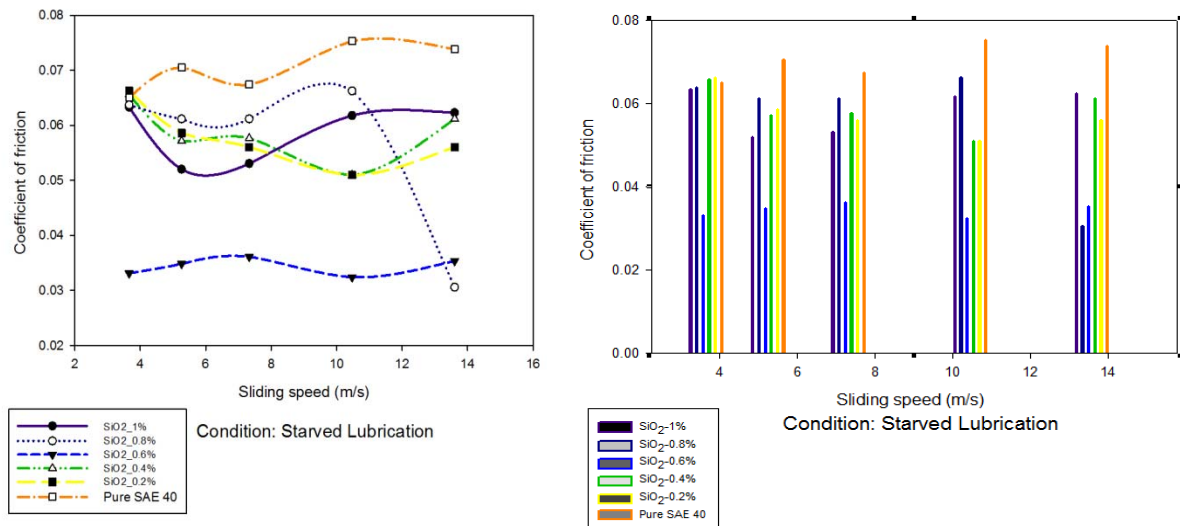


Figure 4: Variation of coefficient of friction with sliding speed for various compositions of Nanofluid in starved condition.

3.2.4 Study of Specific Wear Rate: Figure 5 shows the variation of Specific Wear Rate with respect to sliding speed at a constant load of 40 N for the different compositions of nanoparticles in the lubricant starting from 1%, 0.8%, 0.6%, 0.4%, 0.2% and Pure SAE 40 for fully flooded lubrication. Figure 6 shows the variation of Specific Wear Rate with respect to sliding speed at a constant load of 40 N for the different compositions of nanoparticles in the lubricant starting from 1%, 0.8%, 0.6%, 0.4%, 0.2% and Pure SAE 40 for starved lubrication. The value specific wear rate is almost negligible due to the no wearing of the contact surfaces as the use of nanoparticles in the lubricant results in the formation of a ceramic layer on the contact surfaces which results as a shielding layer for the tribopairs. The specific wear rate in case of lubricant without nanoparticles was evident due to the non formation of ceramic layer.

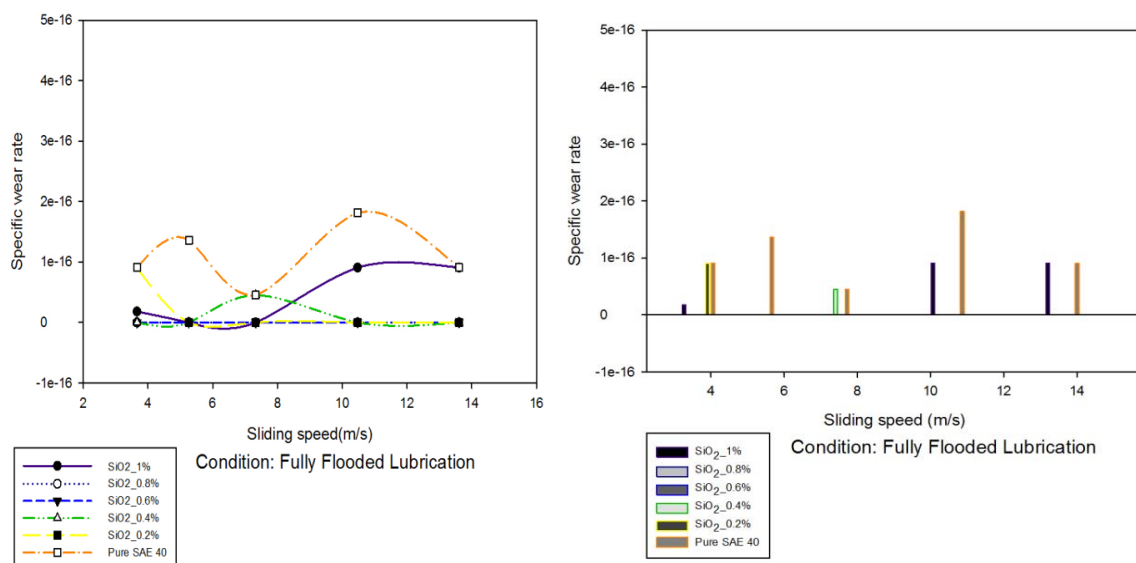


Figure 5: Variation of Specific wear rate with sliding speed for various compositions of nanofluid in Fully Flooded Lubrication.

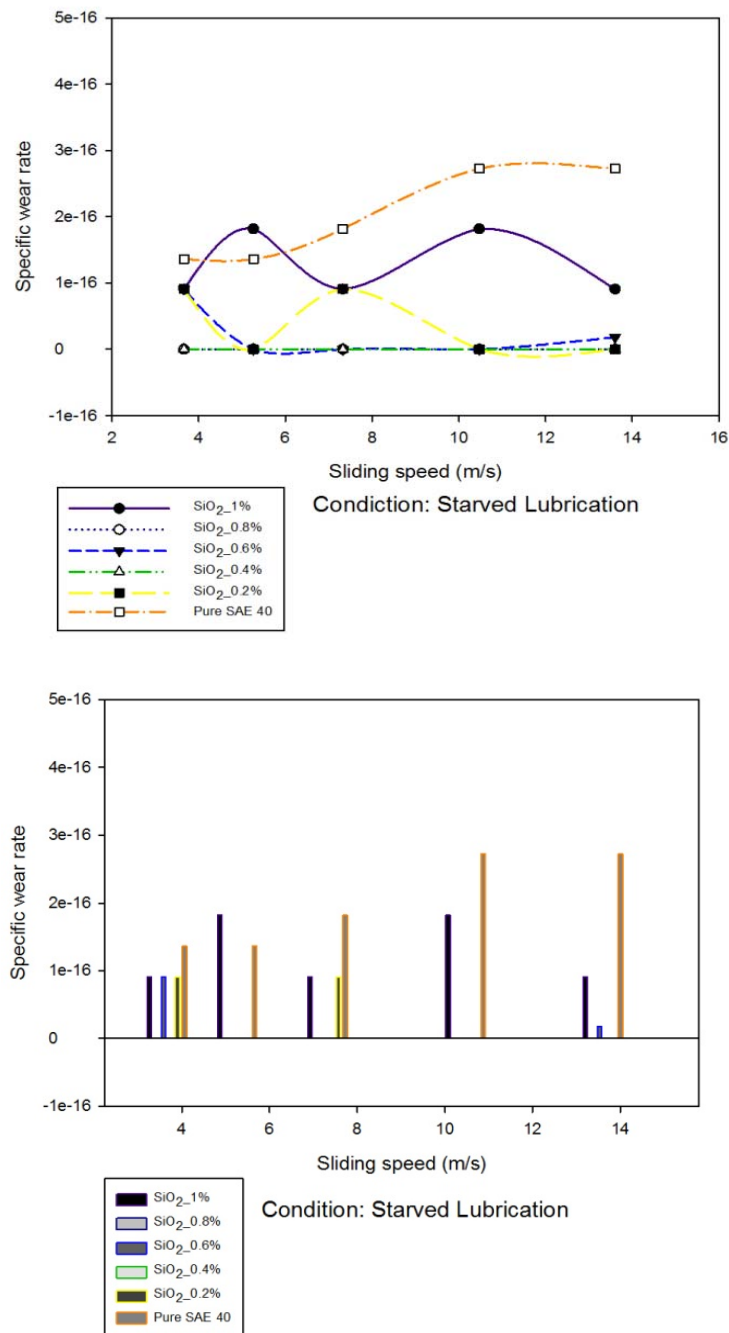


Figure 6: Variation of coefficient of friction with sliding speed for various compositions of Nanofluid in Starved Lubrication.

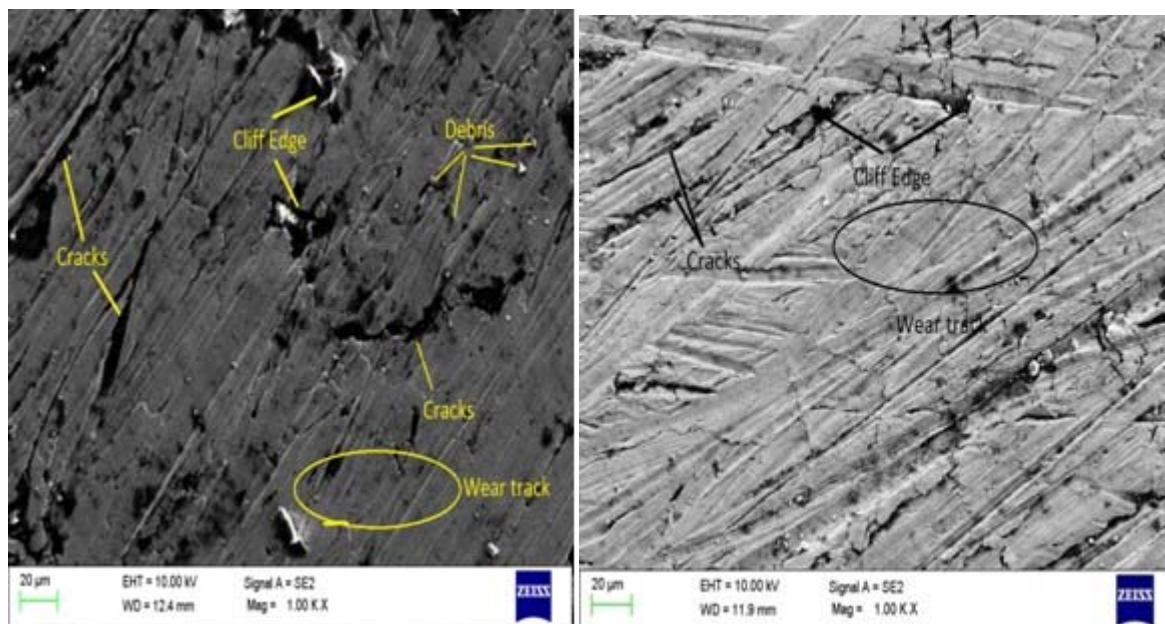


Figure7: SEM imaging of the pin material (a) lubricant without nanoparticles (b) Lubricant with SiO₂ nanoparticles.

In presence of the nanoparticles, there was minimum wear on pin. To study the wear of the pin, the wear pattern of the pin exposed to SEM imaging. The micrographs are shown in Figure7. Wear of the pin was evident in SEM investigation of the pin samples as it showed some wear debris, cliff edge, wear track and cracks. There was a layer of SiO₂ nanoparticles as seen in the SEM imaging of the pin. There were also evidences of the less wearing as the size of cracks, cliff edge and debris were less on the pin which was used with nanoparticles as compared to the pin which was used with plane lubricant. There are also evidences of the healing of cracks on the pin surface by the nanoparticles. All these evidences are the proof for the reduced wear of the tribopairs.

CONCLUSIONS

The experiment has been carried out on the pin on disc wear and friction testing test rig (ASTM G-99) at a constant load of 40 N. The author has observed that the use of nanoparticles in the lubricant improved the tribological properties of the lubricant without harming the service life of the lubricant.

In fully flooded condition the coefficient of friction decreased with the increase in the composition of nanoparticles in the lubricant from 0% to 0.6 % then as the composition was increased further the coefficient of friction starts increasing. The specific wear rate was negligible as with the lubricating oil enriched with nanoparticles as compared to the pure lubricant.

In starved condition, the coefficient of friction has higher values as compared to the fully flooded condition. The coefficient of friction decreased as the composition of nanoparticles in the lubricant increased from 0% to 0.6 % then as the composition was increased further the coefficient of friction starts increasing. The specific wear rate was negligible as with the lubricating oil enriched with nanoparticles as compared to the pure lubricant.

The SEM investigation shows that there was a layer of nanoparticles deposited on the surface of tribopairs that reduced the wear of the pin, moreover the nanoparticles also heals the cracks present on the surface of the tribopairs.

Acknowledgement: The Author is thankful to CSIR for its financial support.

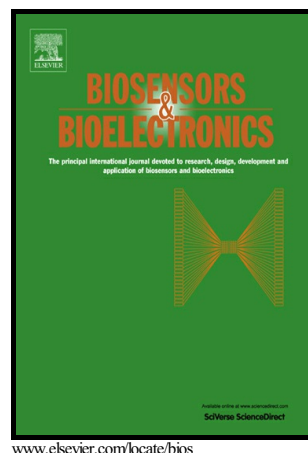
REFERENCES

- [1] K. Holmberg, P. Andersson, N. Nylund, K. Mäkelä, and A. Erdemir, "Tribology International Global energy consumption due to friction in trucks and buses," *Tribology Int.*, vol. 78, pp. 94–114, 2014.
- [2] K. Holmberg, R. Siilasto, T. Laitinen, P. Andersson, and J. Ari, "Tribology International Global energy consumption due to friction in paper machines," vol. 62, pp. 58–77, 2013.
- [3] V. Van Linden and L. Herman, "A fuel consumption model for off-road use of mobile machinery in agriculture," *Energy*, vol. 77, pp. 880–889, 2014.
- [4] T. Q. Tang, Q. Yu, S. C. Yang, and C. Ding, "Impacts of the vehicle's fuel consumption and exhaust emissions on the trip cost allowing late arrival under car-following model," *Phys. A Stat. Mech. its Appl.*, vol. 431, pp. 52–62, 2015.
- [5] D. Singh, K. A. Subramanian, and S. K. Singal, "Emissions and fuel consumption characteristics of a heavy duty diesel engine fueled with Hydroprocessed Renewable Diesel and Biodiesel," *Appl. Energy*, vol. 155, no. April 2003, pp. 440–446, 2015.
- [6] K. Na et al., "Impact of biodiesel and renewable diesel on emissions of regulated pollutants and greenhouse gases on a 2000 heavy duty diesel truck," *Atmos. Environ.*, vol. 107, no. x, pp. 307–314, 2015.
- [7] J. Tharajak, T. Palathai, and N. Sombatsompop, "Recommendations for h-BN loading and service temperature to achieve low friction coefficient and wear rate for thermal-sprayed PEEK coatings," *Surf. Coatings Technol.*, vol. 321, pp. 477–483, 2017.

- [8] A. Erdemir, "Review of engineered tribological interfaces for improved boundary lubrication," *Tribol. Int.*, vol. 38, no. 3, pp. 249–256, 2005.
- [9] R. C. Singh, R. K. Pandey, and S. Maji, "Experimental Studies for Accessing the Influence of Micro-Dimple Area Density on Tribological Performance of Mating Contacts," vol. 1, no. 1, pp. 1–12, 2013.
- [10] U. Pettersson and S. Jacobson, "Influence of surface texture on boundary lubricated sliding contacts," *Tribol. Int.*, vol. 36, no. 11, pp. 857–864, 2003.
- [11] B. V. Deryaguin, V. V. Karashev, N. N. Zakhavaeva, and V. P. Lazarev, "The mechanism of boundary lubrication and the properties of the lubricating film. Short- and long-range action in the theory of boundary lubrication," *Wear*, vol. 1, pp. 277–290, 1957.
- [12] V. G. Shram, A. V. Lysyannikov, and M. A. Kovaleva, "The Mechanism of Lubricants Protective Layers Formation in Friction Sliding," *Procedia Eng.*, vol. 150, pp. 458–463, 2016.
- [13] K. T. Miklozic, J. Graham, and H. Spikes, "Chemical and physical analysis of reaction films formed by molybdenum dialkyl-dithiocarbamate friction modifier additive using Raman and atomic force microscopy," *Tribol. Lett.*, vol. 11, no. 2, pp. 71–81, 2001.
- [14] C. Grossiord, K. Varlot, J. Martin, T. Le Mogne, and C. Esnouf, "MoS₂ single sheet lubrication by molybdenum," *Tribol. Int.*, vol. 31, no. 12, pp. 737–743, 1999.
- [15] B. Sharma and K. Doll, "Oxidation, friction reducing, and low temperature properties of epoxy fatty acid methyl esters," *Green Chem.*, vol. 9, no. 5, pp. 469–474, 2007.
- [16] T. Katafuchi and N. Shimizu, "Evaluation of the antiwear and friction reduction characteristics of mercaptocarboxylate derivatives as novel phosphorous-free additives," *Tribol. Int.*, vol. 40, no. 7, pp. 1017–1024, 2007.
- [17] C. L. Li, L. P. Xiong, H. Liu, L. T. Xiong, and W. Wang, "Tribological Study of Xanthate-Containing Acetic Ester as Additives in Hydrogenated Oil," *Appl. Mech. Mater.*, vol. 236–237, pp. 123–127, 2012.
- [18] Z. Tang and S. Li, "A review of recent developments of friction modifiers for liquid lubricants (2007-present)," *Curr. Opin. Solid State Mater. Sci.*, vol. 18, no. 3, pp. 119–139, 2014.
- [19] W. Marx, "The Effect of WS₂ Nanoparticles on Friction Reduction in Various Lubrication Regimes," *Eur. Sci. Ed.*, vol. 38, no. 2, pp. 35–37, 2012.
- [20] D. Guo, G. Xie, and J. Luo, "Mechanical properties of nanoparticles: basics and applications," *J. Phys. D: Appl. Phys.*, vol. 47, no. 1, p. 13001, 2014.
- [21] H. Kato and K. Komai, "Tribofilm formation and mild wear by tribo-sintering of nanometer-sized oxide particles on rubbing steel surfaces," *Wear* vol. 262, no. 1–2, pp. 36–41, 2007.
- [22] D. X. Peng, Y. Kang, R. M. Hwang, S. S. Shyr, and Y. P. Chang, "Tribological properties of diamond and SiO₂ nanoparticles added in paraffin," *Tribol. Int.*, vol. 42, no. 6, pp. 911–917, 2009.
- [23] W. W. Gerberich et al., "Superhard silicon nanospheres," *J. Mech. Phys. Solids*, vol. 51, no. 6, pp. 979–992, 2003.
- [24] W. M. Mook et al., "Compressive stress effects on nanoparticle modulus and fracture," *Phys. Rev. B - Condens. Matter Mater. Phys.*, vol. 75, no. 21, pp. 1–10, 2007.
- [25] H. Xie, B. Jiang, J. He, X. Xia, and F. Pan, "Lubrication performance of MoS₂ and SiO₂ nanoparticles as lubricant additives in magnesium alloy-steel contacts," *Tribol. Int.*, vol. 93, pp. 63–70, 2016.
- [26] D. Peng, C. Chen, Y. Kang, Y. Chang, and S. Chang, "Size effects of SiO₂ nanoparticles as oil additives on tribology of lubricant," *Ind. Lubr. Tribol.*, vol. 62, no. 2, pp. 111–120, 2010.

Fabrication of Sensitive Bioelectrode Based on Atomically Thin CVD Grown Graphene for Cancer Biomarker Detection

Vijay K. Singh, Saurabh Kumar, Sumit Kumar Pandey, Saurabh Srivastava, Monu Mishra, Govind Gupta, B.D. Malhotra, R.S. Tiwari, Anchal Srivastava



PII: S0956-5663(18)30018-6
DOI: <https://doi.org/10.1016/j.bios.2018.01.014>
Reference: BIOS10207

To appear in: *Biosensors and Bioelectronics*

Received date: 25 October 2017
Revised date: 5 January 2018
Accepted date: 8 January 2018

Cite this article as: Vijay K. Singh, Saurabh Kumar, Sumit Kumar Pandey, Saurabh Srivastava, Monu Mishra, Govind Gupta, B.D. Malhotra, R.S. Tiwari and Anchal Srivastava, Fabrication of Sensitive Bioelectrode Based on Atomically Thin CVD Grown Graphene for Cancer Biomarker Detection, *Biosensors and Bioelectronics*, <https://doi.org/10.1016/j.bios.2018.01.014>

This is a PDF file of an unedited manuscript that has been accepted for publication. As a service to our customers we are providing this early version of the manuscript. The manuscript will undergo copyediting, typesetting, and review of the resulting galley proof before it is published in its final citable form. Please note that during the production process errors may be discovered which could affect the content, and all legal disclaimers that apply to the journal pertain.

Fabrication of Sensitive Bioelectrode Based on Atomically Thin CVD Grown Graphene for Cancer Biomarker Detection

Vijay K. Singh^a, Saurabh Kumar^b, Sumit Kumar Pandey^a, Saurabh Srivastava^b, Monu Mishra^c, Govind Gupta^c, B.D. Malhotra^b, R.S.Tiwari^{a*}, Anchal Srivastava^{a*}

^aDepartment of Physics, Institute of Science, Banaras Hindu University, Varanasi– 221005, India

^bNanobioelectronics Laboratory, Department of Biotechnology, Delhi Technological University, Shahbad Daultapur, Delhi - 110042, India

^cAdvanced Materials and Devices Division, CSIR-National Physical Laboratory, Dr. K. S. Krishnan Marg, New Delhi – 110012, India.

Abstract:

Motivation behind the present work is to fabricate a cost effective and scalable biosensing platform for an easy and reliable detection of cancer biomarker Carcinoembryonic antigen (CEA). Here, we report the sensitive and selective detection of CEA using graphene based bio-sensing platform. Large sized ($\sim 2.5 \times 1.0 \text{ cm}^2$), uniform, continuous, single and few layers graphene films have been grown on copper (Cu) substrate employing chemical vapor deposition (CVD) technique using hexane as a liquid precursor. Functional group has been created over Graphene/Cu substrate through π - π stacking of 1- pyrenebutanoic acid succinimidyl ester (PBSE). Further, to make the sensor specific to CEA, antibody of CEA (anti-CEA) has been covalently immobilized onto PBSE/Graphene/Cu electrode. Selective and sensitive detection of CEA is achieved by anti-CEA/PBSE/Graphene/Cu electrode through electrochemical impedance spectroscopy (EIS) measurements. Under optimal condition, the fabricated sensor shows linear response in the physiological range $1.0 - 25.0 \text{ ng mL}^{-1}$ (normal value $\sim 5.0 \text{ ng mL}^{-1}$), revealing sensitivity $563.4 \Omega \text{ ng}^{-1} \text{ mL cm}^{-2}$ with a correlation coefficient of 0.996 and limit of detection (LOD) 0.23 ng mL^{-1} . In this way, one step electrode fabrication with high specific surface area provides a light weight, low cost, reliable and scalable novel

biosensing platform for sensitive and selective detection of CEA. We believe that this bioelectrode equipped with specific recognition elements could be utilized for detection of other biomolecules too.

Keywords: Graphene, CEA, EIS, Label-free detection, Biosensor.

*Corresponding authors:

E-Mail ID: rstiwariphy@yahoo.com (Prof. R.S. Tiwari), anchalbhu@gmail.com (Prof. Anchal Srivastava) Phone No.: +91-9415991746, +91-9453203122,

1. Introduction:

Cancer disease, characterized by the uncontrolled growth and spread of abnormal cells, is one of the major threats to the human life worldwide. The early and accurate detection of cancer is extremely important for clinical diagnosis, effective toxicity monitoring, and ultimately for the successful treatment of cancer. CEA is one of the cancer biomarkers, which has been extensively used for diagnostic purposes in gastrointestinal, breast and lung cancer (Aquino et al. 2004; Duffy 2001). In an adult nonsmoker human serum, the normal level of CEA is less than 2.5 ng mL⁻¹ and for a smoker it is less than 5.0 ng mL⁻¹ (Loewenstein and Zamcheck 1978; Su et al. 2008). The accurate and sensitive detection of CEA level can lead to the diagnosis of cancer in its early stage. In recent years, immense efforts have been made for the development of CEA sensing methods with high sensitivity and specificity (Liu et al. 2012; Zhang and Cui 2011; Zheng et al. 2005). In comparison to the presently used methods specifically, the polymerase chain reaction method, culturing and colony counting method, and the enzyme-linked immunosorbent assay (ELISAs) which are tiresome and need more time (typically hours to days), on the other hand the bioelectrode based biosensing approach offers rapid and sensitive measurements. Several nanoelectronic biosensors have been developed based on various

nanostructured materials such as nanowires (Wanekaya et al. 2006; Zhang et al. 2011; Zhang et al. 2010a; Zhang et al. 2010b; Zheng and Lieber 2011), nanotubes (Allen et al. 2007; Singh et al. 2013), quantum dots (Hansen et al. 2006; Yang et al. 2012), graphene oxide (GO) (Feng et al. 2011; Jung et al. 2010), reduced graphene oxide (RGO) (Kumar et al. 2015; Zhou et al. 2009) etc. However, bioelectrodes based on these nanomaterials suffer several drawbacks such as, bioelectrode fabrication of these materials requires some supporting substrate such as indium tin oxide (ITO), glassy carbon electrode (GCE), and gold electrodes etc., which are costly and also requires costly binders (nafion) as an adhesive materials.

The discovery of graphene by Geim et al. (Geim 2009), which is a flat atomically thin sheet of carbon atoms arranged in two-dimensional (2D) honeycomb lattice, has stimulated a huge amount of research in biosensing due to its extraordinary structural, electrical, physical, optical and biocompatible properties (Huang et al. 2011; Lee et al. 2008; Neto et al. 2009a; Neto et al. 2009b). Graphene has also added a new dimension to the field of electrochemical sensing because of its perfect 2D structure, which provides large detection area and enables facile and homogeneous functionalization of a variety of aromatic biomolecules through $\pi - \pi$ interaction (Van der Waals force) (Ajayan and Tour 2007). Graphene based devices have potential of portability, rapid diagnostic point-of-care sensing compared to the presently used ELISAs which are time consuming and labor intensive.

For realizing any potential applications of graphene, an easy and less toxic synthesis method is required. Till date, several synthesis methods for producing graphene have been reported such as; mechanical exfoliation (Novoselov et al. 2004), chemical exfoliation (Schniepp et al. 2006), chemical vapor deposition (CVD) (Srivastava et al. 2010) etc. Among these, CVD is one of the novel synthesis routes for producing good quality, large area, mono and few layers

graphene. The advantage of CVD grown graphene over other chemically derived graphene such as RGO, GO etc. is that it gives one atom thick, monolithic and continuous membrane without any discontinuity. This also facilitates reproducibility while scaling it from laboratory to industry which is a major challenge for the synthesis of most of the nanomaterials.

Keeping the above points in view, in this work, good quality large area mono and few layers graphene films have been synthesized on Cu substrate adopting liquid precursor CVD route (Srivastava et al. 2010). To the best of our knowledge, there is no report of using graphene directly on metallic substrate as biosensing platform. In the present method, as synthesized graphene films on Cu substrate have been used as an electrode material, which does not require any further tedious processing such as transferring of graphene onto an insulating substrate SiO_2/Si etc. However, there are several techniques for electrode fabrication from precursor material such as spin coating, electrophoretic deposition, screen printing, inkjet printing etc. (Ge et al. 2012; Kumar et al. 2013; Setti et al. 2005; Zhang et al. 2000), but these techniques are costly, require sophisticated instrumentations and not scalable too. Few reports are also available on graphene based FET devices (Feng et al. 2013; Sui and Appenzeller 2009; Yang et al. 2010; Yeh et al. 2016), but such devices require transferring of graphene from metallic to SiO_2/Si substrate. This process creates many wrinkles and defects in graphene film, which greatly reduces the electrical conductivity and hence potential performance of graphene. Such device fabrication is also very tedious and not cost effective. Therefore, one step electrode fabrication employed in the present work is an added advantage over other known methods of electrode fabrication. The bioelectrode fabricated on metal substrate in present study is also environment friendly and there is no issue of disposability. Further, this CVD synthesized graphene on Cu substrate has been applied to demonstrate as an efficient, easy and reliable label free biosensing

platform for detection of CEA with high sensitivity and specificity having the potential of scalability (Table-1).

2. Materials and methods

2.1. Synthesis of graphene

Large-sized graphene films were grown on Cu foils by CVD technique using hexane as a liquid precursor for carbon (Srivastava et al. 2010). Cu foils were loaded into a quartz tube furnace and initially quartz tube was purged with hydrogen (H_2) gas at a constant flow of 100 sccm. Furnace temperature was raised up to 980 °C under a constant heating rate of 20 °C/min. Temperature of the furnace was stabilized at 980 °C for 30 minutes to anneal the Cu foil. Further, CVD growth of graphene was started by directing hexane vapor for 5 min into the furnace, followed by cooling the furnace to the room temperature under the H_2 atmosphere.

2.2. Fabrication of Immunosensor (anti-CEA/PBSE/Graphene/Cu)

Graphene/Cu electrode was dipped into the PBSE solution (2 mg mL^{-1}) for 2 h. The PBSE was used as the noncovalent functionalization reagent, which adsorbed onto the graphene sheets through π - π stacking resulting in a stable PBSE-graphene composite. The functional groups of PBSE were used to conjugate antibodies of CEA to form anti-CEA/PBSE/Graphene/Cu electrode (Chen et al. 2001; Yang et al. 2008; Yang and Gong 2010). The anti-CEA antibodies ($30 \text{ }\mu\text{L}$, $100 \text{ }\mu\text{g mL}^{-1}$ in phosphate buffer; 50 mM, pH 7.2, 0.9% NaCl) were covalently immobilized onto PBSE/Graphene/Cu electrode as shown in Fig.1. The anti-CEA/PBSE/Graphene/Cu was then rinsed with phosphate buffer (PBS, 50 mM, pH 7.2, 0.9% NaCl) to remove the unbounded antibodies, and 1% of bovine serum albumin (BSA) in PBS was added to the antibody-modified electrode to block unspecific sites. After rinsing again with PBS, electrodes were stored at 4 °C.

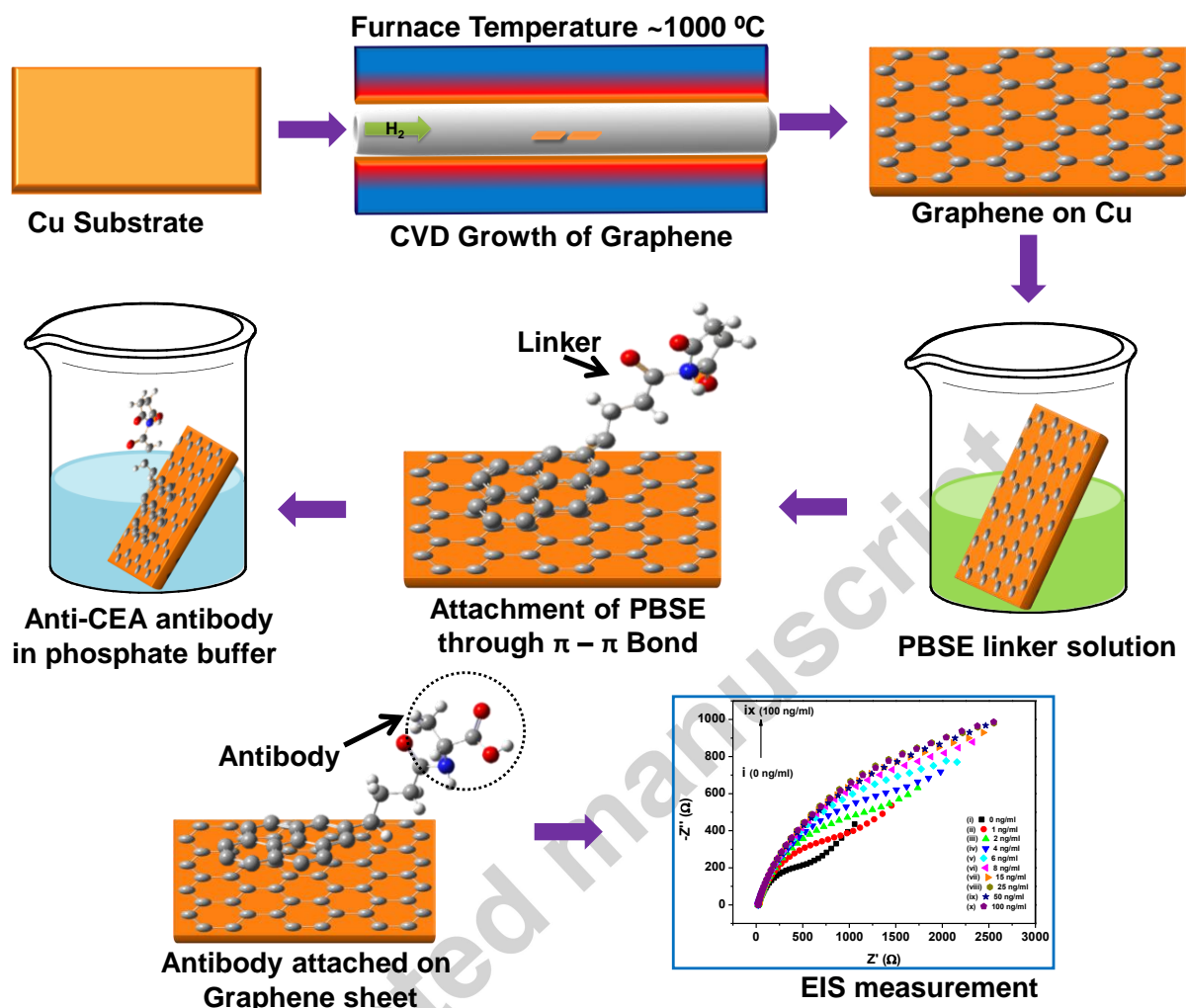


Fig.1. Schematic of biosensor fabrication and EIS measurements.

2.3.Characterization

The surface morphology of graphene was observed using Optical microscope (Dewinter, Italy), Scanning electron microscope (SEM) (ZEISS, Germany), Transmission electron microscope (TEM) (FEI, USA) and Atomic force microscope (AFM) (NT-MDT, Russia). Spectroscopic characterization of the as grown graphene films were carried out using Raman spectroscopy (RenishawinVia, Germany). Presence of functional groups on fabricated bioelectrodes were analyzed using Fourier-transform infrared (FTIR) spectrometer (Frontier,

Perkin Elmer, USA) in Attenuated total reflectance (ATR) mode. The X-Ray photoelectron spectroscopic (XPS) measurements were performed in Multiprobe Surface Analysis System (Scienta Omicron, Germany) operated at a base pressure of 5×10^{-11} Torr. High resolution XPS spectra were recorded using monochromatic $AlK\alpha$ (1486.7 eV) radiation source. The pass energy of the scans were kept at 20 eV with an ultimate spectral resolution of ~ 0.3 eV. The calibration of spectrometer was performed via standard gold sample as described earlier (Mishra et al. 2017).

The electrochemical behavior of the fabricated biosensors were investigated employing an Autolab Potentiostat/Galvanostat (Metrohm, Netherlands) using a conventional three-electrode cell with the BSA/anti-CEA/PBSE/Graphene/Cu as working electrode, platinum as auxiliary electrode and Ag/AgCl as the reference electrode in phosphate buffer saline (PBS, 50 mM, pH 7.4) containing 5 mM $[Fe(CN)_6]^{3-/4-}$.

3. Results and discussion

3.1. Optical and Electron microscopy

The optical, SEM, TEM and HR-TEM images obtained for the graphene film have been shown in Fig.2. Optical image Fig.2(a) shows that graphene film is homogeneous in large area with wrinkles on its surface. The SEM image Fig. 2(b) shows the presence of few multilayer (ML) islands (darker regions) over the uniform single layer (SL) graphene film. Further, for the TEM investigation, graphene film was transferred from Cu foil to lacey carbon coated TEM grid. TEM analysis reveals that graphene film is uniform with folded layers in few regions Fig.2(c). HR-TEM image shown in Fig.2(d) confirms the presence of 2-3 layers in graphene film, which is consistent with Raman and AFM results.

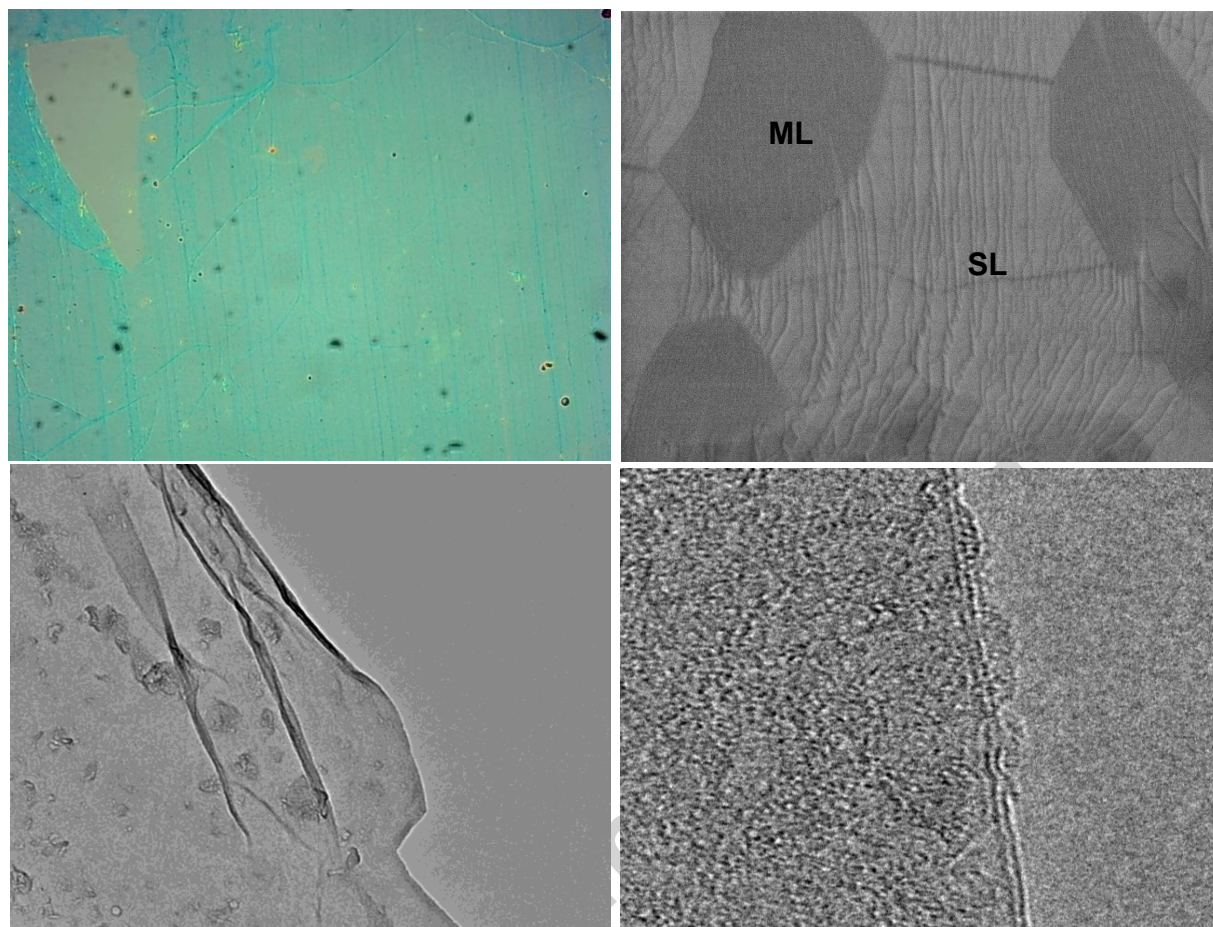


Fig.2. (a) Optical image of graphene film transferred on SiO₂/Si substrate, (b) SEM image showing uniform film of graphene (c) TEM image of graphene film transferred on lacey carbon coated TEM grid where darker region showing folded graphene layer and lighter region indicating the uniform monolayer graphene, (d) HR-TEM image showing bilayer and trilayer graphene films.

3.2. AFM analysis

AFM micrograph of graphene (transferred from Cu foil to SiO₂/Si wafer) has been shown in Fig.3(b). In the AFM image, number of wrinkles are visible that may have been emerged during the synthesis due to the wide difference in thermal expansion coefficient of Cu and graphene (Chae et al. 2009). Wrinkles in graphene film may also occur during the transferring

process. The thickness profile measurement shown in Fig.3(c) indicates that graphene is 3 layers thick (~1.6 nm) (Novoselov et al. 2004).

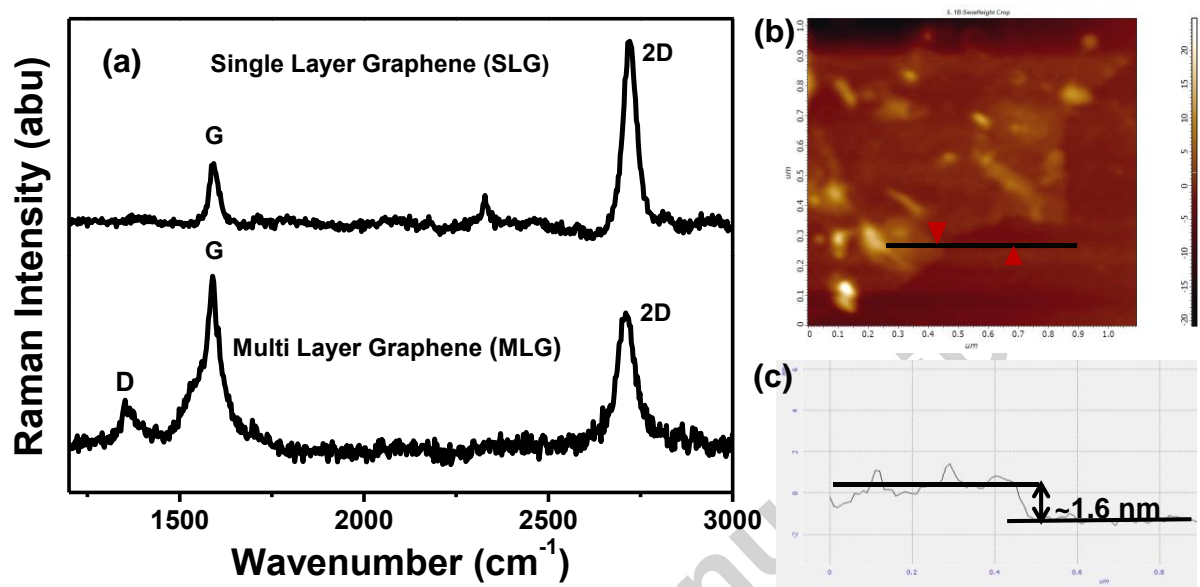


Fig.3. (a) Raman spectra of single and multi-layer graphene, (b) AFM image of graphene, (c) Thickness profile of graphene layer.

3.3. Raman Spectroscopic Analysis

Raman spectroscopy of the as-grown graphene on Cu foil was performed using 514 nm laser excitation to observe the quality and thickness of graphene film and results have been shown in Fig.3(a). The two most prominent peaks observed at $\sim 1590 \text{ cm}^{-1}$ and $\sim 2700 \text{ cm}^{-1}$ correspond to the G and 2D bands of graphene, respectively. The peak seen at $\sim 1350 \text{ cm}^{-1}$ appears due to the defect in graphene film, and known as D band. In our sample, for single layer D band is nearly absent, which indicates that graphene layer is quite homogenous. In the case of multilayer graphene, appearance of D band suggests the presence of few defects in graphene film. Moreover, information regarding the number of layers in graphene film can be extracted from the width and line-shape of 2D band.

In the case of single layer graphene, 2D band has Lorentzian shape with FWHM $\sim 42 \pm 2$ cm^{-1} . Also the intensity ratio of 2D and G band is found to be greater than 2 (i.e. $I_{2D}/I_G > 2$), which confirms the presence of single layer graphene (Ferrari et al. 2006; Malard et al. 2009). In multilayer graphene 2D band has FWHM $\sim 56 \pm 2$ cm^{-1} and the intensity ratio of 2D and G band is less than 1 (i.e. $I_{2D}/I_G < 1$), which confirms the presence of multilayer islands (darker regions of SEM image) over the single layer graphene on Cu foil.

3.4. FT-IR Analysis

FT-IR spectra of bare Cu, Graphene/Cu, PBSE/Graphene/Cu and anti-CEA/PBSE/Graphene/Cu films have been shown in Fig.4. There are no functional groups present on Cu and Graphene/Cu films. However, in the case of PBSE functionalized Graphene/Cu film (PBSE/Graphene/Cu), peaks at 1154 cm^{-1} , 1268 cm^{-1} correspond to C-O stretching. Peaks at 1407 cm^{-1} , 1335 cm^{-1} and 1514 cm^{-1} are due to O-H bend, symmetric and asymmetric stretching of N-O group of PBSE, respectively. The peak at 2928 cm^{-1} has been assigned to the C-H stretching. After immobilization of anti-CEA on PBSE/Graphene/Cu film characteristic peaks of amide-I and amide-II have been found at 1568 cm^{-1} and 3240 cm^{-1} , respectively (Singh et al. 2013). These amide peaks confirm the functionalization of anti-CEA on PBSE/Graphene/Cu electrode.

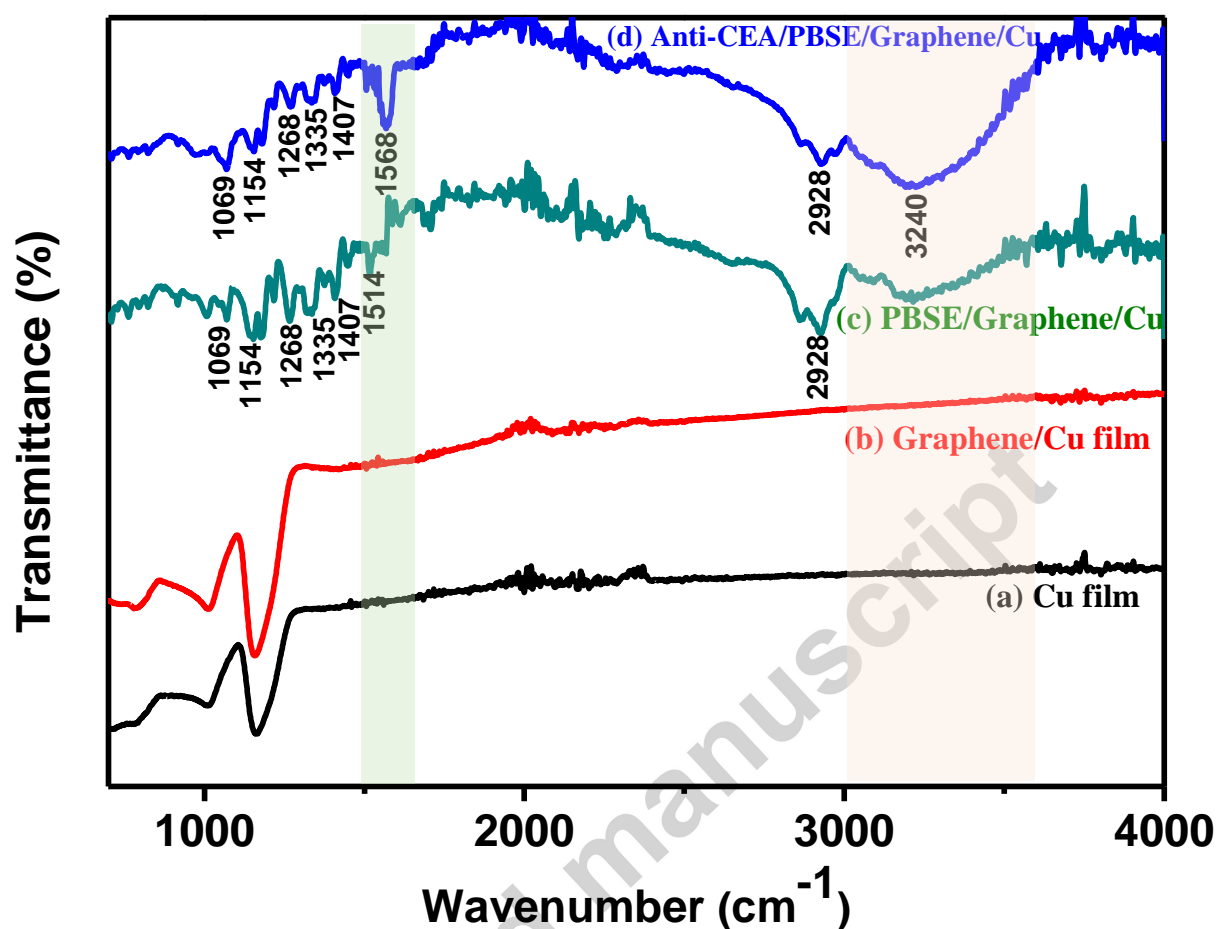


Fig.4. FT-IR spectra of (a) bare Cu film, (b) Graphene/Cu film, (c) PBSE/Graphene/Cu film (d) anti-CEA/PBSE/Graphene/Cu film.

3.5. XPS Studies

An XPS characterization was carried out to study the interaction of PBSE and antibody through graphene layer. The presence of PBSE is confirmed by the characteristic N1s peak at around 400 eV (Fig. 5a) (Liu et al. 2014). The C1s regions of both the electrodes (PBSE/Graphene/Cu and anti-CEA/PBSE/Graphene/Cu electrodes) were deconvoluted into characteristic peaks which have been discussed below.

In the case of PBSE/Graphene/Cu electrode, peaks observed at 284.7 eV, 285.7 eV, 288.8 eV shown in Fig 5(b) correspond to the in-plane sp^2 C=C, C=O and O=C-O bonds, respectively

and a weak peak at 286.8 eV is due to the C-N bond present in PBSE. In the anti-CEA/PBSE/Graphene/Cu electrode (Fig. 5c), the binding energy peaks were almost similar to the spectra of the PBSE/Graphene/Cu electrode. Moreover, an additional dominant wide peak seen at 287.9 eV is attributed to the amide bond formation between PBSE terminated graphene sheet and the NH₂ terminated Fab (fragment, antigen-binding) region of anti-CEA (Fig.1) (Singh et al. 2017). The fitting of the XPS spectra of C1s peaks binding energies (eV) and relative atomic percentages (%) of various functional groups present in PBSE/Graphene/Cu and anti-CEA/PBSE/Graphene/Cu films have been summarized in Table S1 in supplementary part. The relative atomic percentage of the C=O group present in the PBSE terminated graphene sample reduces from ~18.5% to ~12.3 % in the anti-CEA/PBSE/Graphene/Cu sample, indicating the removal of succinimide ester (see the supplementary information Fig S2) during covalent bonding with NH₂ terminated Fab region of anti-CEA. Further, the relative atomic percentage of the C-N bond present in PBSE/Graphene/Cu sample increased from ~2.4% to ~19.8 % in anti-CEA/PBSE/Graphene/Cu sample. This may be attributed to the presence of amide bond in the polypeptide chain of antibody (anti-CEA) and amide bond formation between aminated antibody and PBSE terminated graphene.

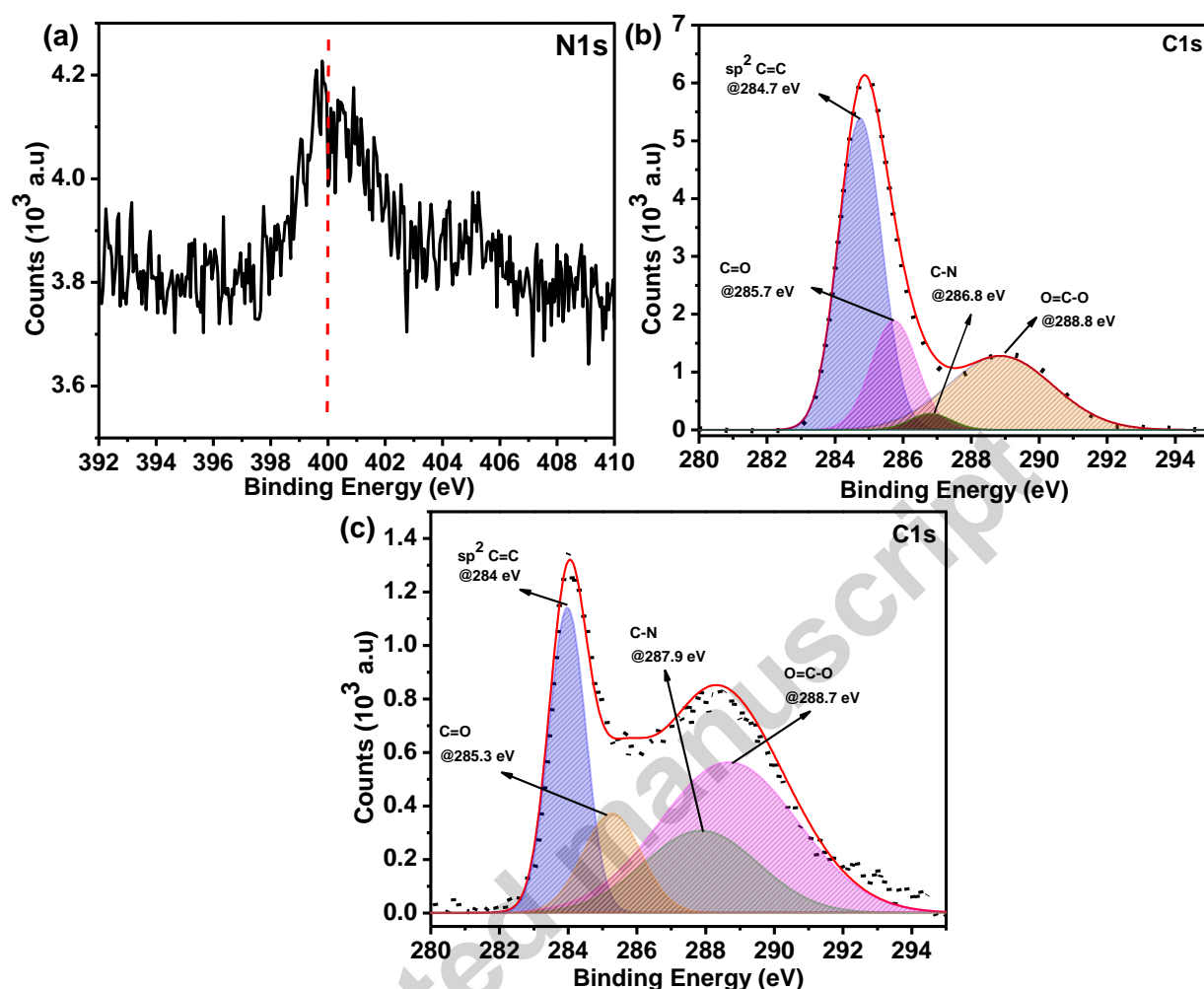


Fig.5. (a) N1s spectrum of PBSE modified graphene and C1s XPS spectrum of (b) PBSE/Graphene/Cu (c) anti-CEA/PBSE/Graphene/Cu.

3.5. Electrochemical Studies

To investigate the charge transfer phenomena at the modified surface/solution interface electrochemical impedance spectroscopy (EIS) were conducted in the frequency range, 1×10^5 -0.1 Hz with amplitude of 0.01. The Randles circuit is mainly used as a fitting model in EIS measurement for the interpretation of the Nyquist plot. It is an equivalent electrical circuit comprising of an active electrolyte resistance (R_s) in series with the parallel combinations of

double layer capacitance (C_{dl}) or also replaced with constant phase element (CPE) of a Faradic reaction and charge transfer resistance (R_{CT}) (Randles 1947). The plot obtained between real and imaginary values of impedance is called Nyquist plot and the diameter of semicircle in the Nyquist plot gives the magnitude of charge transfer resistance (R_{CT}) (Moisel et al. 2008). Fig.6(a) shows the Nyquist plot of Cu, Graphene/Cu, PBSE/Graphene/Cu and anti-CEA/PBSE/Graphene/Cu electrodes. The value of R_{CT} for Graphene/Cu is found to be 1.1 K Ω which is lower than that of the Cu electrode (5.6 K Ω). This result indicates that deposition of graphene over Cu electrode enhances the charge transfer from solution to the electrode due to high conductivity and electrochemical behavior of graphene, which increases the permeability of $[Fe(CN)_6]^{3-/4-}$ to the surface of Graphene/Cu electrode. Thus, the modified surface can be correlated with the charge transfer resistance confirming the deposition of graphene over Cu electrode. It can be seen that R_{CT} value for PBSE/Graphene/Cu electrode (2.1 K Ω , curve c) is larger than Graphene/Cu (1.1 K Ω , curve b) electrode. This increase in the R_{CT} value is attributed to the hindrance in charge transfer after PBSE binding. Further, the value of R_{CT} (733.5 Ω , curve d) of the anti-CEA/PBSE/Graphene/Cu immunoelectrode is lower than the PBSE/Graphene/Cu electrode (2.1 K Ω , curve c). The decrease in the value of R_{CT} may be attributed to the spatial orientation of the antibody molecules that perhaps stimulates charge transfer rate to the antibody immobilized surface.

3.6. Electrochemical impedimetric response of the BSA/anti-CEA/PBSE/Graphene/Cu immunoelectrode:

The electrochemical response studies (Fig.6(b)) were conducted on BSA/anti-CEA/PBSE/Graphene/Cu immunoelectrode as a function of carcinoembryonic antigen (CEA) concentrations (1-100 ng mL⁻¹) in phosphate buffer saline (PBS, 50 mM, pH 7.4, 0.9% NaCl) using EIS. The magnitude of R_{CT} was found to be increased after addition of CEA which may be

attributed to the formation of electrically insulating immunocomplex, produced from the specific antigen-antibody interaction (CEA - anti-CEA immunocomplex) blocking electron transfer. Fig.6(c),(d) show the calibration curves obtained between R_{CT} and CEA concentrations, revealing linearity from 1-25 ng mL^{-1} having sensitivity of $563.4 \Omega \text{ ng}^{-1} \text{ mL cm}^{-2}$ with a correlation coefficient of 0.996. Detection limit of the biosensor has been calculated using equation (S1) and LOD is found to be 0.23 ng mL^{-1} .

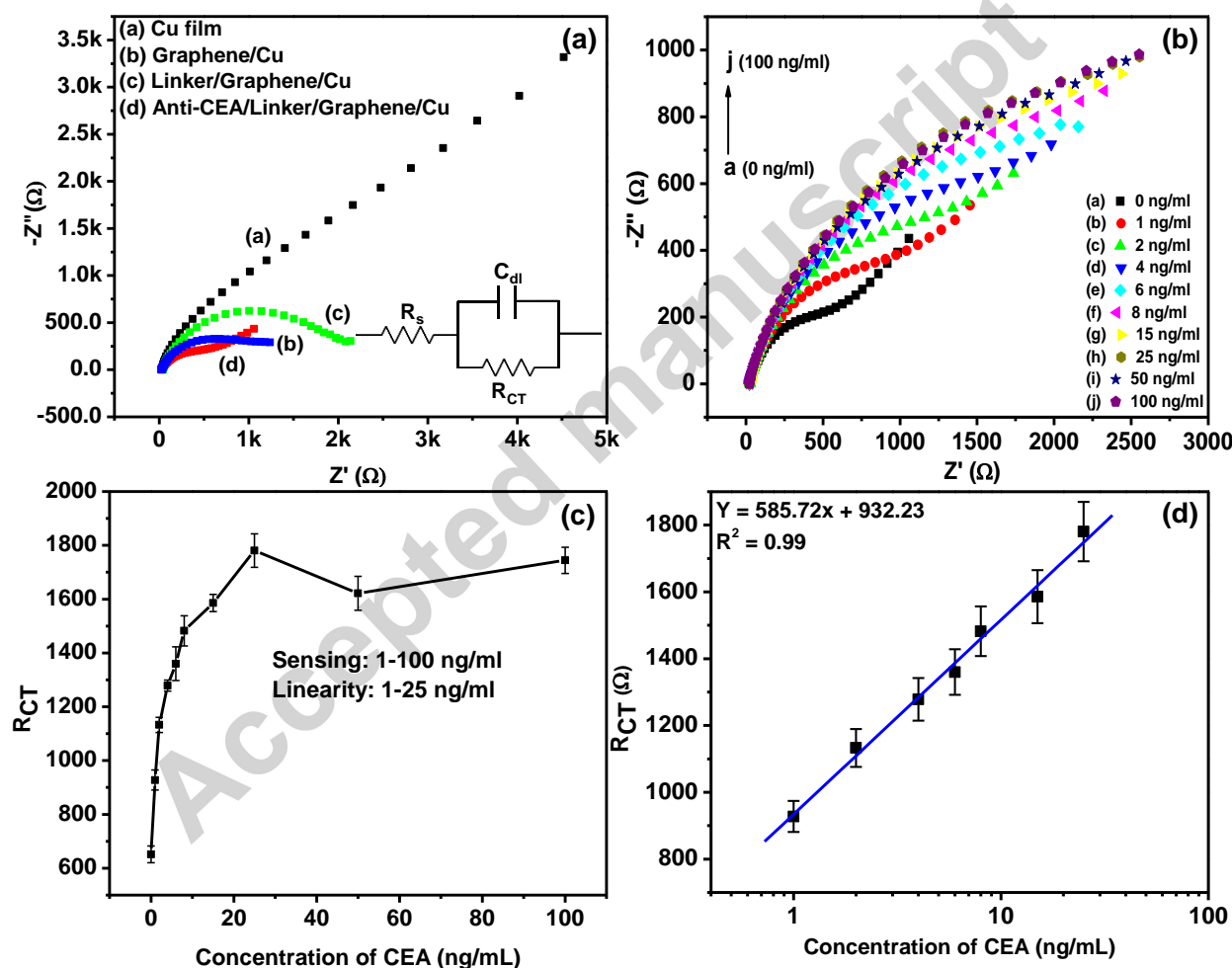


Fig.6. (a) Electrochemical impedance spectra of Cu, Graphene/Cu, PBSE/Graphene/Cu, anti-CEA/PBSE/Graphene/Cu. (b) Electrochemical response studies of BSA/anti-CEA/PBSE/Graphene/Cu bioelectrode obtained as a function of CEA concentrations ($1-100 \text{ ng mL}^{-1}$) and (c) R_{CT} with

respect to CEA concentrations (d) calibration plot between R_{CT} recorded at various CEA concentrations.

3.7. Reproducibility, selectivity and stability studies:

The reproducibility of the BSA/anti-CEA/PBSE/Graphene/Cu immunoelectrode was investigated by measuring the EIS response in the presence of CEA (25 ng mL^{-1}) on four independently fabricated immunoelectrodes under identical conditions (Fig. 7(a)). The reproducibility is evaluated in terms of relative standard deviation (RSD). An average R_{CT} of 1850.1Ω with a RSD of 3.20 % has been found (Fig. 6(b)), which is within the acceptable error range under the tested conditions, suggesting a good reproducible assay.

The selectivity of the fabricated sensor has been examined by monitoring the R_{CT} responses of immunoelectrodes in presence of different interferents present in blood serum such as KCl (8.38 mM), CYFRA-21-1 (2.0 ng mL^{-1}) and CTnI (10.0 ng mL^{-1}) as shown in Fig 7(c). Upon addition of 1.0 ng mL^{-1} CEA, the significant change in the R_{CT} value of immunoelectrode was found. However, upon successive addition of the KCl, CYFRA-21-1 and CTnI interferents, no prominent changes in R_{CT} values have been observed. This indicates that the BSA/anti-CEA/PBSE/Graphene/Cu immunoelectrode specifically interacts with CEA and the response is not affected due to the presence of other potential interferents.

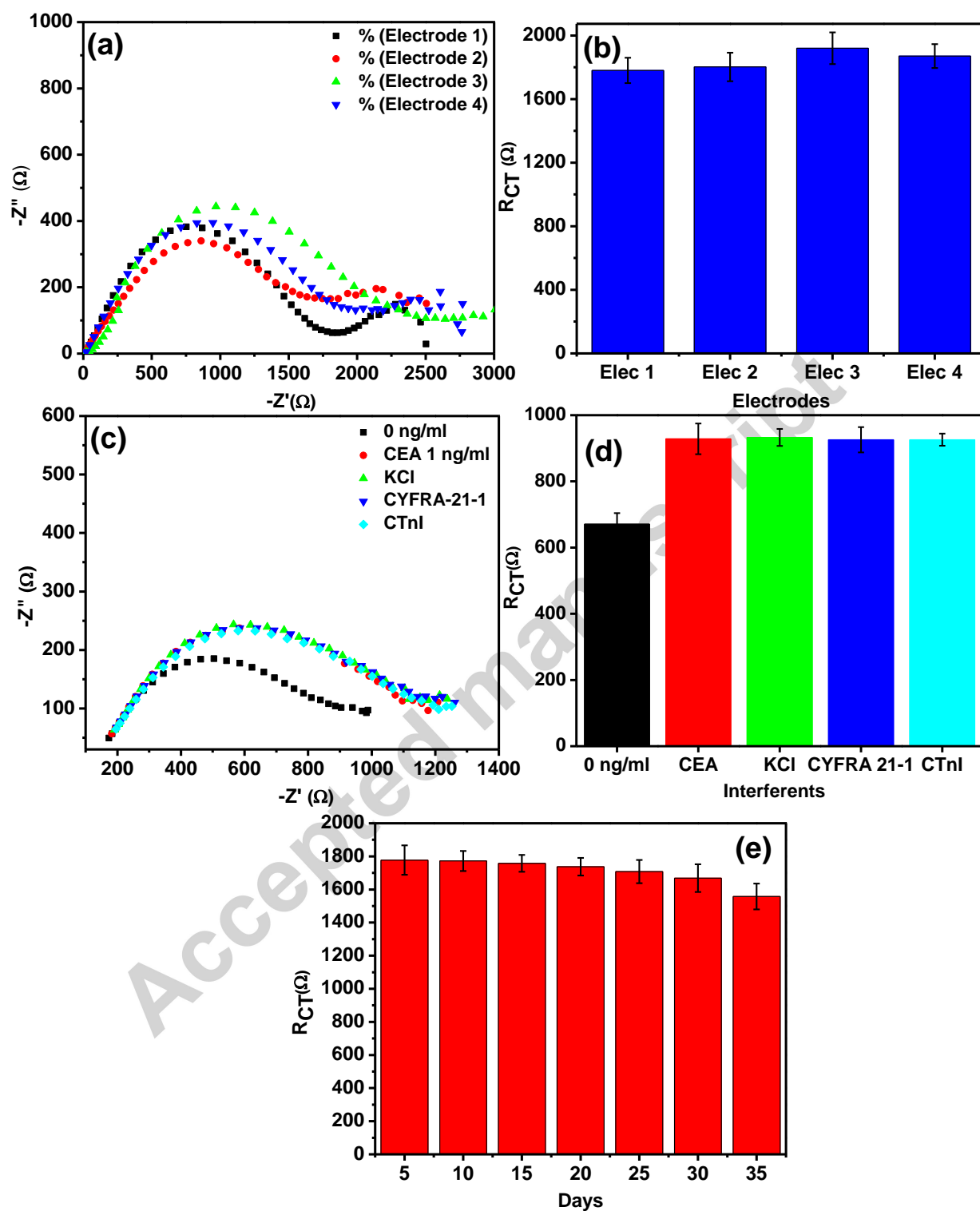


Fig.7. (a), (b) EIS responses of four independently fabricated BSA/anti-CEA/PBSE/Graphene/Cu electrodes in presence of 25.0 ng mL⁻¹ CEA and their R_{CT} values, respectively, (c) and (d)

Selectivity study of BSA/anti-CEA/PBSE/Graphene/Cu electrode in presence of different interferents such as: KCl, CYFRA-21-1 and CTnI (e) Storage stability of BSA/anti-CEA/PBSE/Graphene/Cu electrodes at regular interval of 5 days till 35 days.

The storage stability of the BSA/anti-CEA/PBSE/Graphene/Cu immunoelectrode has also been monitored by measuring EIS response in presence of 25.0 ng mL^{-1} CEA with a regular interval of 5 days (Fig. 7(e)). The immunoelectrode retains its activity upto 30 days with the decrement in R_{CT} of 6.13% when stored in refrigerated conditions at 4°C . After 35 days, 12.37 % decrement in R_{CT} values was found, this indicates that the storage stability of the fabricated immunoelectrodes is 30 days.

Table1. Comparison of sensing behavior of proposed bioelectrode with the other reported works.

S.N o.	Substrate	Materials	Fabrication Method	Detection Method	Linear Range	Detection Limit	Referen ce
1	GCE	MWCNT, Chitosan, Glutaraldehyde, THAMP, Ferrocenecarboxylic acid, Dopamine, AuNPs, HRP	Drop cost	CV, EIS	$0.01 - 80 \text{ ng mL}^{-1}$	0.002 ng mL^{-1}	(Feng et al. 2015)
2	Si/SiO ₂	HRP, AuNPs, Carboxylic magnetic beads, Graphene, Hexacyanoferrate	Drop cost	EIS	$5-60 \text{ ng mL}^{-1}$	5.0 ng mL^{-1}	(Jin et al. 2014)
3	GCE	AuNPs, MWCNTs, Chitosan	Drop cost	CV, EIS, DPV	$0.3-2.5 \text{ ng mL}^{-1}$ and $2.5-20 \text{ ng mL}^{-1}$	0.01 ng mL^{-1}	(Huang et al. 2010)
4	GCE	AuNPs,	Dip coating	CV, EIS,	$1 \text{ fg mL}^{-1} - 10$	0.015 fg	(Liu and

		PATP, hexacyanoferrates		DPV	ng mL ⁻¹	mL ⁻¹	Ma 2013)
5	Cu film	Graphene	Dip Coating	EIS	1.0 – 25.0 ng mL ⁻¹	0.23 ng mL ⁻¹	Present Work

The comparison of present work with the other reports (shown in Table-1) suggests that our biosensor is highly sensitive, selective and linear in the physiological range.

4. Conclusions

In the present study, we have fabricated anti-CEA/PBSE/Graphene/Cu immunosensing platform for sensitive and specific detection of cancer related biomarker CEA using EIS technique. Graphene has been synthesized on Cu film using CVD technique and anti-CEA has been immobilized over it using PBSE as a linker. The EIS studies of the fabricated electrodes reveal the sensitivity of $563.4 \Omega \text{ ng}^{-1} \text{ mL cm}^{-2}$ with detection limit of 0.23 ng mL^{-1} , which meets the requirements of clinical diagnosis of cancer. Due to high sensitivity, specificity, ease of fabrication, and short analysis time this biosensor could be applied as potential candidate for clinical diagnosis of cancer at its early stage. It would be interesting to utilize this bioelectrode equipped with specific recognition elements for detection of other biomolecules too.

Acknowledgements

V.K.S. acknowledges UGC for providing Junior Research Fellowship (Fellowship Grant No: F.25-1/2014-15/(BSR)/5-127/2007/(BSR)). S.S. acknowledges DST, for the financial support (DST/INSPIRE Faculty Award/2014/MS-34). A.S. acknowledges DST, India for funding (Project Code: DST/TSG/PT/2012/68), DST-SERB India (Project Code: EMR/2016/007720), DST-PURSE-5050 and BHU.

References:

- Ajayan, P.M., Tour, J.M., 2007. Materials science: nanotube composites. *Nature* 447(7148), 1066-1068.
- Allen, B.L., Kichambare, P.D., Star, A., 2007. Carbon nanotube field-effect-transistor-based biosensors. *Advanced Materials* 19(11), 1439-1451.
- Aquino, A., Formica, V., Prete, S.P., Correale, P.P., Massara, M.C., Turriziani, M., De Vecchis, L., Bonmassar, E., 2004. Drug-induced increase of carcinoembryonic antigen expression in cancer cells. *Pharmacological research* 49(5), 383-396.
- Chae, S.J., Güneş, F., Kim, K.K., Kim, E.S., Han, G.H., Kim, S.M., Shin, H.J., Yoon, S.M., Choi, J.Y., Park, M.H., 2009. Synthesis of large-area graphene layers on poly-nickel substrate by chemical vapor deposition: wrinkle formation. *Advanced Materials* 21(22), 2328-2333.
- Chen, R.J., Zhang, Y., Wang, D., Dai, H., 2001. Noncovalent sidewall functionalization of single-walled carbon nanotubes for protein immobilization. *Journal of the American Chemical Society* 123(16), 3838-3839.
- Duffy, M.J., 2001. Carcinoembryonic antigen as a marker for colorectal cancer: is it clinically useful? *Clinical chemistry* 47(4), 624-630.
- Feng, L., Chen, Y., Ren, J., Qu, X., 2011. A graphene functionalized electrochemical aptasensor for selective label-free detection of cancer cells. *Biomaterials* 32(11), 2930-2937.
- Feng, L., Wu, L., Qu, X., 2013. New horizons for diagnostics and therapeutic applications of graphene and graphene oxide. *Advanced Materials* 25(2), 168-186.
- Feng, T., Qiao, X., Wang, H., Sun, Z., Hong, C., 2015. Multi-walled carbon nanotubes–chitosan with a branched structure modified with ferrocenecarboxylic acid for carcinoembryonic antigen detection. *Analytical Methods* 7(23), 10032-10039.
- Ferrari, A., Meyer, J., Scardaci, V., Casiraghi, C., Lazzeri, M., Mauri, F., Piscanec, S., Jiang, D., Novoselov, K., Roth, S., 2006. Raman spectrum of graphene and graphene layers. *Physical review letters* 97(18), 187401.
- Ge, S., Ge, L., Yan, M., Song, X., Yu, J., Huang, J., 2012. A disposable paper-based electrochemical sensor with an addressable electrode array for cancer screening. *Chemical Communications* 48(75), 9397-9399.
- Geim, A.K., 2009. Graphene: status and prospects. *science* 324(5934), 1530-1534.
- Hansen, J.A., Wang, J., Kawde, A.-N., Xiang, Y., Gothelf, K.V., Collins, G., 2006. Quantum-dot/aptamer-based ultrasensitive multi-analyte electrochemical biosensor. *Journal of the American Chemical Society* 128(7), 2228-2229.
- Huang, K.-J., Niu, D.-J., Xie, W.-Z., Wang, W., 2010. A disposable electrochemical immunosensor for carcinoembryonic antigen based on nano-Au/multi-walled carbon nanotubes–chitosans nanocomposite film modified glassy carbon electrode. *Analytica chimica acta* 659(1), 102-108.
- Huang, Y., Dong, X., Liu, Y., Li, L.-J., Chen, P., 2011. Graphene-based biosensors for detection of bacteria and their metabolic activities. *Journal of Materials Chemistry* 21(33), 12358-12362.

- Jin, B., Wang, P., Mao, H., Hu, B., Zhang, H., Cheng, Z., Wu, Z., Bian, X., Jia, C., Jing, F., 2014. Multi-nanomaterial electrochemical biosensor based on label-free graphene for detecting cancer biomarkers. *Biosensors and Bioelectronics* 55, 464-469.
- Jung, J.H., Cheon, D.S., Liu, F., Lee, K.B., Seo, T.S., 2010. A graphene oxide based immuno-biosensor for pathogen detection. *Angewandte Chemie International Edition* 49(33), 5708-5711.
- Kumar, S., Jagadeesan, K.K., Joshi, A.G., Sumana, G., 2013. Immuno-CoPS (conducting paper strips) for futuristic cost-effective cancer diagnostics. *Rsc Advances* 3(29), 11846-11853.
- Kumar, S., Kumar, S., Srivastava, S., Yadav, B.K., Lee, S.H., Sharma, J.G., Doval, D.C., Malhotra, B.D., 2015. Reduced graphene oxide modified smart conducting paper for cancer biosensor. *Biosensors and Bioelectronics* 73, 114-122.
- Lee, C., Wei, X., Kysar, J.W., Hone, J., 2008. Measurement of the elastic properties and intrinsic strength of monolayer graphene. *science* 321(5887), 385-388.
- Liu, Y., Dong, X., Chen, P., 2012. Biological and chemical sensors based on graphene materials. *Chemical Society Reviews* 41(6), 2283-2307.
- Liu, Y., Yuan, L., Yang, M., Zheng, Y., Li, L., Gao, L., Nerngchamnong, N., Nai, C.T., Sangeeth, C.S., Feng, Y.P., 2014. Giant enhancement in vertical conductivity of stacked CVD graphene sheets by self-assembled molecular layers. *Nature communications* 5, 5461.
- Liu, Z., Ma, Z., 2013. Fabrication of an ultrasensitive electrochemical immunosensor for CEA based on conducting long-chain polythiols. *Biosensors and Bioelectronics* 46, 1-7.
- Loewenstein, M., Zamcheck, N., 1978. Carcinoembryonic antigen (CEA) levels in benign gastrointestinal disease states. *Cancer* 42(S3), 1412-1418.
- Malard, L., Pimenta, M., Dresselhaus, G., Dresselhaus, M., 2009. Raman spectroscopy in graphene. *Physics Reports* 473(5), 51-87.
- Mishra, M., Gundimeda, A., Krishna, S., Aggarwal, N., Gahtori, B., Dilawar, N., Aggarwal, V.V., Singh, M., Rakshit, R., Gupta, G., 2017. Wet chemical etching induced stress relaxed nanostructures on polar & non-polar epitaxial GaN films. *Physical Chemistry Chemical Physics* 19(13), 8787-8801.
- Moisel, M., de Mele, M.L., Müller, W.D., 2008. Biomaterial interface investigated by electrochemical impedance spectroscopy. *Advanced engineering materials* 10(10), B33-B46.
- Neto, A.C., Guinea, F., Peres, N., Novoselov, K.S., Geim, A.K., 2009a. The electronic properties of graphene. *Reviews of modern physics* 81(1), 109.
- Novoselov, K.S., Geim, A.K., Morozov, S.V., Jiang, D., Zhang, Y., Dubonos, S.V., Grigorieva, I.V., Firsov, A.A., 2004. Electric field effect in atomically thin carbon films. *science* 306(5696), 666-669.
- Randles, J.E.B., 1947. Kinetics of rapid electrode reactions. *Discussions of the faraday society* 1, 11-19.
- Schniepp, H.C., Li, J.-L., McAllister, M.J., Sai, H., Herrera-Alonso, M., Adamson, D.H., Prud'homme, R.K., Car, R., Saville, D.A., Aksay, I.A., 2006. Functionalized single graphene sheets derived from splitting graphite oxide. *The Journal of Physical Chemistry B* 110(17), 8535-8539.

- Setti, L., Fraleoni-Morgera, A., Ballarin, B., Filippini, A., Frascaro, D., Piana, C., 2005. An amperometric glucose biosensor prototype fabricated by thermal inkjet printing. *Biosensors and Bioelectronics* 20(10), 2019-2026.
- Singh, C., Srivastava, S., Ali, M.A., Gupta, T.K., Sumana, G., Srivastava, A., Mathur, R., Malhotra, B.D., 2013. Carboxylated multiwalled carbon nanotubes based biosensor for aflatoxin detection. *Sensors and Actuators B: Chemical* 185, 258-264.
- Singh, R., Hong, S., Jang, J., 2017. Label-free detection of influenza viruses using a reduced graphene oxide-based electrochemical immunosensor integrated with a microfluidic platform. *Scientific reports* 7, 42771.
- Srivastava, A., Galande, C., Ci, L., Song, L., Rai, C., Jariwala, D., Kelly, K.F., Ajayan, P.M., 2010. Novel liquid precursor-based facile synthesis of large-area continuous, single, and few-layer graphene films. *Chemistry of Materials* 22(11), 3457-3461.
- Su, F., Xu, C., Taya, M., Murayama, K., Shinohara, Y., Nishimura, S.-I., 2008. Detection of carcinoembryonic antigens using a surface plasmon resonance biosensor. *Sensors* 8(7), 4282-4295.
- Sui, Y., Appenzeller, J., 2009. Screening and interlayer coupling in multilayer graphene field-effect transistors. *Nano letters* 9(8), 2973-2977.
- Wanekaya, A.K., Chen, W., Myung, N.V., Mulchandani, A., 2006. Nanowire-based electrochemical biosensors. *Electroanalysis* 18(6), 533-550.
- Yang, C., Xu, C., Wang, X., Hu, X., 2012. Quantum-dot-based biosensor for simultaneous detection of biomarker and therapeutic drug: first steps toward an assay for quantitative pharmacology. *Analyst* 137(5), 1205-1209.
- Yang, J., Pang, F., Zhang, R., Xu, Y., He, P., Fang, Y., 2008. Electrochemistry and Electrocatalysis of Hemoglobin on 1-Pyrenebutanoic Acid Succinimidyl Ester/Multiwalled Carbon Nanotube and Au Nanoparticle Modified Electrode. *Electroanalysis* 20(19), 2134-2140.
- Yang, M., Gong, S., 2010. Immunosensor for the detection of cancer biomarker based on percolated graphene thin film. *Chem. Commun.* 46(31), 5796-5798.
- Yang, W., Ratinac, K.R., Ringer, S.P., Thordarson, P., Gooding, J.J., Braet, F., 2010. Carbon nanomaterials in biosensors: should you use nanotubes or graphene? *Angewandte Chemie International Edition* 49(12), 2114-2138.
- Yeh, C.-H., Kumar, V., Moyano, D.R., Wen, S.-H., Parashar, V., Hsiao, S.-H., Srivastava, A., Saxena, P.S., Huang, K.-P., Chang, C.-C., 2016. High-performance and high-sensitivity applications of graphene transistors with self-assembled monolayers. *Biosensors and Bioelectronics* 77, 1008-1015.
- Zhang, B., Cui, T., 2011. An ultrasensitive and low-cost graphene sensor based on layer-by-layer nano self-assembly. *Applied Physics Letters* 98(7), 073116.
- Zhang, G.-J., Huang, M.J., Liu, E.T., Desai, K.V., 2011. Self-assembled monolayer-assisted silicon nanowire biosensor for detection of protein-DNA interactions in nuclear extracts from breast cancer cell. *Biosensors and Bioelectronics* 26(7), 3233-3239.

Zhang, G.-J., Luo, Z.H.H., Huang, M.J., Tay, G.K.I., Lim, E.-J.A., 2010a. Morpholino-functionalized silicon nanowire biosensor for sequence-specific label-free detection of DNA. *Biosensors and Bioelectronics* 25(11), 2447-2453.

Zhang, G.-J., Zhang, L., Huang, M.J., Luo, Z.H.H., Tay, G.K.I., Lim, E.-J.A., Kang, T.G., Chen, Y., 2010b. Silicon nanowire biosensor for highly sensitive and rapid detection of Dengue virus. *Sensors and Actuators B: Chemical* 146(1), 138-144.

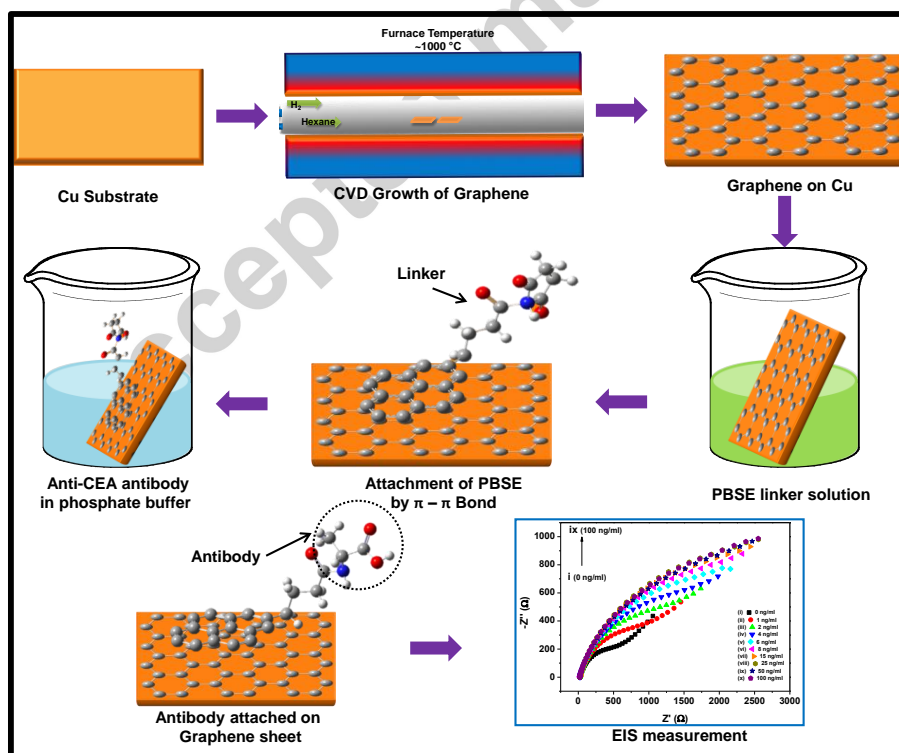
Zhang, S., Wright, G., Yang, Y., 2000. Materials and techniques for electrochemical biosensor design and construction. *Biosensors and Bioelectronics* 15(5), 273-282.

Zheng, G., Lieber, C.M., 2011. Nanowire biosensors for label-free, real-time, ultrasensitive protein detection. *Nanoproteomics*, pp. 223-237. Springer.

Zheng, G., Patolsky, F., Cui, Y., Wang, W.U., Lieber, C.M., 2005. Multiplexed electrical detection of cancer markers with nanowire sensor arrays. *Nature biotechnology* 23(10), 1294-1301.

Zhou, M., Zhai, Y., Dong, S., 2009. Electrochemical sensing and biosensing platform based on chemically reduced graphene oxide. *Analytical chemistry* 81(14), 5603-5613.

Graphical Abstracts



Implementation of Extended Kalman Filter on Stochastic Model of LPF

^{*}Rahul Bansal¹, Sudipta Majumdar²

ECE Department, Delhi Technological University, Delhi-110042, India

¹rahulbansal1591@gmail.com, ²korsudipta@rediffmail.com

Abstract

This paper presents output voltage estimation of RC low pass filter (LPF). For this, extended Kalman filter (EKF) has been used on stochastic model of RC LPF. At first, deterministic model of RC low pass circuit has been derived and it is transformed into stochastic model by adding white Gaussian noise to input source and circuit elements. Thereafter, EKF is applied for output voltage estimation. MATLAB simulation results show that estimated output of RC circuit using noisy input gives approximately same output as PSPICE simulated output (actual output).

Keywords: RC LPF; EKF; stochastic parameter estimation

1. INTRODUCTION

RC circuit is an important circuit component in different electronic circuits. Jiang [1] used RC low pass circuits in class D amplifier for loop stability. Farajollahiet al. [2] proposed a RC circuit based transmission line model for prediction of polymer based electrode and actuators behavior. It is also used in resistance switching interface circuit [3]. Besides these it is also used in CMOS bulk lowpass analogue filter [4], flexible voltage controlled oscillators [5], flyback inverter [6], Chebyshev ladder active RC band pass filter [7], wireless receiver [8] etc.

Stochastic modelling is an approach for optimization problems by including uncertainty. As electronic circuits are affected by different types of noise, the stochastic modelling helps to study the effect of random fluctuations of individual circuit elements and voltage sources. Stochastic modelling of nonlinear rectifier circuit is given in [9]. Bonnin [10] presented the amplitude and phase description for nonlinear oscillator under white Gaussian noise. Tao *et al.* [11] proposed a stochastic approach to accelerate the design of lithium ion battery capacity fading dynamics model. Li-ion battery. Djurhuuset al. [12] analyzed the stochastic resonance of bistable electrical circuit. Rawat *et al.* [13] proposed stochastic modelling of linear RLC circuit.

EKF is broadly used for parameter estimation of nonlinear systems in different applications. Stojanovic and Nedic [14] presented a EKF based joint state and parameter estimation of stochastic nonlinear system with time varying parameters. Chatziset al. [15] proposed stochastic parameter estimation of radar tracking using continuous-discrete EKF. In [16], Liu et al. studied the stochastic stability condition for EKF. In [17], Baccoucheet al. proposed online state of charge estimation of aLi-ion battery using EKF. Yin et al. [18] studied the effect of observability properties of non-smooth systems in the convergence of EKF and Unscented Kalman Filter (UKF).

This paper is organized as follows: Deterministic and stochastic model of RC low pass filter circuit has been derived in Section 2. Brief introduction to EKF is presented in section 3. Implementation of EKF in RC circuit stochastic model is given in Section 4. Simulation results are given in section 5. Section 6 concludes the paper.

2. State Space Model of RC Circuit

2. A. Deterministic Model of RC circuit

Fig. 1 (a) shows the second order RC low pass circuit having input voltage source $u_1(t)$, resistors R_1 , R_2 and capacitors C_1 , C_2 . V_{c_1} and V_{c_2} are the capacitor voltages.

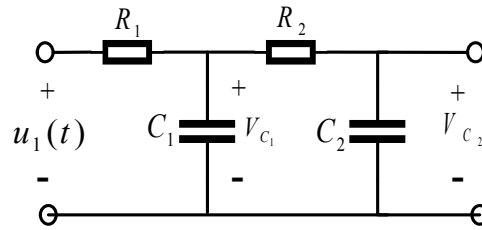


Fig. 1. RC low pass filter

Applying Kirchhoff's law to the circuit in Fig 1, we have

$$\frac{v_{c_1}(t) - u_1(t)}{R_1} + \frac{v_{c_1}(t) - v_{c_2}(t)}{R_2} + C_1 \frac{dv_{c_1}}{dt} = 0 \quad (1)$$

$$\frac{v_{c_2}(t) - v_{c_1}(t)}{R_2} + C_2 \frac{dv_{c_2}}{dt} = 0 \quad (2)$$

Or, (1) and (2) can be written as

$$\frac{dv_{c_1}}{dt} = v_{c_1}(t) \left(-\frac{1}{R_1 C_1} - \frac{1}{R_2 C_1} \right) + v_{c_2}(t) \left(\frac{1}{R_2 C_1} \right) + u_1(t) \left(\frac{1}{R_1 C_1} \right) \quad (3)$$

$$\frac{dv_{c_2}}{dt} = v_{c_1}(t) \left(\frac{1}{R_2 C_2} \right) + v_{c_2}(t) \left(-\frac{1}{R_2 C_2} \right) \quad (4)$$

$$y = v_{c_2}(t) \quad (5)$$

Where, y is the measured output. Above equations can be represented in following matrix notation as

$$\frac{dv(t)}{dt} = Av(t) + B(t) \quad (6)$$

Where $dv(t)$ is given as

$$dv(t) = [dv_{c_1}(t) \quad dv_{c_2}(t)]^T$$

$$A = \begin{bmatrix} \left(-\frac{1}{R_1 C_1} - \frac{1}{R_2 C_1} \right) & \frac{1}{R_2 C_1} \\ \frac{1}{R_2 C_2} & -\frac{1}{R_2 C_2} \end{bmatrix} \quad (7)$$

$$B = \begin{bmatrix} \frac{v_1(t)}{R_1 C_1} & 0 \end{bmatrix} \quad (8)$$

1. 2. B. Stochastic model of RC circuit

White Gaussian noise has been added to input source and elements of the RC circuit to convert deterministic ordinary differential equation into stochastic differential equation. The correlated process i.e. colored noise is added to circuit elements as

$$A_j^* = A_j + k_j w_j(t), \quad 1 \leq j \leq n$$

Where A_j^* is the noisy circuit element, A_j is circuit element, k_j is the constant that denotes the intensity of noise, $w_j(t)$ is the zero-mean correlated process and u_1 is input to the circuit.

$$R_1^* = R_1 + k_1 w_1(t) \quad (9)$$

$$R_2^* = R_2 + k_2 w_2(t) \quad (10)$$

$$C_1^* = C_1 + k_3 w_3(t) \quad (11)$$

$$C_2^* = C_2 + k_4 w_4(t) \quad (12)$$

$$u_1^*(t) = u_1(t) + k_5 w_5(t) \quad (13)$$

The correlated process $w_j(t)$ is mathematically represented by stochastic differential equation (SDE) in terms of white Gaussian noise.

$$dw_j(t) = \rho_j w_j(t)dt + \sigma_j \rho_j dB_j(t) \quad (14)$$

Where, $B_j(t)$ is the Brownian motion process. $B_j(t)$ is continuously differentiable, therefore equation (14) becomes

$$\frac{dw_j(t)}{dt} = \rho_j w_j(t) + \sigma_j \rho_j N_j(t) \quad (15)$$

Where, $N_j(t) = \frac{d}{dt} B_j(t)$ and defined as white Gaussian noise. Substituting (9) - (13) into (3) to (5), we get

$$\begin{aligned} \frac{dv_{c_1}}{dt} = & v_{c_1}(t) \left(-\frac{1}{(R_1 + k_1 w_1(t))(C_1 + k_3 w_3(t))} - \frac{1}{(R_2 + k_2 w_2(t))(C_1 + k_3 w_3(t))} \right) + \\ & + v_{c_2}(t) \left(\frac{1}{(R_2 + k_2 w_2(t))(C_1 + k_3 w_3(t))} \right) + \left(\frac{u_1(t) + k_5 N_5(t)}{(R_1 + k_1 w_1(t))(C_1 + k_3 w_3(t))} \right) \end{aligned} \quad (16)$$

$$\begin{aligned} \frac{dv_{c_2}}{dt} = & v_{c_1}(t) \left(\frac{1}{(R_2 + k_2 w_2(t))} \times \frac{1}{(C_2 + k_4 w_4(t))} \right) \\ & + v_{c_2}(t) \left(-\frac{1}{(R_2 + k_2 w_2(t))} \times \frac{1}{(C_2 + k_4 w_4(t))} \right) \end{aligned} \quad (17)$$

To convert (16) and (17) into stochastic differential equation (SDE), we multiply these equations by dt , therefore get

$$\begin{aligned}
 dv_{c_1}(t) = & v_{c_1}(t) \left(-\frac{1}{(R_1 + k_1 w_1(t))(C_1 + k_3 w_3(t))} - \frac{1}{(R_2 + k_2 w_2(t))(C_1 + k_3 w_3(t))} \right) dt \\
 & + v_{c_2}(t) \left(\frac{1}{(C_1 + k_3 w_3(t))} \times \frac{1}{(C_1 + k_3 w_3(t))} \right) dt \\
 & + \left(\frac{u_1(t) + k_5 w_5(t)}{(R_1 + k_1 w_1(t))(C_1 + k_3 w_3(t))} \right) dt
 \end{aligned} \quad (18)$$

$$\begin{aligned}
 dv_{c_2}(t) = & v_{c_1}(t) \left(\frac{1}{(R_2 + k_2 w_2(t))} \times \frac{1}{(C_2 + k_4 w_4(t))} \right) dt \\
 & + v_{c_2}(t) \left(-\frac{1}{(R_2 + k_2 w_2(t))} \times \frac{1}{(C_2 + k_4 w_4(t))} \right) dt
 \end{aligned} \quad (19)$$

Combining (14), (18) and (19), we have

$$dX(t) = A(t)X(t)dt + z(t)dt + K(t)dB(t) \quad (20)$$

Where

$$X(t) = [w_1(t) \ w_2(t) \ w_3(t) \ w_4(t) \ v_{c_1}(t) \ v_{c_2}(t)]^T \quad (21)$$

$$A(t) = \begin{bmatrix} -\rho_1 & 0 & 0 & 0 & 0 & 0 \\ 0 & -\rho_2 & 0 & 0 & 0 & 0 \\ 0 & 0 & -\rho_3 & 0 & 0 & 0 \\ 0 & 0 & 0 & -\rho_4 & 0 & 0 \\ 0 & 0 & 0 & 0 & A_{55} & A_{56} \\ 0 & 0 & 0 & 0 & A_{65} & A_{66} \end{bmatrix} \quad (22)$$

where

$$\begin{aligned}
 A_{55} = & -\frac{1}{(R_1 + k_1 w_1(t))(C_1 + k_3 w_3(t))} - \frac{1}{(R_2 + k_2 w_2(t))(C_1 + k_3 w_3(t))} \\
 A_{56} = & \frac{1}{(R_2 + k_2 w_2(t))(C_1 + k_3 w_3(t))} \\
 A_{65} = & \frac{1}{(R_2 + k_2 w_2(t))(C_2 + k_4 w_4(t))} \\
 A_{66} = & -\frac{1}{(R_2 + k_2 w_2(t))(C_2 + k_4 w_4(t))}
 \end{aligned}$$

$$Z(t) = \begin{bmatrix} 0 & 0 & 0 & 0 & \frac{u_1(t)}{(R_1 + k_1 w_1(t))(C_1 + k_3 w_3(t))} & 0 \end{bmatrix}^T \quad (23)$$

$$dB(t) = [dB_1(t) \ dB_2(t) \ dB_3(t) \ dB_4(t) \ dB_5(t) \ 0]^T \quad (24)$$

The discrete time state space matrix is obtained by using Euler-Maruyama method. Therefore, the discrete version of A and B are

$$A_D(k) = e^{A\Delta T}, \quad B_D(k) = \left(\int_0^{\Delta T} e^{A\tau} d\tau \right) B \text{ respectively.}$$

The discrete state space model of above SDE becomes

$$X(k+1) = A(k)X(k) + z(k) + K(k)B(k) \quad (26)$$

$$Y(k) = C(k)X(k) \quad (27)$$

Where

$$X(k) = [w_1(k) \ w_2(k) \ w_3(k) \ w_4(k) \ v_{c_1}(k) \ v_{c_2}(k)]^T \quad (28)$$

$$A(k) = \begin{bmatrix} 1 - \Delta T \rho_1 & 0 & 0 & 0 & 0 & 0 \\ 0 & 1 - \Delta T \rho_2 & 0 & 0 & 0 & 0 \\ 0 & 0 & 1 - \Delta T \rho_3 & 0 & 0 & 0 \\ 0 & 0 & 0 & 1 - \Delta T \rho_4 & 0 & 0 \\ 0 & 0 & 0 & 0 & 1 + \Delta T A_{55} & A_{56} \\ 0 & 0 & 0 & 0 & A_{65} & 1 + \Delta T A_{66} \end{bmatrix} \quad (29)$$

$$\begin{aligned} A_{55} &= -\frac{1}{(R_1 + k_1 w_1(k))(C_1 + k_3 w_3(k))} - \frac{1}{(R_2 + k_2 w_2(k))(C_1 + k_3 w_3(k))} \\ A_{56} &= \frac{1}{(R_2 + k_2 w_2(k))(C_1 + k_3 w_3(k))} \\ A_{65} &= \frac{1}{(R_2 + k_2 w_2(k))(C_2 + k_4 w_4(k))} \\ A_{66} &= -\frac{1}{(R_2 + k_2 w_2(k))(C_2 + k_4 w_4(k))} \\ Z(k) &= \begin{bmatrix} 0 & 0 & 0 & 0 & \frac{\Delta T u_1(k)}{(R_1 + k_1 w_1(k))(C_1 + k_3 w_3(k))} & 0 \end{bmatrix}^T \end{aligned} \quad (30)$$

$$K(k) = \begin{bmatrix} -\Delta T \sigma_1 \rho_1 & 0 & 0 & 0 & 0 & 0 \\ 0 & -\Delta T \sigma_2 \rho_2 & 0 & 0 & 0 & 0 \\ 0 & 0 & -\Delta T \sigma_3 \rho_3 & 0 & 0 & 0 \\ 0 & 0 & 0 & -\Delta T \sigma_4 \rho_4 & 0 & 0 \\ 0 & 0 & 0 & 0 & \Delta T k_{56} & 0 \\ 0 & 0 & 0 & 0 & 0 & 0 \end{bmatrix} \quad (31)$$

$$K_{56} = \frac{k_5}{(R_1 + k_1 w_1(k))(C_1 + k_3 w_3(k))}$$

$$B(k) = [B_1(k) \ B_2(k) \ B_3(k) \ B_4(k) \ B_5(k) \ 0]^T \quad (32)$$

$$C(k) = [0 \ 0 \ 0 \ 0 \ 1 \ 0] \quad (33)$$

3. EXTENDED KALMAN FILTER

EKF, an extension of KF, is used for nonlinear state estimation.

In general, nonlinear discrete time system is defined as

$$X(k) = f(X(k-1), u(k-1)) + w(k-1) \quad (33)$$

$$Y(k-1) = g(X(k-1), u(k-1)) + v(k-1) \quad (34)$$

where $f(\cdot)$ and $g(\cdot)$ are the nonlinear functions of input and previous state. $u(k)$ and $Y(k)$ are the control input and measured output respectively. $w(k)$ and $v(k)$ are the process and measurement noise (white Gaussian noise) with zero mean and covariance $R(k)$ and $Q(k)$. Linear state space equation are obtained from (33)-(34) by applying partial derivatives of function f and g with respect to $x(k)$ and $u(k)$ to get Jacobian matrix.

The transformed equations are

$$X(k) = A(k-1)X(k-1) + B(k-1)u(k-1) + w(k-1) \quad (35)$$

$$Y(k-1) = C(k-1)X(k-1) + D(k-1)u(k-1) + v(k-1) \quad (36)$$

Where

$$A(k-1) = \frac{\partial f(X(k-1), u(k-1))}{\partial XP^-(k)}, B(k-1) = \frac{\partial f(X(k-1), u(k-1))}{\partial u(k-1)}$$

$$C(k-1) = \frac{\partial g(X(k-1), u(k-1))}{\partial x(k-1)}, D(k-1) = \frac{\partial g(X(k-1), u(k-1))}{\partial u(k-1)}$$

3. A. EKF general steps:

Estimation through EKF algorithm broadly consists of two steps

- Time update
- Measurement update

At first states $X(k-1)$ are initiated to some value $\hat{X}^0(k-1)$ with error covariance $\hat{P}^0(k-1)$.

1. Time update:

1 (a). State estimation time update:

$$\hat{X}^-(k) = A(k-1)\hat{X}^+(k-1) + B(k-1)u(k-1) + Q(k-1) \quad (37)$$

Where $\hat{X}^-(k)$ is the priori and posteriori state estimate at the time $k-1$ and k respectively. Superscript “-” and “+” represent priori and posteriori values that are approximated before and after measurement.

1 (b). Error covariance time update:

$$P^-(k) = A(k-1)P^+(k-1)A^T(k-1) + Q(k-1) \quad (38)$$

Where $P^-(k)$ and $P^+(k-1)$ are the priori and posteriori error covariance time k and $k-1$ respectively.

1 (c). Output state prediction:

$$\hat{Y}^+(k-1) = C(k-1)\hat{X}^+(k-1) + R(k-1) \quad (39)$$

2. Measurement update

2 (a). Calculation of Kalman gain:

$$K_k = P^-(k)C^T(k-1)[C(k-1)P^-(k)C^T(k-1) + Q_{k-1}]^{-1} \quad (40)$$

Where K_k is the Kalman gain.

2 (b). State estimate measurement update:

$$\hat{X}^+(k) = \hat{X}^-(k) + K_k[Y(k-1) - C(k-1)\hat{X}^-(k)] \quad (41)$$

Where, $\hat{X}^+(k)$ is the posteriori estimated state, $\hat{X}^-(k)$ is the priori estimated state and $Y(k)$ is the real time measured output.

2 (c). Error covariance measurement update:

$$P^+(k) = [I - K_kC(k-1)]P^-(k) \quad (42)$$

In this step, posteriori error covariance, $P^+(k)$, is estimated. These steps are repeated until we get best approximated output.

3. B. Applying EKF in RC circuit:

For applying EKF to RC circuit equations (26) and (27) are modelled as

$$X(k) = A(k-1)X(k-1) + z(k-1) + K(k-1)B(k-1) + w(k-1) \quad (43)$$

$$Y(k-1) = C(k-1)X(k-1) + v(k-1) \quad (44)$$

Where stochastic differential equation (26) and (27) are added with process noise $w(k)$ and measurement noise $v(k)$. After that, step-1 (time update) followed by step 2 (measurement update) from equation (37) - (42) is applied to get best estimated output.

4. SIMULATION RESULTS

Output voltage estimation of RC LPF has been done by applying EKF using stochastic model of the circuit. RC circuit element values are $R_1 = 1M\Omega$, $R_2 = 1M\Omega$, $C_1 = 1\mu F$, $C_2 = 1\mu F$, $\sigma_j = 1$ and $\rho_j = 1$. Estimated output voltage is compared to simulated PSPICE data, which shows that estimated output through EKF is immune to white Gaussian noise. Fig. 2(a) gives comparison of EKF estimated output to simulated output when resistance R_1 is affected by white Gaussian noise. Similarly, Fig. 2(b), Fig. 2(c), Fig. 2(d), Fig. 2(e) gives comparison of simulated output and circuit elements resistance R_2 , capacitance R_1 , capacitance R_1 , input source modelled by zero mean correlated process. Table I shows the SNR for different circuit elements modelled by different noise intensity. It shows that SNR is least when input source is affected by white Gaussian noise as compared to other circuit elements added with zero mean correlated process.

Table I. Signal to Noise Ratio For Different Circuit Element Modelled By White Gaussian Noise

S. No.	Circuit element intensity of noise	SNR (dB)
1.	$k_1 = 1$	56.22
2.	$k_2 = 1$	58.39
3.	$k_3 = 1$	62.46
4.	$k_4 = 1$	65.95
5.	$k_5 = 1$	50.64

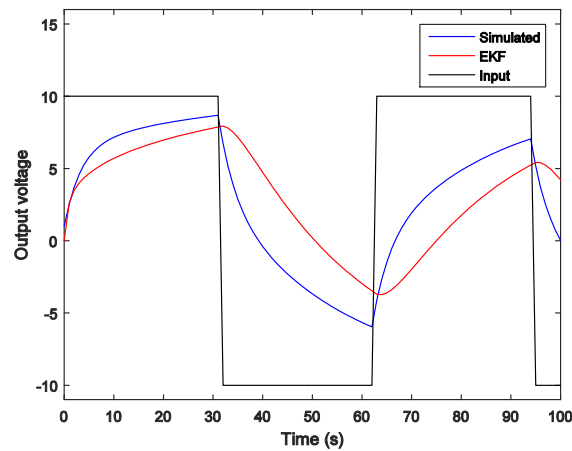


Fig. 2(a). RC LPF PSPICE simulated and stochastic estimated output for $k_1 = 1$ and other k 's are zero.

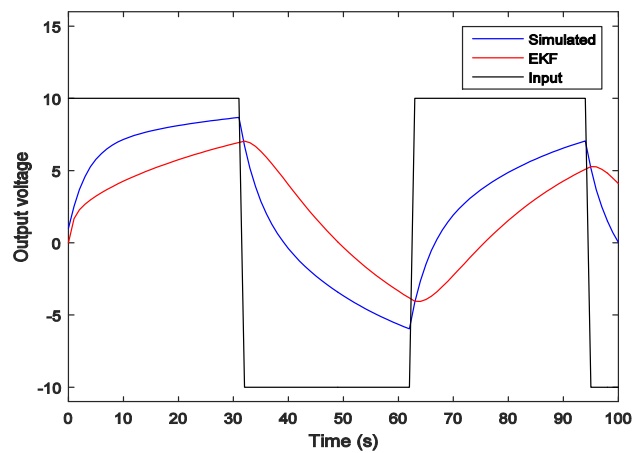


Fig. 2(b). RC LPF PSPICE simulated and stochastic estimated output for $k_2 = 1$ and other k 's are zero.

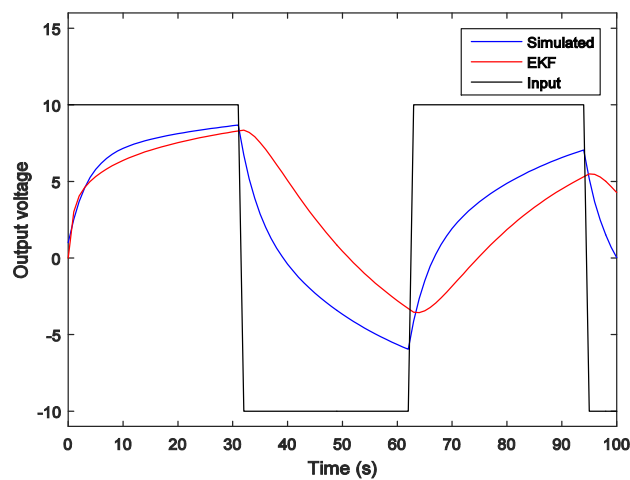


Fig. 2(d). RC LPF PSPICE simulated and stochastic estimated output for $k_3 = 1$ and other k 's are zero.

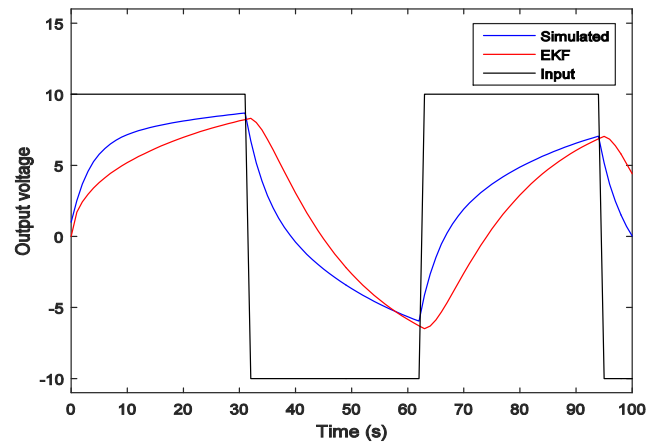


Fig. 2(e). RC LPF PSPICE simulated and stochastic estimated output for $k_4 = 1$ and other k 's are zero.

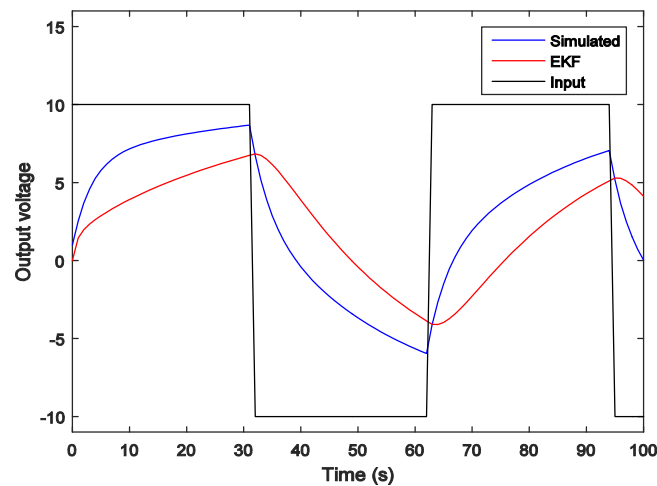


Fig. 2(c). RC LPF PSPICE simulated and stochastic estimated output for $k_5 = 1$ and other k 's are zero.

5. CONCLUSION

Output voltage of RC LPF is estimated using EKF when input source and circuit elements are added with white Gaussian noise. MATLAB and PSPICE simulation results show that EKF work effectively in case of stochastic modelled RC circuit. SNR is computed for each case when either any of the circuit element is affected by white Gaussian noise. The advantage of the proposed method is that it gives good estimation as EKF is a stochastic approach of parameter estimation. Also, it requires small computations and easy to implement. Further, it can be used for real time implementation.

ACKNOWLEDGMENT

The first author would like to thank CSIR (Council for Scientific Industrial Research, Government of India) for financial support in terms of SRF (Senior Research Fellowship).

References

- [1] X. Jiang, "Fundamentals of audio class D amplifier design", IEEE Solid-State Circuits Magazine, (2017), pp. 14-25.
- [2] M. Farajollahi, F. Sassani, N. Naserifar, A. Fannir, C. Plesse, G. T. Nguyen and J. D. Madden, "Nonlinear two dimensional transmission line model for electrochemically driven conducting polymer actuators", IEEE Trans. On Mechatronics, vol.-22, no. 2, (2017), pp. 705-716.
- [3] Y. Meng and R. N. Dean, "A technique for improving the linear operating range for a relative phase delay capacitive sensor interface circuit", IEEE Transactions on Instrumentation and Measurement, vol. 65 no. 3, (2016), pp. 624-630.
- [4] D. Matteis, M., A. Donno, S. D'Amico, and A. Baschirotto, "0.9 V third-order 132 MHz single-OPAMP analogue filter in 28 nm CMOS", Electronics Letters 53, no. 2, (2016), pp. 77-79.
- [5] S. Knobelspies, C. Gonnelli, C. Vogt, A. Daus, N. Münzenrieder and G. Tröster. "Geometry-based tunability enhancement of flexible thin-film varactors", IEEE Electron Device Letters 38, no. 8 (2017), pp. 1117-1120.
- [6] S. H. Lee, W. J. Cha, B. H. Kwon and M. Kim, "Discrete-time repetitive control of flyback CCM inverter for PV power applications", IEEE Transactions on Industrial Electronics 63, no. 2, (2016), pp. 976-984.
- [7] B. Wu and Y. Chiu, "A 40 nm CMOS derivative-free IF active-RC BPF with programmable bandwidth and center frequency achieving over 30 dBm IIP3", IEEE Journal of Solid-State Circuits 50, no. 8 (2015), pp. 1772-1784.
- [8] Y. Wang, L. Ye, H. Liao, R. Huang and Y. Wang, "Highly reconfigurable analog baseband for multistandard wireless receivers in 65-nm CMOS", IEEE Transactions on Circuits and Systems II: Express Briefs 62, no. 3, (2015), pp. 296-300.
- [9] A. Rathee and H. Parthasarathy, "Perturbation-based stochastic modeling of nonlinear circuits", Circuits, Systems, and Signal Processing 32, no. 1, (2013), pp. 123-141.
- [10] M. Bonnin, "Amplitude and phase dynamics of noisy oscillators." International Journal of Circuit Theory and Applications 45, no. 5, (2017), pp. 636-659.
- [11] L. Tao, Y. Cheng, C. Lu, Y. Su, J. Chong, H. Jin, Y. Lin and A. Noktehdan, "Lithium-ion battery capacity fading dynamics modelling for formulation optimization: A stochastic approach to accelerate the design process", Applied Energy 202, (2017), pp. 138-152.
- [12] T. Djurhuus and V. Krozer, "Numerical analysis of stochastic resonance in a bistable circuit", International Journal of Circuit Theory and Applications 45, no. 5, (2017), pp. 625-635.
- [13] T. K. Rawat & H. Parthasarathy, "On stochastic modelling of linear circuits". International Journal of Circuit Theory and Applications, vol. 38, no. 3, (2010), pp. 259-274.
- [14] V. Stojanovic, N. Nedic, "Joint state and parameter robust estimation of stochastic nonlinear systems", International Journal of Robust and Nonlinear Control, vol. 26, no. 14, (2016), pp. 3058-3074
- [15] G. Y. Kulikov, M. V. Kulikov, "The accurate continuous-discrete extended Kalman filter for radar tracking", IEEE Transactions on Signal Processing, vol. 64, no. 4, (2016), pp. 948-958.

- [16] X. Liu, L. Li, Z. Li, T. Fernando, H. H. Iu, "Stochastic stability condition for the extended Kalman filter with intermittent observations", IEEE Transactions on Circuits and Systems II: Express Briefs, vol. 64, no. 3, (2017), pp. 334-338.
- [17] H. J. Kushner, Approximations to optimal non-linear filters. IEEE Trans. Automat. Contr., vol. 12, no. 5, **(1967)**, pp. 546–556.
- [18] M. N. Chatzis, E. N. Chatzi and S. P. Triantafyllou. "A Discontinuous Extended Kalman Filter for non-smooth dynamic problems." Mechanical Systems and Signal Processing, 92, **(2017)**, pp. 13-29.

Influence of Interface Trap Charge Density on Reliability Issues of Transparent Gate Recessed Channel (TGRC) MOSFET

Ajay Kumar¹, M.M. Tripathi¹ and Rishu Chaujar^{2*}

¹Electrical Engineering Department, ^{2*}Engineering Physics Department, Delhi Technological University, Delhi, India

Abstract—This paper examines the reliability issues of In₂O₅Sn (ITO) gate electrode (Transparent Gate) Recessed Channel (TGRC) MOSFET by considering the influence of interface trap charges polarity and density present at the Si/SiO₂ interface. The reliability of TGRC MOSFET is observed in terms of Linearity and distortion FOMs such as g_m , g_{m3} , VIP3, IIP3, HD3, IMD3. Results so obtained revealed that the existence of interface trap charges alter the flat band voltage and thus the threshold voltage; thereby modifying the linearity performance of the device. Moreover, it is also observed that as trap charge density increases, performance escalates considerably. It is found that with positive trap density of $3 \times 10^{12} \text{ cm}^{-2}$, VIP3, IIP3 degrades owing to high distortions (g_{m3}). Thus, results signify that TGRC MOSFET is more reliable to negative trap charges at the Si/SiO₂ interface as compared to positive trap charges.

Keywords—Interface trap charges, ITO, Temperature, TGRC-MOSFET.

I. INTRODUCTION

Trapping of the charges is an important reliability issue for Si-based transistor technology [1]. Traps are created during the fabrication at Si/SiO₂ interface. Interface trap charges are prompted due to, radiation tempted damage [2], stress tempted damage, process tempted damage, and hot carrier tempted damage [3]. These traps either charged (positive or negative) or neutral which hinder the device performance. Sometimes trap charges may improve the device performance (in the case of donor trap charges) only when the device is reliable for these defects. Mostly, devices are fails when the density of trap charges is increased (more defects are created). To reduce this failure mechanism (due to induced trap charges), there is need some engineering schemes in MOSFET devices. Recessed Channel (RC) MOSFET is most promising for extending the scaling limit of conventional CMOS technology due to tremendous gate controllability, lessened SCEs, and ease of fabrication feasibility of RC MOSFET [4]. Though in RC-MOSFET, the efficiency of carrier transport, and current driving capability both are limited owing to high-density field lines owing to two potential barriers which are created at the two corners [5]. Thus carriers required additional energy to cross these barriers and hence results in low current driving capability. Therefore, there is a necessity of incorporating some device engineering schemes onto RC MOSFET. Hence, gate -metal engineering scheme is incorporated by

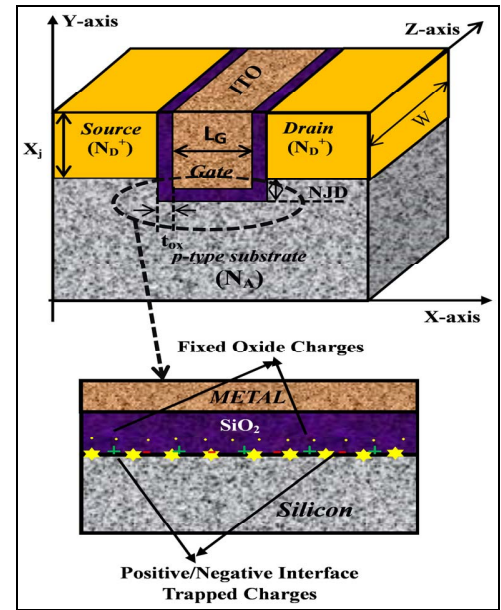


Fig. 1: Device design of TGRC MOSFET (3D device) with interface traps charges. Here, L_{gap} is the length of Nano-gap cavity (8 nm), $t_{\text{ox}} = 2$ nm, and $L_G = 30$ nm. Doping of the source region and drain regions are high with $5 \times 10^{19} \text{ cm}^{-3}$ (an n-type impurity) and the doping of the substrate is $1 \times 10^{17} \text{ cm}^{-3}$ (with a p-type impurity). NJD=10 nm, $V_{\text{gs}} = 0.7$ V and $V_{\text{ds}} = 0.2$ V have been taken in to account.

introducing In₂O₅Sn (ITO) as a gate material which has the highest conductivity and transparency as well. ITO needs low deposition temperature [6, 7], has a high concentration (10^{21} cm^{-3}), the resistivity is very low ($10^{-5} \Omega\text{-cm}$), and the Hall mobility ($53.5 \text{ cm}^2 \text{ V}^{-1} \text{ s}^{-1}$) is very high [8]. In addition, shrinking the device size is the chief reason towards the reduction of the circuit, portability and low cost [9]. To overcome such problems and to improve the linearity, a new device called TGRC-MOSFET [10] was proposed where In₂O₅Sn is used as a gate electrode.

The reliability issues of TGRC-MOSFET have been examined in this work by analyzing the influence of interface trap charge density present at the Si/SiO₂ interface. However many research publications have been reported on linearity analysis and temperature analysis of RC-MOSFET [11], the influence of ITCs density on RC-MOSFET with gate engineering scheme (transparent gate) has been sightseen for the first time in this paper.

II. SIMULATION METHODOLOGY AND CALIBRATION

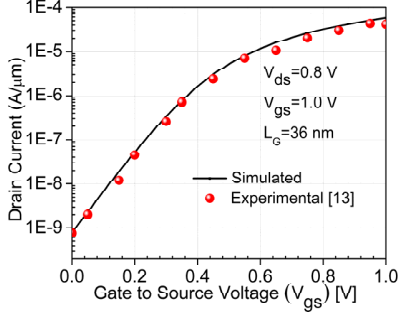
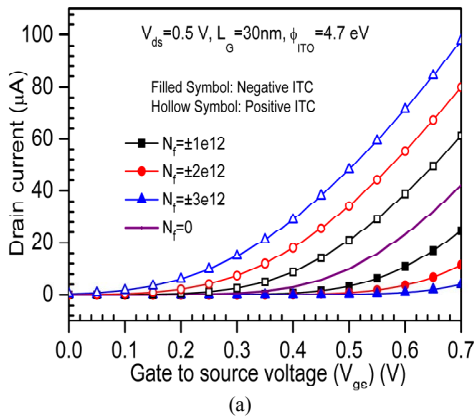


Fig. 2. Calibrated transfer characteristics of recessed channel MOSFET (36 nm gate length) with experimental and simulation data.

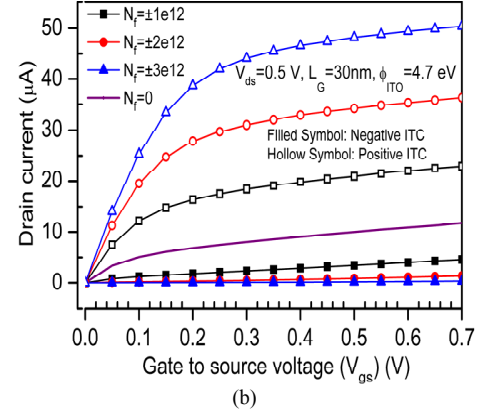
ATLAS is a powerful simulation tool which is used for the extracting of reliability results and all figure of merits (FOMs) [12]. Various simulation models have been used such as Lombardi CVT model is used to consider all the mobilities such as scattering mechanism which is caused by the parallel and perpendicular field applied on the device. For carrier generation-recombination, we have used Shockley-Read-Hall (SRH) Recombination. Fermi-Dirac statistics is used in case of very highly doped material. In order to consider the information about the low energy (temperature) of the carriers, we have used Energy balance transport (EBT) model [12]. The calibration of Pphysical Model parameters of the simulated device with the experimental results by Joerg Appenzeller et al. in 2002 [13] shown in Fig. 2. So as to validate the simulations results, the statistics has been drawn-out [13] for 36 nm groove MOSFET and then plotted as evident in Fig. 2. It is detected from the Fig. 2 that simulated results almost matched with the experimental results in sub-40 nm groove MOSFET thus validating the simulation models.

III. SIMULATION RESULTS AND DISCUSSION

The influence of ITCs polarity and density is observed on TGRC MOSFET. It is observed From Fig. 3(a-b) that, in the presence of positive trap charges, drain current enhances significantly due to the more (low) control of gate bias voltage.



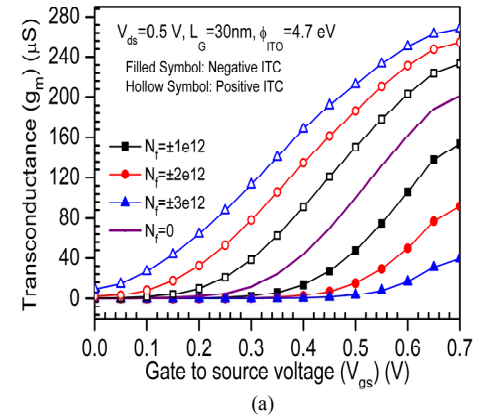
(a)



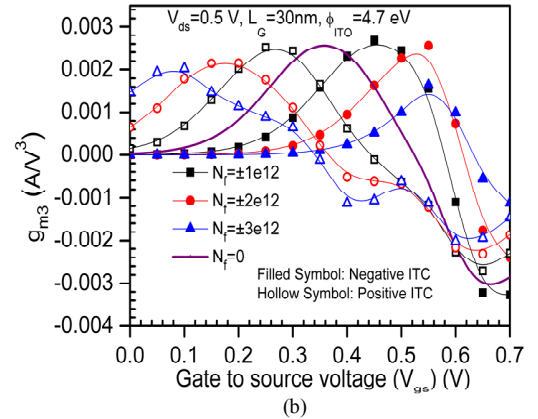
(b)

Fig. 3 (a) Transfer characteristics w.r.t. source voltage (V_{gs}), (b) Output characteristics w.r.t. source voltage (V_{ds}) for TGRC MOSFET.

Drain current further increases (decreases) with an increase in positive (negative) trap charge density as shown in Fig 3(a-b). It is found that input and output characteristics are more prone to positive charges in comparison to negative charges. Fig. 4(a-b) reflects the effect of trap charges polarity / density on linearity FOMs. Fig. 4(a) shows that the transconductance (g_m) is high (low) for positive (negative) traps owing to reduced (enhanced) flat band voltage due to more (low) gate bias.



(a)



(b)

Fig. 4 Impact of interface trap charges for TGRC MOSFET on (a) transconductance (g_{m1}) and (b) g_{m3} .

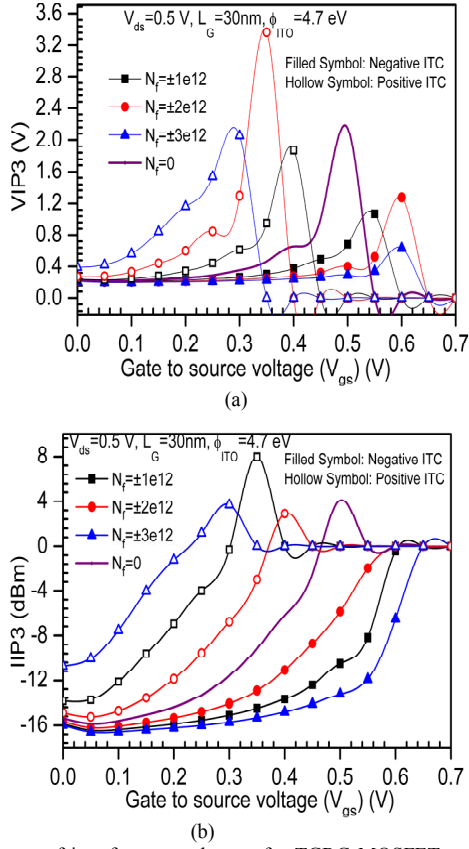


Fig. 5 Impact of interface trap charges for TGRC MOSFET on (a) VIP3 and (b) IIP3.

To assure higher linearity, higher order transconductance coefficient (g_{m3}) must be minimal because g_{m3} decides the dc bias point for optimal operation of the device and regulates the limits on the distortion. It is apparent from Fig. 4(b) that in the existence of positive (negative) trap charges, g_{m3} peak reduces (enhances) appreciably and the effect of density variation is more (less) observed for positive (negative) trap charge density. Thus, signifies that TGRC MOSFET is less prone to negative trap density.

From the dc parameters, VIP3 is used to evaluate the distortion characteristics. Higher VIP3 and IIP3 but lower IMD3 and HD3 are required for lower distortion. The device linearity FOMs are evaluated from Eq. 1 to 4 [11]. The peak amplitude of VIP3 and IIP3 is higher for higher trap density as compared to lower trap density, and it is also found that in the presence of positive trap charges, linearity performance improves owing to improved current driving capability but more reliable for negative trap charges as shown in Fig. 5(a) and (b). In addition, IMD3 is also analyzed considering the influence of both interface trap density and polarity. Integral function method (IFM) is used for the calculation of the distortion since this approach authorizations for the extraction of distortion from DC measurements deprived of an AC characterization, dissimilar to Fourier-based methods [14] as shown in Eq. 4 and 5. Fig. 6(a) reveals that IMD3 reduces in TGRC-

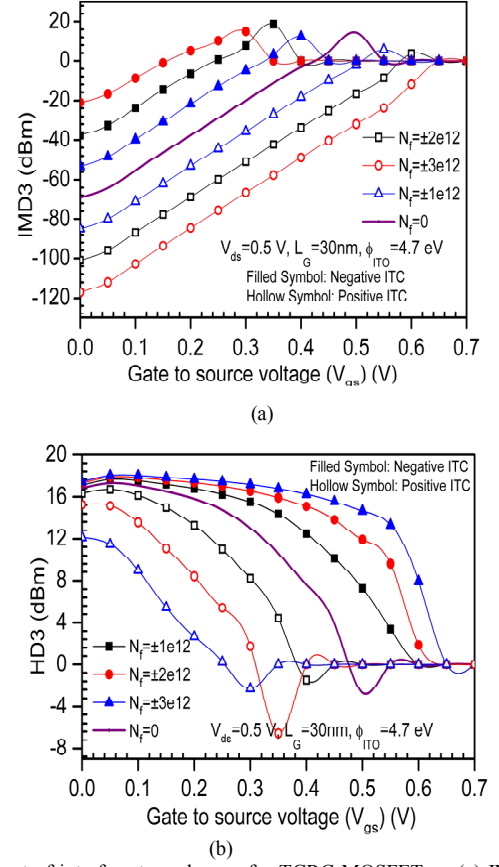


Fig. 6 Impact of interface trap charges for TGRC MOSFET on (a) IMD3, and (b) HD3.

MOSFET owing to the reduced g_{m3} value in comparison to VIP3 which dominates the value of IMD3 (Fig. 4(b)). Meanwhile, it is also observed that TGRC shows reduced (increase) HD3 when positive (negative) trap charges are considered with high density and exhibit the very little effect of traps charges as shown in Fig. 6(b). TGRC exhibits improved linearity and distortion-less performance in the presence of negative trap charge density. Thus, TGRC is more reliable for negative traps as compared to positive traps.

$$VIP3 = \sqrt{\frac{24 \times g_{m1}}{g_{m3}}} \quad \dots (1)$$

$$IIP3 = \frac{2}{3} \frac{g_{m1}}{g_{m3} \times R_s} \quad \dots (2)$$

$$IMD3 = \left(\frac{9}{2} \times (VIP3)^3 \times g_{m3} \right)^2 \times R_s \quad \dots (3)$$

$$\text{where } g_{m1} = \frac{\partial I_d}{\partial V_{gs}} \text{ and } g_{m2} = \frac{\partial^2 I_d}{\partial V_{gs}^2} \cdot g_{m3} = \frac{\partial^3 I_d}{\partial V_{gs}^3}$$

$$HD3 = 0.25 V_a^2 \frac{\left(\frac{d^2 g_{m1}}{dV_{gs}^2} \right)}{6 g_{m1}} \quad \dots (4)$$

where $R_s=50\ \Omega$ for analog and RF applications. V_a is the amplitude of AC signal and considered about 50mV (which is minuscule) for IFM analysis.

IV. CONCLUSION

This work examines the reliability of ITCs (present at the interface of Si/SiO₂) density variation with different polarity (acceptor and donor) on TGRC-MOSFET at room temperature. The results are obtained in terms of linearity performance and intermodulation distortions. The proposed device structure (TGRC-MOSFET) reflects the better reliability in the presence of negative ITCs as compared to positive ITCs. On the basis of obtained results, it is found that TGRC-MOSFET is more reliable when defects are created even though the density of defects is increased. Thus, TGRC-MOSFET is a promising candidate for high linearity and low distortion applications.

ACKNOWLEDGEMENTS

The authors are gratified to University Grand Commission (UGC), Electrical Engineering Department, Microelectronics Research Lab, and Delhi Technological supporting this work.

REFERENCES

- [1] R. Stradiotto, G. Pobegen, C. Ostermaier, M. Wärtl, A. Grill, and T. Grasser, "Characterization of Interface Defects With Distributed Activation Energies in GaN-Based MIS-HEMTs," *IEEE Transactions on Electron Devices*, vol. 64, pp. 1045-1052, 2017.
- [2] Y. H. Lho and K. Y. Kim, "Radiation effects on the power MOSFET for space applications," *ETRI journal*, vol. 27, pp. 449-452, 2005.
- [3] S. Naseh, M. J. Deen, and C.-H. Chen, "Hot-carrier reliability of submicron NMOSFETs and integrated NMOS low noise amplifiers," *Microelectronics Reliability*, vol. 46, pp. 201-212, 2006.
- [4] S. Veeraraghavan and J. G. Fossum, "Short-channel effects in SOI MOSFETs," *IEEE Transactions on Electron Devices*, vol. 36, pp. 522-528, 1989.
- [5] R. Chaujar, R. Kaur, M. Saxena, M. Gupta, and R. Gupta, "Laterally amalgamated DUAL material Gate concave (L-DUMGAC) MOSFET for ULSI," *Microelectronic Engineering*, vol. 85, pp. 566-576, 2008.
- [6] V. Singh, C. Suman, and S. Kumar, "Indium Tin Oxide (ITO) films on flexible substrates for organic light emitting diodes," in *Proc. of ASID*, 2006, p. 388.
- [7] R. Murali and J. D. Meindl, "Modeling the effect of source/drain junction depth on bulk-MOSFET scaling," *Solid-state electronics*, vol. 51, pp. 823-827, 2007.
- [8] T. Minami, "Transparent conducting oxide semiconductors for transparent electrodes," *Semiconductor Science and Technology*, vol. 20, pp. S35-S44, 2005.
- [9] G. E. Moore, "Progress in digital integrated electronics," in *Electron Devices Meeting*, 1975, pp. 11-13.
- [10] A. Kumar, N. Gupta, and R. Chaujar, "TCAD RF performance investigation of Transparent Gate Recessed Channel MOSFET," *Microelectronics Journal*, vol. 49, pp. 36-42, 2016.
- [11] R. Chaujar, R. Kaur, M. Saxena, M. Gupta, and R. Gupta, "TCAD assessment of Gate Electrode Workfunction Engineered Recessed Channel (GEWE-RC) MOSFET and its multi-layered gate architecture, Part II: Analog and large signal performance evaluation," *Superlattices and Microstructures*, vol. 46, pp. 645-655, 2009.
- [12] I. SILVACO, "ATLAS User's Manual," *Santa Clara, CA, Ver*, vol. 5, 2011.
- [13] J. Appenzeller, R. Martel, P. Avouris, J. Knoch, J. Scholvin, J. A. del Alamo, *et al.*, "Sub-40 nm SOI V-groove n-MOSFETs," *IEEE Electron Device Letters*, vol. 23, pp. 100-102, 2002.
- [14] A. Cerdeira, M. A. Alemán, M. Estrada, and D. Flandre, "Integral function method for determination of nonlinear harmonic distortion," *Solid-State Electronics*, vol. 48, pp. 2225-2234, 2004.



Influence of various Carbon and Nitrogen sources on Lipid productivity of *Chlorella minutissima* and *Scenedesmus* sp. and their FAME analysis

Tushita Attre, Arpita Roy, Navneeta Bharadvaja*

Plant Biotechnology Laboratory, Department of Biotechnology, Delhi Technological University, Delhi-110042.

*Corresponding author- navneetab@dtu.co.in

Abstract

Green fuels are getting greater attention day by day due to increase in energy demands and environmental problems. In the current study, *Chlorella minutissima* and *Scenedesmus* sp., were cultivated in BBM medium. The impact of various nitrogen (Sodium Nitrate, Potassium Nitrate, Yeast Extract, Glycine and Urea) and carbon (Glucose, Glycerol, Fructose, Maltose, Starch, Sodium acetate and Sucrose) sources was seen on lipid productivity and FAME analysis. The lipid content was analyzed utilizing Folch strategy by changing the solvent system and amongst the six solvent systems used, Chloroform: Methanol (2:1) was seen demonstrating the best outcomes and was further utilized for extraction. Maximum lipid content and productivity was found in Potassium nitrate nitrogen source (50.08%, 1350.96mg/L/day) for *Chlorella minutissima* and Urea as a nitrogen source (79.05 %, 4027.31 mg/L/day) for *Scenedesmus* sp. Among organic carbon sources, the maximum lipid content and productivity was found in Glucose (36.79% and 2577.27mg/L/day respectively) for *Chlorella minutissima* and Maltose as a carbon source (27.4%, 1690.18 mg/L/day respectively) for *Scenedesmus* sp. Further, it was observed both the algae contained fatty acids from C: 16 to C: 18 which are essential for biodiesel production.

Keywords: Biodiesel, Biomass growth,; *Chlorella minutissima*; *Scenedesmus* sp.; Lipid extraction; FAME analysis

Introduction

Microalgae utilises sunlight and fix CO₂ during photosynthesis and produces biomass more efficiently and rapidly than terrestrial plants. They have been considered for biomass to energy production, based on their fast growth rate, biomass productivity and compatibility for the various kinds of biofuels. (Kumar L, et al., 2017). Power is backbone of each United States's financial improvement and prosperity. India is the sector's 5th largest primary energy patron and fourth largest petroleum consumer after U.S.A, China and Japan (Sharma P. et al., 2015). With an outlook for slight to robust monetary boom and a growing population, growing infrastructural and socio-financial improvement will stimulate an boom in power intake throughout all main sectors of the Indian economic system (Muhit I.B, et al.,2014).Transportation is one of the fastest growing sectors the usage of 27% of the primary electricity (Antoni D,et al.,2007). At the present notable rates of utilization, the world fossil oil holds are probably going to be depleted in below forty five years (BP Statistical overview of the world vitality, 2008). In this way, the growing energy (gas) emergency and ecological debasement have represented an intense problem to our doable improvement and survival. So attention has now moved to the choice powers like biodiesel, bio-ethanol and biogas. Biodiesel is synthesis of unsaturated fat of ethyl or methyl ester produced the usage of virgin or utilized vegetable oil (either palatable or non-consumable).

The most of the biodiesel manufacturing are primarily based on fit to be eaten oil like soybean oil, rapeseed oil, canola oil or sunflower oil in developed countries (Sharma P. et al., 2015). In India, the palatable oil request is better than its actual technology. So there's no chance of occupying this oil for generation of bio diesel. The precept item warm spots for bio diesel can be non-consumable oils obtained from vegetation that may supplant the neighborhood oil makers. There are numerous species, which bear seeds wealthy in oil content and out of those some encouraging tree species had been distinguished. Those are *Jatropha curcas* (Ratanjyot), *Pongamia pinnata* (Karanja), *Calophyllum inophyllum* (Nagchampa or Polanga), Mahua, Castor, Seamarouba and etc (Sharma P. et al., 2015).

Utilizing the ebb and waft yields, mammoth measures of land and crisp water might be expected to create sufficient oil to absolutely supplant petroleum spinoff use. It'd require double the land vicinity of America to be dedicated to soybean technology, or sixty six% to be devoted to rapeseed advent, to meet modern US warming and transportation needs. Microalgae are an emerging source for biodiesel manufacturing in recent years as because of higher biomass and lipid productiveness, and the dearth of opposition with meals plants for agriculture lands and sparkling water resources as they may be develop on non-arable land using saline or waste water (Abdelazi A.E. et al., 2013; Amaro H.M. et al., 2011; Leite G.B. et al., 2013). Microalgae

are photoautotrophic sunlight-driven mobile factories which can convert carbon dioxide to diverse merchandise along with lipids, carbohydrates, proteins, fatty acids, nutrients, antibiotics, and antioxidants (Chisti Y. 2007).

The lipid content has been elevated in many microalgae as a response to excessive way of life conditions which include CO₂, nitrogen awareness and mild depth (Yoo et al., 2010). For the fast accumulation of lipid, microalgae had been cultured in increase-restricting environment such as nitrogen depletion, (Illman AM. et al., 2000; Takagi M. et al., 2000; Li Y. et al., 2008), high mild depth (Khotimchenko et al., 2005), low temperature (Renaud SM. et al., 2002), excessive salt awareness (Takagi M. et al., 2006) and high iron awareness (Liu ZY. et al., 2008). It has been seen that carbon and nitrogen source changes highly influence the biomass and lipid technology of microalgae.

Various carbon sources including Glucose, Sucrose, Fructose, Starch, Maltose, Sodium Acetate and Glycerol and nitrogen sources such as Urea, Yeast Extract, Glycine, Potassium Nitrate, Sodium Nitrate, and Malt Extract had been used. The growth of these resources was recorded by taking absorbance at 680nm on alternate days and additionally through recording dry cell weight on alternate days. The biomass content, lipid content and productivity were additionally calculated for each source. Eventually FAME evaluation confirmed how much percent of fatty acids are present in each alga using various unique carbon and nitrogen sources.

Materials and methods

1. Micro algal strain and culture condition

Pure cultures of *Chlorella minutissima*, *Scenedesmus* sp., were collected from IARI, New Delhi and The Energy and Resources Institute (TERI), Delhi (India) respectively. These species after collection were sub cultured on BBM agar media plates under laboratory conditions (with initial pH of 6.8) and at 25 °Celsius under (~ 1935 lux) light intensity and 12/12 light dark cycle. All the strains were transferred from agar plates to the medium and incubated under the same conditions of temperature and light in 5L culture flasks. Liquid cultures were used as the inoculums for the designed experiments. *Chlorella minutissima* showed better biomass production in 24 hours of illumination of white light of 20 W tube light and shaking periods of 2 hours in Erlenmeyer flasks (Saxena G, 2016)

2. Carbon sources and concentration

The effect at single carbon concentration (0.5g/L) was seen using several sources of carbon in culturing *Chlorella minutissima* and *Scenedesmus* sp. The carbon sources used were Glucose, Fructose, Sucrose, Maltose, Glycerol, Sodium acetate, and Starch. This was done in order to investigate their effect on lipid content and productivity because the inclusion of carbon sources in BBM media showed an increase in lipid production. As there is no carbon sources present in the BBM media the addition of these sources is an added benefit for higher biomass and thus lipid production. The growth and lipid productivity of these species under different carbon sources was recorded and compared.

3. Nitrogen sources and concentration

The effect at single nitrogen concentration (0.25g/L) was seen with several sources of nitrogen such as Yeast extract, Malt extract, Urea, Glycine, Sodium nitrate and Potassium nitrate along with Glucose (0.5g/L) in order to investigate the effect of nitrogen sources on the lipid production of *Chlorella* and *Scenedesmus* sp. The lipid content and productivity of these species under different nitrogen sources was recorded and compared

4. Assessment of combination of solvent systems using Folch method

Lipid was extracted by using Folch method (Folch et al. 1957). As per this method, a weighed amount of biomass i.e. around 250 mg was taken and 5 ml chloroform/methanol (2:1 v/v) was added and vortex for 30 s. This was followed by keeping the mixture for 15–20 min at room temperature. The mixture was then centrifuged at 4000 rpm for 10 min to isolate cell trash from supernatant. This supernatant was washed by 0.9 % NaCl arrangement/water and vortex for few moments. Then this mixture was centrifuged at 3000 rpm for 5 min. Lower chloroform layer with lipid was evacuated deliberately and gathered in 20 ml pre-weighted glass vial. The biomass was re-extricated with 2.5 ml chloroform/methanol (1:1 v/v) until biomass became white. The supernatant was gathered in same vial. The supernatant was then air dried until consistent weight of lipid was attained. The lipid content was calculated gravimetrically. The standard solvent system was changed with different solvent systems such as: Dichloromethane: Methanol (Bligh and Dyer Method); Chloroform: Methanol (Folch method); Hexane: Isopropanol; Cyclohexane: Isopropanol; Hexane: Ethanol; Petroleum Ether.

5. Kinetic parameter :

The relationship developed between OD 680 and biomass (g/l) is given as follows:

The maximum specific growth rate (μ_{\max} day⁻¹) was calculated as follows:

$$\mu_{\max} (\text{day}^{-1}) = (\ln X_2 - \ln X_1) / (t_2 - t_1)$$

Where X_1 and X_2 were the dry biomass weight (g/l) at time t_1 and t_2 respectively.

The doubling time (TD, days) was calculated as follows:

$$TD \text{ (days)} = \ln(2)/\mu_{\max}$$

$$\text{Lipid content } (C_{\text{lipid}}) = (\text{Weight of lipid} / \text{Weight of sample}) \times 100$$

$$\text{Lipid productivity (mg/l/day)} = (C_{\text{lipid}} \times DCW) / t$$

$$\text{Lipid yield (mg/L)} = [\text{Weight of lipid} / \text{Volume of sample}] \times 1000$$

$$\text{Biomass yield or Dry Cell Weight (mg/L)} = [\text{weight of dry sample (mg)} / \text{weight of culture (ml)}] \times 1000$$

6. Sudan test

After completion of extraction of lipid, it was also confirmed whether the extracted material is actually the desired lipid or not. For this conformation, Sudan test which uses Sudan IV dye was performed. This dye is not soluble in water however it is soluble in lipids. 100 ml stock solution of 1mg/ml concentration of Sudan dye was prepared. Lipid sample was prepared by dissolving the extracted lipid in ethanol for each case of above mentioned experiments. For confirmation of lipid, 5ml water is added in a test tube and then the lipid sample dissolved in ethanol was added in to it very slowly. Due to difference in chemical nature, two different phases were formed. Upper phase was lipid phase and lower phase was water. The 20 drops of Sudan IV dye were added slowly with the help of micropipette. The dye was absorbed by the lipid available in upper phase and rest of it was settled in the bottom of the test tubes. This retention or absorbance of dye by the upper phase confirmed that the extracted material was lipid.

7. Fatty Acid Methyl Ester (FAME) analysis of potential lipid yielding algal biomass

Based on the results of potential lipid yielding culture conditions experiment was set for FAME production and analysis.

5-10ml of algae grown under various conditions is taken and centrifuged in order to obtain the biomass and remove all the media from it. 5-10ml of algae was harvested and was collected in screw cap glass tubes in accordance to the density of the material. 2% of Methanolic HCl was added to this algae and the tube caps were tightened properly. These glass tubes are incubated at 80 degree Celcius for 1 hr and 1 ml of 0.9% NaCl in water is added to it. Followed by vortexing the mixture 2 ml of Hexane was added to it. After vortexing the tube is spun at 2000 rpm for 2 minutes for phase separation. After phase separation the upper phase (hexane) is pipetted out in new tube. It is further dried under nitrogen flow and 50 μ l of Hexane is added to it. For FAME analysis only 1 μ L of sample is injected in the GC.

Once the analysis is done all the fatty acids composition is calculated and tabulated in order to find out the percentage of MUFA, PUFA and Saturated fatty acids.

Result and discussion

Growth curve

Potential of microalgae for the production of high and low value commercial products is very huge but effect of environmental conditions on productivity is a great hurdle. The environmental stress affects the biomass productivity as well as final productivity of the commercial product. So identification of potential culture conditions is primary requirement of algal cultivation. All the microalgae species *Chlorella minutissima* and *Scenedesmus sp* were cultured in BBM media and nitrogen source (NaNO_3) was replaced with other nitrogen sources and also different carbon sources were added externally. The cultures in different sources were grown in 250 ml flasks for 2 weeks and the results revealed that in some sources the algae had reached the exponential phase between 7-11 days and in some sources the algae reached exponential phase after that.

Chlorella minutissima

Carbon Sources

In case of carbon sources used in *Chlorella minutissima* Maltose, Glucose, Sucrose and Fructose show a better growth than the control (no carbon source added to it) in which Maltose and Glucose show the best growth curve. Sodium acetate did show good results up-to 7 days but after that it started to decline.

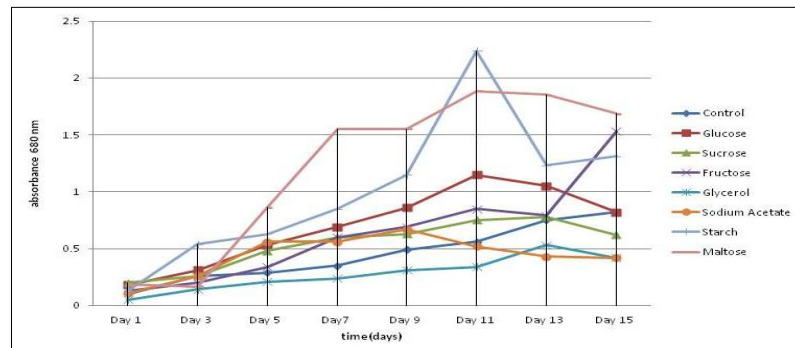


Fig 1. Growth curve of *Chlorella minutissima* under Carbon sources

Nitrogen sources

In case of nitrogen sources, every component showed a better and increased growth than the control but Urea and Yeast extract continued to grow even after 14 days which indicate that they might prove to be better nitrogen source for the growth of *Chlorella minutissima*. Malt extract was also considered as a nitrogen source but it showed no growth after 3 days, i.e the algae grew only for 3 days and after that it started to go in death phase. The experiment using Malt extract was repeated three times and still the algae did not grow after 3 days.

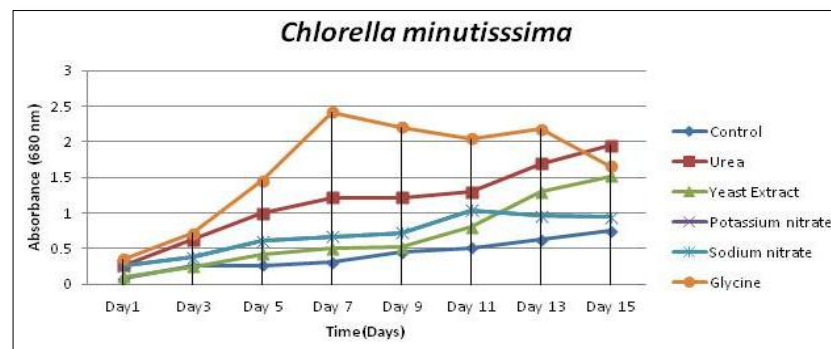


Fig 2. Growth of *Chlorella minutissima* under various nitrogen sources

Growth curve of *Scenedesmus sp.*

Carbon Sources

In case of carbon sources, all except Sodium acetate, Glycerol and Fructose showed a better and increased growth in *Scenedesmus sp.* than control (having no carbon source). But best growth was observed in Maltose, Glucose and Sucrose

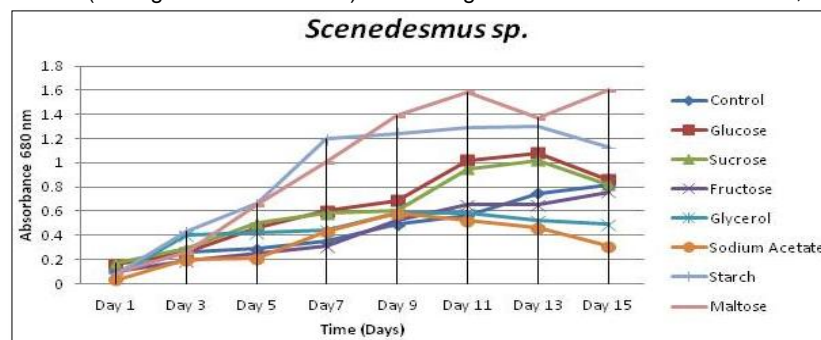


Fig 3. Growth of *Scenedesmus sp.* under various carbon sources

.Nitrogen sources

In case of nitrogen sources Urea and Yeast extract showed an increasing growth and tend to increase even after a time frame of 7 days. Malt extract was also considered as a nitrogen source but it showed no growth after 3 days, i.e the algae grew only for 3 days and after that it started to go in death phase. The experiment using Malt extract was repeated three times and still the algae did not grow after 3 days

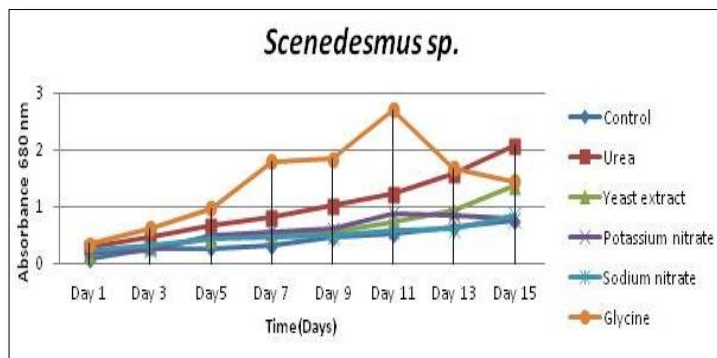


Fig 4. Growth of *Scenedesmus sp.* under various nitrogen species

Lipid yield and productivity

Firstly the lipid productivity for *Chlorella minutissima* and *Scenedesmus sp.* was checked for the best solvent and the further lipid extraction was done accordingly.

Table 1: lipid productivity for *Chlorella minutissima* and *Scenedesmus sp.*(Dry biomass)

Solvent System	Lipid Content (%) of <i>Chlorella sp.</i>	Lipid Content,(%) of <i>Scenedesmus sp.</i>
S1	8.42	9.8
S2	9.42	11.58
S3	8.5	4.66
S4	8.65	8.65
S5	8.038	7.03
S6	1.64	3.6

Table 2: lipid productivity for *Chlorella minutissima* and *Scenedesmus sp.*(Wetbiomass)

Solvent System	Lipid Content (%) of <i>Chlorella sp.</i>	Lipid Content,(%) of <i>Scenedesmus sp.</i>
S1	7.4	8.9
S2	12.08	12.8
S3	11.28	7.6
S4	12.01	11.2
S5	11.09	10.4
S6	1.8	3.8

Looking at this data it can be seen that Chloroform:Methanol (2:1) is the most appropriate solvent system for lipid extraction both using dry and wet biomass . Though wet biomass shows better results but it poses problem of having high moisture content and the results are not accurate and due to this reason dry biomass is used for lipid extraction.

Chlorella minutissima

Carbon Sources

Glucose shows the highest amount of lipid yield and productivity followed by Fructose and Sucrose for *Chlorella minutissima*. The lipid content calculated was 36.79% and lipid productivity was 2577.27mg/L/day.

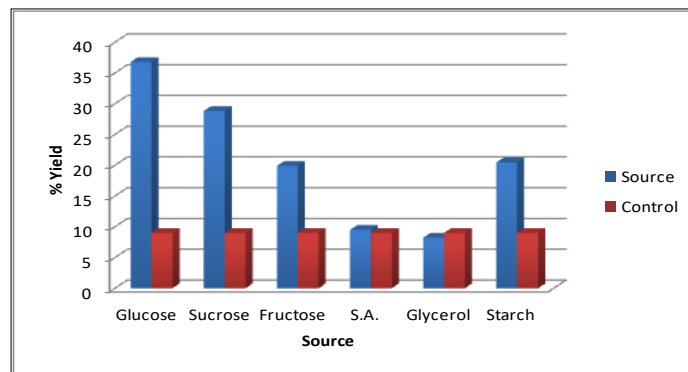


Fig5. Lipid yield for *Chlorella minutissima* under various carbon sources

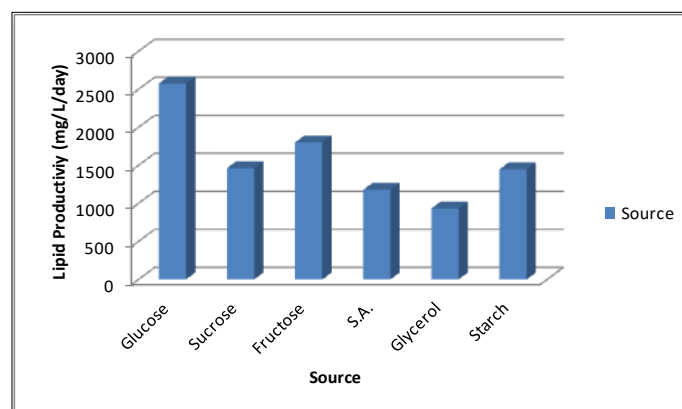


Fig 6 Lipid productivity for *Chlorella minutissima* under various carbon sources

Nitrogen sources

Urea showed best lipid productivity followed by Potassium nitrate and Sodium nitrate for *Chlorella minutissima*. The lipid productivity was 381.5 mg/L/day and potassium nitrate showed maximum lipid content 50.08 %.

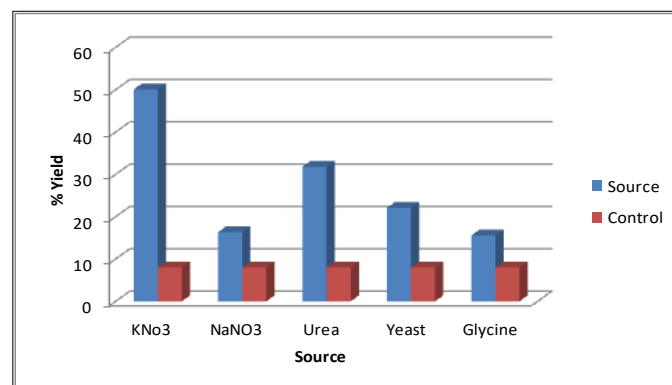


Fig 7 Lipid yield for *Chlorella minutissima* under various nitrogen sources

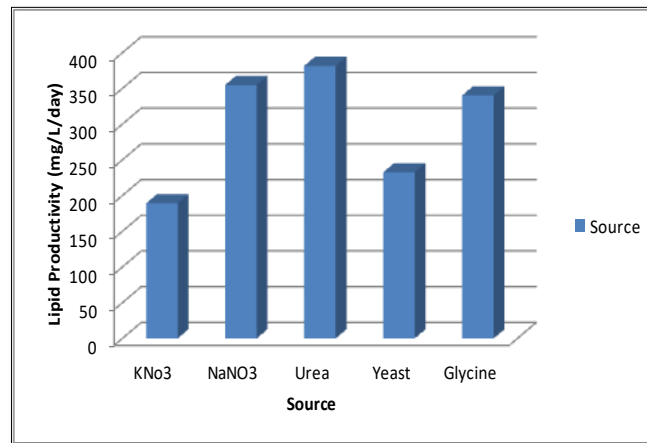


Fig 8 Lipid productivity for *Chlorella minutissima* under various nitrogen sources

Scenedesmus sp.

Carbon Sources

Glucose and sucrose showed better lipid content and productivity for carbon sources in *Scenedesmus sp.*

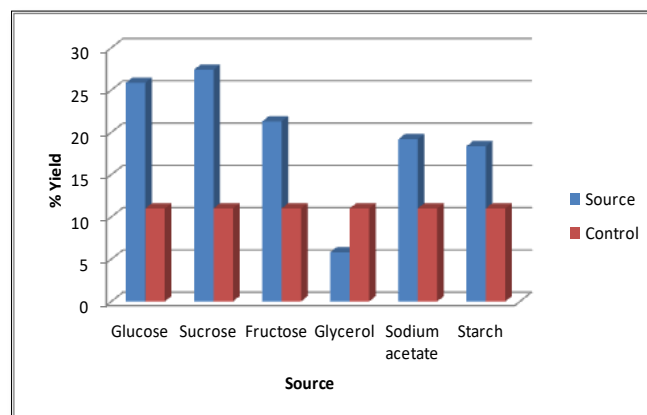


Fig 9 Lipid yield for *Scenedesmus sp.* under various carbon sources

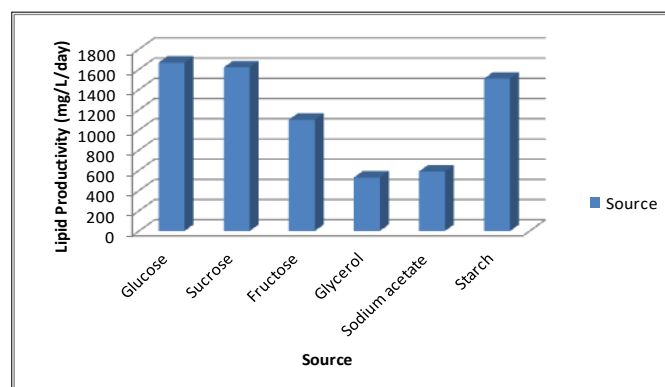


Fig 10 Lipid productivity for *Scenedesmus sp.* under various carbon sources

Nitrogen sources

Urea showed maximum lipid productivity (4027.31 mg/L/day) and lipid content (79.05%).

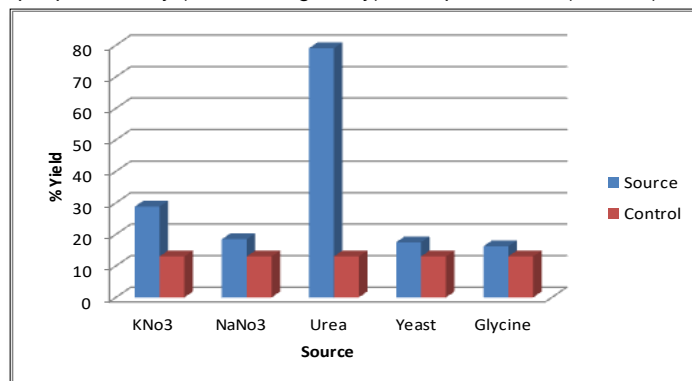


Fig 11 Lipid yield for *Scenedesmus sp.* under various nitrogen sources

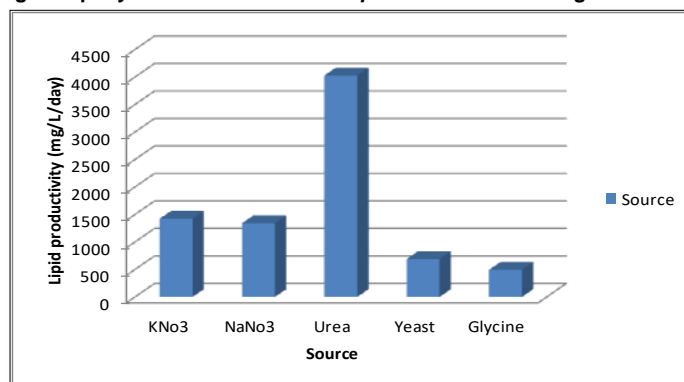


Fig 12 Lipid productivity for *Scenedesmus sp.* under various nitrogen sources

Extraction Process

Among the various combinations of solvent tested, combination of Chloroform: Methanol in the ratio of 2:1 was found most suitable for lipid extraction from *Chlorella minutissima* and *Scenedesmus sp* microalgae. The procedure of extracting lipid utilizes different volume of organic solvents. So for easy comparison, the results were projected on using 5 ml of organic solvents. This extraction process via organic solvents was also combined with the best method of cell disruption i.e. sonication which helped in increasing the lipid yield. These data are supported by the fact that nitrogen starvation condition results in more lipid accumulation (Converti et al. 2009; Chen et al. 2011; Feng et al. 2011; Kumari et al. 2011; Li et al. 2012). The selection of carbon and nitrogen sources depends upon various factors such as the target product, growth rate, and medium cost. However, nitrogen is the key factor in growth medium and also a limiting nutrient affecting the lipid productivity of various microalgae (Griffiths and Harrison 2009). Qiang Lin examined the effects of nitrogen source ((NH₄)₂CO₃, urea, NaNO₃, urea and NaNO₃ mixture) and concentration on the ash free dry biomass (AFDB) and oil accumulation and productivity of a *Scenedesmus rubescens* and found that the microalgae nurtured with the mixture of urea-N and NaNO₃-N had the highest AFDB productivity of 0.539 ± 0.040 g/L/d and the content of fatty acid methyl esters (FAME) (%) fed with (NH₄)₂CO₃-N increased continuously for 17 days and reached 42.94 ± 2.05% in the indoor photo-bioreactors (Qiang Lina, b et al., 2011). Muthu Arumugam also investigated the influence of different nitrogen source (potassium nitrate, sodium nitrate, urea, calcium nitrate, ammonium nitrate and ammonium chloride) of varying concentrations on biomass production of green algae *Scenedesmus* and found nitrate was the promising source for growth of *Scenedesmus* at low concentration (Arumugam, Muthu et al., 2013)



Fig 13 Extraction of lipids

Sudan Test

The presence of brown and red color on the upper phase of the test tube showed the presence of lipids in the sample.

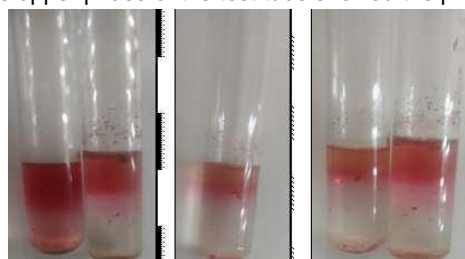


Fig 14 Sudan Test for lipids

Kinetic Parameters

In the study of Dittamart et. al. (2014) the most suitable carbon source was found to be 0.05M glucose, giving a yield of 2.78 ± 0.86 g./l of biomass and 233.68 ± 35.34 mg.L⁻¹ of crude lipid (Dittamart, Doungpen et al., 2014). Gim et. al. (2014) also cultivated *Chlorella vulgaris* in different organic carbon sources and observed glucose as better source for growth enhancement (Geun Ho Gim et al., 2013). This is mainly due to that the glucose is a simple hexose monosaccharide, which is first catabolized glucose-6-phosphate (important intermediate product for various metabolic precursors) and subsequently to pyruvate through anaerobic glycolysis process, and then entered into TCA cycle followed by mitochondrial oxidative phosphorylation for ATPs production (Geun Ho Gim et al., 2013; Droop MR et al., 1974; Neilson AH et al., 1974).

Table 3. Kinetic Parameters of *Chlorella minutissima*

Media	Specific Growth Rate (day ⁻¹)	Doubling Time (day)	Lipid Content (%)	Lipid Yield (mg/L)	Volumetric Lipid Productivity (mg/L/d)
Glucose	0.2801	2.47	36.79	360.83	2577.27
Sucrose	0.2990	2.31	28.82	205	1463.98
Fructose	0.2939	2.35	19.89	255.66	1802.29
Glycerol	0.2995	2.31	8.21	130.75	933.25
Sodium acetate	0.2911	2.38	9.49	165.25	1179.30
Starch	0.2769	2.50	20.45	261.33	1447.93
KNO ₃	0.3022	2.29	50.08	189.16	1350.96
NaNO ₃	0.2942	2.35	16.34	354.75	2532.50
Urea	10.2761	2.51	31.78	381.5	2726.83
Yeast	0.2983	2.32	22.08	232.41	1659.41
Glycine	0.3220	2.15	15.56	340.15	1001.95

Table 4. Kinetic Parameters of *Scenedesmus* sp.

Media	Specific Growth Rate (day ⁻¹)	Doubling Time (Days)	Lipid Content (%)	Lipid Yield (mg/L)	Volumetric Lipid Productivity (mg/L/d)
Glucose	0.2943	3.35	25.86	233.33	1666.58
Sucrose	0.3183	2.17	27.4	226.66	1619.04
Fructose	0.3152	2.19	21.28	154.16	1100.98
Glycerol	0.2918	2.37	5.82	74.25	529.89
Sodium acetate	0.2910	2.38	19.18	82.5	589.1
Starch	0.2794	2.48	18.34	78.24	1508.24
KNO ₃	0.3203	2.16	28.78	199.16	1422.55
NaNO ₃	0.2843	2.43	18.44	187.75	1340.41
Urea	0.3158	2.19	79.05	566	4027.31
Yeast	0.3259	2.12	17.48	96.58	689.62
Glycine	0.2987	2.32	16.21	92.45	493.44

Fame analysis

The FAMES were not measured from the samples of days 8 and 10 because within 6 days, all cultures reached the late exponential growth period or stationary growth period (Hsieh, C.-H et al., 2009) which is well known as the maximum lipid production period in the cells.

The analysis of fatty acid from different Carbon and Nitrogen sources in algae species: *Chlorella minutissima* and *Scenedesmus* sp. by GC-MS showed that they contain various fatty acid methyl esters including Pentadecanoic acid, Octadecadienoic acid, Hexadecanoic acid, Octadecatrienoic acid in major concentration. Heptadecanoic acid and Methyl stearate are present in less concentration. Unsaturated fatty acid Octadecadienoic and Octadecatrienoic acid are the most important essential fatty acids as our body cannot synthesize these fatty acids.

The GC-MS result of FAME sample of both algae are given in below figures.

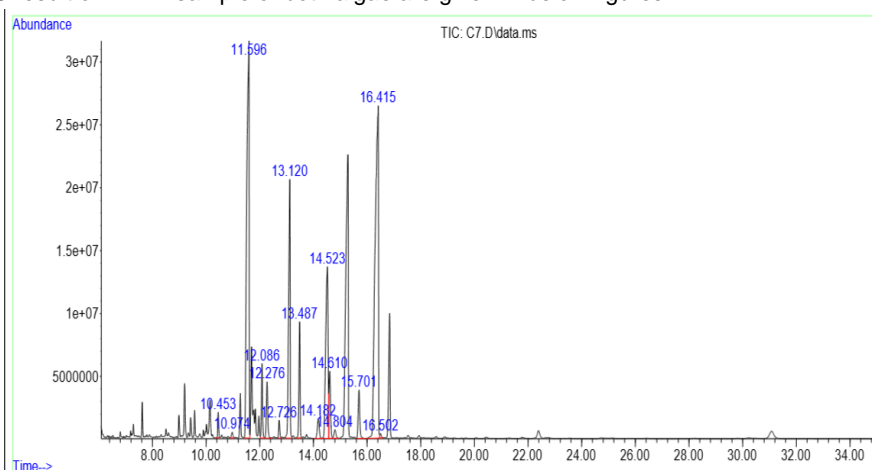


Fig 15 FAME analysis for *Chlorella minutissima*

Table 5: Percentage of Methylated fatty acids in C7 sample : *Chlorella minutissima*

Fatty acid	Common name of Fatty Acid	Carbon number and bonds	Relative %age Content of Fatty acid
Pentadecanoic acid	Pentadecylic acid	C15:0	0.657
Hexadecanoic acid	Palmitic acid	C16:0	27.285
9-Hexadecanoic acid	-	C16:1	2.351
7,10 hexadecadienoic acid	-	C16:2	2.301
Heptadecanoic acid	Margaric acid	C17:0	0.592
7,10,13-Hexadecatrienoic acid	-	C17:3	11.490
Methyl stearate	-	C19:0	1.105
9-Octadecenoic acid, methyl ester	Oleic acid	C18:1	11.886
gamma.-Linolenic acid	-	C18:3	2.269
9,12,15-Octadecatrienoic acid	Alpha linolenic acid	C18:3	32.238
Total			92.174
Saturated Fatty Acid Total			29.639
Monounsaturated Fatty Acid (MUFA) Total			14.237
Polyunsaturated Fatty Acid (PUFA) Total			48.298

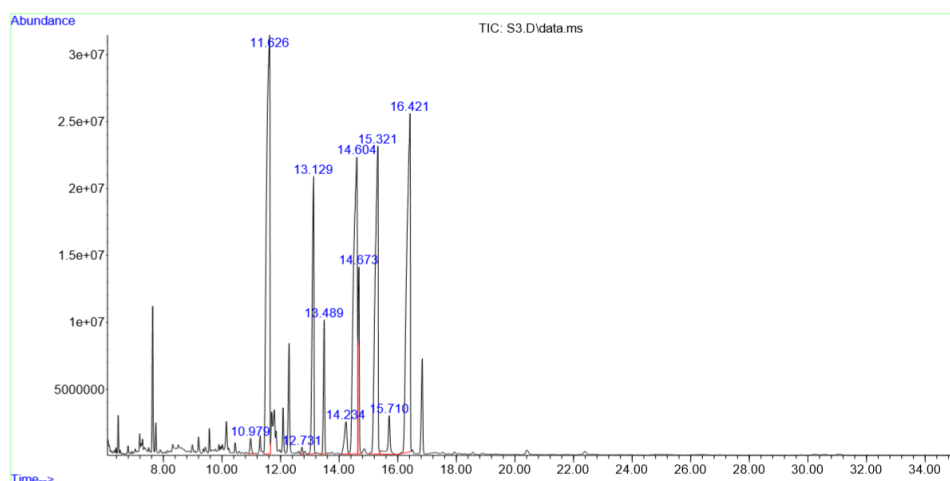


Fig 16. FAME analysis for *Scenedesmus* sp.

Table 6 : Percentage of Methylated fatty acids in S3 sample : *Scenedesmus* sp.

Fatty acid	Common name of Fatty acid	Carbon number and bonds	Relative %age Content of Fatty acid
Pentadecanoic acid	-	C15:0	0.421
Hexadecanoic acid	Palmitic acid	C16:0	24.330
9,12-Octadecadienoic acid	Linolenic acid	C18:2	16.267
Heptadecanoic acid	Margaric acid	C17:0	0.174
7,10,13-Hexadecatrienoic acid	Roughanic acid	C16:3	8.627
Methyl 4,7,10,13-hexadecatetraenoate	-	C17:3	2.830
Methyl stearate	-	C19:0	1.484
9-Octadecenoic acid, methyl ester	Oleic acid	C18:1	19.469
gamma.-Linolenic acid	-	C18:3	1.556
9,12,15-Octadecatrienoic acid	Alpha-linolenic acid	C18:3	20.791
Total			95.949
Saturated Fatty Acid Total			26.409
Monounsaturated Fatty Acid Total			19.469
Polyunsaturated Fatty Acid Total			50.071

Conclusion

Several studies reviewed the effect of C/N ratios in alga-based biodiesel productivity (Xu, H et al., 2006; Yoo, C., et al., 2010). However, the increase of oleic acid content to total FAMES produced by microalgae in media having high C/N ratios has never been reported before this study, even though it was referred to indirectly by Piorreck and Pohl (Piorreck, M. and P. Pohl. 1984). On the other hand, the increase of oleic acid to total FAMES in *Chlorella vulgaris* has already been reported as the response of temperature increase from 25°C to 38°C (Converti, A., A et al., 2009). It has been previously reported that the fatty acid composition produced by microalgae varies with their physiological status and culture conditions, even with extraction methods for recovery of fatty acids (Converti, A., et al., 2009; Hu, Q., et al., 2008; Mulbry, W et al., 2008; Piorreck, M. et al., 1984; Tran, H. L et al., 2009).

Chloroform: Methanol (2:1) was seen to be the best extracting solvent for lipid extraction. Using this maximum lipid content and productivity was found in Potassium nitrate nitrogen source (50.08%, 1350.96mg/L/day) for *Chlorella minutissima* and Urea as a nitrogen source (79.05 %, 4027.31 mg/L/day) for *Scenedesmus* sp. Among organic carbon sources, the maximum lipid content and productivity was found in Glucose (36.79% and 2577.27mg/L/day respectively) for *Chlorella minutissima* and Maltose as a carbon source (27.4%, 1690.18 mg/L/day respectively) for *Scenedesmus* sp. Further it was observed both the algae contain Fatty acid from C: 16 to C: 18 which are essential for biodiesel production.

Acknowledgement

Authors are highly thankful to our Head of Department Prof. D.Kumar and Dr. Navneeta Bharadvaja, our Project guide Department of Biotechnology for their continuous encouragement and valuable mentorship. A special thanks to DR Girish Mishra for providing the GC-MS facility.

References

1. Abdelaziz, A.E., Leite, G.B., Hallenbeck, P.C 2013, Addressing the challenges for sustainable production of algal biofuels: I. Algal strains and nutrient supply. Env. Technol., **34**:1783–1805.

2. Amaro, H.M., Guedes, A., Malcata, F.X., 2010, Advances and perspectives in using microalgae to produce biodiesel. Appl. energy, **88**: 3402–3410.
3. Amit Kumar Sharma, Pradeepta Kumar Sahoo, Shailey Singhal Jan-Feb 2015, Influence Of Different Nitrogen And Organic Carbon Sources On Microalgae Growth And Lipid Production, IOSR-JPBS, Volume 10, Issue 1 Ver. 1 PP 48-53.
4. Antoni. D.; Zverlov, V.V.: 2007, Schwarz, H. Biofuels from Microbes. Appl. J. Microbiol. Biotechnol. , **77**, 23-352
5. BP Statistical Review of the world energy; June 2008.
6. Chisti, Y., 2007. Biodiesel from microalgae J. Biotechnol. Adv. 2007, **25**, 294–306
7. Converti, A., A. A. Casazza, E. Y. Ortiz, P. Perego, and M. D. Borghi. 2009, Effect of temperature and nitrogen concentration on the growth and lipid content of *Nannochloropsis oculata* and *Chlorella vulgaris* for biodiesel production. Chem. Eng. Process. **48**: 1146-1151.
8. Doungpen Dittamart, Chayakorn Pumas, Jeeraporn Pekkoh and Yuwadee Peerapornpisal, 2014, Effects of organic carbon source and light-dark period on growth and lipid accumulation of *Scenedesmus* sp. AARL G022, Maejo Int. J. Science Technol. **8(02)**: 198-206
9. Droop MR 1974, Heterotrophy of carbon. In: Stewart WDP (ed).Algal physiology biochemistry. Blackwell Scientific Oxford, UK, pp 530–559.
10. Geun Ho Gim , Jung Kon Kim , Hyeon Seok Kim, Mathur Nadarajan Kathiravan , Hetong Yang , Sang-Hwa Jeong , Si Wouk Kim 2014, Comparison of biomass production and total lipid content of freshwater green microalgae cultivated under various culture conditions, Bioprocess Biosyst. Eng. **37**:99–106.
11. Hsieh, C.-H. and W.-T. Wu. 2009 Cultivation of microalgae for oil production with a cultivation strategy of urea limitation. Bioresour. Technol. **100**: 3921-3926.
12. Hu, Q., M. Sommerfeld, E. Jarvis, M. Ghirardi, M. Posewitz, M. Seibert, and A. Darzins. 2008, Microalgal triacylglycerols as feedstocks for biofuel production: Perspectives and advances. Plant Journal **54**: 621-639.
13. I.B. Muhit, D. Baidya, Nurangir Nahid, 2014, Prospect of Algal Biodiesel Production in Bangladesh: Overview from Developed Countries, IOSR-JMCE,**11(1)**, 49-54.
14. Illman AM, Scragg AH, Shales SW 2000, Increase in *Chlorella* strains calorific values when grown in low nitrogen medium. Enzyme Microbial. Technol., **27**, 631–635.
15. Khotimchenko SV, Yakovleva IM 2005, Lipid composition of the red alga *Tichocarpus crinitus* exposed to different levels of photon irradiance. Phytochemistry **66**:73–79.
16. Kumar L, Roy A, Saxena G, Kundu K, Bharadvaja N, 2017, Isolation, Identification and biomass productivity analysis of microalga *Scenedesmus rubescens* from DTU Lake, J. Algal Biomass Utln. , **8(3)**: 56- 67
17. Leite, G.B., M.Abdelaziz, A.E., Hallenbeck, P.C, 2013, Algal biofuels; challenges and opportunities. Bioresour. Technol.. **145**: 134–141.
18. Li Y, Horsman M, Wang B, Wu N, Lan CQ 2008, Effects of nitrogen sources on cell growth and lipid accumulation of greenalga *Neochloris oleoabundans*. Appl. J. Microbiol. Biotechnol. **81**, 629–636.
19. Liu ZY, Wang GC, Zhou BC , 2008 Effect of iron on growth and lipid accumulation in *Chlorella vulgaris*, Bioresour. Technol. **99**, 4717–4722.
20. Mulbry, W., S. Kondrad, and J. Buyer. 2008. Treatment of dairy and swine manure effluents using freshwater algae: Fatty acid content and composition of algal biomass at different manure loading rates. J. Appl. Phycology **20**: 1079-1085.
21. Muthu Arumugam, Ankur Agarwal , Mahesh Chandra Aryaa, Zakwan Ahmed, 2013, Influence of nitrogen sources on biomass productivity of microalgae *Scenedesmus bijugatus*, Bioresour. Technol., **131**: 246–249.
22. Neilson AH, Lewin RA 1974, The uptake and utilization of organic carbon by algae: an essay in comparative biochemistry. Phycologia **13**: 227–264.
23. Piorreck, M. and P. Pohl. (1984) Formation of biomass, total protein, chlorophylls, lipids and fatty acids in green and bluegreen algae during one growth phase. Phytochemistry **23**: 217-223.
24. Qiang Lina, b and Junda Lin 2011, Effects of nitrogen source and concentration on biomass and oil production of a *Scenedesmus rubescens* like microalga, , Bioresour. Technol. **102(2)**: 1615-1621
25. Saxena G, Kumar L, Hariri SM, Roy A, Kundu K and Bharadvaja N, 2016, Identification of Potential Culture Conditions for Enhancing the Biomass Production of Microalga *Chlorella minutissima*, Expert Opin Environ Biol , S1-005
26. Takagi M, Karseno, Yoshida T , 2006 Effect of salt concentration on intracellular accumulation of lipids and triacylglyceride in marine microalgae *Dunaliella* cells,. J. Bioscience Bioeng. **101**, 223–226

27. Takagi M, Watanabe K, Yamaberi K, Yoshida T (2000) Limited feeding of potassium nitrate for intracellular lipid and triglyceride accumulation of *Nannochloris* sp. UTEX LB1999. *Appl. Microbiol. Biotechnol.* **54**, 200, 112–117.
28. Tran, H. L., S. J. Hong, and C. G. Lee. 2009 Evaluation of extraction methods for recovery of fatty acids from *Botryococcus braunii* LB572 and *Synechocystis* sp. PCC 6803. *Biotechnol Bioprocess Eng* **14**: 187-192
29. Xu, H., X. Miao, and Q. Wu. 2006 High quality biodiesel production from a microalga *Chlorella protothecoides* by heterotrophic growth in fermenters. *J. Biotechnol.* **126**: 499-507.
30. Yoo C, Jun SY, Lee JY, Ahn CY, Oh HM 2010 Selection of microalgae for lipid production under high levels carbon dioxide. *Bioresour. Technol.* **101**, 71–74.

Micro-Diversity Analysis of Error Probability and Channel Capacity over Hoyt-Gamma Fading

Sandeep KUMAR¹, Sanjay Kumar SONI², Priyanka JAIN¹

¹Dept. of Electronics and Communication, Delhi Technological University, Delhi, India

²Dept. of Electronics and Communication, G.B. Pant Engineering College, Pauri, UK, India

sann.kaushik@gmail.com, sksoni98fece@gbpec.ac.in, priyajain2000@rediffmail.com

Submitted January 24, 2017 / Accepted May 1, 2017

Abstract. In wireless communication system, various parameters such as average symbol/bit error probability (ASEP/ABEP), outage probability and average channel capacity, etc. are studied for its performance analysis. In this paper, the performance of L-Hoyt/Gamma (HG) composite fading channel with Maximum Ratio Combining (MRC) employing micro-diversity is analyzed. Closed-form expressions for distribution function, moments, outage probability and channel capacity are derived in terms of hypergeometric functions. Further, the expressions of ASEP/ABEP for all formats of coherent and non-coherent modulation techniques involving Q -functions and Marcum Q -function are derived over the composite fading channel. Monte-Carlo simulations are performed to validate our analytical results. The analytical results produced here can be useful in several wireless applications where multipath and shadowing are characterized by Hoyt/Gamma distribution.

Keywords

Wireless communication system, shadowing, composite fading, diversity combining, MRC, channel capacity

1. Introduction

Composite fading environments are frequently encountered in mobile radio propagation in which multipath fading is superimposed on shadowing [1]. Multipath fading is captured by several distributions like Rayleigh, Weibull, Nakagami-m and Hoyt. Hoyt distribution is commonly used to model the short-term fading characteristics of wireless communication systems with more severe fading conditions [2], [3]. Closed-form expressions for probability distribution function (PDF), moment generating function (MGF) and high-order moments of Hoyt distribution were obtained in [1], [4], and the expression for cumulative distribution function (CDF) was presented in [5]. The closed-form analysis for the outage probability of Hoyt fading channel under Rayleigh interference and Rayleigh fading channel under mixed Rayleigh and Hoyt interference were evaluated in [6], [7].

In shadowed fading, large-scale signal variation can be described in the form of two distributions [2]. These statistical models are lognormal distribution and Gamma distribution. Shadowing has usually been modeled using lognormal distribution. However, using the lognormal PDF often leads to analytical complexities, because it is not possible to write the closed-form mathematical expressions for performance parameters of the system [2]. An alternate approach was adopted in [8], [9], where shadowing is modeled by cascading short-term fading, while Holtzman approximation was used in [10] to find the closed-form expressions of the Weibull-lognormal composite fading channel. All the above approaches have their own limitations in the sense that they do not give accurate results over the whole range of the composite fading parameters. Gamma distribution is the most acceptable approximation of lognormal distribution and is most widely used in literature to model shadowing effects [11]. The performance of several composite distributions like K [11], generalized-K [12] and the Weibull-Gamma [13] using gamma function have been analyzed in literature. Specifically, in [14] a general model of a class of composite fading such as η - μ /Gamma is carried out, where the result, as a special case, reduced to Hoyt-Gamma case is derived.

Short-term fading is mitigated through micro-diversity while macro-diversity approach is used to overcome the effect of long-term fading. Hinging on the fact that selection combining (SC) diversity enjoys the lowest implementation complexity, the performance of macro-diversity and micro-diversity systems using SC were studied in [15], [16]. MRC gives the best performance of all the diversity techniques, and in [17], the performance of MRC receiver over Hoyt fading was studied. However, to the best of author's knowledge, performance analysis of wireless communication system with micro-diversity, operating over Gamma shadowed Hoyt multipath fading channels is not reported in open literature.

Motivated by this fact, we have derived closed-form solution of L-HG composite fading, where Hoyt represents multipath fading and Gamma captures the shadowing effect. Performance metrics such as the amount of fading (AF), channel capacity and outage probability in terms of output signal-to-noise ratio (SNR) have been derived. The

symbol error rates (SER) of coherent schemes are evaluated in the closed-form, and a single generalized result, encompassing all linear modulation formats is presented. Further, closed-form expressions of error probability of non-coherent techniques involving Marcum Q-function are derived and compared with the coherent schemes.

The rest of the paper is organized as follows. In Sec. 2, the L -HG distribution is derived, and the performance parameters such as AF and outage probability, have been calculated. Channel Capacity has been discussed in Sec. 3. In Sec. 4, ASE/ABEP of coherent modulation schemes are derived, and in Sec. 5 mathematical expressions for non-coherent schemes are evaluated. In Sec. 6, we present the discussion on the closed-form results obtained in the preceding sections. Finally, Section 7 concludes the work.

2. HG Statistics

PDF of received SNR per symbol of conditional Hoyt fading channel is given by [1]

$$p_{\gamma_l}(\gamma_l/w) = \frac{1+q^2}{2qw} \exp\left[-\left(\frac{(1+q^2)^2 \gamma_l}{4q^2 w}\right)\right] I_0\left(\frac{(1-q^4) \gamma_l}{4q^2 w}\right), \gamma_l \geq 0 \quad (1)$$

where γ_l is the instantaneous received SNR of the l^{th} branch and w is the average received SNR of the conditional Hoyt distribution. q is the Hoyt fading parameter, having the value from 0 to 1 and $I_0(\cdot)$ is the modified Bessel of the first type and zeroth order. Short-term fading is mitigated through micro-diversity approaches using multiple antennas at the receiver [2]. When MRC diversity is used, the overall SNR at the output of the receiver is the sum of SNR of all the individual branches multiplied by their proportional weights. Instantaneous output SNR(γ) of MRC detector is given by [1]

$$\gamma = \sum_{l=1}^L \gamma_l. \quad (2)$$

L is the total number of independent and identically distributed (i.i.d.) branches used in diversity combiner. The instantaneous received SNR of the l^{th} branch can be written as

$$\gamma_l = X_l^2 + Y_l^2, \quad l = 1, 2, \dots, L. \quad (3)$$

X_l and Y_l are independent and normally distributed random variables having zero mean and variance σ_x^2 and σ_y^2 , respectively. The fading parameter is related to the variance as $q = \sigma_y / \sigma_x$ and $\sigma_y^2 = w[q^2 / (1 + q^2)]$. The closed-form expression for the conditional PDF of γ is given by [15]

$$p_{\gamma}(\gamma/w) = \left(\frac{1+q^2}{2qw}\right)^L \frac{\exp\left[-\left(\frac{(1+q^2)\gamma}{2q^2 w}\right)\right]}{\Gamma(L)} \gamma^{(L-1)} {}_1F_1\left(\frac{L}{2}; L; \frac{(1-q^4)\gamma}{2q^2 w}\right), \quad \gamma \geq 0 \quad (4)$$

where ${}_1F_1(\cdot; \cdot; \cdot)$ is the confluent hypergeometric function and $\Gamma(\cdot)$ is gamma function. Here, shadowing is modeled using Gamma distribution with PDF given by [2]

$$p_w(w) = \frac{w^{(m-1)}}{\bar{\gamma}^m \Gamma(m)} \exp\left(-\frac{w}{\bar{\gamma}}\right), \quad m \geq 0 \quad (5)$$

where $\bar{\gamma}$ is average received SNR and m is shaping parameter. Composite PDF of γ can be easily evaluated by [1]

$$p_{\gamma}(\gamma) = \int_0^{\infty} p_{\gamma}(\gamma/w) p_w(w) dw. \quad (6)$$

Substituting (4) and (5), into (6), we get

$$p_{\gamma}(\gamma) = \int_0^{\infty} \left(\frac{1+q^2}{2qw}\right)^L \frac{\exp\left[-\left(\frac{(1+q^2)\gamma}{2q^2 w}\right)\right]}{\Gamma(L)} \gamma^{(L-1)} {}_1F_1\left(\frac{L}{2}; L; \frac{(1-q^4)\gamma}{2q^2 w}\right) \frac{w^{(m-1)}}{\bar{\gamma}^m \Gamma(m)} \exp\left(-\frac{w}{\bar{\gamma}}\right) dw \quad (7)$$

where the hypergeometric function ${}_1F_1(\cdot; \cdot; \cdot)$ can be simplified using [18, /9.210/1]. Transforming each exponential term by G-function using [19, /07.34.03.0228.01] and rearranging the terms, (7) can be simplified as

$$p_{\gamma}(\gamma) = \sum_{n=0}^{\infty} \frac{s^L t^n \gamma^{(L+n-1)} \left(\frac{L}{2}\right)_n}{\Gamma(L+n) \Gamma(m) \bar{\gamma}^m n!} \int_0^{\infty} w^{(m-L-n)-1} G_{0,1}^{1,0}\left[\frac{s\gamma}{qw} \middle| 0\right] G_{0,1}^{1,0}\left[\frac{w}{\bar{\gamma}} \middle| 0\right] dw \quad (8)$$

where $s = (1+q^2)/2q$, $t = (1-q^4)/2q^2$ and $G(\cdot)$ is Meijer G-function, whereas $(x)_n$ denotes the Pochhammer's symbol. Using [18, /9.31/2] and [19, /07.34.21.0011.01] and after some mathematical manipulations, (8) can be written as

$$p_{\gamma}(\gamma) = \sum_{n=0}^{\infty} \frac{t^n \left(\frac{L}{2}\right)_n q^{(n+L-m)} \gamma^{m-1}}{\Gamma(L+n) \Gamma(m) \bar{\gamma}^m n! s^{n-m}} G_{0,2}^{2,0}\left[\frac{s\gamma}{q\bar{\gamma}} \middle| 0, n+L-m\right]. \quad (9)$$

By putting $q = 1$ in the definition of s and t equation (9) can be simplified to PDF of K distribution.

2.1 CDF

Substituting (9) in the definitions of CDF,

$$P_{\gamma}(\gamma) = \int_0^{\gamma} p_{\gamma}(\gamma) d\gamma \text{ and using [20] yields}$$

$$P_{\gamma}(\gamma) = \sum_{n=0}^{\infty} \frac{t^n \left(\frac{L}{2}\right)_n q^{(n+L-m)}}{\Gamma(L+n) \Gamma(m) n! s^{n-m}} \left(\frac{\gamma}{\bar{\gamma}}\right)^m \cdot G_{1,3}^{2,1}\left[\frac{s\gamma}{q\bar{\gamma}} \middle| 0, n+L-m, -m\right]. \quad (10)$$

Outage probability is the probability that the instantaneous SNR falls below a predetermined threshold γ_{th} , and it can be easily obtained using (10).

2.2 Moments

The i^{th} moment of γ is defined by [1] as $E[\gamma^i] = \int_0^\infty \gamma^i p_\gamma(\gamma) d\gamma$. With the aid of (9) and [19, /07.34.21.0009.01] it can be easily evaluated as

$$E[\gamma^i] = \sum_{n=0}^{\infty} \frac{t^n \left(\frac{L}{2}\right)_n q^{(n+L+i)} \bar{\gamma}^i}{\Gamma(L+n) \Gamma(m) n! s^{n+i}} \cdot \frac{1}{[\Gamma(m+i)][\Gamma(n+L+i)]}. \quad (11)$$

The AF is used to measure the severity of the channel and is defined as $AF = E[\gamma^2]/E[\gamma]^2 - 1$. AF of the L -HG composite fading channel can be easily evaluated using (11).

3. Channel Capacity

Shannon's channel capacity gives the theoretical upper bound to the maximum rate of data transmission over a given channel with small error probability. It is an important performance parameter which is kept in mind while designing the system. Motivated by this fact, the closed-form of channel capacity under optimal rate adaptation (ORA) and channel inversion fixed rate (CIFR) are presented here.

3.1 ORA

This scheme is more practical since the transmit power remains constant. The average capacity of a fading channel is a function of the bandwidth B and γ . The channel capacity under this definition is expressed as [1]

$$C_{ora} = B \int_0^\infty \log_2(1+\gamma) p_\gamma(\gamma) d\gamma. \quad (12)$$

Putting (9) in (12), and using [19, /07.34.03.0456.01], [19, /07.34.21.0011.01], the above equation can be simplified as

$$\frac{C_{ora}}{B} = \sum_{n=0}^{\infty} \frac{t^n \left(\frac{L}{2}\right)_n q^{(n+L-m)}}{\Gamma(L+n) \Gamma(m) \bar{\gamma}^m n! s^{n-m}} \cdot G_{2,4}^{4,1} \left[\frac{s}{q\bar{\gamma}} \middle| \begin{matrix} -m, 1-m \\ 0, n+L-m, -m, -m \end{matrix} \right]. \quad (13)$$

3.2 CIFR

Under this policy, transmitter allocates higher power to the channel with low SNR and lower power to higher SNR such that the constant received power is maintained. It

is the capacity which gives lower bound of data rate through any channel. The channel capacity under CIFR scheme is defined as [1]

$$C_{cifr} = B \log_2 \left(1 + \frac{1}{\int_0^\infty p_\gamma(\gamma) / \gamma d\gamma} \right). \quad (14)$$

Using the result of (11) for $E[1/\gamma]$ in (14), one can easily find out the final expression of C_{cifr} .

4. ASEP of Coherent Modulation Scheme

In this section, we derive the closed-form expression of the coherent modulation scheme. The general formula for ASEP/ABEP is given by [1]

$$P_{ave} = E[P_e(\gamma)] = \int_0^\infty P_e(\gamma) p_\gamma(\gamma) d\gamma \quad (15)$$

where $P_e(\gamma)$ is the instantaneous Symbol/Bit error rate of the modulation scheme and $p_\gamma(\gamma)$ is the PDF of the fading channel. The generalized probability of error for coherent modulation schemes is given by [21]

$$P_e(\gamma) = \sum_{d=1}^D \alpha_d \left[Q(\sqrt{c_0 \gamma}) \right]^d. \quad (16)$$

Here D , α_d and c_0 have their usual meaning as in [21]. It is analytically difficult to perform the averaging of instantaneous error probability in (15) by directly applying (16) in terms of Q-function. Thus, we need to resort to the approximate form of Q-function. There are various approximations to this Q-function suggested in the open literature [22–25]. However, all these approximations are not very precise as compared to second-order analytical approximation (as is evident from [23, Fig. 2 and 3]). The $Q(\cdot)$ function is approximated using [21], [23] as

$$Q(\sqrt{t}) \approx \frac{a_1}{2} \exp(-b_1 t/2) + \frac{a_2}{2} \exp(-b_2 t). \quad (17)$$

Here $a_1 = 0.3070$, $a_2 = 0.4389$ and $b_1 = 1.0510$. ASEP can be found by substituting (9) and (16) into (15) and using the approximate form of Q-function as in (17). The resultant expression is given by

$$P_{ave} \approx \sum_{n=0}^{\infty} \frac{t^n \left(\frac{L}{2}\right)_n q^{(n+L-m)}}{\Gamma(L+n) \Gamma(m) \bar{\gamma}^m n! s^{n-m}} \cdot \int_0^\infty \gamma^{m-1} G_{0,2}^{2,0} \left[\frac{s\gamma}{q\bar{\gamma}} \middle| \begin{matrix} - \\ 0, n+L-m \end{matrix} \right] \cdot \sum_{d=1}^D \alpha_d \left[\frac{a_1}{2} \exp\left(-\frac{b_1 c_0 \gamma}{2}\right) + \frac{a_2}{2} \exp(-b_2 c_0 \gamma) \right]^d d\gamma. \quad (18)$$

This integral can be solved by expanding the square bracket of the integrand using Binomial expansion

$(x+y)^n = \sum_{k=0}^n C(n,k) x^{n-k} y^k$. Transforming each exponential term by G-function using [19, /07.34.03.0228.01] and then using the results of integral of the product of two G-functions in [19, /07.34.21.0011.01], generalized closed-form solution of ASEP for all formats of coherent modulation techniques is given by

$$P_{\text{ave}} \approx \sum_{n=0}^{\infty} \frac{t^n \left(\frac{L}{2}\right)_n q^{(n+L)}}{\Gamma(L+n)\Gamma(m)n!s^n} \sum_{d=1}^D \alpha_d \cdot \sum_{r=0}^d C(d,r) \left(\frac{a_1}{2}\right)^{d-r} \left(\frac{a_2}{2}\right)^r \cdot G_{2,1}^{1,2} \left[\frac{(d+r)b_1 c_0 q \bar{\gamma}}{2s} \middle| 1-m, 1-n-L \right] \quad (19)$$

where $C(d,r)$ is the combination of r objects from a set of d objects. The next section deals with the derivation of the average probability of error for non-coherent modulation techniques.

5. ASEP/ABEP of Non-Coherent Modulation Scheme

There are certain situations in wireless communication where phase recovery at the receiver cannot be tracked accurately. In such scenarios, the wireless communication system must depend on the non-coherent reception, such as square-law detection of Frequency-shift-keying (FSK) signal [22] or differential coherent modulation technique such as Differential phase-shift-keying (DPSK). Some of the related works in evaluating the closed-form expressions of the non-coherent techniques has been carried out in the past [23], [26], [27]. In this section, we have proposed the analytical formulas for non-coherent schemes over composite HG fading with diversity.

5.1 Multiple-FSK (MFSK)

The instantaneous symbol error probability of MFSK is given by [22]

$$P_e(\gamma) = \sum_{p=1}^{M-1} C(M-1,p) \frac{(-1)^{p+1}}{p+1} \exp\left(-\frac{p}{p+1}\gamma\right). \quad (20)$$

Here, each symbol of MFSK represents $(\log_2 M)$ bits. The ASEP expression for MFSK is obtained by substituting (20) and (9) into (15) and using [19, /07.34.03.0228.01], [19, /07.34.21.0011.01]

$$P_{\text{ave}} = \sum_{n=0}^{\infty} \frac{t^n \left(\frac{L}{2}\right)_n q^{(n+L)}}{\Gamma(L+n)\Gamma(m)n!s^n} \sum_{p=1}^{M-1} C(M-1,p) \frac{(-1)^{p+1}}{p+1} \cdot G_{2,1}^{1,2} \left[\frac{pq\bar{\gamma}}{(p+1)s} \middle| 1-m, 1-n-L \right]. \quad (21)$$

5.2 Differential-QPSK (DQPSK)

Bit error probability for non-coherent DQPSK is given by [22]

$$P_e(\gamma) = Q_1(a\sqrt{\gamma}, b\sqrt{\gamma}) - \frac{1}{2} I_0(ab\gamma) \exp\left(-\frac{a^2+b^2}{2}\gamma\right) \quad (22)$$

where $Q_1(a\sqrt{\gamma}, b\sqrt{\gamma})$ is the Marcum Q-function of the first order and $a = \sqrt{2(1-1/\sqrt{2})}$, $b = \sqrt{2(1+1/\sqrt{2})}$. Substituting (22) and (9) into (15) and using the expressions of Marcum Q-function and modified Bessel function [22], one can write the resulting expression as

$$P_{\text{ave}} = \int_0^{\infty} \sum_{n=0}^{\infty} \frac{t^n \left(\frac{L}{2}\right)_n q^{(n+L-m)} \gamma^{m-1}}{\Gamma(L+n)\Gamma(m)\bar{\gamma}^m n! s^{n-m}} \cdot G_{0,2}^{2,0} \left[\frac{s\gamma}{q\bar{\gamma}} \middle| 0, n+L-m \right] \cdot \left\{ \exp(-x\gamma) \sum_{k=0}^{\infty} \left(\frac{a}{b}\right)^k \sum_{l=0}^{\infty} \frac{(r\gamma)^z}{l! \Gamma(l+k+1)} \right\} d\gamma \quad (23)$$

$$\left\{ -\frac{1}{2} \exp(-x\gamma) \sum_{p=0}^{\infty} \frac{(r\gamma)^{2p}}{(p!)^2} \right\}$$

where $x = (a^2 + b^2)/2$, $r = ab/2$, and $z = 2l + k$. Using [19, /07.34.03.0228.01] and [19, /07.34.21.0011.01], we can obtain the final result for ABEP of DQPSK as

$$P_{\text{ave}} = \sum_{n=0}^{\infty} \frac{t^n \left(\frac{L}{2}\right)_n q^{(n+L)}}{\Gamma(L+n)\Gamma(m)n!s^n} \cdot \left\{ \sum_{k=0}^{\infty} \left(\frac{a}{b}\right)^k \sum_{l=0}^{\infty} \frac{(r)^z}{l! \Gamma(l+k+1)} \left(\frac{q\bar{\gamma}}{s}\right)^z \cdot G_{2,1}^{1,2} \left[\frac{xq\bar{\gamma}}{s} \middle| 1-(z+m), 1-(z+n+L) \right] \right\} \quad (24)$$

$$\left\{ -\frac{1}{2} \sum_{p=0}^{\infty} \frac{(r)^{2p}}{(p!)^2} \left(\frac{q\bar{\gamma}}{s}\right)^{2p} \cdot G_{2,1}^{1,2} \left[\frac{xq\bar{\gamma}}{s} \middle| 1-(2h+m), 1-(2h+n+L) \right] \right\}$$

6. Numerical Results and Discussion

In this section, we confirm the validity of our performance parameters. All the computations and simulations were carried out in MATLAB (version R2014a). The default value of $\bar{\gamma}$ is taken as unity in all the calculations. To validate the accuracy of the derived expressions, Monte-Carlo simulations are also included with 10^7 numbers of samples for generating L -HG composite distribution. It can be observed that the simulation results are in close match with the numerical results obtained by keeping enough number of terms in the infinite series. In Fig. 1, outage probability is plotted against the normalized outage thresh-

old ($\gamma_{th}/\bar{\gamma}$) for several values of m and q using closed-form expression (10). It is evident from the results that outage probability increases with the increase in γ_{th} indicating an increase in the likelihood of failure to achieve a given threshold level.

As expected, the outage probability is shown to decrease with increase in m and q , hinting an improvement in performance of the receiver. The effect of channel condition improvement with diversity is clearly shown in the plot. AF is plotted as a function of m for several values of q in Fig. 2. It can be easily observed that AF reduces as m and L increases, showing improved performance. Furthermore, as q increases, AF plot shifts downwards, while it can also be observed that the gap among the curves decreases as L increases. Moreover, in Fig. 3 the impact of the fading parameter q on the channel capacity is illustrated for various values of diversity order L based on (13). The graph reveals that increasing the values of q or L both helps overcome the effects of fading. Figure 4 depicts the average channel capacity as a function of the average received SNR for the ORA and CIFR schemes with different values of the fading parameter q . The outputs of Monte-Carlo

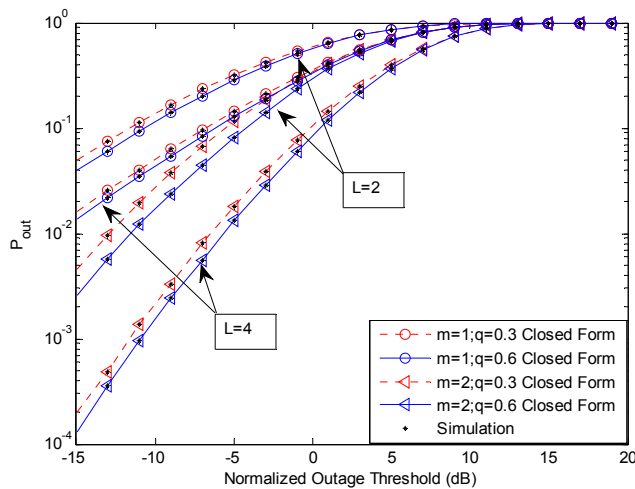


Fig. 1. Diversity effect on outage probability for several values of m and q .

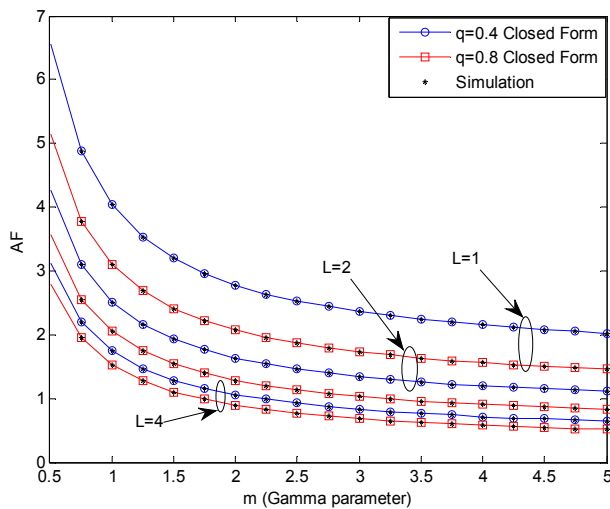


Fig. 2. AF versus m for several values of q and L .

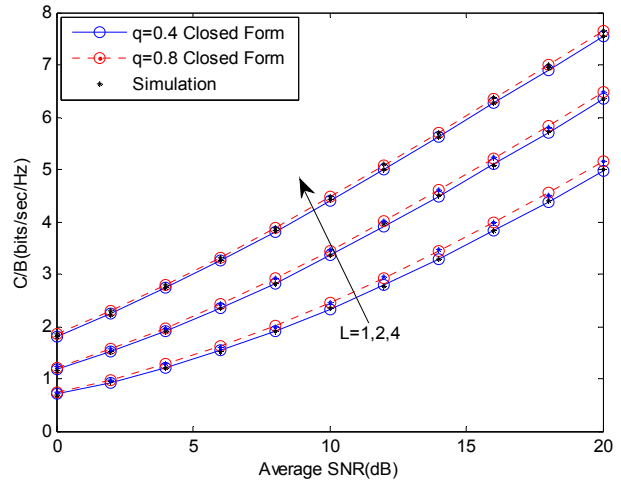


Fig. 3. Effect of diversity and fading parameter on channel capacity with ORA for $m = 1$.

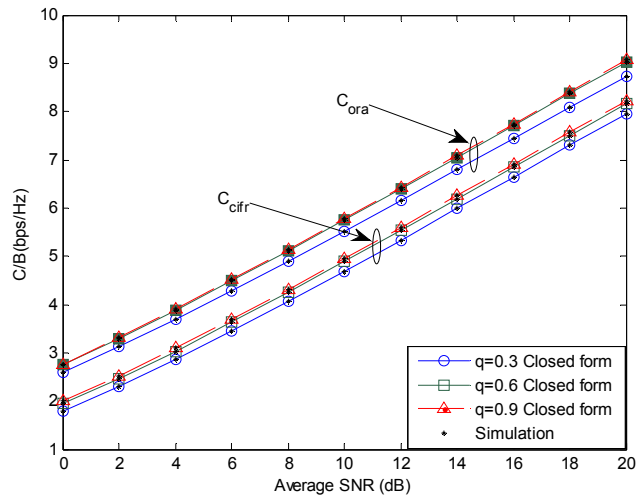


Fig. 4. Channel capacity with ORA and CIFR as a function of average SNR for $m = 2$ and $L = 4$.

simulations are also provided and shown to exactly match with the analytical results. It is evident that, as the average received SNR increases, the capacity of both the transmission schemes improves. We also find that CIFR achieves the lower capacity than ORA. This is because of the fact that CIFR uses a fixed transmission data rate, whereas a large amount of transmitting power is required to compensate for the deep channel fades.

Comparison of QPSK and DQPSK (non-coherent) schemes for different values of L is shown in Fig. 5. As observed, an excellent match between the analytical results produced by putting closed-form expression (19) for QPSK and (24) for DQPSK with the simulations results are achieved. It is observed that the performance of the system improves with an increase in L as shown by downshifting of the plots. Secondly, QPSK outperforms DQPSK significantly. In Fig. 6, ASEP of DEQPSK has been plotted over the composite fading channel for several values of m , q and L . The theoretical curves have been constructed based on expression (19). It is observed that the plots shift downwards with the increase in the fading and shape parameters indicating an improvement in the system performance.

Figure 7 demonstrates the plots for M -ary QAM using the analytical expression (19) over L -HG composite fading channel under the various constellation size $M = 2, 4$ and 8 . It is noted from the results that the plot shifts upwards for the higher constellation.

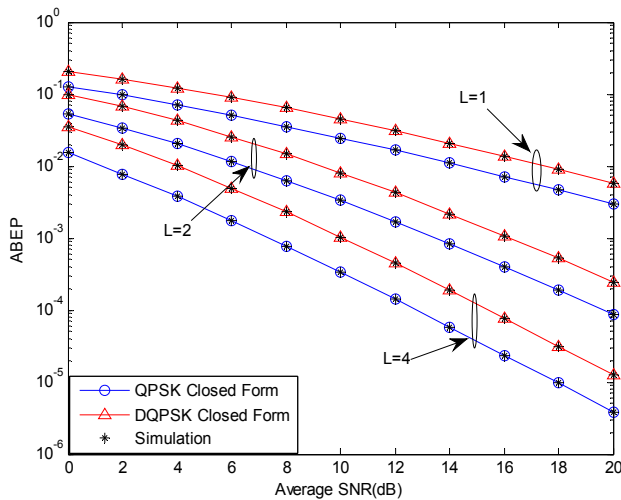


Fig. 5. ABEP Comparison between QPSK (coherent) and DQPSK (non-coherent) for different values of L .

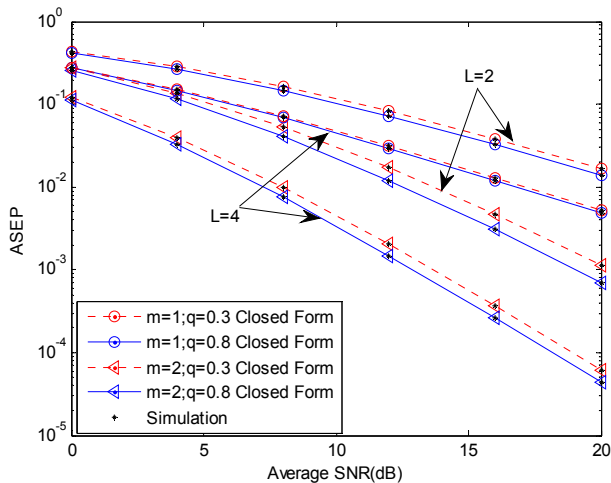


Fig. 6. ASEP of DEQPSK for HG for several values of m , q and L .

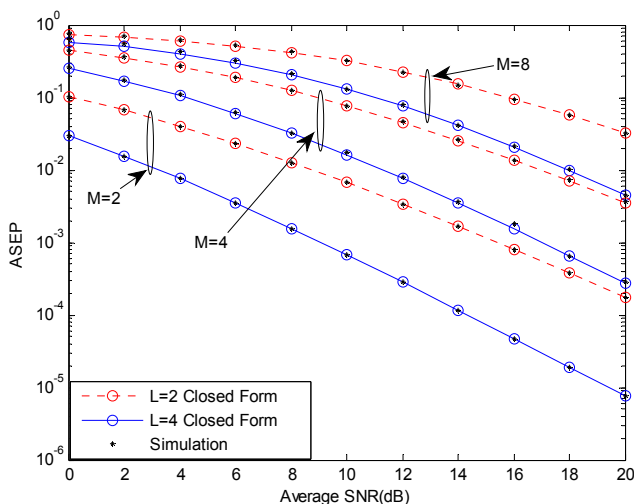


Fig. 7. ASEP of M -QAM for various values of M and L .

Modulation	$L = 1$		$L = 4$	
	$q=0.4$	$q=0.8$	$q=0.4$	$q=0.8$
BPSK (19)	14	2	26	4
QPSK (19)	16	3	29	5
8-PSK (19)	20	4	35	6
2-PAM (19)	11	2	21	3
8-PAM (19)	22	4	39	6
2-QAM (19)	14	2	27	4
8-QAM (19)	21	4	37	6
DEQPSK (19)	17	3	31	5
BFSK (21)	15	3	29	5
DQPSK (24)	13	2	27	4

Tab. 1. Number of terms (N) required for accuracy at 7th place of the decimal digit in the numerical evaluation of (19), (21) and (24).

ABEP/ASEP expressions presented herein are given in terms of infinite series. We have truncated the series by including the finite number of terms N ensuring to achieve accuracy at the seventh place of the decimal digit. In Tab. 1, we have calculated the number of terms required to achieve this accuracy in (19), (21) and (24) as a function of q and L with $m = 1$. The number of terms needed to be summed to achieve the desired accuracy depends on q , L and the modulation technique being used. The value of N decreases with increase in q , indicating that more number of terms are required for more severe fading conditions. It can be observed that we need more number of terms for higher diversity order system.

7. Conclusions

Taking note of the fact that Hoyt is known to capture the severe multipath fading and Gamma distribution is most widely used to model shadowing, we have analyzed the performance of L -HG composite fading model. Closed-form expressions for PDF of instantaneous SNR, outage probability, AF, channel capacity and ASEP/ABEP of the composite L -HG were obtained in terms of generalized hypergeometric functions and the corresponding results are demonstrated. These expressions can be useful in the performance evaluation of L -HG composite fading environment. Moreover, the analytical results are found to be in close agreement with the simulation results.

Acknowledgments

The authors would like to thank Vidhi Rana and Pushpraj Chauhan and the anonymous reviewers for their useful suggestions for improving the presentation of the material in this paper.

References

- [1] SIMON, M. K., ALOUINI, M. S. *Digital Communication over Fading Channels*. 2nd ed. New York: John Wiley & Sons, 2004. ISBN: 0-471-64953-8

- [2] SHANKAR, P. *Fading and Shadowing in Wireless Systems*. New York: Springer, 2012. ISBN: 978-1-4614-0366-1
- [3] YOUSSEF, N., ELBAHRI, W., PATZOLD, M., ELASMI, S. On the crossing statistics of phase processes and random FM noise in Nakagami-q mobile fading channels. *IEEE Transactions on Wireless Communications*, 2005, vol. 4, no. 1, p. 24–29. DOI: 10.1109/TWC.2004.840251
- [4] NAKAGAMI, M. The m-distribution—A general formula of intensity distribution of rapid fading. In Hoffman, W. G., Ed. *Statistical Methods in Radio Wave Propagation*. Pergamon Press, 1960, p. 3–36. DOI: 10.1016/B978-0-08-009306-2.50005-4
- [5] PARIS, J. Nakagami-q (Hoyt) distributions function with applications. *Electronics Letters*, 2009, vol. 45, no. 4, p. 749–751. DOI: 10.1049/el:20093427
- [6] PARIS, J., JIMENEZ, D. Outage probability analysis for Nakagami-q (Hoyt) fading channels under Rayleigh interference. *IEEE Transactions on Wireless Communications*, 2010, vol. 9, no. 4, p. 1272–1276. DOI: 10.1109/TWC.2010.04.090295
- [7] RADAYDEH, R. Performance of cellular mobile systems employing SNR-based GSC in the presence of Rayleigh and Nakagami-q co-channel interferers. *IEEE Transactions on Vehicular Technology*, 2009, vol. 58, no. 6, p. 3081–3088. DOI: 10.1109/TVT.2008.2011276
- [8] SHANKAR, P. M. A Nakagami-N-gamma model for shadowed fading channels. *Wireless Personal Communications*, 2012, vol. 64, no. 5, p. 665–680. DOI: 10.1007/s11277-010-0211-5
- [9] SHANKAR, P. M. An overview of shadowed fading wireless channels in terms of a cascaded approach. *Physical Communication*, June 2015, vol. 15, no. C, p. 59–65. DOI: 10.1016/j.phycom.2015.02.001
- [10] SINGH, R., SONI, S. K., RAW, R. S., KUMAR, S. A new approximate closed-form distribution and performance analysis of a composite Weibull/log-normal fading channel. *Wireless Personal Communications*, 2017, vol. 92, no. 3, p. 883–900. DOI: 10.1007/s11277-016-3583-3
- [11] ABDI, A., KAVEH, M. K distribution: an appropriate substitute for Rayleigh-lognormal distribution in fading-shadowing wireless channels. *Electronics Letters*, 1998, vol. 34, no. 9, p. 851–852. DOI: 10.1049/el:19980625
- [12] BITHAS, P., SAGIAS, N., MATHIOPOULOS, P., KARAGIANNIDIS, G., RONTOGIANNIS, A. On the performance analysis of digital communications over generalized-K fading channels. *IEEE Communications Letters*, 2006, vol. 4, no. 10, p. 353–355. DOI: 10.1109/LCOMM.2006.1633320
- [13] BITHAS, P. Weibull-Gamma composite distribution: alternative multipath/shadowing fading model. *Electronics Letters*, 2009, vol. 45, no. 14, p. 749–751. DOI: 10.1049/el:2009.0534
- [14] ZHANG, J., MATTHAIYOU, M., TAN, Z., WANG, H., KAVEH, M. Performance analysis of digital communication systems over composite η - μ /gamma fading channels. *IEEE Transactions on Vehicular Technology*, 2012, vol. 61, no. 7, p. 3114–3124. DOI: 10.1109/TVT.2012.2199344
- [15] STEFANOVIC, C., JAKSIC, B., SPALEVIC, P., PANIC, S., TRAJCEVSKI, Z. Performance analysis of selection combining over correlated Nakagami-m fading channels with constant correlation model for desired signal and cochannel interference. *Radioengineering*, 2013, vol. 22, no. 4, p. 1176–1181.
- [16] JAKSIC, B., STEFANOVIC, D., STEFANOVIC, M., SPALEVIC, P., MILENKOVIC, V. Level crossing rate of macrodiversity system in the presence of multipath fading and shadowing. *Radioengineering*, 2015, vol. 24, no. 1, p. 185–191. DOI: 10.13164/re.2015.0185
- [17] SUBADAR, R., SAHU, P. R. Performance of L-MRC receiver over independent Hoyt fading channels. In *Proceedings of the National Conference on Communications*. Chennai (India), 2010, p. 1–5. DOI: 10.1109/NCC.2010.5430232
- [18] GRADSHTEYN, S., RYZHIK, I. *Table of Integrals, Series, and Products*. 6th ed. New York: Academic Press 2000. ISBN: 0-122-94757-6
- [19] WOLFRAM. *Wolfram function site*. [Online] Cited 2017-01. Available at: <http://functions.wolfram.com/PDF/MeijerG.pdf>
- [20] ADAMCHIK, V., MARICHEV, O. The algorithm for calculating integrals of hypergeometric type functions and its realization in REDUCE system. In *Proceedings of International Conference on Symbolic and Algebraic Computation*. New York (USA), 1990, p. 212–224. DOI: 10.1145/96877.96930
- [21] KHANDELWAL, V., KARMESHU. A new approximation for average symbol error probability over log-normal channels. *IEEE Wireless Communications Letters*, 2014, vol. 3, no. 1, p. 58–61. DOI: 10.1109/WCL.2013.111113.130525
- [22] PROAKIS, J. G., SALEHI, M. *Digital Communications*. 5th ed. New York: McGraw-Hill, 2008. ISBN: 978-0-07-295716-7
- [23] OLABIYI, O., ANNAMALAI, A. Invertible exponential-type approximations for the Gaussian probability integral Q(x) with applications. *IEEE Wireless Communications Letters*, 2012, vol. 1, no. 5, p. 544–547. DOI: 10.1109/WCL.2012.080112.120232
- [24] PADMAPRIYA, S., TAMILARASI, M. Co-channel interference avoidance algorithm for closed access femtocell networks. *IETE Technical Review*, 2015, vol. 33, no. 3, p. 280–296. DOI: 10.1080/02564602.2015.1088413
- [25] LAOURINE, A., STEPHENNE, A., AFFES, S. Estimating the ergodic capacity of log-normal channels. *IEEE Communications Letters*, 2007, vol. 11, no. 7, p. 568–570. DOI: 10.1109/LCOMM.2007.070302
- [26] HELIOT, F., GHAVAMI, M., NAKHAI, M. R. An accurate closed-form approximation of the average probability of error over log-normal fading channel. *IEEE Transactions on Wireless Communications*, 2008, vol. 7, no. 5, p. 1495–1500. DOI: 10.1109/TWC.2008.061019
- [27] SIMON, M. K., ALOUINI, M. S. A unified approach to the probability of error for non-coherent and differentially coherent modulations over generalized fading channels. *IEEE Transactions on Communications*, 1996, vol. 46, no. 12, p. 1625–1638. DOI: 10.1109/26.737401

About the Authors...

Sandeep KUMAR was born in Delhi, India in 1983. He received his Bachelor of Technology in Electronics and Communication from Kurukshetra University, India in 2004 and Master of Engineering in Electronics and Communication from Thapar University, Patiala, India in 2007. He is currently pursuing Ph.D. from Delhi Technological University, India. Presently he is working as a Member (Research Staff) at the Central Research Laboratory, Ghaziabad, Bharat Electronics Limited. His research interest includes the study of wireless channels, performance modeling of fading channels and radio network planning.

Sanjay Kumar SONI was born in UP, India in 1975. He received his Bachelor of Engineering in Electronics Engineering from Madan Mohan Malviya Engineering College, Gorakhpur in 1997, M. Tech. degree in Communication Engineering from IIT Kanpur in 2004, and Ph.D. in Wireless Communication Engineering from IIT Kharagpur in

2011. Currently, he is an Associate Professor in the Department of Electronics and Communication in G. B. Pant Engineering College, Pauri (Uttarakhand). He has more than 14 years teaching experience. His research interest includes propagation modeling and characterization of wireless channel, time-domain analysis of propagation channel for UWB signals.

Priyanka JAIN received B.E. degree in Electronics & Telecommunication, M.Tech. in Microwave Engineering

from Delhi University, and Ph.D. from Guru Gobind Singh Indraprastha University, Delhi. She has over 9 years of teaching experience at Indira Gandhi Institute of Technology, GGSIP University. At present, she is an Assistant Professor in ECE department, Delhi Technological University. She has published a large number of papers in national and international journal in the field of digital signal processing. Her teaching and research are in the area of signal processing, analog electronics and microwave.



Movie recommender system with metaheuristic artificial bee

Rahul Katarya¹

Received: 30 October 2017 / Accepted: 28 December 2017
© The Natural Computing Applications Forum 2018

Abstract

Recommender systems are information retrieval tool that allocates accurate recommendations to the specific users. Collaborative movie recommender systems support users in accessing their popular movies by suggesting similar users or movies from their past common ratings. In this research work, a hybrid recommender system has been proposed which utilized k-means clustering algorithm with bio-inspired artificial bee colony (ABC) optimization technique and applied to the Movielens dataset. Our proposed system has been described systematic manner, and the subsequent results have been demonstrated. The proposed system (ABC-KM) is also compared with existing approaches, and the consequences have been examined. Estimation procedures such as precision, mean absolute error, recall, and accuracy for the movie recommender system delivered improved results for ABC-KM collaborative movie recommender system. The experiment outcomes on Movielens dataset established that the projected system provides immense achievement regarding scalability, performance and delivers accurate personalized movie recommendations by reducing cold start problem. As far as our best research knowledge, our proposed recommender system is novel and delivers effective fallouts when compared with already existing systems.

Keywords Recommender systems · Collaborative filtering · K-mean · Artificial bee colony

1 Introduction

Recommender systems are effective data filtering tools that are responsible for handling online data and information overload [1–5]. The determination of a recommender system is to create recommendations automatically of things for users preferences. Movie suggestion is the most broadly used interfaces united with web-based portals that intention is to support online library [6–8]. The mainstream of current systems is based on a collaborative filtering (CF) methodology that has been magnificently established [9–15]. It accumulates assessments of films given by an individual and then endorses specific films to the specific user. However, most of the time, recommender systems are suffered from integral restrictions such as reduced scalability and cold start complications [3, 16–19]. We have developed a hybrid collaborative movie recommender

system with improved movie prediction accuracy. In our collaborative movie recommender system, we have employed k-mean and artificial bee colony (ABC) to design an effective ABC-KM-based movie recommender systems. The collaborative algorithms are based on similar users and the person who has similar tastes as their friends have. Present approaches for recommendation systems are either memory based or model based. Model-based techniques use a set of constraints, and these constraints can be reduced using basic reduction techniques. Model-based techniques handle the sparsity issues in a better way than memory-based technologies [20, 21]. User-based collaborative filtering is functional on Movielens and other e-commerce applications [22, 23]. ABC is the most recent optimization procedure that encourages detecting the smart foraging conduct of a honey bee swarm and that is why it is used in research work for optimization [24–27]. ABC is also a bio-inspired algorithm, and bio-inspired means the intelligent algorithms which are motivated by the biological working of bees and apply in optimization and computing [28–33]. There are numerous domains in which ABC has been applied for better results. The various domains are such as image processing, computer and

✉ Rahul Katarya
rahulkatarya@dtu.ac.in

¹ Department of Information Technology, Delhi Technological University, Delhi, India

sensor networks, power distribution, data clustering, industrial engineering, mechanical engineering, and protein structure. The purpose of this research work is to employ user-based collaborative filtering with ABC algorithm and obtain the results by computing similarity in a set of users with Pearson similarity on the set of users. Sometimes, user-item matrix with collaborative filtering can be enormous and leads to the sparse and cold start problems [34]. Collaborative filtering-based recommender systems are mostly affected by cold start problem, in which new users will need to rate an adequate number of items to permit the system to detect their choices accurately and then the only system will deliver trustworthy recommendations. This paper is arranged as Sect. 2 explains the survey work that was performed on collaborative recommender system and clustering-based collaborative endorsements. The suggested system is named as a k-mean-ABC movie recommender system and explained in Sect. 3. In Sect. 4, experiment fallouts performed on Movielens dataset are described and finally summarization of this article with and the upcoming work is highlighted in Sect. 5.

2 Related work

Recommender systems (RS) are most effective knowledge management systems that help users to filter unusable data and contribute to avoiding information overloading and deliver personalized ideas [35, 36]. Currently, CF is the furthestmost operative procedure engaged by movie recommender systems, which is operated by the nearest-neighbor method [37–42]. There are two most popular techniques adopted by CF. Some authors improved memory-based procedures for recommender systems by determining the data sparsity issue in which they utilized support vector machine that computed likenesses between items and enhanced basic memory-based technique [43]. The deficiency of effective approaches for searching the right content may lead to a continuous damage of users, and the authors provided a study on this issue [44]. Computational intelligence has shown a significant impact in the field of data mining and e-commerce applications. In similar scenario, artificial immune system has shown significant influence on recommendation systems. Authors also proposed new mathematical expressions for analyzing immune network by utilizing Pearson correlation coefficient for Movielens and EachMovie datasets [45]. The k-mean algorithm has been widely used clustering approach in data mining [46, 47]. A hybrid movie recommender system was offered by utilizing k-means clustering and genetic algorithms (GAs) with principal component analysis (PCA) on Movielens dataset [7]. A competent incremental collaborative filtering recommender system

was presented which was based on a weighted clustering method [48]. Computational intelligence also showed a significant role in various interdisciplinary environments like movie-based collaborative recommender systems. A collaborative filtering framework was proposed which assimilates both subjective and independent knowledge to produce recommendations for the user that solved the problem of sparsity and the cold start problem by using Movielens datasets [49]. ABC is the furthestmost introduced optimization procedure that checks the brilliant expression of a honey bee swarm. We have utilized swarm optimization procedure in the proposed collaborative movie recommender system which showed the better and improved results when compared to the existing methods [24, 25].

3 k-means-artificial bee colony collaborative filtering framework

To overcome the limitations of a collaborative recommender system, we presented a hybrid cluster and optimization-based technique to advance movie prediction correctness. Our motive is to design a unified model solution that incorporates user ratings from the Movielens dataset for predictions. We used K-mean and ABC as optimization procedure and then apply to Movielens dataset for improved efficient recommender systems. Primarily, k-means clustering algorithm is applied to Movielens dataset for clustering of users into different clusters. The clusters are selected randomly at initial then users are checked one by one by calculating the differences in their ratings and the centroid of the clusters, and if their difference is lowest, then the user is assigned to the cluster to which they are nearby. However, at this instant not assure that each user has been assigned to the correct cluster with the lowest difference of centroid. So each user's distance is compared to cluster mean and displace the users according to the minimum distance from any cluster's mean. Now, this iterative repositioning would now continue from this new partition until no more rearrangements occur. After a point, if no more relocations occurred then that point is the point of completion of the clustering process. The k-means algorithm's necessary steps are presented in Fig. 1.

Next ABC algorithm is employed to the resultant of the k-means procedure for optimizing the results. The cluster is prepared but not optimized, so a function is developed, called as fitness function that helps in improving the user's centroid distances. Fitness function transforms the previous centroids for a limited number of iteration (i.e., relocation of centroids to users). Then, it classifies the users again by calculating the minimum centroid differences or applying k-means again. An artificial bee colony optimization

Fig. 1 Presentation of K-mean procedure

1. For clustering, Put K marks into the area characterized by the users. These marks symbolize a primary set of centroids.
2. Allocate individual user to the collection (cluster) that has the nearby centroid.
3. When totally users have been allocated, recomputed the locations of K centroids for the separate cluster.
4. Replicate stages 2 and 3 til no development in centroids. Group (clusters) is created.

algorithm may be described by using the following three idealized rules [24].

Initialize.

Repeat.

(a) Put the working bees on the nourishment bases in the memory;

(b) Put the observer bees on the nourishment bases in the memory;

(c) Dispatch the pathfinders to the hunt area for noticing new nourishment sources.

Till (necessities are met).

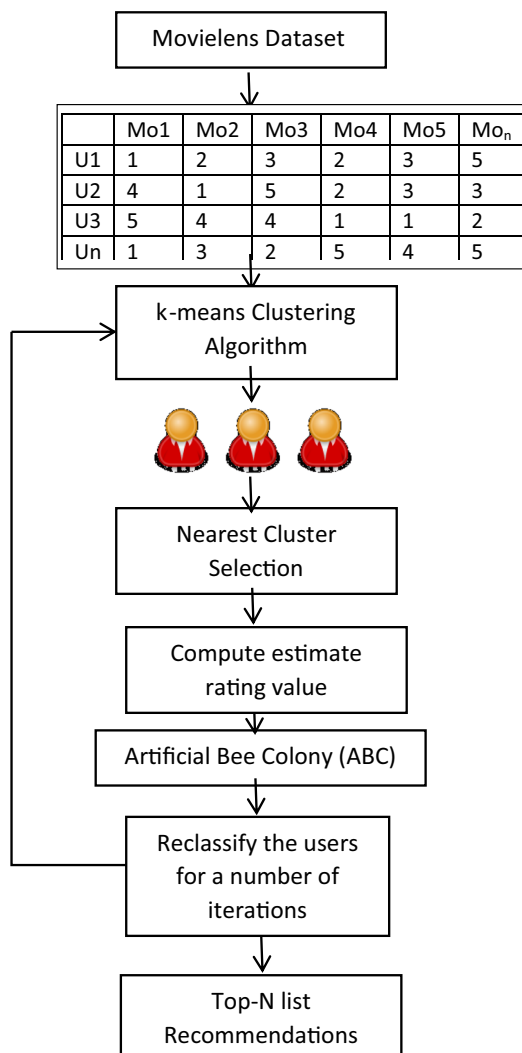
**Fig. 2** Overview of proposed movie recommender system framework

Figure 2 shows a flowchart that displays the stepwise process that how artificial bee colony algorithm is applied. Figure 2 shows the above-described approach, which is being implemented to the Movielens dataset. The Movielens dataset is recorded by reading the file, and dataset is divided into clusters by using k-means clustering algorithm which results in k clusters so that each cluster has a centroid. The space between the user and the centroid is computed, and the user is placed in the cluster whose centroid is the least distance away from him. When all such users have been relocated, the centroids are repositioned, and the new positions are also calculated. Consequently, the estimated rating that the user will give is calculated, and framework is optimized using artificial bee colony algorithm. We have calculated various evaluation expressions for expecting the truth of recommender system such as precision, MAE, recall and accuracy that are acceptable and efficient when compared with already existing methodologies.

ABC determines a community of preliminary resolution vectors with superior results and neighbor exploration methodology, and then continuously proceeds by reducing an objective function (Fig. 3). The objective function $f(\vec{z})$ should be reduced by detecting vector (\vec{z}) .

$$\text{minimize } f(\vec{z}), (\vec{z}) = (z_1, z_2, \dots, z_i, \dots, z_{n-1}, z_n) \in R^n \quad (1)$$

which is controlled by the succeeding similarities and equivalences:

$$li \leq zi \leq ui, i = 1, \dots, n \quad (2)$$

$$\text{substance as : } gy(\vec{z}) \leq 0, \text{ for } y = 1, \dots, p \quad (3)$$

$$hy(\vec{z}) = 0, \text{ for } y = p + 1, \dots, q \quad (4)$$

K-means clustering procedure relies on the preliminary locations and continuously congregates to the nearby local prime from the early point. Users require presetting the k value and centering points, which will often have an immense impact on cluster results. Hence, in the procedure of users gathering, we employed ABC procedure to conquer the K-mean clustering procedure. Therefore, in our proposed system, we employed ABC procedure to regulate the optimum value of center points and the resolutions compare with group's centers. The

Algorithm: ABC-KM Collaborative Filtering Pseudo Code

```

For each movie Mo1 in User U1's list
    For each user U2 who rated Mo1
        For each movie Mo2 purchased by
            User U1
                Record that a user rated Mo1 and Mo2
    For each movie Mo2
        Compute the similarity between Mo1 and Mo2

```

Cluster Initialization:

```

Reset the center of the clusters
Represent every close cluster as a data point
Compute mean of all data points and detect the location of the cluster.
Repeat above phases until convergence.

```

Population Initialisation:

```

Prepare the communities  $z_{i,j}$ ,  $i = 1 \dots SN, j = 1 \dots D$ 
Estimate communities
period=1
iteration
Generate fresh results  $v_{i,j}$  for the laboring bees by Equation 2 and compute
Execute the greedy choice procedure (GCP)
Compute the probability by Equation 1.
Compute fresh answers  $v_{i,j}$  from the  $z_{i,j}$ .
Apply the GCP
Regulate the unrestrained answer for the scout, if occurs, and interchange with a fresh result  $x_{i,j}$  by (3)
Learn the finest answer
period = period + 1
until period=MPN(Maximum period Number)

```

Fig. 3 Pseudocode of proposed system

working of our proposed system with ABC and k-mean can be précised as follows: First, initialize randomly the locations of food bases (each food base being a set of centroids), employ the k-means algorithm to complete clustering task for all created locations, and compute the fitness value of particular group of centroids. In the next step, bees hunt fresh food bases and inform the place of food bases by working bees. We applied k-means clustering algorithm to estimate new fitness values and match them with the original ones. Enhanced food bases will be supplied to onlooker bees. Then, we determined the probability values of food sources and updated their place according to the probability values by onlooker bees. Again, the k-means algorithm was applied to finish clustering process, estimate new fitness values, and compare them with the original ones to update them. We checked the trial counter of food sources, formed a new nourishment foundation (set of centroids), and repeated the steps until the termination criterion is encountered. Therefore, Figs. 2 and 3 illustrate the user and movie behavior who adopted the same working flow as we explained above.

4 Experiment and results

We adopted the publically available Movielens dataset as it has 100,000 ratings, 943 consumers, and 1682 movies of scale 1–5 (<http://grouplens.org/datasets/movielens/>). As discussed in the previous section, we presented a hybrid framework of k-means with ABC algorithm to achieve an improved movie recommendation system. Framework mentioned in the former section is used the Movielens dataset where data are considered from u_1 to u_5 and U_a to U_b . To measure the performance of recommender system, mean absolute error, precision, recall, and accuracy were computed. Comprehensive analysis and behavior of recommender system framework are given below. In Table 1 and Fig. 4, precision values of our proposed system are better than those of existing methods.

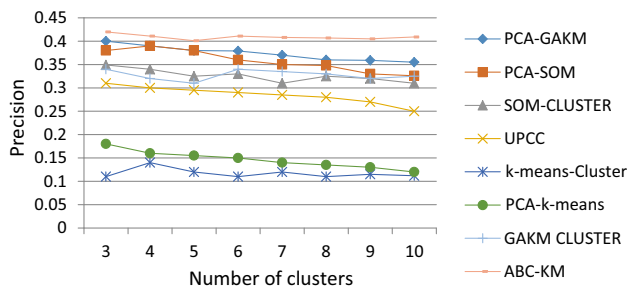
$$\text{Precision} = \frac{|\text{interesting} \cap \text{TopN}|}{N} \quad (5)$$

$$\text{Recall} = \frac{|\text{interesting} \cap \text{TopN}|}{|\text{interesting}|} \quad (6)$$

We concluded from Table 2 and Fig. 5 that recall for different clusters is better for our proposed system when compared with existing methods.

Table 1 Precision for different approaches for diverse values of k

System/cluster	3	4	5	6	7	8	9	10
PCA-GAKM	0.4	0.39	0.38	0.379	0.37	0.36	0.359	0.355
PCA-SOM	0.38	0.39	0.38	0.36	0.35	0.348	0.33	0.326
SOM-CLUSTER	0.349	0.34	0.325	0.33	0.31	0.325	0.32	0.31
UPCC	0.31	0.3	0.295	0.29	0.285	0.28	0.27	0.25
k-means cluster	0.11	0.14	0.12	0.11	0.12	0.11	0.115	0.112
PCA-k-means	0.18	0.16	0.155	0.15	0.14	0.135	0.13	0.12
GAKM CLUSTER	0.34	0.32	0.31	0.34	0.335	0.33	0.32	0.325
ABC-KM	0.42	0.411	0.401	0.411	0.408	0.407	0.405	0.409

**Fig. 4** Comparison of precision with various methods

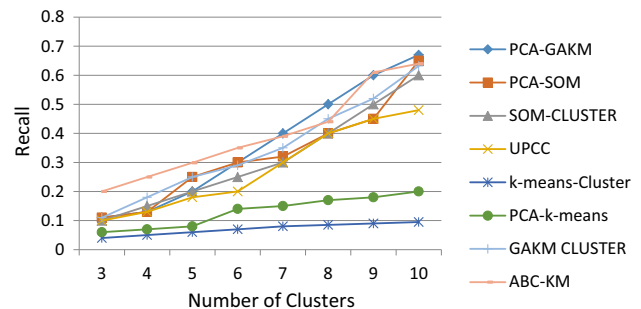
We compared the performance of our proposed system with the already existing systems. We need to investigate the MAE of the proposed routine and then compare it against MAE of other legacy systems.

$$MAE = \frac{\sum |\tilde{P}_{ij} - r_{ij}|}{M} \quad (7)$$

where M is the quantity of films, r_{ij} is the actual rating, and P_{ij} is the predicted rating of user i on movie j . We concluded that Table 3 and Fig. 6 show better MAE values for ABC-KM system when compared to other existing methods.

With an increasing amount of ratings, ABC-KM performed well in Fig. 7.

In Table 4, the performance of various methods has been presented which were performed on the Movielens dataset. We estimated the behavior of all procedures on a machine that has a configuration as an i3 processor with

**Fig. 5** Comparison of recall with various methods

1.9 GHz and 8 GB RAM. The ABC-KM system has efficient speed performance when compared to existing systems and can perform better if the proposed system is implemented in the high-configuration-processing environment.

5 Conclusion and future scope

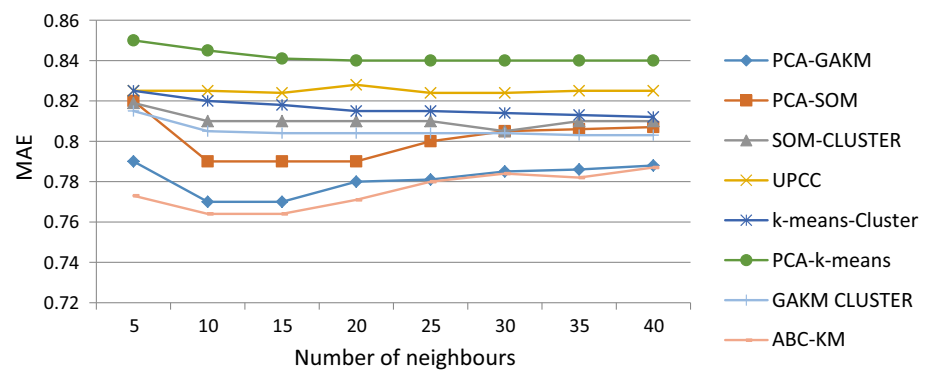
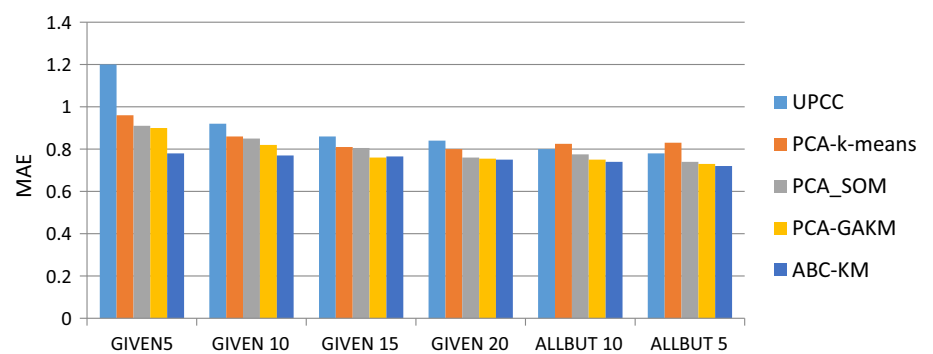
In this article, ABC-KM with k-means and artificial bee colony optimization is proposed with the Movielens dataset that results in an improved movie recommendation system. We measured the performance of our technique with mean absolute error, precision, recall, and accuracy. The experiment outcomes on the Movielens dataset indicated that our proposed recommender system offered high performance regarding accuracy, reliability, and personalization for

Table 2 Recall for different approaches for diverse values of k

System/cluster	3	4	5	6	7	8	9	10
PCA-GAKM	0.11	0.13	0.2	0.3	0.4	0.5	0.6	0.67
PCA-SOM	0.11	0.13	0.25	0.3	0.32	0.4	0.45	0.65
SOM-CLUSTER	0.1	0.15	0.2	0.25	0.3	0.4	0.5	0.6
UPCC	0.1	0.13	0.18	0.2	0.3	0.4	0.45	0.48
k-means cluster	0.04	0.05	0.06	0.07	0.08	0.085	0.09	0.095
PCA-k-means	0.06	0.07	0.08	0.14	0.15	0.17	0.18	0.2
GAKM CLUSTER	0.11	0.18	0.25	0.29	0.35	0.45	0.52	0.632
ABC-KM	0.2	0.25	0.299	0.35	0.39	0.44	0.61	0.64

Table 3 MAE for different approaches for diverse standards of k

System/cluster	5	10	15	20	25	30	35	40
PCA-GAKM	0.79	0.77	0.77	0.78	0.781	0.785	0.786	0.788
PCA-SOM	0.82	0.79	0.79	0.79	0.8	0.805	0.806	0.807
SOM-CLUSTER	0.819	0.81	0.81	0.81	0.81	0.805	0.81	0.81
UPCC	0.825	0.825	0.824	0.828	0.824	0.824	0.825	0.825
k-means cluster	0.825	0.82	0.818	0.815	0.815	0.814	0.813	0.812
PCA-k-means	0.85	0.845	0.841	0.84	0.84	0.84	0.84	0.84
GAKM CLUSTER	0.815	0.805	0.804	0.804	0.804	0.804	0.803	0.803
ABC-KM	0.773	0.764	0.764	0.771	0.78	0.784	0.782	0.787

Fig. 6 Comparison of MAE with various methods**Fig. 7** MAE for the different rating level**Table 4** Comparisons of speed for different methods for Movielens dataset

Methods	PCA-GAKM	PCA-SOM	SOM-CLUSTER	UPCC	k-means cluster	PCA-k-means	GAKM CLUSTER	ABC-KM
Speed (in seconds)	26.32	141.73	76.92	159.34	16.25	55.56	355.71	53.22

movie recommendations with the specific number of clusters. For future work, our system's performance may be evaluated on advance high-configuration machine by

including other important characteristics of users, such as privacy and context with cross-domain data.

Compliance with ethical standards

Conflict of interest The author declares that he has no conflict of interest.

References

- Lu J, Wu D, Mao M, Wang W, Zhang G, Nu S (2015) Recommender system application developments. *Decis Support Syst* 74:12–32. <https://doi.org/10.1016/j.dss.2015.03.008>
- Beel J, Gipp B, Langer S, Breiteringer C (2015) Research-paper recommender systems: a literature survey. *Int J Digit Libr*. <https://doi.org/10.1007/s00799-015-0156-0>
- Bobadilla J, Ortega F, Hernando A, Gutiérrez A (2013) Recommender systems survey. *Knowl-Based Syst* 46:109–132. <https://doi.org/10.1016/j.knosys.2013.03.012>
- Katarya R, Verma OP (2016) Recent developments in affective recommender systems. *Phys A Stat Mech Appl* 461:182–190. <https://doi.org/10.1016/j.physa.2016.05.046>
- Katarya R, Verma OP (2017) Efficient music recommender system using context graph and particle swarm. *Multimed Tools Appl*. <https://doi.org/10.1007/s11042-017-4447-x>
- Colombo-Mendoza LO, Valencia-García R, Rodríguez-González A, Alor-Hernández G, Samper-Zapater JJ (2014) RecomMetz: a context-aware knowledge-based mobile recommender system for movie showtimes. *Expert Syst Appl* 42:1202–1222. <https://doi.org/10.1016/j.eswa.2014.09.016>
- Wang Z, Yu X, Feng N, Wang Z (2014) An improved collaborative movie recommendation system using computational intelligence. *J Vis Lang Comput* 25:667–675. <https://doi.org/10.1016/j.jvlc.2014.09.011>
- Katarya R, Verma OP (2016) A collaborative recommender system enhanced with particle swarm optimization technique. *Multimed Tools Appl*. <https://doi.org/10.1007/s11042-016-3481-4>
- Liu H, Kong X, Bai X, Wang WEI (2015) Context-based collaborative filtering for citation recommendation. *IEEE Access* 3:1695–1703
- Li Y, Zhai CX, Chen Y (2014) Exploiting rich user information for one-class collaborative filtering. *Knowl Inf Syst* 38:277–301. <https://doi.org/10.1007/s10115-012-0583-9>
- Aguilar J, Valdiviezo-Díaz P, Riofrio G (2017) A general framework for intelligent recommender systems. *Appl Comput Inform*. <https://doi.org/10.1016/j.aci.2016.08.002>
- Katarya R, Verma OP (2017) Effectual recommendations using artificial algae algorithm and fuzzy c-mean. *Swarm Evol Comput*. <https://doi.org/10.1016/j.swevo.2017.04.004>
- Kunaver M, Požrl T (2017) Diversity in recommender systems—a survey. *Knowl-Based Syst* 123:154–162. <https://doi.org/10.1016/j.knosys.2017.02.009>
- Rubio JE, Alcaraz C, Lopez J (2017) Recommender system for privacy-preserving solutions in smart metering. *Pervasive Mob Comput*. <https://doi.org/10.1016/j.pmcj.2017.03.008>
- Katarya R, Verma OP (2016) A collaborative recommender system enhanced with particle swarm optimization technique. *Multimed Tools Appl* 75:1–15. <https://doi.org/10.1007/s11042-016-3481-4>
- Bao J, Zheng Y, Wilkie D, Mokbel M (2015) Recommendations in location-based social networks: a survey. *Geoinformatica*. <https://doi.org/10.1007/s10707-014-0220-8>
- Abbas A, Zhang L, Khan SU (2015) A survey on context-aware recommender systems based on computational intelligence techniques. *Computing*. <https://doi.org/10.1007/s00607-015-0448-7>
- Katarya R, Verma OP (2016) Recommender system with grey wolf optimizer and FCM. *Neural Comput Appl*. <https://doi.org/10.1007/s00521-016-2817-3>
- Katarya R, Verma OP (2016) An effective web page recommender system with fuzzy c-mean clustering. *Multimed Tools Appl*. <https://doi.org/10.1007/s11042-016-4078-7>
- Liu D, Liang D, Wang C (2015) A novel three-way decision model based on incomplete information system. *Knowl-Based Syst* 91:32–45. <https://doi.org/10.1016/j.knosys.2015.07.036>
- Mao K, Chen G, Hu Y, Zhang L (2016) Music recommendation using graph based quality model. *Sig Process* 120:1–8. <https://doi.org/10.1016/j.sigpro.2015.03.026>
- Qiao Z, Zhang P, Cao Y, Zhou C, Guo L (2014) Improving collaborative recommendation via location-based user-item subgroup. *Procedia Comput Sci* 29:400–409. <https://doi.org/10.1016/j.procs.2014.05.036>
- Mukherjee R, Sajja N, Sen S (2003) A movie recommendation system—an application of voting theory in user modeling. *User Model User-Adapt Interact* 13:5–33. <https://doi.org/10.1023/A:1024022819690>
- Karaboga D, Ozturk C, Basturk B, Kiran MS, Findik O, Karaboga D et al (2009) A powerful and efficient algorithm for numerical function optimization: artificial bee colony (ABC) algorithm. *Appl Soft Comput* 11:454–462. <https://doi.org/10.1016/j.asoc.2007.05.007>
- Karaboga D, Ozturk C (2011) A novel clustering approach: artificial Bee Colony (ABC) algorithm. *Appl Soft Comput* 11:652–657. <https://doi.org/10.1016/j.asoc.2009.12.025>
- Rajasekhar A, Lynn N, Das S, Suganthan PN (2017) Computing with the collective intelligence of honey bees—a survey. *Swarm Evol Comput* 32:25–48. <https://doi.org/10.1016/j.swevo.2016.06.001>
- Zhou A, Qu B, Li H, Zhao S, Nagarathnam P (2011) Multiobjective evolutionary algorithms: a survey of the state of the art. *Swarm Evol Comput* 1:32–49. <https://doi.org/10.1016/j.swevo.2011.03.001>
- Mavrovouniotis M, Li C, Yang S (2017) A survey of swarm intelligence for dynamic optimization: algorithms and applications. *Swarm Evol Comput* 33:1–17. <https://doi.org/10.1016/j.swevo.2016.12.005>
- Gotmare A, Bhattacharjee SS, Patidar R, George NV (2017) Swarm and evolutionary computing algorithms for system identification and filter design: a comprehensive review. *Swarm Evol Comput* 32:68–84. <https://doi.org/10.1016/j.swevo.2016.06.007>
- Cosma G, Brown D, Archer M, Khan M, Pockley AG (2017) A survey on computational intelligence approaches for predictive modeling in prostate cancer. *Expert Syst Appl* 70:1–19. <https://doi.org/10.1016/j.eswa.2016.11.006>
- Bandaru S, Ng AHC, Deb K (2017) Data mining methods for knowledge discovery in multi-objective optimization: part B—new developments and applications. *Expert Syst Appl* 70:119–138. <https://doi.org/10.1016/j.eswa.2016.10.016>
- Rakshit P, Konar A, Das S (2017) Noisy evolutionary optimization algorithms—a comprehensive survey. *Swarm Evol Comput* 33:18–45. <https://doi.org/10.1016/j.swevo.2016.09.002>
- Ander AR, Leser ULF, Graefe G (2017) Optimization of complex dataflows with user-defined functions. *ACM Comput Surv* 50:38
- Deng S, Huang L, Xu G (2014) Social network-based service recommendation with trust enhancement. *Expert Syst Appl* 41:8075–8084. <https://doi.org/10.1016/j.eswa.2014.07.012>
- Park DH, Kim HK, Choi IY, Kim JK (2012) A literature review and classification of recommender systems research. *Expert Syst Appl* 39:10059–10072
- Bauer J, Nanopoulos A (2014) Recommender systems based on quantitative implicit customer feedback. *Decis Support Syst*. <https://doi.org/10.1016/j.dss.2014.09.005>

37. Ekstrand MD (2010) Collaborative filtering recommender systems. *Found Trends® Hum Comput Interact* 4:81–173. <https://doi.org/10.1561/1100000009>
38. Adomavicius G, Tuzhilin A (2005) Toward the next generation of recommender systems: a survey of the state-of-the-art and possible extensions. *Adapt Web* 69:253–260. https://doi.org/10.1007/978-3-540-72079-9_9
39. Sánchez-Moreno D, Gil González AB, Muñoz Vicente MD, López Batista VF, Moreno García MN (2016) A collaborative filtering method for music recommendation using playing coefficients for artists and users. *Expert Syst Appl* 66:234–244. <https://doi.org/10.1016/j.eswa.2016.09.019>
40. Wu H, Pei Y, Li B, Kang Z, Liu X, Li H (2015) Item recommendation in collaborative tagging systems via heuristic data fusion. *Knowl-Based Syst* 75:124–140. <https://doi.org/10.1016/j.knosys.2014.11.026>
41. Polatidis N, Georgiadis CK (2015) A multi-level collaborative filtering method that improves recommendations. *Expert Syst Appl* 48:100–110. <https://doi.org/10.1016/j.eswa.2015.11.023>
42. Liang X, Xia Z, Pang L, Zhang L, Zhang H (2016) Measure prediction capability of data for collaborative filtering. *Knowl Inf Syst*. <https://doi.org/10.1007/s10115-016-0920-5>
43. Ghazarian S, Nematbakhsh MA (2015) Enhancing memory-based collaborative filtering for group recommender systems. *Expert Syst Appl* 42:3801–3812. <https://doi.org/10.1016/j.eswa.2014.11.042>
44. Soares M, Viana P (2014) Tuning metadata for better movie content-based recommendation systems. *Multimed Tools Appl*. <https://doi.org/10.1007/s11042-014-1950-1>
45. Chen M-H, Teng C-H, Chang P-C (2015) Applying artificial immune systems to collaborative filtering for movie recommendation. *Adv Eng Inform* 29:830–839. <https://doi.org/10.1016/j.aei.2015.04.005>
46. Kanungo T, Mount DM, Netanyahu NS, Piatko CD, Silverman R (2002) Wu a. Y. An efficient k-means clustering algorithm: analysis and implementation. *IEEE Trans Pattern Anal Mach Intell* 24:881–892. <https://doi.org/10.1109/TPAMI.2002.1017616>
47. Ahmad A, Dey L (2007) A k-mean clustering algorithm for mixed numeric and categorical data. *Data Knowl Eng* 63:503–527. <https://doi.org/10.1016/j.datak.2007.03.016>
48. Salah A, Rogovschi N, Nadif M (2015) A dynamic collaborative filtering system via a weighted clustering approach. *Neurocomputing* 175:206–215. <https://doi.org/10.1016/j.neucom.2015.10.050>
49. Cheng L, Wang H (2014) A fuzzy recommender system based on the integration of subjective preferences and objective information. *Appl Soft Comput J* 18:290–301. <https://doi.org/10.1016/j.asoc.2013.09.004>



New Configuration for OFCC-Based CM SIMO Filter and its Application as Shadow Filter

Deva Nand¹ · Neeta Pandey¹

Received: 26 June 2017 / Accepted: 21 December 2017
© King Fahd University of Petroleum & Minerals 2018

Abstract

This paper puts forward a new operational floating current conveyor (OFCC)-based current mode (CM) single input multiple output (SIMO) filter configuration which uses two grounded capacitors, three grounded resistors and three OFCCs. The attractive features of the proposed filter are—use of grounded passive elements; availability of low pass, band pass, high pass and notch filter responses simultaneously at high output impedance; and independent adjustment of filter parameters. These features make the proposed filter suitable from fabrication viewpoint and allow easy cascading. Effect of nonidealities on proposed filter response is also examined. A CM shadow filter is also built by introducing an OFCC-based amplifier and connecting it in a feedback loop of the proposed SIMO filter. This configuration allows adjustment of filter parameters through gain of amplifier. MOS-based implementation of grounded resistors is incorporated to facilitate electronic tuning of filter parameters. The operation of the proposed filters is verified through SPICE simulations using 0.5 μm technology model parameters from MOSIS (AGILENT). Proposed CM SIMO filter is prototyped using commercially available IC AD844, and experimental response is found to be in close agreement with theoretical ones.

Keywords Current mode filter · Shadow filter · Single input multiple output · Operational floating current conveyor

1 Introduction

The development of current mode active element has added new dimensions to analog signal processing, specially the analog filters that find extensive use in communications and control engineering [1–3]. The current mode (CM) filter circuits process the information in terms of time varying currents that enables the system to have wide bandwidth and better signal linearity. Considering these advantageous feature, researchers have designed and developed a wide variety of CM SIMO filters presented in [3–32] and references cited therein. The topologies [3–32] employ differential voltage current conveyor (DVCC) [3,30], current conveyor transconductance amplifier (CCTA) [4,24], current conveyors and its variants [5,7–9,13–19,21,22,25–27,29], current follower transconductance amplifier (CFTA) [6,28], oper-

ational transconductance amplifier (OTA) [10,29], Z-copy current follower transconductance amplifier (ZC-CFTA) [11, 23] and Z-copy current inverter transconductance amplifier (ZC-CITA) [12], multiple output current follower (MO-CF) [20], operational floating current conveyor (OFCC) [31,32] as active elements. The features of CM SIMO filters [3–32] differ in terms of number of active and passive elements used; types of active elements used; input/output impedances; simultaneous availability of output responses; and independent adjustment of the filter parameters. The observations are summarized in Table 1.

It may be noted that

1. Single active element is used in [4], [5, Fig. 2, 3], [28], whereas multiple active elements of different and similar types are employed in [7,18,19,22,27,29] and [6,11], [16, Fig. 5a, 9a], [21, Fig. 3], respectively.
2. Number of simultaneously available responses: two in [5,6], three in [3,4,8–10,12–20] [21, Fig. 2], [23–26,28–30,32], four in [31] and all the five in [7,11], [21, Fig. 3 & 4], [22,27].
3. Some of the responses are available through components in [4], [5, Fig. 2, 3], [10,28,31]. Therefore, additional

✉ Deva Nand
devkamboj07@gmail.com

Neeta Pandey
n66pandey@rediffmail.com

¹ Department of Electronics and Communications, Delhi Technological University, Bawana Road, Delhi, India

Table 1 Comparative analysis of CM SIMO Filters

References	Number and type of active element (s)	Number of passive elements—resistors (R), capacitors(C), floating element	I/O Impe-dance, high (H), low (L)	Available responses ⁺	Possible addi-tional responses	Independent adjustment of filter parameters
[3]	3 DVCC	4R, 2C	H/H	LP, HP, BP	Notch, AP	No
[4]	1 CCTA	2R, 2C	H/L	LP, HP(C), BP(R,C)	Notch, AP	Yes
[5]	(i) 1 CCIII+ or – (Fig. 2, 3)	1R, 2C, 1R Floating	H/L	LP(R), BP(C).	N.A.	No
	(ii) 3 CCIII+ (Fig. 9)	1R, 2C, 1R Floating	H/H	LP, BP	N.A.	No
[6]	4 CFTA	2C	L/H	LP, BP	HP, Notch, AP	Yes
[7]	2 CCCII, 1 MOCCA	2C	L/H	LP, HP, BP, Notch, AP	N.A.	Yes
[8]	3 MOCCII	3R, 2C, 2R Floating	L/H	LP, BP, Notch	HP, AP	No
[9]	3CCII	3R, 2C	L/H	LP, BP, Notch	HP, AP	Yes
[10]	2 OTA	2C	L/L	LP, HP (C), BP	Notch, AP	No
[11]	4 ZC-CFTA	2C	L/H	LP, HP, BP, Notch, AP	N.A.	Yes
[12]	2 ZC-CITA	2C	L/H	LP, HP, BP	Notch, AP	No
[13]	3 MOCC	2R, 2C	L/H	LP, HP, BP	Notch, AP	No
[14]	3 MOCC	4R, 2C	H/H	LP, HP, BP	Notch, AP	No
[15]	3 MOCCCII	1R, 2C	H/H	LP, HP, BP	Notch, AP	No
[16]	Case-I (Sec 2.1, 2.2) & Case-II (Sec 3.1, 3.2). *3–5 CCII+/-	Floating R & C (2.1, 2.2) & Grounded R & C (3.1, 3.2). **2–5 R, 2–3 C	L/H	LP, HP, BP (for all sections)	Notch, AP (for all sections)	No (2.1, 3.1) & Yes (2.2, 3.2)
[17]	3 MOCCII	2R, 2C	L/H	LP, HP, BP	Notch, AP	No
[18]	2 DOCCII, 1 DOCCIII	2R, 2C	L/H	LP, HP, BP	Notch, AP	No
[19]	2 CCII, 1 MOCCCA	2R, 2C	L/H	LP, HP, BP	Notch, AP	Yes
[20]	3 MO-CF	2C, 2R floating	L/H	LP, HP, BP	Notch, AP	No
[21]	(i) 3 DOCCCII (Fig. 2)	2C	L/H	LP, HP, BP	Notch, AP	No
	(ii) 4 CCCII (Fig. 3)	2C	L/H	LP, HP, BP, Notch, AP	N.A.	No
	(iii) 3 CCCII (Fig. 4)	2C	L/H	LP, HP, BP, Notch, AP	N.A.	No
[22]	2 CCCII, 1 CCCII with controlled current gain	2C	L/H	LP, HP, BP, Notch, AP	N.A.	Yes
[23]	3 ZC-CFTA	2C	L/H	LP, HP, BP	Notch, AP	Yes
[24]	2 CCCCTA	2C	H/H	LP, BP, Notch	HP, AP	Yes
[25]	3 DOCCII	3R, 2C	L/H	LP, BP, Notch	HP	Yes
[26]	3 DO-ICCI	3R, 2C	L/H	LP, BP, Notch	HP	Yes
[27]	2 CCCII, 1 CCCII with controlled current gain	2C	L/H	LP, HP, BP, Notch, AP	N.A.	Yes
[28]	1 CFTA	2C	H/L	LP, HP (C), BP	N.A.	No
[29]	2 OTA, 1 ICCIII	1R, 2C	L/H	LP, BP, Notch	HP, AP	Yes
[30]	2 DVCCs	2R, 2C, 1R floating	H/H	LP, BP, Notch	HP, AP	Yes
[31]	3 OFCC	2R, 2C	L/L	LP, HP(C), Notch, BP	AP	No
[32]	2 MO-OFC	2R, 2C	H/H	LP, Notch, BP	HP, AP	No
Prop-osed	3 OFCC	3R, 2C	L/H	LP, HP, BP, Notch	AP	Yes

N.A. not available; ⁺low pass (LP), high pass (HP), band pass (BP), notch and all pass (AP); [16]* :- 5 CCII+/- in Fig. 5a, 9a and [16]** :- 4R,2C Fig. 12, 3R,3C Fig. 15, 5R, 2C Fig. 18

active element would be required to process output further.

4. The desired condition of low input impedance in CM filters is not maintained in [3–5,10,14,15,24,28,30,32].
5. The configurations [5,8,16,20,30] use floating passive elements which are not suitable from fabrication viewpoint.
6. Refs. [3,5,8,10,12–18,20,21,28,31,32] do not support independent adjustment of filter parameters. The parameters adjustment is possible in [6,7,11,19,22–24,27] and [4,9], [16, sec. 2.2, 3.2], [25,26,29,30] through transconductance (g_m) or internal resistance of active element.

It is clear from above discussion that only one SIMO filter [11] is available that uses similar active elements and provides four or more output responses at high output impedance and allows independent adjustment of filter parameters. This configuration, however, uses four active elements. This paper presents a SIMO filter which uses three active elements of same type and provides four output responses simultaneously. Further, it possesses independent adjustment of filter parameters and presents output at high impedance.

The contents are arranged in 4 sections including the introduction. Section 2 briefly reviews the port relationship and circuit symbol of OFCC. It also includes proposed filter and the effect of nonidealities. An application of proposed filter as shadow band pass filter is also put forward in this section. The functional verification of proposed filters is done through simulation and experimentation; and the results are placed in Sect. 3. Conclusions are drawn in Sect. 4.

2 Circuit Description

2.1 OFCC

The circuit symbol of OFCC [33–35] is shown in Fig. 1 where two input ports and five output ports are available. The input impedance of port X (Y) is low (high) which makes it suitable for processing current input (voltage input). The voltage output at low impedance port W is multiplication of input current at port X and open loop transimpedance gain Z_t . Ports Z1, Z2, Z3 and Z4 are high-impedance-current output ports.

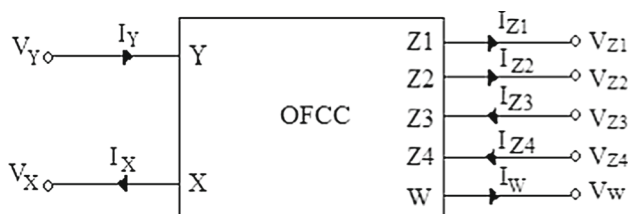


Fig. 1 OFCC Circuit symbol

The port relationships of the OFCC are described by matrix given in (1). It may be noted that the port X tracks the voltage of Y terminal and current at port W is copied to ports Z1 and Z2 in phase and to ports Z3 and Z4 out of phase. So this block offers voltage tracking at input port and current tracking at output ports.

$$\begin{bmatrix} I_Y \\ V_X \\ V_W \\ I_{Z1} \\ I_{Z2} \\ I_{Z3} \\ I_{Z4} \end{bmatrix} = \begin{bmatrix} 0 & 0 & 0 & 0 & 0 & 0 \\ 1 & 0 & 0 & 0 & 0 & 0 \\ 0 & Z_t & 0 & 0 & 0 & 0 \\ 0 & 0 & 1 & 0 & 0 & 0 \\ 0 & 0 & 1 & 0 & 0 & 0 \\ 0 & 0 & -1 & 0 & 0 & 0 \\ 0 & 0 & -1 & 0 & 0 & 0 \end{bmatrix} \begin{bmatrix} V_Y \\ I_X \\ I_W \\ V_{Z1} \\ V_{Z2} \\ V_{Z3} \\ V_{Z4} \end{bmatrix} \quad (1)$$

2.2 Proposed OFCC-Based CM SIMO Filter

Proposed OFCC-based CM SIMO filter is presented in Fig. 2. It uses three OFCCs, three grounded resistors and two grounded capacitors.

For this CM SIMO filter, transfer functions are derived through routine analysis for various current outputs as in (2) to (6).

$$T_{\text{low_pass}} = \frac{I_1}{I_{\text{in}}} = \frac{-R_3}{s^2 C_1 C_2 R_1 R_2 R_3 + s C_1 R_1 R_2 + R_3} \quad (2)$$

$$T_{\text{high_pass}} = \frac{I_2}{I_{\text{in}}} = \frac{-s^2 C_1 C_2 R_1 R_2 R_3}{s^2 C_1 C_2 R_1 R_2 R_3 + s C_1 R_1 R_2 + R_3} \quad (3)$$

$$T_{\text{band_pass}} = \frac{I_3}{I_{\text{in}}} = \frac{-s C_1 R_1 R_3}{s^2 C_1 C_2 R_1 R_2 R_3 + s C_1 R_1 R_2 + R_3} \quad (4)$$

$$T_{\text{notch}} = \frac{I_4}{I_{\text{in}}} = \frac{s^2 C_1 C_2 R_1 R_2 R_3 + R_3}{s^2 C_1 C_2 R_1 R_2 R_3 + s C_1 R_1 R_2 + R_3} \quad (5)$$

and

$$T_{\text{all_pass}} = \frac{I_5}{I_{\text{in}}} = \frac{s^2 C_1 C_2 R_1 R_2 R_3 - s C_1 R_1 R_3 + R_3}{s^2 C_1 C_2 R_1 R_2 R_3 + s C_1 R_1 R_2 + R_3} \quad (6)$$

where $I_5 = I_3 + I_4$.

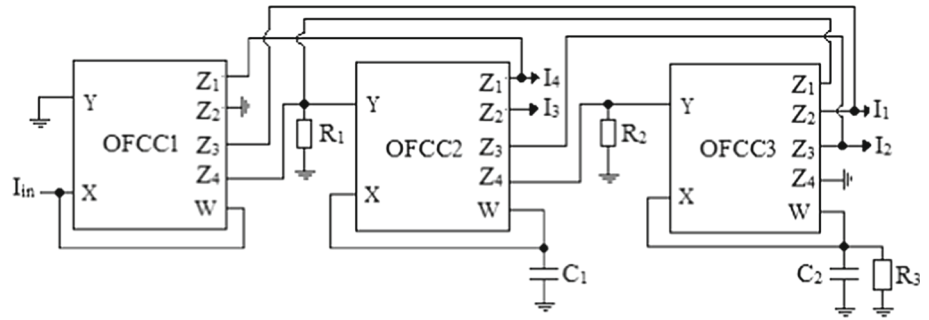
It is clear from (2) to (6) that low pass, high pass, band pass and notch responses are available simultaneously at high output impedance; therefore, these can easily be cascaded. The all pass response may be obtained by simply joining notch and band pass responses together. The filter responses are characterized by pole frequency (ω_o), quality factor (Q_o) and bandwidth ($BW = \omega_o / Q_o$) as given in (7) and (8)

$$\omega_o = \sqrt{\frac{1}{C_1 C_2 R_1 R_2}} \quad \& \quad Q_o = R_3 \sqrt{\frac{C_2}{C_1 R_1 R_2}} \quad (7)$$

$$BW = \frac{\omega_o}{Q_o} = \frac{1}{C_2 R_3} \quad (8)$$



Fig. 2 Proposed OFCC-based CM SIMO Filter



As seen from (7), ω_o and Q_o can be tuned by varying R_1 and R_2 without affecting ω_o/Q_o . Further Q_o can be tuned by varying R_3 while keeping ω_o fixed.

The sensitivity of the proposed filter parameters ω_o and Q_o for passive components used is computed as:

$$\begin{aligned} S_{R_1}^{\omega_o} &= S_{R_2}^{\omega_o} = S_{C_1}^{\omega_o} = S_{C_2}^{\omega_o} = S_{R_1}^{Q_o} \\ &= S_{R_2}^{Q_o} = S_{C_1}^{Q_o} = -\frac{1}{2}, \quad S_{R_3}^{Q_o} = S_{C_2}^{Q_o} = \frac{1}{2} \end{aligned} \quad (9)$$

It is clear from (9) that all the passive sensitivities are less than unity in magnitude; thus, the proposed circuit may be termed as insensitive.

2.3 Effect of Nonidealities

The nonidealities of OFCC can be of two types: first type is finite transimpedance gain ($Z_t(s)$) and second is presence of various parasites. Effect of these nonidealities is examined in the following subsection.

2.3.1 Effect of Finite Transimpedance Gain

The transfer functions given in Sect. 2.2 are obtained by considering ideal value of transimpedance gain. Practically, value of transimpedance gain is frequency dependent and finite. With single pole model, the $Z_t(s)$ [43] is expressed as

$$Z_t(s) = \frac{Z_{to}}{1 + s/\omega_{tc}} \quad (10)$$

where Z_{to} and ω_{tc} correspond to the dc open loop transimpedance gain and transimpedance cutoff frequency, respectively. For high-frequency applications, $Z_t(s)$ is approximated as:

$$Z_t(s) \cong \frac{1}{s/(Z_{to}\omega_{tc})} \quad (11)$$

or

$$Z_t(s) \cong \frac{1}{sC_p} \quad (12)$$

Taking (12) into account, the transfer function (4) modifies to

$$T_{\text{band_pass}} = \frac{I_3}{I_{in}} = \frac{-s(C_1 + C_p)R_1R_3}{D_n(s)} \quad (13)$$

where

$$\begin{aligned} D_n(s) &= s^2(C_1 + C_p)(C_2 + C_p)R_1R_2R_3 \\ &+ s(C_1 + C_p)R_1R_2 + R_3 \end{aligned} \quad (14)$$

It may be observed that the C_p is appearing in parallel to external capacitors so by choosing $C_1, C_2 \gg C_p$, the effect of $Z_t(s)$ may be accommodated and transfer function given in (13) reduces to (4), i.e., ideal response.

2.3.2 Effect of Parasites

The effect of parasites on filter responses is dependent on circuit topology. The parasites are manifested as parallel combination of resistor and capacitor at terminals Y, Z_i ($i = 1, 2, 3, 4$) (i.e., $R_Y, C_Y, R_{Z_i}, C_{Z_i}$). The proposed filter topology of Fig. 2 modifies to Fig. 3 in presence of parasites. It may be noted that R_1 and R_2 in Fig. 2 changes to R_{eq1}/C_{para1} and R_{eq2}/C_{para2} , respectively. The parasites appear in parallel at respective terminals and show their presence and hence modify the values of resistors R_1 as R_{eq1}/C_{para1} and R_2 as R_{eq2}/C_{para2} . Here, $R_{eq1} = R_1/R_{Y2}/R_{Z41}/R_{Z13}$, $R_{eq2} = R_2/R_{Y3}/R_{Z42}$, $C_{para1} = C_{Y2}/C_{Z41}/C_{Z13}$ and $C_{para2} = C_{Y3}/C_{Z42}$. The subscripts i and j with Z terminal correspond to j th Z terminal of i th OFCC.

By taking parasites, denominator of transfer function (2)–(6) modifies to

$$\begin{aligned} D_{n_para}(s) &= s^2(R_{eq1}R_{eq2}R_3(C_1C_2 + C_{para1}C_{para2})) \\ &+ s(C_1R_{eq1}R_{eq2} + R_{eq2}R_3C_{para1} \\ &+ R_{eq2}R_3C_{para2}) + R_3 \end{aligned} \quad (15)$$

where n_para denotes nonideal effect due to parasites only.

So in the presence of parasites, pole frequency modifies to

$$\omega_o^2|_{n_{\text{para}}} = \frac{1}{R_{\text{eq1}} R_{\text{eq2}} R_3 C_1 C_2} \left[1 + \frac{C_{\text{para1}} C_{\text{para2}}}{C_1 C_2} \right]^{-1} \quad (17)$$

$$\omega_0^2|_{n_{\text{para}}} = \frac{1}{R_{\text{eq1}} R_{\text{eq2}} R_3 C_1 C_2} \quad (18)$$
$$\frac{\omega_0}{Q} \bigg|_{n_para} = \frac{C_1 R_{eq1} R_{eq2} + C_{para1} R_{eq2} R_3 + C_{para2} R_{eq2} R_3}{R_{eq1} R_{eq2} C_1 C_2 R_3} \quad (19)$$

$$\begin{aligned} \left. \frac{\omega_o}{Q} \right|_{n_para} &= \frac{1}{C_2 R_3} + \frac{C_{para1}}{C_1 C_2 R_{eq1}} + \frac{C_{para2}}{C_1 C_2 R_{eq1}} \\ &= \frac{1}{C_2 R_3} + \frac{1}{R_{eq1}} \left[\frac{C_{para1}}{C_1 C_2} + \frac{C_{para2}}{C_1 C_2} \right] \end{aligned} \quad (20)$$

$$\left. \frac{\omega_0}{Q} \right|_{n \text{ para}} \approx \frac{1}{C_2 R_3} \quad (21)$$
$$\frac{1}{C_2 R_3} \gg \frac{1}{R_{eq1}} \left[\frac{C_{para1}}{C_1 C_2} + \frac{C_{para2}}{C_1 C_2} \right] \quad (22)$$

$$C \gg \frac{1}{R_{\text{eq1}}} (C_{\text{para1}} + C_{\text{para2}}) \frac{Q}{\omega_0} = C_D \quad (23)$$

2.4 OFCC-Based CM Shadow Band Pass Filter

Connecting the low pass current (I_1) to the amplifier input results in low pass controlled shadow band pass response and the governing transfer function is obtained as

$$\left(\frac{I_{\text{BP_shadow}}}{I_{\text{in}}}\right)_{\text{BP_LPC}} = \frac{-s/(C_2 R_2)}{s^2 + \frac{s}{C_2 R_3} + \frac{(1+A)}{C_1 C_2 R_1 R_2}} \quad (24)$$

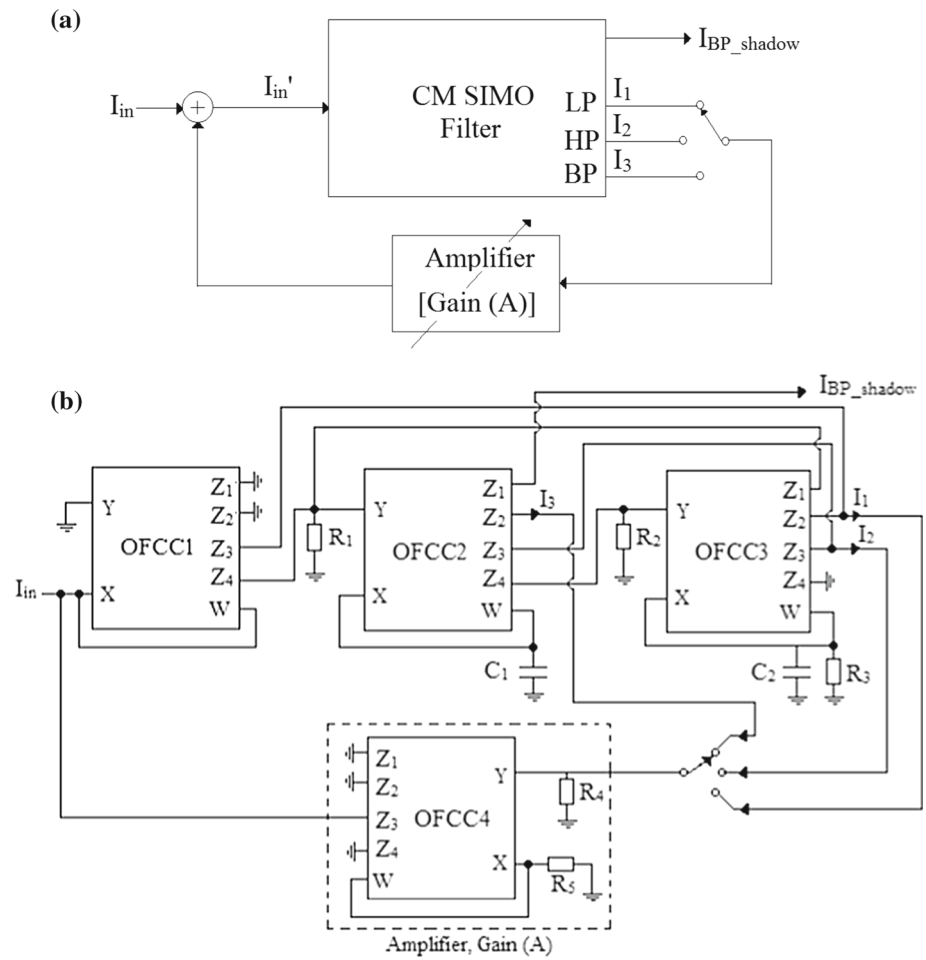
The pole frequency, quality factor and bandwidth of the low pass controlled shadow band pass filter are represented by ω_{o_LPC} , Q_{o_LPC} and $BW_{LPC} = \omega_{o_LPC}/Q_{o_LPC}$, respectively, and are computed from Eq. (24) as

$$\omega_{\text{o_LPC}} = \sqrt{\frac{(1+A)}{C_1 C_2 R_1 R_2}} \quad (25)$$

$$Q_{0_LPC} = R_3 \sqrt{\frac{C_2(1+A)}{C_1 R_1 R_2}} \quad (26)$$

$$\text{BW}_{\text{LPC}} = \frac{\omega_{0_ \text{LPC}}}{Q_{0_ \text{LPC}}} = \frac{1}{C_2 R_3} \quad (27)$$

Fig. 4 **a** Generalized scheme of shadow filter [36], **b** Proposed OFCC-based CM shadow band pass filter



It is clear from (25) to (27) that ω_{o_LPC} and quality factor Q_{o_LPC} can be adjusted via amplifier gain while keeping bandwidth BW_{LPC} same as original bandwidth (BW).

Connecting the high pass current (I_2) to the amplifier input results in high pass controlled shadow band pass response and the governing transfer function is obtained as

$$\left(\frac{I_{BP_shadow}}{I_{in}} \right)_{BP_HPC} = \frac{-s / (C_2 R_2 (1 + A))}{s^2 + \frac{s}{C_2 R_3 (1 + A)} + \frac{1}{C_1 C_2 R_1 R_2 (1 + A)}} \quad (28)$$

where legend BP_HPC represents high pass controlled shadow band pass filter.

From Eq. (28), pole frequency (ω_{o_HPC}) quality factor (Q_{o_HPC}) and bandwidth $BW_{HPC} (= \omega_{o_HPC} / Q_{o_HPC})$ of the high pass controlled shadow band pass filter are computed as

$$\omega_{o_HPC} = \sqrt{\frac{1}{C_1 C_2 R_1 R_2 (1 + A)}} \quad (29)$$

$$Q_{o_HPC} = R_3 \sqrt{\frac{C_2 (1 + A)}{C_1 R_1 R_2}} \quad (30)$$

$$BW_{HPC} = \frac{\omega_{o_HPC}}{Q_{o_HPC}} = \frac{1}{C_2 R_3 (1 + A)} \quad (31)$$

It is observed from (29) to (31) that all filter parameters vary with amplifier gain. The change in ω_{o_HPC} and Q_{o_HPC} is opposite in nature i. e. with increase in gain ω_{o_HPC} decreases while Q_{o_HPC} increases.

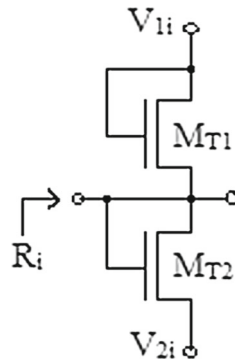
Connecting the band pass current (I_3) to the amplifier input results in band pass controlled shadow band pass response and the governing transfer function is obtained as

$$\left(\frac{I_{BP_shadow}}{I_{in}} \right)_{BP_BPC} = \frac{-s / (C_2 R_2)}{s^2 + \frac{s(1+A)}{C_2 R_3} + \frac{1}{C_1 C_2 R_1 R_2}} \quad (32)$$

where BP_BPC represents band pass controlled shadow band pass filter.

From Eq. (32), pole frequency (ω_{o_BPC}) quality factor (Q_{o_BPC}) and bandwidth $BW_{BPC} (= \omega_{o_BPC} / Q_{o_BPC})$ of the high pass controlled shadow band pass filter are computed as

Fig. 5 MOS-based resistor implementation [42]



$$\omega_{o_BPC} = \sqrt{\frac{1}{C_1 C_2 R_1 R_2}} \quad (33)$$

$$Q_{o_BPC} = \frac{R_3}{(1+A)} \sqrt{\frac{1}{C_1 R_1 R_2}} \quad (34)$$

$$BW_{BPC} = \frac{\omega_{o_BPC}}{Q_{o_BPC}} = \frac{(1+A)}{C_2 R_3} \quad (35)$$

It is clear from (33) and (34) that $\omega_{o_BPC} = \omega_o$ while Q_{o_BPC} may be varied independent of ω_{o_BPC} .

All the grounded resistors used in both of the circuits are implemented using two diode connected MOS transistor structure operating in saturation region and shown in Fig. 5 [42].

$$R_i = \frac{1}{2\mu_n C_{ox} (W/L) (V_{1i} - V_T)} \quad (36)$$

In (36), for calculation of R_i assume bias voltages as $V_{1i} = -V_{2i}$ ($i = 1, 2, 3, 4, 5$), μ is carrier mobility, W/L is aspect ratios of M_{T1} and M_{T2} , C_{ox} is gate capacitance per unit area and V_T is threshold voltage. So by varying the bias voltages, R_i can be varied to tune the circuit parameters electronically.

Table 2 MOS transistors aspect ratios of the structure shown in Fig. 6 [43]

Transistor	$W (\mu m) / L (\mu m)$
$M1, M2$	50/1
$M3, M4, M11, M12, M14, M16, M18, M20, M22, M24$	50/2.5
$M5, M7, M10, M15, M17, M19, M21, M23, M25$	20/2.5
$M6, M8$	40/2.5
$M9, M13$	100/2.5

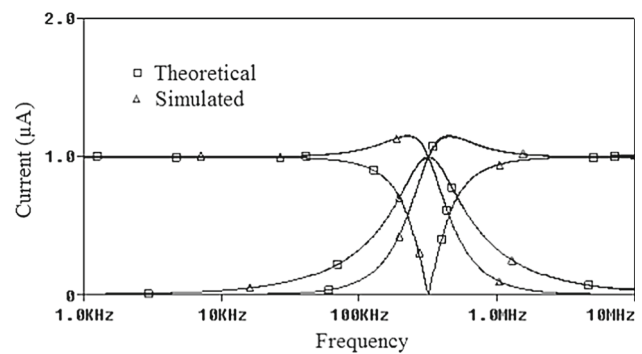


Fig. 7 Theoretical and simulated responses of CM SIMO filter

3 Functional Verification

The operation of proposed filters was verified through SPICE simulations using CMOS-based implementation of OFCC [43]. The schematic is reproduced as Fig. 6 for ready reference. Model parameters of 0.5 μm technology from MOSIS (AGILENT) are used. The aspect ratios of the various transistors are given in Table 2 [43]. The supply voltages (V_{DD} and V_{SS}) are taken as $\pm 1.5V$ and bias voltages (V_{B1} and V_{B2}) of $\pm 0.8V$ are considered.

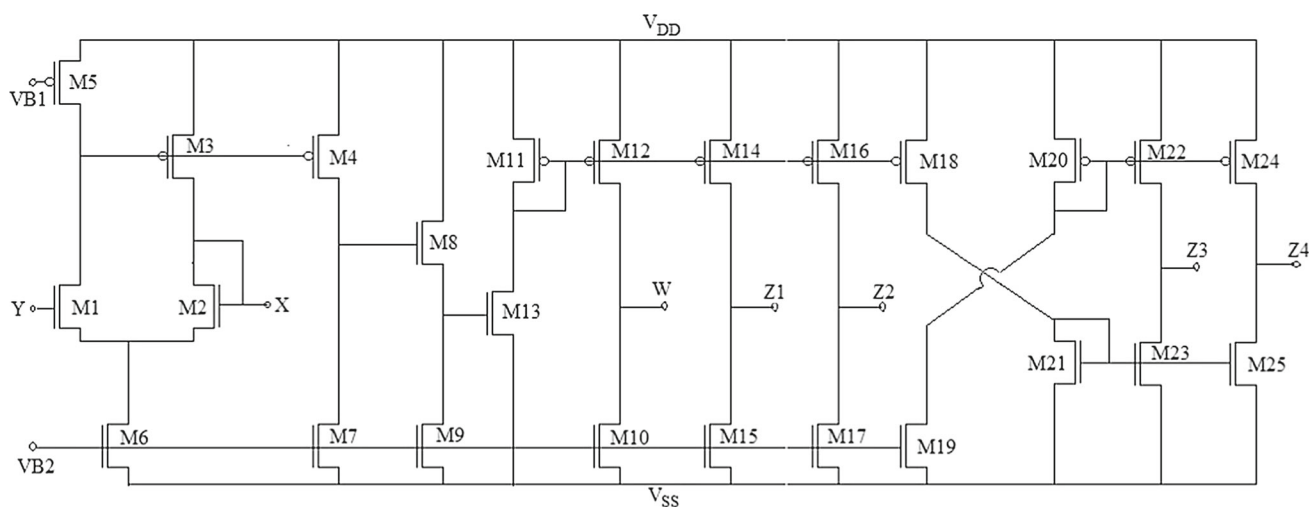
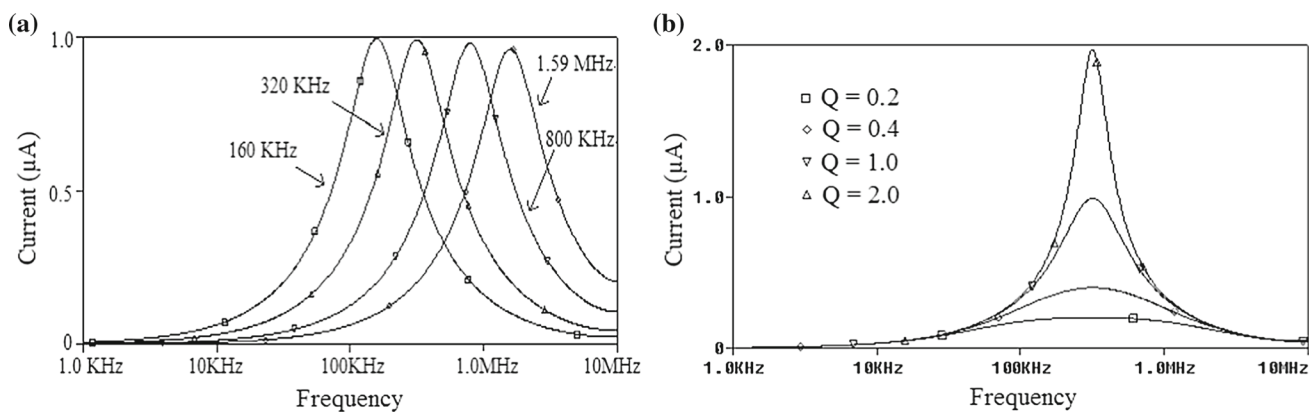
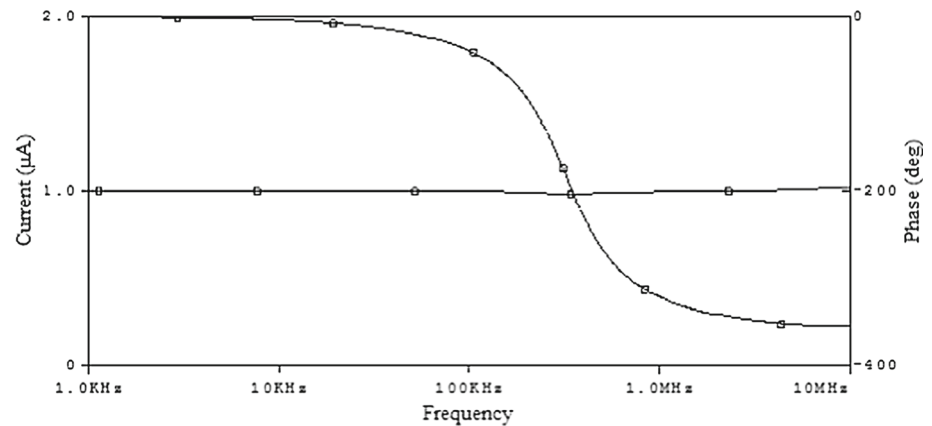


Fig. 6 CMOS-based structure of OFCC [43]

Fig. 8 Simulated magnitude and phase plots of all pass response**Fig. 9** Tuning of f_o and Q_o . **a** Tuning of f_o with R_1 and R_2 **b** Tuning of Q_o with R_3 **Table 3** Simulation settings for independent adjustment of filter parameters

Orthogonal adjustment of f_o with Q_o ($Q_o = 1$)				Orthogonal adjustment of Q_o with f_o ($f_o = 320$ KHz) ($R_1 = R_2 = 5$ k Ω)			
$V_{11} = V_{12} =$ V_{13} *(V)	$V_{21} = V_{22} =$ V_{23} *(V)	$R_1 = R_2 =$ R_3 (k Ω)	f_o (KHz)	V_{13} *(V)	V_{23} *(V)	R_3 (k Ω)	Q_o
1.310	-1.310	1	1590	1.310	-1.310	1	0.2
0.869	-0.869	2	800	0.869	-0.869	2	0.4
0.726	-0.726	5	320	0.726	-0.726	5	1
0.711	-0.711	10	160	0.711	-0.711	10	2

* V_{1i} and * V_{2i} refer to bias voltages corresponding to resistance R_i .

The proposed CM SIMO filter was simulated for pole frequency of 320 KHz using $C_1 = C_2 = 100$ pF and MOS-based resistors of values $R_1 = R_2 = R_3 = 5$ k Ω by selecting bias voltages V_{1i} and V_{2i} in Fig. 5 as ± 0.726 V, respectively.

Theoretical and simulated results for low pass, high pass, band pass and notch frequency responses are shown in Fig. 7. The simulation results agree quite well with the theoretical analysis. The magnitude and phase plot of all pass response is given in Fig. 8.

Simulation results for independent adjustment of filter parameters is shown in Fig. 9 with setting enlisted in Table 3. The adjustment of f_o for Q_o fixed at unity is achieved by

keeping $R_1 = R_2 = R_3$ and varying these simultaneously. The Q_o adjustment for given f_o is obtained by keeping R_1 and R_2 fixed and varying R_3 . Time domain behavior of proposed filter is verified by applying sinusoidal current excitation of 2 μ A amplitude and 500 KHz frequency and corresponding transient responses of low pass, high pass and band pass filter is shown in Fig. 10. The frequency spectrum shown in Fig. 11 confirms effectiveness of the proposed filter for mixed sinusoidal current input of 2 μ A amplitude and 50, 500 KHz, 2.85 MHz frequencies.

The circuit of Fig. 2 is prototyped using commercially available IC AD844-based OFCC implementation [44]. The

Fig. 10 Transient responses for Sinusoidal current input of $2\mu\text{A}$, 500 KHz

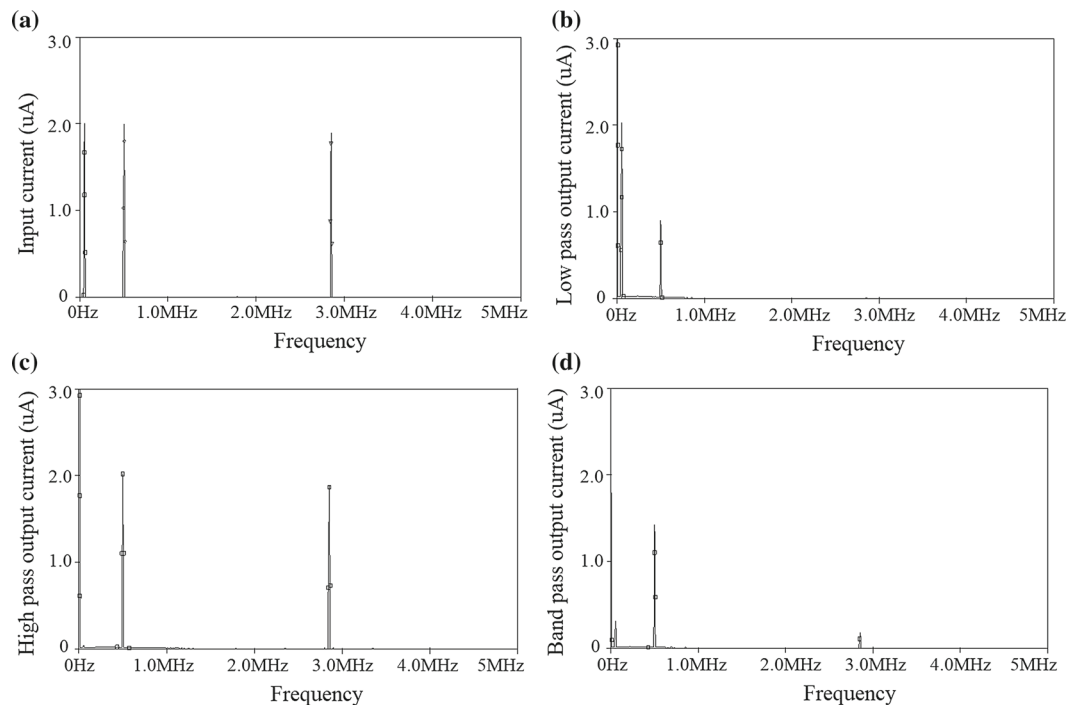
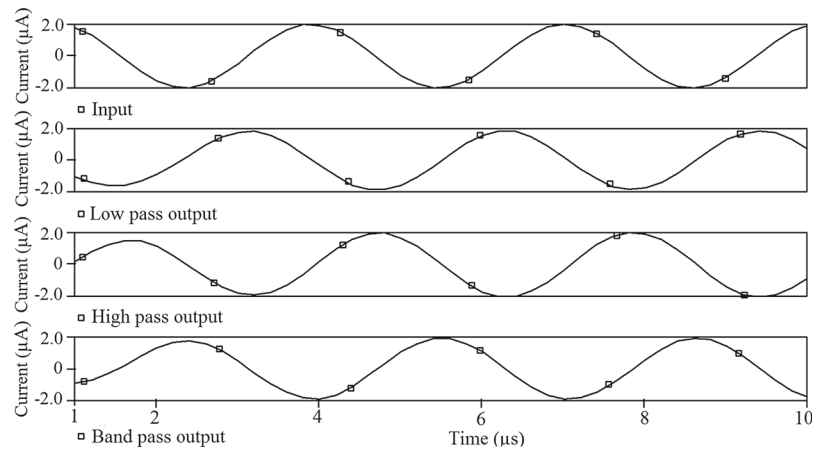


Fig. 11 Frequency spectrum of **a** input **b** low pass **c** high pass and **d** band pass output

component values are kept same as those used for simulations. The theoretical and experimental frequency response for bandpass output are depicted in Fig. 12. The slight deviation in the responses is observed which is due to nonidealities.

To test the functionality of CM shadow band pass filter of Fig. 4b, the original filter pole frequency is chosen as 320 KHz by employing component values ($C_1 = C_2 = 100\text{ pF}$ and $R_1 = R_2 = R_3 = 5\text{ k}\Omega$). For amplifier block where R_4, R_5 are electronically controlled and keeping $R_4 = 1\text{ k}\Omega$ while R_5 is electronically varied as 1, 2 and 3 $\text{k}\Omega$ to control the gain of the amplifier. The gain of the amplifier can also be varied using R_4 or R_5 or both. The variation in LP, HP and BP controlled shadow band pass filter parameters with gain is depicted in Figs. 13, 14 and 15, respectively. The simulated

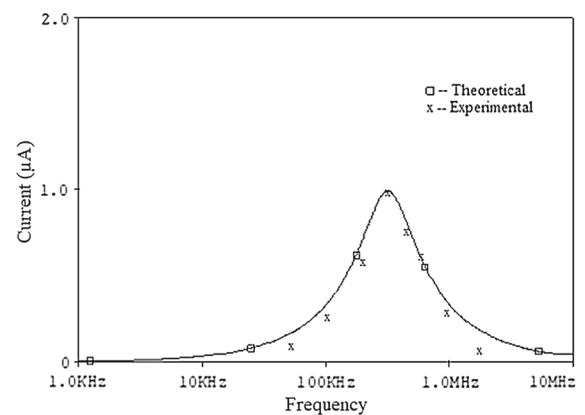


Fig. 12 Simulated and experimental bandpass frequency response

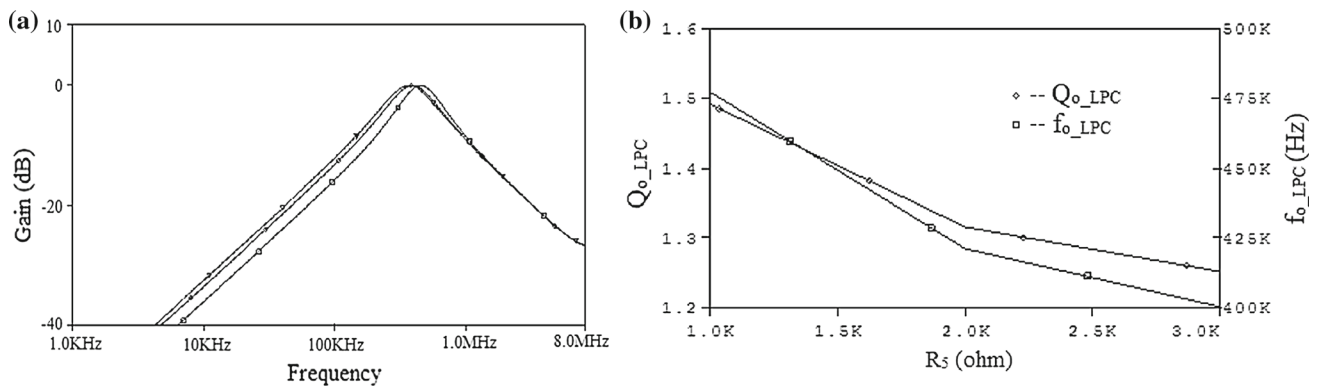


Fig. 13 LP controlled shadow BP response

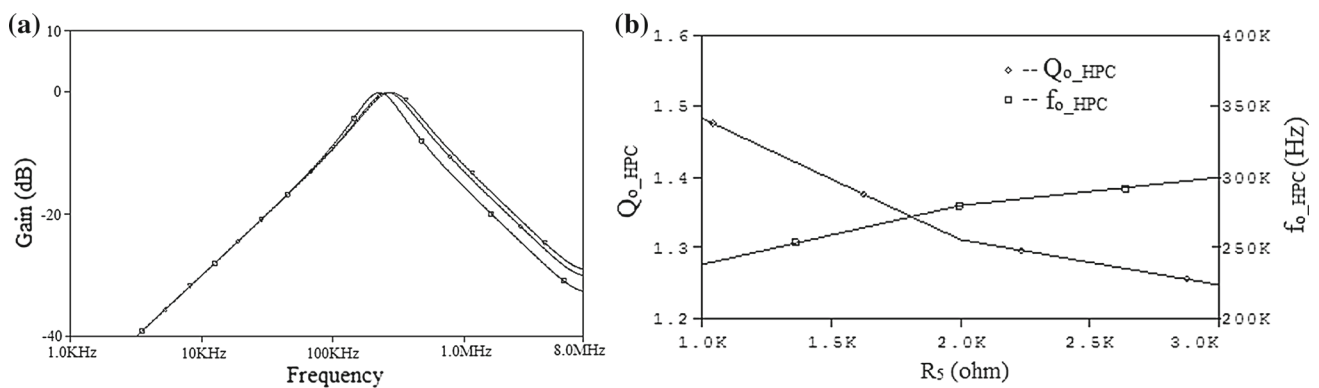


Fig. 14 HP controlled shadow BP response

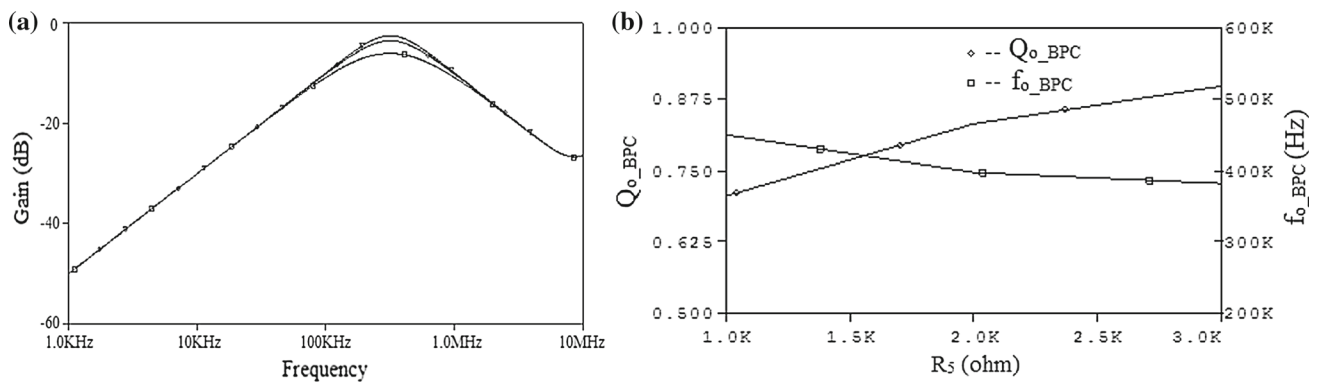


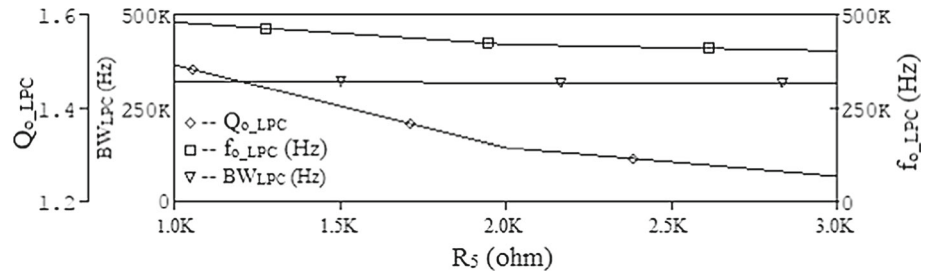
Fig. 15 BP controlled shadow BP response

Table 4 Tuning of shadow filter parameters

$V_{14} = -V_{24} * (V)$ $R_4(K\Omega)$ $V_{15} = -V_{25} * (V)$ $R_5(K\Omega)$ Gain (A)					$Q_o = 1, f_o = 320 \text{ KHz}(R_1 = R_2 = R_3 = 5k\Omega, C_1 = C_2 = 100 \text{ pF})$					
					LP controlled BP		HP controlled BP		BP controlled BP	
					Q_{o_LPC}	$f_{o_LPC} \text{ (KHz)}$	Q_{o_HPC}	$f_{o_HPC} \text{ (KHz)}$	Q_{o_BPC}	$f_{o_BPC} \text{ (KHz)}$
1.310	1	1.310	1	1	1.49	477.61	1.48	238.56	.706	449.75
1.310	1	0.869	2	0.5	1.31	421.21	1.31	280.44	.831	398.02
1.310	1	0.803	3	0.33	1.25	400.63	1.24	300.12	.898	382.75

* V_{1i} and * V_{2i} refer to bias voltages corresponding to resistance R_i .

Fig. 16 LP controlled shadow BP response with bandwidth (BW_{LPC}) independent of ω_{o_LPC} and Q_{o_LPC}



filter parameters of shadow band pass filter with values of tuning resistor R_4 and R_5 are given in Table 4.

It may be noted that the proposed filter and shadow filter have similar characteristics. By examining the expression of ω_o , ω_o/Q_o and Q_o , it is observed that low pass controlled shadow band pass offers one unique feature of constant bandwidth (BW_{LPC}) which is independent of ω_{o_LPC} and Q_{o_LPC} . This fact is pictorially represented in Fig. 16 by including ω_o/Q_o in Fig. 13b.

4 Conclusion

An OFCC-based current mode electronically tunable SIMO filter configuration is presented in this paper. In proposed SIMO filter, all the five standard filter responses are available and only three OFCCs, two grounded capacitors and three grounded resistors are used. MOS-based implementation of grounded resistors is used for electronic tuning. An application of proposed SIMO filter namely shadow band pass filter is also suggested wherein the filter parameters are controlled by amplifier gain instead of varying components of constituent filter. The amplifier in shadow band pass filter is realized using an OFCC and two grounded resistors. The proposed configurations are functionally verified through SPICE simulations. The CM SIMO filter is also examined via prototyping it with commercially available IC AD844.

References

- Sedra, A.S.; Smith, K.C.: Microelectronic Circuits. Oxford University Press, Oxford (2004)
- Ferri, G.; Guerrini, N.C.: Low Voltage Low Power CMOS Current Conveyors. Kluwer Academic Publishers, Boston (2003)
- Ibrahim, M.A.; Minaei, S.; Kuntman, H.: A 22.5 MHz current-mode KHN-biquad using differential voltage current conveyor and grounded passive elements. *AEU Int. J. Electron. Commun.* **59**(5), 311–318 (2005)
- Herencsar, N.; Koton, J.; Vrba, K.: Single CCTA-based universal biquadratic filters employing minimum components. *Int. J. Comput. Electr. Eng.* **1**(3), 307–310 (2009)
- Yüce, E.; Metin, B.; Cicekoglu, O.: Current-mode biquadratic filters using single cciii and minimum numbers of passive elements. *Frequenz* **58**(9–10), 225–228 (2004)
- Tangsrirat, W.: Single-input three-output electronically tunable universal current-mode filter using current follower transconductance amplifiers. *AEU Int. J. Electron. Commun.* **65**, 783–787 (2011)
- Wang, C.; Xu, J.; Keskin, A.U.; Du, S.; Zhang, Q.: A new current-mode current-controlled SIMO-type universal filter. *AEU Int. J. Electron. Commun.* **65**, 231–234 (2011)
- Hong, J.W.: Current-mode and transimpedance-mode universal biquadratic filter using multiple outputs CCIIs. *Indian J. Eng. Materials Sci.* **17**(3), 169–174 (2010)
- Abdalla, K.K.; Bhaskar, D.R.; Senani, R.: Configuration for realising a current-mode universal filter and dual-mode quadrature single resistor controlled oscillator. *IET Circuits Devices Syst.* **6**(3), 159–167 (2012)
- Qadir, A.; Altaf, T.: Current mode canonic OTA-C universal filter with single input and multiple outputs. In: *Proceedings of International Conference on Electronic Computer Technology (ICECT'10)* pp. 32–34 (2010)
- Satansup, J.; Tangsrirat, W.: Single-input five-output electronically tunable current-mode biquad consisting of only ZC-CFTAs and grounded capacitors. *Radioengineering* **20**(3), 650–656 (2012)
- Biolek, D.; Biolkova, V.; Kolka, Z.; Bajer, J.: Single-input multi-output resistorless current-mode Biquad. In: *Proceedings of IEEE European Conference on Circuit Theory and Design*, pp. 225–228 (2009)
- Senani, R.; Singh, A.K.: A new universal current mode biquad filter. *Frequenz* **56**, 55–59 (2002)
- Senani, R.; Singh, A.K.; Singh, V.K.: New tunable SIMO type current mode universal biquad using only three MOCCs and all grounded passive elements. *Frequenz* **57**(7–8), 160–161 (2003)
- Senani, R.; Singh, V.K.; Singh, A.K.; Bhaskar, D.R.: Novel electronically controllable current-mode universal biquad filter. *IEICE Electron. Express* **1**, 410–415 (2004)
- Soliman, A.M.: Current-mode universal filters using current conveyors: classification and review. *Circuits Syst. Signal Process.* **27**, 405–427 (2008)
- Sağbaş, M.; Köksal, M.: Current-mode state-variable filter. *Frequenz* **62**, 37–42 (2008)
- Chunhua, W.; Keskin, A.U.; Yang, L.; Qiuqing, Z.; Sichun, D.: Minimum configuration insensitive multifunctional current mode biquad using current conveyors and all-grounded passive components. *Radioengineering* **19**(1), 178–184 (2010)
- Abdalla, K.K.: Universal current-mode biquad employing dual output current conveyors and MO-CCCA with grounded passive elements. *Circuits Syst.* **4**, 83–88 (2013)
- Jerabek, J.; Sotner, R.; Vrba, K.: Comparison of the SITO current-mode universal filters using multiple-output current followers. In: *Proceedings of the 35th International Conference Telecommunication Signal Process (TSP'12)*, pp. 406–410 (2012)
- Yuce, E.: Current-mode electronically tunable biquadratic filters consisting of only CCCIs and grounded capacitors. *Microelectronics J.* **40**, 1719–1725 (2009)



22. Kumngern, M.: A new current-mode universal filter with single-input five-output using trans-linear current conveyors. *Aust. J. Electr. Electron. Eng.* **9**(2), 177–184 (2012)
23. Senani, R.; Singh, B.; Singh, A.K.: New universal current-mode biquad using only three ZC-CFTAs. *Radioengineering* **21**(1), 273–280 (2012)
24. Singh, S.V.; Maheshwari, S.; Chauhan, D.S.: Current-processing current-controlled universal biquad filter. *Radioengineering* **21**(1), 317–323 (2012)
25. Chen, H.P.: Versatile current-mode universal biquadratic filter using DO-CCIIs. *Int. J. Electron.* **100**(7), 1010–1031 (2013)
26. Chen, H.P.: Current-mode dual-output ICCII-based tunable universal biquadratic filter with low-input and high-output impedances. *Int. J. Circuit Theory Appl.* **42**(4), 376–393 (2014)
27. Kumngern, M.; Phasukkit, P.; Junnapiya, S.; Khateb, F.; Tungjitkusolmun, S.: ECCCII-based current-mode universal filter with orthogonal control of ω_0 and Q . *Radioengineering* **23**(2), 687–696 (2014)
28. Singh, S.V.; Tomar, R.S.; Chauhan, D.S.: Single CFTA based current-mode universal biquad filter. *J. Eng. Res.* **13**(2), 172–186 (2016)
29. Arora, T.S.; Gupta, M.; Gupta, S.: Current mode universal filter employing operational transconductance amplifier and third generation current conveyor. In: *IEEE International Conference on Power Electronics, Intelligent Control and Energy Systems (ICPE-ICES)*, IEEE, pp. 1–4, (2016)
30. Abaci, A.; Yuce, E.: A new DVCC+ based second-order current-mode universal filter consisting of only grounded capacitors. *J. Circuits Syst. Comput.* **26**(9), 1750130 (2017)
31. Pandey, N.; Nand, D.; Khan, Z.: Single input four output current mode filter using operational floating current conveyor. *J. Act. Passiv. Compon.* **2013**, 1–8 (2013)
32. Parveen, T.: OFC based high output impedance current mode simo universal biquadratic filter. In: *International Conference on Multimedia, Signal Processing and Communication Technologies (IMPACT)*, IEEE, pp. 134–136 (2011)
33. Toumazou, C.; Payne, A.; Lidgey, F.J.: Operational floating conveyor. *Electron. Lett.* **27**(8), 651–652 (1991)
34. Khan, A. A.; Al-Turaigi, M. A.; El-Ela, M. A.: Operational floating current conveyor: characteristics, modelling and applications. In: *Proceedings of IEEE Instrumentation and Measurement Technology Conference*, Hamamatsu, Japan, pp. 788–790 (1994)
35. Ghallab, Y. H.; El-Ela, M. A.; Elsaid, M.H.: Operational floating current conveyor: characteristics, modeling and experimental results. In: *Proceedings of 11th International Conference Microelectron (ICM'99) IEEE*, Kuwait pp. 59–62 (1999)
36. Lakys, Y.; Fabre, A.: Multistandard transceivers: State of the art and a new versatile implementation for fully active frequency agile filters. *Analog Integr. Circuits Signal Process.* **74**(1), 63–78 (2012)
37. Pandey, N.; Sayal, A.; Choudhary, R.; Pandey, R.: Design of CDTA and VDTA based frequency agile filters. *Adv. Electron.* **2014**, 1–15 (2014)
38. Roy, S.C.D.: 'Shadow' filters—a new family of electronically tunable filters. *IETE J. Education.* **51**(2–3), 75–78 (2010)
39. Lakys, Y.; Fabre, A.: Shadow filters generalisation to Nth-class. *Electron. Lett.* **46**(14), 985–986 (2010)
40. Abuelma'atti, M.T.; Almutairi, N.R.: New current-feedback operational-amplifier based shadow filters. *Analog Integr. Circuits Signal Process.* **86**(3), 471–480 (2016)
41. Lakys, Y.; Fabre, A.: Shadow filters—a new family of second order filters. *Electron. Lett.* **46**(4), 276–277 (2010)
42. Wang, Z.: 2-MOSFET transresistor with extremely low distortion for output reaching supply voltages. *Electron. Lett.* **26**(13), 951–952 (1990)
43. Hassan, H.M.; Soliman, A.M.: Novel CMOS realizations of operational floating current conveyor and applications. *J. Circuits Syst. Comput.* **14**(6), 1113–1143 (2005)
44. Pandey, N.; Nand, D.; Pandey, R.: Generalised operational floating current conveyor based instrumentation amplifier. *IET Circuits Dev. Syst.* **10**(3), 209–219 (2016)



Optimal automatic generation control of two-area power systems with energy storage units under deregulated environment

Yogendra Arya, Narendra Kumar, and S. K. Gupta

Citation: [Journal of Renewable and Sustainable Energy](#) **9**, 064105 (2017);

View online: <https://doi.org/10.1063/1.5018338>

View Table of Contents: <http://aip.scitation.org/toc/rse/9/6>

Published by the [American Institute of Physics](#)

Articles you may be interested in

[Performance of coordinated FACTS and energy storage devices in combined multiarea ALFC and AVR system](#)

[Journal of Renewable and Sustainable Energy](#) **9**, 064101 (2017); 10.1063/1.4986889

[Comparison of different dynamic models for floating wind turbines](#)

[Journal of Renewable and Sustainable Energy](#) **9**, 063304 (2017); 10.1063/1.5002750

[An Alaska case study: Biomass technology](#)

[Journal of Renewable and Sustainable Energy](#) **9**, 061705 (2017); 10.1063/1.4986578

[Wind power project size and component costs: An Alaska case study](#)

[Journal of Renewable and Sustainable Energy](#) **9**, 061703 (2017); 10.1063/1.4986579

[An Alaska case study: Solar photovoltaic technology in remote microgrids](#)

[Journal of Renewable and Sustainable Energy](#) **9**, 061704 (2017); 10.1063/1.4986577

[Preface: Technology and cost reviews for renewable energy in Alaska: Sharing our experience and know-how](#)

[Journal of Renewable and Sustainable Energy](#) **9**, 061501 (2017); 10.1063/1.5017516

Optimal automatic generation control of two-area power systems with energy storage units under deregulated environment

Yogendra Arya,^{1,2,a)} Narendra Kumar,^{2,b)} and S. K. Gupta^{3,c)}

¹Department of Electrical and Electronics Engineering, Maharaja Surajmal Institute of Technology, C-4, Janakpuri, New Delhi 110058, India

²Department of Electrical Engineering, Delhi Technological University, Shahbad Daulatpur, Main Bawana Road, Delhi 110042, India

³Department of Electrical Engineering, Deenbandhu Chhotu Ram University of Science and Technology, Murthal, Sonapat, Haryana 131039, India

(Received 7 May 2017; accepted 4 December 2017; published online 26 December 2017)

An attempt is made in this paper to present the application, design, and performance analysis of a novel optimal controller (OC) for automatic generation control (AGC) of interconnected two-area electrical power systems in a deregulated power environment with energy storage units. The OC is designed via full state vector feedback strategy to carry out the study. Swift acting energy storage units such as redox flow batteries (RFBs) are integrated into the power system models, and their efficacy in boosting AGC performance is executed and compared. Initially, the efficacy of OC is investigated in a restructured two-area single-source thermal system, and then, the study is extended to a proposed more realistic restructured two-area multi-source thermal-hydro-diesel-gas power system. It is observed that OC is able to satisfy the AGC requirement under different power contracts in the open electricity market and shows better performance in comparison to a recently published artificial cooperative search algorithm optimized proportional integral controller. MATLAB simulation results demonstrate the improvements in the dynamic performance of the system in the presence of RFB. Sensitivity analysis reveals the robustness of OC under ample variations in the system parameters, initial loading and size and positions of uncontracted load power demands. *Published by AIP Publishing.* <https://doi.org/10.1063/1.5018338>

NOMENCLATURE

a_i, c_i	constants of the valve positioner
b_i	time constant of the valve positioner
B_i	frequency bias constant ($= \beta_i$)
D_i	system damping constant
F^0	nominal frequency
H_i	power system inertia constant
i	subscript referring to area- i ($i = 1, 2$)
K_{Pi}	power system gain
K_{ri}	high pressure thermal turbine power fraction
P_{ri}	rated area capacity
$R_{t/h/d/gi}$	governor regulation parameter
T_{CDi}	gas turbine compressor discharge volume time constant
T_{CRi}	gas turbine combustion reaction time delay

^{a)}Email: mr.y.arya@gmail.com

^{b)}Email: dnk_1963@yahoo.com

^{c)}Email: drskgupta.ee@dcrustrm.org

T_{Fi}	gas turbine fuel time constant
T_{ti}	thermal turbine time constant
T_{gdi}	diesel speed governor time constant
T_{GHi}	hydro turbine speed governor main servo time constant
T_{gi}	thermal speed governor time constant
T_{Pi}	power system time constant
T_{RHi}	hydro turbine speed governor transient droop time constant
T_{ri}	reheat thermal turbine time constant
T_{Ri}	hydro turbine speed governor reset time
T_{tdi}	diesel engine time constant
T_{Wi}	nominal starting time of water in penstock
X_i	gas turbine speed governor lead time constant
Y_i	gas turbine speed governor lag time constant
$2\pi T_{12}$	tie-line power synchronizing coefficient
α_{12}	area size ratio coefficient
β_i	area frequency response characteristic
ΔP_{FCi}	incremental change in the internal state of the fuel system and the combustor of the gas turbine
ΔP_{Rti}	incremental change in thermal turbine output
$\Delta P_{Tt/hi}$	incremental change in the internal state of the thermal/hydro turbine
ΔP_{VPi}	incremental change in output of the valve positioner of the gas turbine
$\Delta X_{h/RHi}$	incremental change in the internal state of the mechanical hydraulic governor
ΔX_{gi}	incremental change in the internal state of the gas turbine speed governor
$\Delta X_{t/di}$	incremental change in thermal/diesel governor output

I. INTRODUCTION

Automatic generation control (AGC) is one of the crucial control issues in electric power system operation and control. Because of incessant inequality between total generation and power demands claimed, frequency, generation, and tie-line power digress from their pre-determined values. Consequently, it is necessary to hold the system integrity by matching generation and load demands plus associated losses in real time. A departure in frequency from its nominal range may directly impact the reliability of the power system run. A significant divergence in frequency may lead the system to an unstable state. So, hasty preservation of the scheduled values of frequency and tie-line power exchanges with neighboring control areas are the two chief intentions of an AGC scheme.¹ Rapid acting energy storage units, such as redox flow batteries (RFBs), can proficiently damp out frequency and tie-line power fluctuations caused by small load perturbations in a power system, as they provide the source of active power in addition to the kinetic energy of the generator rotor coupled with the turbine. RFBs recently have emerged as one of the most promising storage technologies to decipher a wide spectrum of operational problems faced by contemporary power systems. An array of articles extensively explore the importance and effects of RFB on the dynamic performance of traditional and restructured power generating systems.¹⁻⁵

In traditional picture, control of generation, transmission, and distribution of electric power are possessed by a single monopolistic entity termed as vertically integrated utility (VIU) which sells power at regulated tariff. Since some decades, with the appearance of deregulation, the VIU configuration no longer exists and several independent entities like distribution companies (DISCOs), generation companies (GENCOs), transmission companies (TRANSCOs), and independent system operators (ISOs) are introduced to create competition among market players.^{4-10,15-18} Due to the availability of a number of GENCOs and DISCOs in the deregulated environment, a DISCO has the freedom to sign contract with any GENCO in its own or other pool for the transaction of electrical power. Due to this fact, in an open market scenario, consumers are supposed to buy power at reduced rates. ISO, a disinterested entity, is accountable

for security and stability of the power system. It offers various ancillary services, out of them frequency regulation or AGC is the one.

In addition to the impact of energy storage units in power systems, the control strategy adopted for AGC influences the system performance notably. To tackle the AGC issue in the restructured system, researchers have proposed various conventional and intelligent methodologies such as the artificial cooperative search algorithm (ACSA),¹ opposition-based harmonic search (OHS),⁴ gradient Newton algorithm,⁶ active disturbance rejection,⁸ ANFIS,¹⁰ and fruit fly optimization (FFO).¹⁸ However, optimal control strategies implemented on restructured systems show superior and robust dynamic performance compared to other methods.^{5,7,9,15–17}

Most of the AGC works in the deregulated regime reported in the literature show simulations of single type of sources i.e., thermal or hydro plants in a control area.^{1,6–10} However, in modern power generation picture, a control area usually has diversity of generating sources such as thermal, gas, diesel, nuclear, and renewable, and hence, denoting a control area only by single type of sources may not be a good AGC design of study. Recently, some researchers have studied the AGC of traditional power systems considering photovoltaic-diesel,¹¹ thermal-hydro-wind/diesel,¹² and thermal-hydro-gas.^{13,14} However, they did not consider the AGC scheme under a deregulated scenario. In a deregulated power system set-up, some multi-source AGC schemes prevalent in the literature are thermal-hydro-gas,^{4,5,15} thermal-hydro,¹⁶ thermal-hydro/gas,¹⁷ and thermal-hydro-nuclear.¹⁸ However, no research is abundant in the literature about the incorporation of thermal, hydro, diesel, and gas diverse sources in a restructured configured system.

Literature discussion indicates that scarce articles have been published so far incorporating the RFB in AGC of restructured systems.^{1,4,5} Hence, in this paper, the impact of RFB is analyzed to palliate the fluctuations in frequency, generation, and tie-line power signals at step load demands under AGC operation in two-area electric power generating systems interconnected in the deregulated mode. Due to the simplicity in implementation and robust recital, the optimal controller (OC) is effectively designed and applied in AGC of two-area deregulated systems. Moreover, the present study is the extension of the work done by the authors in Ref. 5. Initially, OC is designed on a two-area restructured thermal system, and the superiority of OC is demonstrated over a recently published artificial cooperative search algorithm (ACSA) based proportional integral (PI) controller. Further, a more realistic interconnected power system with multi-source power generations is proposed for AGC in the deregulated power environment. Each area of the proposed system includes the more feasible multi-source combination of reheat thermal, hydro, diesel, and gas generating units. OC is designed to conduct an extensive investigation of AGC, incorporating all possible power transactions taking place in a deregulated power market. State space models of the proposed multi-source and existing thermal restructured systems are utilized for OC design, considering all the interface signals and possible contracts. The MATLAB simulation outcomes are legitimated by the calculated values of generations and tie-line powers. A sensitivity analysis is performed to divulge the robustness of OC under a broad deviation in the system loading, parameters, and uncontracted load power demands.

II. SYSTEM MODELS

Investigations are carried out on two-area single-source thermal and proposed two-area multi-source thermal-hydro-diesel-gas electric power systems in the deregulated power environment. The thermal system contains one reheat unit and one non-reheat unit in each area, while each area of the proposed multi-source system is equipped with reheat thermal, mechanical governor based hydro, diesel, and gas power generating units. Two and four DISCOs are considered in each area of thermal and multi-source systems, respectively. The schematic/transfer function model of the thermal system with RFB installed in both areas is shown in Fig. 1, whereas the model of the multi-source system is revealed in Fig. 4. The nominal parameters of the systems are depicted in the Appendix. MATLAB software version 7.5.0 (R2007b) is used for SIMULINK models and workspace programs to obtain various system dynamic responses.

Each area of the power systems under study comprises a speed governor, turbine, generator, and load, as shown in Figs. 1(b) and 4(b). To transform the frequency domain analysis in

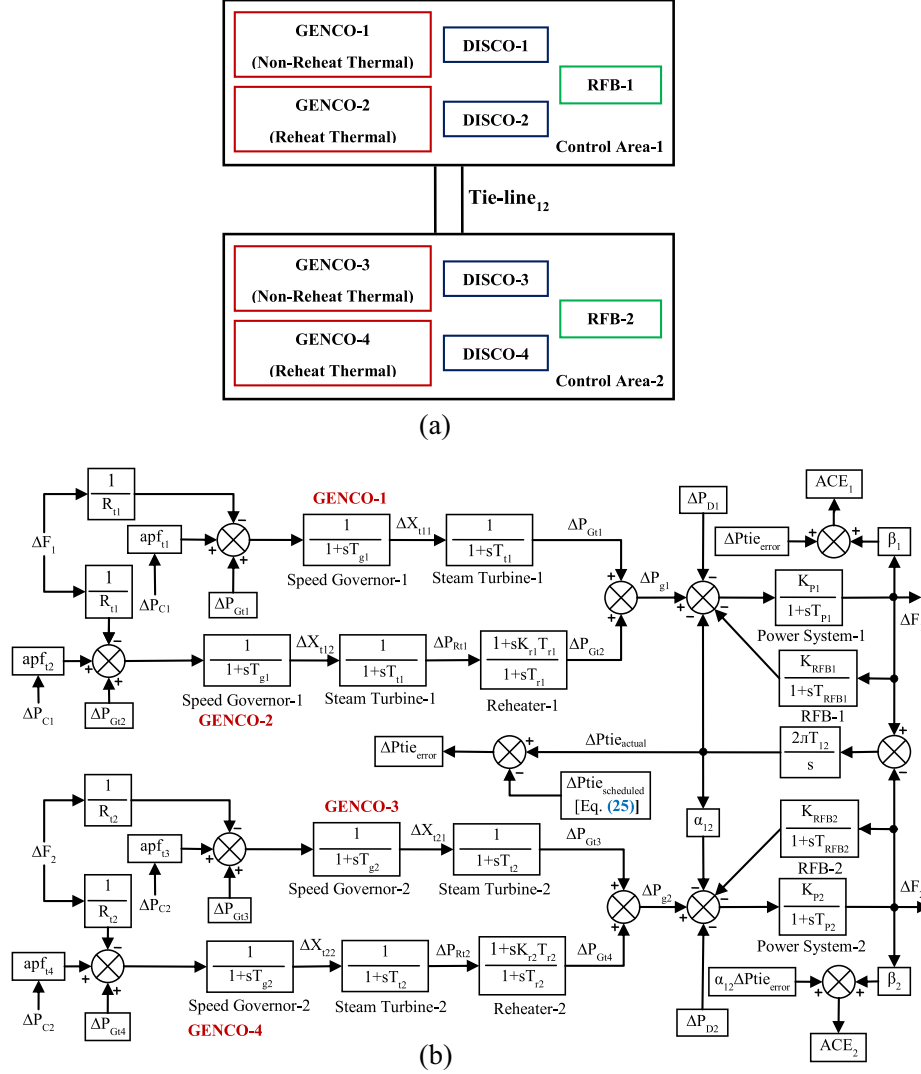


FIG. 1. (a) Schematic demonstration of a two-area interconnected thermal system in the deregulated environment. (b) Block diagram of the restructured two-area power system consisting of identical thermal plants in each area.

an easier form, transfer function blocks are employed to model every component of both the power system models. The transfer functions of different blocks used in each area of the two-area single-source restructured thermal power system are stated as follows:^{1,5}

The generator and load or power system are represented by the transfer function

$$G_{PS} = \frac{K_P}{1 + sT_P}. \quad (1)$$

The speed governor transfer function

$$G_{TG} = \frac{1}{1 + sT_g}. \quad (2)$$

Steam turbine transfer function

$$G_{TT} = \frac{1}{1 + sT_t}. \quad (3)$$

Reheater transfer function

$$G_{TTr} = \frac{1 + sK_r T_r}{1 + sT_r}. \quad (4)$$

Each area of the two-area multi-source restructured thermal-hydro-diesel-gas power system owns four generating units. For the system, the transfer functions of the power system, thermal speed governor, steam turbine, and reheater have been expressed in Eqs. (1)–(4). However, the transfer function of the reheater expressed here is given in the split form to simplify the state space model of the system. Hence, Eq. (4) will change to Eq. (5) for thermal units as⁵

$$G_{TTr} = \frac{1 - K_r}{1 + sT_r} + K_r. \quad (5)$$

The transfer function blocks used for the hydro unit are given as follows:^{5,13}

The mechanical hydraulic governor transfer function in the split form

$$G_{HG} = \left[\frac{1}{1 + sT_{RH}} \right] \left[\left(\frac{1 - \frac{T_R}{T_{GH}}}{1 + sT_{GH}} \right) + \frac{T_R}{T_{GH}} \right]. \quad (6)$$

The hydro turbine transfer function in the split form

$$G_{HT} = \frac{3}{1 + 0.5sT_W} - 2. \quad (7)$$

The transfer function blocks used for the diesel unit are given as follows:¹¹

Diesel governor transfer function

$$G_{DG} = \frac{1}{1 + sT_{gd}}. \quad (8)$$

Diesel generator transfer function

$$G_{DGen} = \frac{1}{1 + sT_{td}}. \quad (9)$$

The transfer function blocks used for the gas unit are given as follows:^{5,13,20}

Gas turbine speed governor transfer function in the split form

$$G_{GG} = \frac{1 - \frac{X}{Y}}{1 + sY} + \frac{X}{Y}. \quad (10)$$

Valve positioner transfer function

$$G_{VP} = \frac{a}{c + sb}. \quad (11)$$

Fuel system and combustor transfer function in the split form

$$G_{FC} = \frac{1 + \frac{T_{CR}}{T_F}}{1 + sT_F} - \frac{T_{CR}}{T_F}. \quad (12)$$

Gas turbine transfer function

$$G_{GT} = \frac{1}{1 + sT_{CD}}. \quad (13)$$

Each area of the two-area systems has four inputs such as the change in controller input (ΔP_C) via the area control error (ACE) participation factor (apf) block, change in the load power demand (ΔP_D), change in GENCO output (ΔP_G), and change in tie-line power (ΔP_{tie_actual}) and two outputs such as the change in generator frequency ΔF and ACE. The GENCOs constantly regulate their power outputs to meet the contracted/uncontracted load demand of DISCOs. In the normal condition, the area generation (ΔP_g) maintains balance with the area load demand (ΔP_D). The divergence between these powers will cause deviation in system frequency and tie-line power flows in negative or positive sides. The list of symbols used in transfer function block diagrams is provided and explained in the Nomenclature. The detailed description of the models and derivation of the transfer function are provided in Refs. 11, 19, and 20.

III. DESIGN OF THE OPTIMAL CONTROLLER

The optimal controller (OC) is designed based on the state vector feedback strategy utilizing the performance index minimization criterion.^{5,7,9,13,16,17} The control problem is to design OC feedback gain matrix K of appropriate dimensions. According to optimal control theory, the control law given by

$$U = -KX \quad (14)$$

is used to minimize a performance index

$$J = \int_0^\infty \frac{1}{2} [X^T Q X + U^T R U] dt, \quad (15)$$

where J is always a scalar. The implementation of Pontryagin's minimum principle for the infinite time problem results in the subsequent algebraic Riccati equation (ARE)²¹

$$A^T P + P A - P B R^{-1} B^T P + Q = 0, \quad (16)$$

where P is the unique positive semi-definite matrix solution to the ARE, Q is a positive semi-definite symmetric state cost weighting matrix, and R is a positive definite symmetric control cost weighting matrix. Both Q and R are square and symmetric diagonal matrices of appropriate dimensions. The dimensions of Q and R matrices depend on the number of state and control variables of the system, respectively. The elements of Q and R in OC are important components as they are largely responsible for the dynamic performance of the system and hence are essentially the tuning parameters for OC. The choice of selection of these elements allows the relative weighting of individual state variables and individual control inputs, respectively. The choice of Q and R influences largely the feedback gain matrix K which is responsible for the closed loop system outcome. The larger the values of Q and R , the more penalized the state and control signals, respectively. Selecting a large value for R means trying to stabilize the system with less (weighted) energy, which is termed as the expensive control approach, while opting a small value for R means not penalizing the control signal, i.e., cheap control approach. Correspondingly, choosing a large value for Q means attempting to stabilize the system with the least probable deviations in the states, and large Q implies less worry about the deviations in the states. There should be a trade-off between the two, which should be maintained to get the desired solution.

In the current study, the selection of parameters of matrices Q and R is based on the consideration of giving equal importance to all the system states and control variables participating in the control action. Therefore, the structures of Q and R are considered as the identity (I) matrices of dimensions 29×29 and 2×2 , respectively, for the multi-source system. For the

single-source power system, the Q matrix is I having dimensions of 15×15 and the R matrix is I having dimensions of 2×2 .

The solution of Eq. (16) yields a positive definite symmetric matrix P , and the optimal control law is given by

$$U \text{ or } \Delta P_C = -R^{-1}B^T P X. \quad (17)$$

Hence, the required optimal feedback gain matrix is given by

$$K = R^{-1}B^T P. \quad (18)$$

The acceptable solution of K is that for which the system remains stable and eigenvalues of the closed loop system should have negative real parts.

IV. STATE SPACE MODELING

The state space model of an interconnected power system is characterized by the following standard state space differential equations:

$$\dot{X} = AX + BU + \Gamma P_D, \quad (19)$$

$$Y = CX, \quad (20)$$

where X , U , P_D , and Y are the state, control, disturbance, and output vectors with dimensions 15×1 , 2×1 , 6×1 , and 15×1 for the single-source system, respectively, and 29×1 , 2×1 , 10×1 , and 29×1 for the multi-source system, respectively. A , B , C , and Γ are system, input distribution, output, and disturbance distribution matrices having dimensions of 15×15 , 15×2 , 15×15 , and 15×6 for the single-source system, respectively, and 29×29 , 29×2 , 29×29 , and 29×10 for the multi-source system, respectively.

In the application of optimal control theory, the term ΓP_D in Eq. (19) will vanish by redefining the states and controls in terms of their steady state values taking place after the disturbance. Hence, Eq. (20) will not alter; however, Eq. (19) will change as follows:

$$\dot{X} = AX + BU, \quad X(0) = -X_{ss}, \quad (21)$$

where new state vector X is equal to the old state vector minus its steady state value X_{ss} . In the present work, an optimal controller based on full-state vector feedback control is designed by employing all the states of the systems which are assumed to be available for the measurement. The structures of X , U , and P_D vectors for thermal and multi-source systems are selected as

State vectors:

Thermal system

$$[X] = \left[\Delta F_1 \Delta P_{Gt1} \Delta P_{Gt2} \Delta P_{Rt1} \Delta X_{t11} \Delta X_{t12} \Delta F_2 \Delta P_{Gt3} \Delta P_{Gt4} \Delta P_{Rt2} \Delta X_{t21} \Delta X_{t22} \Delta P_{tie_actual} \right. \\ \left. \int ACE_1 dt \int ACE_2 dt \right]^T.$$

Multi-source system

$$[X] = \left[\Delta F_1 \Delta F_2 \Delta P_{tie_actual} \Delta P_{Tt1} \Delta P_{Rt1} \Delta X_{t1} \Delta P_{Th1} \Delta X_{h1} \Delta X_{RH1} \Delta P_{Gd1} \Delta X_{d1} \Delta P_{Gg1} \Delta P_{FC1} \Delta P_{VP1} \Delta X_{g1} \right. \\ \left. \Delta P_{Tt2} \Delta P_{Rt2} \Delta X_{t2} \Delta P_{Th2} \Delta X_{h2} \Delta X_{RH2} \Delta P_{Gd2} \Delta X_{d2} \Delta P_{Gg2} \Delta P_{FC2} \Delta P_{VP2} \Delta X_{g2} \int ACE_1 dt \int ACE_2 dt \right]^T.$$

Control vectors:

Thermal and multi-source systems

$$[U] = [\Delta P_{C1} \Delta P_{C2}]^T \text{ and}$$

Disturbance vectors:

Thermal system

$$[P_D] = [\Delta P_{L1} \Delta P_{L2} \Delta P_{L3} \Delta P_{L4} \Delta P_{UC1} \Delta P_{UC2}]^T.$$

Multi-source system

$$[P_D] = [\Delta P_{L1} \Delta P_{L2} \Delta P_{L3} \Delta P_{L4} \Delta P_{L5} \Delta P_{L6} \Delta P_{L7} \Delta P_{L8} \Delta P_{UC1} \Delta P_{UC2}]^T,$$

where ΔP_C is the area control signal, ΔP_L is the power demand of a DISCO, and ΔP_{UC} is the uncontracted power demand in a control area. The other abbreviations used for various states stated earlier are shown in Figs. 1(b) and 4(b) and are described in the Nomenclature.

V. AGC IN THE DEREGULATED SCENARIO

To advance the effectiveness of operation and control of the existing traditional power system scenario, deregulation principles are commenced into the new power system framework. In the deregulated market, consumers or DISCOs have chances to buy power at reduced rates due to the competitive environment generated among various GENCOs. The GENCOs may or may not contribute in the AGC task, and DISCOs have the freedom to ink contracts with any GENCOs of their own pool termed as poolco transaction or any other control area which is termed as bilateral transaction.¹ The GENCOs and DISCOs negotiate various combinations of poolco/bilateral contracts, and they have to submit the agreement obligatorily to ISO to seek approval.⁴⁻⁶ The contracts among GENCOs and DISCOs can be realized successfully via the DISCO participation matrix (DPM) and the area control error participation factor (apf) as proposed by Donde *et al.*⁶ The DPM clarifies the details of the contracts signed between DISCOs and GENCOs. The row and columns of the DPM stand for the number of GENCOs and DISCOs, respectively. The two-area restructured thermal system with two numbers of GENCOs and two numbers of DISCOs in each area [Fig. 1(a)] is represented by the following equation:

$$DPM = \begin{bmatrix} cpf_{11} & cpf_{12} & cpf_{13} & cpf_{14} \\ cpf_{21} & cpf_{22} & cpf_{23} & cpf_{24} \\ cpf_{31} & cpf_{32} & cpf_{33} & cpf_{34} \\ cpf_{41} & cpf_{42} & cpf_{43} & cpf_{44} \end{bmatrix}. \quad (22)$$

The entries of DPM are termed as the contract participation factor (cpf), which designates a fraction of total power contracted by a DISCO with a GENCO. Consequently, the sum of the entries of a column of DPM is unity. The diagonal entries of the DPM correspond to the poolco contracts, and the off diagonal entries correspond to the bilateral contracts.

The total load demand of DISCOs in an area is represented by ΔP_D . For the thermal system

$$\Delta P_{D1} = \Delta P_{L1} + \Delta P_{L2} + \Delta P_{UC1}, \quad (23)$$

$$\Delta P_{D2} = \Delta P_{L3} + \Delta P_{L4} + \Delta P_{UC2}. \quad (24)$$

The scheduled steady state power flow on the tie-line is given as^{1,4-6}

$$\begin{aligned}
\Delta P_{\text{tie_scheduled}} &= (\text{Demand of DISCOs of area-2 from GENCOs in area-1}) \\
&\quad - (\text{Demand of DISCOs of area-1 from GENCOs in area-2}) \\
&= (\text{cpf}_{13} + \text{cpf}_{23})\Delta P_{L3} + (\text{cpf}_{14} + \text{cpf}_{24})\Delta P_{L4} - (\text{cpf}_{31} + \text{cpf}_{41})\Delta P_{L1} \\
&\quad - (\text{cpf}_{32} + \text{cpf}_{42})\Delta P_{L2}.
\end{aligned} \tag{25}$$

The actual tie-line power flow signal shown in Figs. 1 and 4 is stated by

$$\Delta P_{\text{tie_actual}} = \frac{2\pi T_{12}}{s} (\Delta F_1 - \Delta F_2). \tag{26}$$

The tie-line power flow error at any instant is given by¹⁰

$$\Delta P_{\text{tie_error}} = \Delta P_{\text{tie_actual}} - \Delta P_{\text{tie_scheduled}}. \tag{27}$$

$\Delta P_{\text{tie_error}}$ disappears in the steady state when $\Delta P_{\text{tie_actual}}$ reaches $\Delta P_{\text{tie_scheduled}}$. The $\Delta P_{\text{tie_error}}$ signal is used to create the particular area control error (ACE) signal similar to the traditional scenario

$$\text{ACE}_1 = \beta_1 \Delta F_1 + \Delta P_{\text{tie_error}}, \tag{28}$$

$$\text{ACE}_2 = \beta_2 \Delta F_2 + \alpha_{12} \Delta P_{\text{tie_error}}. \tag{29}$$

The ACE signal acts as the input to OC, while the control signal of the controller is to be distributed among GENCOs of the area as per their participation in the AGC task. Coefficients that distribute the control signal to GENCOs are termed as apfs. In a control area, the sum of apfs is equal to 1. Hence, for the thermal system, $\text{apf}_{t1} + \text{apf}_{t2} = \text{apf}_{t3} + \text{apf}_{t4} = 1$.

VI. LINEARIZED MODEL OF RFB FOR AGC

Redox flow batteries (RFB) are rechargeable batteries with an outstanding short-time overload capability. To suppress the oscillations, an active power source with a quick response such as RFB can be expected to be the most effective one during dynamic periods in a power system. They are found to be better than the other energy storage units such as superconducting magnetic energy storage (SMES) because of their normal temperature operation, small losses, and long service life.¹

They offer the following features different from other conventional power storage batteries. They are not aged by fast/frequent charging and discharging deviations, the depth of discharge does not affect their lifetime, and they can operate for decades. The cell and tank sections can be separated to provide flexibility in installations, and because of that, the output can easily be tailored according to the requisite output and capacity via increasing/decreasing the numbers of electrolytic tanks. The plastic tanks employed for holding the electrolytes have long life. The charged electrolyte is stored in detached +ve and -ve tanks, and hence, no self-discharge takes place during extended idling nor needed auxiliary power while stoppage. The electronics and software to manage the RFB system are upgradable like any computer.

The block diagram of the RFB system is shown in Fig. 2. The reactions that occur in the battery cell during charging and discharging are also shown in Fig. 2. RFB stores energy by utilizing redox couples, V^{2+}/V^{3+} in the -ve and V^{4+}/V^{5+} in the +ve half cells stored in mild sulfuric acid solutions, i.e., electrolytes. During the charging/discharging, H^+ ions are exchanged between the two electrolyte tanks via the hydrogen ion permeable polymer membrane. During normal load conditions, RFBs get charged, while during the peak or sudden load demands, they deliver the energy back to the system instantly. AC/DC or DC/AC conversions are performed by a dual converter as shown in Fig. 2. RFBs provide an alternative solution to the problem of mismatch of power generation and sudden load requirements. Hence, they can be suggested to be incorporated in the power system to improve AGC performance and to ensure enhanced

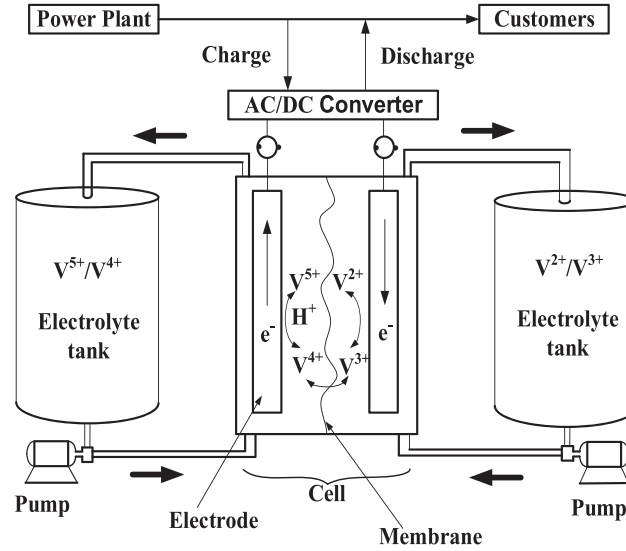


FIG. 2. General block diagram of RFB in AGC.

power quality. In this work, the transfer function model of RFB represented by first order lag is given as^{1,3,5}

$$G_{\text{RFB}}(s) = \frac{K_{\text{RFB}}}{1 + sT_{\text{RFB}}}, \quad (30)$$

where K_{RFB} is the gain and T_{RFB} is the time constant of RFB. In the present study, RFB is supposed to be available in both areas of the restructured two-area systems and the ΔF_i signal is directly used as the input command for the RFB in AGC.^{3,5}

VII. SIMULATION RESULTS AND ANALYSIS

A. Two-area single-source system

The restructured two-area multi-unit thermal system with one non-reheat (GENCO-1 and GENCO-3) and one reheat (GENCO-2 and GENCO-4) generating units in each area is taken from Ref. 1 to compare the suggested method with the existing one. The schematic diagram of the two-area power system interconnected via a tie-line in the deregulated environment with two GENCOs, two DISCOs, and one RFB unit in each area is presented in Fig. 1(a). However, the detailed system is shown in Fig. 1(b). The system with Scenario-III in Ref. 1 is considered, where all four DISCOs individually demand a power (ΔP_{Li}) of 10% in the bilateral contract with contract violation. Additionally, DISCO-1 demands 10% uncontracted power, i.e., $\Delta P_{UC1} = 0.1$ per unit megawatt (puMW). So, the total power demanded in area-1 will be $\Delta P_{D1} = 0.3$ puMW and $\Delta P_{D2} = 0.2$ puMW. The DPM is given as follows:

$$\text{DPM} = \begin{bmatrix} 0.5 & 0.25 & 0 & 0.3 \\ 0.2 & 0.25 & 0 & 0 \\ 0 & 0.25 & 1 & 0.7 \\ 0.3 & 0.25 & 0 & 0 \end{bmatrix}. \quad (31)$$

It is implicit that all four GENCOs participate in AGC as per $\text{apf}_{t1} = 0.75$, $\text{apf}_{t2} = 0.25$, and $\text{apf}_{t3} = \text{apf}_{t4} = 0.5$. The optimized feedback gain matrix K of OC for the system with and without RFB is given in Table I. Utilizing the system data given in the Appendix and K , the system dynamic responses with/without RFB are shown in Fig. 3. To compare the effectiveness of OC

TABLE I. Optimal feedback gain matrices K for the restructured thermal system.

Without RFB	[1.5095	1.8973	3.3580	-0.7078	0.4254	0.2171	-0.3422	-0.3352	-0.4154	0.0389	-0.0659
RFB	-0.0330	0.5591	3.1619	-0.0460;	-0.2825	-0.2841	-0.3521	0.0329	-0.0565	-0.0283	1.4425
	1.9013	3.5310	-0.7896	0.4346	0.2223	-0.4257	0.0460	3.1619]			
With RFB	[1.8472	2.3397	3.8991	-0.7556	0.5085	0.2587	-0.5125	-0.4423	-0.5471	0.0508	-0.0840
	-0.0421	5.6398	7.9046	-0.1298;	-0.4644	-0.3864	-0.4736	0.0422	-0.0721	-0.0361	1.7479
	2.3262	4.0616	-0.8409	0.5173	0.2638	-5.4095	0.1298	7.9046]			

with the recently published artificial cooperative search algorithm (ACSA) optimized PI controller,¹ the results with RFB due to the ACSA based PI controller are also incorporated in Fig. 3. Critical investigations of all the responses, especially Figs. 3(a) and 3(b), without RFB confess that OC shows somewhat inferior performance compared to the ACSA tuned PI controller

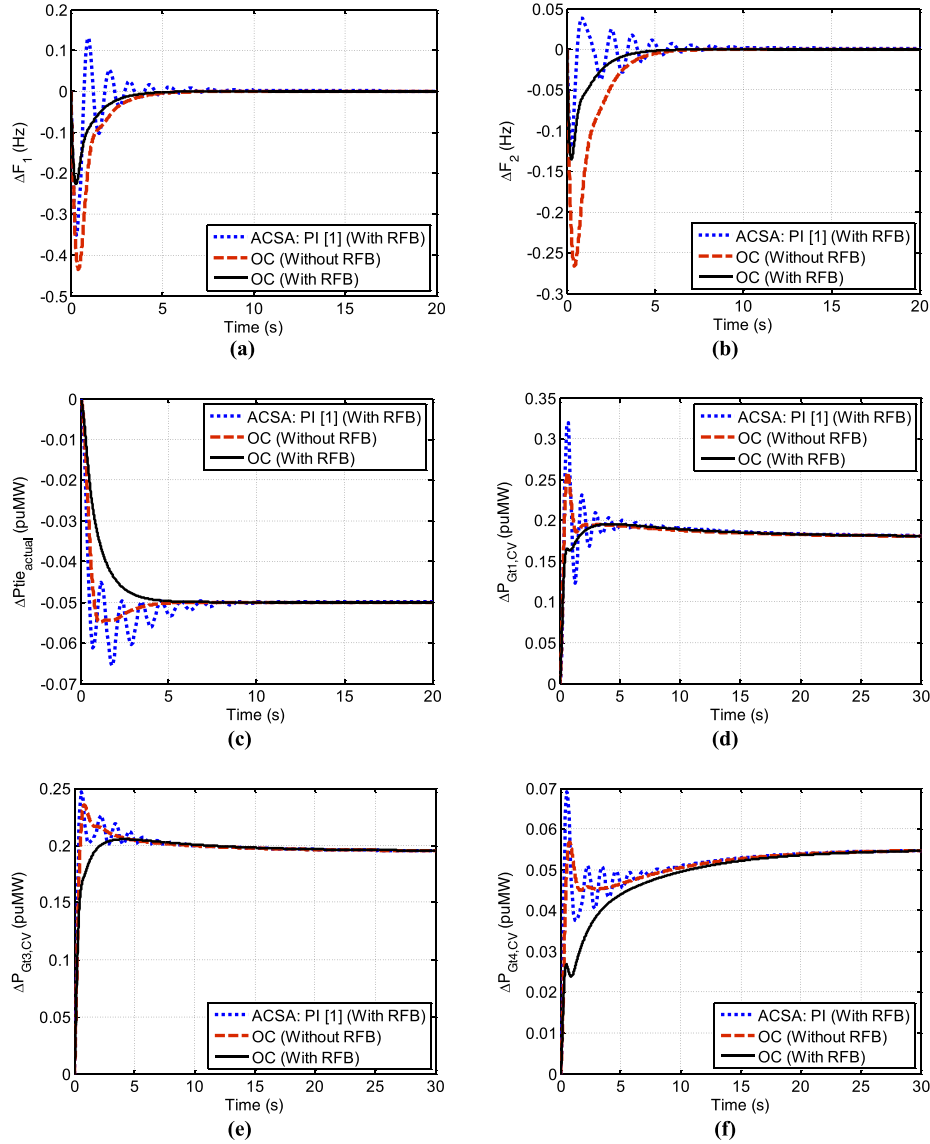


FIG. 3. Dynamic responses of the restructured two-area single-source thermal system with different controllers (a) ΔF_1 , (b) ΔF_2 , (c) ΔP_{tie_actual} , (d) $\Delta P_{G1,CV}$, (e) $\Delta P_{G3,CV}$, and (f) $\Delta P_{G4,CV}$.

(with RFB). However, the performance of OC with RFB is far superior to that of the PI controller with RFB in terms of shorter settling time, peak overshoots/undershoots, and damped out oscillations. In the steady state, the deviations in frequencies of both areas remain zero, while contracted generations of different GENCOs can be defined using the following equation:

$$\Delta P_{Gti} = \text{cpf}_{i1} \Delta P_{L1} + \text{cpf}_{i2} \Delta P_{L2} + \text{cpf}_{i3} \Delta P_{L3} + \text{cpf}_{i4} \Delta P_{L4}. \quad (32)$$

Hence, in the steady state, $\Delta P_{Gt1} = 0.105$ puMW, $\Delta P_{Gt2} = 0.045$ puMW, $\Delta P_{Gt3} = 0.195$ puMW, and $\Delta P_{Gt4} = 0.055$ puMW. However, as per industrial practice, an uncontracted demand (ΔP_{UC1}) of 10% made by DISCO-1 must be supplied by area-1 GENCOs based on their respective apfs. Therefore, under contract violation (CV), $\Delta P_{Gt1,CV} = \Delta P_{Gt1} + \text{apf}_{t1} \Delta P_{UC1} = 0.105 + 0.075 = 0.18$ puMW and $\Delta P_{Gt2,CV} = 0.045 + 0.025 = 0.07$ puMW. However, $\Delta P_{Gt3,CV} = \Delta P_{Gt3}$ and $\Delta P_{Gt4,CV} = \Delta P_{Gt4}$. The simulation results of power outputs of three GENCOs shown with/without RFB in Figs. 3(d)–3(f) match with the above desired values in the steady state. Further, Fig. 3(c) shows $\Delta P_{tie,actual} = -0.05$ puMW which in the steady state is equal to $\Delta P_{tie,scheduled}$ as defined by Eq. (25).

The closed loop system modes of the ACSA tuned PI controller with RFB and OC with/without RFB are shown in Table II. It is observed that all the system modes lie in the left half of the “s” plane, and hence, the system is stable with ACSA¹ and OC with/without RFB. It is also revealed that most of the system modes due to OC with RFB are highly negative compared to the ACSA tuned PI controller with RFB and OC without RFB. Hence, the power system with OC incorporating RFB in control areas shows significantly higher stability margins with excellent damping in comparison to that of the ACSA method.

B. Two-area multi-source system

To confirm the capability of the optimal controller (OC) to cope with the multi-source system, the study is further extended to a restructured two-area multi-source thermal-hydro-diesel-gas system as shown in Fig. 4. The schematic diagram of the two-area power system interconnected via a tie-line in the deregulated environment with four GENCOs, four DISCOs, and one RFB unit in each control area is presented in Fig. 4(a). In the power system model, GENCOs 1 and 5 are single reheat thermal plants, GENCOs 2 and 6 are mechanical governor based hydro plants, GENCOs 3 and 7 are diesel plants, and GENCOs 4 and 8 are gas plants. The detailed transfer function model of the power system model is shown in Fig. 4(b). The effectiveness of OC is tested in five cases related to three possible transactions available in an open market environment.

TABLE II. Pattern of closed-loop system modes for the restructured thermal system.

OC (With RFB)	ACSA: PI ¹ (With RFB)	OC (Without RFB)
-14.3713	-14.4100	-13.6904
-14.2482	-14.6690	-13.6473
-4.3210 ± 6.0578i	-0.4735 ± 5.6195i	-2.1858 ± 4.7822i
-4.4733 ± 5.6826i	-1.2445 ± 4.8690i	-2.5231 ± 4.1187i
-2.2033	-1.6722	-1.9202
-1.0103	-0.5479	-0.9617
-0.8994	-0.4397	-0.8537
-0.1143	-0.1143	-0.1143
-0.1334	-0.1388	-0.1334
-12.5000	-12.5000	-12.5000
-12.5000	-12.5000	-12.5000
-3.3333	-3.3333	-3.3333
-3.3333	-3.3333	-3.3333



FIG. 4. (a) Schematic demonstration of a two-area interconnected multi-source power system in the deregulated environment. (b) Block diagram of the restructured two-area power system consisting of identical thermal-hydro-diesel-gas plants in each area.

Case 1: poolco based transactions—In this case, DISCOs negotiate contracts with GENCOs of their own control area.^{1,4-6,15-18} It is assumed that the load is demanded by DISCOs in area-1 only. Let $\Delta P_{L1} = \Delta P_{L2} = \Delta P_{L3} = \Delta P_{L4} = 0.05$ puMW. The related DPM is given as follows:

$$\text{DPM} = \begin{bmatrix} 0.3 & 0.5 & 0.5 & 0.5 & 0 & 0 & 0 & 0 \\ 0.4 & 0.2 & 0.2 & 0.2 & 0 & 0 & 0 & 0 \\ 0.1 & 0.1 & 0.1 & 0.1 & 0 & 0 & 0 & 0 \\ 0.2 & 0.2 & 0.2 & 0.2 & 0 & 0 & 0 & 0 \\ 0 & 0 & 0 & 0 & 0 & 0 & 0 & 0 \\ 0 & 0 & 0 & 0 & 0 & 0 & 0 & 0 \\ 0 & 0 & 0 & 0 & 0 & 0 & 0 & 0 \\ 0 & 0 & 0 & 0 & 0 & 0 & 0 & 0 \end{bmatrix}. \quad (33)$$

Note that DISCOs of area-1 do not demand power from GENCOs of area-2; hence, the corresponding cpfs of DPM are taken to be zero. For all cases, ACE participation factors are selected as $\text{apf}_{t1} = 0.5$, $\text{apf}_{h1} = 0.2$, $\text{apf}_{d1} = 0.1$, $\text{apf}_{g1} = 0.2$, $\text{apf}_{t2} = 0.25$, $\text{apf}_{h2} = 0.25$, $\text{apf}_{d2} = 0.25$, and $\text{apf}_{g2} = 0.25$. Eqs. (25) and (32) stated for $\Delta P_{\text{tie_scheduled}}$ and steady state power generations, respectively, will be modified for the multi-source system as

$$\begin{aligned} \Delta P_{\text{tie_scheduled}} = & (\text{cpf}_{15} + \text{cpf}_{25} + \text{cpf}_{35} + \text{cpf}_{45})\Delta P_{L5} + (\text{cpf}_{16} + \text{cpf}_{26} + \text{cpf}_{36} + \text{cpf}_{46})\Delta P_{L6} \\ & + (\text{cpf}_{17} + \text{cpf}_{27} + \text{cpf}_{37} + \text{cpf}_{47})\Delta P_{L7} + (\text{cpf}_{18} + \text{cpf}_{28} + \text{cpf}_{38} + \text{cpf}_{48})\Delta P_{L8} \\ & - (\text{cpf}_{51} + \text{cpf}_{61} + \text{cpf}_{71} + \text{cpf}_{81})\Delta P_{L1} - (\text{cpf}_{52} + \text{cpf}_{62} + \text{cpf}_{72} + \text{cpf}_{82})\Delta P_{L2} \\ & - (\text{cpf}_{53} + \text{cpf}_{63} + \text{cpf}_{73} + \text{cpf}_{83})\Delta P_{L3} - (\text{cpf}_{54} + \text{cpf}_{64} + \text{cpf}_{74} + \text{cpf}_{84})\Delta P_{L4}, \end{aligned} \quad (34)$$

$$\begin{aligned} \Delta P_{\text{Gti}} = & \text{cpf}_{i1}\Delta P_{L1} + \text{cpf}_{i2}\Delta P_{L2} + \text{cpf}_{i3}\Delta P_{L3} + \text{cpf}_{i4}\Delta P_{L4} + \text{cpf}_{i5}\Delta P_{L5} + \text{cpf}_{i6}\Delta P_{L6} \\ & + \text{cpf}_{i7}\Delta P_{L7} + \text{cpf}_{i8}\Delta P_{L8}, \quad i = 1, 5, \end{aligned} \quad (35)$$

$$\begin{aligned} \Delta P_{\text{Ghi}} = & \text{cpf}_{i1}\Delta P_{L1} + \text{cpf}_{i2}\Delta P_{L2} + \text{cpf}_{i3}\Delta P_{L3} + \text{cpf}_{i4}\Delta P_{L4} + \text{cpf}_{i5}\Delta P_{L5} + \text{cpf}_{i6}\Delta P_{L6} \\ & + \text{cpf}_{i7}\Delta P_{L7} + \text{cpf}_{i8}\Delta P_{L8}, \quad i = 2, 6, \end{aligned} \quad (36)$$

$$\begin{aligned} \Delta P_{\text{Gdi}} = & \text{cpf}_{i1}\Delta P_{L1} + \text{cpf}_{i2}\Delta P_{L2} + \text{cpf}_{i3}\Delta P_{L3} + \text{cpf}_{i4}\Delta P_{L4} + \text{cpf}_{i5}\Delta P_{L5} + \text{cpf}_{i6}\Delta P_{L6} \\ & + \text{cpf}_{i7}\Delta P_{L7} + \text{cpf}_{i8}\Delta P_{L8}, \quad i = 3, 7, \end{aligned} \quad (37)$$

$$\begin{aligned} \Delta P_{\text{Ggi}} = & \text{cpf}_{i1}\Delta P_{L1} + \text{cpf}_{i2}\Delta P_{L2} + \text{cpf}_{i3}\Delta P_{L3} + \text{cpf}_{i4}\Delta P_{L4} + \text{cpf}_{i5}\Delta P_{L5} + \text{cpf}_{i6}\Delta P_{L6} \\ & + \text{cpf}_{i7}\Delta P_{L7} + \text{cpf}_{i8}\Delta P_{L8}, \quad i = 4, 8. \end{aligned} \quad (38)$$

Considering Eqs. (34)–(38), GENCOs must generate powers in the steady state as $\Delta P_{\text{Gt1}} = 0.09$ puMW, $\Delta P_{\text{Gh1}} = 0.05$ puMW, $\Delta P_{\text{Gd1}} = 0.02$ puMW, $\Delta P_{\text{Gg1}} = 0.04$ puMW, and $\Delta P_{\text{Gt2}} = \Delta P_{\text{Gh2}} = \Delta P_{\text{Gd2}} = \Delta P_{\text{Gg2}} = \Delta P_{\text{tie_scheduled}} = 0$ puMW. The optimal feedback gains of OC for the system with/without RFB are depicted in Table III. Dynamic system responses incorporating RFB in both control areas due to OC are shown in Fig. 5. For case 1, system responses for the deviation in frequency of area-1 [Fig. 5(a)] and area-2 [Fig. 5(b)] settle to zero, while all generations [Figs. 5(e)–5(l)] attain their desired values in the steady state. The steady state scheduled tie-line power flow [Fig. 5(c)] is zero because no power is demanded by areas-1 and 2 from areas-2 and 1. Additionally, the actual tie-line power is equal to the scheduled tie-line power, and hence, tie-line power error turns equal to zero as indicated in Fig. 5(d). All dynamic responses are smooth, non-oscillatory, and fast due to the presence of RFB.

TABLE III. Optimal feedback gain matrices K for the restructured multi-source system.

Without RFB	[0.6954	-0.0476	-2.2558	4.6395	1.0432	0.4709	2.4519	-0.1870	-6.2209	4.5127	0.0854
	1.2792	1.3619	0.3328	0.9991	-0.5330	-0.1352	-0.0355	-0.2829	0.2256	4.1628	-0.5062
	-0.0044	-0.1980	-0.1758	-0.0322	0.0703	0.9999	-0.0171;	0.1126	0.3360	2.1940	-0.3035
	-0.0516	-0.0169	-0.1153	0.0069	-1.9149	-0.2908	-0.0030	-0.0593	-0.1107	-0.0235	0.0334
	4.8375	0.8658	0.3477	2.2391	0.4051	10.1211	4.7113	0.1550	1.0280	1.3298	0.3553
	1.3943	0.0171	0.9999]								
With RFB	[0.0066	-0.0491	0.6238	2.1310	0.3140	0.3068	0.4689	0.1896	7.4866	1.9777	0.0660
	0.1958	0.3078	0.1239	0.5846	-0.5197	-0.0486	-0.0116	-0.1310	-0.0217	-0.0885	-0.5188
	-0.0050	-0.0599	-0.0609	-0.0123	-0.1832	0.9996	-0.0278;	-0.0443	-0.0241	-0.6416	-0.4537
	-0.0404	-0.0084	-0.1174	-0.0211	-0.9246	-0.4666	-0.0051	-0.0533	-0.0551	-0.0113	-0.1727
	2.1962	0.2199	0.1781	0.4236	0.2553	10.9765	2.0508	0.1388	0.1601	0.3098	0.1428
	0.6719	0.0278	0.9996]								

Case 2: poolco-bilateral transactions—In this case, DISCOs have the liberty to make contracts with GENCOs of their own and other control areas.^{1,4-6,8-10,15-18} In this case, the power demand of all DISCOs is presumed equal to 0.05 puMW. The DPM for this case is given as

$$\text{DPM} = \begin{bmatrix} 0.25 & 0 & 0.4 & 0.2 & 1 & 0 & 0.2 & 0.5 \\ 0.1 & 0 & 0.1 & 0.2 & 0 & 0 & 0 & 0.2 \\ 0.05 & 0 & 0 & 0.1 & 0 & 0 & 0 & 0 \\ 0.1 & 0 & 0.1 & 0.2 & 0 & 1 & 0 & 0 \\ 0.25 & 1 & 0.2 & 0.1 & 0 & 0 & 0.8 & 0.3 \\ 0.1 & 0 & 0.1 & 0.1 & 0 & 0 & 0 & 0 \\ 0.05 & 0 & 0 & 0.05 & 0 & 0 & 0 & 0 \\ 0.1 & 0 & 0.1 & 0.05 & 0 & 0 & 0 & 0 \end{bmatrix}. \quad (39)$$

For the above DPM, GENCOs must generate contracted powers of $\Delta P_{Gt1} = 0.1275$ puMW, $\Delta P_{Gh1} = 0.03$ puMW, $\Delta P_{Gd1} = 0.0075$ puMW, $\Delta P_{Gg1} = 0.07$ puMW, $\Delta P_{Gt2} = 0.1325$ puMW, $\Delta P_{Gh2} = 0.015$ puMW, $\Delta P_{Gd2} = 0.005$ puMW, $\Delta P_{Gg2} = 0.0125$ puMW, and $\Delta P_{tie_scheduled} = 0.035$ puMW. The values of $\Delta P_{tie_scheduled}$, ΔP_{tie_actual} , ΔP_{tie_error} , and GENCO outputs are verified using simulated responses shown in Figs. 5(c)–5(l). Figures 5(a) and 5(b) show larger undershoots and settling times in case 2 compared to case 1 due to the existence of load demands in both areas. It is noticed that in the deregulated atmosphere, the type of contract affects not only the load demand of an area but also the GENCO output and scheduled tie-line power flow. Further, in the absence of uncontracted power demands, the apf value does not influence the steady state behavior, but only the transient behavior of the system will be affected.

Case 3: contract violation—In some circumstances, DISCOs may breach a contract by demanding excess power than that specified in the contract. This excess DISCO demand which is not contracted to none of the GENCOs must be supplied only by the GENCOs operating in the same area as DISCOs.^{1,4-6,8-10,15-18} Consider case 2 once again with an amendment that DISCO-1 and DISCO-5 demand 0.05 puMW excess power, i.e., $\Delta P_{UC1} = \Delta P_{UC2} = 0.05$ puMW. Hence, $\Delta P_{D1} = \Delta P_{D2} = 0.2 + 0.05 = 0.25$ puMW. Fig. 5 also consists of the stabilized dynamic responses with RFB in the event of contract violation. With OC, AGC requirement is satisfied as ΔF_1 , ΔF_2 , and ΔP_{tie_error} settle to zero in the steady state. All generation in the steady state will deflect from case 2 values due to the excess power demands in both areas, and values of apfs in area-1 and 2 will decide the contribution of the uncontracted load among GENCOs in the area. Therefore, $\Delta P_{Gt1,CV} = 0.1275 + (0.5 \times 0.05) = 0.1525$ puMW and $\Delta P_{Gh1,CV} = 0.03 + (0.2 \times 0.05) = 0.04$ puMW. Similarly, $\Delta P_{Gd1,CV} = 0.0125$ puMW, $\Delta P_{Gg1,CV} = 0.08$ puMW, $\Delta P_{Gt2,CV} = 0.145$ puMW, $\Delta P_{Gh2,CV} = 0.0275$ puMW, $\Delta P_{Gd2,CV} = 0.0175$ puMW, and

$\Delta P_{G2,CV} = 0.025$ puMW; however, the steady state $\Delta P_{tie,scheduled}$ value will not change. The uncontracted demand in both areas is revealed in output power signals of all eight GENCOs as shown in Figs. 5(e)–5(l). It also confirms the fruitfulness of OC. From Figs. 5(f) and 5(j), it is also observed that the results of hydro power generations are characterized by an initial fast negative dip followed by slower exponential enlargement. This is due to the non-minimum phase characteristic of hydro turbines. Hence, hydro power plants compared to thermal/diesel/gas need more time to meet desired power generations. Compared to case 2, in case 3, all responses are observed substandard due to the presence of uncontracted power demands in both areas. Further, on comparing Figs. 3 and 5, it is observed that the results of more realistic multi-source power systems are more oscillatory or inferior in comparison to the results of the thermal power system.

Case 4: case 3 without RFB—To compare the system responses with and without RFB, case 3 is again simulated without considering the effect of RFB. The system model is simulated

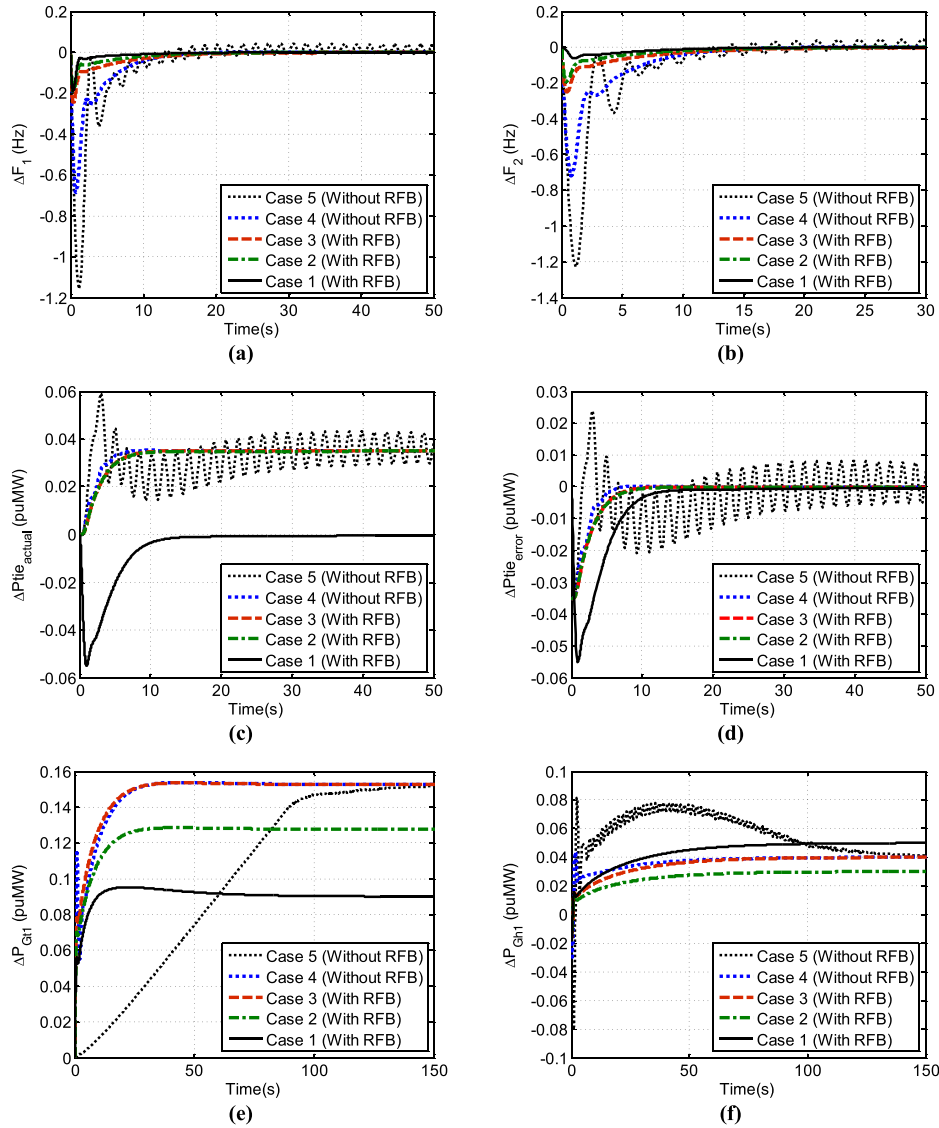


FIG. 5. Dynamic responses of the restructured two-area multi-source hydro-thermal-diesel-gas system with OC for different cases (a) ΔF_1 , (b) ΔF_2 , (c) ΔP_{tie_actual} , (d) ΔP_{tie_error} , (e) ΔP_{G1} , (f) ΔP_{G2} , (g) ΔP_{Gd1} , (h) ΔP_{Gd2} , (i) ΔP_{Gt1} , (j) ΔP_{Gt2} , (k) ΔP_{Gd2} , and (l) ΔP_{Gg2} .

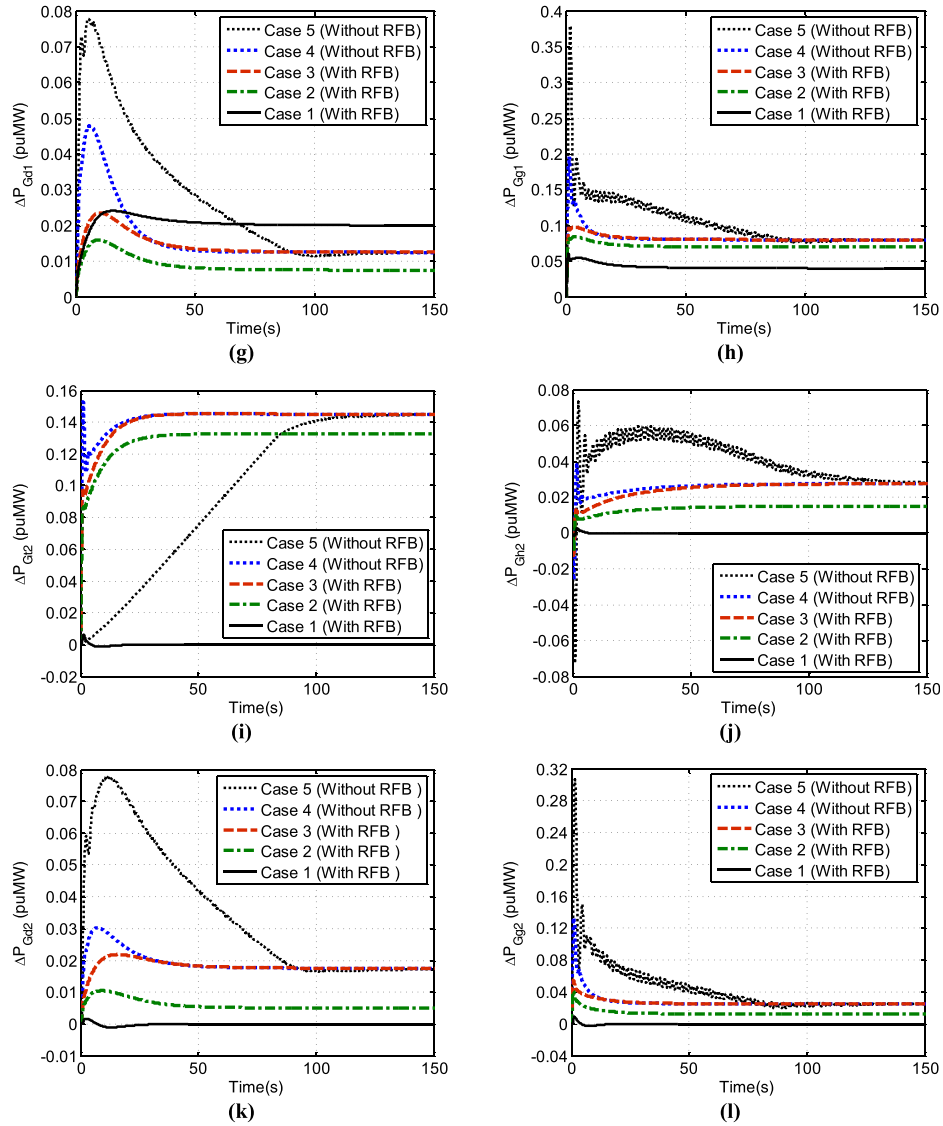


FIG. 5. (Continued.)

with OC utilizing the optimized feedback gains given in Table III for “without RFB” tag. On comparing the dynamic responses with and without RFB shown in Fig. 5 for case 3, it is concluded that high-quality results are obtained with RFB, i.e., case 3 compared to the results obtained without considering RFB, i.e., case 4. Hence, the use of RFB in the power system can be advocated to alleviate the oscillations caused at sudden load demands.

Case 5: case 4 with the generation rate constraint (GRC) and time delay (TD)—In practical power systems with steam or hydro power plants, a maximum limit, termed as the generation rate constraint (GRC), subsists on the rate of the change in the power generation. In the absence of GRC, undesirably, generators are anticipated to chase large momentary disturbances. Therefore, GRC must be integrated in a pragmatic AGC study. In the majority of research studies, the effect of GRC in restructured systems is neglected.^{1,6,7,9,10,15} The GRC for the hydro unit for raise and lower generations is considered +0.045 pu/s and −0.06 pu/s, respectively, while ± 0.0005 pu/s GRC is considered for single reheat thermal plants of the studied multi-source thermal-hydro-diesel-gas system. Due to the rising intricacy of interconnected power system in the restructured scenario, communication channel delays become a major challenge

in the AGC performance analysis. Time delays (TDs) can corrupt a system's performance and even cause system instability.¹⁷ In view of the above, a time delay of 0.2 s is considered in the output signal of OC, i.e., ΔP_{Ci} in addition to GRC. Here, the system described in case 4 is again simulated with the optimized gains obtained in case 4 (see "Without RFB" in Table III) and considering GRC and TD. Simulation results for case 5 are also shown in Fig. 5. It is observed that for case 5, i.e., case 3 without RFB and with GRC and TD, degraded system dynamic performance is observed compared to the system performance without GRC and TD. Close examination of these dynamic responses clearly appraises that without RFB and with GRC and TD, area frequencies, tie-line power flows, and power output signals suffer from large oscillation, longer settling time, higher peak overshoot, and peak undershoot. However, OC shows favorable performance under this worst condition.

1. Sensitivity analysis

A sensitivity analysis is performed to substantiate the robustness of the optimum feedback gains of OC obtained at a nominal condition for ample alterations in the system parameters.^{5,14,17,18} The relations specified in the Appendix indicate that the deviation in initial loading influences the power system damping constant (D_i), power system gain (K_{Pi}), power system time constant (T_{Pi}), and area frequency response characteristic (β_i). These parameters to be used in the thermal system model are calculated for different initial loadings. Selecting one at a time, initial system loading and the speed governor regulation parameter (R_i) for the single-source thermal system and time constants of the thermal speed governor (T_{gi}) and the diesel governor (T_{gdi}) for the multi-source system are changed from their nominal values in the range of $\pm 25\%$. The single-source thermal system dynamic responses without considering RFB for ΔF_2 and ΔP_{tie_actual} are shown in Figs. 6(a) and 6(b) for the altered operating conditions of nominal R_i and system loading, respectively. However, the multi-source system dynamic responses (for case 4) for ΔF_1 and ΔP_{Gg2} are shown in Figs. 6(c) and 6(d) for changed operating conditions of T_{gi} and T_{gdi} , respectively. Critical examination of the responses clearly unveils that all these responses show undetectable variations. So, it can be concluded that optimized feedback gains obtained at the nominal loading of 50% and nominal parameters need not be retuned for broad changes in the system loading or system parameters.

In realistic restructured power generating systems, uncontracted power demands can occur in any one area or in all the areas concurrently.^{5,17} If the controller is not designed to undertake such cases, the system will definitely turn unstable. Here, systems under study are simulated for four contract violation/non-violation situations such as (a) $\Delta P_{UC1} = 0.1$ puMW, $\Delta P_{UC2} = 0$ puMW, (b) $\Delta P_{UC1} = 0$ puMW, $\Delta P_{UC2} = 0.1$ puMW, (c) $\Delta P_{UC1} = \Delta P_{UC2} = 0.1$ puMW, and (d) $\Delta P_{UC1} = \Delta P_{UC2} = 0.15$ puMW. Because of more likelihood of system instability, the success of OC is tested on the systems without RFB. Figure 6(e) shows the GENCO-2, i.e., ΔP_{Gt2} response of the single-source thermal system, and Fig. 6(f) shows the GENCO-3, i.e., ΔP_{Gd1} response of the multi-source thermal-hydro-diesel-gas system for case 4. Evaluation of Figs. 6(e) and 6(f) clearly reveals the efficacy of OC under higher intensity and changed locations of contract violation demands (ΔP_{UCi}). To save space, only two dynamic responses are shown for the rationale of this statement.

VIII. CONCLUSION

The effect of redox flow batteries (RFBs) on AGC performance enrichment of two-area power systems in the deregulated power environment is explored. A novel optimal control strategy is implemented to perform the simulations. Initially, a restructured two-area four-unit thermal system is investigated, and the superiority of the optimal controller (OC) is demonstrated over the artificial cooperative search algorithm (ACSA) tuned PI controller. The benefit of OC over ACSA tuned PI is corroborated through the simulation results in terms of appreciably smooth and fast responses with a minimal settling time. Further, since RFB can contribute to instant power demands, ameliorating system performance is observed with RFB in contrast to the system without RFB. Next, system mode analysis shows a substantial improvement in the

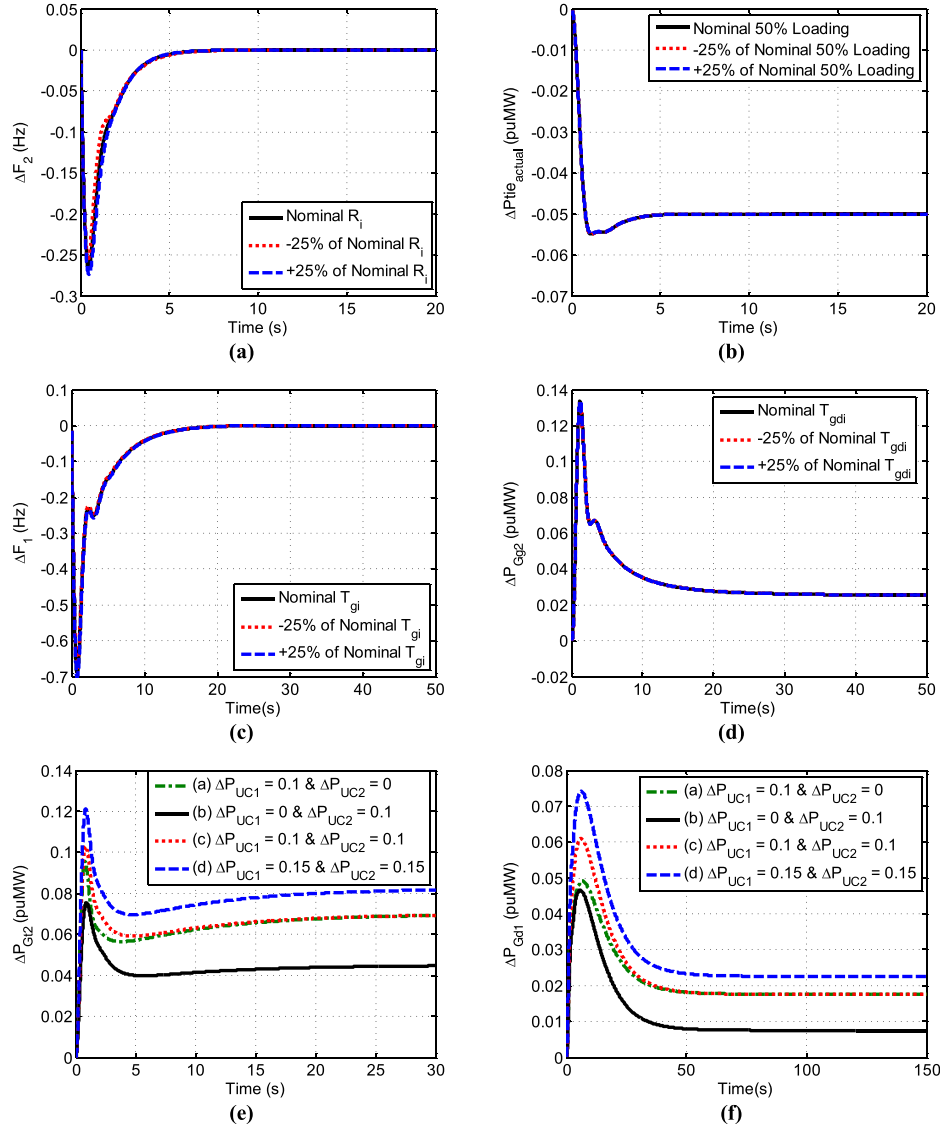


FIG. 6. Dynamic responses with OC during sensitivity analysis (a) ΔF_2 of the single-source system, (b) ΔP_{tie_actual} of the single-source system, (c) ΔF_1 of the multi-source system, (d) ΔP_{Gg2} of the multi-source system, (e) ΔP_{Gg2} of the single-source system, and (f) ΔP_{Gd1} of the multi-source system.

system stability margins with OC compared to the ACSA PI strategy. To demonstrate the ability of OC to cope with the multi-source system, the study is further extended to a more realistic restructured two-area multi-source thermal-hydro-diesel-gas system. An extensive analysis is performed for the AGC scheme considering poolco, poolco-bilateral, and contract violation transactions with/without RFB/GRC-TD. It is established that in all the cases, the area frequencies turn to zero in the steady state, which satisfies the AGC requirements. It is also established that the simulated actual values of generations and scheduled tie-line powers of GENCOs under different transaction match with the corresponding desired values. Finally, sensitivity analysis reveals that OC with the optimized feedback gains acquired at the nominal loading of 50% is robust enough and need not be reset if the system is subjected to broad variations in the system's initial loading or parameters from the nominal values. The robustness of OC is also established at a bigger size and changed positions of uncontracted power demands.

APPENDIX: SYSTEM DATA

Nominal parameters of single/multi-source power system models under investigation^{1,11,13,15}
 $P_{r1} = P_{r2} = 2000 \text{ MW}$, $P_{tie_{max}} = 200 \text{ MW}$, Base power = 2000 MVA, initial loading (ΔP_{Di}^0) = 50%, $F^0 = 60 \text{ Hz}$, $\alpha_{12} = -1$, $D_i = 8.33 \times 10^{-3} \text{ puMW/Hz}$, $H_i = 5 \text{ MWs/MVA}$, $T_{gi} = 0.08 \text{ s}$, $T_{ti} = 0.3 \text{ s}$, $K_{ri} = 0.5$, $T_{ri} = 10 \text{ s}$, $R_{ti} = R_{hi} = R_{gi} = 2.4 \text{ Hz/puMW}$, $R_{di} = 2.5 \text{ Hz/puMW}$, $K_{Pi} = 120 \text{ Hz/puMW}$, $T_{Pi} = 20 \text{ s}$, $B_i = \beta_i = 0.425 \text{ puMW/Hz}$, $2\pi T_{12} = 0.545 \text{ puMW/Hz}$, $T_{RHi} = 28.75 \text{ s}$, $T_{GHi} = 0.2 \text{ s}$, $T_{Ri} = 5 \text{ s}$, $T_{Wi} = 1 \text{ s}$, $a_i = 1$, $b_i = 0.05 \text{ s}$, $c_i = 1$, $X_i = 0.6 \text{ s}$, $Y_i = 1 \text{ s}$, $T_{CRi} = 0.01 \text{ s}$, $T_{Fi} = 0.23 \text{ s}$, $T_{CDi} = 0.2 \text{ s}$, $K_{RFB} = 0.6787$, $T_{RFB} = 0 \text{ s}$, $T_{gd} = 0.1 \text{ s}$, $T_{td} = 8 \text{ s}$, $T_{Pi} = 2H/F^0 D_i \text{ s}$, $K_{Pi} = 1/D_i \text{ Hz/puMW}$, $D_i = \Delta P_{Di}^0/F^0 \text{ puMW/Hz}$, $\beta_i = D_i + 1/R_i \text{ puMW/Hz}$.

■.

- ¹R. K. Selvaraju and G. Somaskandan, "Impact of energy storage units on load frequency control of deregulated power systems," *Energy* **97**, 214–228 (2016).
- ²A. Lucas and S. Chondrogiannis, "Smart grid energy storage controller for frequency regulation and peak shaving, using a vanadium redox flow battery," *Int. J. Electr. Power Energy Syst.* **80**, 26–36 (2016).
- ³I. A. Chidambaram and B. Paramasivam, "Control performance standards based load-frequency controller considering redox flow batteries coordinate with interline power flow controller," *J. Power Sources* **219**, 292–304 (2012).
- ⁴R. Shankar, K. Chatterjee, and R. Bhushan, "Impact of energy storage system on load frequency control for diverse sources of interconnected power system in deregulated power environment," *Int. J. Electr. Power Energy Syst.* **79**, 11–26 (2016).
- ⁵Y. Arya and N. Kumar, "Optimal AGC with redox flow batteries in multi-area restructured power systems," *Eng. Sci. Technol., Int. J.* **19**(3), 1145–1159 (2016).
- ⁶V. Donde, M. A. Pai, and I. A. Hiskens, "Simulation and optimization in an AGC system after deregulation," *IEEE Trans. Power Syst.* **16**(3), 481–489 (2001).
- ⁷B. Tyagi and S. C. Srivastava, "A LQG based load frequency controller in a competitive electricity environment," *Int. J. Emerging Electr. Power Syst.* **2**(2), (2005).
- ⁸W. Tan, Y. Hao, and D. Li, "Load frequency control in deregulated environments via active disturbance rejection," *Int. J. Electr. Power Energy Syst.* **66**, 166–177 (2015).
- ⁹Ibraheem, P. Kumar, N. Hasan, and Y. Singh, "Optimal automatic generation control of interconnected power system with asynchronous tie-lines under deregulated environment," *Electr. Power Compon. Syst.* **40**(10), 1208–1228 (2012).
- ¹⁰A. Pappachen and A. P. Fathima, "Load frequency control in deregulated power system integrated with SMES-TCPS combination using ANFIS controller," *Int. J. Electr. Power Energy Syst.* **82**, 519–534 (2016).
- ¹¹M. Datta, T. Senjyu, A. Yona, and T. Funabashi, "A fuzzy based method for leveling output power fluctuations of photovoltaic-diesel hybrid power system," *Renewable Energy* **36**(6), 1693–1703 (2011).
- ¹²B. Mohanty, S. Panda, and P. K. Hota, "Differential evolution algorithm based automatic generation control for interconnected power systems with non-linearity," *Alexandria Eng. J.* **53**(3), 537–552 (2014).
- ¹³Ibraheem Nizamuddin and T. S. Bhatti, "AGC of two area power system interconnected by AC/DC links with diverse sources in each area," *Int. J. Electr. Power Energy Syst.* **55**, 297–304 (2014).
- ¹⁴P. N. Topno and S. Chanana, "Load frequency control of a two-area multi-source power system using a tilt integral derivative controller," *J. Vib. Control* (published online, 2016).
- ¹⁵K. P. S. Parmar, S. Majhi, and D. P. Kothari, "LFC of an interconnected power system with multi-source power generation in deregulated power environment," *Int. J. Electr. Power Energy Syst.* **57**, 277–286 (2014).
- ¹⁶Y. Arya and N. Kumar, "AGC of a multi-area multi-source hydrothermal power system interconnected via AC/DC parallel links under deregulated environment," *Int. J. Electr. Power Energy Syst.* **75**, 127–138 (2016).
- ¹⁷Y. Arya, N. Kumar, and Ibraheem, "AGC of a two-area multi-source power system interconnected via AC/DC parallel links under restructured power environment," *Optim. Control Appl. Methods* **37**(4), 590–607 (2016).
- ¹⁸B. Mohanty and P. K. Hota, "Comparative performance analysis of fruit fly optimisation algorithm for multi-area multi-source automatic generation control under deregulated environment," *IET Gener., Transm. Distrib.* **9**(14), 1845–1855 (2015).
- ¹⁹P. Kundur, *Power System Stability and Control*, 12th reprint (Tata McGraw-Hill, New Delhi, 2011).
- ²⁰G. Lalor, J. Ritchie, D. Flynn, and M. J. O'Malley, "The impact of combined cycle gas turbine short term dynamics on frequency control," *IEEE Trans. Power Syst.* **20**(3), 1456–1464 (2005).
- ²¹B. D. O. Anderson and J. B. More, *Optimal Control: Linear Quadratic Methods* (Dover Publications, Inc., Mineola, New York, 2014).

See discussions, stats, and author profiles for this publication at: <https://www.researchgate.net/publication/322400233>

PID Based Impedance Control Scheme for Flexible Single Arm Underwater Robot Manipulator

Conference Paper · January 2018

CITATIONS

0

READS

21

3 authors, including:



Sunil Kumar

Sant Longowal Institute of Engineering and Tec...

21 PUBLICATIONS 7 CITATIONS

[SEE PROFILE](#)



Rastogi Vikas

Delhi Technological University

57 PUBLICATIONS 165 CITATIONS

[SEE PROFILE](#)

Some of the authors of this publication are also working on these related projects:



Right now, we are working in area of Heavy Vehicle Modeling and control, railway dynamics and ride comfort and turbine blade vibrations [View project](#)



Right now, we are working in area of turbine blade vibrations [View project](#)

PID Based Impedance Control Scheme for Flexible Single Arm Underwater Robot Manipulator

Sunil Kumar¹, Vikas Rastogi², Pardeep Gupta³

^{1,3}Department Mechanical Engineering Sant Longowal Institute of Engineering & Technology, Longowal Punjab, India

²Department of Mechanical Engineering, Delhi Technological University, Delhi, India

¹sunil_thappa@yahoo.com

Abstract: This paper deals with force and position control of an end effector of a single flexible arm robot manipulator in underwater medium. The interactions with the environment are affected by the different underwater conditions such as hydrodynamic forces and other disturbances. This work is an attempt to control the force and position of an end-effector of a robot manipulator during interaction with environment. The control strategy presents extended impedance controller with PID control for more stable conditions through bond graph modeling technique. An environmental condition includes a fixed distance maintained during interaction from the virtual wall. The scheme developed is further implemented on single arm flexible underwater robot manipulator. Simulation study has been carried out which reveals some effective stability of system.

Keywords: Manipulator; Flexible; Underwater rob; PID; Bond graph

1. INTRODUCTION

Interaction with its surrounding environment by underwater robot is very significant for complete autonomous mission. Underwater robots have been un-mitigated in past decades in the number of applications, in underwater conditions. The robot end-effectors have to make contact or keep constant distance with the environment required in many engineering applications. Interactions with underwater environment deal with some nonlinear conditions, which are of great interest to the modeling and scientific community. The modelling and design for force control of underwater robots requires consideration of nonlinear conditions so as insist of the controller may be investigated effectively.

Numbers of interaction control schemes exist for force control [1] like direct force control, hybrid force/position control, parallel force/position control and impedance control, which are studied by many researchers for interaction control [2]. Hogen [3, 4 and 5] has developed an approach to facilitate the application of robots involving static and dynamic interaction between the manipulator and

its environment considering impedance components of the manipulator. By applying impedance between robot end-effector position and constant force, a controlled interaction can be achieved [6]. Kinematic constraints can be exerted on the manipulator and force/position tracking can also be realized using state feedback relying as per the environment geometry [7]. Using pneumatic actuator with passivity properties such as impact and force control, a desired interaction force can be achieved for stable and dissipative contact tasks with an arbitrary environment [8]. To cope with the uncertainties arising from free-flyers dynamics, Wang and Xie [9] have investigated force/position track control using an adaptive Jacobian controller and multiple impedance control. In the practical case of contact with friction, velocity/force can be used to determine the surface normal direction [10]. Asymptotic stability of force regulator using a PI force plus PD- position feedback can be effectively done in a condition, where environment is not so rigid [11]. Robot finger contracting a compliant surface with stiffness and kinematics uncertainties has been studied by Doulgeri et al. [12].

Y. Cui et al [13] has investigated effectiveness of impedance controller on UVMs through simulation has been and an explicit force control scheme is one of the robust scheme for considering occurrence of unexpected impact and can be further extended with adaptive motion control [14 and 15]. Multiple impedance control was customized by the Farivarnejad and Moosavian [16] for the heavy object in underwater structure in case of inevitable contact. Pathak et al [17] has discussed impedance control of a space robot using virtual base in controller domain and further Amit Kumar [18] has presented a scheme for torque control by impedance at the interaction point between flexible space robot tip and space structure using a virtual foundation. In this paper PID based impedance control scheme has been developed for single arm flexible underwater robot manipulator extending further the work done by Kumar [18]. Overwhelming control strategies have been extended to impedance control for the interaction of end-effector with the environmental conditions. In order to achieve an effective stability during interaction PID

controller has been embedded in the system. Bond graph model has been created and simulated on SYMBOL SONATA (R) software. An extensive simulation has been performed for effective in the underwater environment. The next section provides the detailed methodology of PID based impedance controller.

2. IMPEDANCE CONTROL WITH PID

The force/position tracking problem of the underwater robot manipulator in the nonlinear dynamic and environment condition has been explored in this section. As reported by Mukherjee et al. [19] and Pathak [20] an overwhelming control strategy can be extended to impedance control using bond graph. The passive foundation concept is used for modelling underwater robot. To achieve good stability Proportional-Integral-Derivative (PID) controller based system is applied to control the underwater robot using a high feedforward gain μh .

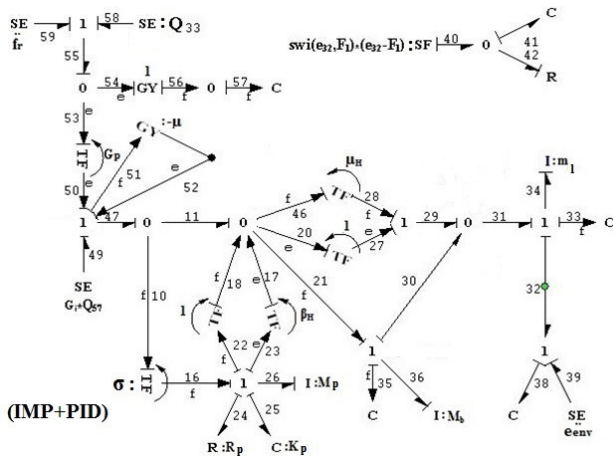


Fig. 1. Bond graph model of PID Impedance controller.

Figure 1 shows the depicted bond graph model of impedance controller with PID. In bond graph model SE39 is used to contradict the effort of environmental stiffness by C38. Mb is mass of the base and ml is the mass of the link. Mp, Kp and Rp are the mass, stiffness and damping of passive foundation. The passive foundation velocity is sensed and feedback to the controller through passive foundation compensation gain σ as flow activated transformer between the bonds 10 and 16. Taking into account the impedance modulates the limit force of interaction [21 and 22]. The PID control is attached to the impedance controller in which flow activated C element on bonds 33 and 35 provide the tip and base displacements respectively. The integrated flow signal of displacement is given by Q57 activated bond which converts the effort signal to the flow signal between bond 54 and bond 56. SE49 corresponds to the effort applied on the system, which is proportional to the integral of the error signal. The activation on bond 51 and 52 take care of the derivative action by accommodating the velocity without applying any force on the system. Reference velocity is represented by fr

which is represented by SE59. One may obtain the transfer function of PID controller $P(s)$ through by signal flow diagram of PID, which is attached to Impedance controller. Figure 2 shows the signal flow graph of the system with only derivative feedback.

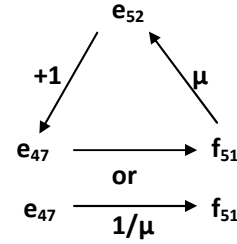


Fig. 2. Signal flow graph for derivative feedback of PID controller

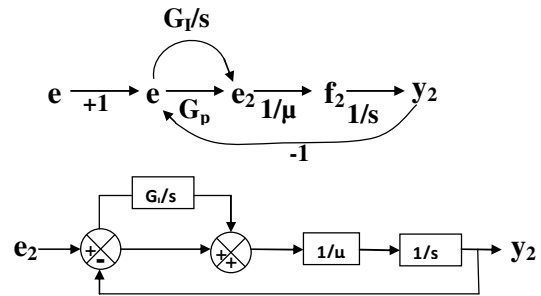


Fig. 3. Flow graph and block diagram for the PID controller attached to Impedance controller

Using Mason's formula, the transfer function for the derivative feedback can be written as

$$\frac{f_{51}}{e_{47}} = \frac{1}{-\mu} \quad (1)$$

The integrated and proportional control action is added to derivative feedback the signal flow graph and block diagram shown in figure 3.

The transfer function of PID controller using Mason's formula may be expressed as

$$\frac{P(s)}{e_{ref}} = \frac{G_p s + G_i}{-\mu s^2 + G_p s + G_i} \quad (2)$$

$$\text{Also } e_{ref} = \frac{y_{ref}}{s} \quad (3)$$

From equation no. 2 and 3 one may obtain the $P(s)$ as

$$P(s) = \frac{G_p s + G_i}{-\mu s^2 + G_p s + G_i} * \frac{y_{ref}}{s} \quad (4)$$

The impedance at the interaction point is defined as the ratio of tip velocity to the environmental condition represented as

$$\frac{f_{tip}}{e_{env}} = \frac{R(s)[1 + (1 - \sigma)\beta_h F_{pf}(s)P(s) + \mu_h P(s)F_b(s)]}{1 + \mu_h P(s)R(s) + (1 - \sigma)\beta_h F_{pf}(s)P(s) + \mu_h P(s)F_b(s)} \quad (5)$$

In Eq. (5) $R(s) = \frac{1}{m_1 s}$ is transfer function of the underwater welding robot,
 $F_{pf}(s) = s/(M_{pf}s^2 + R_{pf}s + K_{pf})$ is transfer function of the passive foundation,
 $F_b(s) = 1/M_b s$ is transfer function for the base of underwater welding robot,
 μ_h = High feedforward gain related to the physical domain,
 β_h = High gain related to the passive foundation,
 σ = Feedback compensation from passive foundation to controller

One may achieve through Eq. (5), modulation of impedance to accommodate interaction force which is possible for $\sigma < 1$ and trajectory control is achieved at $\sigma = 1$ by rejecting passive foundation characteristic

3. PID IMPEDANCE CONTROL OF FLEXIBLE ARM UNDERWATER ROBOT MANIPULATOR

Implementation of impedance control with PID on the underwater flexible single arm robot manipulator is composed of models of a base of underwater robot, flexible link and impedance controller with PID. In underwater robot modeling it is assumed that the system has single manipulator with revolute joints and consists of an open kinematic chain configuration. Bond graph modeling of base and flexible link was done by considering different aspects of kinematics and dynamics with underwater condition [23]. Subsystems (capsules) of the model were created and connected to each other bonds as shown in a block diagram of figure 4.

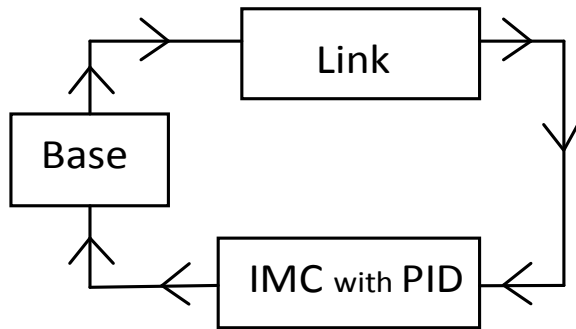


Fig. 4. Block diagram of the proposed scheme

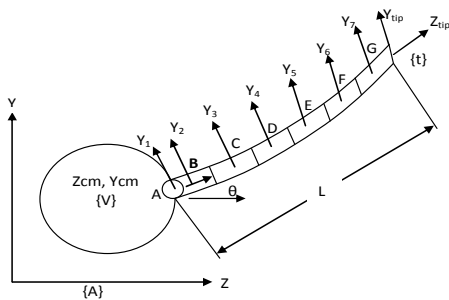


Fig. 5. Schematic representation physical model of one arm flexible underwater robot

Figure 5 shows the schematic sketch of a physical model of a single link flexible underwater robot divided into six equal segments. In the Figure 5 {A} represents the absolute frame, {V} represents the robot frame. The frame {t} locates the tip of the robot. L is the length of the flexible link and r is the distance between the robot base and centre of mass (CM) of the underwater vehicle and θ be the joint angle as shown in Figure 5.

3.1 Modeling of base

Figure 6 shows the bond graph sub-system (capsule) of base of underwater welding robot manipulator. Z_{cm} and Y_{cm} are the coordinates of the base with respect to absolute frame {A} as shown in Figure 5. The external force SE attached at the 1-junctions represents the net force acting due to resultant of buoyant force, hydrostatic force and gravity represented by $f(SE)$ in the Figure 6.

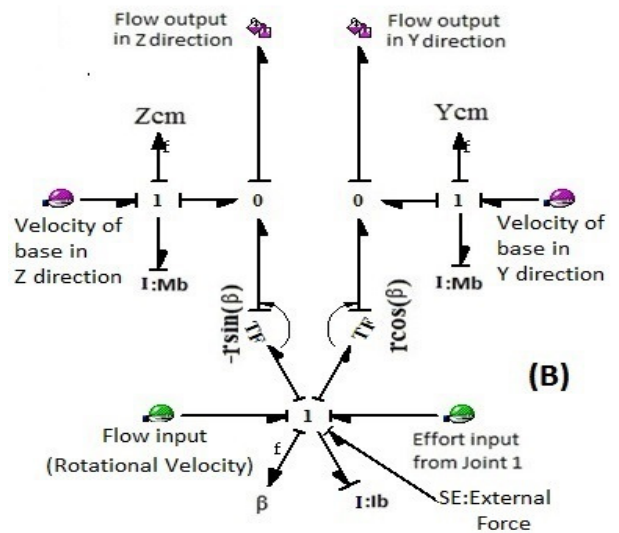


Fig. 6. Bond graph sub-system for Base of underwater robot

3.2 Modeling of flexible link

The bond graph model was based on the physical model shown in Figure 5 and the equations related to kinematic and dynamic modeling are discussed in this section. The flexible link of underwater robot has been modeled as uniform Euler-Bernoulli beam with flexible rigidity EI, density ρ and cross-section area A.

Kinematic

The kinematic analysis of flexible link is performed in order to make the bond graph and to find kinematic relationship of base with link. The absolute velocities at junction of link can be evaluated using the velocity equations 1 and 2. z_{cm} and y_{cm} are the co-ordinate of the center of mass of the underwater robot with respect to absolute frame. The velocity of the flexible link at mid of

first segment of link in z and y-direction with respect to frame {A} may be represented as

$$\dot{z}_{11} = \dot{z}_{CM} - (r \sin \beta) \dot{\beta} - \dot{y}_{11} \sin(\theta_1 + \beta) \quad (6a)$$

$$\dot{y}_{11} = \dot{y}_{CM} + (r \cos \beta) \dot{\beta} + \dot{y}_{11} \cos(\theta_1 + \beta) \quad (6b)$$

In above equations β represents the rotation of base where as θ_1 represents the joint angle. The segment angles of link are $\gamma_{11}, \gamma_{12}, \gamma_{13}, \gamma_{14}, \gamma_{15}, \gamma_{16}$ has been used in the module of transformers in Figure 7. The CM velocity perpendicular to link is represented by \dot{y}_{11} . The velocities in z and y direction at tip of the link (end-effector) with respect to frame {A} can be evaluated as

$$\dot{z}_{tip} = \dot{z}_{16} - \left(\frac{L}{12} \sin \gamma_{16}\right) \dot{\gamma}_{16} \quad (7a)$$

$$\dot{y}_{tip} = \dot{y}_{16} + \left(\frac{L}{12} \cos \gamma_{16}\right) \dot{\gamma}_{16} \quad (7b)$$

Here \dot{z}_{16} and \dot{y}_{16} are the velocities in the z and y direction at the midpoint of sixth segment of a link.

Dynamic

The dynamics of underwater robot manipulator are highly complex and nonlinear. Different methods can be used for study of dynamics of underwater robots like Euler, Lagrange, Newton and Kane methods. The dynamic

equation for underwater robot manipulator is conveniently expressed by different researchers [24 and 25] as

$$(P, \tau) = (m)(\ddot{V}, \dot{\omega}) + (m_c)(V, \omega) + B\dot{y} + G + Hs \quad (8)$$

Where, (P, τ) : External input forces and torques, (m) : body inertial and added mass is 6x6 inertia matrices, (m_c) : Coriolis and centripetal matrices, $B\dot{y}$: Buoyancy force matrix, G : Gravity force matrix, and Hs : hydrostatic force.

When the motion of rigid body is to be simulated in an underwater environment, number of additional forces must be considered which are governed by the various hydrostatic and hydrodynamic effects. In present work it is assumed that the welding is performed at a depth of 10 meters, so the effect of surface waves is ignored further it is assumed that fluid is irrotational, unbounded and still. The effect of drag and fluid acceleration is not considered. The buoyancy force is easily expressed in the earth-fixed frame in the Z direction as

$$f_b = -\rho g v \quad (9)$$

Where ρ is the fluid density, v the body volume and g the gravity acceleration

Similarly the gravity force and hydrostatic force are expressed with respect to the earth-fixed frame

$$f_g = G \text{ and } f_h = \rho g A_s \quad (10)$$

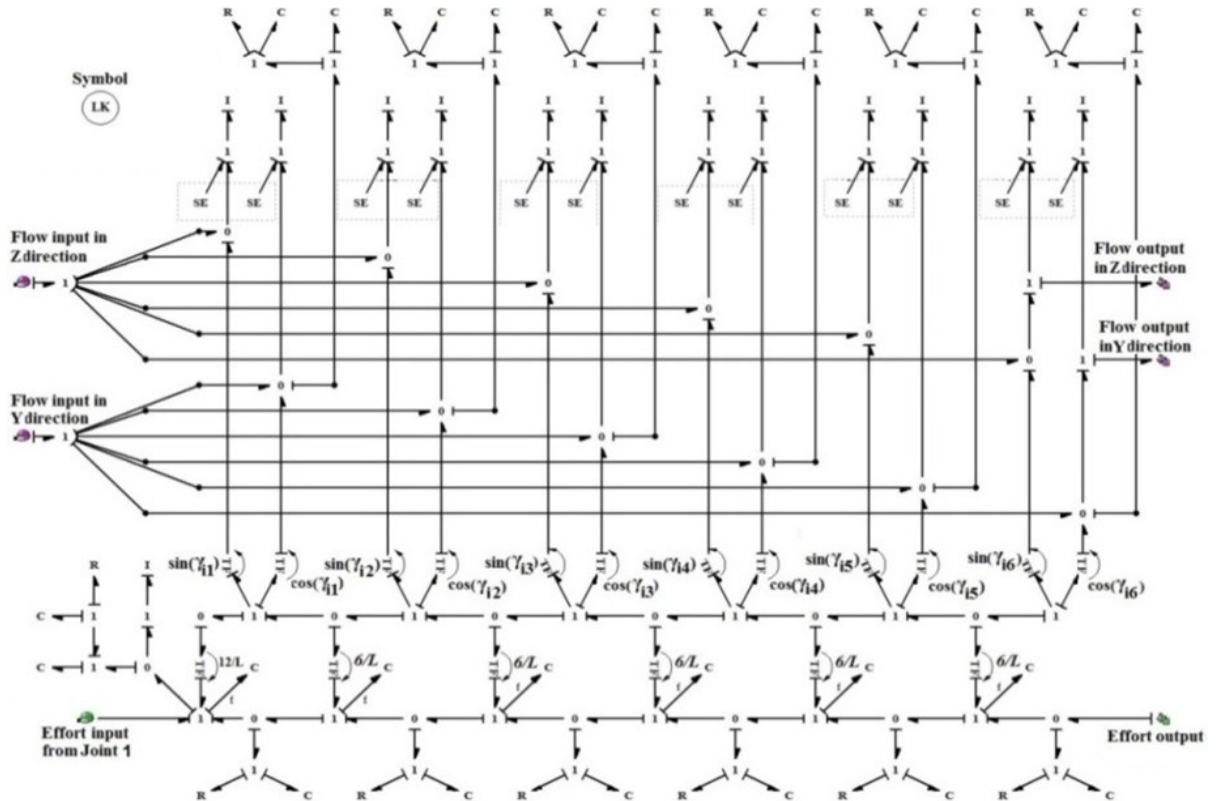


Fig. 7. Bond graph sub system model of flexible link for underwater robot

Where, G is gravitational force and A_s is surface of arm on which water pressure is acting.

The SE attached to bond 1 at the top of the bond graph of arm sub-system shown in Figure 7 on each segment represents dynamic of manipulator SE attached to the base sub-system to bond 1 at the bottom in Figure 6 represents dynamic of underwater robot.

3.3 Bond Graph Modeling

The arm of underwater robot has been modeled as flexible link using Euler-Bernoulli beam theory to create bond graph shown in Figure 7. Lumped inertia of the beam is taken into account but rotary inertia and shear deformation are neglected. The interface shear forces are represented by corresponding 0-junctions in the bond graph model shown in Figure 7. The 1-junctions along the upper line of the ladder structure represent the velocities of the mass centers of the reticules in z and y-direction to which corresponding inertia elements are attached. The 1-junctions along the lower line represent reticule interface rotations. The C elements at 0-junctions along the lower line model represent the flexural stiffness of the reticules. The mass of the both the links for each segment ($\rho AL/6$) along with buoyancy force, gravity force and hydrostatic force are attached to "1" junction corresponding to the segment velocities. In the bond graph model R elements are also shown to represent the internal damping present in the flexible link. In this model Pads (Rpad and Cpad) are used for computational simplicity i.e., to avoid the differential causality. In the bond graph of link shown in Figure 7 SE represents the resultant of hydrostatic force, gravity force and buoyancy force acting on each segment.

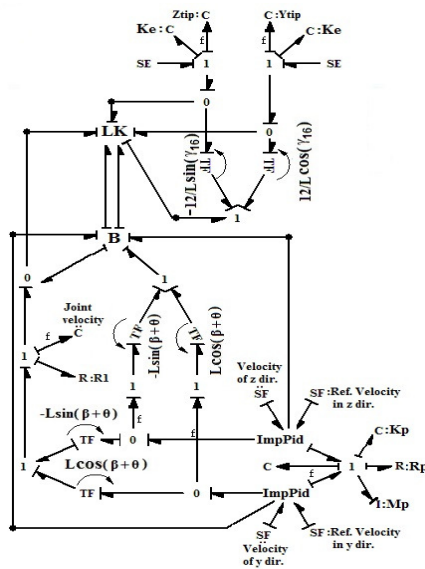


Fig. 8. Integrated Bond graph model of single arm flexible underwater welding robot.

4. INTEGRATED BOND GRAPH

In underwater conditions environmental forces are generated which are to be controlled along with the tangent direction of end effector position. Impedance is used to control either environmental forces or velocity of end effector at the interaction point. The modulation of impedance is done by compensation gain (σ). When gain (σ) value is 1 impedance is changed which leads to control of trajectory. In another situation, when compensation gain (σ) value is more than 1 force at the end effector remains controlled. The scheme discussed for ground manipulator may be used to model a force/position control of underwater single arm flexible robot manipulator. The Figure 8 shows the integrated bond graph model for underwater robot manipulator. Modelling is done as per the strategy shown in Figure 1. The sub system of PID impedance controller is linked with the sub system of a base of underwater robot manipulator (B) and flexible arm (LK). The SE's attached at the 1-junctions represents the forces require for contradicting the effort of environmental stiffness $Keas$ shown in Figure 8. The flow activated C elements provides trajectory in Y and Z direction respectively.

5. SIMULATION AND RESULT

The parameters used in simulation are shown in table 1.

TABLE 1: Parameters used for modeling of single arm flexible underwater robot manipulator.

Sr. No.	Parameters	Nomenclature	Value
1	Modulus of Elasticity	E	$7 \times 10^{10} N/m^2$
2	Link Length	L	0.5m
3	Moment of inertia of cross-section of link	I	$2.13 \times 10^{-7} m^4$
5	Density of Aluminium(alloy)	ρ_l	$2700 kg/m^3$
6	Cross section area of link	A	$1.6 \times 10^{-3} m^2$
7	Surface Area of link	A_s	0.02
8	Mass of link	Mlink	0.5kg
9	Volume of link	Vlink	$8 \times 10^{-4} m^3$
10	Mass of base	Mb	50kg
11	Moment of Inertia of base	Ib	$10 kg \cdot m^2$
12	Radius of base	r	0.1m
13	Joint Resistance	JR	0.1 Nm/(rad/s)
14	Gain value	μ_h	
15	Passive foundation characteristics	Kp, Rp	1000 Nm/rad 100 Nm/(radians/s)

Sr. No.	Parameters	Nomenclature	Value
		I_p	40 Kg m^2
		M_p	200 Kg
16	Gain modulations	K_{ini}	0.9
		K_{gi}	0.4
		K_{gp}	0.6
17	Interaction force limit	F_{limt}	500 N
18	Input Reference Angular Velocity	ω	1 rad/s
19	Force error integration	K_t	100 N/m
		R_t	80 N(m/s)
20	PID gain modulations	G_p	0.001
		G_i	0.1
		μ	7
21	Environment stiffness	K_e	4000 N/m
22	Location of underwater robot from obstruction (Wall)	y_w	0.1 m
15	Passive foundation characteristics	K_p , R_p I_p M_p	1000 Nm/rad 100 Nm/(radians/s) 40 Kg m^2 200 Kg

To show the efficacy of the proposed impedance control scheme, simulation study has been carried out. The

reference displacement for the tip was considered to follow the half rectified sine wave path in Y direction with amplitude A, which may be expressed as

$$y = A * \sin\left(\frac{\pi}{2}t\right) * swi[\sin\left(\frac{\pi}{2}t\right), 0] \quad (11)$$

The reference velocity obtained may be written as

$$f_r = \dot{y} = A \left(\frac{\pi}{2}\right) * \cos\left(\frac{\pi}{2}t\right) * swi[\sin\left(\frac{\pi}{2}t\right), 0] \quad (12)$$

In the beginning the tip trajectory is set to reference trajectory. It is assumed that wall is at y_w distance from the initial tip location. To contradict the effort of environmental stiffness effort element, SE42 is given represented as

$$SE42 = swi(Q33, w) * K_e * w \quad (13)$$

The simulation is carried out for 10 seconds as per the underwater condition discussed. The initial position of the tip is assumed to be zero radians. From Figure 9(a) shows the comparison of reference tip displacement and actual tip displacement in side water. It is observed that in underwater condition the tip follows the reference trajectory in underwater environment till 8 mm from initial tip position. As soon as the limit force is reached, it follows straight path with small dip as reference trajectory, which starts moving back ward from the amplitude. The tip again follows the reference trajectory as reference trajectory which reaches 10mm distance from wall as force reduce to the limited force.

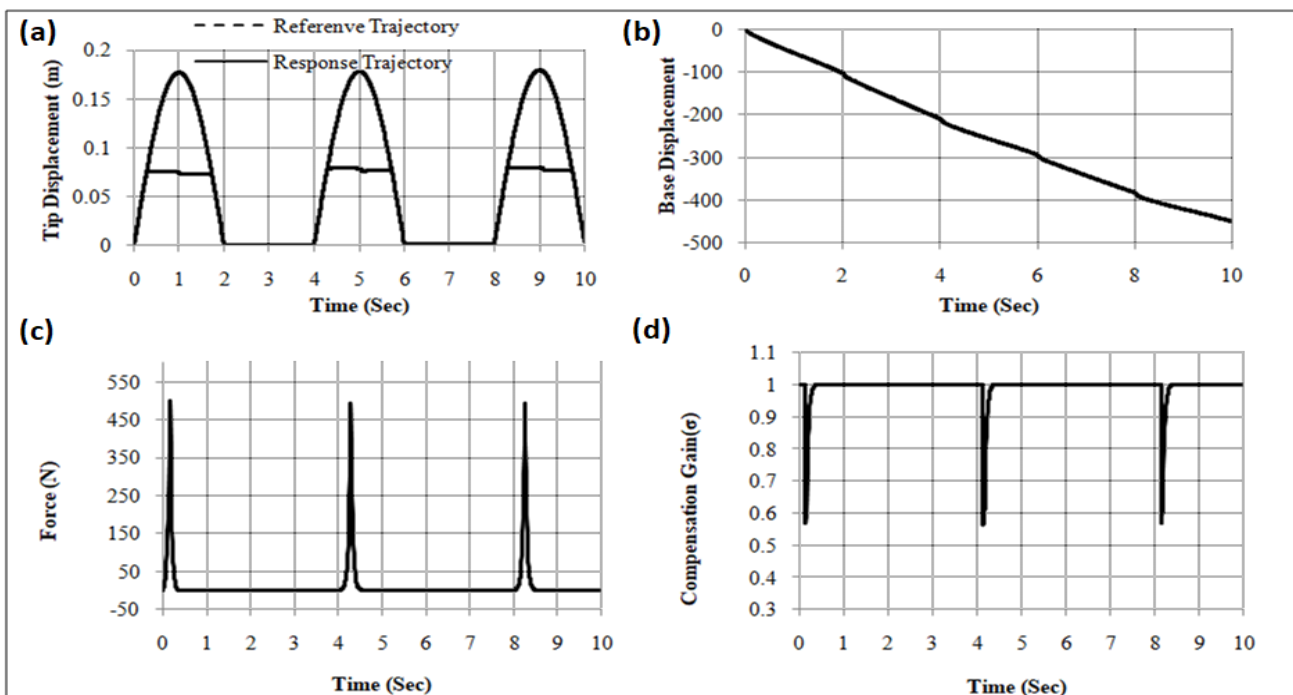


Fig. 9. Plots for the results obtained for flexible one arm underwater welding robot manipulator: (a) Plot of tip trajectory versus time, (b) Plot of Base Displacement versus time; (c) Plot of Force versus time and (d) Plot of compensation gain versus time.

Figure 9(b) shows the base displacement with respect to time. As interaction force is passed to the base of robot manipulator leading to move from its starting position as shown in Figure 9(b). Figure 9(c) shows the relation of contact force between tip and environment with time in underwater condition. It is observed that force rise till it reaches limited force i.e. 500 N and when the tip reaches wall the contact force becomes zero. As the reference trajectory reaches its amplitude that is distance between the wall and the tip force almost becomes zero till next cycle starts. From Figure 9(c) and Figure 9(d), it is observed that compensation gain and interaction force are interrelated. Compensation gain modulated as the interaction force reaches its limited value and keeps interaction force less than 500 N which is the limit force.

6. CONCLUSIONS

PID base impedance controller has presented in this study. The scheme is suitable for the implementation in underwater robot manipulators. The constraints that arise in underwater conditions are taken into account like hydrostatic force and disturbances. PID impedance controller has been implemented to achieve force and position control. A methodology for force control by impedance control at the interaction point between the tip of single arm flexible robot manipulator tip and the wall has been presented in the paper. The methodology is derived by taking analogy from a ground robot. The impedance control of underwater robot is achieved by a passive foundation base. The PID Impedance Control in flexible underwater robot manipulator has been demonstrated through simulation results, which showed the efficacy of the scheme. The compensation gain also included to show the dynamics of the system. Controller was able to restrict the interaction force to its limited value. Due to the interaction between the underwater robot manipulator tip and the wall, the forces acting on the tip gets transferred to the base through links and lead to the change in position of the base.

REFERENCES

- [1] B. Siciliano, L. Villani, Robot force control, Boston, MA:Kluwer, 1999.
- [2] Gianluca Antonelli, Nilanjan Sarkar, Stefano Chiaverini, External force control for Underwater vehicle-manipulator system", Proceedings of 38th conference on decision & control Phoenix, Arizona USA (1999) 2975-2980.
- [3] Neville Hogan, Impedance control: An approach to manipulation: part I-theory, Journal of dynamic systems, measurement and control 107 (1985) 1-7.
- [4] Neville Hogan, Impedance control: An approach to manipulation: part II-theory, Journal of dynamic systems, measurement and control 107 (1985) 8-16.
- [5] Neville Hogan, Impedance control: An approach to manipulation: part III-theory, Journal of dynamic systems, measurement and control 107 (1985) 17-24.
- [6] N. Hogan, Impedance control: An approach to manipulation, Journal of Dynamic Systems and Measurement Control 107(1985)1-24.
- [7] N.H. McClamroch, D. Wang, Feedback stabilization and tracking of constrained robots, IEEE Transactions on Automatic Control 33 (1988)419-426.
- [8] Yong Zhu, Eric J. Barth, Passivity-based impact and force control of a pneumatic actuator, Journal of dynamic systems, measurement and control 130 (2008) 1-7.
- [9] Hanlei Wang, YongchunXie, Adaptive jacobian position/force tracking control of free-flying manipulators, Journal of Robotics and Autonomous systems57 (2009) 173-181.
- [10] T. Yoshikawa, A. Sudou, Dynamic hybrid position/force control of robot manipulators on-line estimation of unknown constraint, IEEE Transactions on Robotics and Automation 9 (2) (1993)220-226.
- [11] S. Chiaverini, B. Siciliano, L. Villani, Force/position regulation of compliant robot manipulators, IEEE Transactions on Automatic Control 39 (1994) 647-652.
- [12] Z. Doulgeri, Y. Karayiannidis, Force/position tracking of a robot in compliant contact with unknown stiffness and surface kinematics, IEEE International Conference on Robotics and Automation, Roma, Italy (2007) 4190-4195.
- [13] Y. Cui, T. Podder, N. Sarkar, Impedance control of underwater vehicle-manipulator systems (UVMS), Proceeding IEEE/RSJ international conference Intelligent robots and systems (1997) 148-153.
- [14] Gianluca Antonelli, Stefano Chiaverini, Nilanjan Sarkar, An external force control scheme for Underwater vehicle-manipulator system", International conference on intelligent robots and systems, Kyongji, Korea, 1999.
- [15] Gianluca Antonelli, Stefano Chiaverini, Nilanjan Sarkar, External force control for Underwater vehicle-manipulator systems with adaptive motion control, IEEE Hong-Kong symposium on robotics and control, Hong-Kong (1999) 361-366.
- [16] HamedFarivarnejad, A. Sli A. Moosavian, Multiple impedance control for object manipulation by a dual arm underwater vehicle-manipulator system, Ocean Engineering 89 (2014) 82-89.
- [17] P.M. Pathak, A. Mukherjee, A Dasgupta, Impedance control of space robots using passive degrees of freedom in controller domain, Transactions of ASME 127 (2005) 564-578.

- [18] Amit Kumar, Modeling and control of flexible space robots, PhD thesis, Department of mathematics, Indian institute of technology Roorkee, 2010.
- [19] Amalendu Mukherjee, Ranjit Karmakar, Arun Kumar Samantaray, Bond graph in modelling simulation and fault identification, I.K. International publishing house Pvt. Ltd., New Delhi, 2006.
- [20] Pushparaj Mani Pathak, Strategies for Trajectory, Attitude, and Impedance Control of Space Robots, Ph.D. thesis, Department of Mechanical Engineering, Indian Institute of Technology, Kharagpur, 2004.
- [21] C. S. Kumar, Shaping the Interaction Behavior of Manipulators through Additional Passive Degrees of Freedom: A New approach to Impedance Control, PhD thesis, Department of Mechanical Engineering, Indian Institute of Technology, 1994.
- [22] C.S. Kumar, A. Mukherjee, M.A. Faruqi, Some Finer Aspects of Impedance Modulation on Hybrid Tracking and Force Controlled Manipulators, Proceedings of International Conference on Bond Graph Modeling and Simulation (ICBGM), California, pp. 214-219, January 17-20, 1993.
- [23] Sunil Kumar, Vikas Rastogi, Pardeep Gupta, Trajectory Control of Single Arm Underwater Flexible Welding Robot using Bond Graphs, The Proceedings of the 2014 International conference on bond graph modelling and simulation (ICBGM'2014), Simulation Series, Vol. 46 (8) (2014) 79-84.
- [24] Fang Wang, Ye Li, Lei Wan, Yuru Xu, Modeling and Motion Control Strategy for Autonomous Underwater Vehicles, Proceedings of International Conference on Mechatronics and Automation, August 9-12, Changchun, China, pp. 4851-4856, 2009.
- [25] Nilanjan Sharkar, Tarun Kanti Podder, Coordinated Motion Planning and Control of Autonomous Underwater Vehicle-Manipulator Systems Subject to Drag Optimization, IEEE Journal of Oceanic Engineering 26 (2) (2001) 228-239.

See discussions, stats, and author profiles for this publication at: <https://www.researchgate.net/publication/322526521>

Realization of Current Mode Universal Filter and a Dual-Mode Single Resistance Controlled Quadrature Oscillator Employing...

Article in *Advances in Electrical and Electronic Engineering* · January 2018

DOI: 10.15598/aeer.v15i5.2397

CITATIONS

0

READS

34

2 authors:



Manish Gupta

Inderprastha Engineering College, Ghaziabad

8 PUBLICATIONS 17 CITATIONS

[SEE PROFILE](#)



Tajinder Singh Arora

Maharaja Surajmal Institute Of Technology

19 PUBLICATIONS 26 CITATIONS

[SEE PROFILE](#)

Some of the authors of this publication are also working on these related projects:



New Single Input Multiple Output Type Current Mode Biquad Filter Using OTAs [View project](#)

REALIZATION OF CURRENT MODE UNIVERSAL FILTER AND A DUAL-MODE SINGLE RESISTANCE CONTROLLED QUADRATURE OSCILLATOR EMPLOYING VDCC AND ONLY GROUNDED PASSIVE ELEMENTS

Manish GUPTA¹, Tajinder Singh ARORA²

¹Department of Electronics and Communication Engineering, Inderprastha Engineering College,
Surya Nagar Flyover Road, Ghaziabad, 201004 Uttar Pradesh, India

²Department of Electronics and Communication Engineering, Maharaja Surajmal Institute of Technology,
Lal Sain Mandir Marg, Janakpuri, 110058 New Delhi, India

guptamanish2004@gmail.com, tajarora@gmail.com

DOI: 10.15598/aece.v15i5.2397

Abstract. *The manuscript presents a circuit that can act as a universal filter as well as a single resistance controlled oscillator by unpretentiously changing the switch positions. The circuit employs only two active devices and all grounded passive elements. The utilization of only grounded passive components makes this circuit a better choice for integrated circuit implementation. The current mode biquadratic filter offers all the five basic responses along with independent tunability of its quality factor. The dual-mode quadrature sinusoidal oscillator offers explicit current outputs along with voltage outputs. The circuit also offers a simple and uncoupled condition of oscillation and frequency of oscillation. The typical analysis such as non-ideal, sensitivity and parasitic analysis along with the regular simulation results as well as experimental results are exposed here, to strengthen the design idea.*

Keywords

Current Mode circuits, single resistance controlled oscillator, universal filter, voltage differencing current conveyor.

1. Introduction

From last few decades, there has been a predominance of digital signal processing over analog signal processing. But this does not pose any threat to it; rather it gave more challenges and opportunity to the designer and researcher of analog circuits. Analog signal pro-

cessing, where natural/ analog signals are handled as per the specifications, has its own advantages such as higher bandwidth, faster speed of operation etc. In the domain of analog circuits, some of the most widely employed applications are active filters, sinusoidal oscillator, non-linear waveforms generator, synthetic inductor realization [1], [2], [3], [4] and [5]. Frequency selective filters and sinusoidal oscillator, since long, have found impeccable application in communication receiver, control systems etc. [6]. Frequency selective filters, as the name implies, is the block that passes /attenuates any specific frequency or a band of frequencies whereas oscillator is a circuit that generates the undamped waveform of any designed frequency.

The reference no. [7] exposed a gateway to the upcoming future devices; Voltage Differencing Current Conveyor (VDCC) is one of them. So many applications of this active device [8], [9], [10], [11], [12], [13], [14], [15], [16], [17], [18], [19], [20], [21] and [22], and references cited therein, are made available in the open literature. But still as per authors' perception, this active device has to be much more explored and exploited for analog signal processing applications, in future.

Out of these [8], [9], [10], [11], [12], [13], [14], [15], [16], [17], [18], [19], [20], [21] and [22], synthetic inductor is realized in [8], [9] and [10], passive element simulator in [11] and [12], active filter was presented in [13], [14], [15], [16] and [17], and sinusoidal oscillator in [18], [19], [20] and [21]. The behavioral model of the active device is discussed in detail in [22]. Comparison of the designed universal filter circuit with the earlier work done on VDCC based filters is as follows. In [13] a voltage mode universal active filter using single

Tab. 1: Comparison table of literature survey (Active Filter).

Ref. No.	Mode of operation	All five types of responses available	Number of VDCC employed	Number of passive elements used	Whether all passive elements grounded	Matching of impedances at input and output level	Is Q_0 independently tunable
[13]	Voltage mode	Yes	1	3	No	No	No
[14]	Current mode	Yes	1	3	Yes	No	No
[15]	Current mode	Yes	2	4	Yes	No	Yes
[16]	Voltage mode	No	2	7	No	No	Yes
Proposed circuit	Current mode	Yes	2	4	Yes	Yes	Yes

Tab. 2: Comparison table of literature survey (Sinusoidal Oscillator).

Ref. No.	Number of VDCC employed	Whether all passive elements grounded	Non-interacting CO and FO	Availability of explicit quadrature outputs	Is operation in CM/VM both mode	Any significant remarks
[18]	1	Yes	No	No	No	Availability of BP and LP responses in transconductance mode
[19]	2	Yes	Yes	Yes	Yes	-
[20]	1	Yes	No	Yes	No	Multiphase Oscillator (Linear Control of FO)
[21]	1	Yes	No	Yes	No	-
Proposed circuit	2	Yes	Yes	Yes	Yes	Availability of current mode Universal filter

VDCC is presented but it suffers from the drawback of the utilization of floating passive elements. A current mode universal filter with less number of active devices is presented in [14] but the circuit has a drawback that the filter parameters are not independently tunable. The circuit given in [15] uses the same number of active and passive devices but input current is not injected at low impedance port. Additionally, circuit can perform one function only. In [16] higher numbers of passive elements were used. First ever, first order all-pass filter using single VDCC is presented in [17]. A qualitative comparison of parameters with given literature survey is shown in Tab. 1.

Now the comparison of the proposed oscillator with the earlier published work is given as follows. The quadrature oscillator, employing all grounded passive elements, which is not having non-interacting CO and FO (also known as fully uncoupled) and its tuning capability is limited with passive grounded element only, is presented in [18] and [21]. In [19], the same number of active and passive elements are utilized, but works as a sinusoidal oscillator only (can't perform the function of active filter). In [20], a multiphase oscillator using controlled gain VDCC was proposed but requires a matching condition to the linear control of oscillation frequency. A comparative analysis is also presented in Tab. 2.

The purpose of this manuscript is to present one such circuit that can work as a universal filter along with a sinusoidal oscillator. In conclusion, the circuit offers various features, when used as an active filter, such as:

- Availability of all five responses in current mode i.e. low pass, high pass, band pass, band reject and all pass filter function.
- Independent tunability of its quality factor (Q_0).
- Orthogonal tunability of its center frequency (ω_0).
- Availability of explicit current output.
- Use of only grounded passive elements.
- Availability of low impedance at input port and high impedance at output port.

Whereas when the same circuit acts as sinusoidal oscillator reflects some useful characteristics e.g.

- Availability of explicit current output.
- Use of only grounded passive elements.
- Availability of quadrature current output (explicit).
- Availability of voltage mode quadrature output.
- Simple Condition of Oscillation (CO) and Frequency of Oscillation (FO).
- Uncoupled CO and FO.
- FO can be tuned either electronically or by use of grounded passive resistor.
- CO can also be adjusted by grounded passive resistor or by electronic tunability.

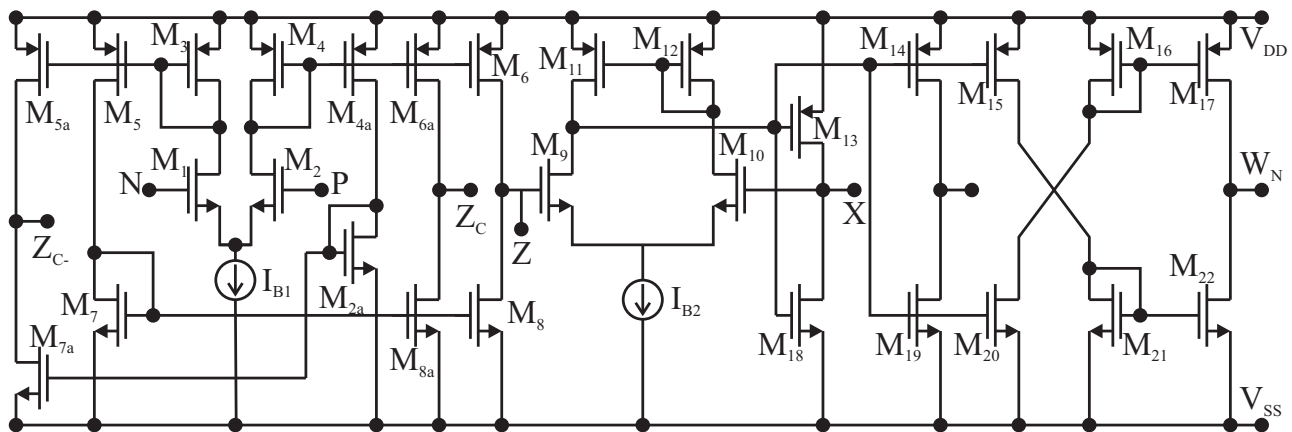


Fig. 1: MOS realization of the Voltage Differencing Current Conveyor [15].

Full manuscript is divided into five main sections. At the outset, the present section gives the introduction of analog signal processing and comparison between previous work and presented work. Section 2. presents the active device i.e. VDCC along with the proposed circuit. Non-ideal and sensitivity analysis is depicted in Sec. 3. . Section 4. states the effects of parasitic of the active device under consideration, on the proposed circuit. To verify the theoretical analysis, Sec. 5. contains all the simulation results. Experimental results are given in Sec. 6. At last, conclusion is provided in Sec. 7.

2. Proposed Circuit

The electrical combination of an Operational Transconductance Amplifier (OTA) and a second generation Current Conveyor (CCII) is known as VDCC. The block diagram along with its functional circuit diagram, employing CMOS transistors, are shown in Fig. 2 and Fig. 1 respectively. Equation (1) represents the natural characteristics of the active device. Here g_m is the transconductance factor of the device; additionally, this is electronically tunable with the help of the bias current i.e. I_{B1} (Fig. 2).

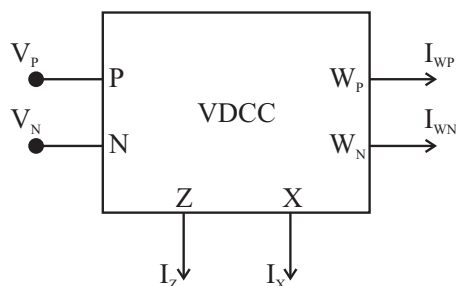


Fig. 2: Block Diagram of VDCC [8].

$$\begin{bmatrix} I_P \\ I_N \\ I_Z \\ V_X \\ I_{WP} \\ I_{WN} \end{bmatrix} = \begin{bmatrix} 0 & 0 & 0 & 0 \\ 0 & 0 & 0 & 0 \\ g_m & -g_m & 0 & 0 \\ 0 & 0 & 1 & 0 \\ 0 & 0 & 0 & 1 \\ 0 & 0 & 0 & -1 \end{bmatrix} \begin{bmatrix} V_P \\ V_N \\ V_Z \\ I_X \end{bmatrix}. \quad (1)$$

The proposed circuit that can work as a current mode universal filter, as well as single resistance controlled oscillator, by simply altering the switch position, is shown in Fig. 3. Table 3 shows the basic combination of switches, as shown in Fig. 3, so that the circuit can provide the desired nature of the operation.

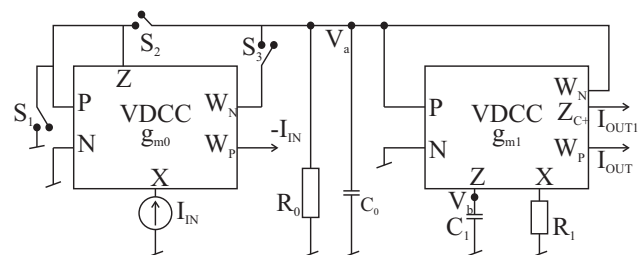


Fig. 3: Proposed realization of filter cum Oscillator Circuit.

Tab. 3: Characteristic table (for the circuit shown in Fig. 3).

S. No.	Switches			Operation
	S1	S2	S3	
1.	ON	OFF	ON	Current mode universal filter
2.	OFF	ON	OFF	Dual mode quadrature oscillator

When the switch combination as given in S.No. 1 of Tab. 3 is applied, the circuit behaves as an active filter. To get all the desired transfer functions, we simply apply the basics of circuit theory on the Fig. 3, utilizing the characteristic equation of VDCC i.e. given in Eq. (1). All five desired transfer function of a universal filter i.e. low pass, high pass, band pass, band stop

and all pass are presented in Eq. (2), Eq. (3), Eq. (5), Eq. (7) and Eq. (9). The common denominator polynomial, expression for the center frequency and quality factor are given by Eq. (10), Eq. (11) and Eq. (12). It is evident from Eq. (12) that the Q_0 is independent of ω_0 and its value can be varied by varying a grounded passive resistor i.e. R_0 . The gain of the given Band Pass (H_{BP}) and Low Pass (H_{LP}) filter function is given in Eq. (13).

$$\frac{I_{OUT1}}{I_{IN}} = \frac{I_{BP}}{I_{IN}} = \frac{s \cdot g_{m1}}{D(s)}. \quad (2)$$

$$\frac{I_{OUT}}{I_{IN}} = \frac{I_{LP}}{I_{IN}} = \frac{g_{m1}}{D(s)}. \quad (3)$$

If $g_{m1}R_0 = 1$,

$$I_{HP} = -I_{IN} + I_{BP} + I_{LP}, \quad (4)$$

$$\frac{I_{HP}}{I_{IN}} = -\frac{s^2}{D(s)}. \quad (5)$$

$$I_{BS} = I_{HP} - I_{BP}, \quad (6)$$

$$\frac{I_{BS}}{I_{IN}} = -\frac{s^2 + \frac{s}{R_0C_0}}{D(s)}. \quad (7)$$

$$I_{AP} = -I_{HP} - I_{BP} + I_{LP}, \quad (8)$$

$$\frac{I_{AP}}{I_{IN}} = \frac{s^2 - \frac{s}{R_0C_0} + \frac{g_{m1}}{R_1C_0C_1}}{D(s)}. \quad (9)$$

$$D(s) = s^2 + \frac{s}{R_0C_0} + \frac{g_{m1}}{R_1C_0C_1}. \quad (10)$$

$$\omega_0 = \sqrt{\frac{g_{m1}}{R_1C_0C_1}}. \quad (11)$$

$$Q_0 = R_0 \sqrt{\frac{g_{m1}C_0}{R_1C_1}}. \quad (12)$$

$$\left. \begin{aligned} H_{LP} &= 1 \\ H_{BP} &= g_{m1}R_0 \end{aligned} \right\}, \quad (13)$$

where ω_0 is the center frequency in $\text{rad}\cdot\text{s}^{-1}$ and Q_0 is the quality factor.

When the appropriate switch combination of Tab. 3 (S.No.2) is applied, the proposed circuit works as a Single Resistance Controlled Oscillator (SRCO). The characteristic equation of the proposed SRCO is given by Eq. (14). The Condition of Oscillation (CO) and Frequency of Oscillation (FO) are simple and uncoupled to each other, represented by Eq. (15) and Eq. (16) respectively. Here, it is evident that the CO, as well as

FO, can be tuned electronically (g_{m0} for CO and g_{m1} for FO) as well as with the help of grounded passive resistor (R_0 for CO and R_1 for FO), without affecting each other. The circuit offers two explicit current outputs that are in 90° phase shift to each other. These two quadrature outputs are I_{OUT} and I_{OUT1} ; namely. The relationship between them is shown by Eq. (17). Here it is worth noting that the derived circuit can also offer quadrature voltage outputs V_a and V_b . The relationship between the both is justified by Eq. (18).

$$s^2 + \frac{s}{C_0} \left(\frac{1}{R_0} - g_{m0} \right) + \frac{g_{m1}}{R_1C_0C_1} = 0. \quad (14)$$

$$\text{C.O.} \quad \left(\frac{1}{R_0} - g_{m0} \right) = 0. \quad (15)$$

$$\text{F.O.} \quad \omega_0 = \sqrt{\frac{g_{m1}}{R_1C_0C_1}}. \quad (16)$$

$$\frac{I_{OUT}}{I_{OUT1}} = \frac{1}{sC_1R_1}. \quad (17)$$

$$\frac{V_b}{V_a} = \frac{g_{m1}}{sC_1}. \quad (18)$$

3. Non-Ideal and Sensitivity Analysis

The deviation between ideal and non-ideal values of the active device can be checked through its given mathematical equation. Equation (19) represents the characteristics equations of VDCC where ' i ' represents the number of the active device that could be 0 and 1. The non-ideal factors are defined as α , β , γ_P and γ_N . The ideal values of α , β , γ_P and γ_N are in unity only.

$$\left. \begin{aligned} I_Z &= \alpha_i \cdot g_{mi}(V_P - V_N) \\ V_X &= \beta_i \cdot V_Z \\ I_{WP} &= \gamma_{Pi}I_X \\ I_{WN} &= -\gamma_{Ni}I_X \end{aligned} \right\}. \quad (19)$$

When Eq. (19) is used for analyzing the proposed circuit, as given in Fig. 3, by circuit theory fundamentals, non-ideal transfer functions are obtained. Equation (20) and Eq. (21) represent the transfer functions of band pass and low pass filters, whereas, frequency and quality factor along with common denominator polynomial are given by Eq. (22), Eq. (23) and Eq. (24).

$$\frac{I_{OUT1}}{I_{IN}} = \frac{\alpha_1 \cdot \gamma_{NO} \left(\frac{sg_{m1}}{C_0} \right)}{D'(s)}. \quad (20)$$

$$\frac{I_{OUT}}{I_{IN}} = \frac{\alpha_1 \cdot \beta_1 \cdot \gamma_{P1} \cdot \gamma_{NO} \left(\frac{g_{m1}}{C_0C_1R_1} \right)}{D'(s)}. \quad (21)$$

$$\omega'_0 = \sqrt{\frac{\alpha_1 \cdot \beta_1 \cdot g_{m1} \cdot \gamma_{N1}}{C_0 C_1 R_1}}. \quad (22)$$

$$Q'_0 = R_0 \sqrt{\frac{C_0 \alpha_1 \cdot \beta_1 \cdot g_{m1} \cdot \gamma_{N1}}{C_1 R_1}}. \quad (23)$$

$$D'(s) = s^2 + s \left(\frac{1}{C_0 R_0} \right) + \frac{\alpha_1 \cdot \beta_1 \cdot \gamma_{N1} g_{m1}}{C_0 C_1 R_1}. \quad (24)$$

While doing the non-ideal analysis for the proposed sinusoidal oscillator, we get the following characteristic equation, given by Eq. (25). From Eq. (25), non-ideal CO and FO can be easily deduced, which are represented in Eq. (26) and Eq. (27) respectively.

$$s^2 + \frac{s}{C_0} \left(\frac{1}{R_0} - \alpha_0 \cdot g_{m0} \right) + \frac{\alpha_1 \cdot \beta_1 g_{m1} \gamma_{N1}}{R_1 C_0 C_1} = 0. \quad (25)$$

$$\text{C.O.} \quad \left(\frac{1}{R_0} - \alpha_0 \cdot g_{m0} \right) \geq 0. \quad (26)$$

$$\text{F.O.} \quad \omega_0 = \sqrt{\frac{\alpha_1 \cdot \beta_1 \cdot g_{m1} \gamma_{N1}}{R_1 C_0 C_1}}. \quad (27)$$

Sensitivity analysis was also carried out for both the proposed applications of VDCC. The sensitivity equations for the derived current mode universal filter are given by Eq. (28), Eq. (29), Eq. (30), Eq. (31), Eq. (32) and Eq. (33) and for SRCO derived sensitivity equations are represented by Eq. (34) to Eq. (35). All the derived sensitivity figures are under considerable limits.

$$S_{\alpha_1}^{\omega'_0} = S_{\beta_1}^{\omega'_0} = S_{\gamma_{N1}}^{\omega'_0} = \frac{1}{2}. \quad (28)$$

$$S_{g_{m1}}^{\omega'_0} = \frac{1}{2}; \quad S_{R_1}^{\omega'_0} = S_{C_1}^{\omega'_0} = S_{C_0}^{\omega'_0} = -\frac{1}{2}. \quad (29)$$

$$S_{\alpha_1}^{Q'_0} = S_{\beta_1}^{Q'_0} = S_{\gamma_{N1}}^{Q'_0} = \frac{1}{2}. \quad (30)$$

$$S_{g_{m1}}^{Q'_0} = S_{C_0}^{Q'_0} = \frac{1}{2}. \quad (31)$$

$$S_{C_1}^{Q'_0} = S_{R_1}^{Q'_0} = -\frac{1}{2}. \quad (32)$$

$$S_{R_0}^{Q'_0} = 1. \quad (33)$$

$$S_{\alpha_1}^{\omega'_0} = S_{\beta_1}^{\omega'_0} = S_{\gamma_{N1}}^{\omega'_0} = \frac{1}{2}. \quad (34)$$

$$S_{g_{m1}}^{\omega'_0} = \frac{1}{2}; \quad S_{R_1}^{\omega'_0} = S_{C_1}^{\omega'_0} = S_{C_0}^{\omega'_0} = -\frac{1}{2}. \quad (35)$$

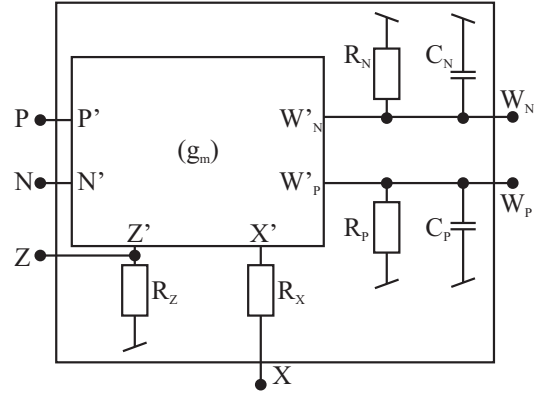


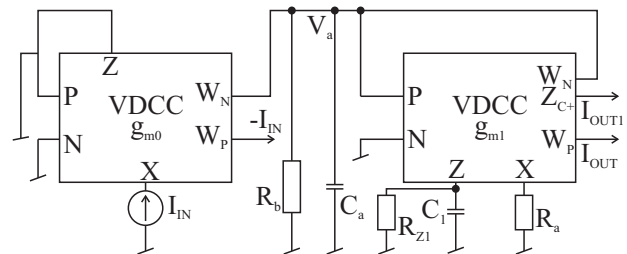
Fig. 4: Parasitic model of VDCC [19].

4. Parasitic Analysis

A well known parasitic model of VDCC [19] has been taken into consideration, shown in Fig. 4, to explore the effect of parasitic on designed circuits.

The next scheme shows the proposed circuit including parasitic effects. It is evidently shown that the proposed current mode universal filter and sinusoidal oscillator reflects good performance under the influence of parasitic.

4.1. Parasitic Analysis for Universal Filter



Assumptions:

$$R_a = R_1 + R_{X1}.$$

$$R_b = R_0 || R_{N0} || R_{N1}.$$

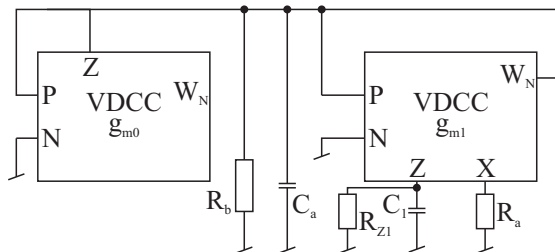
$$C_a = C_0 + C_{N0} + C_{N1}.$$

$$I_{OUT1} = \frac{\left[\frac{1}{R_{Z1}} + sC_1 \right] \frac{g_{m1}}{C_a C_1}}{\tilde{D}(s)}.$$

$$I_{OUT} = \frac{\frac{g_{m1}}{R_a C_1 C_a}}{\tilde{D}(s)}.$$

$$\begin{aligned}\tilde{D}(s) &= s^2 + s \left[\frac{1}{C_1 R_{Z1}} + \frac{1}{C_a R_b} \right] + \frac{1}{C_a C_1} \left[\frac{g_{m1}}{R_a} + \frac{1}{R_{Z1} R_b} \right] \cdot S_{R_a}^{\tilde{\omega}_0} = -S_{g_{m1}}^{\tilde{\omega}_0} = -\frac{1}{2} \frac{\frac{g_{m1}}{R_a C_1 C_a}}{\frac{1}{C_a C_1} \left[\frac{1}{R_{Z1}} \left(\frac{1}{R_b} - g_{m0} \right) + \frac{g_{m1}}{R_a} \right]} \\ \tilde{\omega}_0 &= \sqrt{\frac{1}{C_1 C_a} \left[\frac{g_{m1}}{R_a} + \frac{1}{R_{Z1} R_b} \right]} \\ \tilde{Q}_0 &= \frac{1}{\left[\frac{1}{C_1 R_{Z1}} + \frac{1}{C_a R_b} \right]} \sqrt{\frac{1}{C_1 C_a} \left[\frac{g_{m1}}{R_a} + \frac{1}{R_{Z1} R_b} \right]} \\ S_{C_1}^{\tilde{\omega}_0} &= S_{C_a}^{\tilde{\omega}_0} = -\frac{1}{2} \\ S_{R_a}^{\tilde{\omega}_0} &= -S_{g_{m1}}^{\tilde{\omega}_0} = -\frac{1}{2} \frac{\frac{g_{m1}}{R_a C_1 C_a}}{\frac{1}{C_1 C_a} \left[\frac{g_{m1}}{R_a} + \frac{1}{R_{Z1} R_b} \right]} \\ S_{R_b}^{\tilde{\omega}_0} &= -S_{R_{Z1}}^{\tilde{\omega}_0} = -\frac{1}{2} \frac{\frac{1}{C_1 C_a R_{Z1} R_b}}{\frac{1}{C_1 C_a} \left[\frac{g_{m1}}{R_a} + \frac{1}{R_{Z1} R_b} \right]} \\ S_{g_{m0}}^{\tilde{\omega}_0} &= -\frac{1}{2} \frac{\frac{g_{m0}}{R_{Z1} C_1 C_a}}{\frac{1}{C_a C_1} \left[\frac{1}{R_{Z1}} \left(\frac{1}{R_b} - g_{m0} \right) + \frac{g_{m1}}{R_a} \right]}\end{aligned}$$

4.2. Parasitic Analysis for Sinusoidal Oscillator



Assumptions:

$$R_a = R_1 + R_{X1}.$$

$$R_b = R_0 || R_{Z0} || R_{N1}.$$

$$C_a = C_0 + C_{N1}.$$

$$\text{CO: } \frac{1}{C_a}[g_{m0} - R_b] = \frac{1}{C_1 R_{z1}}.$$

$$\text{FO: } \tilde{\omega}_0^2 = \frac{1}{C_a C_1} \left[\frac{1}{R_{Z1}} \left(\frac{1}{R_b} - g_{m0} \right) + \frac{g_{m1}}{R_a} \right].$$

$$S_{C_1}^{\tilde{\omega}_0} = S_{C_a}^{\tilde{\omega}_0} = -\frac{1}{2}.$$

5. Simulation Results

Feasibility of the proposed filter cum oscillator circuit, with all grounded passive components, has been tested and simulated using Cadence PSPICE simulation software. The CMOS version shown in Fig. 1, using 0.18 μm TSMC MOS process parameters [23], is utilized for generating the graphical results. The aspect ratios, used in Fig. 1, are presented in Tab. 4 [8]. For simulation, supply voltage of ± 0.9 V and bias current of 50 μA (I_{B1}) and 100 μA (I_{B2}), shown in Fig. 1, are used and the corresponding value of transconductance gain (g_m) is 277 $\mu\text{A}\cdot\text{V}^{-1}$. All the simulation results of the derived circuit are mainly divided into two parts - former depict universal filter's simulation results and latter shows the simulation graphs for the oscillator circuit.

For the testing of the universal filter, the passive components were selected as $R_0 = R_1 = 3.6 \text{ k}\Omega$, $C_0 = 21.9 \text{ pF}$, $C_1 = 87.6 \text{ pF}$ and the transconductance gain of the active device is $277 \text{ }\mu\text{A}\cdot\text{V}^{-1}$. Figure 5 demonstrates that the designed current mode circuit can be utilized as a low pass, high pass, band pass and band stop filter. Here the center frequency was chosen as 1 MHz and the value of the quality factor is 0.5 . The proposed circuit can also act like an all pass filter whose gain as well as phase response is depicted in Fig. 6. Figure 5 and Fig. 6 collectively justify the design of a universal filter using VDCC with all grounded passive components. As given in Eq. (12), Q_0 can be varied with the help of resistance R_0 without altering the center frequency. So the variation of the quality

factor by changing the value of grounded passive resistor R_0 is shown in Fig. 7. Table 5 gives the range of R_0 and their corresponding value of Q_0 .

Tab. 4: Aspect ratios of the MOS devices [8].

CMOS transistors	W/L (in μm)
M1–M4	3.6/1.8
M5, M6	7.2/1.8
M7, M8	2.4/1.8
M9, M10	3.06/0.72
M11, M12	9.0/0.72
M13–M17	14.4/0.72
M18–M22	0.72/0.72

Tab. 5: Q_0 tunability (passive Components values).

Q_0	R_0 (in $\text{k}\Omega$)
0.25	1.8
0.35	2.54
0.5	3.6
0.707	5.09
1	7.2
1.414	10.18

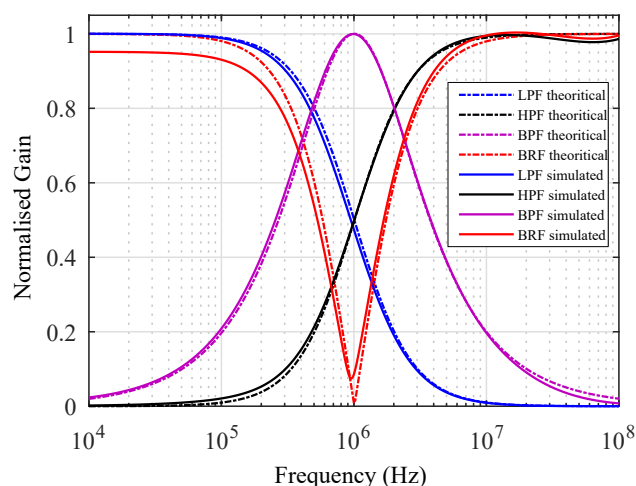


Fig. 5: Current mode filter responses of low pass, high pass, band pass and band reject functions.

Apart from Q_0 tunability, the center frequency of the designed filter can also be varied, as shown in Fig. 8. The passive elements values selected for Fig. 8 are given in Tab. 6. The transient response of the band pass filter is also simulated at 1 MHz, represented in Fig. 9. Figure 9 depicts that at input current of 25 μA , the output is distortion free. Total Harmonic Distortion (THD) of the designed current mode filter circuit is also calculated. The graph plotted between input current versus existing percentage of THD, is depicted in Fig. 10. Figure 10 shows that up to 80 μA of input current the THD is significantly low.

The proposed circuit can also be utilized as a single resistance controlled oscillator with all grounded com-

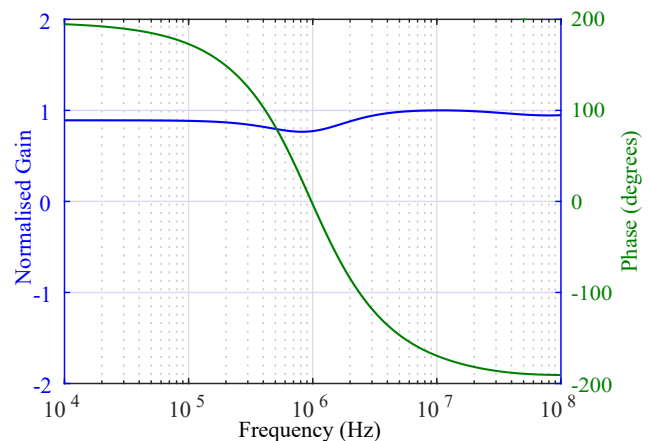


Fig. 6: Gain and phase response of an all pass filter function.

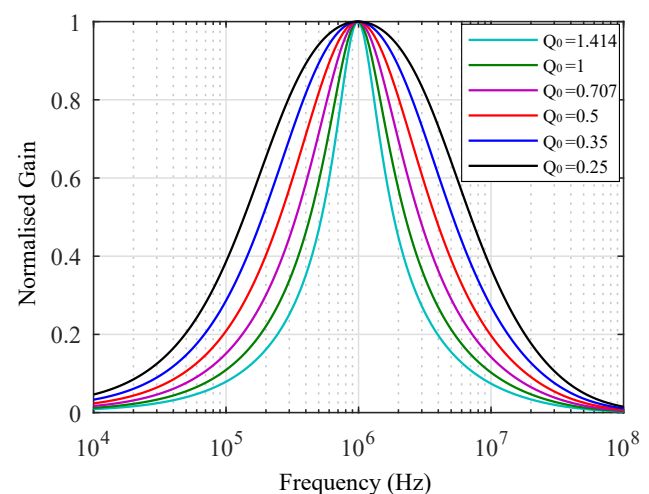


Fig. 7: Q_0 tunability with fixed center frequency at 1 MHz.

Tab. 6: Passive Components values for the tunability of the center frequency.

Frequency (MHz)	0.63	1	1.48
R_0 ($\text{k}\Omega$)	5.72	3.6	2.45
R_1 ($\text{k}\Omega$)	7.2	3.6	1.8
g_m ($\mu\text{A}\cdot\text{V}^{-1}$)	220	277	299
Q_0	0.5	0.5	0.5

ponents. The passive components values for the designed sinusoidal oscillator were chosen as $R_1 = 15 \text{ k}\Omega$, $C_0 = C_1 = 21.9 \text{ pF}$ and the transconductance gain of the active device is $277 \mu\text{A}\cdot\text{V}^{-1}$. The transient and the steady state responses, with explicit current output are shown in Fig. 11 and Fig. 12, respectively. Additionally, Fig. 12 represents the quadrature outputs in current mode. As discussed in Sec. 2., the designed oscillator can also deliver the voltage mode quadrature output, represented in Fig. 13. Lissajous patterns for the current and voltage mode quadrature outputs are also plotted in Fig. 14 and Fig. 15, respectively. It can be seen from last two figures that there are no tilts in the ellipses, hence verifying the quadrature relation-

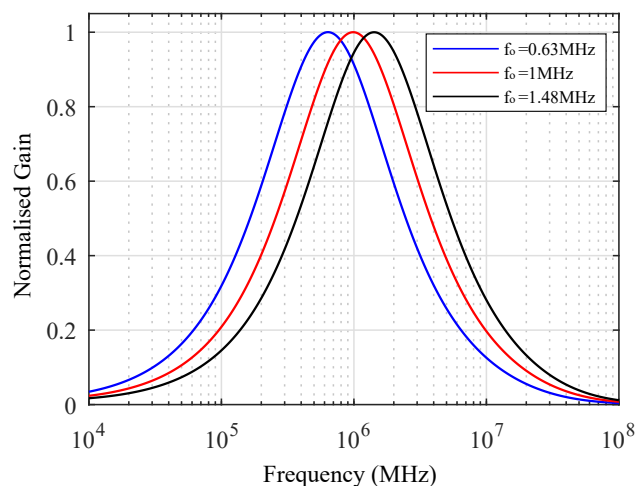


Fig. 8: Variation of center frequency with fixed Q_0 .

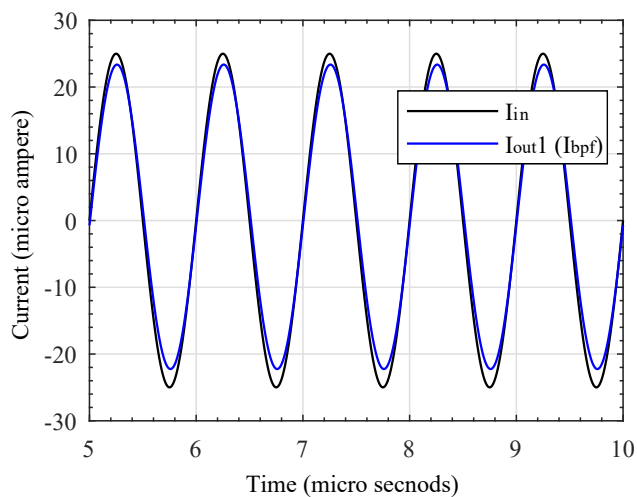


Fig. 9: Transient response of the band pass filter.

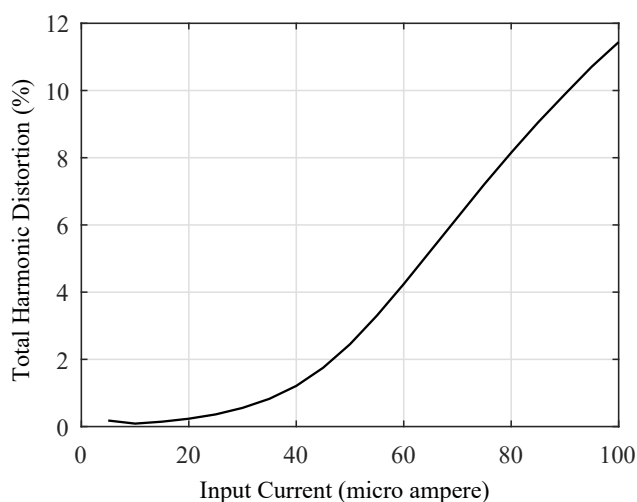


Fig. 10: THD curve for a band pass filter function.

ships. The measured phase angle is 88.3° and 89.4° respectively for Fig. 12 and Fig. 13.

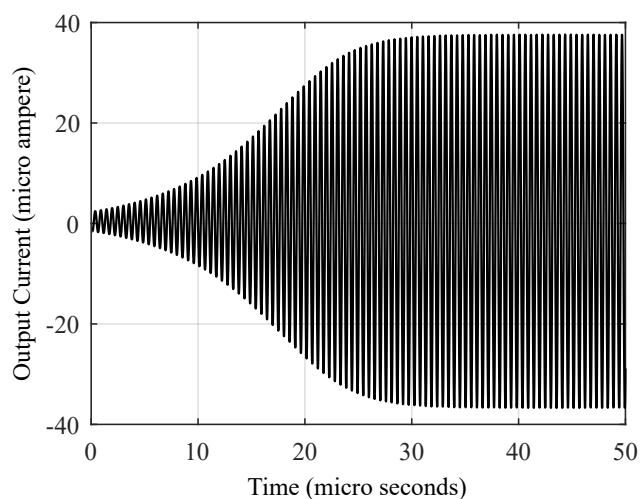


Fig. 11: Transient response of the current mode sinusoidal oscillator.

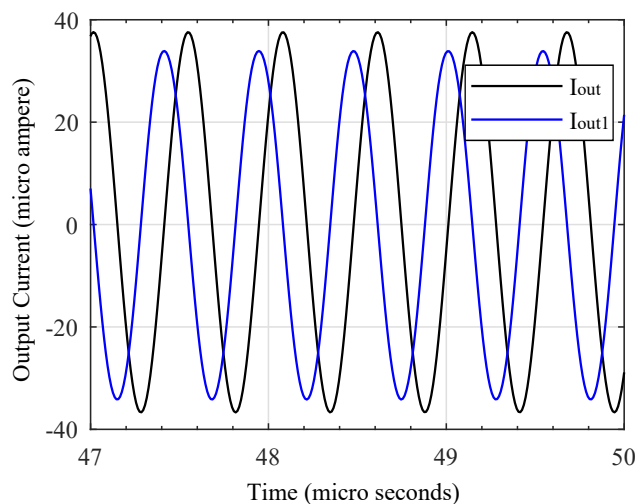


Fig. 12: Steady state response of the quadrature current outputs.

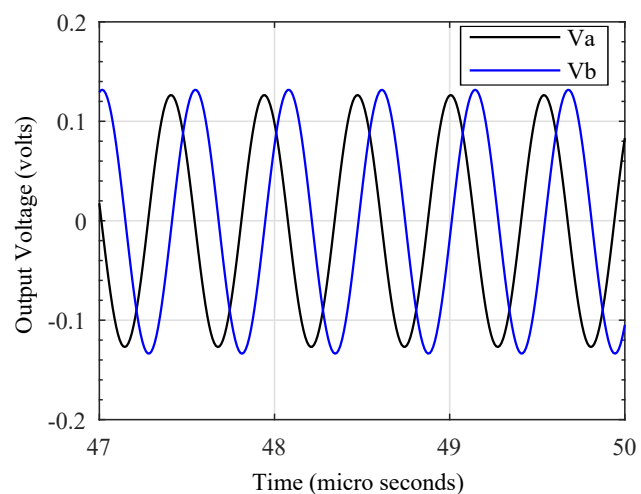


Fig. 13: Steady state response of the quadrature voltage outputs.

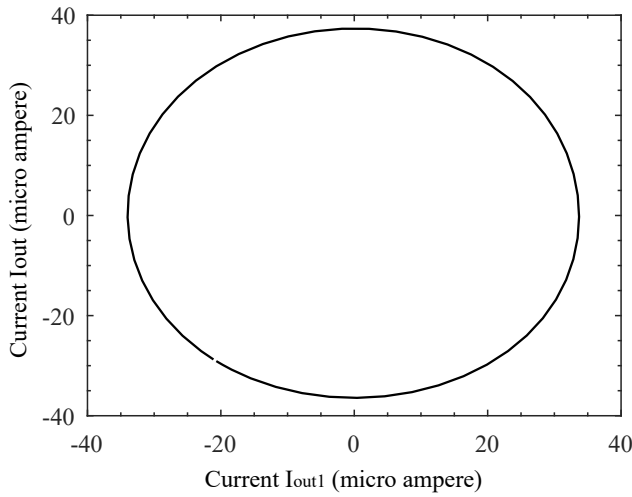


Fig. 14: Lissajous Pattern for current mode outputs.

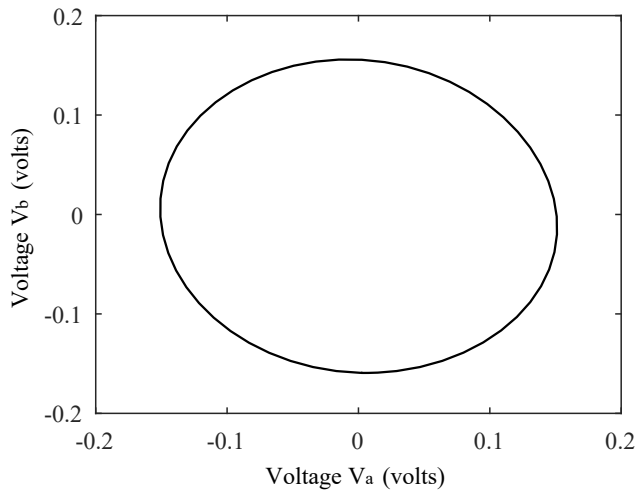


Fig. 15: Lissajous Pattern for voltage mode outputs.

The FFT representation of the explicit current output sinusoidal oscillator is shown in Fig. 16 (for better clarity and to see the availability of harmonics, y-axis has been taken in log domain). It is evident from Eq. (16) that the FO of the derived circuit can be varied with the help of grounded passive resistor i.e. R_1 and same can also be achieved by electronic tunability using g_{m1} . Figure 17 shows the variation of FO with respect to grounded resistor R_1 whereas Fig. 18 represents the electronic tunability of FO with respect to bias current of g_{m1} i.e. I_{B1} . In Fig. 17, for the entire range of R_1 the FO is calculated and maximum error between simulated and calculated values of FO is found to be 6.78 % only. The variation of frequency, under the influence of parasitics, has also been computed. The values of parasitic elements ($R_X = 43 \Omega$, $R_Z = 362 \text{ k}\Omega$, $R_N = 141 \text{ k}\Omega$, $C_P = C_N = 0.92 \text{ pF}$) have been taken from [8]. In Fig. 18, for ideal frequency of 1.86 MHz (for $C_0 = C_1 = 21.9 \text{ pF}$, $R_1 = 3.6 \text{ k}\Omega$ and $g_{m1} = 236 \mu\text{A}\cdot\text{V}^{-1}$ at I_{B1} of 35 μA) we get the sim-

ulated value as 1.84 MHz and including the effect of parasitic we get the FO 1.82 MHz with an error of 2.58 % with respect of ideal frequency.

The total harmonic distortion was also calculated for the entire usable range of the sinusoidal oscillator, as shown in Fig. 19. Figure 19 depicts that the THD is significantly low for the entire range of frequencies which strengthens the designed idea. However, the fluctuation presented in Fig. 19 can be reduced by introducing an additional AGC network as given in [20].

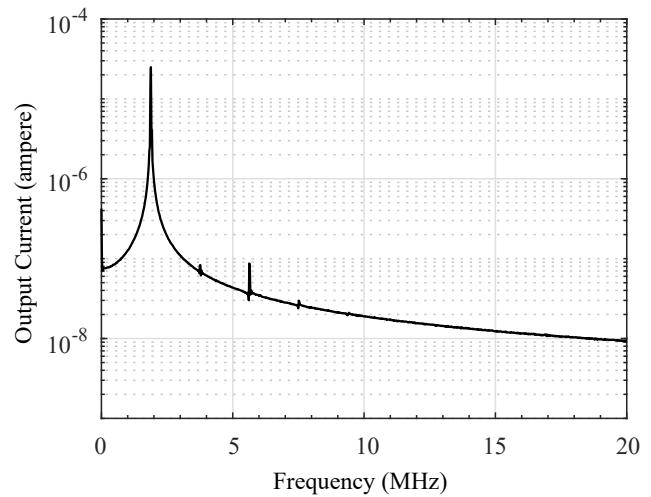


Fig. 16: FFT representation of the explicit current output of sinusoidal oscillator.

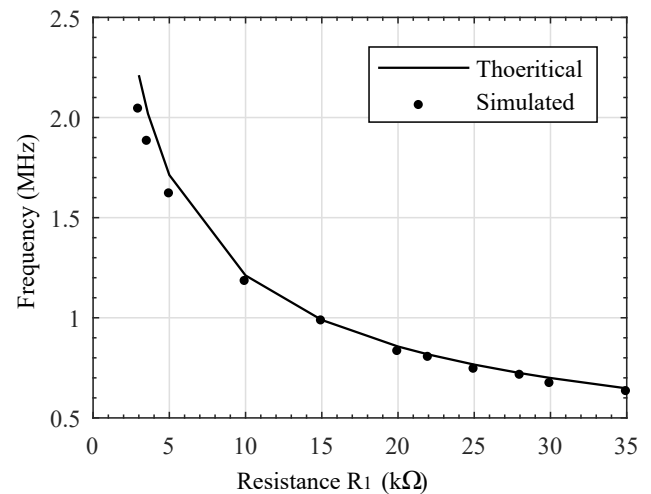


Fig. 17: Variation of FO with respect to a grounded resistor R_1 .

6. Experimental Results

For practical implementation of VDCC as a block, a readily available integrated circuit i.e. OPA860 (see

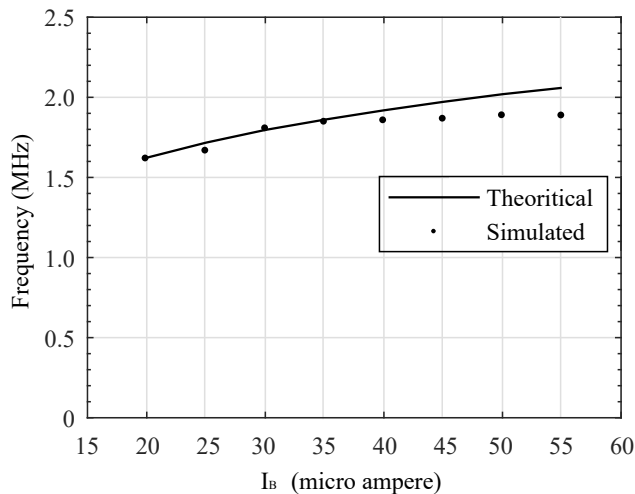


Fig. 18: Variation of FO with respect to the input bias current I_{B1} .

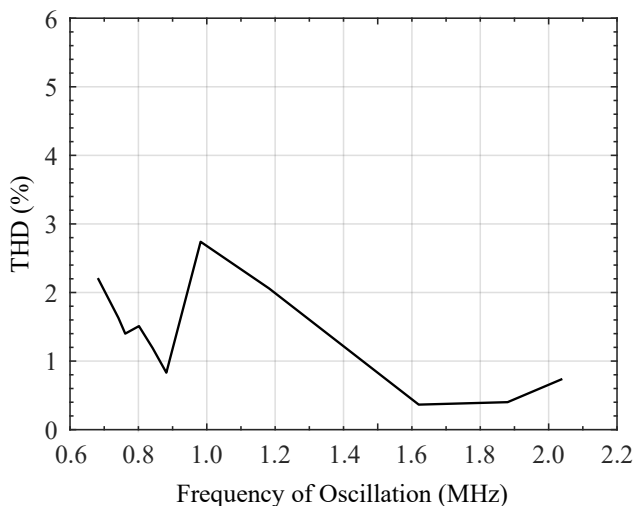


Fig. 19: Variation of FO with respect to calculated THD.

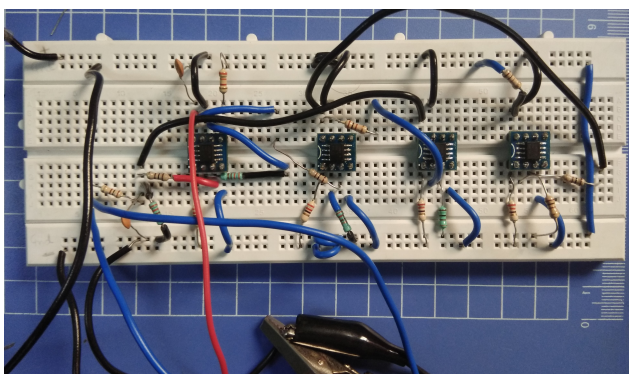


Fig. 20: Experimental setup for Active filter using VDCC.

Fig. 13 of [13]) have been used here. OPA860 is basically a diamond transistor [24]. Here it is worth mentioning that the resistors of $100\ \Omega$ are connected in series to the bases of OTA and buffers inputs [24]. The

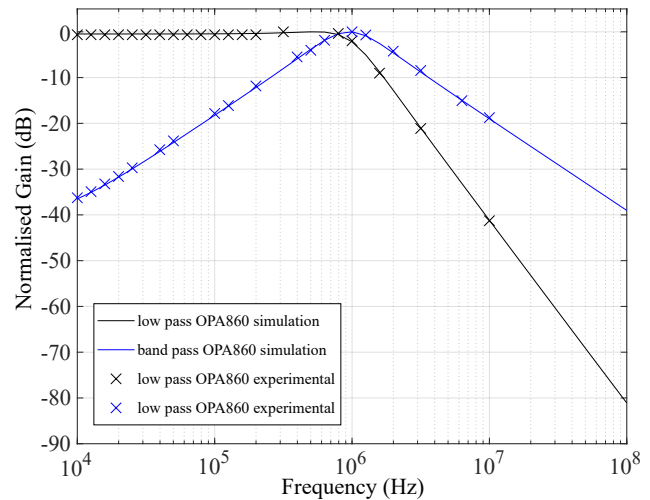


Fig. 21: Filter responses of low pass and band pass responses.

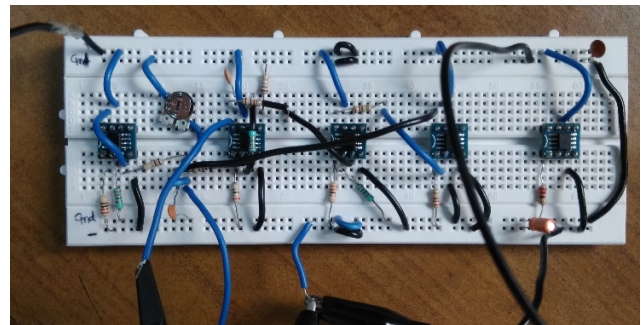


Fig. 22: Experimental setup for sinusoidal oscillator using VDCC.

value of R_{OFFSET} is also taken as $100\ \Omega$ (Fig. 13 of [13]).

For a generation of hardware results, we have used SCIENTIFIC Multiple power supply (PSD3304), SCI-ENTECH function generator (4061), SCIENTIFIC Oscilloscope (30 MHz, SM410). The passive component values, used in experimentation for the active filter, are $C_1 = C_2 = 470\ \text{pF}$, $R_{m1} = 1/g_{m1} = 330\ \Omega$ and $R_1 = R_0 = 330\ \Omega$. For the implementation of SRCO following passive elements have been taken, $C_1 = C_2 = 470\ \text{pF}$, $R_{m1} = 1/g_{m1} = R_{m0} = 1/g_{m0} = 330\ \Omega$ and $R_1 = 330\ \Omega$. Figure 20 and Fig. 22, respectively, shows the experimental setup for the active filter and sinusoidal oscillator using OPA860. The two (explicit) responses i.e. low pass and band pass are simulated using the PSPICE library file of OPA 860 obtained from www.ti.com. The results obtained are very much close to reality, as one can see in Fig. 21. For the purpose of experimentation low pass and band pass (explicit outputs, obtained experimentally) are also marked in Fig. 21. The frequency of operation was chosen as 1 MHz. Figure 23 shows the steady state quadrature output of the experimentally realized oscillator using OPA860. Here the frequency of operation is also cho-

sen as 1.03 MHz (ideally) and the achieved frequency through simulation (using OPA860 macro model) is 935 kHz (with an error of 6.5 %). When the same is performed experimentally, the frequency of operation comes out to be 914 kHz (with an error of 2.2 % with respect to OPA860 simulation). To check the wide range of the oscillator, the graph between frequency of operation and a grounded passive resistor R_1 is plotted, shown in Fig. 24. The simulated and experimental values are in good agreement to each other.

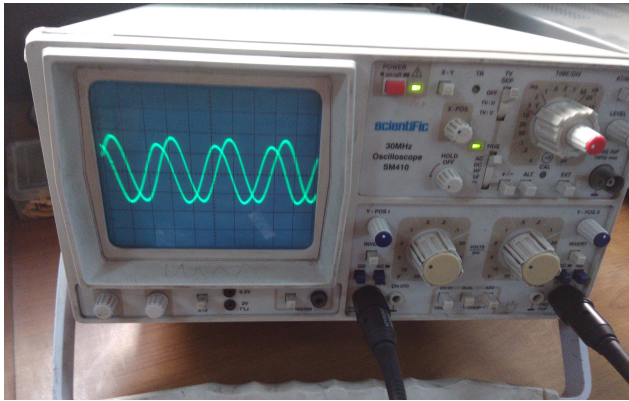


Fig. 23: Steady state output of the oscillator.

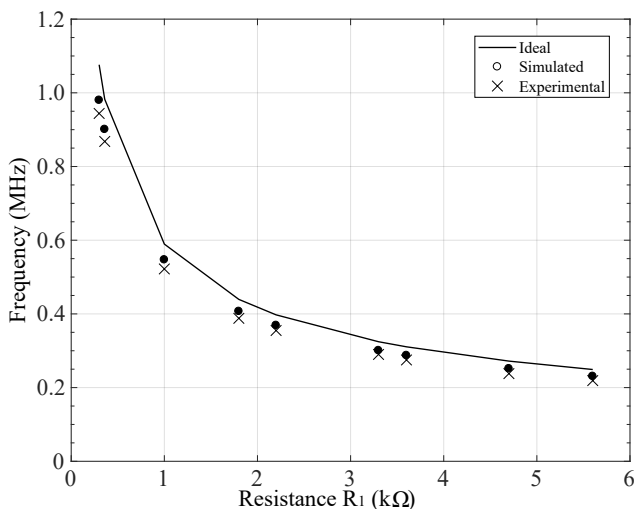


Fig. 24: Variation of FO with respect to a grounded resistor R_1 .

7. Conclusion

This manuscript presents a realization of a current mode universal filter and a single resistance controlled oscillator successively, by altering the positions of the passive switches. Both the designed circuits employ only grounded passive elements and two active devices. Availability of explicit current outputs makes it a better proposition. The designed universal filter can pro-

duce all the five basic responses along with independent control of its quality factor. The derived SRCO has quadrature outputs in current mode (explicit output) as well as in voltage mode. The CO and FO of the oscillator are totally uncoupled and can be governed by a passive grounded resistor. The additional electronic tunability of CO and FO is also available. Regular mathematical analysis and typical simulation and experimental results justify the theoretical idea.

Acknowledgment

All the experimental work was performed at Electronic Devices and Circuits Lab of the department of Electronics and Communication Engineering, Inderprastha Engineering College, Ghaziabad, Uttar Pradesh (India).

References

- [1] SENANI, R., D. R. BHASKAR and A. K. SINGH. *Current conveyors: variants, applications and hardware implementations*. New York: Springer, 2014. ISBN 978-3-319-08683-5.
- [2] ARORA, T. S. and R. K. SHARMA. An all-mode KHN equivalent biquad using third generation current conveyor and all grounded passive elements. *Proceedings of the National Academy of Sciences, India Section A: Physical Sciences*. 2017, vol. 87, iss. 1, pp. 98–107. ISSN 0369-8203.
- [3] SENANI, R., D. R. BHASKAR, M. GUPTA and A. K. SINGH. Canonic OTA-C sinusoidal oscillators: generation of new grounded-capacitor versions. *American Journal of Electrical and Electronic Engineering*. 2015, vol. 3, iss. 6, pp. 137–146. ISSN 2328-7365.
- [4] ARORA, T. S. and R. K. SHARMA. A novel cubic generator realised by CCIII-based four quadrant analog multiplier and divider. *Indian Journal of Science and Technology*. 2016, vol. 9, iss. 38, pp. 1–8. ISSN 0974-6846. DOI: 10.17485/ijst/2016/v9i38/100026.
- [5] PATHAK, J. K., A. K. SINGH and R. SENANI. New canonic lossy inductor using a single CDBA and its application. *International Journal of Electronics*. 2016, vol. 103, iss. 1 pp. 1–13. ISSN 0020-7217. DOI: 10.1080/00207217.2015.1020884.
- [6] SENANI, R., D. R. BHASKAR, A. K. SINGH and R. K. SHARMA. *Sinusoidal oscillators and waveform generators using modern electronic circuit*

- building blocks*. Berlin: Springer. 2015. ISBN 978-3-319-23711-4.
- [7] BIOLEK, D., R. SENANI, V. BIOLKOVA and Z. KOLKA. Active elements for analog signal processing: classification, review and new proposals. *Radioengineering*. 2008, vol. 17, iss. 4, pp. 15–32. ISSN 1210-2512.
 - [8] KACAR, F., A. YESIL, S. MINAEI and H. KUNTMAN. Positive/negative lossy/lossless grounded inductance simulators employing single VDCC and only two passive elements. *AEU-International Journal of Electronics and Communications*. 2014, vol. 68, iss. 1, pp. 73–78. ISSN 1434-8411. DOI: 10.1016/j.aeue.2013.08.020.
 - [9] JERABEK, J., R. SOTNER, R. PROKOP, V. KLEDROWETZ, A. KARTCI and U. E. AYTEN. Inductance simulator based on dual controlled CMOS voltage differencing current conveyor. In: *IEEE 59th International Midwest Symposium on Circuits and Systems (MWSCAS)*. Abu Dhabi: IEEE, 2016, pp. 16–19. ISBN 978-1-5090-0916-9. DOI: 10.1109/MWSCAS.2016.7870087.
 - [10] PRASAD, D. and J. AHMAD. New electronically-controllable lossless synthetic floating inductance circuit using single VDCC. *Circuits and Systems*. 2014, vol. 5, iss. 1, pp. 13–17. ISSN 2153-1285. DOI: 10.4236/cs.2014.51003.
 - [11] KARTCI, A., U. E. AYTEN, N. HERENC SAR, R. SOTNER, J. JERABEK and K. VRBA. Application possibilities of VDCC in general floating element simulator circuit. In: *European Conference on Circuit Theory and Design (ECCTD)*. Trondheim: IEEE, 2015, pp. 1–4. ISBN 978-1-4799-9877-7. DOI: 10.1109/ECCTD.2015.7300064.
 - [12] SRIVASTAVA, M., P. BHANJA and S. F. MIR. A new configuration for simulating passive elements in floating state employing VDCCs and grounded passive elements. *1st IEEE International Conference on Power Electronics, Intelligent Control and Energy Systems (ICPEICES-2016)*. Delhi: IEEE, 2016, pp. 1–4. ISBN 978-1-4673-8587-9. DOI: 10.1109/ICPEICES.2016.7853402.
 - [13] KACAR, F., A. YESIL and K. GURKAN. Design and experiment of VDCC-based voltage mode universal filter. *Indian Journal of Pure and Applied Physics*. 2015, vol. 53, iss. 5, pp. 341–349. ISSN 0975-1041.
 - [14] LAMUN, P., P. PHATSORNSIRI and U. TORTEANCHAI. Single VDCC-based current-mode universal biquadratic filter. In: *7th International Conference on Information Technology and Electrical Engineering (ICITEE)*. Chiang Mai: IEEE, 2015, pp. 122–125. ISBN 978-1-4673-7863-5. DOI: 10.1109/ICITEED.2015.7408926.
 - [15] RANA, S., A. K. KUMAWAT and P. KUMAR. A Universal current mode KHN biquad filter using voltage differencing current conveyor. In: *1st IEEE International Conference on Power Electronics, Intelligent Control and Energy Systems (ICPEICES-2016)*. Delhi: IEEE, 2016, pp. 3965–3970. ISBN 978-1-4673-8587-9. DOI: 10.1109/ICPEICES.2016.7853506.
 - [16] JAIN, R. and P. KUMAR. VDCC based voltage mode Tow-Thomas biquad filter. In: *1st IEEE International Conference on Power Electronics, Intelligent Control and Energy Systems (ICPEICES-2016)*. Delhi: IEEE, 2016, pp. 3971–3974. ISBN 978-1-4673-8587-9. DOI: 10.1109/ICPEICES.2016.7853464.
 - [17] SOTNER, R., N. HERENC SAR, J. JERABEK, K. VRBA, T. DOSTAL, W. JAIKLA and B. METIN. Novel first-order all-pass filter applications of z-copy voltage differencing current conveyor. *Indian Journal of Pure & Applied Physics (IJPAP)*. 2015, vol. 53, iss. 8, pp. 537–545. ISSN 0975-1041.
 - [18] PRASAD, D., D. R. BHASKAR and M. SRIVASTAVA. New single VDCC-based explicit current-mode SRCO employing all grounded passive components. *Electronics*. 2014, vol. 18, iss. 2, pp. 81–88. ISSN 2079-9292.
 - [19] SRIVASTAVA, M. and D. PRASAD. VDCC based dual-mode quadrature sinusoidal oscillator with outputs at appropriate impedance levels. *Advances in Electrical and Electronic Engineering*. 2016, vol. 14, no. 2, pp. 168–177. ISSN 1804-3119. DOI: 10.15598/aece.v14i2.1611.
 - [20] SOTNER, R., J. JERABEK, J. PETRZELA, N. HERENC SAR, R. PROKOP and K. VRBA. Second-order simple multiphase oscillator using z-copy controlled-gain voltage differencing current conveyor. *Elektronika IR Elektrotechnika*. 2014, vol. 20, iss. 9, pp. 13–18. ISSN 1392-1215. DOI: 10.5755/j01.eee.20.9.8709.
 - [21] SOTNER, R., J. JERABEK, R. PROKOP and V. KLEDROWETZ. Simple CMOS voltage differencing current conveyor-based electronically tunable quadrature oscillator. *Electronics Letters*. 2016, vol. 52, iss. 12, pp. 1016–1018. ISSN 0013-5194.
 - [22] JERABEK, J., R. SOTNER, N. HERENC SAR, K. VRBA and T. DOSTAL. Behavioral model

for emulation of ZC-CG-VDCC. *IEICE Electronic Express*. 2016, vol. 13, iss. 18, pp. 1–6. ISSN 1349-2543. DOI: 10.1587/elex.13.20150859.

- [23] MINAEI, S. and E. YUCE. Novel voltage-mode all-pass filter based on using DVCCs. *Circuits Systems and Signal Processing*. 2010, vol. 29, iss. 3, pp. 391–402. ISSN 1531-5878.
- [24] OPA860-Wide bandwidth Operational Transconductance Amplifier (OTA) and Buffer. In: *National Instruments* [online]. Dallas: National Instruments, 2008. Available at: <http://www.ti.com/lit/ds/sbos331c/sbos331c.pdf>.

About Authors

Manish GUPTA was born 1975 in Ghaziabad, Uttar Pradesh, India. He obtained B.Tech Degree in Electronics and Communication Engineering from Delhi College of Engineering, Delhi, (presently D.T.U. Delhi), M.Tech with specialization in Signal Processing from Netaji Subhas Institute of Technology,

New Delhi and Ph.D. in area of Analog Integrated Circuits and Signal Processing from Jamia Millia Islamia, New Delhi, India. Currently he is working as an Associate Professor with Department of Electronics and Communication Engineering, Inderprastha Engineering College, Ghaziabad, Uttar Pradesh, India. His research interests are in the area of Bi-polar and CMOS, analog integrated circuits, current mode signal processing.

Tajinder Singh ARORA was born 1979 in Dehradun, Uttarakhand, India. He obtained B.Tech. Degree (Electronics and Communication Engineering) from Dehradun Institute of Technology, Dehradun, M.Tech. (Signal Processing) from Netaji Subhas Institute of Technology, New Delhi and Ph.D. (Analog Signal Processing) from Uttarakhand Technical University, Dehradun. He is currently working as an Associate Professor with Department of Electronics and Communication Engineering, Maharaja Surajmal Institute of Technology, New Delhi, India. His research interests are in the area of Analog and Digital signal processing He has authored or co-authored 20 research papers in International Journals and Conferences.



Contents lists available at ScienceDirect

Materials Research Bulletin

journal homepage: www.elsevier.com/locate/matresbu

Significant enhancement in structural, dielectric, piezoelectric and ferromagnetic properties of $\text{Ba}_{0.9}\text{Sr}_{0.1}\text{Zr}_{0.1}\text{Ti}_{0.9}\text{O}_3\text{-CoFe}_2\text{O}_4$ multiferroic composites

Aditya Jain^a, Amrish K. Panwar^{a,*}, A.K. Jha^b^a Department of Applied Physics, Delhi Technological University (Formerly Delhi College of Engineering), Bawana Road, Delhi, 110042, India^b Department of Applied Science, A.I.A.C.T.R. Geeta Colony, Delhi, 110031, India

ARTICLE INFO

Keywords:

Perovskite
Ferrite
Multiferroic
Ferroelectric
Ceramic

ABSTRACT

Multiferroic composites $(1-x)\text{Ba}_{0.9}\text{Sr}_{0.1}\text{Zr}_{0.1}\text{Ti}_{0.9}\text{O}_3\text{-}(x)\text{CoFe}_2\text{O}_4$ ($x = 0.0, 0.05, 0.10, 0.20$ & 0.30) were prepared using mechanochemical activation method. Rietveld refined XRD patterns confirm the diphasic nature of composite samples. All of the diffraction peaks of $(1-x)\text{BSZT-(x)CFO}$ can be identified for the separate perovskite (BSZT) and inverse spinel (CFO) phases and no other impurity phase were observed for the composites. $(1-x)\text{BSZT-(x)CFO}$ sample with $x = 0.05$ have shown significant improvement in microstructural, dielectric, ferroelectric and piezoelectric properties over the pristine BSZT sample. Such an improvement in electrical properties can be attributed to larger grain size, improved density and easier ferroelectric domain wall motion inside the grain. Dielectric breakdown strength of the composites also shows a similar trend and is observed to be maximum for the sample with $x = 0.05$ CFO concentration. The composite samples also show a substantial enhancement in ferromagnetic characteristics and increases progressively with increase in ferrite (CFO) content.

1. Introduction

Ferroelectric and piezoelectric ceramic materials have been extensively investigated and considered as important multifunctional materials for various electronics and microelectronics applications such as micro electromechanical systems (MEMS), non-volatile random access memory (NVRAM), ceramic capacitors, actuators, sonar sensors, etc. A significant amount of research has been devoted to the study of BaTiO_3 based materials over the last decade to develop improved ceramic materials for ferroelectric, ferromagnetic and piezoelectric applications [1,2]. Further, Ecological considerations and an ever-increasing demand to improve device performance are motivating researchers to explore lead-free BaTiO_3 based materials. BaTiO_3 is a classic ferroelectric as well as piezoelectric material with a characteristic tetragonal distortion of the perovskite structure. Moreover, owing to the miniaturization of multilayer ceramic capacitors (MLCCs) and for nano-electronics applications, most of the efforts are directed towards the study the tetragonal phase and cubic phase of barium titanate based materials. One of the most effective ways to improve materials performance is by the addition of suitable substituent/dopants into the lattice [3]. BaTiO_3 based perovskite compounds such as $\text{A}_x\text{A}_{1-x}'\text{B}_y\text{B}_{1-y}'\text{O}_3$ with $0 \leq x, y \leq 1$ are of high commercial and

technological interests because of their better ferroelectric, optical and magnetic properties as well as better performance compared to the simple ABO_3 perovskite compounds [4]. $\text{BaZr}_{1-x}\text{Ti}_x\text{O}_3$ (BZT) and $\text{Ba}_{1-x}\text{Sr}_x\text{TiO}_3$ (BST) has replaced BaTiO_3 in many applications including the fabrication of multi-layered ceramic capacitors because Zr^{4+} is chemically more stable as compared to Ti^{4+} , in addition BZT possess better dielectric properties compared to pure BaTiO_3 [5,6]. Further, BST is one of the promising candidate for tunable microwave devices and dynamic RAM applications. So, combining the properties of both BZT and BST may result in some new characteristics. BTO has diverse applications in the field of ferroelectrics, however, its applicability in piezoelectric and magnetic devices is limited due to its low piezoelectric constant and poor magnetic properties. Moreover, the ceramics based on BaTiO_3 are well-known for their better dielectric and ferroelectric properties, exhibit higher polarization, low losses and good mechanical/chemical stability in a wide frequency range [7,8]. Therefore, efforts have been directed towards improving the multiferroic properties of the materials under study.

In the present work, we have investigated double phase ceramic composites of $(1-x)\text{Ba}_{0.9}\text{Sr}_{0.1}\text{Zr}_{0.1}\text{Ti}_{0.9}\text{O}_3\text{-}x\text{CoFe}_2\text{O}_4$ ($0 \leq x \leq 0.3$). Since BSZT exhibit no ferromagnetism and so the addition of CoFe_2O_4 (CFO) into BSZT by forming a composite is an effective way to induce the

* Corresponding author.

E-mail address: amrish.phy@dce.edu (A.K. Panwar).

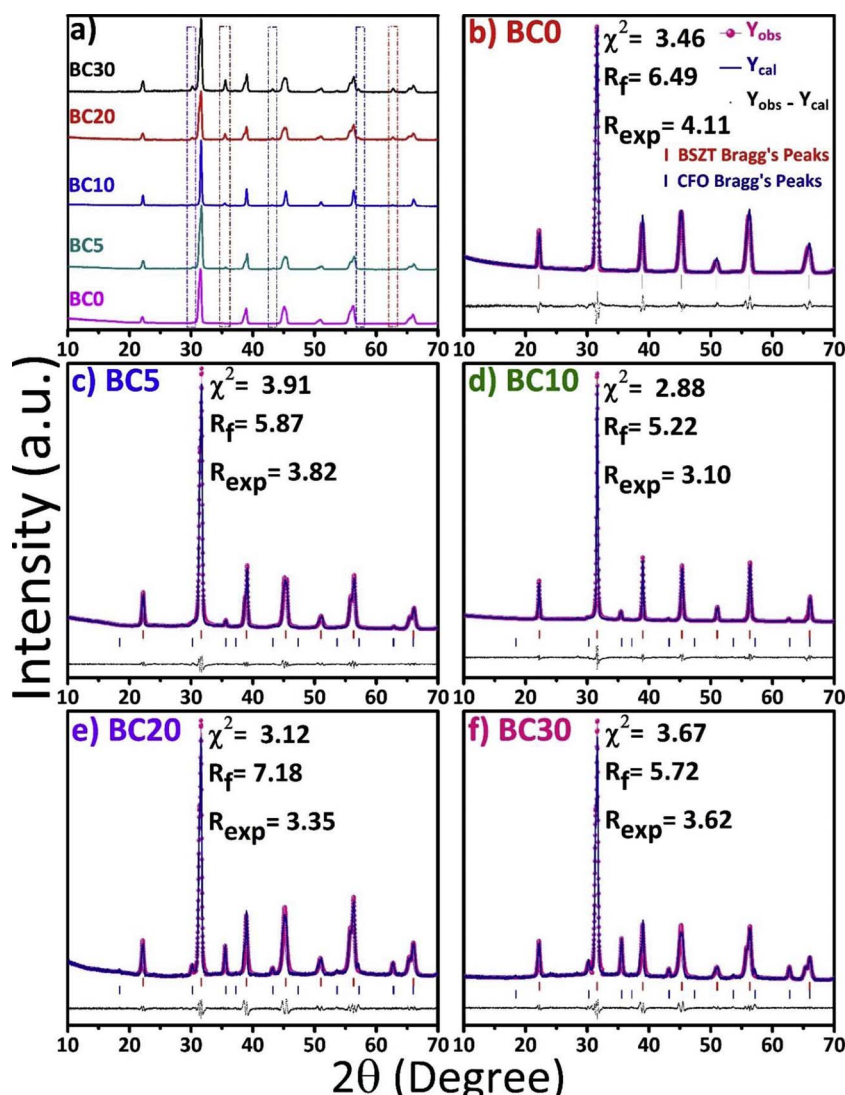


Fig. 1. Comparative and Rietveld refined X-ray diffraction (XRD) patterns of (1-x)BSZT-(x)CFO composites: (a) combined XRD pattern of five synthesized samples, (b) BC0, (c) BC5, (d) BC10 (e) BC20 and (f) BC30.

ferromagnetism. Cobalt ferrite is a hard magnetic material with a high coercive field and large saturation magnetization and owing to this, it is widely used as piezomagnetic constituent [9]. Furthermore, the multiferroic composite materials, which possess better ferroelectric and ferromagnetic properties compared to single phase materials, are currently attracting a great deal of attention.

The ferroelectric, piezoelectric and magnetic properties of any material depend on microstructure, purity, morphology and size of the particle [10]. Synthesis method can produce drastic effects on these parameters. Mechanochemical activation route of synthesis has been known to be a viable method for the production of ceramic materials and can be used to produce ultrafine particles with uniform distribution, high purity and controlled morphology. Such a uniform distribution of grains combined with ultrafine particle size are suitable and well suited for use in modern green fabrication technique namely inkjet printing, tape casting, etc. Moreover, the sintering temperature required to synthesize the material is lower than those needed to sinter conventionally produced materials (up to 100–250 °C lower in some cases) [11]. In the present study, we have made an attempt to solve the inherent problems occurring in BSZT by making composites of BSZT and CFO. After a detailed literature survey, it has been found that this composition had not yet been reported. The aim of the present study is to investigate the structural, dielectric, ferroelectric and ferromagnetic properties of (1-x)Ba_{0.9}Sr_{0.1}Zr_{0.1}Ti_{0.9}O₃-xCoFe₂O₄ (x=0.0, 0.05, 0.1, 0.2 and 0.3). Apart from these studies, the authors have carried out a

detailed Rietveld refinement of all the synthesized compositions in order to analyze the structural transition occurring in the composites.

2. Experimental

Composite materials with Ba_{0.9}Sr_{0.1}Zr_{0.1}Ti_{0.9}O₃ (BSZT) as ferroelectric phase and CoFe₂O₄ (CFO) as magnetic phase were synthesized using mechanochemical activation method. Ba_{0.9}Sr_{0.1}Zr_{0.1}Ti_{0.9}O₃ was synthesized by using AR grade (Sigma-Aldrich make) BaCO₃ (99.5%), SrCO₃ (99.0%), ZrO₂ (99.99%) and TiO₂ (99.0%) as the starting precursors. All the raw materials were taken in required proportion and milling of the samples were carried out in air environment at 425 rpm for effective 24 h. Retsch planetary ball mill PM100 was used to carry out ball milling of raw materials. A cylindrical zirconia vial with approximately 45 mm diameter and 120 Zirconia balls with 5 mm diameter were used as milling medium. The ferroelectric phase BSZT powder was first calcined at 1050 °C for 4 h followed by sintering at 1200 °C for 3 h in a muffle furnace.

Highly pure AR grade CoO (99.9%) and Fe₂O₃ (99.9%) in stoichiometric proportion were milled with toluene to prepare the magnetic phase CoFe₂O₄ for 25 h in zirconia media. CoFe₂O₄ was calcined at 1100 °C for 5 h followed by sintering at 1250 °C for 10 h. Finally, the multiferroic composites (1-x)Ba_{0.9}Sr_{0.1}Zr_{0.1}Ti_{0.9}O₃-(x)CoFe₂O₄ (where x=0, 0.05, 0.1, 0.2 and 0.3) were obtained by thoroughly mixing the constituent phases BSZT and CFO in desired weight ratios in a ball mill

Table 1
Rietveld refined XRD parameters for bare BSZT and BSZT-CFO composite samples.

Sample	Space group	Crystal structure	Lattice parameters (Å)	Cell volume (Å ³)	Theoretical density (gm/cm ³)	χ^2	R _{exp}	R _f	R _{Bragg}
BC0	<i>P4mm</i>	Tetragonal	a = 4.0034 c = 4.0246	64.5031	5.4823	3.46	4.11	6.49	1.82
BC5	BSZT phase	<i>P4mm</i>	a = 4.0011 c = 4.0222	64.3889	5.5359	3.91	3.82	5.87	3.15
	CFO phase	<i>Fd-3m</i>	a = 8.3632	584.948					2.64
BC10	BSZT phase	<i>P4mm</i>	a = 3.9926 c = 4.0183	64.0551	5.5214	2.88	3.10	5.22	4.23
	CFO phase	<i>Fd-3m</i>	a = 8.3749	587.406					3.66
BC20	BSZT phase	<i>P4mm</i>	a = 3.9911 c = 4.0181	64.0038	5.4436	3.12	3.35	7.18	2.44
	CFO phase	<i>Fd-3m</i>	a = 8.3792	588.311					3.94
BC30	BSZT phase	<i>P4mm</i>	a = 3.9878 c = 4.0143	63.8385	4.4241	3.67	3.62	5.72	1.79
	CFO phase	<i>Fd-3m</i>	a = 8.3857	589.682					3.56

for 4 h. The resulting powders were then thoroughly mixed with 3 wt% polyvinyl alcohol (PVA) solution and squeezed into disk-shaped pellets of around 10 mm diameter and nearly 1.2 mm thickness by using a hydraulic press. The cylindrical disks of BSZT-CFO composites were annealed at 800 °C with heating rate of 6 °C/min for 2 h in air environment. Hereafter, these composites are identified as BC0, BC5, BC10, BC20 and BC30 for $x = 0.0, 0.05, 0.10, 0.20$ and 0.30 , respectively.

The crystallographic structure and phase identification of BCx composites were analyzed by *Bruker D8 Advance* X-ray diffractometer having $\text{CuK}\alpha_1$ radiation with the wavelength of 1.541 Å. Lattice constants were evaluated by using X-ray diffraction data with the help of *X'Pert Highscore Plus* software followed by Rietveld analysis. The microstructural features and surface characteristics of high temperature sintered pellet samples were analyzed with the help of *Hitachi S-3700N* scanning electron microscope. A computer program package *ImageJ* has been used to perform grain size distribution of composite samples. The pellet samples were polished to approximate thickness of 1 mm and slightly viscous silver paste was coated on both sides of sintered pellets to form electrodes. Following the electrode formation, the pellets were cured at 140 °C for 30 min. These disk-shaped pellets were further used to carry out dielectric measurement at multiple frequencies by using *Keysight E4980* LCR meter. Temperature dependent dielectric properties were examined over a wide temperature range of 27–225 °C. The ferroelectric characteristics of the samples were investigated using a Sawyer-Tower circuit based P-E loop equipment. Magnetic hysteresis loops of the sintered pellets at room temperature were recorded using a PAR 155 vibrating sample magnetometer (VSM).

3. Result and discussion

3.1. X-ray diffraction (XRD)

In order to clearly understand the phase and structural modification on the substitution of CFO in BSZT, we have performed structural refinement by Rietveld method using *X'Pert Highscore Plus* software. Figs. 1(a)–(f) shows the combined XRD patterns and Rietveld-refined XRD pattern of $(1-x)\text{Ba}_{0.9}\text{Sr}_{0.1}\text{Zr}_{0.1}\text{Ti}_{0.9}\text{O}_3 - x\text{CoFe}_2\text{O}_4$ ($x = 0.0, 0.05, 0.10, 0.20$ and 0.30) specimens. Clear intense peaks with high peak to noise ratio are observed, indicating the high crystallinity of the synthesized solid solutions as the intensity of XRD peaks is closely related to the crystallinity of particles in sintered powder. Barium titanate (JCPDS no. 00-005-0626) and cobalt ferrite (JCPDS no. 00-002-1045) were taken as the reference patterns and the Pseudo-Voigt function was used to refine diffraction peaks. The Rietveld refined X-ray diffraction pattern of BC0 sample shows a well-recognized tetragonal phase with

P4mm space group. However, as the CFO content is increased, the peaks of cobalt ferrite begin to appear. The BSZT-CFO composite samples prepared through the mechanochemical activation method shows a mixed perovskite-inverse spinel phase without any traces of impurities. The calculated and observed d values in pure and CFO added BSZT compounds indicate that there is no transformation in the basic crystal structure (tetragonal) as x changes from 0.05 to 0.30. Although, the tetragonality of the specimens i.e. lattice constants 'a' and 'c' varies with the CFO addition. All of the diffraction peaks of $(1-x)\text{BSZT}-(x)\text{CFO}$ can be identified for the separate perovskite (BSZT) and inverse spinel (CFO) phases and no other intermediate phase was found for the composites. This confirms the successful synthesis of the di-phase multiferroic composites and it also indicates that both the constituent phases have retains their identity in the composites and no undesirable reaction has taken place between the perovskite BSZT and ferrite CFO phases during the final sintering process. In composite samples, the BSZT retained a tetragonal perovskite structure with *P4mm* space group while CFO crystallizes in a cubic inverse-spinel structure with *Fd-3m* space group. It is also observed that the peak intensity of ferrite phase increases as CFO concentration increases. The detailed structural parameters obtained after Rietveld refinement are listed in Table 1.

The presence of individual phases in the composites also indicate that a limited reaction takes place between ferroelectric BSZT and ferrite CFO phase. This is because BSZT shows a perovskite structure while CFO exhibits inverse spinel structure and therefore these compounds demonstrate a little solubility with one another. Further, the small change in lattice parameters and c/a ratio also confirms the limited solubility of BSZT and CFO phases. Fig. 2(a) & 2(b) shows the unit cell crystal structure of BSZT and CFO. The crystal structures have been drawn using VESTA software from the atomic positions obtained after the Rietveld refinement of BC5 sample. The crystal structures shown in Fig. 2(a,b) further confirms that BSZT exhibits a tetragonal phase and CFO displays an inverse spinel phase. The tiny grey stripes at tetrahedral and octahedral positions of Fe and Co atoms signify the deficit in occupancy that may be ascribed to weight loss of the compound during high-temperature calcination and sintering process.

3.2. Microstructural studies

The typical SEM micrographs of sintered pellets of BSZT-CFO multiferroic composites are shown in Fig. 3(a)–(e). The images show that all the samples possess a fairly homogeneous polygonal grain type morphology and excellent dispersity. The grain size of BSZT-CFO composites did not show any definite pattern in terms of size and the average grain size was found to be approximately 412, 468, 345, 376 and 334 nm for BC0, BC5, BC10, BC20 and BC30, respectively. A notable

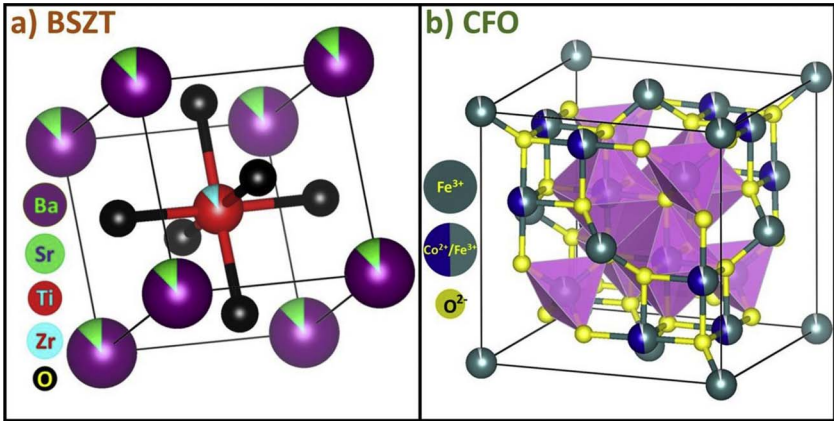


Fig. 2. Crystal structures of (a) $\text{Ba}_{0.9}\text{Sr}_{0.1}\text{Zr}_{0.1}\text{Ti}_{0.9}\text{O}_3$ and (b) CoFe_2O_4 .

increase in grain size is observed for BC5 sample however, the grain size decreases on further CFO addition. These results do indicate that higher CFO concentration inhibits the grain growth formation. It is worth noting that CFO addition in BSZT compound leads to a significant change in surface morphology of the material. In a polycrystalline material, both intrinsic and extrinsic factors affect the ferroelectric and piezoelectric properties of the material [12,13]. The grain size of the material is an extrinsic parameter and it strongly influences the electrical properties. Further, it is observed that coarse-grained ceramics often exhibit better ferroelectric and piezoelectric characteristics as compared to fine-grained ceramics [14]. The reason being that the coarse-grained ceramics offer improved domain mobility as well as polarization, resulting in higher degree of dipole movement and hence

Table 2
Room temperature saturation polarization (P_s), remnant polarization ($2P_r$), electric coercive field ($2E_c$), saturation magnetization ($2M_s$), remnant magnetization ($2M_r$), Magnetic coercive field ($2H_c$), breakdown strength (E_{bd}) and piezoelectric constant (d_{33}) for (1-x)BSZT-(x)CFO composites.

Sample	$2P_s$ ($\mu\text{C}/\text{cm}^2$)	$2P_r$ ($\mu\text{C}/\text{cm}^2$)	$2E_c$ (kV/cm)	$2M_s$ (emu/gm)	$2M_r$ (emu/gm)	$2H_c$ (kOe)	E_{bd} (kV/cm)	d_{33} (pC/N)
BC0	16.38	4.70	16.22	—	—	—	235	269
BC5	16.80	5.86	20.14	3.66	2.01	3.84	273	281
BC10	16.14	8.28	30.02	6.06	3.12	3.85	267	209
BC20	12.84	8.46	37.38	11.48	6.08	3.85	239	117
BC30	11.38	9.44	48.32	14.42	7.54	3.86	178	64

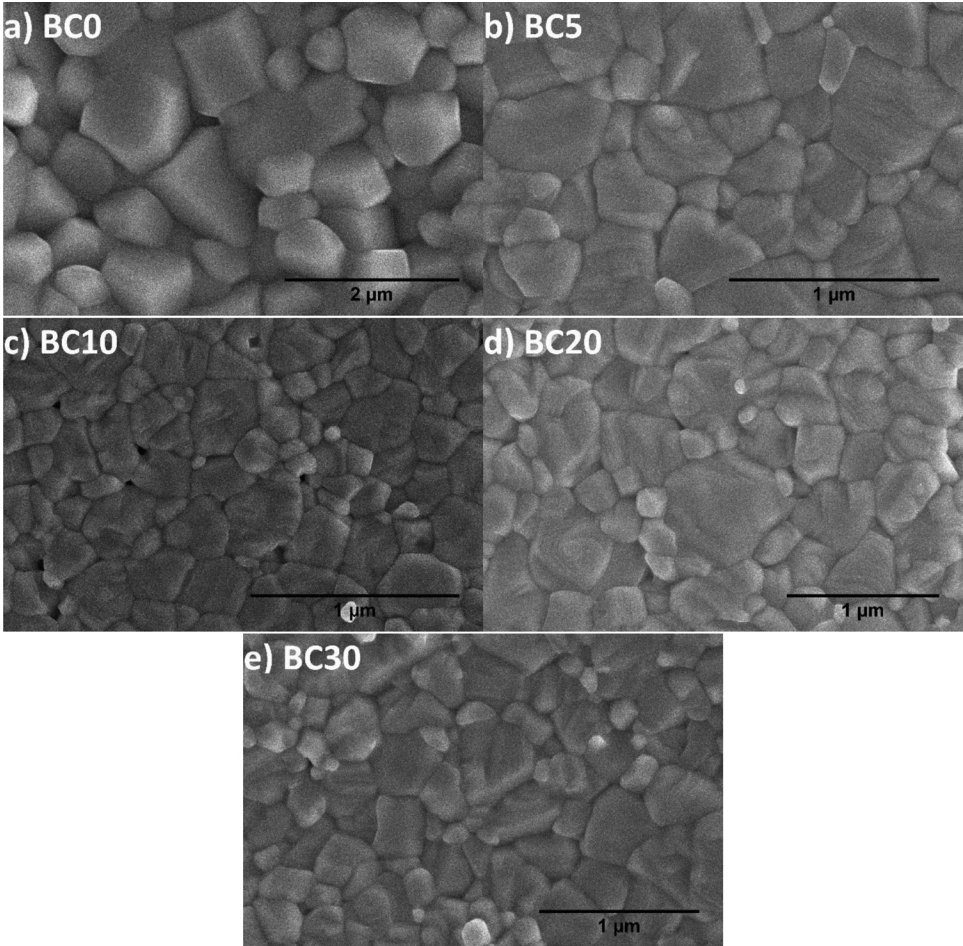


Fig. 3. SEM micrograph of high temperature sintered pellets of (1-x)BSZT-(x)CFO composites: (a) BC0, (b) BC5, (c) BC10 (d) BC20 and (e) BC30.

improved electrical properties [15,16]. Additionally, it is observed that the sintering temperature and soaking period at the peak temperature also affect the grain size of the ceramics [17,18]. The above two factors also modify the surface characteristics of the final sintered material and consequently they affect the electrical properties of the ceramics. The grains in all the sample are attached closely to each other and therefore exhibit a very dense microstructure. The theoretical density measured from XRD data shows an irregular variation and was found to be maximum for BC5 sample and minimum for BC10 sample. The as obtained theoretical density values are listed in Table 2. In composite samples, the existence of two different kinds of grains may be due to the fact that the grains of one compound (either BSZT or CFO) has a higher probability of growing as compared to other and hence bigger grain grows at the cost of smaller one. Moreover, in composite materials, it is typically difficult to attain a homogeneous surface morphology because of the substantial difference in thermal expansion coefficient and sintering condition of two different compounds.

Further, on magnifying the SEM images of composite samples, two types of magnetic domains i.e. circular and maze shaped domains with 180° domain wall structure can be observed. The difference in the morphology of single phase BC0 and other composite samples as observed from SEM images may be attributed to variation in the axis orientation of the five synthesized samples. Generally, in order to reduce the internal stray field energy due to demagnetizing field inside the domains, a maze shaped structures are observed [19]. Whereas, circular domain structures are observed due to the presence of substantially high electric field [20,21]. Furthermore, the domain walls are discontinuous near to grain boundaries, which may be due to the presence of non-magnetic BSZT phase resulting from high temperature sintering process [22].

3.3. Dielectric studies

Dielectric constant and dielectric loss as a function of temperature at multiple frequencies has been measured and is shown in Fig. 4(a)–(j). The composite samples show a rather complex behavior as compared to pure BSZT sample. In Fig. 4(a)–(j), it can be observed that the dielectric constant decreases with increase in frequency. This observed behavior can be explained by Maxwell-Wagner space charge polarization that plays a key role in defining such composite (or heterogeneous) systems [23]. The all four types of polarization namely, (i) electronic, (ii) ionic, (iii) dipolar and (iv) interfacial polarization contribute to the total polarization at low frequency and thus dielectric constant is found to be maximum at low frequency. However, at higher frequencies, some of the polarizations do not contribute. This is because at higher frequencies the dipoles are not capable of aligning themselves in the direction of the rapidly oscillating applied electric field and hence contribution from different polarization components ceases to contribute resulting in decrease of dielectric constant.

Two different regions of dispersion can be clearly seen in BC5 sample. At low frequency and high temperature, the dielectric properties are influenced by conductivity effects that can be identified as gradual slope of dielectric constant curve. Further, at higher frequency, this type of dispersion shifts to higher temperature region and another type of dispersion begin to appear [24]. The primary characteristic of this kind of dispersion is the maxima seen in both dielectric constant and dielectric loss curves that is found to shift to higher temperature with an increase in frequency. This kind of behavior of dielectric constant curve may be ascribed to relaxor or dipolar glass like dispersion [25]. It is worth mentioning here that similar anomaly has been stated in a number of perovskite-based reports [24,26,27]. According to previous reports, this phenomenon is attributed either to interfacial polarization in which free charge carriers accumulate at both the dielectric electrode interfaces or to clustering and migration of oxygen vacancies [28]. Further, it has been observed that BC5 sample possesses the highest dielectric constant among the five synthesized samples

which may be attributed to optimum heterogeneity (i.e. ferroelectric and ferrite phase) of the composite. Heterogeneous interfaces in a composite material are the boundary between the ferroelectric and ferrite phases, which results in the occurrence of interfacial polarization and thus contribute to the high value of dielectric constant. In a material, as an electric field is applied, the space charges provided by CFO phase gathers at the grain boundaries of the two constituent phases because of the different permittivity and conductivity of the compounds which results in interfacial polarization. In the present case, for BC5 sample, amount of space charge provided by CFO increases and consequently a higher value of dielectric constant is achieved. Another possible cause for an enhanced dielectric constant for BC5 sample is the occurrence of hopping conduction mechanism in CFO [29]. Hopping conduction in a material is a thermally activated process. With the increase in temperature, the electron hopping between Fe^{3+} and Fe^{2+} get enhanced. Further, as the electric field is applied, the dipoles $\text{Fe}^{3+}/\text{Fe}^{2+}$ align themselves in the direction same as that of applied electric field and thus resulting in high value of dielectric constant [30]. Besides, in ferrites, at low frequency and high temperature of operation, the ionic polarization also adds up to the polarization value [31]. However, as the temperature increases beyond a certain limit, the dielectric constant begins to decrease which may be attributed to the increased random vibration motion of ions and electrons [32].

The dielectric loss as a function of temperature at some selected frequencies is shown in Figs. 4(b,d,f,h and j). It can be observed that in all the samples, the dielectric loss is minimum at lower temperature and increases abruptly at higher temperature. Interestingly, BC5 sample shows the lowest value of dielectric loss among the five synthesized samples. Pure BSZT sample shows the emergence of dielectric loss peak at the phase transition temperature, however, other four composite samples do not show any such peak. The dielectric loss of the samples decreases for BC5 sample and increases with further increase in CFO content. The density of a material plays a crucial role in determining the dielectric properties. Further, the material with lower density dissipates high energy and thus result in an increase in dielectric loss. It can be seen that dielectric loss values are in good agreement with the theoretical density results obtained from XRD analysis.

To further understand the observed dielectric behavior, degree of diffuseness or diffuseness constant was calculated by using the temperature dependence curve of dielectric constant. The insets of Fig. 4 shows the plot of diffuseness constant evaluated by plotting $\ln(T-T_c)$ vs. $\ln(1/\epsilon - 1/\epsilon_{\max})$. The increasingly diffused nature of phase transition peak may be ascribed to perturbed localized dynamics and polar structural distortion of $\text{TiO}_6/\text{ZrO}_6$ octahedra due to A-site and B-site substitution in BaTiO_3 as well as ferrite addition in the perovskite unit cell. According to modified Curie-Weiss law, the diffuseness parameter can be calculated using the equation as follows [33]:

$$\frac{1}{\epsilon} - \frac{1}{\epsilon_m} = \frac{(T-T_c)^\gamma}{C'} \quad (1)$$

where, T_c signifies the Curie-Weiss temperature, γ represents diffuseness parameter and C' denotes the Curie constant. The diffuseness constant γ provides necessary information on phase transition behavior of any dielectric material. Normal ferroelectric behavior is observed when $\gamma = 1$ and diffuse phase transition when $1 < \gamma < 2$ [33]. The BC5 sample with such superior dielectric properties can be used for the production of multi-layered ceramic capacitors and low loss dielectric materials.

3.4. Ferroelectric studies

Fig. 5(a–c) shows the variation in electric polarization against variation in electric field at 20 Hz test frequency for all the five synthesized samples. The hysteresis loops have been recorded at three different temperatures of 27, 75 and 125 °C. The saturation polarization, remnant polarization and coercive field values of the five synthesized

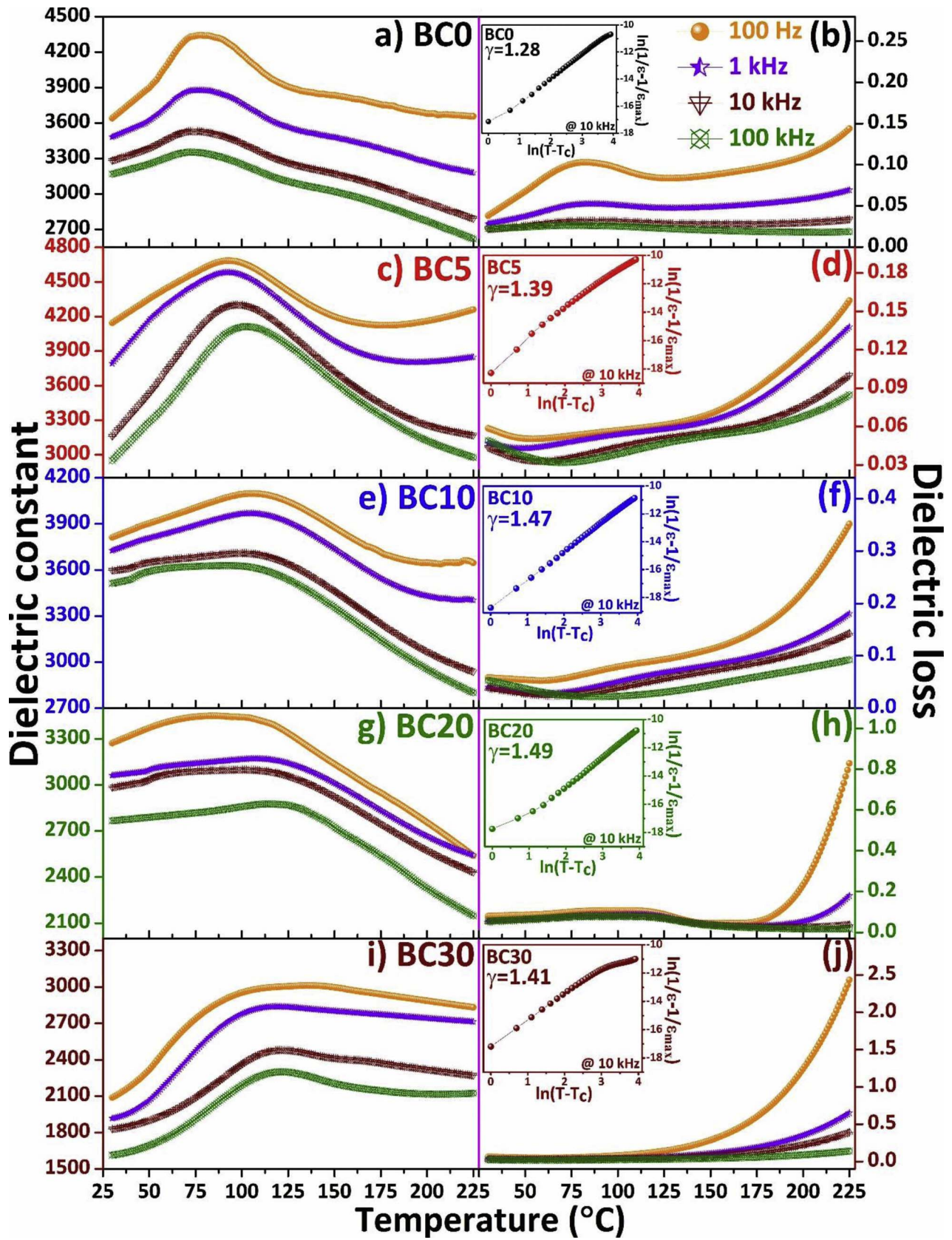


Fig. 4. Temperature dependence of dielectric constant and dielectric loss; inset shows the Plot of $\ln(1/\epsilon' - 1/\epsilon_{\max})$ as a function of $\ln(T - T_c)$ for the (1-x)BSZT-(x)CFO composites: (a & b) BC0, (c & d) BC5, (e & f) BC10 (g & h) BC20 and (i & j) BC30.

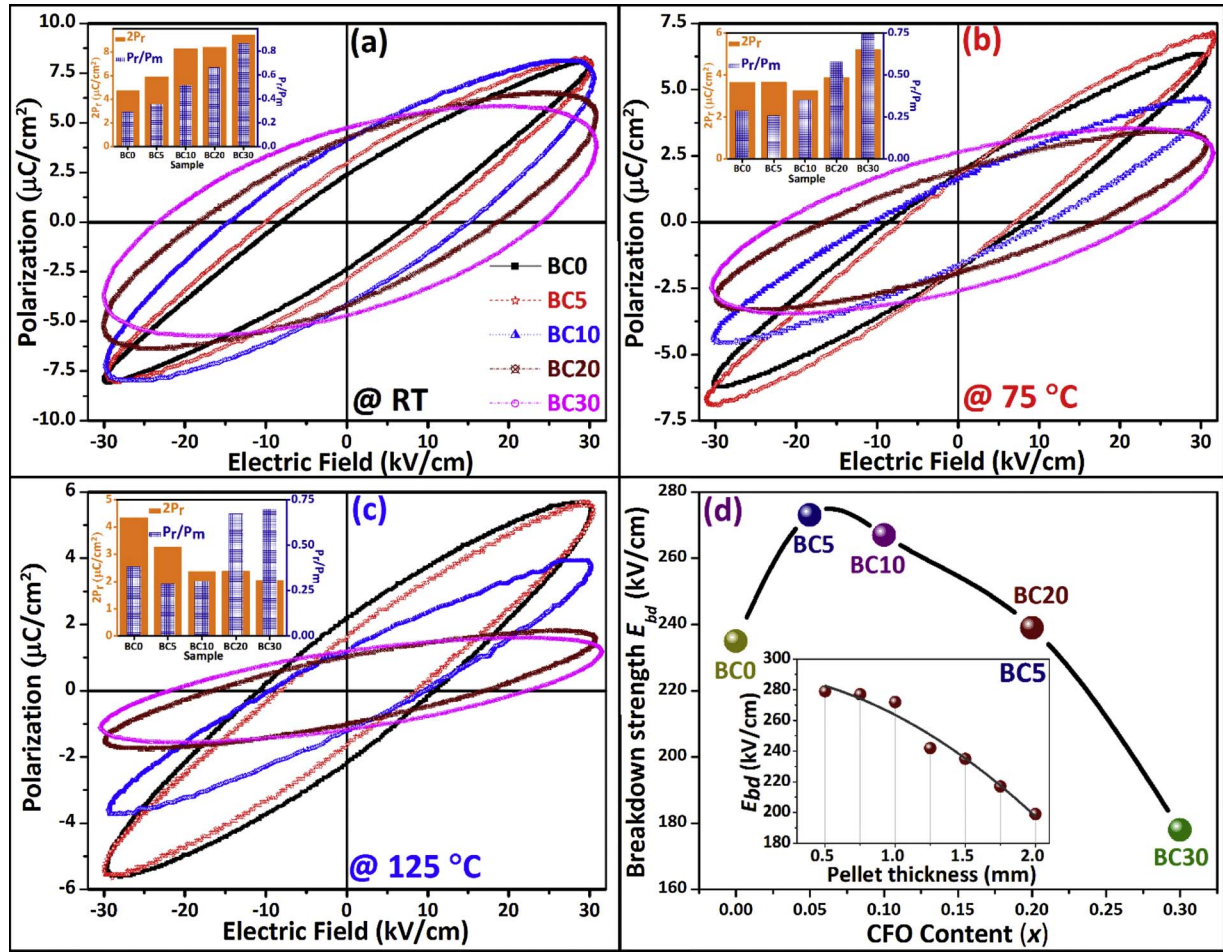


Fig. 5. Ferroelectric hysteresis loops of (1- x)BSZT-(x)CFO composites at three different temperatures: (a) Room temperature, (b) 75 °C and (c) 125 °C; inset shows the variation of remnant polarization ($2P_r$) and P_r/P_m ratio for the five synthesized samples, (d) shows the variation of dielectric breakdown strength and inset shows the effect of pellet thickness on E_{bd} value.

samples are listed in Table 2. At all the three temperatures, under a maximum electric field of 30 kV/cm, the saturation polarization is observed to be maximum for BC5 sample. (1- x)BSZT- x CFO samples with up to $x = 0.10$ show a well-defined saturated hysteresis loop with negligible leakage current indicating an improved ferroelectric character with CFO addition. However, in higher CFO content samples (i.e. BC20 and BC30), the composites show relatively unsaturated oval shaped hysteresis loop with high remnant polarization. The decrease in saturation polarization for higher CFO content samples may be attributed to stronger pinning of domain walls caused by the relatively smaller grain size of the sample. Smaller grain size results in smaller individual ferroelectric domains and therefore contains a higher number of grain boundary regions, which are known to be non-ferroelectric areas [2]. Moreover, in higher CFO content samples, the obtained polarization values indicate that the presence of non-dielectric material considerably affect the polarization characteristics of BaTiO₃ based ceramics. Further, other morphological properties such as low defect density, compositional homogeneity, grain shape, etc. also affect the ferroelectric properties of ceramics [2]. The occurrence of structural transition due to CFO substitution also affect the stability of ferroelectric phase and therefore at higher CFO substitution ferroelectricity gets deteriorated. Further, it has been observed that with CFO addition, the area of the loops has also been increased which may be due to higher conductivity of ferrite phase compared to that of BSZT phase. The variation in remnant polarization and P_r/P_m ratio is depicted in the inset of Fig. 6(a-c).

At higher temperatures of 75 °C and 125 °C, the remnant and saturation polarization decreases compared to room temperature and

shows nearly similar behavior with variation in CFO content. It has been observed that small CFO addition in BSZT lattice leads to an increase in coercive field of the samples which may be ascribed to the occurrence of dipole friction due to domain orientation. Further, the slight reduction in grain size with increase in CFO concentration have also resulted in enhancing the dipole friction during the process of domain orientation [30]. The approximate poling electric field needed for the alignment of ferroelectric domains in BSZT-CFO composites has been evaluated using the coercive field values. Moreover, the coercive field results for the composites indicate that samples with higher CFO content may require higher electric field to align ferroelectric domains.

3.5. Breakdown strength measurement

Dielectric breakdown strength, E_{bd} is of great significance for the commercial applications of dielectric materials as this property governs the maximum allowable energy storage density and operational range of electric field for a dielectric material. The dielectric breakdown strength measurement was carried out in a silicon oil bath at room temperature by applying a rectified ac voltage signal to the disk-shaped pellet sample. A brass made pin type electrode with a rounded tip was used as the high voltage electrode. The ground electrode is made up of stainless steel and consist of a flat surface and is in direct contact with the sample. This whole arrangement is enclosed in a Teflon compartment to avoid flashover. Prior to breakdown strength measurement, the samples were coated with silver paste and heated in an oven at 150 °C for 30 min to ensure proper electrical contact between the electrode and sample surface. The high voltage rectified ac signal was increased at a

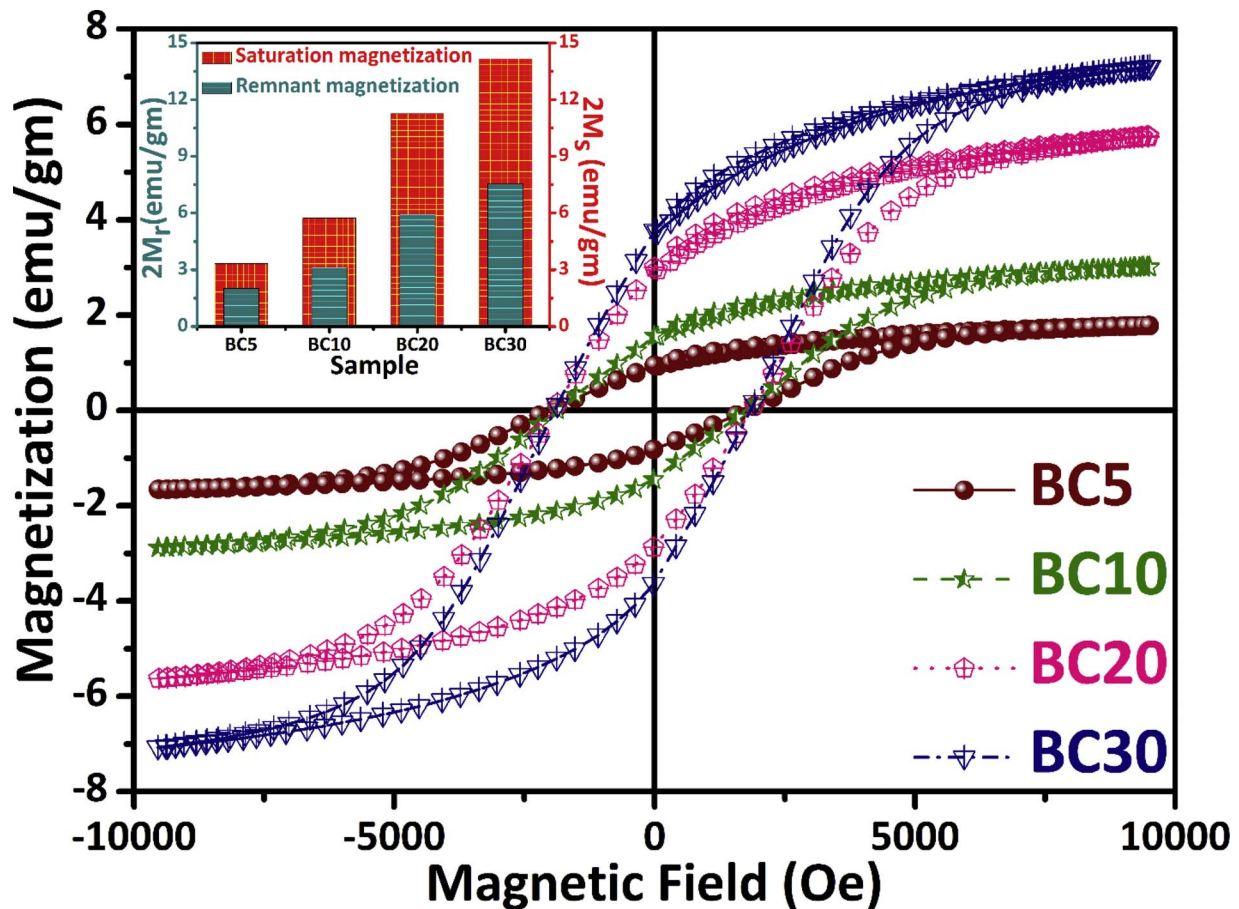


Fig. 6. Ferromagnetic hysteresis (M - H) loop of $(1-x)$ BSZT- (x) CFO composites and the inset shows the variation of remnant and saturation magnetization with an increase in CFO content.

rate of 0.5 kV/s until the specimen undergoes breakdown. The breakdown in the sample is characterized by shorting of the pellet.

Generally, the breakdown strength of ceramic materials is dependent on various internal and external parameters. Grain boundary nature, grain size and porosity comes under the category of internal parameter while electrode configuration, sample area and sample thickness signify external parameters. In the present work, external parameters are kept identical and therefore the change in dielectric strength value can not be ascribed to external effects [34]. Fig. 5(d) shows the variation in dielectric breakdown strength for $(1-x)$ BSZT- x CFO samples. For each sample, the breakdown strength was measured by taking average of the four measurements. The dielectric breakdown strength of the materials increases with slight increase in CFO content, becomes maximum for BC5 sample and decreases on further increase in ferrite content. However, BC10 and BC20 samples show comparable or even higher dielectric breakdown strength as compare to BC0 sample. The increase in dielectric breakdown strength of BC5 sample which is about 16% higher as compare to BC0 sample may be collectively attributed to higher grain size, increased density and decrease in number of pores in the sample. In addition to this, the compact and uniform surface morphology of BC5 sample results in reduction of surface defects and therefore contribute to the increase in dielectric breakdown strength of the material. Following the E_{bd} measurement of whole circular pellets, the same pellets were broken down in few pieces and they were checked for dielectric breakdown strength. Interestingly, some of the broken pieces that are far from the vicinity of electrode pin did not shorted and shown almost comparable dielectric breakdown strength. This observation indicates that the partial discharges at any sectional area did not instantly result in dielectric bulk breakdown and a sample can sustain a certain number of partial discharges before complete breakdown.

The dependence of dielectric breakdown strength on the thickness of pellet sample has been observed for BC5 as it shows the highest dielectric breakdown strength among the five synthesized samples. The sample shows a gradual reduction in dielectric breakdown strength with increase in thickness. Generally, thick dielectric materials possess a higher number of defects like micropores and microcracks and therefore breakdown occurs at relatively lower voltage [35].

3.6. Ferromagnetic studies

The room temperature magnetic hysteresis loops for the four BSZT-CFO composite samples is presented in Fig. 6. The hysteresis loop of BC0 sample is not shown here as it did not show any appreciable magnetization. However, all the composite samples have shown well saturated M-H curve and exhibit a typical ferromagnetic behavior. It is worth mentioning here that the magnetic characteristics of BSZT-CFO composites are solely attributed to ferrite phase. The obtained values of saturation magnetization and coercive magnetic field are still higher without significantly affecting the ferroelectricity of the material and therefore these materials may found application in the field of multi-ferroic devices. The remnant as well as saturation polarization of the composites were found to increase with CFO addition. The inset of Fig. 6 shows the variation of remnant and saturation polarization with an increase in CFO concentration. The magnetic coercivity of a material is the required magnetic field strength for taking over the magnetic anisotropy energy barrier to switch the magnetization [36]. It is to be noted that the coercive field of the composites did not show any significant increase with an increase in CFO content. The addition of CFO in BSZT lattice may have resulted in the origination of oxygen vacancies so as to preserve the charge neutrality of the compound [37]. This increase in number of oxygen vacancies leads to a subsequent increase in

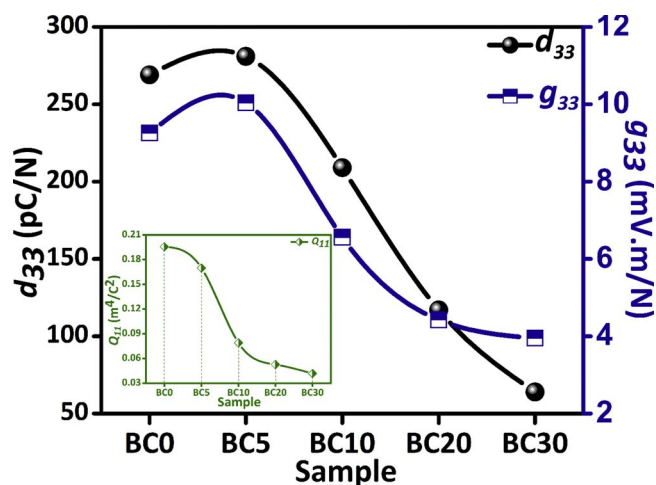


Fig. 7. Variation of piezoelectric constant (d_{33}), piezoelectric voltage coefficient (g_{33}) and electrostrictive coefficient (Q_{11}) (inset) as a function of CFO content.

magnetization of the composites. Priya et al. reported the similar observation where Cu and Dy were doped in BiFeO₃-BaTiO₃ composite [38]. Further, the enhancement in number of oxygen vacancies has resulted in an increase in leakage current leading to the deterioration of ferroelectric properties. Another possibility for the increase in magnetization of higher CFO content samples is the magnetization contribution by the grains of the ferrite phase. These ferrite grains acts as the source of magnetization and therefore the sum of magnetization of these individual grains contribute to the overall magnetization of the materials [39]. Moreover, the coexistence of tetragonal and inverse spinel phase leads to a more complex magnetic arrangement of dipoles which causes a regular arrangement of space modulated spin structure and therefore results in an improvement in ferromagnetism of the composites. The presence of large ferroelectricity and appreciable ferromagnetism at room temperature in the composite samples can provide a possible application in the field of magnetic data storage, multi-state memories, AC/DC magnetic field sensors, etc.

3.7. Piezoelectric studies

Fig. 7 shows the variation of different electromechanical coefficients as a function of CFO content. It is observed that the piezoelectric characteristics of ceramic materials are very much dependent on the poling conditions. Generally, a high uniform electric field is desired for aligning ferroelectric domains. However, at high electric field the materials are prone to electrical breakdown and therefore an optimum electric field is necessary. In addition to this, the poling temperature and time duration of poling also play a vital role in determining piezoelectric properties. After the poling, the ferroelectric domains get aligned in the direction of the electric field. In this work, the pellet specimens were poled at an electric field of ~ 15 kV/mm for 75 min at a poling temperature of $T_p \sim 70$ °C. The d_{33} value was found to saturate after 75 min of poling and did not show any significant change even on further increasing the poling time. The poling of material at an appropriate temperature leads to accumulation of positive and negative charge carriers at the edges of the grains resulting in an internal electric field that can enhance the piezoelectric properties of the material [40,41]. The piezoelectric charge constant, d_{33} is observed to increase slightly with increase in CFO content up to $x = 0.05$ and decreases on further increase in ferrite content. The piezoelectric voltage coefficient, g_{33} also shows similar trend and is observed to decrease at higher CFO concentration. The maximum value of piezoelectric charge coefficient and piezoelectric voltage constant for BC5 sample are observed to be 281 pC/N and 10.03 mV m/N, respectively. The BC5 sample shows $\sim 4.5\%$ increase in d_{33} value compared to BC0 sample. The higher value

of d_{33} may be attributed to larger grain size, increased density and to a little extent the increase in oxygen vacancy formation with the CFO addition [42]. However, in the higher CFO content samples, the number of oxygen vacancies increases but the effect of grain size and density dominates and therefore the piezoelectric charge constant of the materials decreases. The obtained d_{33} and g_{33} values are relatively higher compared to the previous reports on BaTiO₃ based materials [43,44]. Further, the thermodynamic theory of ferroelectricity can be used to relate piezoelectric constant and electrostrictive coefficient of the material and is expressed as follows:

$$d_{33} = 2P_r Q_{11} \epsilon_{33} \quad (2)$$

where, P_r is the remnant polarization, Q_{11} denotes the electrostrictive coefficient, and ϵ_{33} signifies the dielectric permittivity of the specimen. The electrostrictive coefficient of all the synthesized samples shown in the inset of Fig. 7 has been calculated using Eq. 1 and it is found to decrease with increase in CFO concentration. Finally, it can be established that the material with better ferroelectricity and high dielectric constant exhibits superior piezoelectric properties.

4. Conclusion

Mechanochemical activation method was employed to synthesize BSZT-CFO composite ceramics. The effect of CFO addition in BSZT on the microstructure, dielectric, ferroelectric, ferromagnetic and piezoelectric properties have been studied. Rietveld refined XRD pattern of composite samples confirms the formation of mixed phase without any traces of impurity. The addition of CFO has resulted in a remarkable change in surface morphology of the samples. The BC5 sample shows the highest dielectric constant, high saturation polarization, excellent dielectric breakdown strength and large piezoelectric constant among the five synthesized samples. The superior electrical characteristics of BC5 sample may be attributed to larger grain size, high density and to some extent on the increase in number of oxygen vacancies due to CFO addition. In addition to these, the BSZT-CFO composites show a well saturated ferromagnetic characteristics which are solely attributed to the ferrite phase. Finally, it can be concluded that BSZT-CFO composites with excellent electrical properties coupled with significant ferromagnetic properties can prove to be a promising material for multi-ferroic applications.

Acknowledgements

Authors are heartily gratified for the funding of DST-SERB (Grant no. PS/O39/2011), India to carry out this research.

References

- [1] N. Kumar, E.A. Patterson, T. Frömling, D.P. Cann, Conduction mechanisms in BaTiO₃-Bi(Zn_{1/2}Ti_{1/2})O₃ ceramics, *J. Am. Ceram. Soc.* 99 (2016) 3047–3054.
- [2] E. Chandrakala, J. Paul Praveen, B.K. Hazra, D. Das, Effect of sintering temperature on structural, dielectric, piezoelectric and ferroelectric properties of sol-gel derived BZT-BCT ceramics, *Ceram. Int.* 42 (2016) 4964–4977.
- [3] I. Coondoo, N. Panwar, H. Amorín, V.E. Ramana, M. Algueró, A. Kholkin, Enhanced piezoelectric properties of praseodymium-modified lead-free (Ba_{0.85}Ca_{0.15})(Ti_{0.90}Zr_{0.10})O₃ ceramics, *J. Am. Ceram. Soc.* 98 (2015) 3127–3135.
- [4] H. Tian, D. Wang, J. Qi, Y. Wang, H. Chan, C. Choy, Synthesis of BaZr_{0.75}Hf_{0.25}O₃ by a solid-state reaction technique and characterizations of dielectric properties, *J. Alloys Compd.* 402 (2005) 251–255.
- [5] M.D. Glinchuk, E.A. Eliseev, V.A. Stephanovich, Phase diagram of mixed ferro-electrics, *Ferroelectrics* 254 (2001) 27–39.
- [6] X. Tang, J. Wang, X. Wang, H. Chan, Effects of grain size on the dielectric properties and tunabilities of sol-gel derived Ba(Zr_{0.2}Ti_{0.8})O₃ ceramics, *Solid State Commun.* 131 (2004) 163–168.
- [7] A. Jain, A.K. Panwar, A.K. Jha, Structural, dielectric and ferroelectric studies of Ba_{1-x}Sr_xTiO₃ ceramics prepared by mechanochemical activation technique, *J. Mater. Sci. - Mater. Electron.* 27 (2016) 9911–9919.
- [8] A. Jain, A.K. Panwar, A. Jha, Influence of milling duration on microstructural, electrical, ferroelectric and piezoelectric properties of Ba_{0.95}Sr_{0.1}Zr_{0.04}Ti_{0.96}O₃ ceramic, *Ceram. Int.* 42 (2016) 18771–18778.
- [9] N. Adhlakha, K.L. Yadav, R. Singh, Effect of BaTiO₃ addition on structural,

- multiferroic and magneto-dielectric properties of $0.3\text{CoFe}_2\text{O}_4 - 0.7\text{BiFeO}_3$ ceramics, *Smart Mater. Struct.* 23 (2014) 105024.
- [10] P. Pahuja, C. Prakash, R. Tandon, Comparative study of magnetoelectric composite system $\text{Ba}_{0.95}\text{Sr}_{0.05}\text{TiO}_3 - \text{Ni}_{0.8}\text{Co}_{0.2}\text{Fe}_2\text{O}_4$ with ferrite prepared by different methods, *Ceram. Int.* 40 (2014) 5731–5743.
- [11] I. MacLaren, C. Ponton, A TEM and HREM study of particle formation during barium titanate synthesis in aqueous solution, *J. Eur. Ceram. Soc.* 20 (2000) 1267–1275.
- [12] Q.M. Zhang, H. Wang, N. Kim, L.E. Cross, Direct evaluation of domain-wall and intrinsic contributions to the dielectric and piezoelectric response and their temperature dependence on lead zirconate-titanate ceramics, *J. Appl. Phys.* 75 (1994) 454–459.
- [13] G. Arlt, N.A. Pertsev, Force constant and effective mass of 90° domain walls in ferroelectric ceramics, *J. Appl. Phys.* 70 (1991) 2283–2289.
- [14] P. Zheng, J. Zhang, Y. Tan, C. Wang, Grain-size effects on dielectric and piezoelectric properties of poled BaTiO_3 ceramics, *Acta Mater.* 60 (2012) 5022–5030.
- [15] C.A. Randall, N. Kim, J.P. Kucera, W. Cao, T.R. Shrout, Intrinsic and extrinsic size effects in fine-grained morphotropic-phase-boundary lead zirconate titanate ceramics, *J. Am. Ceram. Soc.* 81 (1998) 677–688.
- [16] T.M. Kamel, G. de With, Grain size effect on the poling of soft $\text{Pb}(\text{Zr},\text{Ti})\text{O}_3$ ferroelectric ceramics, *J. Eur. Ceram. Soc.* 28 (2008) 851–861.
- [17] A. Herabut, A. Safari, Processing and electromechanical properties of $(\text{Bi}_{0.5}\text{Na}_{0.5})_{(1-1.5x)}\text{La}_x\text{TiO}_3$ ceramics, *J. Am. Ceram. Soc.* 80 (1997) 2954–2958.
- [18] S. Sarraute, O.T. Sørensen, B.F. Sørensen, E.R. Hansen, Microstructure dependent thermophysical properties of Ni–Zn ferrite– BaTiO_3 functionally graded ceramics, *J. Mater. Sci.* 34 (1999) 99–104.
- [19] J. Coey, M. Viret, S.Von Molnar, Mixed-valence manganites, *Adv. Phys.* 58 (2009) 571–697.
- [20] Z.M. Dang, Y.H. Lin, C.W. Nan, Novel ferroelectric polymer composites with high dielectric constants, *Adv. Mater.* 15 (2003) 1625–1629.
- [21] I. Gul, W. Ahmed, A. Maqsood, Electrical and magnetic characterization of nanocrystalline Ni–Zn ferrite synthesis by co-precipitation route, *J. Magn. Magn. Mater.* 320 (2008) 270–275.
- [22] R. Valenzuela, *Magnetic Ceramics*, Cambridge University Press, 2005.
- [23] S.S. Chougule, B.K. Chougule, Response of dielectric behavior and magnetoelectric effect in ferroelectric rich (x) $\text{Ni}_{0.9}\text{Zn}_{0.1}\text{Fe}_2\text{O}_4 + (1-x)$ PZT ME composites, *J. Alloys Compd.* 456 (2008) 441–446.
- [24] R. Grigalaitis, M.V. Petrović, J. Bobić, A. Dzunuzovic, R. Sobiestianskas, A. Brilingas, B. Stojanović, J. Banys, Dielectric and magnetic properties of $\text{BaTiO}_3 - \text{NiFe}_2\text{O}_4$ multiferroic composites, *Ceram. Int.* 40 (2014) 6165–6170.
- [25] M. Wei, J. Zhang, M. Zhang, Z. Yao, H. Chen, C. Yang, Relaxor behavior of $\text{BaTiO}_3 - \text{BiVO}_3$ perovskite materials for high energy density capacitors, *Ceram. Int.* (2016).
- [26] O. Bidault, P. Goux, M. Kchikech, M. Belkaoui, M. Maglione, Space-charge relaxation in perovskites, *Phys. Rev. B: Condens. Matter* 49 (1994) 7868.
- [27] J. Macutkevicius, J. Banys, R. Grigalaitis, Y. Vysochanskii, Asymmetric phase diagram of mixed $\text{CuInP}_2(\text{S}_x\text{Se}_{1-x})_6$ crystals, *Phys. Rev. B: Condens. Matter* 78 (2008) 064101.
- [28] Z. Yu, C. Ang, P. Vilarinho, P. Mantas, J. Baptista, Dielectric properties of Bi doped SrTiO_3 ceramics in the temperature range 500–800 K, *J. Appl. Phys.* 83 (1998) 4874–4877.
- [29] M. George, S.S. Nair, K. Malini, P. Joy, M. Anantharaman, Finite size effects on the electrical properties of sol–gel synthesized CoFe_2O_4 powders: deviation from Maxwell–Wagner theory and evidence of surface polarization effects, *J. Phys. D: Appl. Phys.* 40 (2007) 1593.
- [30] R. Sharma, P. Pahuja, R.P. Tandon, Structural, dielectric, ferromagnetic, ferroelectric and ac conductivity studies of the $\text{BaTiO}_3 - \text{CoFe}_{1.8}\text{Zn}_{0.2}\text{O}_4$ multiferroic particulate composites, *Ceram. Int.* 40 (2014) 9027–9036.
- [31] K. Patankar, S. Joshi, B. Chougule, Dielectric behaviour in magnetoelectric composites, *Phys. Lett. A* 346 (2005) 337–341.
- [32] A. Gupta, R. Chatterjee, Dielectric and magnetoelectric properties of $\text{BaTiO}_3 - \text{Co}_{0.6}\text{Zn}_{0.4}\text{Fe}_{1.7}\text{Mn}_{0.3}\text{O}_4$ composite, *J. Eur. Ceram. Soc.* 33 (2013) 1017–1022.
- [33] P.A. Jha, P.K. Jha, A. Jha, R. Dwivedi, Dielectric behavior of $(1-x)\text{BaZr}_{0.025}\text{Ti}_{0.975}\text{O}_3 - (x)\text{BiFeO}_3$ solid solutions, *Mater. Res. Bull.* 48 (2013) 101–105.
- [34] X. Wang, Y. Zhang, X. Song, Z. Yuan, T. Ma, Q. Zhang, C. Deng, T. Liang, Glass additive in barium titanate ceramics and its influence on electrical breakdown strength in relation with energy storage properties, *J. Eur. Ceram. Soc.* 32 (2012) 559–567.
- [35] W. Lei, Y.-Y. Yan, X.-H. Wang, W. Lu, Z.-B. Yang, W.-Z. Lu, Improving the breakdown strength of $(\text{Mg}_{0.9}\text{Zn}_{0.1})_2(\text{Ti}_{1-x}\text{Mn}_x)\text{O}_4$ ceramics with low dielectric loss, *Ceram. Int.* 41 (2015) 521–525.
- [36] M.A. Basith, A. Billah, M.A. Jalil, N. Yesmin, M.A. Sakib, E.K. Ashik, S.M.E. Hoque Yousuf, S.S. Chowdhury, M.S. Hossain, S.H. Firoz, B. Ahmmad, The 10% Gd and Ti co-doped BiFeO_3 : A promising multiferroic material, *J. Alloys Compd.* 694 (2017) 792–799.
- [37] M. Guo, W. Liu, X. Xu, P. Wu, H. Zhang, Y. Han, G. Rao, S. Wang, The effect of Fe–O–Fe bond angle on modulating multiferroic properties of Ba–K-codoped BiFeO_3 nanoparticles, *J. Nanopart. Res.* 17 (2015) 460.
- [38] A. Sathya Priya, I.B. Shameem Banu, S. Anwar, Investigation of multiferroic properties of doped $\text{BiFeO}_3 - \text{BaTiO}_3$ composite ceramics, *Mater. Lett.* 142 (2015) 42–44.
- [39] T. Woldu, B. Raneesh, B.K. Hazra, S. Srinath, P. Saravanan, M.V.R. Reddy, N. Kalarikkal, A comparative study on structural, dielectric and multiferroic properties of $\text{CaFe}_2\text{O}_4/\text{BaTiO}_3$ core-shell and mixed composites, *J. Alloys Compd.* 691 (2017) 644–652.
- [40] S. Su, R. Zuo, S. Lu, Z. Xu, X. Wang, L. Li, Poling dependence and stability of piezoelectric properties of $\text{Ba}(\text{Zr}_{0.2}\text{Ti}_{0.8})\text{O}_3 - (\text{Ba}_{0.7}\text{Ca}_{0.3})\text{TiO}_3$ ceramics with huge piezoelectric coefficients, *Curr. Appl. Phys.* 11 (2011) S120–S123.
- [41] J. Wu, D. Xiao, W. Wu, Q. Chen, J. Zhu, Z. Yang, J. Wang, Composition and poling condition-induced electrical behavior of $(\text{Ba}_{0.85}\text{Ca}_{0.15})(\text{Ti}_{1-x}\text{Zr}_x)\text{O}_3$ lead-free piezoelectric ceramics, *J. Eur. Ceram. Soc.* 32 (2012) 891–898.
- [42] C.-M. Weng, C.-C. Tsai, J. Sheen, C.-S. Hong, S.-Y. Chu, Z.-Y. Chen, H.-H. Su, Low-temperature-sintered CuF_2 -doped NKN ceramics with excellent piezoelectric and dielectric properties, *J. Alloys Compd.* 698 (2017) 1028–1037.
- [43] W. Choi, K. Choi, G. Yang, J.C. Kim, C. Yu, Improving piezoelectric performance of lead-free polymer composites with high aspect ratio BaTiO_3 nanowires, *Polym. Test.* 53 (2016) 143–148.
- [44] X. Chen, Y. Wang, F. He, H. Zhou, L. Fang, L. Liu, Effects of $\text{Bi}(\text{Zn}_{0.5}\text{Zr}_{0.5})\text{O}_3$ addition on the structure and electric properties of BaTiO_3 lead-free piezoelectric ceramics, *Ceram. Int.* 39 (2013) 3747–3751.

Source Material Assessment of Heterojunction DG-TFET for Improved Analog Performance

Jaya Madan¹ Skanda Shekhar² and Rishu Chaujar³

Microelectronics Research Lab, Department of Engineering Physics,
Delhi Technological University, Bawana Road, Delhi-110042, India
jayamadan.2012@gmail.com¹ skanda.shekhar15@gmail.com² and rishu.phy@dce.edu³

Abstract— In this work, the viability of different materials as the source region of a Double-Gate Tunnel FET (DG-TFETs) has been studied. The study essentially focuses on obtaining superior current switching ratio (I_{ON}/I_{OFF}), threshold voltage (V_{th}) and subthreshold swing (SS) in DG-TFETs. In this regard, a comparative analysis of electrical and analog parameters of DG-TFETs with Silicon (Si), Germanium (Ge) and Indium-Arsenide (InAs) sources has been carried out. Choice of materials has been made in such a way as to study the effects of both, elemental semiconductors from the 14th group and binary compounds of elements from the 13th and 15th groups of the periodic table respectively. Such a change in the source material allows for the creation of a heterojunction at the source-channel interface, which significantly modifies the band bending in the device on application of gate bias. Using numerical simulation techniques based on the Non-local Band-to-Band Tunneling (BTBT) model, the strong correlation between the properties of the source and the characteristics of the device is examined. While both Ge and InAs source DG-TFETs show significant improvement over standard Si source DG-TFETs, it is assessed that Ge clearly outperforms InAs as a preferable source material.

Keywords—Band to band tunneling, Heterojunction, Source material, Silicon, Germanium, Indium-Arsenide, tunnel FET.

I. INTRODUCTION

The need for faster and more energy efficient computing devices has been a constant motivation for scaling MOSFETs down. While such scaling down of MOSFETs to obtain devices with increasingly impressive device characteristics has been extremely successful, an impasse seems to have been hit in this respect over the past few decades. This is primarily a result of the short channel effects that emerge due the fundamental physics governing the operation of MOSFETs. These effects lead to major difficulties while implementing low-standby power MOSFET devices [1, 2]. Another problem with MOSFETs, and concomitantly the CMOS architecture, is the limitation of SS of the device to a minimum of 60 mV/decade. Since this limitation is fundamental in nature in that it is a consequence of the mechanism of majority carrier injection into the channel of MOSFET, it becomes difficult, if not impossible, to overcome it. Thermal injection is the primary mechanism of majority carrier injection into the channel of MOSFET from the source and this limitation arises as a direct consequence of the Fermi-Dirac statistics that governs majority carrier distribution. Reduction of SS of the device below this fundamental limit becomes imperative for improved switching action of the transistor [3, 4].

These limitations have inspired researchers to explore other paradigms of transistor construction that differ from MOSFETs in the fundamental mechanism of carrier injection, and yet preserve the qualities that make MOSFETs successful candidates in the first place [5, 6]. Another important factor that must be taken into account is the compatibility of the device under consideration with the existing CMOS architecture [7]. A promising candidate in this regard is the Tunnel Field Effect Transistor (TFET). A TFET is a gated p-i-n junction that is operated in reverse bias [8-10]. Majority carriers are injected from the source to the channel through quantum mechanical Band-to-Band Tunneling (BTBT) which is a result of finite, but non-zero, probability of tunneling through a potential barrier. This lifts the aforementioned fundamental limitation of a minimum SS of 60 mV/decade, allowing TFETs to have SS as low as 20 mV/decade [11].

Here, the effects of variation in the material of the source to Germanium and Indium-Arsenide as opposed to the standard TFET design with a Silicon source have been studied. The channel and drain are made of Silicon in all three cases. This creates a heterojunction at the source-channel interface which is responsible for improved device characteristics as also reported earlier [12, 13]. Additionally, the improvement in the switching performance of the device on changing the work function (Φ) of gate electrode has also been demonstrated. This optimization leads to lower V_{th} and SS with a manageable tradeoff in the I_{OFF} and I_{ON} for optimum current switching ratio.

II. DEVICE STRUCTURE AND ITS DESCRIPTION

Fig. 1 shows the two-dimensional view of the device under consideration i.e. DG-TFET. In this work, a standard DG-TFET with three semiconductor regions: the source, the channel and the drain is considered. A second gate offers better gate controllability and thereby allows higher drive current and lower OFF-state current [14]. A p+ (n+) source (drain) with a length and width of 20 nm and 10 nm respectively has been considered. The uniform source (drain) doping is maintained at 10^{20} (5×10^{18}) /cm³. The source material is changed from Si to Ge and InAs respectively in order to assess the feasibility of each material as the source, which is the principal study of this investigation. The channel is made of lightly p-doped Si with a dopant concentration of 10^{15} /cm³. The channel length and width are 50 nm and 10 nm respectively. While investigating the impact of change of

source material from Si to Ge and InAs respectively, other source parameters such as the doping, the length and the width are kept constant. All device parameters have been chosen and are carefully controlled to obtain optimum device performance. This investigation has been performed on Technology Computer Aided Design (TCAD) using ATLAS developed by Silvaco [15].

The simulation environment of ATLAS requires the application of certain mathematical models in order to obtain results that are consistent and can be calibrated with experimental devices. Since the primary mechanism of carrier injection in TFETs is BTBT, it becomes imperative to use models of the phenomenon that are closest to the actual barrier that an electron moving from the source to the channel tunnels through. In this regard, there are two possible alternatives. The first is the Kane model that was developed independently by Kane and Keldysh. Although Keldysh obtained his expression for tunneling probability a year before Kane, Kane's derivation of the expression is considered to be more mathematically rigorous [16]. This model approximates the potential barrier at the source channel interface as a triangular potential barrier. While this model has been widely used in earlier literature in this domain, this approximation can be done away with while using more modern simulators on faster computers. Therefore, here the second alternative, namely the non-local BTBT model, is used in consonance with the Band Gap Narrowing model to simulate BTBT. Non-local BTBT model accounts for the dynamic change in the barrier width at every point in the source-channel interface. Since this is the true physical nature of the potential barrier faced by the electron at the interface, this model provides exceptionally accurate simulation results. In addition, the recombination model used is the Shockley-Read-Hall (SRH) recombination model which accounts for the recombination of majority and minority charge carriers in the device. To account for the heavy doping in the source and the drain, the majority charge carrier distribution is simulated using the Fermi-Dirac statistical model. The simulator solves Poisson and carrier continuity equations in order to simulate the drift and diffusion of charge carriers through the device under the mobility model. All simulations have been performed at an absolute temperature of 300 K and only abrupt junctions have been taken into consideration. At the temperature at which the simulation is performed (300K), Si and Ge are indirect bandgap materials while InAs is a direct bandgap material. By implication, the only material capable of undergoing radiative recombination at 300 K is InAs. However, the high dopant concentration in the source explains the exclusion of any radiative recombination model in the simulation environment as the number of radiative recombination events remains fairly low.

III. RESULT AND DISCUSSION

Fig. 2(a) and 2(b) show the energy band profile of the heterojunction DG-TFET for Si, Ge and InAs sources respectively. Fig. 2(a) shows the profile in the OFF- state @ $V_{gs} = 0.0$ V and $V_{ds} = 1.0$ V while Fig. 2(b) shows the profile in the ON- state @ $V_{gs} = 1.2$ V and $V_{ds} = 1.0$ V. The inset of Fig. 2(b) shows the magnified view of energy band profile at the tunneling junction. It is observed that there is a

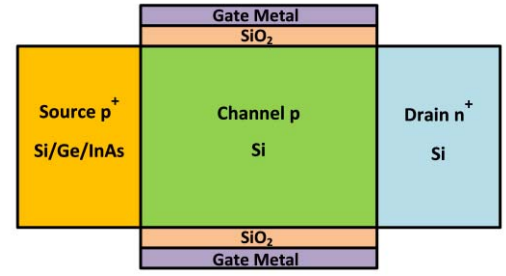


Fig. 1: Schematic 2D view of the DG-TFET under consideration.

distinct modification in the energy bands for Ge and InAs at the source w.r.t Si due to the creation of the heterojunctions. At $V_{gs} = 0.0$ V, the Fermi levels in all three regions are aligned and the energy gap at the source corresponds to that of Si (1.1 eV), Ge (0.67 eV) and InAs (0.36 eV) respectively in the three cases. On application of gate bias, steep bending of bands due to displacement of the Fermi level by the applied potential is observed. Since the potential is applied to the channel alone, a drop in the Fermi level of the channel is observed that causes lowering of the barrier width at the tunnelling junction around the source-channel interface. In this respect, maximum band bending is observed with the Ge source followed by InAs and Si sources respectively. A thought-provoking observation is the presence of a kink in the conduction band of InAs source DG-TFET in both OFF and ON- state. This kink appears as a result of the difference in electron affinities of InAs and Si at the heterojunction. This is indeed the reason behind lower band bending (or higher tunnelling barrier width) in the case of the InAs source DG-TFET even though the bandgap of InAs (0.36 eV) is lower than Ge (0.67 eV). Fig. 3 shows the variation of Non-local BTBT rate of electrons with distance along the channel.

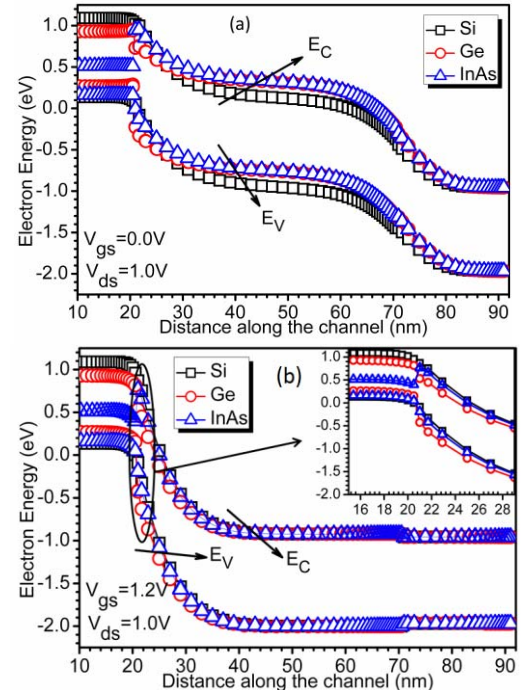


Fig. 2: Energy band profile along the channel for Si, Ge and InAs source DG-TFETs at (a) $V_{gs} = 0.0$ V and $V_{ds} = 1.0$ V (OFF-state) and (b) $V_{gs} = 1.2$ V and $V_{ds} = 1.0$ V (ON-state).

Tunneling of electrons occurs at the source-channel interface due to lowering of the barrier width around the junction. Maximum electron tunneling is observed for the Ge source followed by InAs and Si sources. Quantitatively, the order of magnitude change in the Non-local BTBT rate of electrons is from 10^{27} /cm³s for Si to 10^{29} /cm³s for Ge. However, the tunneling rate in the InAs source DG-TFET is 3.33 times that of the Si source DG-TFET.

Fig. 4 shows a plot of the electric field with the distance along the channel for Si, Ge and InAs sources in the ON and OFF states respectively. The observed variation of electric field is a combined consequence built-up electric field at the interfaces in the device and the potential applied to the drain w.r.t the source. In the OFF-state, the built-up electric field at each interface is a result of the equilibrium of drift and diffusion processes on both sides of the junction. On application of gate bias, this equilibrium is disturbed leading to an overall change in the electric field. Since all equilibrium and non-equilibrium phenomena (like drift and diffusion) in semiconductors are dependent on material properties such as the effective masses of electrons and holes, the electric field changes with change in source material of the DG-TFET.

Since the material of only the source is changed, a variation is seen only in the first peak of the electric field curve. In the ON-state, the electric field peaks further at the source-channel junction while it falls to negligible values at the channel-drain interface. This increase in the electric field at the source-channel interface is responsible for an increase in the electron tunneling probability through the junction. By implication, carriers moving from the channel to the drain face

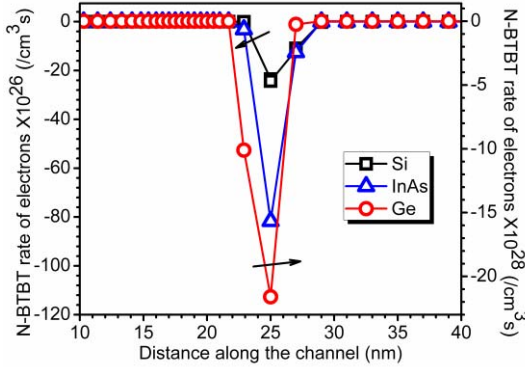


Fig. 3: Rate of Non-local BTBT along the channel for Si, Ge and InAs source DG-TFETs at $V_{gs} = 1.2$ V and $V_{ds} = 1.0$ V.

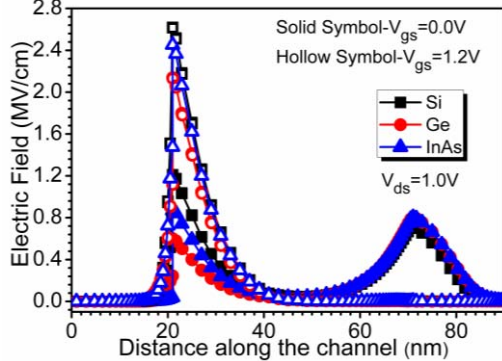


Fig. 4: Variation of electric field with distance along channel for Si, Ge and InAs source DG-TFETs at $V_{gs} = 0.0$ V and $V_{gs} = 1.2$ V.

little resistance therefore contributing to drive current. Here again, maximum electric field at the tunneling junction is obtained for Ge followed by InAs and Si respectively. This leads to maximum tunneling probability in the case of Ge followed by InAs and Si respectively.

Fig. 5 shows the variation of drive current (I_{ds}) with gate voltage (V_{gs}) at constant $V_{ds} = 1.0$ V. The tunneling junction width (L_{BW}) is an important factor determining the tunneling probability. It is observed that maximum drive current is obtained when L_{BW} is minimum i.e. for the Ge source DG-TFET. Moreover, consistent with previous results in this work, the Ge source DG-TFET has highest drive current followed by the InAs and Si source DG-TFETs. The tunneling probability, however, is a result of the interplay of a variety of material properties. Interestingly, the drive current of InAs source DG-TFET is lower than that of the Ge source DG-TFET although the energy bandgap of InAs is lower than that of Ge. This is attributed to the lower L_{BW} for the Ge source DG-TFET than for the InAs source DG-TFET owing to the difference in electron affinities of InAs and Ge in comparison with Si. Therefore, the drive current of DG-TFET depends not only on the bandgap of source material, but also on the properties of the entire heterojunction. These results indicate that a substantial improvement in the drive current of a DG-TFET is observed by changing the material properties of the source. A detour was taken to examine the transfer characteristics of DG-TFET for different work function (Φ) of gate electrode. The motivation behind this detour was to examine the optimization of DG-TFET. It is observed that changing the Φ of the gate metal results in a lateral shift in the I_{ds} - V_{gs} curves for all three source materials.

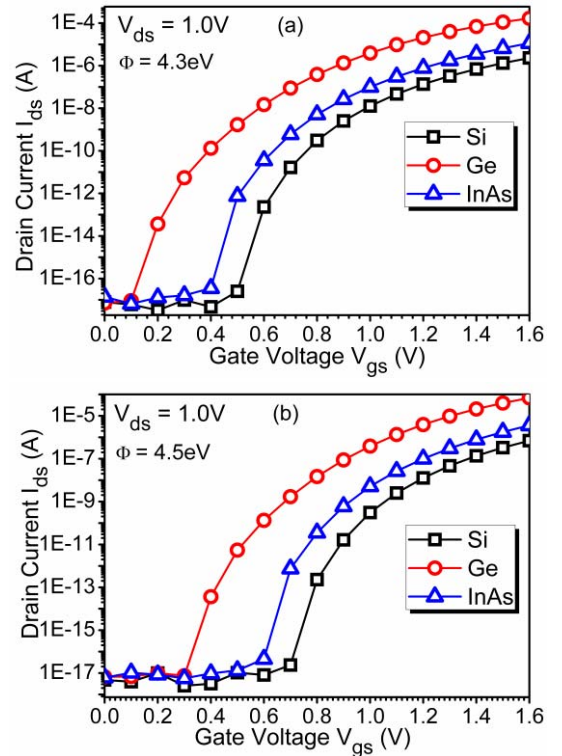


Fig. 5: Influence of gate work function on transfer characteristics of Si, Ge and InAs source DG-TFETs for (a) $\Phi = 4.3$ eV and (b) $\Phi = 4.5$ eV.

This is due to the change in the flatband voltage (V_{fb}) with a change in the Φ of gate electrode. The effective gate voltage i.e. ($V_{gs} - V_{fb}$) is enhanced for lower metal Φ of gate electrodes. Therefore, better transfer characteristics are observed for $\Phi = 4.3$ eV in comparison with $\Phi = 4.5$ eV. Furthermore, the influence of the gate Φ on the current switching ratio (I_{ON}/I_{OFF}) for Si, InAs and Ge source DG-TFETs respectively is shown in Fig. 6. I_{ON}/I_{OFF} is higher with $\Phi = 4.3$ eV as compared to that of 4.5 eV which is attributed to early switching ON of the device for $\Phi = 4.3$ eV. Further, I_{ON}/I_{OFF} is highest for Ge followed by InAs and Si respectively. This is due to the highest drive current for Ge source DG-TFET followed by InAs and Si source DG-TFETs respectively for both values of Φ . Quantitatively, a fivefold enhancement in I_{ON}/I_{OFF} is observed for $\Phi = 4.3$ eV as compared to $\Phi = 4.5$ eV for the Ge source DG-TFET. Additionally, the order of magnitude I_{ON}/I_{OFF} increases from 10^{10} to 10^{12} for the Ge source DG-TFET as compared to the Si source DG-TFET.

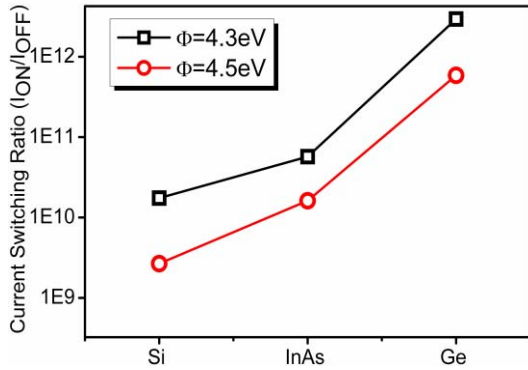


Fig. 6: Influence of gate work function on I_{ON}/I_{OFF} of Si, Ge and InAs source DG-TFETs.

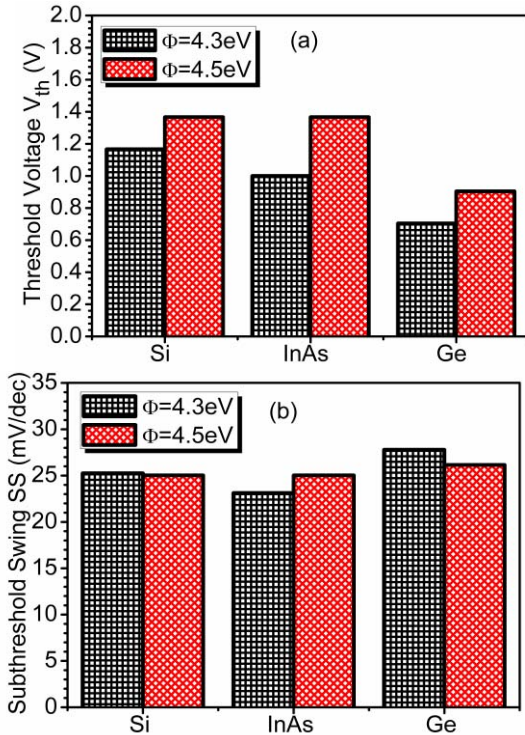


Fig. 7: Influence of gate work function of Si, InAs and Ge source DG-TFETs on (a) V_{th} and (b) SS.

V_{th} is an important parameter that is essential for low power applications. Fig. 7 indicates the impact of Φ on the V_{th} and SS for Si, InAs and Ge source DG-TFETs respectively. The constant current method i.e. $V_{gs} @ I_{ds} = 10^{-7}$ A is used for V_{th} calculation. For all three materials, V_{th} is lower for $\Phi = 4.3$ eV in comparison with $\Phi = 4.5$ eV. Among the three materials under consideration, the Ge source DG-TFET shows the lowest V_{th} followed by the InAs and Si source DG-TFETs respectively. Another important performance parameter of a transistor is SS. A low SS is desirable for fast switching characteristics. The use of a lower Φ does not lead to an enhancement in SS as observed for all other electrical parameters in this investigation. There is a small degradation in SS in the case of Si and Ge source DG-TFETs when a gate with $\Phi = 4.3$ eV is used. However, in the case of the InAs source DG-TFET there is a small improvement in SS when a gate with lower Φ is used. The InAs source DG-TFET has the most favorable SS followed by the Si and Ge source DG-TFETs respectively.

IV. CONCLUSION

In this work, the effects of the source material on the electrical parameters of a DG-TFET have been probed. A strong correlation between the electrical characteristics of the DG-TFET under consideration and the material of the source has been observed. Among the three candidates considered, the Ge source DG-TFET shows highest drive current and superior I_{ON}/I_{OFF} followed by InAs and Si source DG-TFETs respectively. These results make the Ge source DG-TFET an attractive contender for use as transistors in computer chips. A higher drive current implies more current per unit area of the chip and a concomitant ease in scaling the device down with only a negligible performance trade-off. Additionally, the low V_{th} of the Ge source DG-TFET makes it ideal for low power applications. This possibility must be explored further so as to harness the true power of the TFET as a low power, high speed transistor.

ACKNOWLEDGMENT

The authors would like to thank the Microelectronics Research Lab, Department of Engineering Physics, Delhi Technological University (formerly DCE) and one of the authors (Jaya Madan) is grateful to the University Grant Commission (UGC) for providing the necessary financial assistance to carry out this research work.

REFERENCES

- [1] K. Boucart and A. M. Ionescu, "Length scaling of the double gate tunnel FET with a high-k gate dielectric," *Solid-State Electronics*, vol. 51, pp. 1500-1507, 2007.
- [2] W. Y. Choi, B.-G. Park, J. D. Lee, and T.-J. K. Liu, "Tunneling field-effect transistors (TFETs) with subthreshold swing (SS) less than 60 mV/dec," *IEEE Electron Device Letters*, vol. 28, pp. 743-745, 2007.
- [3] K. K. Bhuvalka, J. Schulze, and I. Eisele, "Scaling the vertical tunnel FET with tunnel bandgap modulation and gate workfunction engineering," *IEEE transactions on electron devices*, vol. 52, pp. 909-917, 2005.
- [4] A. Biswas, S. S. Dan, C. Le Royer, W. Grabinski, and A. M. Ionescu, "TCAD simulation of SOI TFETs and calibration of non-local band-to-band tunneling model," *Microelectronic Engineering*, vol. 98, pp. 334-337, 2012.

- [5] A. M. Ionescu and H. Riel, "Tunnel field-effect transistors as energy-efficient electronic switches," *Nature*, vol. 479, pp. 329-337, 2011.
- [6] J. Madan and R. Chaujar, "Temperature Associated Reliability Issues of Heterogeneous Gate Dielectric - Gate All Around - Tunnel FET," *IEEE Transactions on Nanotechnology*, 2017.
- [7] R. Gandhi, Z. Chen, N. Singh, K. Banerjee, and S. Lee, "CMOS-Compatible Vertical-Silicon-Nanowire Gate-All-Around p-Type Tunneling FETs With-mV/decade Subthreshold Swing," *IEEE Electron Device Letters*, vol. 32, pp. 1504-1506, 2011.
- [8] J. Madan and R. Chaujar, "Interfacial Charge Analysis of Heterogeneous Gate Dielectric-Gate All Around-Tunnel FET for Improved Device Reliability," *IEEE Transactions on Device and Materials Reliability*, vol. 16, pp. 227-234, 2016.
- [9] J. Madan and R. Chaujar, "Gate Drain Underlapped-PNIN-GAA-TFET for Comprehensively Upgraded Analog/RF Performance," *Superlattices and Microstructures*, vol. 102, pp. 17-26, 2// 2017.
- [10] J. Madan and R. Chaujar, "Numerical Simulation of N⁺ Source Pocket PIN-GAA-Tunnel FET: Impact of Interface Trap Charges and Temperature," *IEEE Transactions on Electron Devices*, vol. 64, pp. 1482-1488, 2017.
- [11] Y. Khatami and K. Banerjee, "Steep subthreshold slope n-and p-type tunnel-FET devices for low-power and energy-efficient digital circuits," *IEEE Transactions on Electron Devices*, vol. 56, pp. 2752-2761, 2009.
- [12] A. N. Hanna, H. M. Fahad, and M. M. Hussain, "InAs/Si hetero-junction nanotube tunnel transistors," *Scientific reports*, vol. 5, p. 9843, 2015.
- [13] C.-H. Shih and N. D. Chien, "Sub-10-nm tunnel field-effect transistor with graded Si/Ge heterojunction," *IEEE Electron Device Letters*, vol. 32, pp. 1498-1500, 2011.
- [14] K. Boucart and A. M. Ionescu, "Double-Gate Tunnel FET With High-k Gate Dielectric," *IEEE Transactions on Electron Devices*, vol. 54, pp. 1725-1733, 2007.
- [15] A. U. s. Manual, "Silvaco," *Santa Clara, CA*, 2010.
- [16] S. A. Mookerjee, "Band-to-band tunneling field effect transistor for low power logic and memory applications: Design, fabrication and characterization," Citeseer, 2010.

Stability Analysis of Job Shop Problem

Nilam Rathi

Department of Applied Mathematics, Delhi technological University Delhi, India

ABSTRACT

The job-shop problem (JSP) is an optimization technique, in which ideal jobs are assigned to resources at particular times. Practical view of deterministic scheduling process is not valid for every process in practice. In present study, stability analysis has been performed and to test the suitable techniques of optimization which will be applicable for job-shop problem also discussed how parametric relation are affected for two jobs. Comparative study of some existing techniques with present study is also discussed in this paper.

Keyword - Comparative study, Job-shop problem, Optimization, Parametric- relation, Stability analysis

I INTRODUCTION

The problem under consideration is to minimize the value of the given desired function of completion times of n jobs $J = \{1, 2, \dots, n\}$ processed on m machines $N = \{1, 2, \dots, m\}$. First, we assume that processing time $t_{j,k}$ of job $j \in J$ on machine $k \in N$ (i.e., processing time of operation $O_{j,k}$) is known before scheduling.

Operation preemptions are not allowed. This problem is denoted as $J||\varphi$ where φ desired objective function. Let $C_{i,k}$ denote the completion time of the job in position i on machine $k \in N$. We assume that desired function $\varphi(C_{1,m}, C_{2,m}, \dots, C_{n,m})$ is non-decreasing function of job completion times. Such a criterion is called regular.

For the job-shop problem $J|n=1|C_{\max}$ with two jobs and make span desired function $C_{\max} = \max\{C_{1,m}, C_{2,m}, \dots, C_{n,m}\}$, the geometric algorithm was proposed by Akers and Friedman [1] and developed by Brucker [2], Szwarc [7], Hardgrave and Nemhauser [4]. Sotskov [5] generalized the geometric algorithm for the problem $J|n=1|\varphi$ with any given regular criterion. Sotskov [6] proven that both problems:

$$J|n=1|C_{\max} \text{ and } J|n=2|\Sigma C_{i,m} \quad (1)$$

are binary NP-hard. Hereafter, the criterion $\Sigma C_{i,m}$ means minimization of total completion time

$$\sum_{i=1}^n C_{i,m} \quad 2. 2.$$

II METHODOLOGY

Describing geometric model for the case of a flow-shop problem $J|n=1|\varphi$, i.e., when all n jobs have the same technological through m machines, namely, $(1, 2, \dots, m)$.

Let $TM_{j,k}$ denote the sum of the processing times of job $j \in J = \{1, 2\}$ on a subset of k machines $\{1, 2, \dots, k\} \subseteq N$:

$$TM_{j,k} = \sum_{i=1}^k t_{j,i} \quad 1 \leq k \leq m \quad (3)$$

Assuming that $TM_{1,0} = TM_{2,0} = 0$. Introducing a coordinate system xy on the plane, and draw the rectangle with corners $(0, 0)$, $(TM_{1,m}, 0)$, $(0, TM_{2,m})$ and $(TM_{1,m}, TM_{2,m})$. In the rectangle, we draw m rectangles H_k , $k \in \{1, 2, \dots, m\}$, with corners $(TM_{1,k-1}, TM_{2,k-1})$, $(TM_{1,k}, TM_{2,k-1})$, $(TM_{1,k-1}, TM_{2,k})$, $(TM_{1,k}, TM_{2,k})$.

South-west corner $(TM_{1,k-1}, TM_{2,k-1})$ of the rectangle H_k as SW_k , north-west corner $(TM_{1,k-1}, TM_{2,k})$ as NW_k , south east corner $(TM_{1,k}, TM_{2,k-1})$ as SE_k , and north-east corner $(TM_{1,k}, TM_{2,k})$ as NE_k . Obviously, point $(0, 0)$ is SW_1 and point $(TM_{1,m}, TM_{2,m})$ is NE_m .

Using Chebyshev's metric, i.e., the length $d[(x, y), (x', y')]$ of a segment $[(x, y), (x', y')]$ connecting points (x, y) and (x', y') in the rectangle H is calculated as follows:

$$D[(x, y), (x', y')] = \max \{|x - x'|, |y - y'|\}. \quad (4)$$

The length $D[(x_1, y_1), (x_2, y_2), \dots, (x_r, y_r)]$ of a continuous polygonal line $[(x_1, y_1), (x_2, y_2), \dots, (x_r, y_r)]$ is equal to the sum of the lengths of its segments. Since $\varphi(C_{1,m}, C_{2,m})$ is a increasing function, the search for the optimal schedule can be restricted to set S of schedules in which at any time of the interval $[0, \max\{C_{1,m}, C_{2,m}\}]$ at least one job is processed. A schedule from set S can be suitably represented within the rectangle H on the plane xy as a trajectory (Continuous polygonal line) $\tau = [SW_1, (x_1, y_1), (x_2, y_2), \dots, (x_r, y_r), NE_m]$ where either $x_r = TM_{1,m}$ or $y_r = TM_{2,m}$. Let a point (x, y) belong to the trajectory τ and let d be the length of the part of trajectory τ from the point SW_1 to the point (x, y) . The coordinate x (coordinate y) of point (x, y) defines the state of processing job 1 (job 2) as follows.

If $SW_u \leq x \leq SE_u$ and $SW_v \leq y \leq NW_v$, $u \in M$, $v \in M$, then job 1 (job 2) is completed on the machines $1, 2, \dots, u-1$ (on the machines $1, 2, \dots, v-1$) at time d . Moreover at time d , job 1 (job 2) has been processed on machine u (machine v) during $x - SW_u$ (during $y - SW_v$) time units.

Since a machine cannot process more than one job at a time and operation preemptions are not allowed, each straight segment $[(x, y), (x', y')]$ of a trajectory τ may be either

- Horizontal (when only job 1 is processed) or
- Vertical (when only job 2 is processed) or
- Diagonal with slope of 450 (when both jobs are processed simultaneously).

International Conference on Computational and Experimental Methods in Mechanical Engineering

G.L. Bajaj Institute of Technology and Management, Greater Noida (U.P) India

ICCEMME-2017

8th-9th December 2017, www.conferenceworld.in

ISBN: 978-93-86171-85-6

It is clear that a horizontal segment (vertical segment) can only pass along south boundary (west boundary) of the rectangle H_k , $k \in M$, or along north (east) boundary of the rectangle H . The diagonal segment of trajectory τ can only pass either outside rectangle H_k or through point NW_k or point SE_k . Sotskov [5] proven that problem $J|n=1|\Phi$ of finding the optimal schedule or, in other words, of finding the optimal trajectory, can be reduced to the shortest path problem in the digraph (V, A) constructed by the following Algorithm 1. Again for simplicity, we describe this algorithm for the case of a flow-shop problem $F|n=1|\varphi$, when all n jobs have the same technological route through m machines.

Vertex set V of the digraph (V, A) is a subset of set

$$V_0 = \{SW_1, NE_m\} \cup \{NW_k, SE_k : k \in M\} \cup \{(x_k, TM_{2,m}), (TM_{1,m}, y_k) : k \in M\}.$$

III ALGORITHM

1. Set $V = \{SW_1, SE_1, NW_1, NE_m\}$ and $A = \{(SW_1, SE_1), (SW_1, NW_1)\}$.
2. Take vertex $(x, y) \in V \setminus \{NE_m\}$ with zero out degree. If $(x, y) = SE_k$, go to step 3. If $(x, y) = NW_k$, go to step 3.
3. If set $V \setminus \{NE_m\}$ has no vertex with zero out degree.
STOP
4. Draw a diagonal line with slope 450 starting from vertex SE_k until either east boundary $[(TM_{1,m}, 0), NE_m]$ of the rectangle H is reached in some vertex $(TM_{1,m}, y_k)$ or open south boundary (SW_h, SE_h) of the rectangle H_h , $k+1 \leq h \leq m$, is reached. In the former case, set $V := V \cup \{(TM_{1,m}, y_k)\}$ and $A := A \cup \{(SE_k, (TM_{1,m}, y_k)), ((TM_{1,m}, y_k), NE_m)\}$. In the latter case, set $V := V \cup \{SE_h, NW_h\}$ and $A := A \cup \{(SE_k, SE_h), (SE_k, NW_h)\}$. Go to step 2.
5. Draw a diagonal line with slope 450 starting from vertex NW_k until either north boundary $[(0, TM_{2,m}), NE_m]$ of the rectangle H is reached in some vertex $(x_k, TM_{2,m})$ or open west boundary (SW_h, NW_h) of the rectangle H_h , $k+1 \leq h \leq m$, is reached. In the former case, set $V := V \cup \{(x_k, TM_{2,m})\}$ and $A := A \cup \{(NW_k, (x_k, TM_{2,m})), ((x_k, TM_{2,m}), NE_m)\}$. In the latter case, set $V := V \cup \{SE_h, NW_h\}$ and $A := A \cup \{(NW_k, SE_h), (NW_k, NW_h)\}$. Go to step 2.

In order to find the optimal path (i.e., optimal schedule) for the problem $J|n=1|\Phi$ we can use the following Algorithm, where the length of arc $((x, y), (x', y')) \in A$ is assumed to be equal to the length of the polygonal Line constructed by Algorithm with origin in the point (x, y) and with end in the point (x', y') .

International Conference on Computational and Experimental Methods in Mechanical Engineering

G.L. Bajaj Institute of Technology and Management, Greater Noida (U.P) India

ICCEMME-2017

8th - 9th December 2017, www.conferenceworld.in

ISBN: 978-93-86171-85-6

IV STABILITY ANALYSIS

In what follows, we consider stability of an optimal schedule with respect to possible variations of the given vector $t = (t_{1,1}, t_{1,2}, \dots, t_{1,m}, t_{2,1}, t_{2,2}, \dots, t_{2,m})$ of operation processing times.

Let (V_t, A_t) denote the digraph (V, A) constructed by Algorithm 1 for the problem $F|n=2|\varphi$ with vector t of operation processing times. Let P_t be set of all shortest paths from vertex SW1 to the border vertices in the digraph (V_t, A_t) . As follows from Algorithm 1, the same path may belong to sets P_t constructed for different vectors t of operation processing times (since for any vector t we have $V_t \subseteq V_0$). Notation $su(t)$ is used for a schedule defined by path $\tau_u \in P_t$. The objective function value calculated for schedule $su(t)$ is denoted as $\varphi(su(t))$. A schedule is called *active* if none of the operations can start earlier than in this schedule, provided that the remaining operations could start no later. It is known (see Giffler and Thompson [3]) that a set of active schedules is dominant (i.e., it contains at least one optimal schedule) for any regular criterion. The following claim may be proven by induction with respect to number of machines m .

To test whether optimality of the path $\tau_u \in P_t$ is stable takes $O(m \log m)$ time for problem $F|n=1|\Phi$ and $O(m_2 \log m)$ time for problem $J|n=1|\varphi$. Indeed, we can use Algorithm 2 for the vector t of the operation processing times and construct optimal paths with different border vertices. Number of the optimal paths which have to be tested due to theorem is restricted by the number of border vertices asymptotically restricted by $O(m)$ for problem $F|n=1|\varphi$ and by $O(m_2)$ for problem $J|n=1|\varphi$.

It is easy to convince that for the above sufficiency proof of Theorem 2 we can replace increasing function φ by non-decreasing function φ . It should be noted that the most objective functions considered in classical scheduling theory are continuous non-decreasing functions of job completion times, e.g.,

- Make span C_{\max} ,
- Total completion time $\sum_1^n C_{i,m}$
- Maximal lateness $L_{\max} = \max\{C_{i,m} - D_i : i \in J\}$ and
- Total tardiness $= \sum_1^n \max\{0, C_{i,m} - D_i : i \in J\}$ where D_i denotes the given due date for a job i .

And so sufficiency of applicable theorem may be violated in the break points of such a function φ .

REFERENCES

1. S.B. Akers and J. Friedman, A non-numerical approach to production scheduling problems, Operations Research 3, 1955, 429 - 442.
2. P. Brucker, An efficient algorithm for the job-shop problem with two jobs, Computing 40, 1988, 353 - 359.

International Conference on Computational and Experimental Methods in Mechanical Engineering

G.L. Bajaj Institute of Technology and Management, Greater Noida (U.P) India ICCEMME-2017

8th-9th December 2017, www.conferenceworld.in

ISBN: 978-93-86171-85-6

3. B. Giffler and G.L. Thompson, Algorithms for solving production-scheduling problems, Operations Research 8, N 4, 1960, 487 - 503.
4. W.W. Hardgrave and G. Nemhauser, A geometric model and graphical algorithm for a sequencing problem, Operations Research 11, N 6, 1963, 889 - 900.
5. Yu.N. Sotskov, Optimal scheduling two jobs with regular criterion, In: Design Processes Automating, Institute of Engineering Cybernetics, Minsk, 1985, 86 - 95 (in Russian).
6. Yu.N. Sotskov, The complexity of shop-scheduling problems with two or three jobs, European Journal of Operational Research 53, 1991, 326 - 336.
7. W. Szwarc, Solution of the Akers-Friedman scheduling problem, Operations Research 8, 1960, 782 - 788.
8. Yu. N. Sotskov, N. Yu. Sotskova, STABILITY OF AN OPTIMAL SCHEDULE FOR A JOB-SHOP PROBLEM WITH TWO JOBS, International Journal "Information Theories & Applications" Vol.10, pp. 321 - 325.